MINERAL TRAPS FOR GREENHOUSE GASES IN MINE TAILINGS: A PROTOCOL FOR VERIFYING AND QUANTIFYING CO_2 SEQUESTRATION IN ULTRAMAFIC MINES

by

Siobhan Alexandra Wilson

B.Sc. (Honours), McMaster University, 2003
M.Sc., The University of British Columbia, 2005

A THESIS SUBMITTED IN PARTIAL FULFILLMENT OF
THE REQUIREMENTS FOR THE DEGREE OF

DOCTOR OF PHILOSOPHY

in

The Faculty of Graduate Studies

(Geological Sciences)

THE UNIVERSITY OF BRITISH COLUMBIA
(Vancouver)

December 2009

Abstract

Mineralization of CO_2 in ultramafic mine tailings can occur on a scale that is significant relative to the greenhouse gas emissions of a mine. Consequently, some active mining operations may be able to take advantage of carbon mineralization within their tailings to offset part of their greenhouse gas emissions. The secondary Mg-carbonate minerals that form in mine tailings are safe and durable traps for carbon and their presence can represent substantial disposal of atmospheric CO_2. Hydrated Mg-carbonate minerals precipitate within mine tailings from the Diavik Diamond Mine, Northwest Territories, Canada, and the Mount Keith Nickel Mine, Western Australia, Australia. An improved understanding of the carbon cycle in mine tailings, and the contribution of mineralogical and geochemical strategies for assessing carbon mineralization in ultramafic mine tailings, are achieved by studying these sites.

Quantitative mineralogical procedures, which use X-ray powder diffraction data, are developed for quantifying low abundances of mineral traps for CO_2 within mine tailings. Quantitative mineralogical results are used to assess the amount of CO_2 stored within hydrated Mg-carbonate minerals at both mine sites, and to assist in determining which gangue minerals are the primary sources for Mg in these minerals.

Radiocarbon and stable isotopes of carbon and oxygen are used to identify the sources for carbon in secondary Mg-carbonate minerals. Isotopic analogue experiments are used to study the fractionation of stable carbon isotopes during precipitation of dypingite, a hydrated Mg-carbonate mineral, under conditions that simulate those in the tailings storage facilities at Mount Keith. The results of these experiments suggest that hydrated Mg-carbonate minerals may be precipitating out of isotopic equilibrium with the atmosphere. A carbon isotopic fractionation factor obtained for dypingite, and computational models for isotopic mixing scenarios, are used to interpret stable isotope and radiocarbon data for carbonate minerals. Although models for mixing scenarios can provide convincing fits to stable isotopic data, they are commonly inconsistent with field observations, trends in quantitative mineralogical data, and radiocarbon results. Ultimately, radiocarbon data are used to determine that most of the carbon trapped and

stored within hydrated Mg-carbonate minerals at Diavik and Mount Keith is sourced from the modern atmosphere.

Table of Contents

List of Tables

List of Figures

List of Symbols and Abbreviations

A – area

An_{91} – Anorthite-91

apfu – atoms per formula unit

BHPB – BHP Billiton

CHN – Carbon-Hydrogen-Nitrogen

C – elemental concentration

d – Durbin-Watson statistic

d – distance between lattice planes

D – depth

DDMI – Diavik Diamond Mines Inc.

DIC – Dissolved Inorganic Carbon

DOC – Dissolved Organic Carbon

EMP – Electron Microprobe

f – fraction of water remaining in an evaporative system

f_w – fraction of water in a system

f_r – fraction of rock in a system

$F^{14}C$ – Fraction Modern Carbon

Fo_{90} – Forserite-90

FP – Fundamental Parameters

h – relative humidity

ICDD – International Centre for Diffraction Data

ICME – International Council on Metals and the Environment

IPCC – Intergovernmental Panel on Climate Change

IRMS – Isotope Ratio Mass Spectrometer

m or M – mass

MAD – Median Absolute Deviation

MPA – Maximum Potential Acidity

n – molar concentration of an element

NAD – North American Datum

NBS – National Bureau of Standards

NP – Neutralization Potential

p – fraction of carbon from a isotopic reservoir

pfu – per formula unit

PCIGR – Pacific Centre for Isotopic and Geochemical Research

PDF-4+ – Powder Diffraction File, version 4+

PGE – Platinum Group Element

PKC – Processed Kimberlite Containment facility

POM – Particulate Organic Matter

PV – Pseudo-Voigt

Q – water-rock ratio

RIR – Reference Intensity Ratio(s)

R_{wp} – weighted pattern statistic

SEM – Scanning Electron Microscope

SSAMS – Single Stage Accelerator Mass Spectrometer

t – time

T – temperature

TN – Total Nitrogen

TOC – Total Organic Carbon

TSF – Tailings Storage Facility

UNEP – United Nations Environmental Program

VPDB – Vienna Pee Dee Belemnite

VSMOW – Vienna Standard Mean Ocean Water

wt.% – weight percent

WGS – World Geodetic System

X – weight percent abundance of a mineral

XRD – X-Ray Diffraction

XRPD – X-Ray Powder Diffraction

$\alpha_{x\text{-}y}$ – isotopic fractionation factor between substances x and y

$\delta^{13}C$ – delta carbon-13

$\delta^{18}O$ – delta oxygen-18

$\Delta^{13}C_{x\text{-}y}$ – approximately $10^3 \ln\alpha_{x\text{-}y}$ for C

$\Delta^{14}C$ – deviation in ^{14}C composition

$\Delta^{18}O_{x\text{-}y}$ – approximately $10^3 \ln\alpha_{x\text{-}y}$ for O

$\varepsilon_{x\text{-}y}$ – isotopic separation between substances x and y

θ – scattering angle of X-rays

ρ – density

σ – measurement uncertainty

φ – fraction of an element held by water

χ^2 – chi squared statistic

Acknowledgements

This thesis is part of a broader study of CO_2 sequestration within mine tailings, conducted by the Mineral Deposit Research Unit in the Department of Earth and Ocean Sciences, The University of British Columbia, and the Geomicrobiology Group in the Department of Earth Sciences, The University of Western Ontario, London, ON, Canada. This project received funding from the Natural Sciences and Engineering Research Council of Canada (NSERC), Diavik Diamond Mines Inc. (DDMI), and BHP Billiton (BHPB) through a Collaborative Research and Development Grant to Profs. Gregory M. Dipple and Gordon Southam. Further support for this project was provided by a NSERC Discovery Grant to Prof. Mati Raudsepp.

I have been the extremely fortunate recipient of a University Graduate Fellowship from The University of British Columbia, a Foundation Scholarship and a Student Travel/Research Grant from the Mineralogical Association of Canada (MAC), a Grant from the Edward H. Kraus Crystallographic Research Fund from the Mineralogical Society of America (MSA), and an Alexander Graham Bell Canada Graduate Scholarship from NSERC. The generosity of the support that I have received from MAC, MSA, NSERC, and UBC in the past four years still staggers me. Thank you so much for providing me with the opportunity to focus exclusively on my research and for honouring me by showing such confidence in my abilities and my work. I am immensely grateful.

Although I began my doctoral studies in January 2006, I arrived at UBC in the autumn of 2003 to pursue a master's degree. Having been a part of the Department of Earth and Ocean Sciences at UBC for six years, I would like to thank everyone here for their support, assistance, and kindness. First and foremost amongst these individuals are my research supervisors, Greg Dipple and Mati Raudsepp. I still have difficulty imagining what convinced them to take on a master's student who couldn't tell the difference between serpentine and cedar chips. Moreover, it completely escapes me what convinced them to keep her on for a Ph.D. Whatever the reason, as someone who (at least in her own mind) has since mastered the game of "Wood or Fibre?", I am very thankful for their faith in me. Greg, Mati, I cannot fathom ever finding a way to thank you sufficiently for challenging me to expand the scope of my imagination and for giving me every opportunity to hone my abilities and to indulge my curiosity. Thank you, with every fibre (and all the cedar chips) of my being, for your mentorship, your time, and for challenging me to work harder than I ever have in my life. Greg, you have my undying appreciation for finding the time to help me write my thesis while learning how to manage an academic department! Most importantly of all, thanks are due to Greg for teaching me to appreciate beer and fieldwork and to Mati for his stalwart (albeit unsuccessful) efforts to improve my taste in both coffee and hats.

Uli Mayer has been gracious enough to sit on my advisory committee through two degrees. Thank you, Uli, for your time and for providing me with so many excellent papers to read and new ideas to consider. Thank you also for reminding me that minerals do not exist in a vacuum and that water is lurking everywhere. I am indebted to Gordon Southam, at The University of Western Ontario, for sharing his advice and expertise in the course of fieldwork. Thank you, Gordon, for teaching me to always consider the influence of life on geological systems and to remember that minerals and microbes are

often intimately connected. I am also grateful to Jim Mortensen and Al Lewis for taking the time to help me through my comprehensive exam. Thanks to John Kaszuba at The University of Wyoming and Marc Bustin and Greg Lawrence at UBC for participating in my final oral examination and for asking such thoughtful and challenging questions.

Thanks are due to Ben Grguric, Josh Levett, John Tomich, Shona, Red, and all the staff at Mount Keith for their generous and knowledgeable support in the field. Thanks also to Colleen English and her staff at Diavik for giving so freely of their time and expertise.

Ian Power and I have been working together on CO_2 sequestration in mine tailings since 2004 and have engaged in many field-based adventures and mishaps. It has always been a pleasure and a phenomenal learning experience to work with you, Ian, and I hope to continue doing so for a long time to come. You shall always have my particular thanks for putting up with my annoyingly long, contemplative silences in the field, for allowing me to share in the glow of inventing Golden Bear Coffee at Diavik and that absurd desert at Atlin (the one that required a rock hammer and a bottle of Bailey's…), and for pulling me out that time I fell thigh-deep into mine tailings at Mount Keith.

Abraham, Claire Bear, J.T., Jeremy, Joanne, Julio, Lizzie, Lyle, Nina, Shaun, and Stu: Thank you for being such excellent labmates! It's been a pleasure working with you and learning from you. Thank you also to all the undergraduate students (past and present) who have assisted me in the lab: Claire Brown, Moira Cruickshanks, Colin Finkbeiner, Vicky Liu, Shelley Oliver, Mandy Tang, and Joanne Woodhouse. Jenny Lai, Edith Czech, and Elisabetta Pani are thanked for their assistance over the years and for being patient with me on the many occasions when I forgot to return equipment to their lab. Thanks to Gen. Stuart Mills for taking the time to pass on some of his ridiculously extensive knowledge of systematic mineralogy. I am grateful to Shaun Barker for giving so freely of his time, for his support in the laboratory, and for reading parts of this thesis in its earliest incarnations. Shaun, I shall always be grateful to you for upholding the unspoken Fancy Coffee Pact and for saving Jesse and me from Mt. St. Helens. I would also like to thank Johanna and Ellen Dipple for the superb artwork on my office door and for the Avenging Narwhal action figure (this is by far the best desk toy I have ever had).

I could never have finished this thesis without excellent company and daily trips to Tim Horton's and other establishments. In this regard, I am particularly grateful to Gareth Chalmers (above all), Shaun Barker, Stuart Sutherland, James Thom, Lyle Hansen, Stephen "Sphagnum" Moss, Shawn "No.2" Hood, Ayesha Ahmed, Shelley Oliver, Curtis Brett, Daniel Ross, Krista Michol, Nils Peterson, Jackie Dohaney, Swati Singh, Steve Johnston, Holly Peterson, R.-E. Farrell, Geneviève Robert, John Dockrey, Gen. Stuart Mills, Mackenzie Parker, and everyone else with whom I have ever enjoyed coffee (and other beverages) at UBC. My gratitude goes to good friends in distant places: Cathy Lovekin, Di Moscu, Steve Johnston, Jeff Hargot, and Swati Singh – I hope to visit all of you soon. A heartfelt thanks goes to everyone at the False Creek Ku Yu Kai Goju-ryu Karate dojo, and to Julie Zilber Sensei in particular. It has been a delight and an honour to train with you these past five years.

Finally, the love and encouragement that I have received from my parents, Irina and David, my brother, Min, and my partner, Jesse, have sustained me through my Ph.D., and my M.Sc. before that. I could never have done this without your support and your patience. Thank you for everything.

This work is dedicated to my parents, David and Ira,

to Min, my favourite brother,

and to Jesse.

Co-authorship Statement

This thesis consists of four related manuscripts that have been prepared for publication in peer-reviewed international journals.

A version of Chapter 2 has been published in *Applied Geochemistry*. I am the lead author of this manuscript and Mati Raudsepp and Gregory M. Dipple are my co-authors. As the primary author, I designed and conducted all experiments, performed all analyses, and was responsible for the bulk of the text, tables, and figures. M. Raudsepp provided technical advice and suggestions. G.M. Dipple, who initiated the project, provided oversight on applications and implications of the results of this research. All authors contributed to revision of the manuscript. The reference for the manuscript follows:

Wilson, S.A., Raudsepp, M., and Dipple, G.M. (2009) Quantifying carbon fixation in trace minerals from processed kimberlite: A comparative study of quantitative methods using X-ray powder diffraction data with applications to the Diavik Diamond Mine, Northwest Territories, Canada. Applied Geochemistry, 24, 2312-2331. doi:10.1016/j.apgeochem.2009.09.018.

Chapter 3 is intended for submission to a peer-reviewed international journal. I am the lead author and Shaun L.L. Barker, Gregory, M. Dipple, Viorel Atudorei, and James M. Thom are my co-authors. As the first author, I helped to design the experiments and performed most of the sampling. I am responsible for the bulk of the interpretation, for the computational modelling, and for most of the text, figures, and tables. S.L.L. Barker assisted with experimental design, sampling, and interpretation of data. G.M. Dipple provided advice regarding measurement of stable isotopic fractionation factors and assisted with the interpretation of data. V. Atudorei performed all stable isotopic analyses. J.M. Thom conceived of the method by which we precipitated dypingite, by evaporation from a saline brine. S.L.L. Barker, G.M. Dipple, and I have contributed to revision of the manuscript.

Chapter 4 is intended for submission to a peer-reviewed international journal. I am the primary author and Gregory M. Dipple, Shaun L.L. Barker, Ian M. Power, Stewart J. Fallon, Mati Raudsepp, and Gordon Southam are my co-authors. I conducted most of the research and produced most of the text, figures, and tables. I am responsible for much of the interpretation. I received significant assistance with interpretation of results from G.M. Dipple, and further assistance from S.L.L. Barker, I.M. Power, and G. Southam. I.M. Power and I performed most of the fieldwork and were assisted by G. Southam and G.M. Dipple. S.J. Fallon contributed radiocarbon analyses and M. Raudsepp provided advice pertaining to quantitative mineralogical techniques. G.M. Dipple and G. Southam initiated the project. G.M. Dipple, M. Raudsepp, and I have participated in revision of the manuscript.

Chapter 5 is intended for submission to a peer-reviewed international journal. I am the lead author and Gregory M. Dipple, Ian M. Power, Shaun L.L. Barker, Stewart J. Fallon, and Gordon Southam are my co-authors. I am responsible for the bulk of the text, figures, and tables. G.M. Dipple and I developed the geochemical models and I implemented them in MATLAB. G.M. Dipple, I.M. Power, S.L.L. Barker, and G. Southam assisted me with the interpretation of isotopic data and model results. G.M. Dipple and G. Southam initiated the project. I.M. Power and I performed most of the fieldwork and were assisted by G. Southam and G.M. Dipple. S.J. Fallon contributed radiocarbon analyses. In addition, J.R. Gare contributed a function to the code for scenario 3 and helped to make some of the scripts more succinct. G.M. Dipple, S.L.L. Barker, and I have contributed to revision of the manuscript.

Chapter 1

Introduction

1.1 Climate change and carbon capture and storage

Current warming of the Earth's climate has been connected to the emission of anthropogenic greenhouse gases (i.e., CO_2, CH_4, N_2O) into the atmosphere (IPCC 2007). The overwhelming majority of climate scientists support this interpretation (Oreskes 2004) and the national science academies of the G8+5 nations have issued several declarations affirming that current climate change is almost certainly an anthropogenic effect. In 2004, carbon dioxide (CO_2) constituted 77% by mass of total anthropogenic greenhouse gas emissions (IPCC 2007). The global atmospheric concentration of CO_2 increased exponentially from a pre-industrial (i.e., pre-1750) level of 280 ± 20 ppm to 379 ppm by 2005. Approximately two-thirds of this increase has been attributed to the combustion of fossil fuels and one-third to changes in land use since 1750 (IPCC 2007). Coincident with the increasing concentration of atmospheric greenhouse gases, the average surface temperature of the Earth increased by 0.74º ± 0.18ºC between 1906 and 2005, and sea level rose by 0.17 ± 0.05 m over the course of the 20th century (IPCC 2007). The increased concentration of atmospheric CO_2 has also been implicated in a decrease of 0.1 pH units in global average surface ocean water since the pre-industrial era (IPCC 2007).

Pacala and Socolow (2004) suggest that less than double the pre-industrial atmospheric CO_2 concentration (i.e., 500 ± 50 ppm) should be treated as an upper limit in order to prevent the most damaging and irreversible effects of anthropogenic climate change. Strategies for decarbonising energy sources, increasing efficiency of energy production, and trapping and storing CO_2 are required to stabilize concentrations of atmospheric CO_2 within the next century (e.g., Hoffert et al. 2002; Lackner 2003; Pacala and Socolow 2004; Broecker 2007). It will take time to increase the efficiency of, and ultimately to replace, the extant fossil-fuel based energy infrastructure that is in use

today. In the meantime, geologically stable, energy efficient, and cost-effective strategies for sequestering CO_2 must be developed and implemented. The International Energy Agency predicts that nearly 20% of total reductions in greenhouse gas emissions for the next 40 years will need to be achieved through capture and storage of carbon (International Energy Agency 2008).

Anthropogenic CO_2 could be stored within living biomass or sequestered by injection into deep ocean water, seabed sediments, and subterranean geological formations such as saline aquifers and reservoirs for oil and gas (IPCC 2005). Sequestration of CO_2 within biomass has a short characteristic storage time, on the order of 1-100 years, and a relatively limited capacity compared to other technologies (Lackner 2003). Although the ocean's capacity to store CO_2 is significantly larger than that of the biosphere, concerns about leakage and accelerated ocean acidification have curbed development of this option in recent years (Lackner 2003; Sipilä et al. 2008).

The large-scale CO_2 sequestration projects at Weyburn, Saskatchewan, Canada, and Sleipner, in the North Sea, have demonstrated successful storage of CO_2 within subterranean geological reservoirs. At the Weyburn oil field, industrially produced waste CO_2 is injected into a reservoir of shallow marine carbonate rocks. Approximately 5000 t/day of CO_2 have been injected into the Midale Beds at Weyburn since 2000 (Cantucci et al. 2009). At Sleipner, supercritical CO_2 (stripped from mined natural gas) has been injected at a rate of approximately 1 Mt/year since 1996 into the Utsira Sand, which is a ~200 m thick saline aquifer (Bickle 2007). Although storage of supercritical CO_2 within underground wells and saline aquifers has been demonstrated to be stable on the decadal timescale, long-term stability of this method is not assured. Significant uncertainty remains regarding seismic instability of trapping and the potential for migration and leakage of buoyant CO_2 (Lackner 2003). Consequently, wide-scale use of injection-based technologies could require continuous monitoring at storage sites for thousands of years (e.g., Sipilä et al. 2008). Because this is an extremely difficult, if not impossible, commitment for a society to make, more permanent means of storage must be pursued.

Approximately 90% of carbon on Earth is fixed within carbonate minerals (Sundquist 1985; Sudquist 1993) and it is expected that these minerals will be the ultimate sink for most anthropogenic CO_2 on a timescale of one million years (Kump et

al. 2000). Storage of CO_2 in carbonate minerals is recognized as a safe and effective method for the sequestration of anthropogenic carbon (Seifritz 1990; Lackner et al. 1995; Lackner 2003). Furthermore, mineralization of anthropogenic CO_2 within carbonate minerals has the largest capacity and longest storage time of any method yet proposed for capturing and storing carbon (Lackner 2003).

Since carbon mineralization was first proposed as a method for storing CO_2 (Seifritz 1990), most of the work on this subject has focussed on the development of rapid, large-scale methods for trapping and storing CO_2 at industrial point sources (reviewed in Huijgen and Comans 2003, 2005; IPCC 2005; Sipilä et al. 2008). Most processes developed to date are based on reaction of naturally occurring silicate minerals such as forsterite [Mg_2SiO_4], serpentine-group minerals [$Mg_3Si_2O_5(OH)_4$], and wollastonite [$CaSiO_3$] to carbonate minerals like magnesite [$MgCO_3$] and calcite [$CaCO_3$]. In nature, weathering of silicate minerals by dissolution leads to precipitation of carbonate minerals under conditions of atmospheric pressure and temperature. This is one of the most significant mechanisms for geochemical exchange of CO_2 between the atmosphere and lithosphere (Schwartzman and Volk 1989; Berner 1990). However, this is typically a slow process and high-temperature pre-treatment of silicate minerals, or extraction of Mg and Ca from these minerals, is often required to accelerate reaction in the laboratory. Furthermore, high temperatures and pressures are needed to induce carbon mineralization reactions on the short timescales (i.e., hours) required for development and deployment of industrial carbonation reactors (Sipilä et al. 2008). As a result, this approach to carbon mineralization remains both costly and energy intensive (Lackner 2003; Sipilä et al. 2008).

Recently, there has been a shift toward the development of low-temperature, low-pressure procedures for carbon mineralization that emulate or piggyback upon natural processes that occur at the surface of the Earth. Schuiling and Krijgsman (2006) suggest that olivine-group minerals could be incorporated into acidic soils, where they would act as fertilizer and a neutralization agent while reacting with the atmosphere to produce carbonate minerals. Ferrini et al. (2009) have developed an industrial process by which anthropogenic CO_2 may be rapidly and effectively stored within a low-temperature carbonate mineral, nesquehonite [$MgCO_3 \cdot 3H_2O$], by reaction with Mg-rich wastewater

from desalination plants and oil fields. Kelemen and Matter (2008) propose that acceleration of carbon mineralization via natural silicate weathering within ophiolites could consume on the order of 1 Gt of CO_2 per year within peridotite deposits in Oman alone. Of relevance to this thesis, an expanding body of work suggests that *in situ* weathering of silicate minerals, within the mineral waste from some mines, may be used to sequester a significant amount of CO_2.

1.2 Carbon mineralization within mine tailings

Mineral-fluid reactions are greatly accelerated in mine tailings because the milling process leads to a large increase in reactive surface area (e.g., White et al. 1996; Molson et al. 2005). Carbonate minerals are known to precipitate during mineral-fluid reactions in mine tailings at several sites in Canada: the Kidd Creek copper-zinc mine near Timmins, Ontario (Al et al. 2000), the Lower Williams Lake uranium mine near Elliot Lake, Ontario (Paktunc and Davé 2002), and in chrysotile mine tailings at Thetford, Québec (Huot et al. 2003), Clinton Creek, Yukon Territory (Wilson et al. 2004), and Cassiar, British Columbia (Wilson et al. 2005). Wilson et al. (2006) and Rollo and Jamieson (2006) suggest that if atmospheric CO_2 were the primary source of carbon in the carbonate minerals that develop within ultramafic mine tailings, the weathering process by which they result could be used to sequester CO_2. Also, carbonation of bauxite mine residue to calcite and dawsonite (by reaction with atmospheric CO_2) has been proposed as a means by which aluminum mines might neutralize their basic tailings, and offset some portion of their emissions (Jones et al. 2006; Khaitan et al. 2009).

Wilson et al. (2009) used a combination of stable carbon and oxygen isotope, and radiocarbon analyses to demonstrate that tailings from the historical chrysotile mines at Clinton Creek, Yukon Territory and Cassiar, British Columbia are trapping and storing CO_2 from the atmosphere. Previously, Wilson et al. (2006) developed a technique for use with the Rietveld method and X-ray powder diffraction data (Rietveld 1969; Hill and Howard 1987; Bish and Howard 1988) that enables quantitative phase analysis in samples containing disordered minerals (e.g., serpentine-group minerals). Because

ultramafic mine tailings contain abundant serpentine-group minerals, the combination of the quantitative method of Wilson et al. (2006) and the isotopic verification protocol of Wilson et al. (2009) allows the carbonate mineral traps for atmospheric CO_2 in ultramafic mine tailings to be identified and quantified. Measured abundances of these mineral traps obtained with the Rietveld method can then be used to estimate the amount of atmospheric CO_2 trapped within mine tailings.

Deposit types that produce tailings suitable for CO_2 sequestration include, but are not limited to: Cu-Ni-PGE deposits hosted by dunite, serpentinite, and gabbro-norite; serpentinite-hosted chrysotile; diamondiferous kimberlite pipes, and podiform chromite deposits in layered mafic intrusions. The only mineralogical prerequisite to efficient CO_2 sequestration in mine tailings are the high abundance of Mg-silicate minerals. Although, a low abundance of acid-generating sulphide minerals could be considered a further prerequisite, Power et al. (in review) have demonstrated that the addition of an acid generating substance and a microbial catalyst can accelerate weathering of serpentine minerals, while maintaining a neutral to basic pH (under which most carbonate minerals are stable).

1.3 Carbon mineralization in tailings from active mines

Previous investigations into verification and quantification of passive carbon mineralization in ultramafic mines have been undertaken at historical mine sites (Wilson et al. 2006, 2009). There are few data dealing with this phenomenon as it occurs in the tailings from active mines.

Active mining operations may be able to take advantage of carbon mineralization within their tailings to offset part of their greenhouse gas emissions. However, the sources and cycles for carbon in active mining operations are, respectively, more plentiful and more complicated than in historical mine tailings environments. In addition, carbonate minerals are not always present at high abundance, and thus not readily detectable, in the recently deposited tailings from active mining operations. In order to enable mining companies to claim credit for CO_2 sequestration, there must exist an

unbiased scientific protocol for identifying, verifying, and quantifying sequestration of CO_2 within mine tailings. This work seeks to improve our understanding of the carbon cycle in mine tailings, and to make a contribution to mineralogical and geochemical strategies for assessing carbon mineralization in mine tailings.

Carbon is being mineralized within ultramafic mine tailings from the active mining operations at the Mount Keith Nickel Mine, Western Australia, Australia (Fig. 1.1), and the Diavik Diamond Mine, Northwest Territories, Canada (Fig. 1.2).

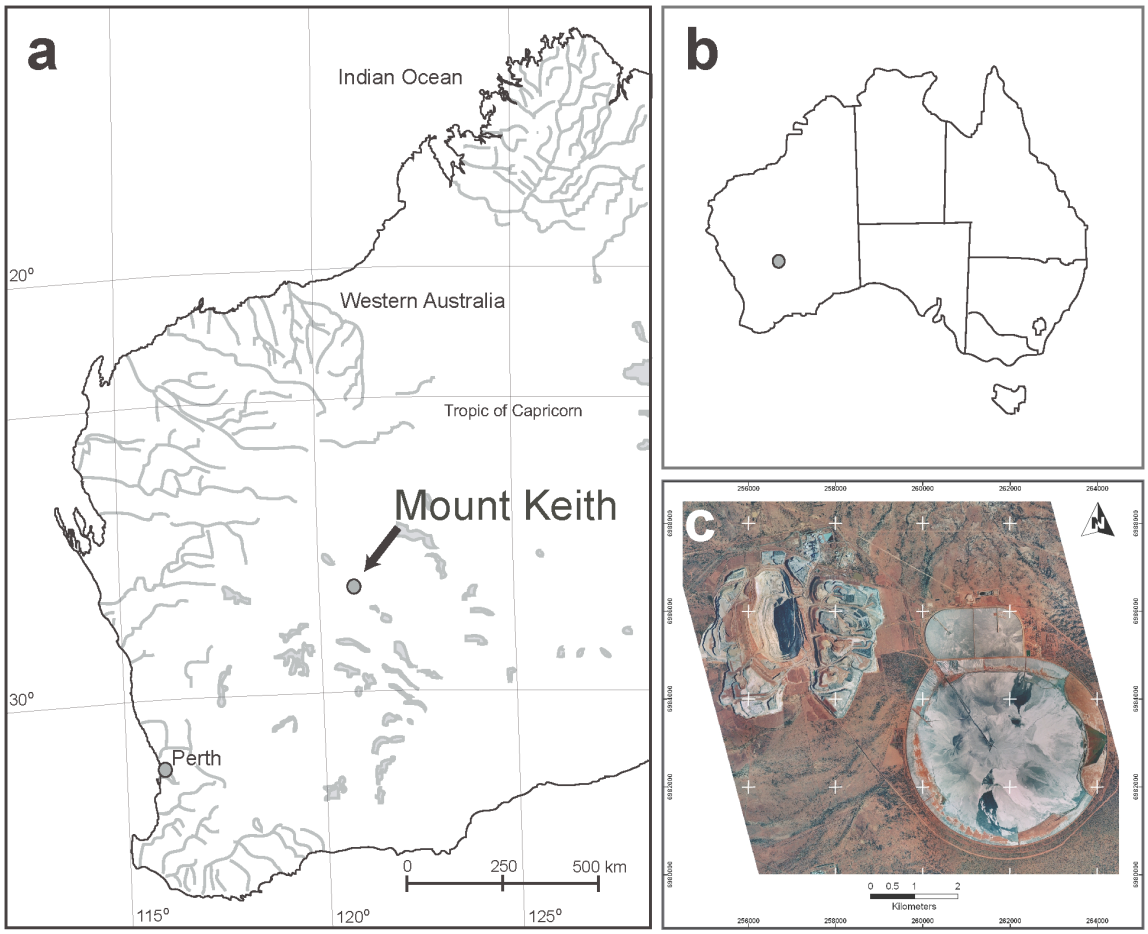

Figure 1.1: (a) and (b) Location of Mount Keith Nickel Mine, Western Australia, Australia. (c) Satellite photograph of the open pit at the MKD5 deposit and tailings storage facility, Mount Keith.

At both sites, which are hosted by ultramafic rocks, hydrated magnesium carbonate minerals develop within mine tailings by weathering of Mg-rich gangue minerals. Differences in climate and tailings management practices have resulted in widespread mineralization and preservation of secondary hydromagnesite

[$Mg_5(CO_3)_4(OH)_2 \cdot 4H_2O$] at Mount Keith, and limited mineralization of nesquehonite [$MgCO_3 \cdot 3H_2O$], calcite, and Na-carbonate minerals in the tailings at Diavik. These mines are characterized by significant contrasts in climate, rock type, and tailings management practices. The goal of this thesis is to exploit these contrasts in order to develop mineralogical and geochemical strategies for identifying, verifying, and quantifying carbon mineralization in tailings from actively producing mines hosted by ultramafic rocks.

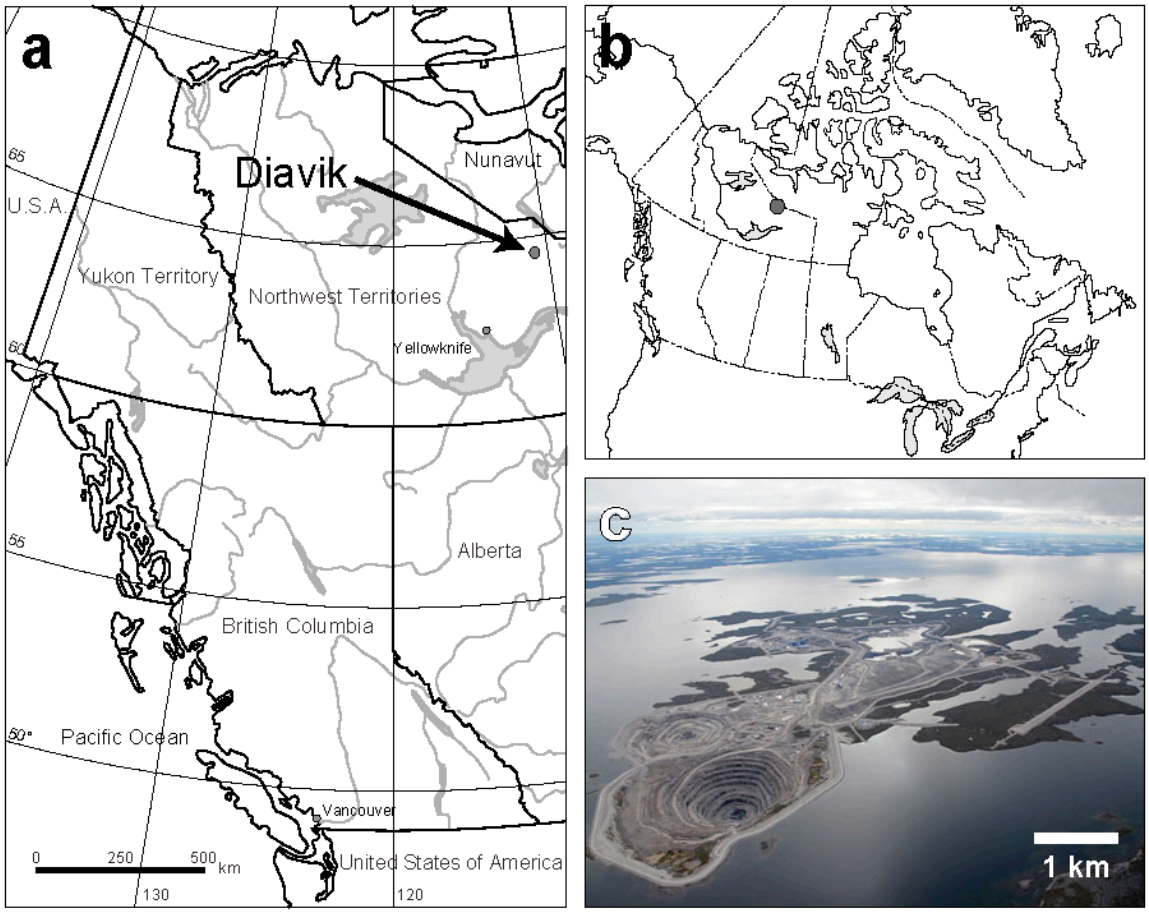

Figure 1.2: (a) and (b) Location of Diavik Diamond Mine, Northwest Territories, Canada. (c) Aerial photograph of the Diavik Diamond Mine (courtesy of Diavik Diamond Mines Inc.).

1.4 Organization and outcomes of this thesis

An approach to estimating CO_2 sequestration within minerals in mine tailings must provide quantitative mineralogical and geochemical information on the sample scale and apply it at the scale of a tailings storage facility. It is necessary to consider the representativeness of samples, the limitations of quantitative mineralogical methods, the potential pitfalls in collecting and interpreting geochemical data, and the physical properties of the materials under study.

The goal of this thesis is to address these concerns in order to outline a strategy by which mining companies may account for the capture and storage of carbon within mine tailings. Four manuscripts are assembled here for this purpose. The second chapter of this thesis (Chapter 2) expands the scope of the mineralogical toolbox for assessing carbon mineralization in mine tailings, the subject of my master's thesis (Wilson 2005), published as Wilson et al. (2006). Chapter 3 presents new data for the fractionation of carbon isotopes in dypingite, a poorly-understood Mg-carbonate mineral which acts as a mineral trap for carbon in mine tailings. In Chapters 4 and 5, the results of the preceding chapters are applied to mine-scale assessments of carbon mineralization at the Mount Keith Nickel Mine, and the Diavik Diamond Mine. Chapter 2 has been published in *Applied Geochemistry*. Chapters 3, 4, and 5 have undergone internal review and are intended for submission to peer-reviewed international journals. Brief descriptions of these manuscript-style chapters follow.

Chapter 2 (published in *Applied Geochemistry*) is a comparative study of quantitative X-ray powder diffraction (XRPD) techniques applied to measurement of trace amounts of a Mg-carbonate mineral. Carbon is being mineralized within trace amounts of nesquehonite [$MgCO_3 \cdot 3H_2O$] in the kimberlite mine tailings at the Diavik Diamond Mine. Although the abundance of nesquehonite in these mine tailings is low, trapping of CO_2 within trace minerals may be offsetting kilotonnes of greenhouse gas emissions at Diavik and other large mines. The applicability and accuracy of three techniques for quantitative phase analysis with XRPD data to the measurement of trace amounts of nesquehonite in kimberlite mine tailings is evaluated. These techniques are tested on synthetic mixtures of pure minerals and are subsequently applied to

measurement of trace nesquehonite in natural kimberlite mine tailings from the Diavik Diamond Mine. Results of quantitative phase analysis are used to estimate trapping of CO_2 within trace mineralization of nesquehonite at Diavik.

Chapter 3 describes the results of mineral synthesis experiments, which are used to obtain a stable isotopic fractionation factor for carbon between the Mg-carbonate mineral, dypingite [$Mg_5(CO_3)_4(OH)_2 \cdot 5H_2O$], and dissolved inorganic carbon. Currently, the only published data for experimentally determined fractionation factors for any Mg-carbonate minerals are those reported by O'Neil and Barnes (1971) for exchange of oxygen between hydromagnesite and water at 0° and 25°C. The lack of isotopic fractionation factors for Mg-carbonate minerals hampers the interpretation of stable isotope data collected from these minerals. This dearth of information also interferes with the development of a consistent and reliable protocol for verifying mineralization of atmospheric CO_2 within dypingite and related minerals in ultramafic mine tailings. To begin bridging this gap, open system precipitation experiments are undertaken to study the partitioning of ^{13}C between dypingite and total dissolved inorganic carbon in an evaporative and saline system. These experiments are designed to simulate the conditions under which atmospheric CO_2 is mineralized within the chemically and structurally related mineral, hydromagnesite, at the Mount Keith Nickel Mine.

Chapter 4 is a detailed site study of carbon mineralization at the Mount Keith Nickel Mine. In this chapter, field observations, stable and radiogenic isotope geochemistry, and extensive use of quantitative mineralogy are combined to fingerprint the source of carbon in secondary hydromagnesite [$Mg_5(CO_3)_4(OH)_2 \cdot 4H_2O$], and are used to estimate the amount of CO_2 that is fixed within this mineral at Mount Keith. In order to estimate the total amount of CO_2 captured within hydromagnesite at this mine, it is necessary that the mineralogy of its tailings storage facilities be well constrained. This requires extensive sampling and the construction of a database of quantitative mineralogical data. Rietveld refinement results for more than 200 samples of mine tailings are used to obtain an empirical rate for mineralization of hydromagnesite, and to estimate the amount of CO_2 trapped and stored within mine tailings. The three-isotope system (i.e., $\delta^{13}C$, $\delta^{18}O$, and $F^{14}C$) employed by Wilson et al. (2009), and the results of Chapter 3, are used to fingerprint the source of CO_2 within hydromagnesite and to

provide more precise constraints on the amount of CO_2 fixed within the tailings at Mount Keith.

In Chapter 5, stable and radiogenic isotope data for primary and secondary carbonate minerals from the Diavik Diamond Mine are examined. The diversity of mineral species identified at Diavik and the input of carbon and oxygen from multiple reservoirs give rise to stable isotopic data that are difficult to interpret. Under such conditions, it can be challenging to implicate specific reservoirs in the precipitation of minerals, and therefore, to assess whether atmospheric CO_2 is being sequestered into secondary carbonate minerals. In this chapter, I model three scenarios by which carbon may be mixed and cycled between different reservoirs in mine tailings (using conditions based on those at Diavik and Mount Keith). These models make use of measured values from Diavik and Mount Keith, published equilibrium fractionation factors, and the fractionation factor obtained for dypingite in Chapter 3. Model results are used to interpret stable carbon and oxygen isotopic data and radiocarbon data for the Diavik Diamond Mine and three other mines: the Mount Keith Nickel Mine (using data from Chapter 4), and the historical chrysotile mines at Clinton Creek and Cassiar (using data from Wilson et al. 2009). Based on comparison of isotopic data with model results, field observations, and quantitative mineralogical results from Chapters 2 and 4, the impact of mechanical mixing and bedrock carbonate recycling on CO_2 sequestration at these four mines is considered. The validity of using stable isotopes of carbon and oxygen as the primary tools for verifying sequestration of atmospheric CO_2 within mine tailings is assessed.

In Chapter 6, the most significant results of this thesis are summarized, and the implications of these results for sequestration of CO_2 within ultramafic mine tailings are discussed. From the conclusions arrived at during this work, suggestions are made for future lines of research.

1.5 References

Al, T.A., Martin, C.J., and Blowes, D.W. (2000) Carbonate-mineral/water interactions in sulfide-rich mine tailings. Geochimica et Cosmochimica Acta, 64, 3933-3948.

Berner, R.A. (1990) Atmospheric carbon dioxide levels over Phanerozoic time. Science, 249, 1382-1386.

Bickle, M., Chadwick, A., Huppert, H.E., Hallworth, M., and Lyle, S. (2007) Modelling carbon dioxide accumulation at Sleipner: Implications for underground carbon storage. Earth and Planetary Science Letters, 225, 164-176.

Bish, D.L. and Howard, S.A. (1988) Quantitative phase analysis using the Rietveld method. Journal of Applied Crystallography, 21, 86-91.

Broecker, W.S. (2007) CO_2 arithmetic. Science, 315, 1371.

Cantucci, B., Montegrossi, G., Vaselli, O., Tassi, F., Quattrocchi, F., and Perkins, E.H. (2009) Geochemical modeling of CO_2 storage in deep reservoirs: The Weyburn Project (Canada) case study. Chemical Geology, 265, 181-197.

Department of Indian Affairs and Northern Development (1993) Guidelines for Acid Rock Drainage Prediction in the North: Northern Mine Environment Neutral Drainage Studies No. 1. Prepared by Steffen, Robertson and Kirsten (B.C.) Inc. Ottawa, ON, Canada.

Ferrini, V., De Vito, C., and Mignardi, S. (2009) Synthesis of nesquehonite by reaction of gaseous CO_2 with Mg chloride solution: Its potential role in the sequestration of carbon dioxide. Journal of Hazardous Materials, 168, 832-837.

Hill, R.J. and Howard, C.J. (1987) Quantitative phase analysis from neutron powder diffraction data using the Rietveld method. Journal of Applied Crystallography, 20, 467-474.

Hoffert, M.I., Caldeira, K., Benford, G., Criswell, D.R., Green, C., Herzog, H., Jain, A.K., Kheshgi, H.S., Lackner, K.S., Lewis, J.S., Lightfoot, H.D., Manheimer, W., Mankins, J.C., Mauel, M.E., Perkins, L.J., Schlesinger, M.E., Volk, T., and Wigley, T.M.L. (2002) Advanced technology paths to global climate stability: energy for a greenhouse planet. Science, 298, 981-987.

Huijgen, W.J.J. and Comans, R.N.J. (2005) Carbon dioxide sequestration by mineral carbonation: Literature review update 2003-2004. Energy Research Centre of the Netherlands, Report ECN-C-05-022.

Huijgen, W.J.J. and Comans, R.N.J. (2003) Carbon dioxide sequestration by mineral carbonation: Literature review. Energy Research Centre of the Netherlands, Report ECN-C-03-016.

Huot, F., Beaudoin, G., Hebert, R., Constantin, M., Bonin, G., and Dipple, G. (2003) Evaluation of Southern Québec asbestos residues for CO_2 sequestration by mineral carbonation; preliminary results. Joint Annual Meeting of the Geological and Mineralogical Associations of Canada, Vancouver, Canada. May 25-28, 2003.

International Energy Agency (2008) Energy Technology Perspectives 2008: Scenarios & Strategies to 2050. Organisation for Economic Co-operation and Development Publishing, 648 p.

IPCC (2007) Climate Change 2007: The Physical Basis. Contribution of Working Group I to the Fourth Assessment Report of the Intergovernmental Panel on Climate Change. Solomon, S., Qin, D., Manning, M., Chen, Z., Marquis, M., Averyt, K.B., Tignor, M., and Miller, H.L., Eds. Cambridge University Press, Cambridge, UK and New York, NY, USA, 996 p.

IPCC (2005) IPCC Special Report on Carbon Dioxide Capture and Storage. Metz, B., Davidson, O., de Coninck, H.C., Loos, M., and Meyer, L.A., Eds. Cambridge University Press, Cambridge, UK and New York, NY, USA, 431 p.

Jones, G., Joshi, G., Clark, M., and McConchie, D. (2006) Carbon capture and the aluminium industry: Preliminary studies. Environmental Chemistry, 3, 297-303.

Kelemen, P.B. and Matter, J. (2008) In situ carbonation of peridotite for CO_2 storage. Proceedings of the National Academy of Sciences of the USA, 105, 17295-17300.

Khaitan, S., Dzombak, D.A., and Lowry, G.V. (2009) Journal of Environmental Engineering, 133, 433-438.

Kump, L.R., Brantley, S.L., and Arthur, M.A. (2000). Chemical weathering, atmospheric CO_2, and climate. Annual Review of Earth and Planetary Sciences, 28, 611-667.

Lackner, K.S. (2003) Climate change: A guide to CO_2 sequestration. Science, 300, 1677-1678.

Lackner, K.S., Wendt, C.H., Butt, D.P., Joyce, G.L., and Sharp, D.H. (1995) Carbon dioxide disposal in carbonate minerals. Energy, 20, 1153-1170.

Molson, J.W., Fala, O., Aubertin, M., and Bussière, B. (2005) Numerical simulations of pyrite oxidation and acid mine drainage in unsaturated waste rock piles. Journal of Contaminant Hydrology, 78, 343-371.

O'Neil, J.R. and Barnes, I. (1971) C^{13} and O^{18} compositions in some fresh-water carbonates associated with ultramafic rocks and serpentinites: western United States. Geochimica et Cosmochimica Acta, 35, 687-697.

Oreskes, N. (2004) Beyond the Ivory Tower: the scientific consensus on climate change. Science, 306, 1686.

Pacala, S. and Socolow, R. (2004) Stabilization wedges: solving the climate problem for the next 50 years with current technologies. Science, 305, 968-972.

Paktunc, A.D. and Davé, N.K. (2002) Formation of secondary pyrite and carbonate minerals in the Lower Williams Lake tailings basin, Elliot Lake, Ontario, Canada. American Mineralogist, 87, 593-602.

Power, I.M., Dipple, G.M., and Southam, G. Bioleaching of ultramafic tailings by *Acidithiobacillus* spp. for CO_2 sequestration. Environmental Science & Technology, in review.

Rietveld, H.M. (1969) A profile refinement method for nuclear and magnetic structures. Journal of Applied Crystallography, 2, 65-71.

Rollo, H.A. and Jamieson, H.E. (2006) Interaction of diamond mine waste and surface water in the Canadian Arctic. Applied Geochemistry, 21, 1522-1538.

Schuiling, R.D. and Krijgsman, P. (2006) Enhanced weathering: An effective and cheap tool to sequester CO_2. Climatic Change, 774, 349-354.

Schwartzman, D.W. and Volk, T. (1989) Biotic enhancement of weathering and the habitability of Earth. Nature, 340, 457-460.

Seifritz, W. (1990) CO_2 disposal by means of silicates. Nature, 345, 486.

Sipilä, J., Teir, S., and Zevenhoven, R. (2008) Carbon dioxide sequestration by mineral carbonation: Literature review update 2005-2007. Åbo Akademi University Heat Engineering Laboratory, Report 2008-1.

Sundquist, E.T. (1993) The global carbon dioxide budget. Science, 259, 934-941.

Sundquist, E.T. (1985) Geological perspectives on carbon dioxide and the carbon cycle. In The Carbon Cycle and Atmospheric CO_2: Natural Variations Archaen to Present. Sundquist, E.T. and Broecker, W.S., Eds. Geophysical Monographs 32, Washington, DC, American Geophysical Union, p. 5-60.

White, A.F., Blum, A.E., Schulz, M.S., Bullen, T.D., Harden, J.W., and Peterson, M.L. (1996) Chemical weathering rates of a soil chronosequence on granitic alluvium: I. Quantification of mineralogical and surface area changes and calculation of primary silicate reaction rates. Geochimica et Cosmochimica Acta, 60, 2533-2550.

Wilson, S.A., Dipple, G.M., Power, I.M., Thom, J.M., Anderson, R.G., Raudsepp, M., Gabites, J.E., and Southam, G. (2009) Carbon dioxide fixation within mine wastes of ultramafic-hosted ore deposits: Examples from the Clinton Creek and Cassiar chrysotile deposits, Canada. Economic Geology, 104, 95-112.

Wilson, S.A., Raudsepp, M., and Dipple, G.M. (2006) Verifying and quantifying carbon fixation in minerals from serpentine-rich mine tailings using the Rietveld method with X-ray powder diffraction data. American Mineralogist, 91, 1331-1341.

Wilson, S.A., Thom, J.M., Dipple, G.M., Raudsepp, M., and Anderson, R.G. (2005) Towards sustainable mining: uptake of greenhouse gases by mine tailings. British Columbia and Yukon Chamber of Mines Mineral Exploration Roundup, Vancouver, Canada. January 24-27, 2005.

Wilson, S. A., Dipple, G.M., Anderson, R.G., and Raudsepp, M. (2004) Characterization of Clinton Creek mine residues and their suitability for CO_2 sequestration. British Columbia and Yukon Chamber of Mines Mineral Exploration Roundup, Vancouver, Canada. January 26-29, 2004.

Chapter 2

Quantifying carbon fixation in trace minerals from processed kimberlite: A comparative study of quantitative methods using X-ray powder diffraction data with applications to the Diavik Diamond Mine, Northwest Territories, Canada[1]

2.1. Introduction

Emission of anthropogenic greenhouse gases (e.g., CO_2, CH_4, and N_2O) has been implicated as a cause of current warming of the Earth's climate. Carbon dioxide (CO_2) is by far the most significant of these greenhouse gases, representing 77% of total anthropogenic emissions in 2004 (Solomon et al. 2007). By 2005, the global atmospheric concentration of CO_2 had increased to 379 ppm from a pre-1750 (i.e., pre-industrial) value of 280 ± 20 ppm. Approximately two-thirds of this increase is attributed to combustion of fossil fuels and one-third to changes in land-use patterns during the past 260 years (Solomon et al. 2007). It has been suggested that strategies for decarbonizing energy sources, increasing energy efficiency, and trapping and storing CO_2 must be developed and implemented in order to stabilize concentrations of atmospheric CO_2 and curtail the most damaging effects of anthropogenic climate change (e.g., Hoffert et al. 2002; Lackner 2003; Pacala and Socolow 2004; Broecker 2007; Solomon et al. 2007).

Approximately 90% of carbon on Earth is fixed within carbonate minerals (Sundquist 1985; Sudquist 1993) and it is expected that these minerals will be the ultimate sink for most anthropogenic CO_2 on a timescale of 10^6 years (Kump et al. 2000). Storage of CO_2 in carbonate minerals is recognized as a safe and effective method for the sequestration of anthropogenic carbon (Seifritz 1990; Lackner et al. 1995; Lackner 2003). Precipitation of carbonate minerals in situ by dissolution of silicate mine residues

[1] A version of this chapter has been published.
Wilson, S.A., Raudsepp, M., and Dipple, G.M. (2009) Quantifying carbon fixation in trace minerals from processed kimberlite: A comparative study of quantitative methods using X-ray powder diffraction data with applications to the Diavik Diamond Mine, Northwest Territories, Canada. Applied Geochemistry, 24, 2312-2331. doi:10.1016/j.apgeochem.2009.09.018.

is one potential implementation of this process. The development of secondary carbonate minerals has been documented in tailings at several mine sites in Canada: at the Kidd Creek copper-zinc mine near Timmins, Ontario (Al et al. 2000), the Lower Williams Lake uranium mine near Elliot Lake, Ontario (Paktunc and Davé 2002), and in chrysotile mine tailings at Thetford, Québec (Huot et al. 2003), Clinton Creek, Yukon Territory (Wilson et al. 2004), and Cassiar, British Columbia (Wilson et al. 2005). The carbon bound within secondary carbonate minerals in the tailings at some of these mines may not have had an atmospheric source. However, Wilson et al. (2009) demonstrate that tailings from the historical chrysotile mines at Clinton Creek, Yukon Territory and Cassiar, British Columbia are trapping and storing CO_2 from the atmosphere. Accelerating the uptake of CO_2 into tailings from active mines could reduce or offset the net greenhouse gas emissions of many mining operations.

Bulk geochemical methods for CO_2 abundance cannot distinguish among various carbonate minerals nor can they discern the difference between atmospheric, bedrock, biological, and industrial sources of carbon within minerals. However, the sources of bound carbon can be distinguished using radiocarbon and stable isotopes of carbon and oxygen (Wilson et al. 2009). Also, automated point-counting techniques (e.g. mineral liberation analysis) cannot be used to quantify fine-grained minerals or hydrous minerals that are easily vaporized by an electron beam. As an alternative to point counting, the amount of CO_2 trapped within fine-grained, hydrous carbonate minerals can be estimated from weight-percent abundances determined with quantitative phase analysis using X-ray powder diffraction (XRPD) data.

At the Diavik Diamond Mine, Northwest Territories, Canada, efflorescent films of Ca, Na, and Mg-carbonate minerals form in the tailings from the fine and coarse Processed Kimberlite Containment facilities (PKC). These minerals precipitate at the surface of kimberlite waste that is beached along the edge of a central pond used for storing process water. Based on our observations, the most common secondary carbonate mineral, and the one best preserved at depth, is nesquehonite ($MgCO_3 \cdot 3H_2O$). Also, geochemical modelling by Rollo and Jamieson (2006) suggests that carbon mineralization may be occurring in waste kimberlite at the nearby EKATI Diamond Mine.

Many studies have demonstrated the accuracy and precision of the Rietveld method for determining mineral abundances from XRPD data (e.g., Hill and Howard 1987; Bish and Howard 1988; Bish and Post 1993; Raudsepp et al. 1999; De la Torre et al. 2001; De la Torre and Aranda 2003; Ufer et al. 2004; Omotoso et al. 2006; Wilson et al. 2006). Processed kimberlite from Diavik contains a variety of minerals that are characterized by one or more of the following: (1) extensive solid solution, (2) structural disorder, and (3) severe preferred orientation. Furthermore, processed kimberlite at Diavik generally contains abundant serpentine and forsterite with minor to trace amounts of many other phases, resulting in complicated XRPD patterns that consist of many overlapped peak profiles. The combination of these factors presents a challenge for quantifying carbon mineralization with the Rietveld method (Rietveld 1969). This is chiefly because the Rietveld method requires that the crystal structures and chemistry of the phases being analyzed be known and also gives less reliable results for minerals present at low abundances (e.g., Raudsepp et al. 1999).

Alternatively, Chung's (1974) method of normalized reference intensity ratios (RIR) and similar methods have been used successfully to quantify trace abundances of minerals in multi-phase mixtures (e.g., Bish and Chipera 1991; Omotoso et al. 2006). Calibration curves produced according to the internal standard method (Alexander and Klug 1948) have also been used successfully to measure trace abundances of minerals (e.g., Sanchez and Gunter 2006). These three methods are typically used in isolation on very different systems of minerals and, as such, it is difficult to recommend the use of one method over another for quantification of low abundances of minerals. Here we assess the ability of Chung's RIR method, the internal standard method, and the Rietveld method to measure minor to trace amounts of nesquehonite using weighed mixtures of pure mineral standards, prepared to simulate processed kimberlite. Based on the results of our tests, we outline a procedure for accurate quantification of CO_2 trapping within trace minerals in kimberlite mine tailings. This procedure is subsequently applied to samples of natural processed kimberlite from the fine and coarse PKC at Diavik. Results of quantitative phase analysis are used to estimate trapping of CO_2 within nesquehonite at Diavik (from stoichiometry of this mineral) and to determine the contribution of

nesquehonite to neutralization potential of the tailings according to the method of Jambor et al. (2007).

2.2 Locality and sampling strategy

The Diavik Diamond Mine is located on East Island, in Lac de Gras, approximately 300 km northeast of Yellowknife, Northwest Territories, Canada (Fig. 2.1). There are four mineable kimberlite pipes on the Diavik property; two of which, A154 North and A154 South, are currently being mined from a single open pit. A third pipe, A418, is located to the south of the A154 pipes and began production in 2008. The fourth pipe, A21, is not currently being developed. The kimberlites at Lac de Gras, including those at Diavik, intrude Late Archean granitoids and supracrustal rocks of the Yellowknife Supergroup in the Slave Structural Province (Graham et al. 1998). Approximately 2 Mt/year of kimberlite ore is being mined from the A154 open pit. After undergoing processing to remove diamonds, the kimberlite is transported to one of two locations for permanent storage. Most of the processed kimberlite is piped, suspended in process water, into a natural basin (termed the fine processed kimberlite containment facility or fine PKC) where it is stored beneath a pond of process water. A much smaller amount of coarse-grained waste material is stored subaerially in a pile (called the coarse processed kimberlite containment facility or coarse PKC). The bulk of the processed kimberlite from the fine PKC is characterized by major abundances of serpentine minerals (predominantly lizardite) and high-Mg forsterite with minor amounts of calcite, Cr-rich diopside, Mg-rich garnets, plagioclase, phlogopite, quartz, and clay minerals (predominantly vermiculite and possibly smectite or interstratified clays). Traces of chromite, dolomite, muscovite, perovskite, and amphibole have also been observed. The mineralogy of the coarse PKC is similar to that of the fine PKC, but differs notably in that trace amounts of pyrite and jarosite have been observed in the course of microscope work on the coarse processed kimberlite.

Efflorescent crusts of secondary minerals are common in the fine PKC and occur occasionally in the coarse PKC at Diavik. These occur in four distinct modes (Fig. 2.2):

(1) white, powdery efflorescences on vertical and horizontal surfaces in the fine PKC, (2) crusts of a white, powdery precipitate just below the surface of the coarse PKC, (3) preserved efflorescent minerals at depth within the fine PKC, and (4) surface crusts in the fine PKC where nutrient-rich waste water from the sewage treatment plant has been deposited. We have observed the presence of nesquehonite ($MgCO_3 \cdot 3H_2O$) in all four types of efflorescence. Nesquehonite is a common low-temperature alteration product of serpentinite and serpentine-rich mine wastes (e.g., Suzuki and Ito 1973; Suzuki and Ito 1974; Inaba et al. 1985; Giester et al. 2000; Wilson et al. 2006; Wilson et al. 2009). Nesquehonite also forms by evaporation in creeks and playa environments that are fed by groundwater derived in part from drainage through ultramafic rock units (e.g., O'Neil and Barnes 1971; Power et al. 2007; Power et al. 2009).

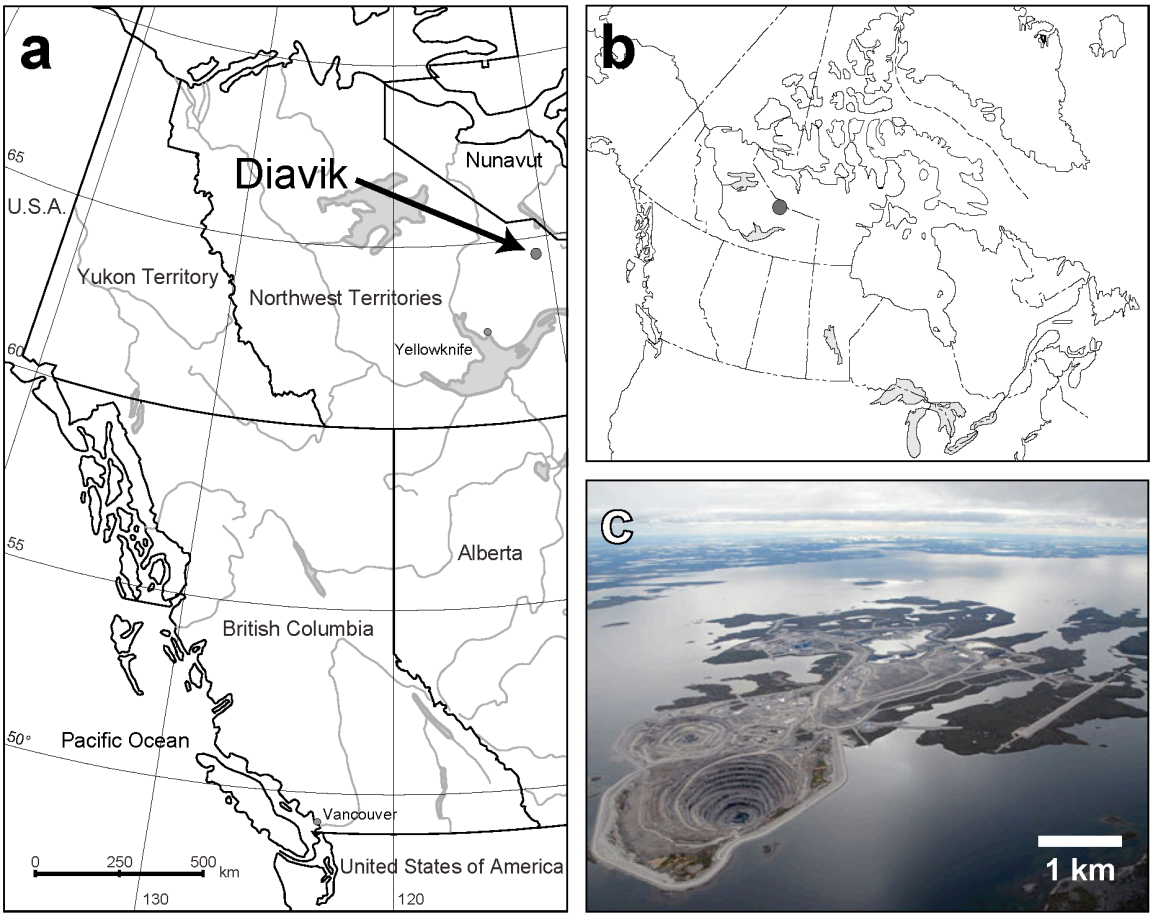

Figure 2.1: (a) and (b) Location of Diavik Diamond Mine, Northwest Territories, Canada. (c) Aerial photograph of the Diavik Diamond Mine (courtesy of Diavik Diamond Mines Inc.).

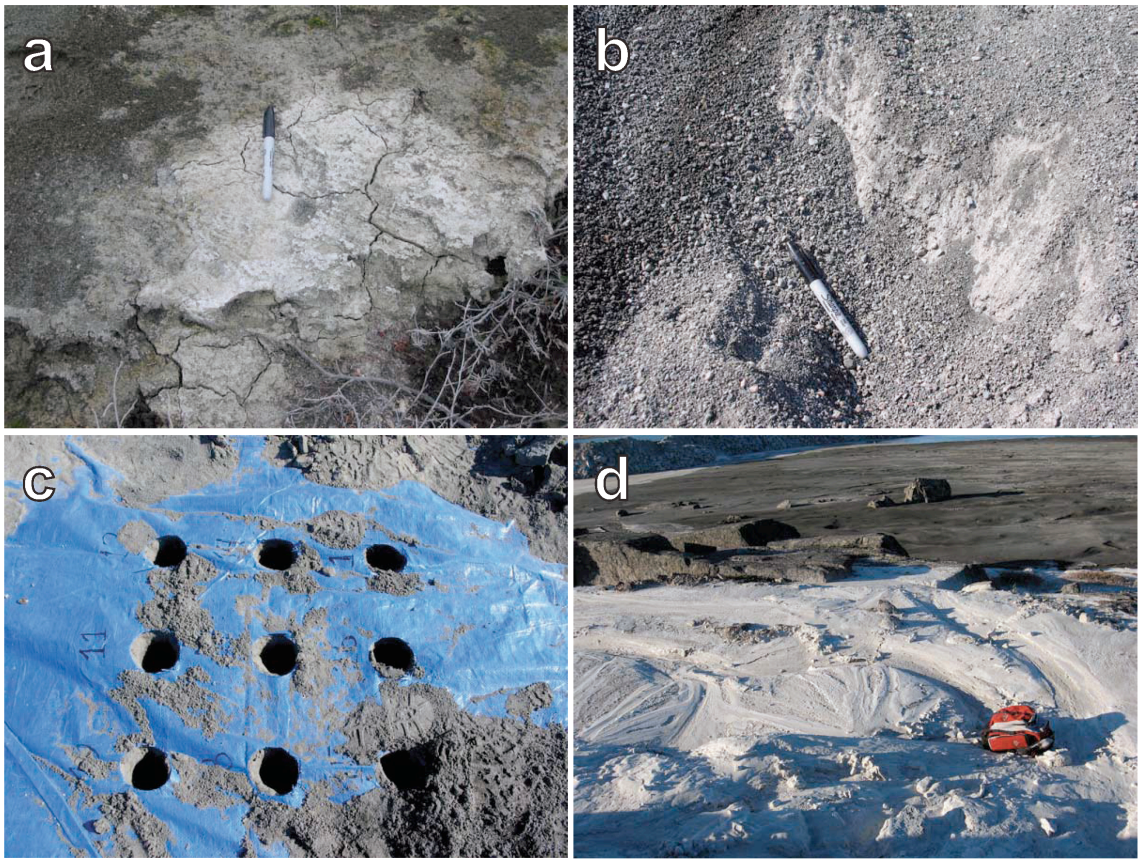

Figure 2.2: Modes in which nesquehonite and other efflorescent minerals have been identified in the processed kimberlite at Diavik: (a) as a white, powdery film on horizontal and vertical surfaces in the fine PKC (Group 1), (b) as horizontally continuous precipitates immediately below the surface of the coarse PKC (Group 2), (c) as preserved efflorescent precipitates at depth beneath the surface of the fine PKC (Group 3, show here as 10-cm diameter core holes), and (d) as discrete deposits of pale-coloured material on some horizontal surfaces in the fine PKC (Group 4, rucksack for scale).

Group 1 efflorescences are widespread at the surface of the fine PKC around the circumference of the pond. They are typically rich in either nesquehonite or sulphate minerals (commonly gypsum). Group 2 efflorescences contain sulphate minerals (variably some combination of anhydrite, gypsum, epsomite, hexahydrite, syngenite, and possibly butlerite) or occasionally nesquehonite. Efflorescences from Groups 1 and 2 are observed as thin films less than 1 mm in thickness. Group 3 comprises efflorescent nesquehonite, preserved in trace amounts at depth within the fine PKC (where trace abundance is defined here as < 0.5 wt.%). Group 4 crusts occur more rarely as thick (> 1 mm), continuous patches near the perimeter wall and road of the fine PKC. These deposits are rich in portlandite and Ca- and Na-carbonate minerals (primarily calcite,

gaylussite, natrite, thermonatrite, trona, and vaterite) with occasional nesquehonite, gypsum, and ettringite.

Although Group 1 and 4 efflorescences cover a significant portion of the surface of the processed kimberlite beached along the circumference of the fine PKC pond, we have found that only Group 3 efflorescences persist at depth. These preserved crusts of nesquehonite likely represent most of the carbon mineralization in either the fine or coarse PKC at Diavik, and are the main focus of this study.

Most of the sampling conducted at Diavik was done in August 2006 in the fine PKC with some additional samples having been collected from the coarse PKC. Limited sampling was carried out in September 2005. Sampling locations for the fine PKC are provided in Figure 2.3. One sample examined in this study was taken from just below the surface of the coarse PKC and three of the samples were collected by trowel from the surface of the fine PKC. The remaining 16 samples were collected with a sediment-coring device, in 10-cm lengths, from depths of either 0 cm (i.e., from 0-10 cm depth) or 100 cm (i.e., from 95-105 cm depth) below the surface of the fine PKC.

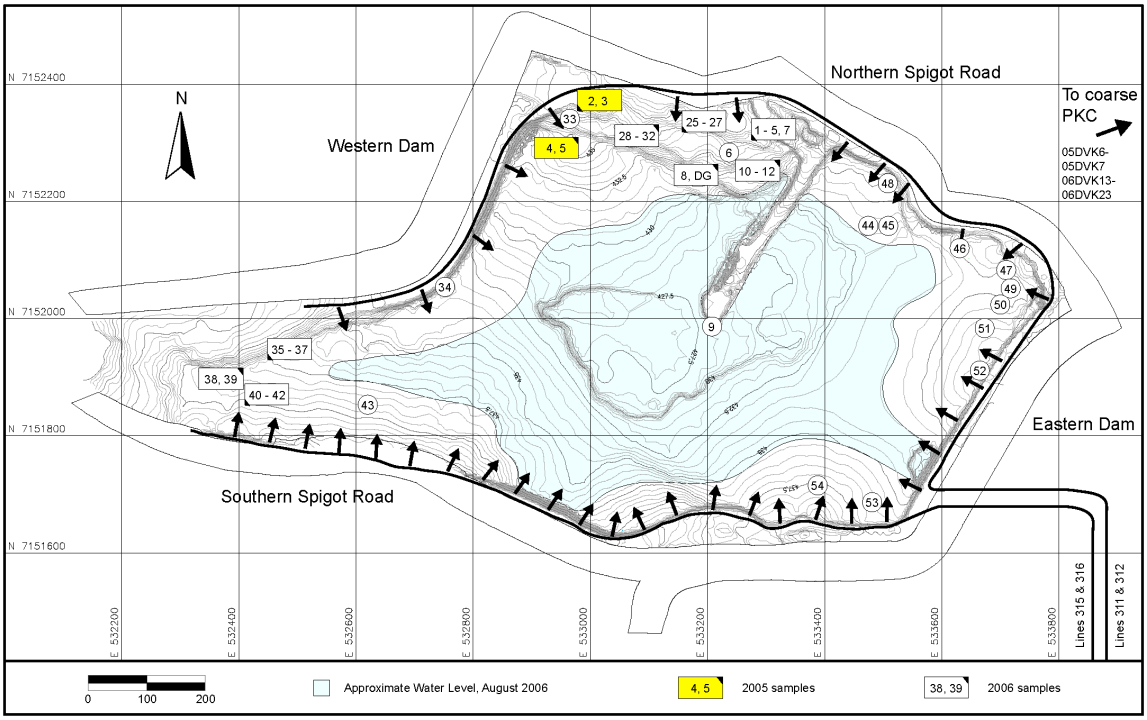

Figure 2.3: Sampling locations within the storage facility for processed kimberlite fines at Diavik (fine PKC). Modified from a report by Reinson (2006) for Golder Associates Ltd. Small arrows indicate locations of discharge spigots. The approximate extent of the tailings pond is shown for late summer 2006. Co-ordinates are given in NAD 83. Bathymetric data were collected in 2005 (from Reinson 2006).

2.3 Experimental method

2.3.1 Sample preparation and data collection

Thirteen mixtures of pure mineral samples were prepared to simulate processed kimberlite (mine tailings) (Table 2.1). Minerals used in these mixtures represent those commonly found in the tailings at Diavik: lizardite, high-Mg forsterite, diopside, almandine-pyrope series garnet, phlogopite, calcite, quartz, oligoclase, and nesquehonite. The abundance of nesquehonite in the synthetic tailings was varied from 0.10 wt.% to 5.00 wt.% in order to assess the applicability of the Rietveld method (1969), Chung's (1974) normalized RIR method (also known as the "adiabatic method"), and the internal standard method (Alexander and Klug 1948) for measuring the abundance of this phase for a range of trace and minor abundances.

Samples of the constituent minerals were checked for purity using X-ray powder diffraction and energy-dispersion X-ray spectroscopy. The serpentine used in the synthetic mixtures and several samples of serpentine from Diavik were identified to be predominantly lizardite using X-ray powder diffraction and dispersive Raman microspectroscopy according to the method of Rinaudo et al. (2003). All crystalline standards, with the exception of the lizardite, were at least 99% pure. Rietveld refinement results indicated that the lizardite contained 1.1 wt.% calcite.

Pure mineral phases were weighed on a scale with ± 0.1 mg precision. Prior to each use, the scale was calibrated and tested for accuracy using a set of weights ranging from 1 mg to 500 mg. Variable amounts of forsterite (30.00, 33.00, 34.00, 34.50, 34.75, and 34.90 wt.%) and nesquehonite (5.00, 2.00, 1.00, 0.50, 0.25, and 0.10 wt.%) were added to the mixtures in Series 1 and 2, such that the abundance of these two phases totalled 35.00 wt.% (Table 2.1). Mixtures containing 0.10-0.50 wt.% nesquehonite were weighed to total 4.00 g, and those containing 1.00-5.00 wt.% nesquehonite totalled 2.00 g (after Bish and Chipera 1991). Samples containing less than 0.10 wt.% nesquehonite were not prepared because large uncertainties would result from weighing and any attempt to homogenize such mixtures.

Table 2.1: Compositions of synthetic processed kimberlite renormalized to exclude corundum and taking account of calcite contamination in lizardite.

Phase	Series 1						Series 2					
	07lsk1r	**07lsk2r**	**07lsk3r**	**07lsk4r**	**07lsk5r**	**07lsk6r**	**07lsk7r**	**07lsk8r**	**07lsk9r**	**07lsk10r**	**07lsk11r**	**07lsk12r**
Lizardite	44.50	44.50	44.50	44.50	44.50	44.50	34.62	34.62	34.62	34.62	34.62	34.62
Forsterite	34.90	34.75	34.50	34.00	33.00	30.00	34.90	34.75	34.50	34.00	33.00	30.00
Nesquehonite	0.10	0.25	0.50	1.00	2.00	5.00	0.10	0.25	0.50	1.00	2.00	5.00
Almandine-Pyrope	5.00	5.00	5.00	5.00	5.00	5.00	5.00	5.00	5.00	5.00	5.00	5.00
Calcite	5.50	5.50	5.50	5.50	5.50	5.50	5.38	5.38	5.38	5.38	5.38	5.38
Diopside							5.00	5.00	5.00	5.00	5.00	5.00
Oligoclase							5.00	5.00	5.00	5.00	5.00	5.00
Phlogopite	5.00	5.00	5.00	5.00	5.00	5.00	5.00	5.00	5.00	5.00	5.00	5.00
Quartz	5.00	5.00	5.00	5.00	5.00	5.00	5.00	5.00	5.00	5.00	5.00	5.00
Total	100.00	100.00	100.00	100.00	100.00	100.00	100.00	100.00	100.00	100.00	100.00	100.00

Each mixture was ground under anhydrous ethanol using agate grinding elements for six minutes in a McCrone micronizing mill to reduce the mean grain size and to ensure homogenization. At this point, grinding was halted and an internal standard of synthetic corundum (prepared from smelter grade alumina according to Australian Standard AS 2879.3-1991) was added to each sample such that it constituted 10 wt.% of the renormalized weight. Each sample was then ground for an additional four minutes, for a total grinding time of 10 minutes. Samples of synthetic processed kimberlite were dried at room temperature under a fume hood and disaggregated with an agate mortar and pestle once dry. One duplicate mixture (Series 1, 07lsk6r-2) and one additional mixture (Series 2, 07lsk12r) were prepared using 10 wt.% of NIST 676a corundum as an internal standard.

Grinding times were chosen to minimize both degradation of the lizardite structure and contamination of the samples by quartz from the grinding elements while optimizing particle-size reduction and homogenization. The micronizing mill was used to reduce the mean particle size of the samples to micron or sub-micron level. Knowledge of the mean grain size of the narrow size distribution afforded by micronizing allows for the use of the Brindley (1945) correction for microabsorption in Rietveld refinements.

Diopside and oligoclase were omitted from the Series 1 mixtures to assess the effect of the (110) reflection of diopside (d≈6.47 Å) and the $(1\,\bar{1}\,0)$, (110), (020), and (001) reflections of oligoclase (d≈6.30, 6.34, 6.38, and 6.39 Å, respectively) on detection and measurement of the (101) and $(10\,\bar{1})$ reflections of nesquehonite (d≈6.48 Å and d≈6.52 Å, respectively).

In addition, 20 samples of processed kimberlite from Diavik were prepared to assess the Rietveld, RIR, and internal standard methods on natural samples of kimberlite mine tailings. Samples were left in a drying hood for a minimum of 48 hours and were then homogenized mechanically with a spatula. Once dried and homogenized, an aliquot of each sample (i.e., 50–100 g) was powdered using a tungsten carbide ringmill. Two-gram aliquots of natural processed kimberlite were ground under ethanol for six minutes in the McCrone micronizing mill. At this point, 10 wt.% of synthetic corundum was added to each sample and the samples were ground for an additional four minutes for a total grinding time of 10 minutes.

Natural and synthetic samples were mounted in a back-loading aluminum cavity holder of the design described by Raudsepp and Pani (2003). Powdered samples were loaded against the roughened surface of a sheet of glass that covered the top of the cavity. Data for Rietveld refinement of synthetic processed kimberlite were collected on specimens prepared in two ways: (1) on specimens that had been serrated with a razor blade along two axes (one parallel to the axis of the diffractometer goniomenter and the second in the perpendicular direction) and (2) on non-serrated specimens. Specimens were serrated to inhibit preferred orientation of crystallites, particularly those of phlogopite. Data for Rietveld refinement of natural processed kimberlite from Diavik were collected from non-serrated specimens. The specimens used to collect data for reference intensity ratios were not serrated with a razor blade so as to preserve the preferred orientation of nesquehonite on {101}, and thus improve detection of the (101) and $(10\bar{1})$ reflections. Additional RIR data were collected for three samples (Series 2, 07lsk7r, 07lsk8r, and 07lsk9r) that were front-loaded into the cavity holder to assess the impact of mounting procedure on preferred orientation and detection of nesquehonite.

XRPD data were collected on a Siemens D5000 θ-2θ diffractometer equipped with a VÅNTEC-1 detector. A long, fine-focus Co X-ray tube was operated at 35 kV and 40 mA and an Fe monochromator foil was employed. All data for Rietveld refinement were collected with a step size of 0.02° 2θ and counting time of 1s/step over a range of 3-80° 2θ. Data for reference intensity ratios and the calibration curve were collected using a step size of 0.02° 2θ and a counting time of 120 s/step over the ranges 15.2-16.5° 2θ and 43.6-45.1° 2θ, for the (101) and $(10\bar{1})$ reflections of nesquehonite and the (110) reflection of corundum, respectively. In order to improve detection of the (101) and $(10\bar{1})$ reflections and confirm the presence of trace nesquehonite in the samples of natural tailings, data were collected on specimens that had been ring-milled and subsequently smear-mounted onto glass slides with anhydrous ethanol. These data were collected using a step size of 0.02° 2θ and a counting time of 40 s/step over the range 15.2-16.5° 2θ. Collection of XRPD data for the RIR method and calibration curve took 6 hours and 12 minutes for the reference peaks of nesquehonite and 6 hours and 34 minutes for the corundum reference peak. Counting times for RIR data were chosen to allow both patterns, for nesquehonite and corundum, to be collected overnight. Data for each

Rietveld refinement were acquired in 1 hour and 12 minutes, taking considerably less time.

2.3.2 Rietveld refinement and quantitative phase analysis

Rietveld refinements were done with Rietveld refinement software Topas Version 3 (Bruker AXS 2004) using the fundamental parameters approach (Cheary and Coelho 1992). Sources of crystal structure data for the phases in synthetic and natural samples are listed in Table 2.2. Refinements were done using the method of Wilson et al. (2006) to compensate for planar disorder in lizardite. Specifically, peak intensities were extracted independently of atomic scattering from an XRPD pattern of the high-purity lizardite standard with the Pawley method (Pawley 1981). The extracted intensities with the cell parameters and space group of lizardite-1T (Mellini and Viti 1994) were used to fit the lizardite in XRPD patterns of synthetic and natural kimberlites as a peaks phase. Fourth-order symmetrized harmonics were used to model anisotropic peak shape in lizardite (Järvinen 1993). Without reference to atomic co-ordinates, the relative intensities of the calculated intensities in a peaks phase are unconstrained by atomic scattering. To prevent interference of lizardite peaks with peaks from other phases, their relative intensities were initially held constant and were refined only after the peaks of the other phases had been fitted. It is important to note that other serpentine minerals (i.e., chrysotile, antigorite, polygonal serpentine) have been observed in the groundmass of kimberlites (e.g., Mitchell 1986; Mitchell and Putnis 1988; Sharp et al. 1990) and may be present in small amounts in the kimberlite at Diavik. As a consequence of using a peaks phase to model the lizardite component of kimberlite samples, other, minor serpentine phases may also be fitted by the lizardite peaks phase. Furthermore, this method cannot be used to quantify more than one disordered phase per sample (e.g., lizardite plus another serpentine mineral) and does not account for additional, X-ray amorphous phases (Wilson et al. 2006).

Table 2.2: Sources of crystal structure data for Rietveld refinement and values used to compute neutralization potential (NP) of processed kimberlite.

Mineral	Source of Structure	NP	Source of NP Data
Albite (Oligoclase)	Armbruster et al. (1990)	1	Jambor et al. (2007)
Almandine-Pyrope	Armbruster et al. (1992)	3	Jambor et al. (2007)
Calcite	Maslen et al. (1995)	1000	By definition
Corundum	Brown et al. (1993)	n/a [a]	n/a [a]
Diopside	Ahn et al. (1986)	5	Jambor et al. (2002, 2007)
Forsterite	Yu (1997)	38	Jambor et al. (2007)
Lizardite-1T	Mellini and Viti (1994)	32	Jambor et al. (2007)
Nesquehonite	Giester et al. (2000)	723	Calculated from Lawrence and Scheske (1997)
Phlogopite-1M	Collins and Catlow (1992)	8	Jambor et al. (2007)
Quartz	Glinnemann et al. (1992)	0	Jambor et al. (2007)
Vermiculite	Shirozu and Bailey (1966)	29	Jambor et al. (2002)

[a] n/a - not applicable to computation of neutralization potential.

Backgrounds for Series 1 synthetic processed kimberlite were modelled using first-order Chebychev polynomials for serrated specimens and second-order Chebychev polynomials for non-serrated specimens with an additional $1/x$ term to aid in the fitting of the background curve at low angles of diffraction. Higher-order Chebychev polynomials (i.e. second-order for serrated specimens and third-order for non-serrated specimens) were necessary to model the backgrounds for the more complex samples in Series 2 and the samples of natural processed kimberlite from Diavik. In each refinement, the zero error was refined and the Lorentzian crystallite size and cell parameters were refined for all phases. Refinement parameters were turned on in the same order for all synthetic and natural processed kimberlites. Preferred orientation of detectable mineral phases was not

corrected for because this effect was relatively minor except in phlogopite. Contamination from the agate grinding elements of the micronizing mill was tested on pure mineral phases used in this study. The amount of contamination by agate when grinding corundum was also assessed. Grinding corundum for under four minutes resulted in less than 1 wt.% contamination by agate while longer grinding times gave rise to more significant contamination. Contamination of other pure mineral phases by agate was considerably less than 1 wt.% using a grinding time of 10 minutes. Because quartz is a minor component of the synthetic and natural tailings, this contamination may result in overestimates of the abundance of this phase.

The crystallinity of the synthetic corundum, which was used as an internal standard, was assessed by Rietveld refinement with reference to NIST 676a synthetic corundum. Two 50-50 wt.% mixtures were prepared for this purpose and XRPD data were collected for each of the following: (1) NIST 676a corundum and an in-house standard of annealed synthetic fluorite and (2) the same synthetic fluorite and the synthetic corundum. NIST 676a is certified to be 99.02 ± 1.11 wt.% crystalline. Refinement of the pattern with NIST corundum and fluorite gave 50.2 wt.% corundum and 49.8 wt.% fluorite. From these values, the in-house fluorite standard was determined to be 98.1 +1.0/-1.1 wt.% crystalline. Refinement of the pattern with synthetic corundum and fluorite gave values of 50.3 wt.% corundum and 49.7 wt.% fluorite. Based on this result, the crystallinity of the synthetic corundum was determined to be 99.3 +1.0/-1.1 wt.%. It is important to note that the Rietveld refinement results for both mixtures are within error of the expected values, as defined empirically by previous studies on weighed mixtures of pure mineral phases (e.g., Hill and Howard 1987; Bish and Howard 1988; Bish and Post 1993; Raudsepp et al. 1999; De la Torre et al. 2001; De la Torre and Aranda 2003; Ufer et al. 2004; Omotoso et al. 2006; Wilson et al. 2006). Therefore, the actual crystallinities of the in-house fluorite standard and the synthetic corundum may differ from calculated values by several weight percent. However, it can be said with confidence that NIST 676a, the synthetic corundum, and the in-house fluorite standard have comparable crystalline fractions. The amount of lizardite in natural samples and most of the synthetic mixtures was calculated based on a spike of 9.93 wt.% of synthetic corundum. The amount of lizardite was calculated based on a 9.90 wt.% spike for the two

mixtures made with NIST 676a corundum (i.e., 07lsk6r-2 and 07lsk12r). When mineral abundances are calculated assuming a 10 wt.% spike of synthetic corundum the values differ only in the third significant figure. Refinement results were recalculated and renormalized for each sample using the method of Gualtieri (2000). Corundum was chosen over fluorite as the spike phase because it gives more peaks over 3-80° 2θ (CoKα) and has fewer overlapped peaks with the constituent minerals of processed kimberlite.

A Brindley radius (Brindley 1945) of 2.5 μm was used to correct for microabsorption in all phases. Scanning electron microscopy, done after milling, on natural samples of processed kimberlite revealed occasional sheets of phlogopite with diameters as great as 40 μm (Fig. 2.4a). In synthetic mixtures, sheets of phlogopite were observed that reached diameters up to 100 μm (Fig. 2.4b). Diameters of other phases in both synthetic and natural samples infrequently exceeded 5 μm. For comparison, laser-diffraction based particle-size analysis was done on two samples at the Norman B. Keevil Institute of Mining Engineering, UBC. Each sample was coned and quartered several times to obtain a representative subsample, which was mixed with distilled water and a small amount of Triton X-100 dispersant. A small, representative aliquot was then taken and analyzed using a Malvern Mastersizer laser diffraction instrument with ultrasonic treatment. Average particle diameters of 3.57 μm (r = 1.79 μm) and 7.83 μm (r = 3.92 μm) were obtained for a natural sample of processed kimberlite fines (05DVK7) and a synthetic mixture (07lsk3r), respectively. Observations made with the scanning electron microscope indicate that phlogopite was the only phase resistant to milling. Rietveld refinement results did not change significantly when the Brindley radius for phlogopite was varied within an order of magnitude of 2.5 μm. As a result, the default radius of 2.5 μm was taken to be representative of the natural samples and synthetic mixtures.

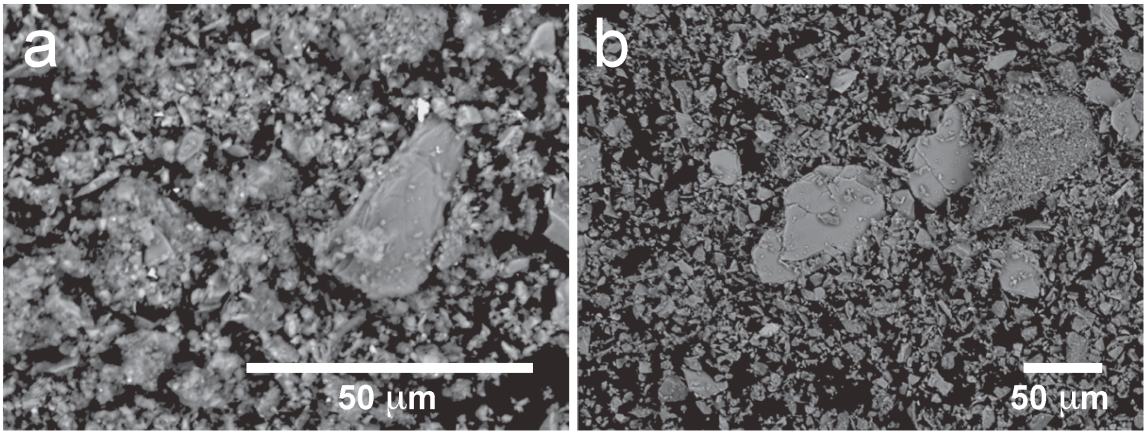

Figure 2.4: Backscattered SEM images of (a) 05DVK7 and (b) 07lsk3r. Large sheets of phlogopite remain after 10 minutes grinding with the McCrone micronizing mill.

2.3.3 Quantitative analysis of nesquehonite using the RIR method and the internal standard method

Reference intensity ratio (RIR) analyses were done using the normalized RIR method (Chung 1974). The RIR is defined as the ratio of the integrated intensity of the overlapping (101) and $(10\bar{1})$ reflections of nesquehonite to the integrated intensity of the (110) peak of synthetic corundum in a 50-50 wt.% mixture. The (101) and $(10\bar{1})$ reflections were chosen because they are the most intense in the X-ray diffraction pattern for nesquehonite. As the more commonly used (113) reflection of corundum overlaps with reflections from other phases in the processed kimberlite, the (110) reflection was used instead.

Peak positions and integrated intensities were determined using Topas Version 3 (Bruker AXS 2004). Peak positions were located using a first-derivative peak search or, in the case of the severely overlapping reference peaks of nesquehonite, located manually based on knowledge of the crystal structure. Profile refinement for reference peaks was done in two ways: using the fundamental parameters approach (Cheary and Coelho 1992) and using a Pseudo-Voigt profile. Peak position, integrated intensity, and Lorentzian crystallite size were refined for each reference peak and the Lorentz polarization correction was applied. RIR values were calculated, using both profile types, as the average of six independent measurements (after Bish and Chipera 1991). RIR values for the (101) and $(10\bar{1})$ reflections of nesquehonite relative to the (110) reflection of corundum were 0.36 ± 0.02 and 0.37 ± 0.02 for fundamental parameters and Pseudo-

Voigt profiles, respectively. Average peak positions (CoKα), using fundamental parameters, were 15.75° ± 0.01° 2θ [($10\bar{1}$), nesquehonite], 15.84° ± 0.01° 2θ [(101), nesquehonite], and 44.10° ± 0.01° 2θ [(110), corundum]. Average peak positions (CoKα), using a Pseudo-Voigt profile, were 15.77° ± 0.01° 2θ [($10\bar{1}$), nesquehonite], 15.85° ± 0.01° 2θ [(101), nesquehonite], and 44.10° ± 0.01° 2θ [(110), corundum]. RIR values were also determined by fitting the overlapping (101) and ($10\bar{1}$) reflections of nesquehonite using a single peak. These values were 0.41 ± 0.02 for fundamental parameters and 0.41 ± 0.05 using a Pseudo-Voigt profile. Profile refinements were visibly and statistically better using the more physically correct two-peak fit for nesquehonite. As such, all data reported fit the overlapping reference reflections of nesquehonite with two peaks. Errors reported on quantitative data obtained using the RIR method are as 1σ.

Profile refinements were done on the synthetic mixtures in Series 1 and 2 using both profile types (i.e., fundamental parameters and Pseudo-Voigt) and using first, second, and fourth-order Chebychev polynomials to model the background. A first-order background gave the most accurate and reproducible results with fundamental parameters and Pseudo-Voigt profile refinements. Therefore, profile refinements for natural samples of processed kimberlite also were done using first-order Chebychev polynomials. Nearby reflections from phases other than nesquehonite and corundum were also fitted in order to properly partition the intensity from partially overlapping peaks.

A calibration curve was constructed by plotting the ratio of the intensities of the (101) and ($10\bar{1}$) reflections of nesquehonite to the (110) reflection of corundum versus the nominal abundance of nesquehonite for Series 1 mixtures (after Alexander and Klug 1948). Intensities extracted using the fundamental parameters approach (as described above) were used to produce the calibration curve.

2.4 Results and discussion

2.4.1 Synthetic mine tailings

2.4.1.1 Rietveld refinement results

Rietveld refinements were initially done on data collected from serrated specimens of synthetic kimberlite tailings. The results for Series 1 and 2 mixtures gave significant overestimates for the abundance of lizardite while underestimating the abundances of forsterite and the minor phases. This effect bore a resemblance to the pattern of misestimates that would have resulted from a weighing error for the internal standard (e.g., Gualtieri 2000; Wilson et al. 2006). More precisely, it appeared as though there had been significantly less than 9.93 wt.% crystalline corundum (or 9.90 wt.% for the two samples spiked with NIST 676a) in all of the synthetic mixtures. However, the minor weighing error and negligible sample loss monitored throughout preparation and analysis of these samples could not account for the magnitude of the misestimates. Also, that the same misestimates were observed in all synthetic tailings to a similar extent suggested that the abundance refined for lizardite was in fact the abundance of lizardite plus a considerable amount of amorphous material in each sample. Furthermore, each mixture phase (with the exception of lizardite) was underestimated to a different and internally consistent extent. Under this interpretation, the weighed abundances for forsterite and the minor phases would have been underestimated because the refined results only accounted for the crystalline component of each mineral standard. Previous studies have identified X-ray amorphous material in association with weathering features in feldspars (e.g., Rimsaite 1979; Kawano and Tomita 1996). Banfield et al. (1990) observed amorphous silica and nanoscale patches of a smectite-group mineral in olivine crystals from Abert Rim, Oregon, USA. Additionally, work by Wang et al. (1991) suggests that mantle-derived pyrope may be partially amorphous and contain structurally-bound water. However, it is unlikely that considerable amounts of amorphous and/or nanocrystalline material would be associated with the large, relatively unaltered, single crystals chosen for use as mineral standards.

Operating under the assumption that the standard minerals could contain undetected material, specimens of each mineral were prepared with the addition of 10 wt.% synthetic corundum to measure the effect of possible amorphous content on Rietveld refinement results. In serrated specimens (and neglecting refinement error), amorphous contents appeared to range from 6.3 +1.2/-0.7 wt.% of the quartz standard to 24.1 +0.9/-0.6 wt.% of the oligoclase (Table 2.3). The known compositions given in Table 2.1 for the synthetic mixtures were recalculated assuming that these misestimates were due to amorphous content associated with the pure mineral standards. Subtracting the supposed amorphous component from the expected concentration of each phase leads to values that are lower than initially expected for forsterite, nesquehonite, almandine-pyrope, calcite, diopside, oligoclase, and quartz. Lizardite concentrations increase when assumed to represent the concentration of lizardite plus the supposed amorphous content associated with the other mineral phases.

Rerunning non-serrated specimens of the synthetic processed kimberlites and the high-purity mineral standards from which they were made gives very different results. Rietveld refinement results for non-serrated specimens of standard minerals plus corundum were well within error, typically being within ± 0.5 wt.% and not exceeding ± 1.0 wt.% of nominal abundances. This result indicates that there is no detectable amorphous and/or nanocrystalline material in any of the pure mineral standards and demonstrates that underestimates were caused by surface roughness introduced by serration. Surface roughness is known to reduce the intensities of Bragg peaks, with the reduction increasing in severity toward small scattering angles (e.g., de Wolff 1956; Suortti 1972). This effect would have led to the variable intensity loss for different mineral phases.

Table 2.3: Crystallinity of internal standard phases and estimates of crystallinity from serrated samples suffering from surface roughness effects.

Phase	Internal Standard	Crystalline (wt.%)	Uncertainty [a] (wt.%)	Amorphous (wt.%)	Uncertainty [a] (wt.%)
NIST 676a α-Al_2O_3 [b]	n/a	99.02	1.11	0.98	1.11
UBC CaF_2 [b,d]	NIST 676a	98.1	+1.0/-1.1	1.9	+1.1/-1.0
Synthetic α-Al_2O_3 [b,e]	UBC CaF2	99.3	+1.0/-1.1	0.7	+1.1/-1.0
Lizardite [c,d]	n/a	unknown	n/a	unknown	n/a
Forsterite (PMM 676) [c,f]	Synthetic α-Al_2O_3	91.2	+0.7/-1.1	9.8	+1.1/-0.7
Nesquehonite (synthetic) [c,g]	Synthetic α-Al_2O_3	89.1	+1.3/-1.9	10.9	+1.9/-1.3
Almandine-Pyrope (PME 20807) [c,f]	Synthetic α-Al_2O_3	88.0	+0.7/-1.1	12.0	+1.1/-0.7
Calcite [c,h]	Synthetic α-Al_2O_3	86.7	+0.7/-1.1	13.3	+1.1/-0.7
Diopside [c,h]	Synthetic α-Al_2O_3	88.1	+0.7/-1.1	11.9	+1.1/-0.7
Oligoclase (CMN F80-22-7) [c,i]	Synthetic α-Al_2O_3	75.9	+0.6/-0.9	24.1	+0.9/-0.6
Phlogopite (Comet Mine, Québec) [c,h]	Synthetic α-Al_2O_3	~100	n/a	none detected	n/a
Quartz [c,h]	Synthetic α-Al_2O_3	93.7	+0.7/-1.2	6.3	+1.2/-0.7

[a] Calculated assuming crystallinity of spike phase cannot exceed 100%.
[b] Non-serrated specimen.
[c] Serrated specimen.
[d] From our laboratory collection.
[e] From C. Kelaart, Bruker Biosciences Pty Ltd (Australia).
[f] From The Pacific Museum of the Earth, University of British Columbia, Vancouver, BC, Canada.
[g] Courtesy of I.M. Power, University of Western Ontario, London, ON, Canada. As described by Power et al. (2007).
[h] From local mineral dealers, Vancouver, BC, Canada.
[i] From The Canadian Museum of Nature, Ottawa, ON, Canada.

Results of quantitative phase analysis on serrated and non-serrated specimens of synthetic processed kimberlites are given in Tables 2.4 and 2.5 and Figures 2.5, 2.6, and 2.7. Much of the deviation in the results for serrated specimens is explained by intensity loss due to surface roughness (which is modelled as "amorphous content" in Fig. 2.5). Refined abundances for non-serrated specimens (Table 2.5 and Fig. 2.6) show significantly less deviation from expected abundances for lizardite, nesquehonite, almandine-pyrope, and oligoclase. Also, refinement results for forsterite and calcite are somewhat improved whereas diopside, phlogopite, and quartz tend to be overestimated. On average, the refinement bias (after Omotoso et al. 2006; Tables 2.4 and 2.5) is nearly halved by running profile refinements on non-serrated specimens (i.e., the average bias is reduced from 19.7 to 11.8). Despite the increase in accuracy, the fit statistics for

refinements done on non-serrated specimens suffer as a consequence of the poor fit to phlogopite. Also, large overestimates (as much as ~50% relative) for quartz result from overlap of the (003) reflection of phlogopite and the (011) reflection of quartz. Because no correction was made for preferred orientation of phlogopite, the (003) reflection was inadequately modelled and the intensity was fitted by the structure of quartz. Other major sources of error in Rietveld refinement may include (1) the large increase in relative error for refinements of minor phases and (2) compositional variation in phases subject to solid solution.

Relative error is known to increase rapidly for Rietveld refinement of the concentrations of minor phases. Raudsepp et al. (1999) and Dipple et al. (2002) found that relative error increases rapidly for concentrations below 6 wt.% for conditions of data collection used in our laboratory. Although relative errors can be high for minor phases (Fig. 2.7), absolute errors are small and seldom exceed 1 wt.% for non-serrated specimens (Table 2.6).

Systematic underestimates of some phases, forsterite and almandine-pyrope in particular, may be due to incorrect compositional information. Electron microprobe (EMP) data were not obtained for the pure mineral standards or for grains of minerals from the processed kimberlite at Diavik. Instead, compositions of the almandine-pyrope and forsterite standards were estimated from energy dispersive X-ray spectroscopy and XRPD data. A large compositional variation in the peridotitic, eclogitic, and crustal garnets found at Diavik (McLean et al. 2007) along with a heterogeneous distribution in the processed kimberlite inhibits attempts at constraining the chemical composition of garnet by Rietveld refinement. The composition of forsterite from kimberlite commonly varies from Fo_{85} to Fo_{95} (Mitchell 1986). At Diavik this composition is generally in the vicinity of Fo_{90} (personal communication, R.C. Brett, UBC). Fo_{90} and almandine-pyrope with Mg/(Mg+Fe) = 0.70 were used in refinements of synthetic mixtures. Because these values also approximate the composition of the forsterite and the predominantly eclogitic garnet at Diavik (McLean et al. 2007), they were retained for refinement of the natural samples. These values are estimates only, and as a result they introduce further uncertainty into the refinements.

Table 2.4: Rietveld refinement results for serrated specimens of synthetic processed kimberlite.

Phase	Series 1							Series 2					
	07lsk1r	07lsk2r	07lsk3r	07lsk4r	07lsk5r	07lsk6r	07lsk6r-2 (NIST)	07lsk7r	07lsk8r	07lsk9r	07lsk10r	07lsk11r	07lsk12r (NIST)
Lizardite + Amorphous	53.2	52.4	53.4	51.1	54.6	54.5	55.9	43.5	43.0	44.9	46.3	44.6	48.7
diff [a]	8.7	7.9	8.9	6.6	10.1	10.0	11.4	8.9	8.4	10.3	11.7	9.9	14.1
Forsterite	30.2	29.9	29.1	30.1	27.0	25.8	25.0	30.3	30.1	29.8	27.6	26.9	24.6
diff	-4.7	-4.8	-5.4	-3.9	-6.0	-4.2	-5.0	-4.6	-4.7	-4.7	-6.4	-6.1	-5.4
Nesquehonite	b/d [b]	b/d [b]	0.5	0.8	1.3	2.7	3.4	b/d [b]	b/d [b]	0.3	0.7	1.4	4.4
diff	-0.1	-0.3	0.0	-0.2	-0.7	-2.3	-1.6	-0.1	-0.3	-0.2	-0.3	-0.6	-0.6
Almandine-Pyrope	4.6	4.2	3.8	3.6	4.3	3.6	4.0	4.0	3.8	3.6	3.6	3.6	3.3
diff	-0.4	-0.8	-1.2	-1.4	-0.7	-1.4	-1.0	-1.0	-1.2	-1.4	-1.4	-1.4	-1.7
Calcite	3.7	4.2	3.7	4.4	3.9	4.0	3.7	4.2	4.2	4.0	3.9	4.1	3.8
diff	-1.8	-1.3	-1.8	-1.1	-1.6	-1.5	-1.8	-1.2	-1.2	-1.4	-1.5	-1.3	-1.5
Diopside								4.9	4.9	4.7	4.2	5.0	3.7
diff								-0.1	-0.1	-0.3	-0.8	0.0	-1.3
Oligoclase								3.7	3.9	4.0	4.0	3.8	2.9
diff								-1.3	-1.1	-1.0	-1.0	-1.2	-2.1
Phlogopite	4.1	4.3	4.8	4.7	4.3	4.4	3.4	4.7	4.6	4.1	4.7	5.8	3.8
diff	-0.9	-0.7	-0.2	-0.3	-0.7	-0.6	-1.6	-0.3	-0.4	-0.9	-0.3	0.8	-1.2
Quartz	4.2	4.9	4.7	5.2	4.6	4.9	4.7	4.7	5.5	4.7	5.1	4.8	4.8
diff	-0.8	-0.1	-0.3	0.2	-0.4	-0.1	-0.3	-0.3	0.5	-0.3	0.1	-0.2	-0.2
Total	100.0	100.0	100.0	100.0	100.0	100.0	100.0	100.0	100.0	100.0	100.0	100.0	100.0
Σ|diff| (bias) [c]	17.4	15.8	17.8	13.6	20.2	20.0	22.8	17.8	17.7	20.5	23.4	21.5	28.1
R_{wp} [d]	7.7	7.1	8.7	8.3	7.8	6.9	7.6	6.6	6.9	6.7	6.9	7.5	7.5
d [e]	0.8	0.9	0.9	0.9	1.0	1.0	1.0	1.2	1.1	1.1	1.1	0.8	1.0
χ^2 [f]	1.6	1.5	1.6	1.6	1.4	1.5	1.5	1.3	1.4	1.4	1.4	1.6	1.4
Chebychev order	1	1	1	1	1	1	1	2	2	2	2	2	2

[a] Difference between refined and expected weight-percent concentrations.
[b] b/d indicates a concentration below the detection limit.
[c] Σ|diff| is the sum of absolute deviations from actual compositions, after the "bias" of Omotoso et al. (2006).
[d] R_{wp} is the weighted pattern index, a function of the least-squares residual.
[e] d is the Durbin-Watson statistic, a measure of serial correlation for the least-squares fit.
[f] χ^2 is the reduced chi-squared statistic for the least-squares fit.

Table 2.5: Rietveld refinement results for non-serrated specimens of synthetic processed kimberlite.

Phase	Series 1							Series 2					
	07lsk1r	07lsk2r	07lsk3r	07lsk4r	07lsk5r	07lsk6r	07lsk6r-2 (NIST)	07lsk7r	07lsk8r	07lsk9r	07lsk10r	07lsk11r	07lsk12r (NIST)
Lizardite + Amorphous	49.3	49.9	43.9	48.6	45.8	50.0	49.8	37.8	37.6	39.6	36.2	39.3	33.6
diff [a]	4.8	5.4	-0.6	4.1	1.3	5.5	5.3	3.1	2.9	5.0	1.5	4.6	-1.0
Forsterite	30.5	30.9	31.5	29.3	29.6	26.2	25.3	31.6	31.1	29.8	30.9	28.4	26.5
diff	-4.4	-3.9	-3.0	-4.7	-3.4	-3.8	-4.7	-3.3	-3.7	-4.7	-3.1	-4.6	-3.5
Nesquehonite	b/d [b]	b/d [b]	1.1	1.1	2.1	3.6	4.0	b/d [b]	b/d [b]	0.4	1.2	1.5	5.1
diff	-0.1	-0.3	0.6	0.1	0.1	-1.4	-1.0	-0.1	-0.3	-0.1	0.2	-0.5	0.1
Almandine-Pyrope	4.9	4.8	6.0	5.1	5.7	4.9	4.5	4.3	5.2	4.7	4.5	4.2	5.5
diff	-0.1	-0.2	1.0	0.1	0.7	-0.1	-0.5	-0.7	0.2	-0.3	-0.5	-0.8	0.5
Calcite	4.4	4.2	4.3	4.6	4.4	4.2	4.2	4.5	4.5	4.3	4.3	4.4	4.4
diff	-1.1	-1.3	-1.2	-0.9	-1.1	-1.3	-1.3	-0.9	-0.8	-1.1	-1.1	-1.0	-1.0
Diopside								5.8	5.5	5.6	5.8	5.5	6.2
diff								0.8	0.5	0.6	0.8	0.5	1.2
Oligoclase								4.8	5.1	4.0	4.3	4.5	4.6
diff								-0.2	0.1	-1.0	-0.7	-0.5	-0.4
Phlogopite	5.2	4.6	5.9	5.0	5.8	5.1	5.9	5.8	5.1	5.8	5.8	6.2	6.5
diff	0.2	-0.4	0.9	0.0	0.8	0.1	0.9	0.8	0.1	0.8	0.8	1.2	1.5
Quartz	5.7	5.6	7.3	6.4	6.6	6.1	6.2	5.4	5.9	5.8	7.1	6.0	7.5
diff	0.7	0.6	2.3	1.4	1.6	1.1	1.2	0.4	0.9	0.8	2.1	1.0	2.5
Total	100.0	100.0	100.0	100.0	100.0	100.0	100.0	100.0	100.0	100.0	100.0	100.0	100.0
Σ|diff| (bias) [c]	11.3	12.0	9.6	11.3	9.0	13.4	15.0	10.4	9.5	14.3	10.9	14.7	11.7
R_{wp} [d]	11.2	11.3	14.5	11.4	13.9	12.0	14.6	10.3	12.1	11.7	15.3	11.6	14.3
d [e]	0.3	0.3	0.2	0.3	0.2	0.3	0.2	0.4	0.3	0.3	0.2	0.3	0.2
χ^2 [f]	2.8	2.8	3.7	2.9	3.5	3.0	3.7	2.5	3.0	2.9	3.8	2.9	3.5
Chebychev order	2	2	2	2	2	2	2	3	3	3	3	3	3

[a] Difference between refined and expected weight-percent concentrations.
[b] b/d indicates a concentration below the detection limit.
[c] Σ|diff| is the sum of absolute deviations from actual compositions, after the "bias" of Omotoso et al. (2006).
[d] R_{wp} is the weighted pattern index, a function of the least-squares residual.
[e] d is the Durbin-Watson statistic, a measure of serial correlation for the least-squares fit.
[f] χ^2 is the reduced chi-squared statistic for the least-squares fit.

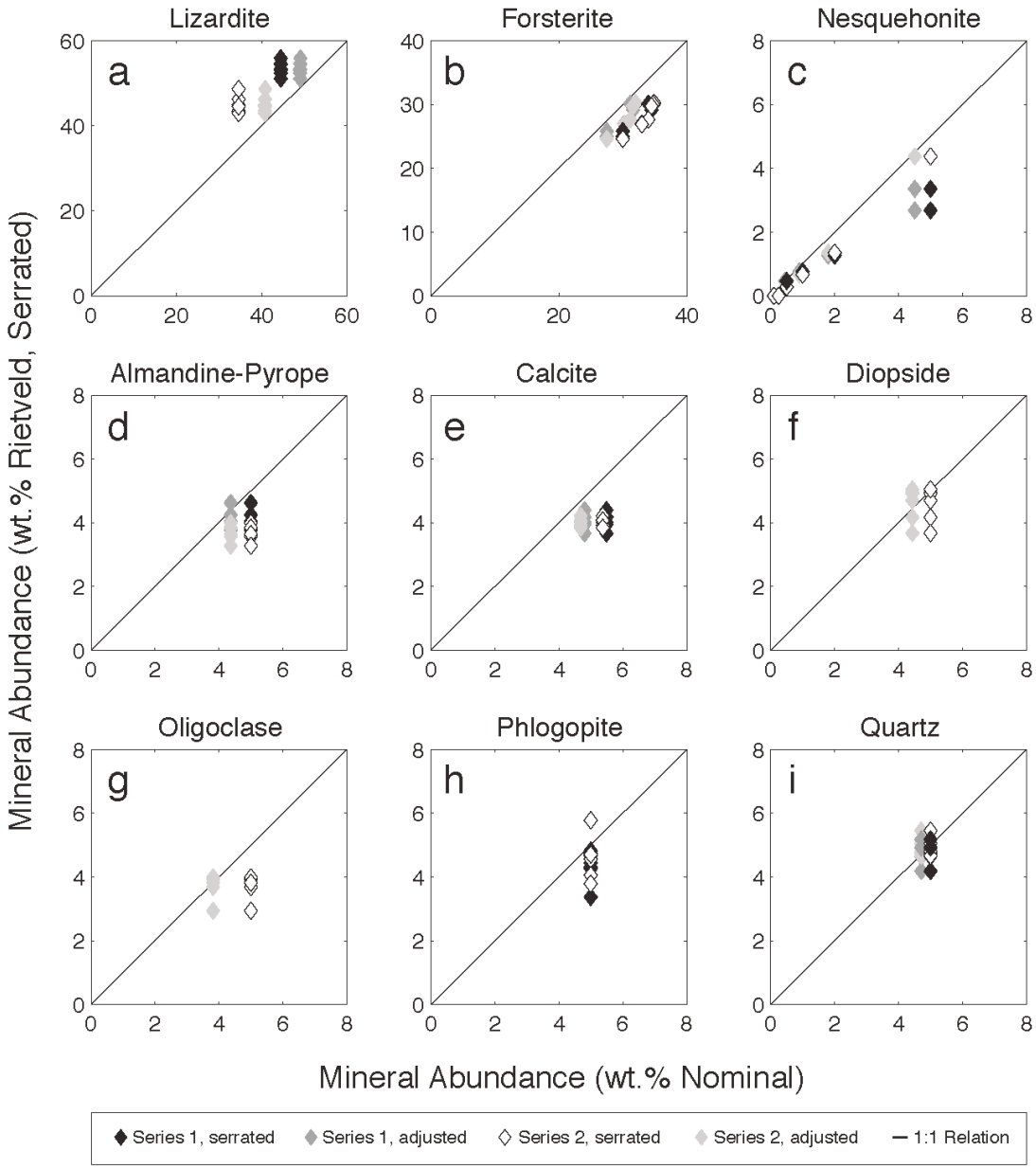

Figure 2.5: Results of Rietveld refinements on serrated specimens of synthetic processed kimberlite. Series 1 indicates 07lsk1r through 6r and Series 2 indicates 07lsk7r through 12r. "Adjusted" results model intensity loss (actually due to surface roughness) as "amorphous content".

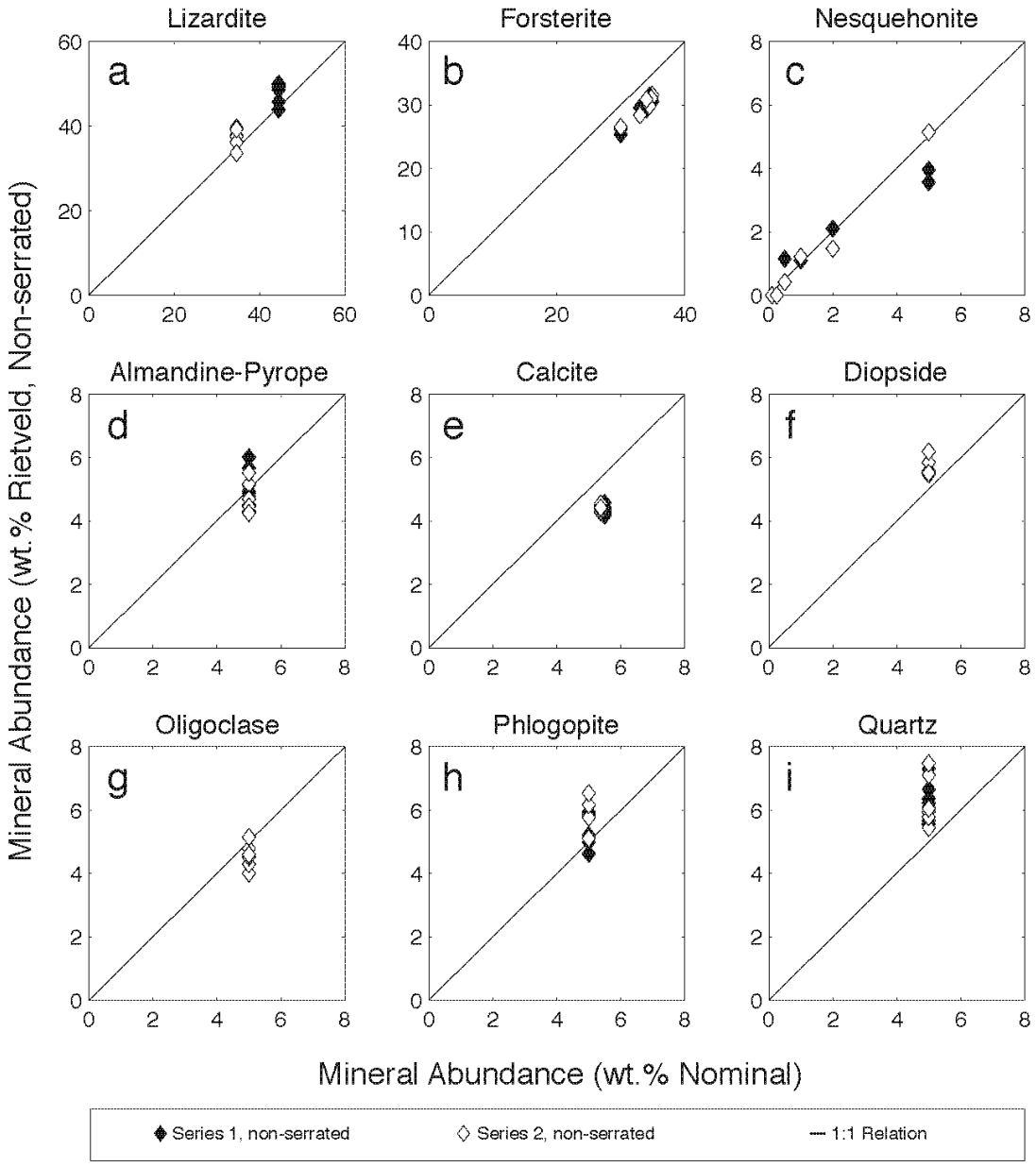

Figure 2.6: Results of Rietveld refinements on non-serrated specimens of synthetic processed kimberlite. Series 1 indicates 07lsk1r through 6r and Series 2 indicates 07lsk7r through 12r.

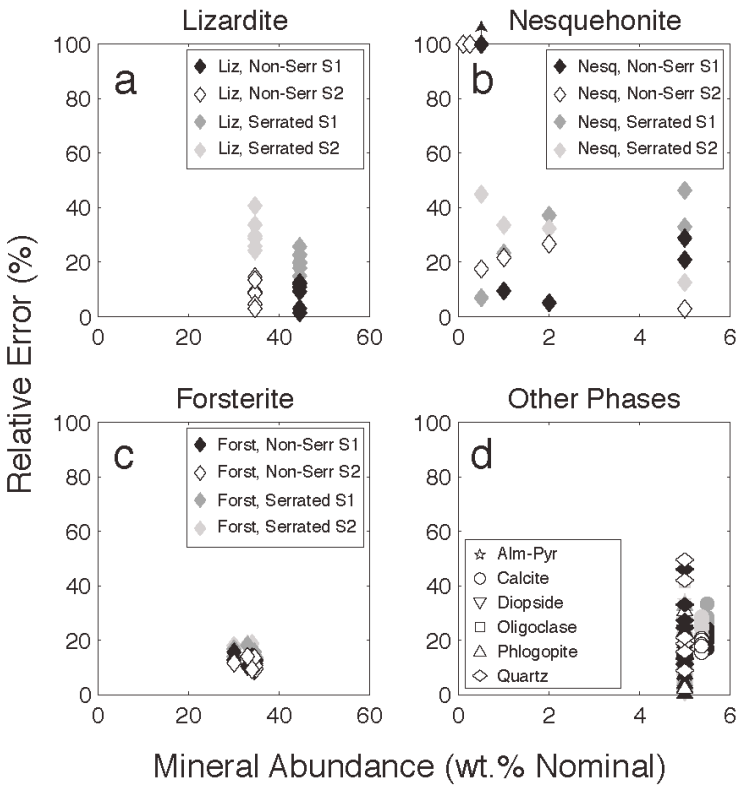

Figure 2.7: Relative error on Rietveld refinement results for each mineral phase in the synthetic processed kimberlites. Results for Series 1 and 2 (and serrated versus non-serrated specimens) are distinguished by the colour of the symbols.

Phlogopite in kimberlite is commonly distorted, kink banded, and partially altered (Mitchell 1986). The phlogopite standard used in the synthetic kimberlites was chosen because it was highly pure and suffered from anisotropic peak broadening. Anisotropic peak broadening can result from stacking faults or anisotropic distribution of crystallite size or strain, which can be symptoms of deformation (e.g., Jerome and Mohanty 1979; Dutta and Pradhan 2003; Couvy et al. 2004). This phlogopite was best modelled using the March-Dollase correction (March 1932; Dollase 1986) for preferred orientation on {001} and a sixth-order symmetrized harmonic expansion (Järvinen 1993) to model peak anisotropy (Fig. 2.8a). Refined results for phlogopite, from a sample prepared with an internal standard of 10 wt.% synthetic corundum, were introduced as a starting model into refinements of synthetic mixtures. The degree of preferred orientation on {001} was refined, but the coefficients of the symmetrized harmonics were held constant. Although this model gave the best fit to the pattern for phlogopite (when tested on synthetic

kimberlite mine tailings), severe overlap of the major reflections of phlogopite with other phases and the use of symmetrized harmonics commonly led to overestimates of several weight percent (Fig. 2.8b). Overestimates worsened when symmetrized harmonics were used to model both preferred orientation and peak anisotropy. Preferred orientation in phlogopite was also modelled using the March-Dollase correction without using symmetrized harmonics to model peak anisotropy (Fig. 2.8c). Again, because of severe overlap with the major reflections of this phase, the model failed to adequately fit the phlogopite. Extreme underestimates (of as much as 4.7 wt.% on a 5.0 wt.% abundance of phlogopite) resulted from overestimates of the degree of preferred orientation. Because of the difficulty in correctly modelling preferred orientation and peak anisotropy for a low abundance of phlogopite in a pattern suffering from severe overlap of peaks, coupled with the difficulty in reducing its particle size, no corrections were applied to phlogopite in the final refinements (Fig. 2.8d). Although the refinement statistics suffered (particularly for data collected from non-serrated specimens), the fit to phlogopite was better constrained and refinement results were more accurate and more consistent.

Other possible sources of error include fluorescence from Cr and Mn-bearing phases (using Co radiation), and difficulty in modelling minor phases due to overlap of reflections in the XRPD patterns. In addition, Wilson et al. (2006) observed that the use of a peaks phase to model a serpentine mineral can cause low-abundance mineral phases to be underestimated in Rietveld refinements. They noted that large misestimates are likely to occur for minerals at abundances below approximately 5 wt.% due to limitations in the fundamental parameters approach, difficulty in modelling preferred orientation, and the tendency of complex systems of peaks to dominate the analysis. These effects, together with the number of low-abundance phases in the synthetic samples, may contribute to systematic overestimates for lizardite.

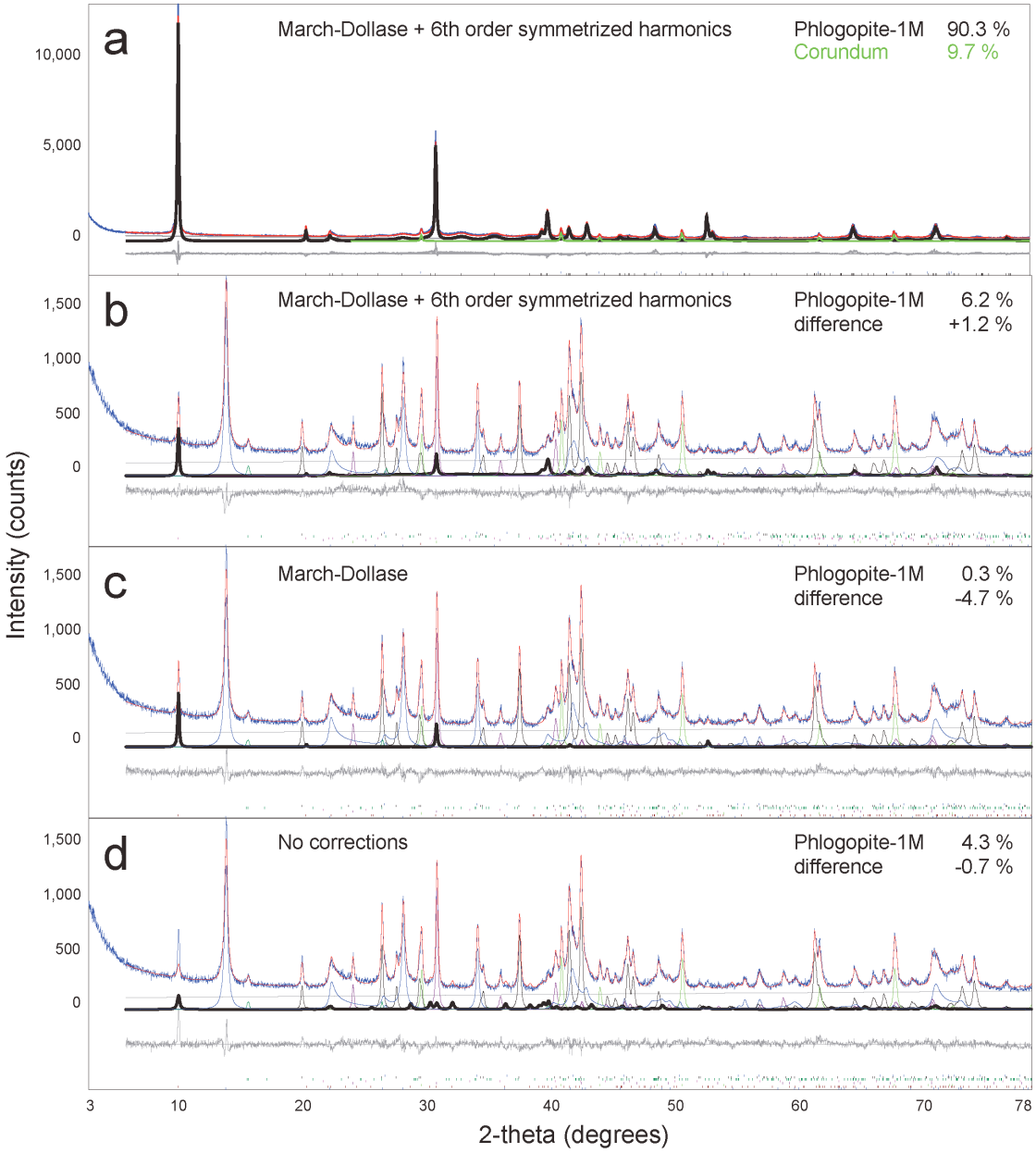

Figure 2.8: Modeling phlogopite in a synthetic kimberlite (07lsk3r). (a) Phlogopite was best fit using the March-Dollase correction for preferred orientation on {001} and a sixth-order symmetrized harmonic expansion to model peak anisotropy; (b) the same model applied to a serrated specimen of 07lsk3r; (c) modeling phlogopite with only the March-Dollase correction, and (d) modeling phlogopite with no corrections for preferred orientation or anisotropic peak shape.

Nesquehonite was not detected at abundances ≤ 0.25 wt.% in the patterns collected for samples 07lsk1r, 07lsk2r, 07lsk7r, and 07lsk8r. The relative error on refined values for the amount of nesquehonite remained consistent for detectable abundances between 0.50 wt.% and 5.0 wt.%. A maximum relative error of approximately 40% was observed for abundances in this range and can be expected for natural samples. This corresponds to an absolute error of 0.2 wt.% for a sample containing 0.50 wt.% nesquehonite and 2.0 wt.% for a sample containing 5.0 wt.% nesquehonite. No significant overall difference in accuracy was observed for Rietveld refinements of Series 1 and 2 samples and the inclusion of additional, low abundance phases (i.e., diopside and oligoclase) in the Series 2 samples had no adverse effect on refinement results. Also, the choice of NIST 676a corundum or synthetic corundum did not have a significant effect on Rietveld refinement results. However, the disparity in the sizes of these two sample subsets makes the effect of differing internal standards difficult to assess. Despite the significant relative errors for nesquehonite, the absolute errors are generally small and are in keeping with results for low abundance phases from previous studies using the Rietveld method for quantitative phase analysis (i.e., Raudsepp et al. 1999; Omotoso et al. 2006; Wilson et al. 2006).

2.4.1.2 Results of quantitative RIR and the internal standard method

Quantitative RIR results for nesquehonite in the synthetic processed kimberlites are given in Table 2.6 and Figure 2.9. No significant difference in accuracy was observed for RIR results using fundamental parameters and Pseudo-Voigt peak fitting. As with Rietveld refinement results (Fig. 2.6), abundances from RIR deviate somewhat from the ideal values. However, RIR results were generally closer to the expected, nominal values than those obtained by Rietveld refinement (Fig. 2.9).

Results for the two samples (07lsk6r-2 and 07lsk12r) that used NIST 676a corundum as the spike phase were significantly worse than for those that used synthetic corundum. The (110) reflection of the NIST 676a corundum was less intense than the same reflection in the synthetic corundum, relative to the reference peaks of nesquehonite. Because the reference intensity ratio was determined using synthetic corundum, the abundance of nesquehonite was overestimated in the samples spiked with

the NIST corundum standard. Even though the results worsened using the NIST standard, the absolute errors on the abundance of nesquehonite were on the same order as those obtained using the Rietveld method. These results could be improved by measuring and using a RIR for nesquehonite that was determined relative to the NIST 676a corundum. Unfortunately, there was insufficient nesquehonite to make a second 50-50 wt.% mixture to determine this RIR.

Table 2.6: Results of Reference Intensity Ratio measurements on synthetic processed kimberlite.

	Sample Name	Nominal (wt.%)	Fundamental Parameters		Pseudo-Voigt	
			X_{nesq}, (wt.%)	$\sigma(X_{nesq})$ (wt.%)	X_{nesq}, (wt.%)	$\sigma(X_{nesq})$ (wt.%)
Series 1	07lsk1r	0.100	0.096	0.005	0.092	0.005
	diff[a]		-0.004		-0.008	
	07lsk2r	0.250	0.081	0.004	0.076	0.004
	diff		-0.169		-0.174	
	07lsk3r	0.500	0.430	0.024	0.425	0.023
	diff		-0.070		-0.075	
	07lsk4r	1.000	0.843	0.047	0.793	0.042
	diff		-0.157		-0.207	
	07lsk5r	2.000	2.010	0.112	1.945	0.103
	diff		0.010		-0.055	
	07lsk6r	5.000	4.824	0.268	4.905	0.261
	diff		-0.176		-0.095	
	07lsk6r-NIST	5.000	5.832	0.325	5.898	0.314
	diff		0.832		0.898	
Series 2	07lsk7r	0.100	0.013	0.001	0.012	0.001
	diff		-0.087		-0.088	
	07lsk8r	0.250	0.041	0.002	0.041	0.002
	diff		-0.209		-0.209	
	07lsk8r-front	0.250	0.090	0.005	0.087	0.005
	diff		-0.160		-0.163	
	07lsk9r	0.500	0.216	0.012	0.205	0.011
	diff		-0.284		-0.295	
	07lsk9r-front	0.500	0.259	0.014	0.250	0.013
	diff		-0.241		-0.250	
	07lsk10r	1.000	0.775	0.043	0.722	0.038
	diff		-0.225		-0.278	
	07lsk11r	2.000	1.865	0.104	1.710	0.091
	diff		-0.135		-0.290	
	07lsk12r-NIST	5.000	6.019	0.335	5.829	0.310
	diff		1.019		0.829	

[a] Difference between refined and expected weight-percent concentrations.

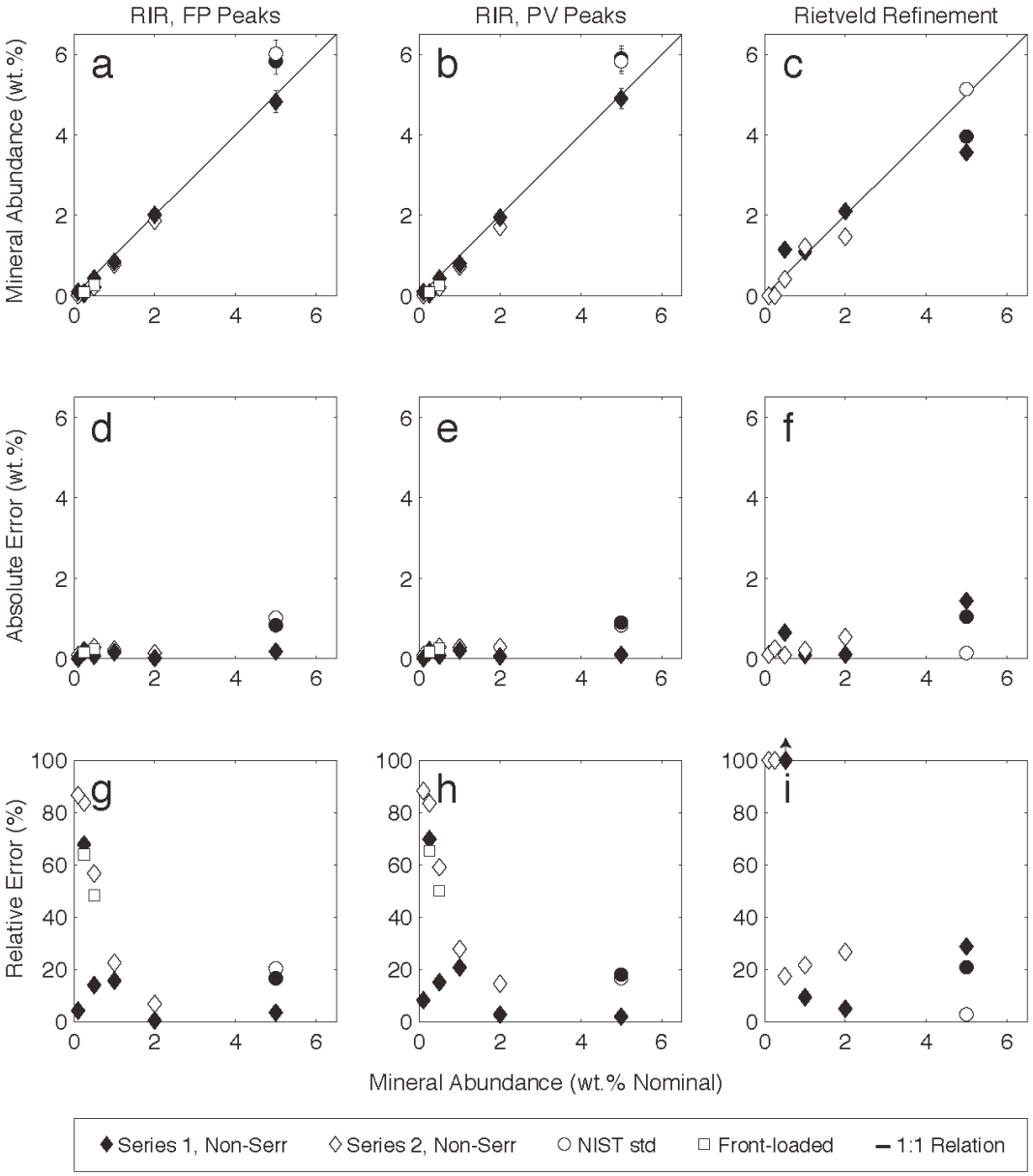

Figure 2.9: RIR and Rietveld refinement results for nesquehonite. RIR results are given for Fundamental Parameters (FP) and Pseudo-Voigt (PV) peak fitting.

Series 1 and 2 mixtures containing nesquehonite at abundances ≥ 0.50 wt.% gave maximum relative uncertainties of ~20%. Accuracy began to decrease dramatically for concentrations ≤ 0.25 wt.% nesquehonite for the Series 1 mixtures and ≤ 0.50 wt.% for the Series 2 mixtures. The RIR result for the Series 1 sample, 07lsk2r (which contained 0.25 wt.% nesquehonite), was underestimated by 68% relative. Underestimates in the vicinity of 50% to 90% relative were observed for samples 07lsk7r, 07lsk8r, and 07lsk9r in Series 2. The reference peaks of nesquehonite were only just detectable at > 3σ above the intensity of the background for sample 07lsk7r. XRPD data were recollected on specimens of 07lsk7r, 07lsk8r, and 07lsk9r that were front-loaded into cavity mounts and pressed flat with a smooth sheet of glass to maximize preferred orientation of crystallites. The estimates for the concentration of nesquehonite in samples 07lsk8r and 07lsk9r were somewhat improved when the data were recollected in this way (Table 2.6 and Fig. 2.9). The nesquehonite peaks were not detected in the data for the front-loaded specimen of 07lsk7r. It is likely that the underestimates on abundances less than 0.50 wt.% are the result of decreased preferred orientation of nesquehonite. At higher abundances, the elongate crystals of nesquehonite tend to orient themselves along [010], giving rise to the preferred orientation observed on {101}. At lower abundances, crystals of nesquehonite could be packed more randomly into a powdered specimen. Also, underestimates of nesquehonite are more severe for the samples in Series 2, which contain more phases and a lower abundance of (preferentially oriented) phyllosilicate minerals than the samples in Series 1. It appears that at abundances less than 0.50 wt.%, the ability to induce a similar degree of preferred orientation to that seen at abundances of 5.0 wt.% or 50 wt.% (as in the RIR standard mixture), is compromised in the samples from Series 1 and particularly in the samples from Series 2. In some systems, it is possible to use a multireflection RIR method to reduce the impact of preferred orientation on quantitative phase analysis (i.e., Chipera and Bish 1995). Unfortunately, the severe overlap of reflections in XRPD patterns for processed kimberlite precludes this option. Thus, we consider the practical lower limit to quantification of nesquehonite to be in the range of 0.25-0.50 wt.% using this RIR method. Below this limit, RIR quantitative results for nesquehonite should be considered as an order of magnitude estimate at best.

At abundances ≥ 0.50 wt.% the RIR method gives results for nesquehonite that are generally more accurate than the Rietveld refinement results (Figs. 2.6 and 2.9). RIR and Rietveld results were typically characterized by relative uncertainties less than 20% and 40%, respectively for nesquehonite in abundances ≥ 0.50 wt.%. For this system of minerals, both the Rietveld and RIR method failed to accurately quantify nesquehonite at abundances below approximately 0.50 wt.%. With the Rietveld method, this is largely a consequence of counting statistics. Rietveld refinement results could be improved and detection limits lowered if a significantly longer time per step was used to acquire XRPD patterns. With the RIR method, the relatively low accuracy for abundances < 0.50 wt.% was likely a consequence of sometimes unpredictable decreases in the preferred orientation of nesquehonite at low abundances.

As a readily available alternative to using RIR or the Rietveld method to measure nesquehonite abundances < 0.50 wt.%, a calibration curve was produced. This was done by plotting the ratio of intensities of the reference peaks for nesquehonite and corundum versus the nominal abundance of nesquehonite for the 6 mixtures from Series 1 that were prepared with synthetic corundum (after Alexander and Klug 1948). The Series 1 mixtures were selected for this purpose because they represent the baseline composition of kimberlite mine tailings and have no peaks in the vicinity of the references peaks of nesquehonite. A best linear fit to these data is given in Figure 2.10a. The amounts of nesquehonite in the Series 2 mixtures prepared with synthetic corundum (which are most similar to the mine tailings at Diavik) were calculated using this calibration curve as a test of its accuracy. The use of a calibration curve for mixtures with 1 wt.% or less nesquehonite (Fig. 2.10b) mitigates the systematic underestimates given by the RIR method (Fig. 2.10c). At abundances ≥ 1.00 wt.%, nesquehonite is underestimated by less than 15% relative (in two samples). At lower abundances, maximum underestimates of approximately 50% relative are observed (in three samples). This represents a significant improvement over maximum underestimates of 90% observed using the RIR method. It should be noted that, because of the small but significant underestimates of nesquehonite calculated for samples from Series 2 using the calibration curve for Series 1 data, the amount of nesquehonite in Diavik tailings may also be slightly underestimated.

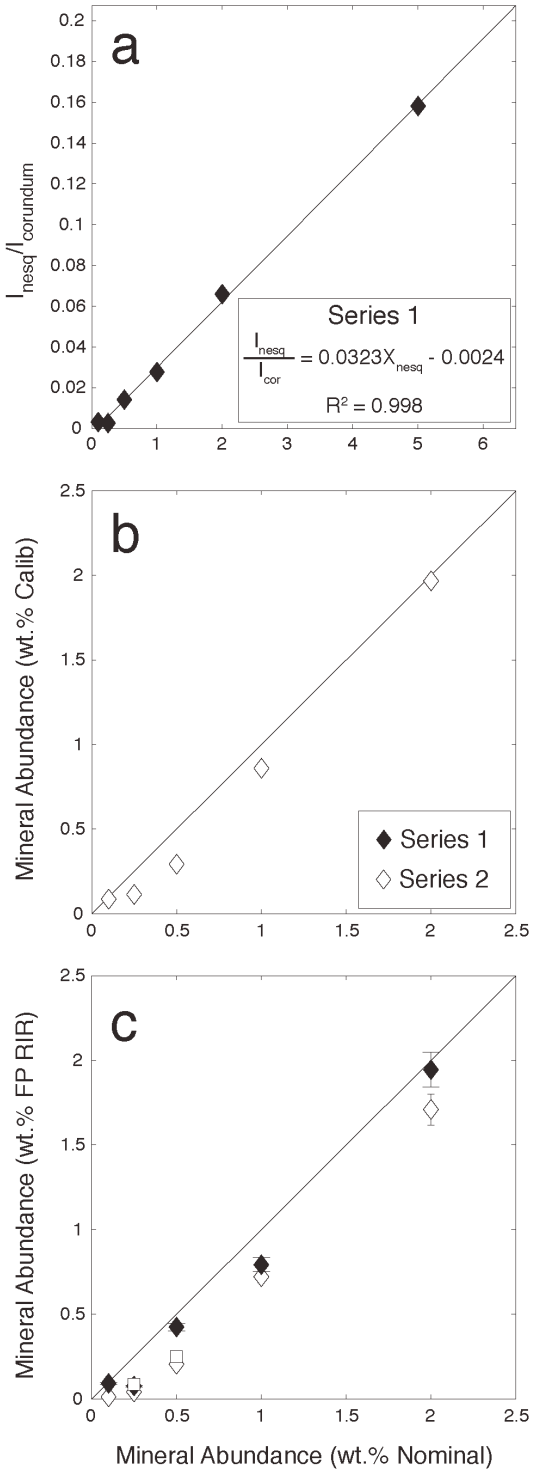

Figure 2.10: Calibration curve for nesquehonite in Series 1 mixtures (a), the calibration curve applied to Series 2 mixtures (b), and FP RIR results (c). An expanded view of Fig. 2.9a is shown in (c) and error bars are 1σ, propagated from repeated measurement of the RIR standard.

Based on our results, the abundance of nesquehonite can be measured using either the RIR method or the Rietveld method when present at ≥ 0.50 wt.%. At abundances < 0.50 wt.%, the use of a calibration curve is likely to give more accurate results.

2.4.2 Natural mine tailings

Twenty samples of processed kimberlite from the Diavik Diamond Mine were analyzed using the Rietveld method, the RIR method of Chung (1974), and a calibration curve according the internal standard method of Alexander and Klug (1948). Analyses were done on data collected from non-serrated specimens. Samples 05DVK4, 06DVK35, and 06DVK36 are samples of fine processed kimberlite covered by a thin, efflorescent film of nesquehonite (Group 1 crusts). Sample 05DVK7 is from a Group 2 crust from the coarse PKC. Samples 06DG1-1, 06DG3-1, 06DG7-1, and 06DG9-1 are 10-cm long core samples, which were collected at the corners of a 5 m x 5 m grid, from the surface of the fine PKC. Samples 06DG1-3, 06DG3-3, 06DG7-3, and 06DG9-3 are 10-cm long core samples collected from a depth of 100 cm below the corresponding samples from the surface of the fine PKC (e.g., 06DG1-3 was collected from an interval 95 to 105 cm beneath 06DG1-1). 06DVK33-1, 06DVK33-3, 06DVK42-1, 06DVK42-3, 06DVK46-1, 06DVK46-3, 06DVK53-1, and 06DVK53-3 are samples collected from four cores (i.e., cores 06DVK33, 06DVK42, 06DVK46, and 06DVK53) taken at four corners of the fine PKC. Again, core samples were collected from the surface and at a depth of 100 cm. Sampling locations are given in Figure 2.3 and the results of quantitative phase analysis are given in Table 2.7.

Rietveld refinement results indicate that samples of fine processed kimberlite from Diavik contain between 40.0 and 76.2 wt.% lizardite and between 12.3 and 46.3 wt.% forsterite. The combined abundance of lizardite and forsterite varies from 76.1 to 93.3 wt.%. Calcite was present at abundances between 1.9 and 4.1 wt.%. Vermiculite, which was detected in 18 samples, was identified by XRPD using a smear-mounted specimen that had been solvated with glycerol for 12 hours at 60˚C, according to the method of Moore and Reynolds (1997). Following solvation, no change in the position of the basal reflection of this clay phase was observed, suggesting that it is vermiculite and discounting the presence of a pure smectite group mineral. However, this does not rule

out the possibility that some of the samples from Diavik may contain interstratified serpentine-smectite of the sort described by Sakharov et al. (2004). Plagioclase feldspar, diopside, and quartz were present at abundances less than 5 wt.%. Pyrope-rich garnet and phlogopite were present at abundances of 0-6.4 wt.% and 1.6-3.5 wt.%, respectively. Based on results for the synthetic mixtures, maximum relative errors of approximately 50% can be expected on refined abundances for these minor phases. At higher abundances, in the vicinity of 5 wt.% and above, relative errors between 5% and 20% are anticipated.

Nesquehonite was present below the detection limit for Rietveld refinement (approximately 0.50 wt.%) in all samples of processed kimberlite. The reference peaks of nesquehonite were detected at > 3σ above background intensity in three samples from the fine PKC (05DVK4, 06DVK36, and 06DVK53-1) and one sample from the coarse PKC (05DVK7) using the long acquisition time for the RIR method. It was not detected in sample 06DVK35, despite its presence having been confirmed by visual inspection and by XRPD analysis of high-graded crust material. Nesquehonite may have been detected at higher than 2σ above the background intensity in sample 06DG3-3. RIR results for the four samples in which nesquehonite was detected give abundances between 0.039 and 0.063 wt.% nesquehonite (Table 2.7). Considering the difficulty in maintaining a relatively constant degree of preferred orientation in nesquehonite and the underestimates that ensued in the synthetic mixtures, it is very likely that the values obtained for the natural samples are underestimated to a comparable extent. In fact, results of a similar magnitude were obtained for synthetic mixtures with 0.10 and 0.25 wt.% nesquehonite (Table 2.6, Figs. 2.9 and 2.10). Use of the calibration curve suggests that nesquehonite is present between approximately 0.11 wt.% and 0.14 wt.% in the four natural samples from Diavik with measurable abundances (Table 2.7).

Table 2.7: Results of quantitative phase analysis of natural samples of processed kimberlite, renormalized to exclude corundum.

Phase	**05DVK4**	**05DVK7**	**06DG1-1**	**06DG1-3**	**06DG3-1**	**06DG3-3**	**06DG7-1**	**06DG7-3**	**06DG9-1**	**06DG9-3**
depth (cm)	surface	surface	surface	100	surface	100	surface	100	surface	100
Lizardite + amorphous	40.0	61.0	72.6	63.8	71.2	61.9	76.2	50.3	75.5	51.4
Forsterite	36.8	15.1	17.5	23.4	18.1	25.4	12.3	35.2	14.5	35.7
Nesq. Rietveld	n/d [a]	n/d	n/d	n/d	n/d	n/d	n/d	n/d	n/d	n/d
Nesq. RIR	0.058	0.043	n/d	n/d	n/d	n/d	n/d	n/d	n/d	n/d
Nesq. Internal Std.	0.133	0.118	n/d	n/d	n/d	n/d	n/d	n/d	n/d	n/d
Nesq. Present? [b]	yes	yes	n/d	yes	n/d	yes	n/d	n/d	n/d	n/d
Almandine-Pyrope	6.4	1.9	1.6	2.3	1.5	2.9	1.3	4.4	1.0	4.3
Calcite	2.2	1.9	2.7	2.6	2.3	2.3	2.6	2.5	2.6	2.2
Diopside	2.6	3.2	1.6	2.0	2.1	1.7	1.8	1.9	1.8	2.0
Phlogopite	2.9	2.7	1.6	2.5	1.9	2.0	2.1	2.7	2.1	1.6
Plagioclase	3.4	3.7	1.1	1.3	1.4	1.5	1.5	1.2	0.8	1.0
Quartz	2.7	2.0	0.9	1.2	0.8	1.3	0.9	1.1	0.9	1.0
Vermiculite	2.9	8.4	0.4	0.9	0.8	1.0	1.2	0.6	0.8	0.7
Total (Rietveld)	100.0	100.0	100.0	100.0	100.0	100.0	100.0	100.0	100.0	100.0
R_{wp} [c]	5.1	4.8	4.9	4.9	4.8	4.7	5.0	5.1	5.1	4.5
d [d]	1.0	1.1	1.1	1.1	1.1	1.1	1.0	1.0	1.0	1.2
χ^2 [e]	1.5	1.4	1.4	1.4	1.4	1.3	1.5	1.5	1.5	1.3
NP, Computed [f]	51.0	47.5	57.7	55.5	55.3	53.2	56.1	54.6	55.7	52.1
NP, Nesq. [g]	1.0	0.9	0	0	0	0	0	0	0	0

[a] n/d indicates that the phase was not detected.

[b] Nesquehonite determined to be present if the (101) and (10 $\bar{1}$) peaks are detected at > 3σ above background in smear-mounted specimens.

[c] R_{wp} is the weighted pattern index, a function of the least-squares residual.

[d] d is the Durbin-Watson statistic, a measure of serial correlation for the least-squares fit.

[e] χ^2 is the reduced chi-squared statistic for the least-squares fit.

[f] NP, Computed is calculated using Rietveld refinement results and abundances of nesquehonite determined from the calibration curve. Units are kg $CaCO_3$/t.

[g] NP, Nesq. is the contribution of nesquehonite to the total computed NP. Units are kg $CaCO_3$/t.

Table 2.7 (continued): Results of quantitative phase analysis of natural samples of processed kimberlite, renormalized to exclude corundum spike.

Phase	**06DVK33-1**	**06DVK33-3**	**06DVK35**	**06DVK36**	**06DVK42-1**	**06DVK42-3**	**06DVK46-1**	**06DVK46-3**	**06DVK53-1**	**06DVK53-3**
depth (cm)	surface	100	surface	surface	surface	100	surface	100	surface	100
Lizardite + amorphous	63.3	65.6	65.1	67.7	47.0	48.5	55.8	55.8	65.8	50.3
Forsterite	27.2	24.0	19.6	15.6	46.3	44.3	32.8	30.7	20.1	33.8
Nesq. Rietveld	n/d [a]	n/d	n/d	n/d	n/d	n/d	n/d	n/d	n/d	n/d
Nesq. RIR	n/d	n/d	n/d	0.039	n/d	n/d	n/d	n/d	0.063	n/d
Nesq. Internal Std.	n/d	n/d	n/d	0.114	n/d	n/d	n/d	n/d	0.138	n/d
Nesq. Present? [b]	n/d	n/d	yes	yes	yes	yes	yes	yes	yes	yes
Almandine-Pyrope	1.6	2.2		0.9	2.1	2.0	1.7	4.0		4.2
Calcite	2.4	2.6	4.0	4.1	2.5	3.1	2.5	2.0	3.9	2.7
Diopside	1.8	1.6	2.2				1.9	1.8		1.9
Phlogopite	1.8	1.6	2.9	3.5	2.0	1.6	1.8	2.5	2.8	2.1
Plagioclase	1.1	0.9	2.1	2.4			1.7	1.4	2.5	1.8
Quartz	0.8	1.0	2.2	2.2		0.5	1.5	1.2	2.5	1.7
Vermiculite		0.6	2.0	3.6	0.1		0.3	0.5	2.3	1.4
Total (Rietveld)	100.0	100.0	100.0	100.0	100.0	100.0	100.0	100.0	100.0	100.0
R_{wp} [c]	4.9	4.7	4.8	5.3	4.9	4.6	4.7	4.9	4.9	4.7
d [d]	1.1	1.1	1.0	0.9	1.0	1.1	1.2	1.1	1.1	1.1
χ^2 [e]	1.4	1.4	1.4	1.5	1.4	1.4	1.4	1.4	1.4	1.4
NP, computed [f]	54.5	56.2	69.1	71.0	58.0	63.4	55.2	50.3	69.7	57.2
NP, Nesq. [g]	0	0	0	0.8	0	0	0	0	1.0	0

[a] n/d indicates that the phase was not detected.

[b] Nesquehonite determined to be present if the (101) and (10 $\bar{1}$) peaks are detected at > 3σ above background in smear-mounted specimens.

[c] R_{wp} is the weighted pattern index, a function of the least-squares residual.

[d] d is the Durbin-Watson statistic, a measure of serial correlation for the least-squares fit.

[e] χ^2 is the reduced chi-squared statistic for the least-squares fit.

[f] NP, Computed is calculated using Rietveld refinement results and abundances of nesquehonite determined from the calibration curve. Units are kg $CaCO_3$/t.

[g] NP, Nesq. is the contribution of nesquehonite to the total computed NP. Units are kg $CaCO_3$/t.

Additional data for nesquehonite were collected on smear-mounted specimens of the 20 natural samples. Samples were smear-mounted in order to induce preferred orientation of nesquehonite. The (101) and $(10\bar{1})$ reflections of nesquehonite were detected in 11 of the 20 samples using a counting time of 40 s/step. RIR data for the reference peaks of nesquehonite were acquired using a counting time of 120 s/step. In sample 06DVK53-1, the reference peaks for nesquehonite are more intense in the pattern collected in 2 hours and 4 minutes on a smear-mounted specimen than in the pattern from a back-loaded specimen collected in 6 hours and 12 minutes (Fig. 2.11). It can be inferred from Figure 2.11 that the detection limit is significantly lower for smear-mounted specimens. Several analytical options are available to improve detection and quantification of nesquehonite. One such option is to use even longer counting times on the specimens loaded into cavity mounts and to measure, empirically, the decrease in preferred orientation with decreasing abundance of nesquehonite. This would need to be done using replicate analyses of standard mixtures. The time and cost involved in this procedure may disqualify its development and routine use. A second option is to induce preferred orientation in standard mixtures and natural samples by smear-mounting onto zero-diffraction quartz plates. This method would improve detection of nesquehonite, but the variation in degree of preferred orientation and the effect of surface roughness would need to be assessed. Also, the very small amounts of sample needed to prepare this type of specimen may result in measurement errors from insufficient homogenization.

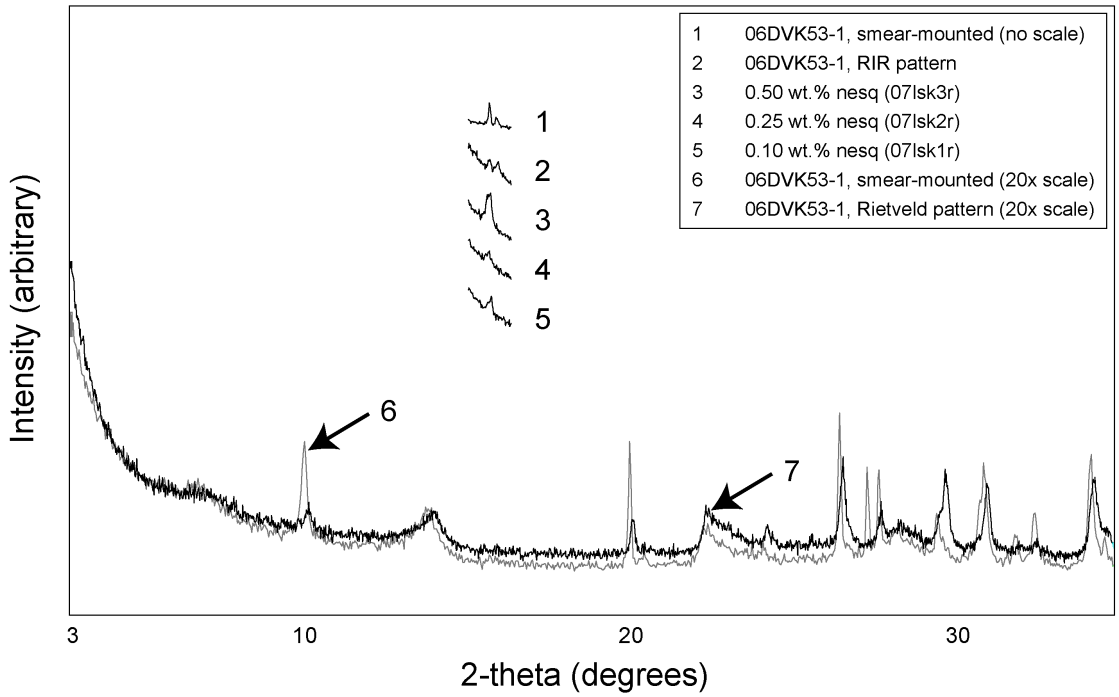

Figure 2.11: XRPD patterns collected for 06DVK53-1. The reference peaks of nesquehonite are relatively less intense in the RIR pattern (2) than in the pattern acquired from a smear-mounted (oriented) aliquot (1). The left-most peak in (1) and (2) and the only peak in (3), (4), and (5) is from the (101) and (10 $\bar{1}$) reflections of nesquehonite. The peak to the right in (1) and (2) is from plagioclase.

2.5 Implications for neutralization potential and carbon dioxide sequestration

Jambor et al. (2007) have demonstrated that the neutralization potential (NP) of a geological sample can be computed from Rietveld refinement results. In their study, they calculated the NP values of geological materials using appropriate values for NP of the individual minerals in each sample. These values were drawn from a library of NP data for pure mineral phases that had been determined using the Sobek method (Sobek et al. 1978). Most of the NP results computed by Jambor et al. (2007) were lower than the measured values, but the authors concluded that they could be used as a baseline estimate of NP.

NP values were calculated using the method of Jambor et al. (2007) for the 20 samples of processed kimberlite from Diavik (Table 2.7). Values used for the NP of individual minerals are from Jambor et al. (2002, 2007) or (in the case of nesquehonite)

are calculated from Lawrence and Scheske (1997) and are listed in Table 2.2. The mean value of NP for the natural samples was 57.0 kg $CaCO_3$/t. The minimum and maximum values were 47.5 kg $CaCO_3$/t and 71.0 kg $CaCO_3$/t, respectively.

The Canadian Department of Indian Affairs and Northern Development (1993) considers mine tailings to be acid generating if they have a ratio of NP to maximum potential acidity (MPA) of 1.2:1 or less. A ratio of 3:1 or less is used to identify waste rock as acid generating. From the calculated NP values, pyrite (which has been observed in the coarse PKC) would need to be present at abundances between 2.4 and 3.5 wt.% for acid mine drainage to be considered a risk in the processed kimberlite at Diavik (Fig. 2.12). Pyrite has not been detected with XRPD in natural samples from either the fine or coarse PKC to a detection limit of approximately 0.5 wt.%. However, gypsum was observed as an efflorescent precipitate at the surface of the processed kimberlites and Baker et al. (2003) have reported gypsum precipitating from dissolved pyrite and calcite in column experiments on freshly processed kimberlite from Diavik. It is not unlikely that some amount of the pyrite initially present in the processed kimberlite had dissolved and been neutralized by calcite to precipitate gypsum. Baker et al. (2003) reported the mean values of NP and MPA for freshly processed kimberlites as 196 ± 131 kg $CaCO_3$/t and 14.8 ± 6.7 kg $CaCO_3$/t, respectively (replotted in Fig. 2.12). The NP values computed as part of this study are considerably lower than those reported by Baker et al. (2003). Some of this decrease may be due to neutralization of calcite; however, the computed NP values should be considered conservative estimates only. Although the calculated NP results are underestimated relative to those of Baker et al. (2003), they can be used (1) to establish whether acid generation may be a risk in localized regions of the tailings or waste rock facilities and (2) to select potentially high-risk samples for kinetic testing.

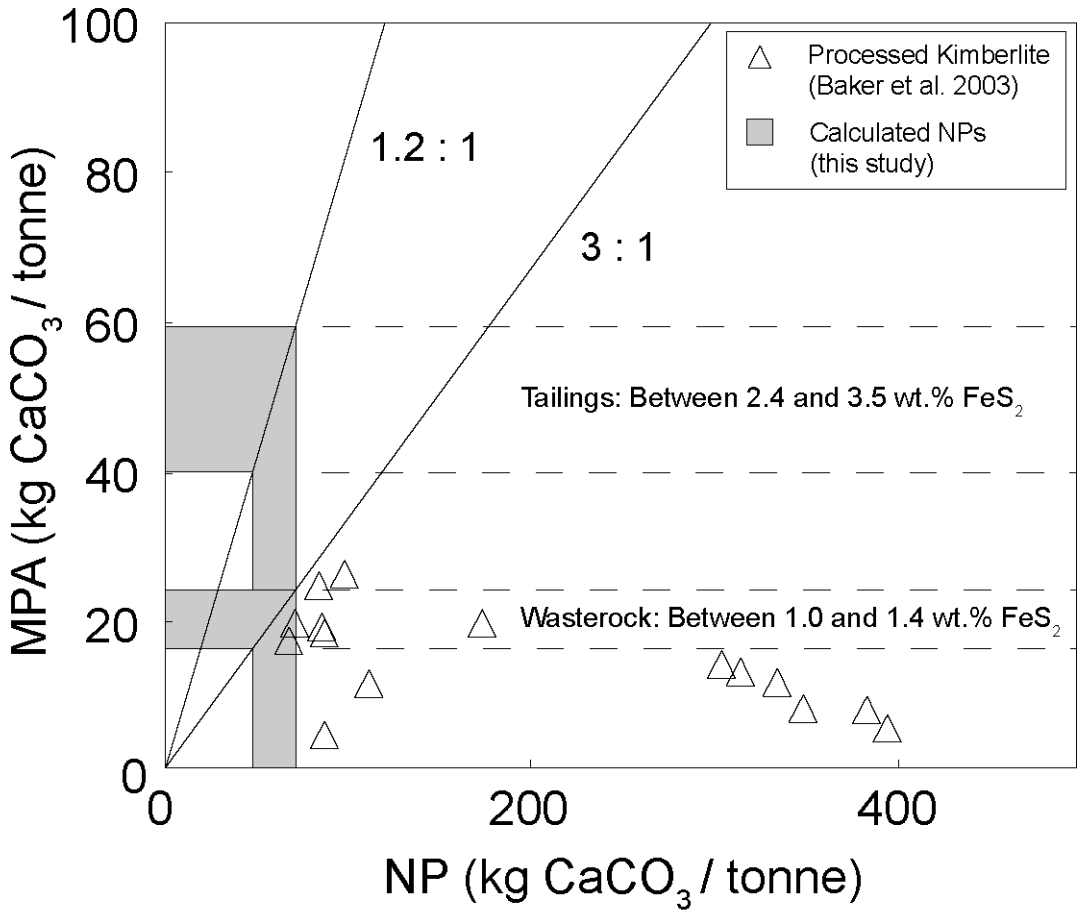

Figure 2.12: Results for neutralization potential (NP) and maximum potential acidity (MPA) of processed kimberlite are replotted from Baker et al. (2003). Ranges for calculated NPs from this study can be used to estimate the minimum threshold at which acid mine drainage could become a concern in the fine PKC at Diavik (i.e., 2.4 wt.% FeS_2).

It is important to note that the development of nesquehonite in the tailings from Diavik may contribute to their potential to neutralize acid mine drainage. Nesquehonite, in the four samples from Diavik with abundances measurable using the calibration curve, may contribute NP on the order of 0.8 to 1.0 kg $CaCO_3$/t, an amount that constitutes 1% to 2% of the NP of these samples (Table 2.7). Although this increase in NP is not large, it is significant considering that it is due to mineralization of 0.11 to 0.14 wt.% of nesquehonite.

Precipitation of nesquehonite is generally induced by evaporation (e.g., Suzuki and Ito 1974; Jull et al. 1988; Grady et al. 1989; McLean et al. 1997; Kloprogge et al. 2003; Power et al 2007). Correspondingly, efflorescent films of nesquehonite are typically found in dry, subaerial conditions in the fine PKC at Diavik and nesquehonite

detected at depth within the processed kimberlite likely represents buried efflorescences from former surfaces in the containment facility. Acero et al. (2007) have used column experiments to demonstrate that efflorescent minerals first precipitate at the surface of unsaturated mine tailings and later begin to infiltrate pore spaces in the underlying material. They attribute this process to the withdrawal of the evaporation front within the column experiments as the mine tailings were drying. Also, Wilson et al. (2009) have described abundant carbon mineralization, including thick crusts (> 1 mm) of efflorescent nesquehonite, in the tailings pile at the Clinton Creek chrysotile mine, Yukon Territory, Canada. Differences in climate and mineralogy of mine residues may play a role in determining the extent to which mineral carbonation is occurring at these sites. However, given that nesquehonite precipitates by evaporation, a further control may be the depth of the vadose zone in a tailings storage facility. The tailings pile at Clinton Creek is located on the slope of a mountainside. Wilson et al. (2009) have excavated within the pile and have described the tailings to be unsaturated by water to a depth of at least 2 m. Contrastingly, most of the volume of the fine processed kimberlite at Diavik is located several metres below the surface of the central pond and is saturated with process water. In addition, samples from several cores of processed kimberlite beached around the perimeter of the pond were located beneath the water table.

Values for modal abundance obtained from quantitative phase analysis can be used to estimate the amount of carbon dioxide that is crystallographically bound in nesquehonite and other carbonate minerals. Wilson et al. (2006) have applied this method to bulk samples of chrysotile mine tailings to estimate the amount of secondary carbonate mineralization occurring per kilogram of tailings material. From these results, they were able to estimate the amount of CO_2 bound within piles of chrysotile mine tailings. At Diavik, this sort of stoichiometric analysis is made possible by the very limited substitution of other divalent cations for Mg in nesquehonite (assessed using energy dispersive X-ray spectroscopy and scanning electron microscopy). Nesquehonite is present below the quantification limit in all samples taken from at depth within the fine PKC. Also, nesquehonite is unlikely to form in tailings saturated with water. A best estimate for the amount of nesquehonite precipitating in the fine PKC at Diavik can be made (1) using the quantitative results calculated from the calibration curve (for three

samples), (2) assuming that samples containing detectable but unquantifiable nesquehonite contain ~0.075 wt.% of this mineral (half way between limits for detection and quantification of nesquehonite, eight samples), and (3) assuming that nesquehonite is present at 0 wt.% in the samples in which it was below detection (eight samples). No estimate was made for CO_2 sequestration in the coarse PKC because only one datum was available (for 05DVK7).

Eleven of the 19 samples analyzed from the fine PKC were taken from the nesquehonite-rich upper 10 cm of this storage facility. Based on our quantitative XRPD results, between 12 and 24 t of CO_2 (depending on packing density) are concentrated within the upper 10 cm of dry, processed kimberlite in the fine PKC. Our results for the deep samples suggest that an additional 1,800 t of CO_2 may be stored within nesquehonite preserved at depth. The Diavik Diamond Mine produces approximately 150,000 tonnes of CO_2 equivalent greenhouse gas emissions each year (Mining Association of Canada 2007). Relative to this value for annual greenhouse gas emissions, a total of approximately 1,800 t of CO_2 trapped within the fine PKC does not seem considerable. In spite of this, it is significant that so much CO_2 has been sequestered within minerals at a site like Diavik, where the extremely cold climate and tailings management procedures may have severely inhibited carbon mineralization. Consequently, detection and quantification of trace carbon mineralization at Diavik makes it possible to establish an approximate baseline for CO_2 sequestration in ultramafic mine tailings that can be applied to subsequent studies.

In general, a tailings storage facility has two purposes in an active mining environment: To act as (1) a permanent storage area for tailings and (2) a temporary storage facility for process water that is due to be either recycled or released into the surrounding environment. Draining the process water from the fine PKC and relocating it to a separate collection pond could enhance precipitation of nesquehonite. Unfortunately, this is not an economical option for an operational mine and would increase Diavik's footprint on the tundra at East Island. However, this strategy could represent a feasible option for promoting CO_2 sequestration within minerals at less environmentally sensitive localities and under more temperate conditions.

2.6 Conclusions

Trace amounts of secondary carbonate minerals in kimberlite mine tailings can be quantified accurately using either the Rietveld method or the method of normalized reference intensity ratios for abundances ≥ 0.5%. A calibration curve, constructed using the internal standard method, provides more accurate results for abundances < 0.5%.

Surface roughness effects, when combined with structureless pattern fitting and the use of an internal standard, can produce a pattern of systematic misestimates in Rietveld refinement results that is similar to that caused by X-ray amorphous content. As a result, surface roughness should not be induced as a measure to compensate for severe preferred orientation of phyllosilicates in specimens intended for quantitative phase analysis.

It may be useful to promote the formation of secondary carbonate minerals at active mines as (1) a passive method for trapping and storing atmospheric CO_2 in sulphide-poor, alkaline tailings or (2) as a defense against acid mine drainage in more sulphide-rich, alkaline or intermediate tailings. At Diavik, nesquehonite was quantifiable in 20% of the samples analyzed (generally surface samples from the fine and coarse PKC) at an abundance of 0.11 wt.% to 0.14 wt.%. Nesquehonite was detectable in another 40% of the samples that were analyzed to a limit of approximately 0.05 wt.%. Based on these results, on the order of 1.8×10^3 tonnes of CO_2 may be trapped in the tailings at Diavik. Although nesquehonite is only present at trace abundance in the tailings at Diavik, it may provide 1-2% of the neutralization potential of tailings in some regions of the PKC.

2.7 References

Acero, P., Ayora, C., and Carrera, J. (2007) Coupled thermal, hydraulic and geochemical evolution of pyritic tailings in unsaturated column experiments. Geochimica et Cosmochimica Acta, 71, 5325-5338.

Al, T.A., Martin, C.J., and Blowes, D.W. (2000) Carbonate-mineral/water interactions in sulfide-rich mine tailings. Geochimica et Cosmochimica Acta, 64, 3933-3948.

Ahn, Y.P., Kim, B.H., and Ishizowa, N. (1986) Structure refinements of solid solutions in the system CaO-MgO-2SiO_2-Al_2O_3. Journal of the Korean Ceramic Society, 23, 25-34.

Alexander, L. and Klug, H.P. (1948) Basic aspects of X-ray absorption in quantitative diffraction analysis of powder mixtures. Analytical Chemistry, 20, 886-889.

Armbruster, T., Buergi, H.B., Kunz, M., Gnos, E., Broennimann, S., and Lienert, C. (1990) Variation of displacement parameters in structure refinements of low albite. American Mineralogist, 75, 135-140.

Armbruster, T., Geiger, C.A., and Lager, G.A. (1992) Single-crystal X-ray structure study of synthetic pyrope-almandine garnets at 100 and 293 K. American Mineralogist, 77, 512-521.

Baker, M.J., Blowes, D.W., Logsdon, M.J., and Jambor, J.L. (2003) Environmental geochemistry of kimberlite materials: Diavik Diamonds Project, Lac de Gras, Northwest Territories, Canada. Exploration and Mining Geology, 10, 155-163.

Banfield, J.F., Veblen, D.R., and Jones, B.F. (1990) Transmission electron microscopy of subsolidus oxidation and weathering of olivine. Contributions to Mineralogy and Petrology, 106, 110-123.

Bish, D.L. and Chipera, S.J. (1991) Detection of trace amounts of erionite using X-ray powder diffraction: erionite in tuffs of Yucca Mountain, Nevada, and Central Turkey. Clays and Clay Minerals, 39, 437-445.

Bish, D.L. and Howard, S.A. (1988) Quantitative phase analysis using the Rietveld method. Journal of Applied Crystallography, 21, 86-91.

Bish, D.L. and Post, J.E. (1993) Quantitative mineralogical analysis using the Rietveld full-pattern fitting method. American Mineralogist, 78, 932-940.

Brindley, G.W. (1945) The effect of grain or particle size on X-ray reflections from mixed powders and alloys, considered in relation to the quantitative determination of crystalline substances by X-ray methods. Philosophical Magazine, 36, 347-369.

Broecker, W.S. (2007) CO_2 arithmetic. Science, 315, 1371.

Brown, A.S., Spackman, M.A., and Hill, R.J. (1993) The electron distribution in corundum. A study of the utility of merging single-crystal and powder diffraction data. Acta Crystallographica Section A: Foundations of Crystallography, A49, 513-527.

Bruker AXS (2004) Topas V. 3.0: General Profile and Structure Analysis Software for Powder Diffraction Data. Bruker AXS, Germany.

Cheary, R.W. and Coelho, A.A. (1992) A fundamental parameters approach to X-ray line-profile fitting. Journal of Applied Crystallography, 25, 109-121.

Chipera, S.J. and Bish, D.L. (1995) Multireflection RIR and intensity normalizations for quantitative analyses: applications to feldspars and zeolites. Powder Diffraction, 10, 47-55.

Chung, F.H. (1974) Quantitative interpretation of X-ray diffraction patterns of mixtures. II. Adiabatic principle of X-ray diffraction analysis of mixtures. Journal of Applied Crystallography, 7, 526-531.

Collins, D.R. and Catlow, C.R.A. (1992) Computer simulation of structures and cohesive properties of micas. American Mineralogist, 77, 1172-1181.

Couvy, H., Frost, D.J., Heidelbach, F., Nyilas, K., Ungár, T., Mackwell, S., and Cordier, P. (2004) Shear deformation experiments at 11 GPa - 1400°C in the multianvil apparatus. European Journal of Mineralogy, 16, 877-889.

De la Torre, A.G. (2003) Accuracy in Rietveld quantitative phase analysis of Portland cements. Journal of Applied Crystallography, 36, 1169-1176.

De la Torre, A.G., Bruque, S., and Aranda, M.A.G. (2001) Rietveld quantitative amorphous content analysis. Journal of Applied Crystallography, 34, 196-202.

de Wolff, P.M. (1956) Measurement of particle absorption by X-ray fluorescence. Acta Crystallographica, 9, 682-683.

Department of Indian Affairs and Northern Development (1993) Guidelines for Acid Rock Drainage Prediction in the North: Northern Mine Environment Neutral Drainage Studies No. 1. Prepared by Steffen, Robertson and Kirsten (B.C.) Inc. Ottawa, ON, Canada.

Dipple, G.M., Raudsepp, M., and Gordon, T.M. (2002) Assaying wollastonite in skarn. In Industrial Minerals in Canada, Canadian Institute of Mining, Metallurgy and Petroleum Special Volume, 53, 303-312.

Dollase, W.A. (1986) Correction of intensities for preferred orientation in powder diffractometry: application of the March model. Journal of Applied Crystallography, 19, 267-272.

Dutta, H. and Pradhan, S.K. (2003) Microstructure characterization of high energy ball-milled nanocrystalline V_2O_5 by Rietveld analysis. Materials Chemistry and Physics, 77, 868-877.

Giester, G., Lengauer, C.L., and Rieck, B. (2000) The crystal structure of nesquehonite, $MgCO_3 \cdot 3H_2O$, from Lavrion, Greece. Mineralogy and Petrology, 70, 153-163.

Glinnemann, J., King, H.E., Jr., Schulz, H., Hahn, T., La Placa, S.J., and Dacol, F. (1992) Crystal structures of the low-temperature quartz-type phases of silica and germanium dioxide at elevated pressure. Zeitschrift für Kristallographie, 198, 177-212.

Government of Canada (1999) The Canadian Environmental Assessment Act: Comprehensive Study Report: Diavik Diamonds Project. Retrieved June 2008 from the website of The Canadian Environmental Assessment Agency: http://www.acee-ceaa.gc.ca/010/0003/0025/archive_e.htm.

Graham, I., Burgess, J.L., Bryan, D., Ravenscroft, P.J., Thomas, E., Doyle, B.J., Hopkins, R., and Armsrong, K.A. (1998) Exploration history and geology of the Diavik kimberlites, Lac de Gras, Northwest Territories, Canada. In J.J. Gurney, J.L. Gurney, M.D. Pascoe, and S.H. Richardson, Eds., Proceedings of the VIIth International Kimberlite Conference, 1, 262-279. Red Roof Design, Cape Town, South Africa.

Grady, M.M., Gibson, E.K., Jr., Wright, I.P., and Pillinger, C.T. (1989) The formation of weathering products on the LEW 85320 ordinary chondrite: evidence from

carbon and oxygen stable isotope compositions and implications for carbonates in SNC meteorites. Meteoritics, 24, 1-7.

Gualtieri, A.F. (2000) Accuracy of XRPD QPA using the combined Rietveld – RIR method. Journal of Applied Crystallography, 33, 267-278.

Hill, R.J. and Howard, C.J. (1987) Quantitative phase analysis from neutron powder diffraction data using the Rietveld method. Journal of Applied Crystallography, 20, 467-474.

Hoffert, M.I., Caldeira, K., Benford, G., Criswell, D.R., Green, C., Herzog, H., Jain, A.K., Kheshgi, H.S., Lackner, K.S., Lewis, J.S., Lightfoot, H.D., Manheimer, W., Mankins, J.C., Mauel, M.E., Perkins, L.J., Schlesinger, M.E., Volk, T., and Wigley, T.M.L. (2002) Advanced technology paths to global climate stability: energy for a greenhouse planet. Science, 298, 981-987.

Huot, F., Beaudoin, G., Hebert, R., Constantin, M., Bonin, G., and Dipple, G. (2003) Evaluation of Southern Québec asbestos residues for CO_2 sequestration by mineral carbonation; preliminary results. Joint Annual Meeting of the Geological and Mineralogical Associations of Canada, Vancouver, BC, Canada. May 25-28, 2003.

Inaba, S., Minakawa, T., and Noto, S. (1985) Nesquehonite and dypingite from Shiraki, Mie Prefecture, Japan. Chigaku Kenkyu, 34, 281-287.

Järvinen, M. (1993) Application of symmetrized harmonics expansion to correction of the preferred orientation effect. Journal of Applied Crystallography, 26, 525-531.

Jambor, J.L. and Blowes, D.W. (1998) Theory and applications of mineralogy in environmental studies of sulfide-bearing mine wastes. In L.J. Cabri and D.J. Vaughn, Eds., Modern Approaches to Ore and Environmental Mineralogy, 27, 367-401. Mineralogical Association of Canada, Ottawa, ON, Canada.

Jambor, J.L. and Blowes, D.W. (1991) Mineralogical study of low-sulphide, high-carbonate, arsenic-bearing tailings from the Delnite minesite, Timmins, Ontario. In Proceedings of the 2nd International Conference on the Abatement of Acidic Drainage (Montréal, Québec, Canada), 4, 173-197.

Jambor, J.L., Dutrizac, J.E., and Raudsepp, M. (2007) Measured and computed neutralization potentials from static tests of diverse rock types. Environmental Geology, 52, 1019-1031.

Jambor, J.L., Dutrizac, J.E., Groat, L.A., and Raudsepp, M. (2002) Static tests of neutralization potentials of silicate and aluminosilicate minerals. Environmental Geology, 43, 1-17.

Jerome, L.E. and Mohanty, G.P. (1979) Deformation-induced structural effects in cerium. Journal de Physique Colloque, C5, 381-382.

Jull, A.J.T., Cheng, S., Gooding, J.L., and Velbel, M.A. (1988) Rapid growth of magnesium-carbonate weathering products in a stony meteorite from Antarctica. Science, 242, 417-419.

Kawano, M. and Tomita, K. (1996) Amorphous aluminum hydroxide formed at the earliest weathering stages of K-feldspar. Clays and Clay Minerals, 44, 672-676.

Kloprogge, J.T., Martens, W.N., Nothdurft, L., Duong, L.V., and Webb, G.E. (2003) Low temperature synthesis and characterization of nesquehonite. Journal of Materials Science Letters, 22, 825-829.

Kump, L.R., Brantley, S.L., and Arthur, M.A. (2000). Chemical weathering, atmospheric CO_2, and climate. Annual Review of Earth and Planetary Sciences, 28, 611-667.

Lackner, K.S. (2003) Climate change: A guide to CO_2 sequestration. Science, 300, 1677-1678.

Lackner, K.S., Wendt, C.H., Butt, D.P., Joyce, G.L., and Sharp, D.H. (1995) Carbon dioxide disposal in carbonate minerals. Energy, 20, 1153-1170.

Lawrence, R.W. and Scheske, M. (1997) A method to calculate the neutralization potential of mining wastes. Environmental Geology, 32, 100-106.

March, A. (1932) Mathematische theorie der regelung nach der korngestalt bei affiner deformation. Zeitschrift für Kristallographie, 81, 285-297.

Maslen, E.N., Streltsov, V.A., Streltsova, N.R., and Ishizawa, N. (1995) Electron density and optical anisotropy in rhombohedral carbonates. III. Synchrotron X-ray studies of $CaCO_3$, $MgCO_3$ and $MnCO_3$. Acta Crystallographica Section B: Structural Science, B51, 929-939.

McLean, H., Banas, A., Creighton, S., Whiteford, S., Luth, R.W., and Stachel, T. (2007) Garnet xenocrysts from the Diavik Mine, NWT, Canada: composition, color, and paragenesis. Canadian Mineralogist, 45, 1131-1145.

McLean, R.J.C., Jamieson, H.E., and Cullimore, D.R. (1997) Formation of nesquehonite and other minerals as a consequence of biofilm dehydration. World Journal of Microbiology and Biotechnology, 13, 25-28.

Mellini, M. and Viti, C. (1994) Crystal structure of lizardite-1T from Elba, Italy. American Mineralogist, 79, 1194-1198.

Mining Association of Canada (2007) Towards Sustainable Mining Progress Report 2007: GHG Emissions and Energy Management Progress Report. Retrieved January 25, 2008 from the website of the Mining Association of Canada: http://www.mining.ca/www/Towards_Sustaining_Mining/Technical_Data_and_Bulletins.php.

Mitchell, R.H. (1986) Kimberlites: Mineralogy, Geochemistry and Petrology. Plenum Press, New York, NY, USA.

Mitchell, R.H. and Putnis, A. (1988) Polygonal serpentine in segregation-textured kimberlite. Canadian Mineralogy, 26, 991-997.

Moore, D.M. and Reynolds, R.C., Jr. (1997) X-ray Diffraction and the Identification and Analysis of Clay Minerals, Second Edition. Oxford University Press, New York, NY, USA.

Omotoso, O., McCarty, D.K., Hillier, S., and Kleeberg, R. (2006) Some successful approaches to quantitative mineral analysis as revealed by the 3rd Reynolds Cup contest. Clays and Clay Minerals, 54, 748-760.

O'Neil, J.R. and Barnes, I. (1971) C^{13} and O^{18} compositions in some fresh-water carbonates associated with ultramafic rocks and serpentinites: western United States. Geochimica et Cosmochimica Acta, 35, 687-697.

Pacala, S. and Socolow, R. (2004) Stabilization wedges: solving the climate problem for the next 50 years with current technologies. Science, 305, 968-972.

Paktunc, A.D. and Davé, N.K. (2002) Formation of secondary pyrite and carbonate minerals in the Lower Williams Lake tailings basin, Elliot Lake, Ontario, Canada. American Mineralogist, 87, 593-602.

Pawley, G.S. (1981) Unit-cell refinement from powder diffraction scans. Journal of Applied Crystallography, 14, 357-361.

Power, I.M., Wilson, S.A., Thom, J., Dipple, G.M., and Southam, G. (2007) Biologically induced mineralization of dypingite by cyanobacteria from an alkaline wetland near Atlin, British Columbia, Canada. Geochemical Transactions, 8, article 13.

Power, I.M., Wilson, S.A., Thom, J.M., Dipple, G.M., Gabites, J.E., and Southam, G. (2009) The hydromagnesite playas of Atlin, British Columbia, Canada: A biogeochemical model for CO_2 sequestration. Chemical Geology, 260, 286-300.

Price, W.A. and Errington, J.C. (1998) Guidelines for metal leaching and acid rock drainage at minesites in British Columbia. Retrived June 6, 2008 from the website of the British Columbia Ministry of Energy, Mines and Petroleum Resources: http://www.em.gov.bc.ca/Subwebs/mining/Project_Approvals/guidelines.htm#Metal%20Leaching%20and%20Acid%20Rock%20Drainage.

Raudsepp, M., Pani, E., and Dipple, G.M. (1999) Measuring mineral abundance in skarn. I. The Rietveld method using X-ray powder-diffraction data. Canadian Mineralogist, 37, 1-15.

Raudsepp, M. and Pani, E. (2003) Application of Rietveld analysis to environmental mineralogy. In J.L. Jambor, D.W. Blowes, and A.I.M. Ritchie, Eds., Environmental Mineralogy of Mine Wastes, 31, 165-180. Mineralogical Association of Canada, Ottawa, ON, Canada.

Reinson, J. (2006) Diavik Diamond Mines Inc. management of the processed kimberlite containment facility: short term management plan, revision A. Prepared by Golder Associates Ltd., document number 05-1328-006/059-2012, report #0024.

Rietveld, H.M. (1969) A profile refinement method for nuclear and magnetic structures. Journal of Applied Crystallography, 2, 65-71.

Rimsaite, J. (1979) Natural amorphous materials, their origin and identification procedures. In M.M. Mortland and V.C. Farmer, Eds., Proceedings of the VIth International Clay Conference, Developments in Sedimentology, 27, 567-577. Elsevier Scientific Publishing Company, Amsterdam, The Netherlands.

Rinaudo, C., Gastaldi, D., and Bulluso, E. (2003) Characterization of chrysotile, antigorite and lizardite by FT-Raman spectroscopy. Canadian Mineralogist, 41, 883-890.

Robertson, J.D., Tremblay, G.A., and Fraser, W.W. (1997) Subaqueous tailing disposal: a sound solution for reactive tailings. In Proceedings of the Fourth International Conference on Acid Rock Drainage, 3, 1027-1044. MEND, Natural Resources Canada, Ottawa, ON, Canada.

Rollo, H.A. and Jamieson, H.E. (2006) Interaction of diamond mine waste and surface water in the Canadian Arctic. Applied Geochemistry, 21, 1522-1538.

Sakharov, B.A., Dubinska, E., Bylina, P., Kozubowski, J.A., Kapron, G., and Frontczak-Baniewicz, M. (2004) Serpentine-smectite interstratified minerals from Lower Silesia (SW Poland). Clays and Clay Minerals, 52, 55-65.

Sanchez, M.S. and Gunter, M.E. (2006) Quantification of amphibole content in expanded vermiculite products from Libby, Montana U.S.A. using powder X-ray diffraction. American Mineralogist, 91, 1448-1451.

Seifritz, W. (1990) CO_2 disposal by means of silicates. Nature, 345, 486.

Sharp, T.G., Otten, M.T., and Buseck, P.R. (1990) Serpentinization of phlogopite phenocrysts from a micaceous kimberlite. Contributions to Mineralogy and Petrology, 104, 530-539.

Shirozu, H. and Bailey, S.W. (1966) Crystal structure of a two-layer Mg-vermiculite. American Mineralogist, 51, 1124-1143.

Sobek, A.A., Schuller, W.A., Freeman, J.R., and Smith, R.M. (1978) Field and laboratory methods applicable to overburdens and minesoils. US Environmental Protection Agency Report EP-600/2-78-054.

Solomon, S., Qin, D., Manning, M., Chen, Z., Marquis, M., Averyt, K.B., Tignor, M., and Miller, H.L., Eds. (2007) Climate Change 2007: The Physical Basis. Contribution of Working Group I to the Fourth Assessment Report of the Intergovernmental Panel on Climate Change. Cambridge University Press, Cambridge, UK and New York, NY, USA.

Sundquist, E.T. (1993) The global carbon dioxide budget. Science, 259, 934-941.

Sundquist, E.T. (1985) Geological perspectives on carbon dioxide and the carbon cycle. In E.T. Sundquist and W.S. Broecker, Eds., The Carbon Cycle and Atmospheric CO_2: Natural Variations Archaen to Present, Geophysical Monographs, 32, 5-60. American Geophysical Union, Washington, DC, USA.

Suortti, P. (1972) Effects of porosity and surface roughness on the X-ray intensity reflected from a powder specimen. Journal of Applied Crystallography, 5, 325-331.

Suzuki, J. and Ito, M. (1973) A new magnesium carbonate hydrate mineral, $Mg_5(CO_3)_4(OH)_2 \cdot 8H_2O$, from Yoshikawa, Aichi Prefecture, Japan. Journal of the Japanese Association of Mineralogists, Petrologists and Economic Geologists, 68, 353-361.

Suzuki, J. and Ito, M. (1974) Nesquehonite from Yoshikawa, Aichi Prefecture, Japan: occurrence and thermal behaviour. Journal of the Japanese Association of Mineralogists, Petrologists and Economic Geologists, 69, 275-284.

Ufer, K., Roth, G., Kleeberg, R., Stanjek, H., Dohrmann, R., and Bergmann, J. (2004) Description of X-ray powder pattern of turbostratically disordered layer structures with a Rietveld compatible approach. Zeitschrift für Kristallographie, 219, 519-527.

Wang, A., Wang, W., and Zhang, A. (1991) Microstructural variations of a pyrope inclusion in diamond, as revealed by a micro-Raman spectroscopic study. Canadian Mineralogist, 29, 517-524.

Wilson, S.A., Dipple, G.M., Power, I.M., Thom, J.M., Anderson, R.G., Raudsepp, M., Gabites, J.E., and Southam, G. (2009) Carbon dioxide fixation within mine tailings at the Clinton Creek and Cassiar chrysotile deposits, Canada. Economic Geology, 104, 95-112.

Wilson, S.A., Raudsepp, M., and Dipple, G.M. (2006) Verifying and quantifying carbon fixation in minerals from serpentine-rich mine tailings using the Rietveld method with X-ray powder diffraction data. American Mineralogist, 91, 1331-1341.

Wilson, S.A., Dipple, G.M., Anderson, R.G., and Raudsepp, M. (2004) Characterization of Clinton Creek mine residues and their suitability for CO_2 sequestration. British Columbia and Yukon Chamber of Mines Mineral Exploration Roundup 2004, Vancouver, BC, Canada. January 26-29, 2004.

Wilson, S.A., Thom, J.M., Dipple, G.M., Raudsepp, M., and Anderson, R.G. (2005) Towards sustainable mining: uptake of greenhouse gases by mine tailings. British Columbia and Yukon Chamber of Mines Mineral Exploration Roundup 2005, Vancouver, BC, Canada. January 24-27, 2005.

Yu, S.C. (1997) Effects of pressure on the crystal structure of olivine in harzburgite xenolith of basalt. Proceedings of the National Science Council, Republic of China, 21, 173-179.

Chapter 3

Carbon isotopic fractionation between dypingite, $Mg_5(CO_3)_4(OH)_2 \cdot 5H_2O$, and aqueous bicarbonate in an evaporative and highly saline system[1]

3.1 Introduction

Dypingite [$Mg_5(CO_3)_4(OH)_2 \cdot 5H_2O$] is the most common intermediate phase in the decomposition of nesquehonite [$MgCO_3 \cdot 3H_2O$] to hydromagnesite [$Mg_5(CO_3)_4(OH)_2 \cdot 4H_2O$] in abiotic precipitation/decomposition experiments (e.g., Davies and Bubela 1973; Canterford et al. 1984; Han and Lee 1985). Dypingite is also found in nature (1) as a weathering product of mafic or ultramafic rocks and mine tailings (Raade 1970; Suzuki and Ito 1973; Inaba et al. 1986; Gore et al. 1996; Wilson et al. 2006, 2009) and (2) in association with cyanobacterial colonies in Mg-rich alkaline wetlands (Power et al. 2007, 2009). In ultramafic mine tailings, dypingite and other hydrous and basic Mg-carbonate minerals can act as traps for atmospheric carbon dioxide (CO_2), potentially storing this greenhouse gas in the long term as a mineral (Wilson et al. 2006, 2009).

Wilson et al. (2009) suggest that accelerated carbonation of Mg-silicate mine tailings may be used by some mining operations to offset their greenhouse gas emissions. They propose that a combination of stable carbon and oxygen isotopes and radiocarbon could be used effectively to verify trapping and storage of atmospheric CO_2 within secondary Mg-carbonate minerals in mine tailings. However, at this time very little is known about the fractionation of stable carbon and oxygen isotopes in hydrous and basic Mg-carbonate minerals like dypingite, hydromagnesite, and nesquehonite. In fact, the only published data for fractionation effects in any hydrous or basic Mg-carbonate

---

[1] A version of this chapter will be submitted for publication.
Wilson, S.A., Barker, S.L.L., Dipple, G.M., Atudorei, V., and Thom, J.M. Carbon isotopic fractionation between dypingite, $Mg_5(CO_3)_4(OH)_2 \cdot 5H_2O$, and aqueous bicarbonate in an evaporative and highly saline system.

minerals are two equilibrium isotopic fractionation factors for exchange of oxygen between hydromagnesite and water at 0˚ and 25˚C (O'Neil and Barnes 1971). The lack of equilibrium or kinetic isotopic fractionation factors for Mg-carbonate minerals hampers the interpretation of stable isotope data collected from these minerals. This dearth of information also interferes with the development of a consistent and reliable protocol for verifying mineralization of atmospheric CO_2 within dypingite and related minerals in ultramafic mine tailings. Here, we give a brief review of available equilibrium fractionation factors for carbonate minerals and suggest which ones may be most applicable to studies of carbon mineralization in mine tailings.

To begin bridging this gap, free drift, open system experiments are undertaken to study the partitioning of ^{13}C between dypingite and total dissolved inorganic carbon. The experiments from which dypingite is formed are conducted between 20˚ and 25˚C and the only source of carbon available to the systems is gaseous CO_2 from the laboratory atmosphere. These experiments are designed to simulate conditions under which atmospheric CO_2 is mineralized within hydrous, basic magnesium carbonate minerals like dypingite and hydromagnesite. More specifically, they simulate evaporation-driven precipitation of these minerals from Mg and Cl-rich, high-pH process water, which can be found in the tailings containment facilities of some ultramafic-hosted mines (e.g., the Mount Keith Nickel Mine, Chapter 4). The results of dypingite precipitation experiments are considered in light of previous studies of carbonate mineral precipitation and an isotopic fractionation factor is reported for exchange of carbon between dypingite and dissolved inorganic carbon. We discuss the implications that these experiments have for verification of CO_2 sequestration in mine tailings using isotopic techniques.

3.2 Review of isotopic fractionation factors for carbonate minerals

Due to the high abundance of calcite within the Earth's crust, its utility as an industrial chemical, and the relative ease of its synthesis, the partitioning of stable carbon and oxygen isotopes during precipitation of calcite has been well studied experimentally. Fractionation factors for low-temperature isotopic exchange of carbon and oxygen

between calcite, gaseous carbon dioxide (CO_2) and aqueous carbonate species (i.e., H_2CO_3, HCO_3^-, and CO_3^{2-}) are well-constrained by experiments for equilibrium precipitation of calcite (e.g., Epstein 1953; Rubinson and Clayton 1969; O'Neil et al. 1969; Deines et al. 1974; Friedman and O'Neil 1977; Romanek et al. 1992; Kim and O'Neil 1997; Jiménez-López et al. 2001). A more complete list of references and an in-depth review of equilibrium fractionation factors for hydrogen, carbon, and oxygen and their pertinence to geological systems is provided by Chacko et al. (2001). Considerable attention has also been given to the study of kinetic fractionation of ^{13}C between aqueous and gaseous carbonate species (e.g., Vogel et al. 1970; Stiller et al. 1985; Zhang et al. 1995), with particular emphasis on isotopic fractionation during precipitation and dissolution of calcite (e.g., Turner 1982; Kim and O'Neil 1997; Skidmore et al. 2004). Equilibrium fractionation factors have also been determined for related minerals like siderite, Mg-calcite, and mixed-cation (Mg-Ca-Fe) carbonate minerals by precipitation at low temperatures using inorganic procedures (e.g., Jiménez-López et al. 2004, 2006; Romanek et al. 2009).

Although isotopic fractionation during low-temperature precipitation of calcite has been well studied, undertaking similar studies of dolomite and magnesite has posed a challenge. The kinetic hurdles to precipitating dolomite and magnesite have yet to be overcome in laboratory experiments under ambient conditions and without mediation by micro-organisms (Land 1998; Romanek et al. 2009). Recently, Vasconcelos et al. (2005) used sulphate-reducing bacteria to mediate the precipitation of dolomite to obtain a temperature-dependent oxygen fractionation factor between dolomite and water over the range of 25˚ to 45˚C. However, carbon isotopic fractionation factors have yet to be reported for dolomite precipitated under these conditions. Comparable experimental results have not been published for magnesite although cyanobacteria have been implicated in mediating its precipitation under ambient conditions (Thompson and Ferris 1990).

Traditionally, factors for isotopic fractionation between magnesite and gaseous or aqueous carbon species have been used as proxies for fractionation effects in hydrated Mg-carbonate minerals and hydrated, basic Mg-carbonate minerals (e.g., Kralik 1989; Braithwaite and Zedef 1996; Zedef et al. 2000; Léveillé et al. 2007; Power et al. 2007,

2009; Wilson et al. 2009). However, the lack of low-temperature, experimentally determined equilibrium fractionation factors for dolomite and magnesite necessitates the use of theoretical results to interpret data for natural occurrences of these minerals. A number of approaches have been used to estimate equilibrium fractionation factors for carbonate minerals, including arguments based on mineral chemistry and observations of natural systems (e.g., Clayton et al. 1968; Sheppard and Schwarcz 1970; Barnes and O'Neil 1971; Zachmann and Johannes 1989; Spötl and Burns 1994; Jiménez-López et al. 2004) and the use of statistical mechanical and quantum chemical modelling (e.g., McCrea 1950; Bottinga 1968; O'Neil et al. 1969; Shiro and Sakai 1972; Golyshev et al. 1981; Kieffer 1982; Chacko et al. 1991; Zheng 1999; Deines 2004; Schauble et al. 2006; Chacko and Deines 2008; Rustad et al. 2008).

Although rapid precipitation of carbonate minerals in open systems has often been linked to isotopic disequilibrium (e.g., Fantidis and Ehhalt 1970; Hendy 1971; Turner 1982; Mickler et al. 2004, 2006; Kosednar-Legenstein et al. 2008), the wide range of possible deviations from isotopic equilibrium is difficult to predict for any given geological system. Because of this, equilibrium fractionation factors are best used as a first approximation to explaining isotopic fractionation effects and may be used to identify isotopic disequilibrium (e.g., Mickler et al. 2006).

In order to assess which of the available equilibrium fractionation factors are most appropriate for use in interpreting stable carbon and oxygen isotopic data for magnesite and other Mg-carbonate minerals, temperature-dependent equilibrium carbon and oxygen isotopic fractionation factors for a variety of carbonate minerals are plotted in Figures 3.1 and 3.2. All fractionation factors for carbon and oxygen isotopes are given as $10^3 \ln\alpha_{\text{mineral-CO}_2}$ and $10^3 \ln\alpha_{\text{mineral-H}_2\text{O}}$, respectively. These are experimentally and theoretically determined equilibrium fractionation factors for aragonite, calcite, dolomite, magnesite, and a number of hydrous (s.s., containing structurally bound water) and basic (s.s., containing structurally bound hydroxyl) carbonate minerals.

3.2.1 Equilibrium carbon isotopic fractionation factors for carbonate minerals

Carbon isotopic fractionation factors for minerals are commonly reported for isotopic exchange between a mineral and an aqueous or gaseous carbonate species. In

order to compare fractionation factors for minerals, values of $10^3 \ln\alpha_{mineral\text{-}CO_2}$ have been calculated from factors reported relative to carbonate species other than CO_2. A number of equilibrium carbon isotopic fractionation factors are plotted in Figure 3.1.

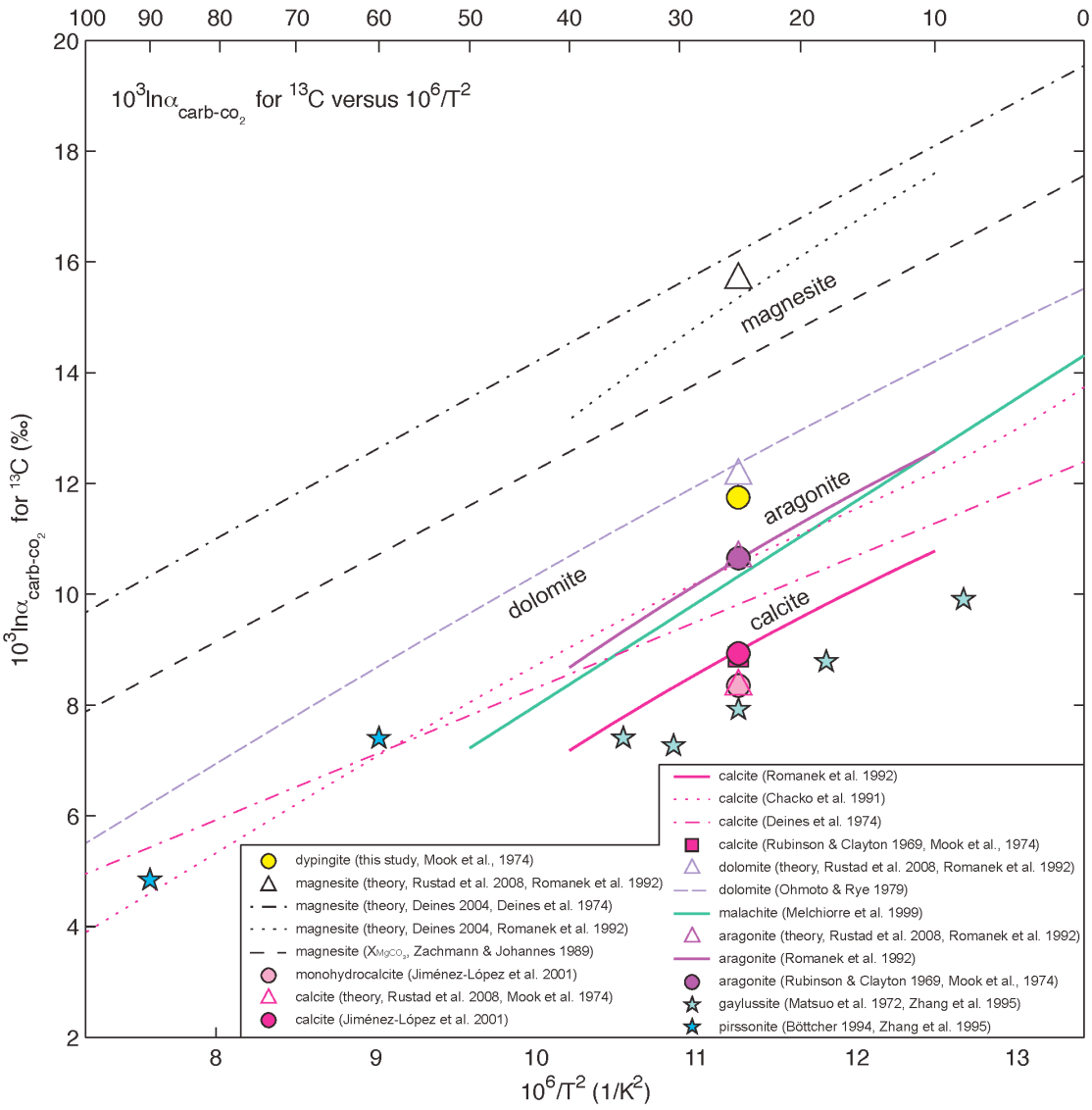

Figure 3.1: Equilibrium carbon isotopic fractionation between carbonate minerals and gaseous CO_2 compiled from experimental and theoretical studies.

The most recent and widely accepted determination of low-temperature fractionation of carbon isotopes between each of aqueous H_2CO_3, HCO_3^-, and CO_3^{2-} and gaseous CO_2 is by Zhang et al. (1995). The results of this experimental study agree very well with previous work by Deuser & Degens (1967), Wendt (1968), Emrich et al.

(1970), Mook et al. (1974), Turner (1982), and Lesniak and Sakai (1989). The fractionation factors of Zhang et al. (1995) were only determined over the range of 5˚-25˚C: however, their results for fractionation between HCO_3^- and CO_2 are in excellent agreement with the earlier results of Mook et al. (1974) in this range of temperatures (Zhang et al. 1995; Chacko et al. 2001). Because Mook et al. (1974) studied the temperature dependence of this fractionation effect from 5˚ to 125˚C, we have applied the Mook et al. (1974) relation to calculations of $10^3 \ln\alpha_{mineral\text{-}CO_2}$ from reported determinations of $10^3 \ln\alpha_{mineral\text{-}HCO_3^-}$. Consequently, values of $10^3 \ln\alpha_{mineral\text{-}CO_2}$ were obtained from fractionation factors between carbonate minerals and aqueous HCO_3^- (Rubinson and Clayton 1969, Rustad et al. 2008 for calcite; Rubinson and Clayton 1969 for dolomite) using the results of Mook et al. (1974) for carbon isotopic fractionation between gaseous CO_2 and aqueous HCO_3^-. Although the experiments of Mook et al. (1974) were conducted at temperatures between 5˚ and 125˚C, we have used their results to extrapolate down to 0˚C.

The experimental results of Romanek et al. (1992) for $10^3 \ln\alpha_{calcite\text{-}CO_2}$ were used to plot theoretical values of $10^3 \ln\alpha_{mineral\text{-}calcite}$ from Deines (2004) and Rustad et al. (2008) (Fig. 3.1). For comparison, the theoretically determined equilibrium fractionation between magnesite and calcite from Deines (2004) was also plotted using the experimental results of Deines et al. (1974) for $10^3 \ln\alpha_{calcite\text{-}CO_2}$.

Values of $10^3 \ln\alpha_{mineral\text{-}CO_2}$ for gaylussite [$Na_2Ca(CO_3)_2 \cdot 5H_2O$] and pirssonite [$Na_2Ca(CO_3)_2 \cdot 2H_2O$] were calculated from experimentally determined values of $10^3 \ln\alpha_{mineral\text{-}CO_3^{2-}}$ for gaylussite (Matsuo et al. 1972) and pirssonite (Böttcher 1994). This was done by extrapolation to higher temperatures of the experimental result of Zhang et al. (1995) for equilibrium fractionation between carbon in aqueous CO_3^{2-} and gaseous CO_2.

3.2.1.1 Ca-carbonate minerals

Experimental data from several low-temperature studies of slow, controlled precipitation of Ca-carbonate minerals from supersaturated solutions are plotted in Fig. 3.1. Among these, results for calcite from Rubinson and Clayton (1969), Romanek et al. (1992), and Jiménez-López et al. (2001) are indistinguishable within experimental error.

The recalculation of Deines et al. (1974) for the temperature dependence of $10^3 \ln\alpha_{calcite\text{-}CO_2}$ used data compiled from a large number of early studies, but it is not in good agreement with more recent results from low-temperature experiments. Also, the theoretical calculations of Chacko et al. (1991) give excellent predictions for fractionation of carbon at high temperatures, but tend to overestimate fractionation effects between calcite and CO_2 at low temperatures (Chacko et al. 2001). Quantum chemical calculations done by Rustad et al. (2008) for $10^3 \ln\alpha_{calcite\text{-}CO_2}$ at 25˚C give a value that is approximately 0.6‰ lower than expected from experiments.

Carbon isotopic fractionation factors for aragonite are similarly well constrained by experiments (e.g., Rubinson and Clayton 1969; Romanek et al. 1992). Also, the theoretical result given by Rustad et al. (2008) for $10^3 \ln\alpha_{aragonite\text{-}CO_2}$ at 25˚C is in very good agreement with experimental fractionation factors from Rubinson and Clayton (1969) and Romanek et al. (1992).

The experimentally determined fractionation factors of Romanek et al. (1992) for calcite and aragonite cover a wide range of low temperatures from 0˚ to 40˚C and are in excellent agreement with results from other experiments. Because of this, we have made use of the results of Romanek et al. (1992) in subsequent calculations involving these minerals.

3.2.1.2 Ca-Mg-carbonate minerals

Ohmoto and Rye (1979) recalculated a fractionation curve for carbon in the system dolomite-CO_2 using results from a field-based study of carbon and oxygen isotopes in paired grains of calcite and dolomite that was done by Sheppard and Schwarcz (1970). The results of Ohmoto and Rye (1979) and Rustad et al. (2008) are mutually consistent for dolomite, but no experimental data are available for direct confirmation. Furthermore, Sheppard and Schwarcz (1970) established that their results were valid over the range of temperatures between 100˚ and 650˚C using the Mg-calcite solvus thermometer. As such, the extrapolation of this curve to significantly lower temperatures, as done by Ohmoto and Rye (1979), may not be valid.

3.2.1.3 Mg-carbonate minerals

Although we do not make direct use of fractionation factors for dolomite in this study, several previous workers have proposed that fractionation factors for magnesite might be derived from those for dolomite. Zachmann and Johannes (1989) argued, based on the stoichiometry of calcite, dolomite, and magnesite, that doubling the co-efficients in the expression of Sheppard and Schwarcz (1970) for $10^3 \ln\alpha_{\text{dolomite-calcite}}$ would produce an approximate expression for $10^3 \ln\alpha_{\text{magnesite-calcite}}$. Deines (2004) used the statistical mechanical approach of Chacko et al. (1991) to compute the temperature dependent fractionation effect for carbon between a number of carbonate minerals and calcite. As with dolomite, no experimental results are available for comparison with theoretical determinations of carbon fractionation between magnesite and CO_2. However, the theoretical fractionation curve of Deines (2004), which is calculated for a large range of temperatures above 0˚C, and that of Rustad et al. (2008) for 25˚C are internally consistent at this temperature (i.e., 25˚C). As noted previously, the fractionation factors computed by Rustad et al. (2008) are in good agreement with experimental results for aragonite and within 0.6‰ of well-established experimental results for calcite. On this basis, we have used the theoretical fractionation curve of Deines (2004) for $10^3 \ln\alpha_{\text{magnesite-calcite}}$ and the experimental curve of Romanek et al. (1992) for $10^3 \ln\alpha_{\text{calcite-}CO_2}$ to estimate the magnitude of carbon isotopic fractionation between magnesite and gaseous CO_2. In the absence of equilibrium fractionation factors, we have adopted the result of Deines (2004) as a rough proxy for the equilibrium fractionation factors of other Mg-carbonate minerals.

3.2.2 Equilibrium oxygen isotopic fractionation factors for carbonate minerals

3.2.2.1 Ca-carbonate minerals

Temperature-dependent equilibrium oxygen isotopic fractionation factors are plotted in Figure 3.2. As with carbon, equilibrium oxygen isotopic fractionation between calcite and water is well-understood. As can be seen from Figure 3.2, the experimental results of Epstein et al. (1953), O'Neil et al. (1969), Kim and O'Neil (1997), and Jiménez-López et al. (2001) are in close agreement at 25˚C. There are, however, small

deviations (on the order of 0.5‰ or less) between several of these curves in the range of 10˚ to 40˚C. The experiments done by Kim and O'Neil (1997) had several advantages over those of previous workers, being stringently controlled to precipitate only calcite, and give internally consistent results for a large number of experiments over a wide range of low temperatures. However, the results of O'Neil et al. (1969) are applicable to a larger range of temperatures. Correspondingly, we have used the results of O'Neil et al. (1969) in any calculations involving $10^3 \ln\alpha_{calcite\text{-}H_2O}$ for oxygen.

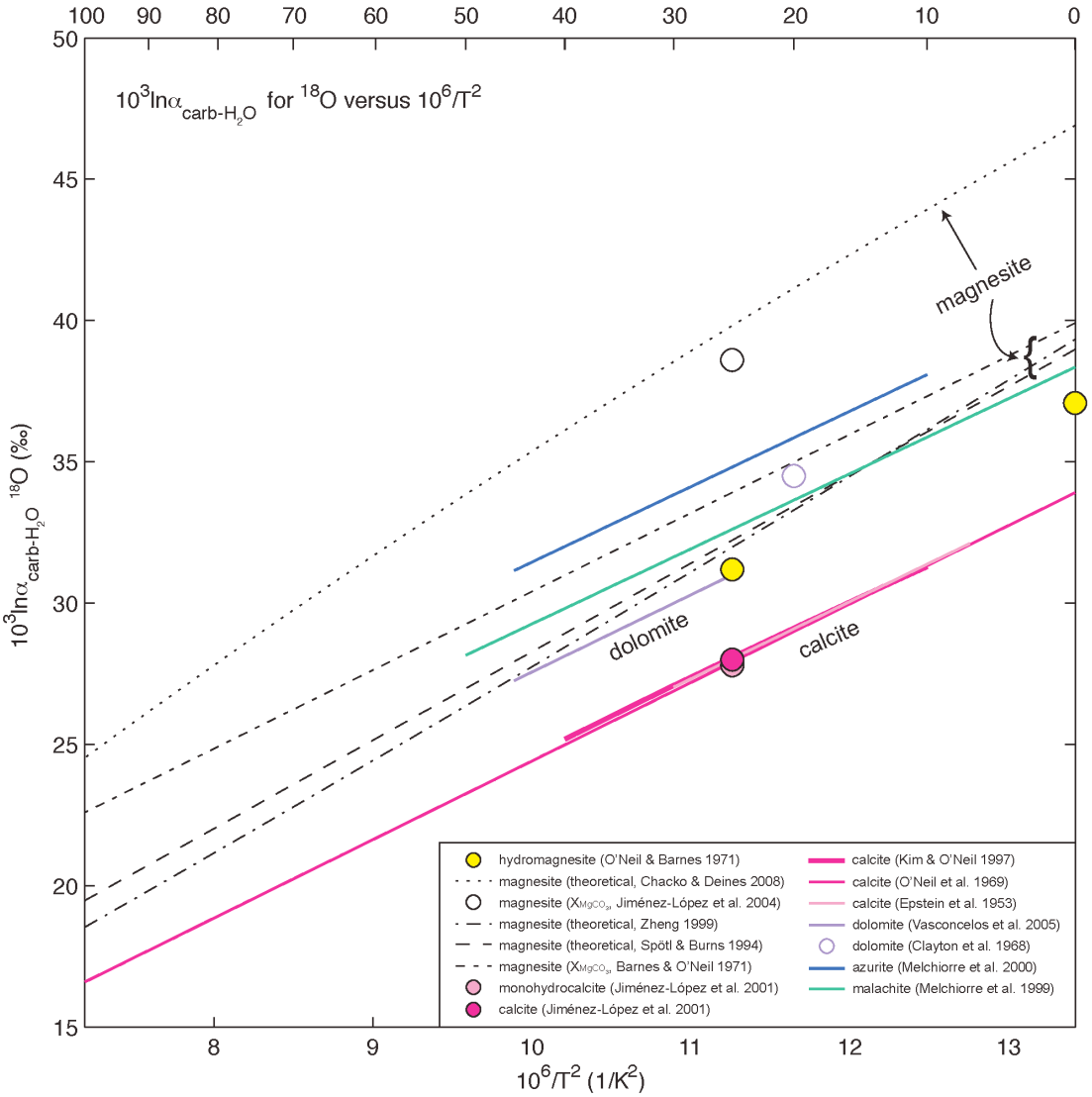

Figure 3.2: Equilibrium oxygen isotopic fractionation between carbonate minerals and gaseous CO_2 compiled from experimental and theoretical studies.

Although we do not make use of fractionation factors for aragonite, it is worth noting the magnitude of the isotopic separation between polymorphs aragonite and calcite. Several studies have been made of oxygen fractionation factors for aragonite in biominerals at low temperatures. Grossman and Ku (1986) obtained an equilibrium oxygen fractionation factor between aragonite and calcite from co-existing aragonitic and calcitic foraminifera. Also, Patterson et al. (1993) determined a fractionation factor for oxygen between aragonite and water by measuring the stable oxygen isotopic composition of fish otoliths and the water in which they lived. Outside of these observations of natural systems, one well-controlled laboratory experiment has been done to obtain a fractionation factor for exchange of oxygen isotopes between aragonite and calcite (Tarutani et al. 1969). This last study indicates that aragonite is enriched in ^{18}O by 0.6‰ over calcite at 25˚C (Fig. 3.2).

3.2.2.2 Ca-Mg-carbonate minerals

An oxygen isotopic fractionation curve for $10^3\ln\alpha_{dolomite\text{-}H_2O}$ from 25˚ to 45˚C has been determined by Vasconcelos et al. (2005) using sulphate-reducing bacteria to overcome kinetic barriers to low-temperature precipitation of dolomite. As expected, and observed for calcite and aragonite (Kim and O'Neil 1997), the temperature dependence (which is indicated by the slopes of the curves) of fractionation factors for dolomite and calcite are very similar at low temperatures. A single estimate of $10^3\ln\alpha_{dolomite\text{-}H_2O}$ for a natural sample of dolomite precipitating from an alkaline lake at 20˚C (Clayton et al. 1968) is inconsistent with the experimental results of Vasconcelos et al. (2005), overestimating the $10^3\ln\alpha_{dolomite\text{-}H_2O}$ relative to the experimental fractionation curve.

On the basis of stoichiometry, Barnes and O'Neil (1971) argue that $10^3\ln\alpha_{mineral\text{-}H_2O}$ for oxygen in dolomite and magnesite could be approximated by combining (1) the oxygen isotopic fractionation factor for calcite-H_2O of O'Neil et al. (1969) with (2) the observation made by Tarutani et al. (1969) that the fractionation between Mg-calcite and water increases by 0.06‰ for every mole-% of $MgCO_3$ in the solid solution. Estimating the fractionation of oxygen between dolomite and water using the stoichiometric argument made by Barnes and O'Neil (1971) gives an estimate of $10^3\ln\alpha_{dolomite\text{-}H_2O}$ = 31.1‰ at 25˚C, which compares favourably to $10^3\ln\alpha_{dolomite\text{-}H_2O}$ = 31.0‰, obtained from

the fractionation curve of Vasconcelos et al. (2005). Therefore, we recommend adoption of the fractionation factor of Vasconcelos et al. (2005).

3.2.2.3 Mg-carbonate minerals

Theoretical values of $10^3 \ln\alpha_{magnesite\text{-}H_2O}$ have been proposed by Barnes and O'Neil (1971), Spötl and Burns (1994), Zheng (1999), and Chacko and Deines (2008). The agreement between the theoretical result of O'Neil and Barnes (1971) and the experiments of Vasconcelos et al. (2005) for $10^3 \ln\alpha_{dolomite\text{-}H_2O}$ suggests that the estimate of $10^3 \ln\alpha_{magnesite\text{-}H_2O}$ made by Barnes and O'Neil (1971) may be an effective proxy for experimental fractionation factors for magnesite (Fig. 3.2). However, more recent work by Jiménez-López et al. (2004) suggests that the equilibrium fractionation between oxygen in Mg-calcite and water may actually be as much as (0.17 ± 0.02)‰ for every mole-% of $MgCO_3$. Estimating $10^3 \ln\alpha_{magnesite\text{-}H_2O}$ using data from Jiménez-López et al. (2004), assuming ideal magnesite stoichiometry and that the fractionation observed for Mg-calcite and water holds over the entire calcite-magnesite solid solution, gives what may be an unrealistically large $10^3 \ln\alpha_{magnesite\text{-}H_2O}$ (Fig. 3.2).

Spötl and Burns (1994), using an approach proposed by Aharon (1988), calculated an oxygen isotope fractionation curve for magnesite-H_2O. This was done by scaling experimentally determined fractionation curves for other divalent metal carbonates according to the known inverse relationship between the ionic radii of divalent cations and the relative oxygen isotopic fractionation of the carbonate minerals that they form. The statistical mechanical computation of Chacko and Deines (2008) for $10^3 \ln\alpha_{dolomite\text{-}H_2O}$ is approximately 2‰ higher than the experimental fractionation factor of Vasconcelos et al. (2005) at 25˚C, suggesting that their fractionation factor for magnesite may also be overestimated. In the absence of experimentally determined fractionation factors for magnesite-H_2O, we recommend the use of fractionation factors proposed by either Barnes and O'Neil (1971) or Spötl and Burns (1994). Although these fractionation factors have not been validated by experiments, they were determined based on careful observation of natural systems and experimental results for chemically and structurally related minerals.

3.2.3 Equilibrium isotopic fractionation factors for hydrous and basic carbonate minerals

Isotopic fractionation factors are provided for the following hydrous and basic carbonate minerals (Figs. 3.1-3.4): hydromagnesite [$Mg_5(CO_3)_4(OH)_2{\cdot}4H_2O$], monohydrocalcite [$CaCO_3{\cdot}H_2O$], gaylussite [$Na_2Ca(CO_3)_2{\cdot}5H_2O$], pirssonite [$Na_2Ca(CO_3)_2{\cdot}2H_2O$], azurite [$Cu_3(CO_3)_2(OH)_2$], and malachite [$Cu_2(CO_3)(OH)_2$]. Fractionation effects between pairs of more and less hydrous carbonate minerals are shown in Figures 3.3 and 3.4. It can be seen from Figure 3.3, that monohydrocalcite is isotopically lighter in carbon than calcite under equilibrium conditions (Jiménez-López et al. 2001). A similar trend can be seen for pirssonite and gaylussite, with the more hydrous gaylussite being isopically lighter than pirssonite.

Oxygen isotopic fraction factors (Fig. 3.4) show the same trend as those for carbon (Fig. 3.3). Measurements of $10^3\ln\alpha_{\text{hydromagnesite-}H_2O}$ (from O'Neil and Barnes 1971) are consistently lower in magnitude than predictions made for magnesite (e.g., Barnes and O'Neil 1971; Spötl and Burns 1994). The fractionation curves from Melchiorre et al. (1999, 2000) show that malachite is isotopically lighter in oxygen than the less hydrous azurite. In all of these cases, the equilibrium fractionation effects are smaller for more hydrous and more basic mineral phases than for related, anhydrous or less hydrous/basic minerals. There is no statistically significant difference in the $10^3\ln\alpha$ values for oxygen isotopic fractionation between calcite and monohydrocalcite and H_2O (Jiménez-López et al. 2001). However, it follows that the presence of more strongly-bonded hydroxyl groups within a mineral's structure may give rise to larger differences in fractionation factors than structural H_2O. If the relationships observed in Figures 3.3 and 3.4 hold for other carbonate minerals, one would expect basic and hydrous Mg-carbonate minerals to be isotopically lighter in both carbon and oxygen than magnesite formed at isotopic equilibrium under the same conditions.

Bonding environment exerts significant control over the energy states of the constituent atoms of a mineral (e.g., Chacko et al. 2001). Because of this, crystal chemistry will influence carbon and oxygen isotopic fractionation in Mg-carbonate minerals. Significant differences in stable carbon and oxygen isotopic fractionation are observed between the $CaCO_3$ polymorphs, calcite (R-3c) and aragonite (Pmcn) (e.g.,

Romanek et al. 1992; Kim and O'Neil 1997). Because of the structural and chemical differences between magnesite and other Mg-carbonate minerals, it cannot be assumed that carbon and oxygen isotopic fractionation effects in these minerals are similar. Consequently, isotopic fractionation factors for specific Mg-carbonate minerals are required for improved analysis of stable isotopic data for these minerals.

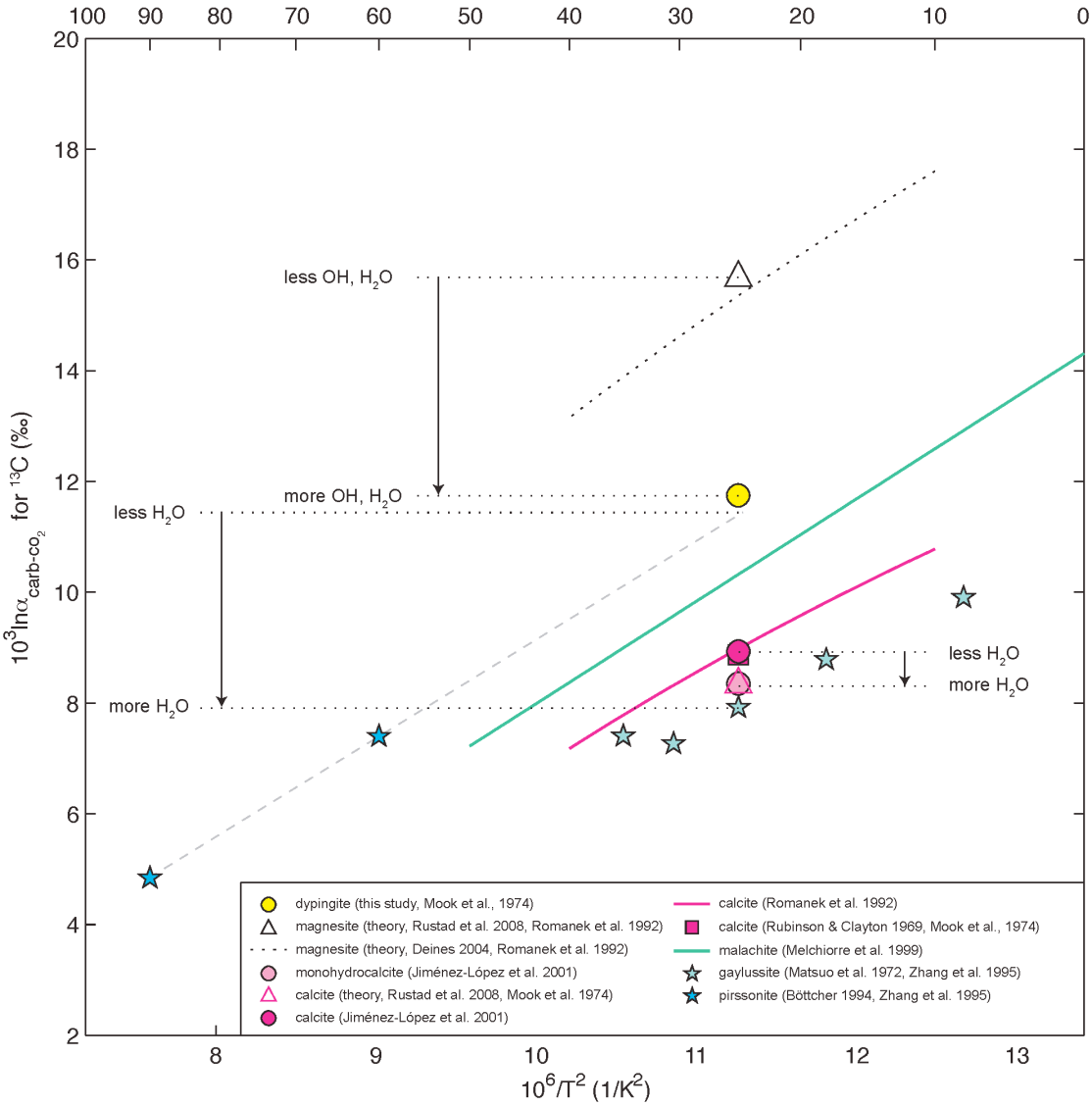

Figure 3.3: Equilibrium carbon isotopic fractionation between hydrous and basic carbonate minerals and gaseous CO_2.

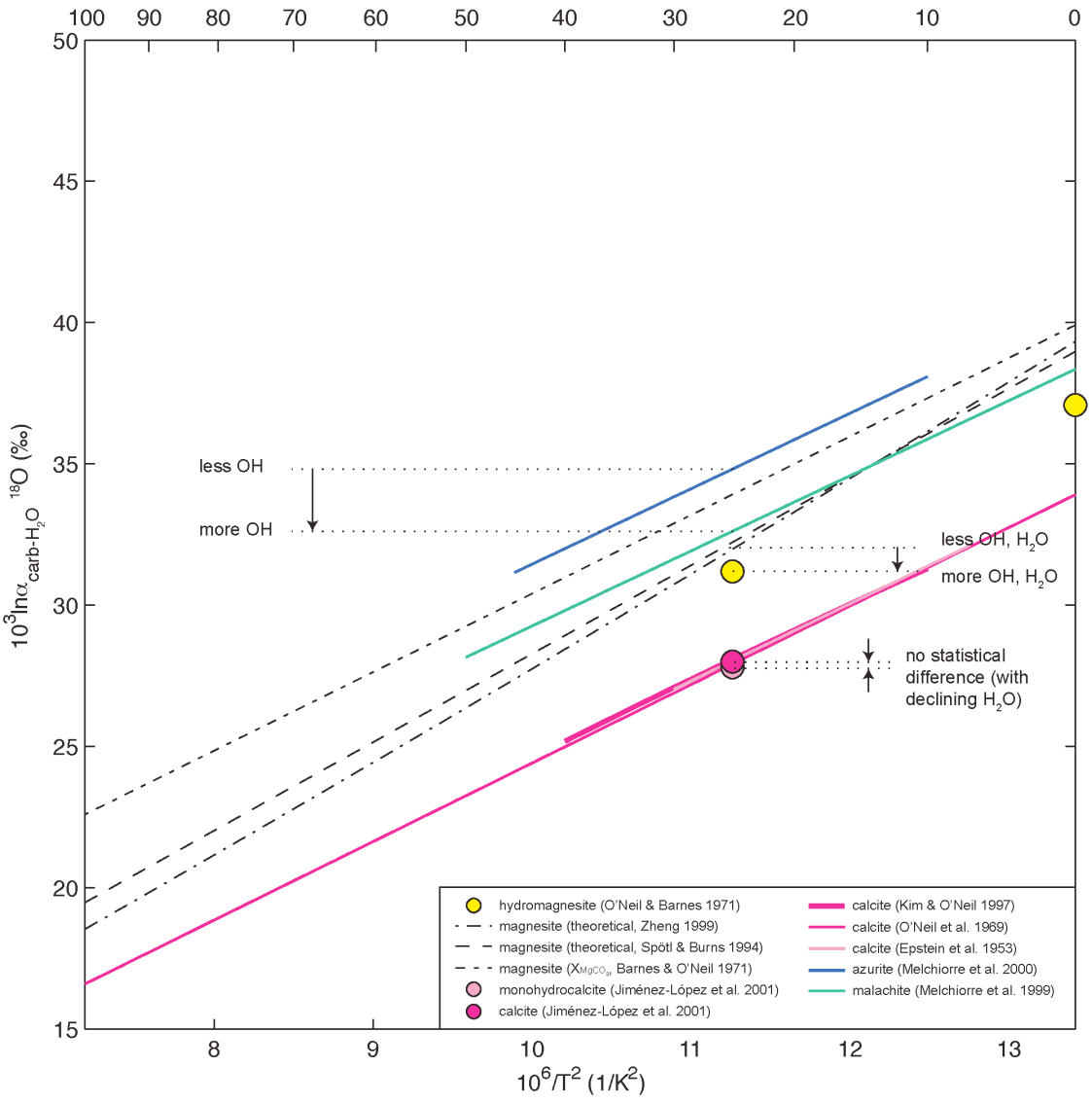

Figure 3.4: Equilibrium oxygen isotopic fractionation between hydrous and basic carbonate minerals and water.

Currently, the only published data for fractionation effects in any hydrous or basic Mg-carbonate minerals are those reported by O'Neil and Barnes (1971) for exchange of oxygen between hydromagnesite and water at 0˚ and 25˚C. It is important to consider here that although O'Neil and Barnes (1971) report precipitation of hydromagnesite within 3 weeks at low temperatures, subsequent studies have not been able to precipitate hydromagnesite below a temperature of 55˚C on such a short timescale (e.g., Botha and Strydom 2001; Li et al. 2003). It should be noted here that the temperature conditions at Mount Keith, and those used in this study, are not as high as

those generally used to precipitate hydromagnesite in the laboratory. However, it is likely that the relative humidity under which Mg-carbonate minerals precipitate exerts some degree of control over the hydration state of these minerals, as it does with hydrous Mg-sulphate minerals. This may explain why hydromagnesite precipitates in the desert at Mount Keith, but dypingite precipitates at comparable temperatures in our laboratory, which is located in a temperate rainforest.

At the time when the results of O'Neil and Barnes (1971) were published, dypingite had only just been recognized as a mineral (Raade 1970). Also, the crystal chemistry and structure of hydromagnesite were still under debate (e.g., Murdock 1954; White 1971; Robie and Hemingway 1972) and were not fully described until publication of the work of Akao et al. (1974), Stephan (1974), and Akao and Iwai (1977b). Until then, "hydromagnesite" was commonly used loosely as a descriptive term for a variety of hydrated and basic Mg-carbonate minerals, a practice that still persists to some extent outside of the mineralogical community. It is not improbable that, at least in the case of the experiment conducted at 25˚C, dypingite was produced instead of hydromagnesite.

3.3 Methods

3.3.1 Procedure for precipitating dypingite

During this study, dypingite was synthesized in two identical bench top precipitation experiments (dyp-may14-09-1 and dyp-may14-09-2) that were run simultaneously under ambient conditions. These initially contained 1.00 mol/L NaCl (Fisher Scientific, Certified ACS Sodium Chloride), 0.100 mol/L $MgCl_2$ (Sigma-Aldrich, Anhydrous Magnesium Chloride assayed at ≥ 98% purity), and 2.5 x 10^2 mol/L NaOH (Fisher Scientific, Certified ACS Sodium Hydroxide). Solutions were prepared gravimetrically from water and reagents that were weighed on a scale with ± 0.1 g precision. Before each experiment commenced, a 2000 mL Pyrex® beaker and a magnetic stir bar were sterilized by rinsing with anhydrous ethanol and were then rinsed three times in Nanopure de-ionized water (17.8 MΩ·cm, prepared using a Barnstead™ E-pure™ water deionization system). A magnetic stir bar and 1500.0 g of Nanopure water

were added to each beaker, whereupon the water was allowed to equilibrate with atmospheric CO_2 by stirring at 500 rpm for approximately 20 minutes using Fisher Scientific magnetic stirplates. At this point, the rotation of the stirbar was reduced to 60 rpm and reagents were added to each beaker as summarized in Table 3.1. A Cole-Parmer Masterflex® L/S® precision standard pump system fitted with two L/S® Easy-Load® II pump heads was used to pump laboratory air into solution. Laboratory air was the sole input of CO_2 into these experiments and is assumed to have had the same composition as the bulk atmosphere (i.e., $P_{CO_2} \approx 4 \times 10^{-4}$ atm). Carbon dioxide in air was introduced into solution using two lengths of Tygon® lab tubing (for each beaker) fit with 0.22 μm Millipore Millex GP sterile syringe filters at their open ends to prevent contamination through the pump. The tubing used had an inner diameter of ~6.4 mm and, with the pump system set to 500 rpm, bubbled approximately 2.8×10^3 mL/min of air through solution (based on specifications from the Cole-Parmer website at www.masterflex.com). Experiments were stirred continuously (at either 60 rpm or 100 rpm), maintained at laboratory temperature, and left open to the atmosphere so that evaporation could drive the solutions to supersaturation with respect to dypingite.

Table 3.1: Starting conditions for experiments dyp-may14-09-1 and dyp-may14-09-2.

Experiment	**m_{H_2O} (g) (±0.1 g)**	**m_{NaCl} (g) (±0.1 g)**	**m_{MgCl_2} (g) (±0.1 g)**	**m_{NaOH} (g) (±0.1 g)**	**m_{total} (g) (±0.1 g)**	**m_{equip}[a] (g) (±0.2 g)**
dyp-may14-09-1	1500.0	87.6	14.4	1.5	2247.9	646.3
dyp-may14-09-2	1500.0	87.6	14.4	1.5	2249.5	647.5

[a] Denotes the combined mass of the beaker and stir bar used in the experiment.

Daily measurements were taken for pH, temperature, and total mass of the experiments before and after sampling. Temperature was monitored using a standard mercury laboratory thermometer with ± 0.5ºC precision. A portable Thermo Scientific Orion 4-Star pH/ISE meter was used to measure pH. The pH meter was calibrated daily against three standard buffer solutions that are traceable to NIST standards at pH 4.00, 7.00, and 10.00 (purchased from Fisher Scientific). Both the thermometer and pH electrode were rinsed thoroughly with Nanopure water and carefully dried with a

Kimwipe before and after each measurement. Samples of water for measurement of total dissolved C, $\delta^{18}O$ of water, and $\delta^{13}C$ on dissolved inorganic carbon (DIC) were collected using sterile single-use syringes (from Henke Sass Wolf) fitted with 0.22 μm Millipore Millex GP sterile syringe filters to remove precipitate. Millipore filtered water was injected into 0.5 dram (1.85 mL) vials, leaving no headspace, and sealed vials were wrapped with Parafilm M® to prevent sample loss by evaporation. During the first four days of experiments dyp-may14-09-1 and dyp-may14-09-2, 3-mL volumes of well-mixed solution were drawn daily from each experiment to sample the precipitates. Because this provided too little material for mineralogical analysis, the procedure was revised so that 20-mL volumes were drawn for subsequent samples. These samples were filtered through Whatman No. 1 qualitative filter paper in order to isolate the precipitate. Samples of precipitate were not rinsed in water because dypingite is susceptible to partial decomposition in deionized water (Suzuki and Ito 1973; this study). Precipitate samples were dried under a hood for at least 24 hours, removed from filter paper with a sterile spatula, and gently disaggregated using an alumina mortar and pestle.

3.3.2 Qualitative X-ray powder diffraction methods

Synthetic mineral phases in all samples of precipitate were identified from X-ray powder diffraction (XRPD) patterns. Finely ground aliquots of sample were mounted as slurry onto a zero-background quartz plate with anhydrous ethanol and allowed to dry at room temperature. XRPD data were collected on a Siemens (Bruker) D5000 θ-2θ diffractometer equipped with a VÅNTEC-1 detector. A long, fine-focus Co X-ray tube was operated at 35 kV and 40 mA and an Fe monochromator foil was employed. Data for mineral identification were collected with a step size of 0.04° 2θ and counting time of 1s/step over a range of 2-45° 2θ. Constituent mineral phases were identified with reference to the ICDD PDF-4+ 2008 database using the program DIFFRAC^{plus} EVA 14 (Bruker AXS 2008).

3.3.3 CHN analyses

A Carlo Erba 1106 automatic analyzer was used to measure the wt.% of carbon, hydrogen, and nitrogen in five specimens of natural and synthetically produced

dypingite. On the order of 1 mg of each pulverized mineral specimen was combusted and the resulting gaseous species were scrubbed, reduced, and separated on a gas chromatograph column for measurement at the instrument's detector. CHN analyses were done in the Microanalytical Unit of the Research School of Chemistry, The Australian National University.

3.3.4 Total inorganic carbon measurements

Measurements of total dissolved inorganic carbon were done on 20 samples of filtered water collected from the two precipitation experiments. Measurements were done in the Department of Civil Engineering, The University of British Columbia, using an IL-550 TOC/TN analyzer. Each sample of water was decanted into a sparge vessel and treated with acid to release dissolved carbon as gaseous CO_2. The amount of CO_2 that resulted was measured using an infrared detector.

3.3.5 Stable isotopic methods

The $\delta^{13}C$ and $\delta^{18}O$ values of experimental precipitates and the $\delta^{13}C$ values of dissolved inorganic carbon were analyzed using a gas bench attached to a Thermo Finnigan DeltaPlus XL isotope ratio mass spectrometer (IRMS) at the Department of Earth and Planetary Sciences, The University of New Mexico. Specimens of synthetic minerals and filtered water were treated with phosphoric acid to liberate CO_2 at 50ºC according to the methods of Révész and Landwehr (2002) and Salata et al. (2000), respectively. Specimens were allowed to react with phosphoric acid for two hours. The external precision (1σ deviation) for isotopic analyses was approximately 0.1‰ for both $\delta^{13}C$ and $\delta^{18}O$, as estimated from repeated analysis of calcite standards. Eight specimens of dypingite-rich precipitates were analyzed for $\delta^{18}O$ and $\delta^{13}C$ compositions and 16 samples of filtered water were analyzed for the $\delta^{13}C$ composition of total dissolved inorganic carbon.

$\delta^{18}O$ values of filtered water were measured using a laser spectroscopic Liquid Water Isotope Analyzer from Los Gatos Research, Inc. at the Pacific Centre for Isotopic and Geochemical Research (PCIGR), The University of British Columbia. Eight specimens of filtered water, including one replicate specimen, were analyzed for their

^{18}O concentrations. Tap water was run between analyses of experimental waters as a precaution against accumulation of salts within the isotope analyzer from combustion of these saline waters. Reproducibility of known values for three water standards was better than 0.3‰ for $\delta^{18}O$.

3.4 Analytical Results

3.4.1 X-ray powder diffraction results

Mineral identifications from X-ray powder diffraction patterns are summarized in the last three columns of Tables 3.2 and 3.3. The crystalline phases precipitated in the two experiments are not naturally occurring and, by definition, are not minerals. Nonetheless, for the sake of clarity, synthetic phases will be referred to by the mineral names of their naturally occurring analogues. XRPD patterns of the final precipitates obtained from experiments dyp-may14-09-1 and dyp-may14-09-2 are plotted in Figure 3.5 with three other XRPD patterns for dypingite: one pattern from naturally occurring dypingite from Yoshikawa, Shinshiro Cho, Aichi Prefecture, Japan and two patterns collected on dypingite that was precipitated in association with cyanobacteria (replotted from Power et al. 2007).

Precipitates were not obtained in sufficient quantity for collection of XRPD patterns from either experiment on days 1-3 and no sampling was done on day 7. Again, insufficient quantities of precipitates were obtained from experiment dyp-may14-09-1 on day 13 and from experiment dyp-may14-09-2 on day 10. From the fourth until the sixteenth day of both experiments, poorly crystalline brucite (characterized by broad, asymmetric peaks) was the most abundant phase in the precipitates and was accompanied by a lesser amount of synthetic halite. Although synthetic halite did not precipitate in the bulk solutions, it did form along the interior walls of the beakers and as a crust on the tubing. Experimental precipitates were carefully filtered and dried, so most of the halite detected with XRPD was likely contamination from the tubing and interior walls of the beakers.

Synthetic dypingite was identified in both experiments on day 16: at low abundance in experiment dyp-may14-09-2 and just above detection in experiment dyp-may14-09-1. By the seventeenth day of both experiments, dypingite was the most abundant phase, the relative amount of brucite had declined, and halite remained present at relatively low abundance.

In experiment dyp-may14-09-1, the amount of brucite continued to decline. On day 19 of this experiment, brucite was observed only at trace abundance and by day 20 it was no longer detectable. Contrastingly, brucite remained detectable in precipitates from experiment dyp-may14-09-2 up to and including the final day (i.e., day 21) of the experiment. Notably, the relative amount of brucite in experiment dyp-may14-09-2 did decline considerably over the final six days, but it was still readily detectable in the XRPD pattern from the final precipitate (Fig. 3.5).

3.4.2 Results of CHN determination

CHN data were obtained for four specimens of synthetic dypingite and for the specimen of naturally occurring dypingite from Yoshikawa, Shinshiro Cho, Aichi Prefecture, Japan (Table 3.4). The four specimens of synthetic dypingite are from three precipitation experiments conducted under the same conditions as experiments dyp-may14-09-1 and dyp-may14-09-2, but which were not sampled for water and from which only the final precipitate was collected and analyzed. The elemental abundances of the five specimens vary between 8.3 and 10.3 wt.% for carbon and 2.7 and 3.1 wt.% for hydrogen. No nitrogen was detected in any of the specimens. Some of this variability can be explained by the presence of halite in the experimental precipitates (i.e., jtdypingite, dyp-feb13-07-2, and the rinsed and unrinsed aliquots of dyp-sept23-07-2). This is evidenced by the higher abundances of carbon and hydrogen reported for (1) the natural, halite-free specimen of dypingite from Yoshikawa and (2) an aliquot of synthetic dypingite (from dyp-sept23-07-2) that was rinsed with distilled water to remove halite. The majority of experimental precipitates were not rinsed because the structure of dypingite tends to decompose on exposure to distilled water (Suzuki and Ito 1973; this study).

Table 3.2: Results of dypingite precipitation experiment dyp-may14-09-1.

Day	Date and Time of Sampling	Time (hours)	pH	DIC (mg/L)	T (˚C) (±0.5˚C)	m_{soli} (g) (±0.2 g)	m_{solr} (g) (±0.2 g)	Δm[b] (g) (±0.4 g)	$\delta^{13}C_{DIC}$ (±0.2‰)	$\delta^{18}O_{H2O}$ (±0.3‰)	$\delta^{13}C_{dyp}$ (±0.2‰)	$\delta^{18}O_{dyp}$ (±0.2‰)	dypingite present?[a]	brucite present?[a]	halite present?[a]
1	5/14/09 18:00	0.0	9.22	–	22.0	1601.6	1592.4	–	-19.2	-10.9 -11.3	–	–	–	–	–
2	5/15/09 16:00	22.0	9.35	11.4	20.0	1548.9	1540.7	43.5	–	–	–	–	–	–	–
3	5/16/09 12:30	42.5	9.35	–	20.0	1501.8	1493.5	38.9	-17.4	–	–	–	–	–	–
4	5/17/09 14:15	68.3	9.25	29.0	21.5	1444.4	1414.4	49.1	–	–	–	–	–	M	m
5	5/18/09 14:30	92.5	9.31	–	21.5	1373.1	1347.7	41.3	–	-10.4	–	–	–	M	m
6	5/19/09 16:45	118.8	9.30	44.4	21.0	1299.2	1274.6	48.5	–	–	–	–	–	M	m
8	5/21/09 15:30	165.5	9.23	–	21.0	1190.9	1166.4	83.7	-16.9	–	–	–	–	M	m
9	5/22/09 18:30	192.5	9.16	75.9	23.0	1117.6	1092.5	48.8	–	–	–	–	–	M	m
10	5/23/09 16:05	214.1	9.12	–	22.0	1055.1	1007.3	37.4	–	-6.8	–	–	–	M	m
11	5/24/09 17:40	239.7	9.08	110.3	22.0	967.1	942.3	40.2	–	–	–	–	–	M	m
12	5/25/09 18:20	264.3	9.01	–	23.0	899.3	873.9	43.0	-16.0	–	–	–	–	M	m
13	5/26/09 16:20	286.3	9.03	134.6	22.5	838.3	813.3	35.6	–	–	–	–	–	–	–
14	5/27/09 14:30	308.5	9.01	–	21.5	772.6	747.5	40.7	–	-2.0	–	–	–	M	m
15	5/28/09 15:50	333.8	8.96	151.7	22.0	704.2	678.9	43.3	–	–	–	–	–	M	m
16	5/29/09 16:30	358.5	8.84	–	23.5	636.3	609.8	42.6	-16.2	–	-14.0	27.0	tr	M	m
17	5/30/09 20:30	386.5	8.86	103.9	22.0	565.0	539.5	44.8	–	–	–	–	M	m	m
18	5/31/09 20:10	410.2	8.84	–	22.0	505.9	480.7	33.6	-18.2	–	-15.2	28.2	M	m	m
19	6/1/09 15:45	429.8	8.73	68.1	23.0	452.0	425.7	28.7	–	–	–	–	M	tr	m
20	6/2/09 16:30	454.5	8.65	–	23.0	387.4	362.7	38.3	-20.0	–	-15.4	28.9	M	–	m
21	6/3/09 16:30	478.5	8.48	51.6	24.5	324.0	6.3	38.7	-20.7	–	-15.2	30.2	M	–	m

[a] Detected from X-ray powder diffraction patterns of precipitates. “M” for “Major” denotes the most abundant phase in the sample, “m” for “minor” denotes a minor phase, and “tr” denotes a phase present at trace abundance (i.e., near detection).

[b] Δm is the mass loss of water due to evaporation between sampling events.

Table 3.3: Results of dypingite precipitation experiment dyp-may14-09-2.

Day	Date and Time of Sampling	Time (hours)	pH	DIC (mg/L)	T (˚C) (±0.5˚C)	m_{soli} (g) (±0.2 g)	m_{solf} (g) (±0.2 g)	Δm^b (g) (±0.4 g)	$\delta^{13}C_{DIC}$ (±0.2‰)	$\delta^{18}O_{H2O}$ (±0.3‰)	$\delta^{13}C_{dyp}$ (±0.2‰)	$\delta^{18}O_{dyp}$ (±0.2‰)	dypingite present?[a]	brucite present?[a]	halite present?[a]
1	5/14/09 18:00	0.0	9.22	–	22.0	1602.0	1593.9	–	-19.3	-10.9 -11.3	–	–	–	–	–
2	5/15/09 16:00	22.0	9.34	10.6	20.5	1550.9	1543.4	43.0	–	–	–	–	–	–	–
3	5/16/09 12:30	42.5	9.36	–	20.0	1504.1	1495.7	39.3	-19.0	–	–	–	–	–	–
4	5/17/09 14:15	68.3	9.30	23.3	22.0	1453.6	1423.3	42.1	–	–	–	–	–	M	m
5	5/18/09 14:30	92.5	9.30	–	22.0	1379.3	1354.9	44.0	–	-9.9	–	–	–	M	m
6	5/19/09 16:45	118.8	9.30	43.1	21.5	1303.7	1278.9	51.2	–	–	–	–	–	M	m
8	5/21/09 15:30	165.5	9.21	–	21.5	1190.3	1164.1	88.6	-18.1	–	–	–	–	M	m
9	5/22/09 18:30	192.5	9.16	71.2	23.0	1115.0	1089.1	49.1	–	–	–	–	–	M	m
10	5/23/09 16:07	214.1	9.12	–	22.5	1052.5	1027.4	36.6	–	-6.8	–	–	–	–	–
11	5/24/09 17:40	239.7	9.10	98.8	22.0	984.4	958.8	43.0	–	–	–	–	–	M	m
12	5/25/09 18:20	264.3	9.01	–	23.5	916.6	890.6	42.2	-17.3	–	–	–	–	M	m
13	5/26/09 16:20	286.3	9.02	118.6	23.0	856.0	830.3	34.6	–	–	–	–	–	M	m
14	5/27/09 14:30	308.5	9.01	–	22.0	791.0	765.5	39.3	–	-3.4	–	–	–	M	m
15	5/28/09 15:50	333.8	8.94	135.4	22.5	727.1	701.8	38.4	–	–	–	–	–	M	m
16	5/29/09 16:30	358.5	8.83	–	24.0	674.0	649.0	27.8	-16.9	–	-12.0	25.8	m	M	m
17	5/30/09 20:30	386.5	8.88	123.4	22.5	604.7	579.5	44.3	–	–	–	–	M	m	m
18	5/31/09 20:10	410.2	8.84	–	23.5	555.1	529.6	24.4	-18.2	–	-15.7	28.3	M	m	m
19	6/1/09 15:45	429.8	8.75	83.0	23.5	504.8	479.1	24.8	–	–	–	–	M	m	m
20	6/2/09 16:30	454.5	8.65	–	23.5	436.7	411.1	42.4	-19.8	–	-15.3	29.5	M	m	m
21	6/3/09 16:30	478.5	8.52	62.5	24.5	372.8	4.4	38.3	-20.3	–	-16.9	29.5	M	m	m

[a] Detected from X-ray powder diffraction patterns of precipitates. “M” for “Major” denotes the most abundant phase in the sample, “m” for “minor” denotes a minor phase, and “tr” denotes a phase present at trace abundance (i.e., near detection).

[b] Δm is the mass loss of water due to evaporation between sampling events.

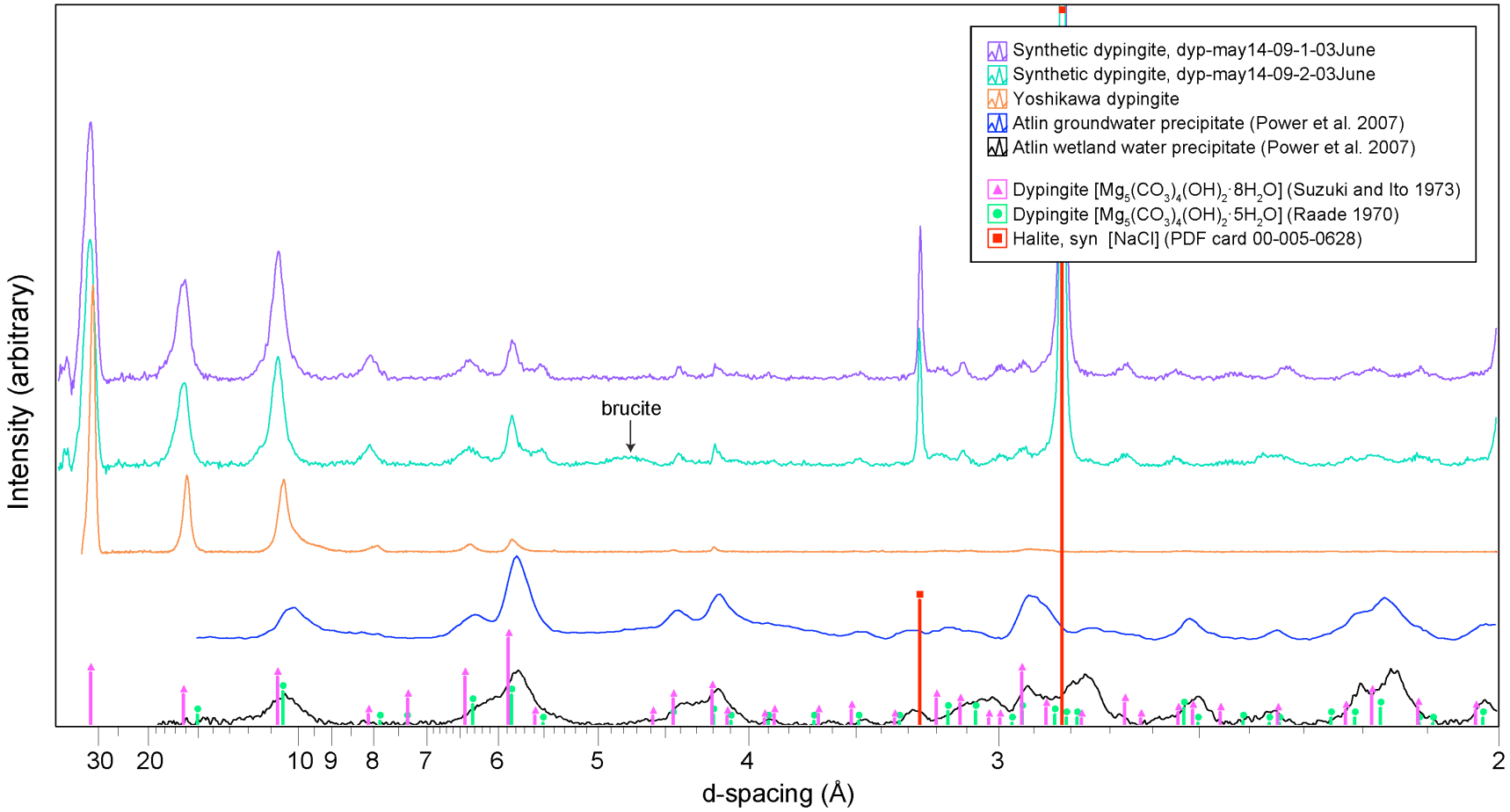

Figure 3.5: X-ray powder diffraction patterns of synthetic and natural dypingite. The two uppermost patterns are of final precipitates from experiments dyp-may14-09-1 and dyp-may14-09-2. The middle pattern is of dypingite from Yoshikawa, Shinshiro Cho, Aichi Prefecture, Japan. The two bottommost patterns are of experimental precipitates formed in association with filamentous cyanobacteria and are replotted from Power et al. (2007).

Table 3.4: CHN data and H-content of dypingite compared to results of previous studies.

Sample Name	C (wt.%)[a]	H (wt.%)[a]	H_{total} (apfu)[b]	H_{OH} (apfu)[b]	H_{H2O} (pfu)[c]	H_2O (pfu)[c]
Yoshikawa dypingite (natural)	10.3	2.9	14	2.0	12	5.8
jtdypingite	8.7	2.7	15	2.0	13	6.4
dyp-feb13-07-2	9.4	3.1	16	2.0	14	6.8
dyp-sept23-07-2 (unrinsed)	8.3	2.8	16	2.0	14	6.9
dyp-sept23-07-2 (rinsed)	9.6	3.1	16	2.0	14	6.8
Raade (1970)			12	2.0	10	5.1
Davies and Bubela (1973)			20	2.0	18	9.1
Suzuki and Ito (1973)			18	2.0	16	7.8
Canterford et al. (1984)			11	2.0	8.7	4.4

[a] Measurement error on C and H determination is approximately ±0.3 wt.%.
[b] Abbreviation of "atoms per formula unit".
[c] Abbreviation of "per formula unit".

3.4.3 Data from monitoring of pH, temperature, and mass loss

Daily measurements of pH, temperature, and mass loss due to evaporation and sampling are summarized in Tables 4.2 and 4.3 and Figures 3.6 and 3.7.

Both experimental solutions began with a pH of 9.22. On the second day of experiments dyp-may14-09-1 and dyp-may14-09-2 this value increased to 9.35 and 9.34, respectively (Fig. 3.6a). The pH of both solutions declined gradually and linearly, reaching values of approximately 8.9 on day 16 when dypingite precipitated. At this point, pH began to change more rapidly – decreasing by approximately 0.4 pH units within six days. On the day the experiments were ended, the pH values for dyp-may14-09-1 and dyp-may14-09-2 were 8.48 and 8.52, respectively.

Solution temperature was controlled by the ambient temperature of the laboratory in which experiments were conducted and was allowed to vary. Temperatures varied between 20.0˚ ± 0.5˚C and 24.5˚ ± 0.5˚C and a general trend toward increasing temperature was observed with time. A temperature gradient of 0.5˚ ± 1.0˚C, which is

undetectable within the precision of our thermometer, may have been present in the laboratory as suggested by consistently lower temperatures measured for experiment dyp-may14-09-1 than for dyp-may14-09-2 (Fig. 3.6b).

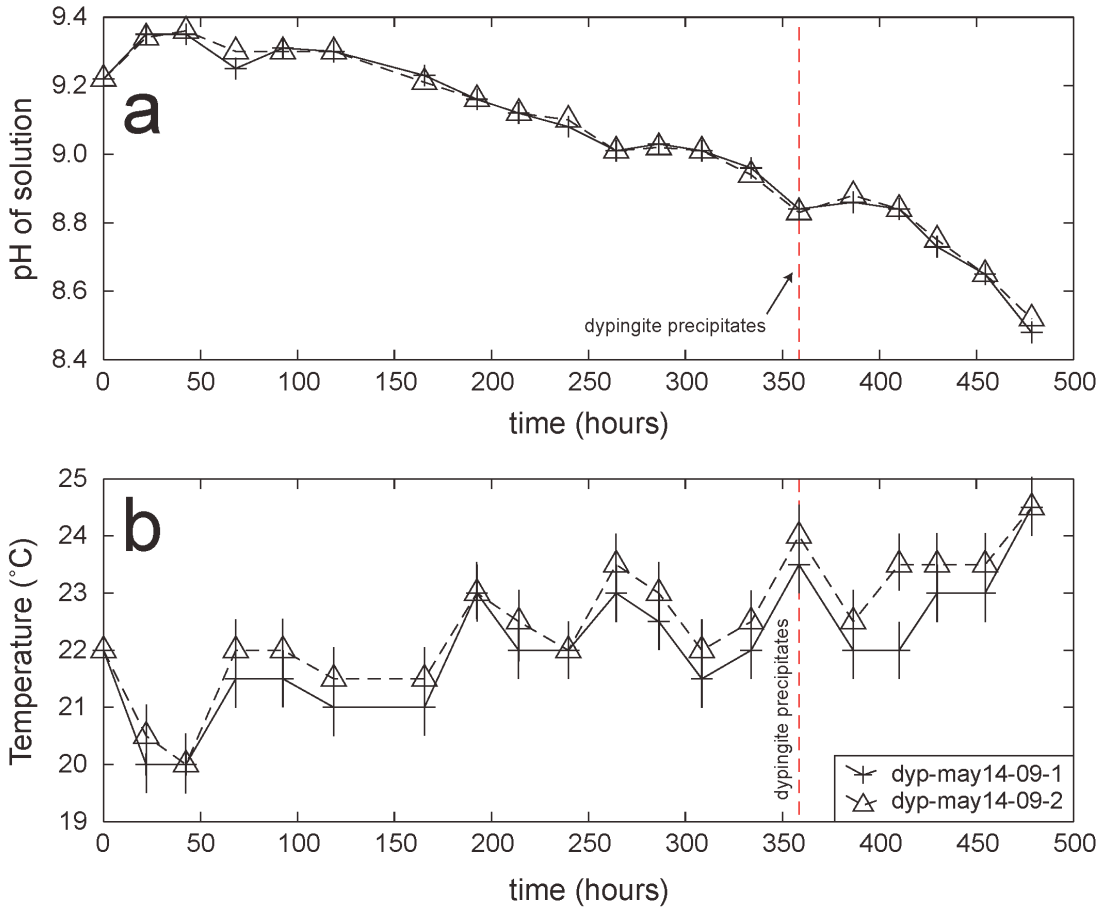

Figure 3.6: pH and temperature (˚C) of solutions over time. Variation of pH with time is plotted in (a) and variation of temperature with time is plotted in (b). The time corresponding to samples in which dypingite was first identified is marked by a dashed line. Measurement errors in (a) are typically smaller than the symbols employed. Uncertainties associated with temperature measurements in (b) are denoted by the extents of the vertical bars.

Figure 3.7a plots the mass of solutions over the duration of the two experiments. A roughly linear decline in mass is observed for both experiments, with a slightly larger negative slope for dyp-may14-09-1. Mass was lost to both evaporation and sampling of solution and precipitates. In experiment dyp-may14-09-1, 1277.6 g (79.8%) of solution plus precipitate were lost over the course of the experiment. The majority, 51.2%, of mass loss resulted from evaporation and the remaining 28.5% was due to sampling.

Experiment dyp-may14-09-2 lost 76.7% of its mass – 49.5% to evaporation and 27.2% to sampling. The average rate of evaporative mass loss is plotted against time in Figure 3.7b. Here, the rate of mass loss due to evaporation is measured between sampling events (typically a 20-30 hour interval). Between 1.4-2.0 g/hour of water were lost to evaporation from experiment dyp-may14-09-1 and 1.0-2.0 g/hour of water were lost from experiment dyp-may14-09-2.

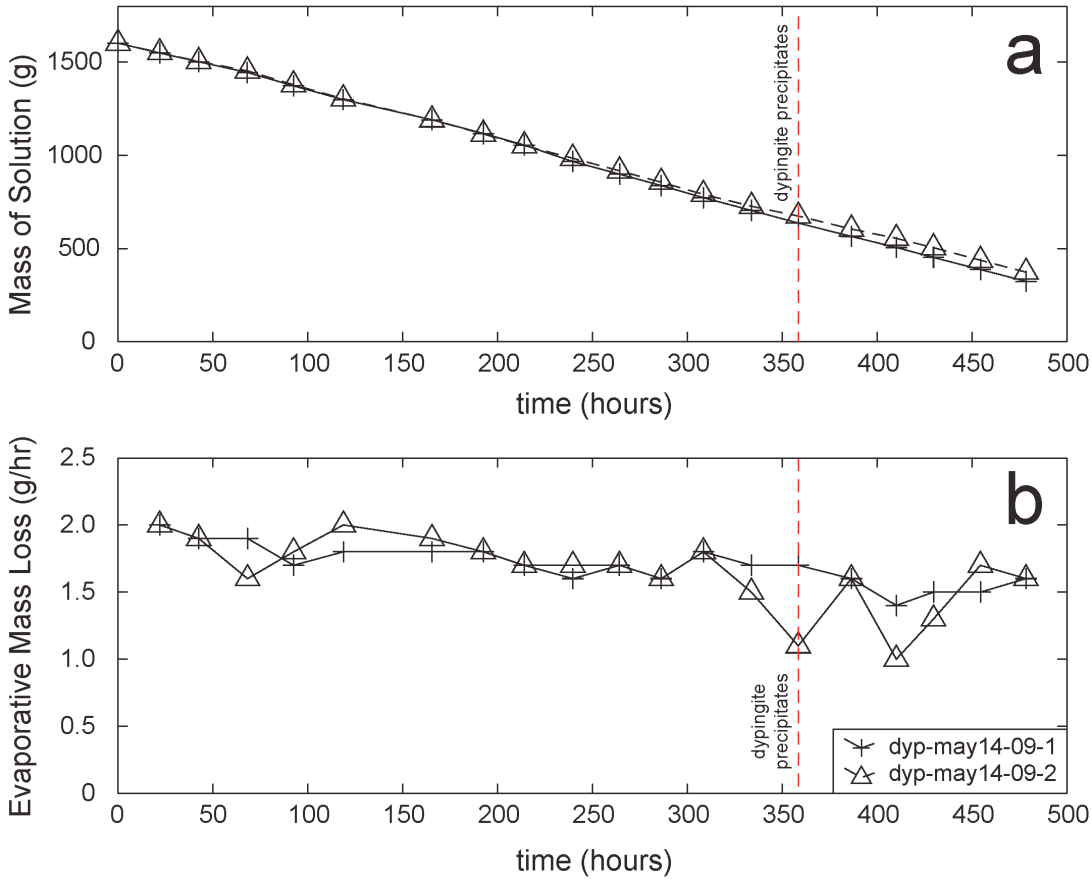

Figure 3.7: Water loss from precipitation experiments over time. (a) Plots the mass of solutions with time and (b) gives average hourly mass loss from solutions between measurements. Uncertainties on measured values are considerably smaller than the symbols employed. The time corresponding to samples in which dypingite was first identified is marked by a dashed line.

3.4.4 Stable isotopic results

The stable carbon isotopic composition of total dissolved inorganic carbon (DIC) was measured for eight samples of filtered water from each experiment (Tables 3.2 and 3.3 and Fig. 3.8). At the onset of experiments dyp-may14-09-1 and dyp-may14-09-2,

$\delta^{13}C_{DIC}$ values were -19.2‰ and -19.3‰, respectively. In both experiments, $\delta^{13}C_{DIC}$ values became progressively more positive over time, reaching maximum measured values on day 16 of the experiments at the onset of dypingite precipitation. Maximum values of $\delta^{13}C_{DIC}$ were -16.2‰ and -16.9‰ for dyp-may14-09-1 and dyp-may14-09-2, respectively. After day 16, $\delta^{13}C_{DIC}$ values became progressively more negative.

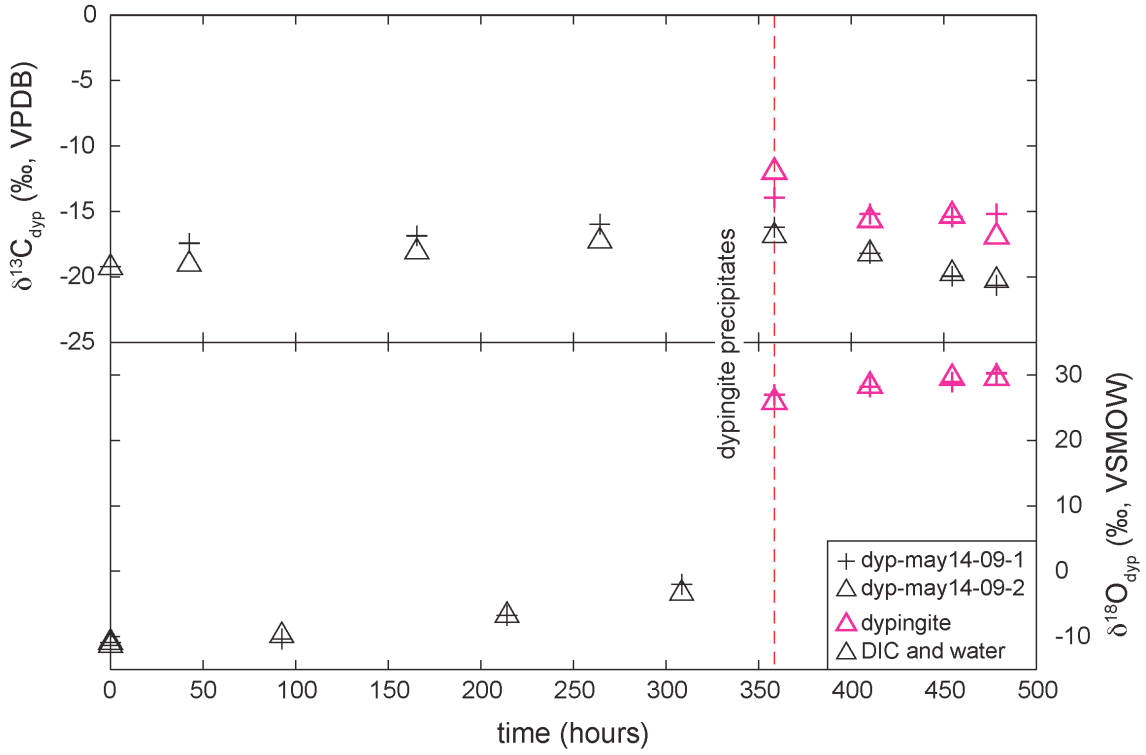

Figure 3.8: Stable carbon and oxygen isotopic data for synthetic dypingite, dissolved inorganic carbon (DIC), and water. Uncertainties on measured values are considerably smaller than the symbols employed. The time corresponding to samples in which dypingite was first identified is marked by a dashed line.

Stable oxygen isotopic compositions were determined for eight samples of filtered water. Results for three samples from each experiment and two identical samples of the Nanopure water used to prepare experimental solutions are listed in Tables 3.2 and 3.3 and plotted in Figure 3.8. Analyses of the duplicate samples of Nanopure water give $\delta^{18}O_{H2O}$ values of -10.9‰ and -11.3‰. Water sampled from experiments dyp-may14-09-1 and dyp-may14-09-2 becomes progressively more enriched in ^{18}O with time. On day 14 of the experiments, the last day for which there are $\delta^{18}O_{H2O}$ data, water from dyp-

may14-09-1 has a value of $\delta^{18}O_{H2O}$=-2.0‰ and water from dyp-may14-09-2 gives $\delta^{18}O_{H2O}$=-3.4‰.

Stable oxygen and carbon isotopic data were obtained for four specimens of dypingite from each experiment. Precipitates of dypingite from days 16, 18, 20, and 21 were analyzed from both experiments (Tables 3.2 and 3.3 and Fig. 3.8). Dypingite from experiment dyp-may14-09-1 gives -15.4‰ ≤ $\delta^{13}C_{dyp}$ ≤ -14.0‰ and 27.0‰ ≤ $\delta^{18}O_{dyp}$ ≤ 30.2‰. Experiment dyp-may14-09-2 yielded dypingite with a broader range of values: -16.9‰ ≤ $\delta^{13}C_{dyp}$ ≤ -12.0‰ and 25.8‰ ≤ $\delta^{18}O_{dyp}$ ≤ 29.5‰.

3.4.5 Results of total dissolved inorganic carbon measurements

The concentration of total dissolved inorganic carbon (DIC) was measured for 10 samples from each experiment (Tables 3.2 and 3.3 and Figs. 3.9 and 3.10). Because only one ~2 mL sample of filtered water was collected each day, measurements of DIC concentrations were made on samples of water collected on alternating days. This approach allowed the remaining samples to be analyzed for stable isotopic concentrations. Over time, DIC concentrations in experiment dyp-may14-09-1 rose steadily from 11.4 mg/L on day 2 to a measured maximum of 151.7 mg/L on day 15. Likewise, DIC concentrations in experiment dyp-may14-09-2 rose from 10.6 mg/L on day 2 to a measured maximum of 135.4 mg/L on day 15. Day 16 saw the onset of dypingite precipitation, and the next measured values of DIC concentration (on day 17) had declined to 103.9 mg/L and 123.4 mg/L for experiments dyp-may14-09-1 and dyp-may14-09-2, respectively. DIC concentrations continued to decline until the experiments were concluded. Final DIC concentrations measured for day 21 of the experiments were 51.6 mg/L and 62.5 mg/L.

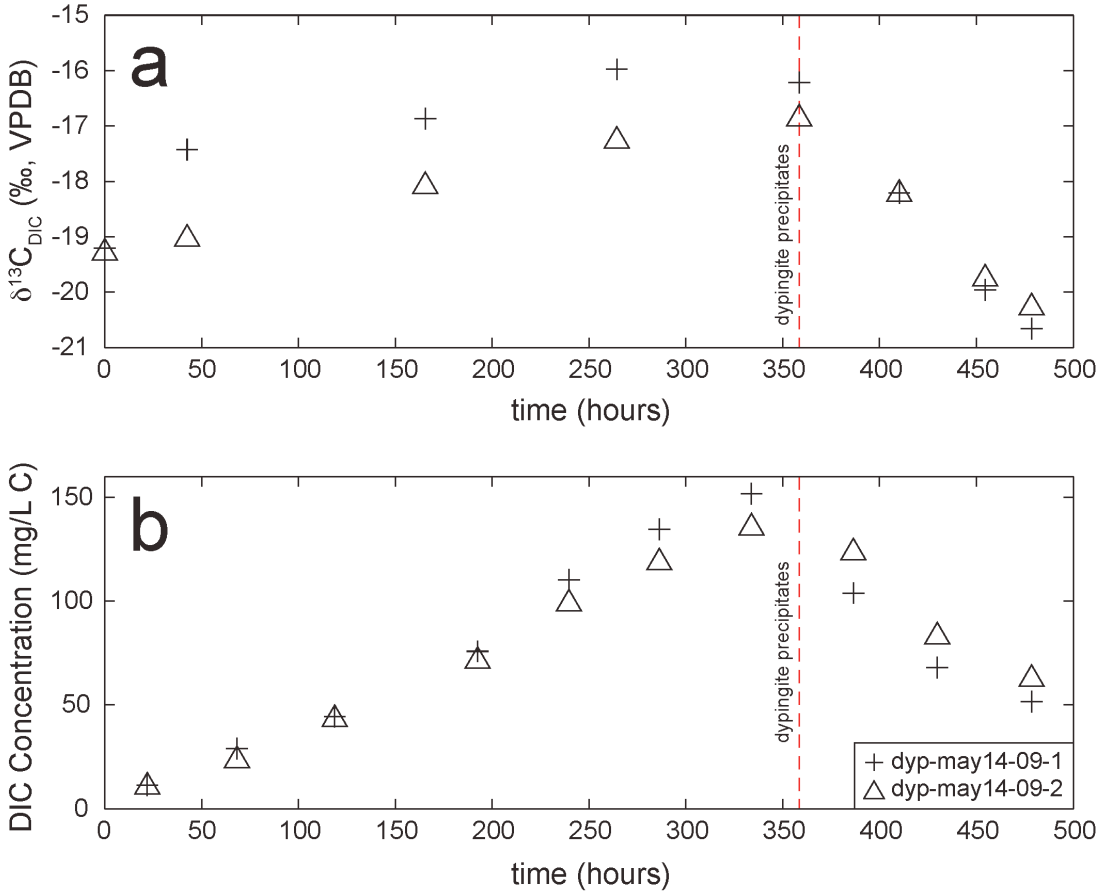

Figure 3.9: Stable carbon isotopic data and concentrations of dissolved inorganic carbon (DIC) over time. $\delta^{13}C$ values of DIC are given in (a) and concentrations of DIC in solution are given in (b). Uncertainties on measured values are considerably smaller than the symbols employed. The time corresponding to samples in which dypingite was first identified is marked by a dashed line.

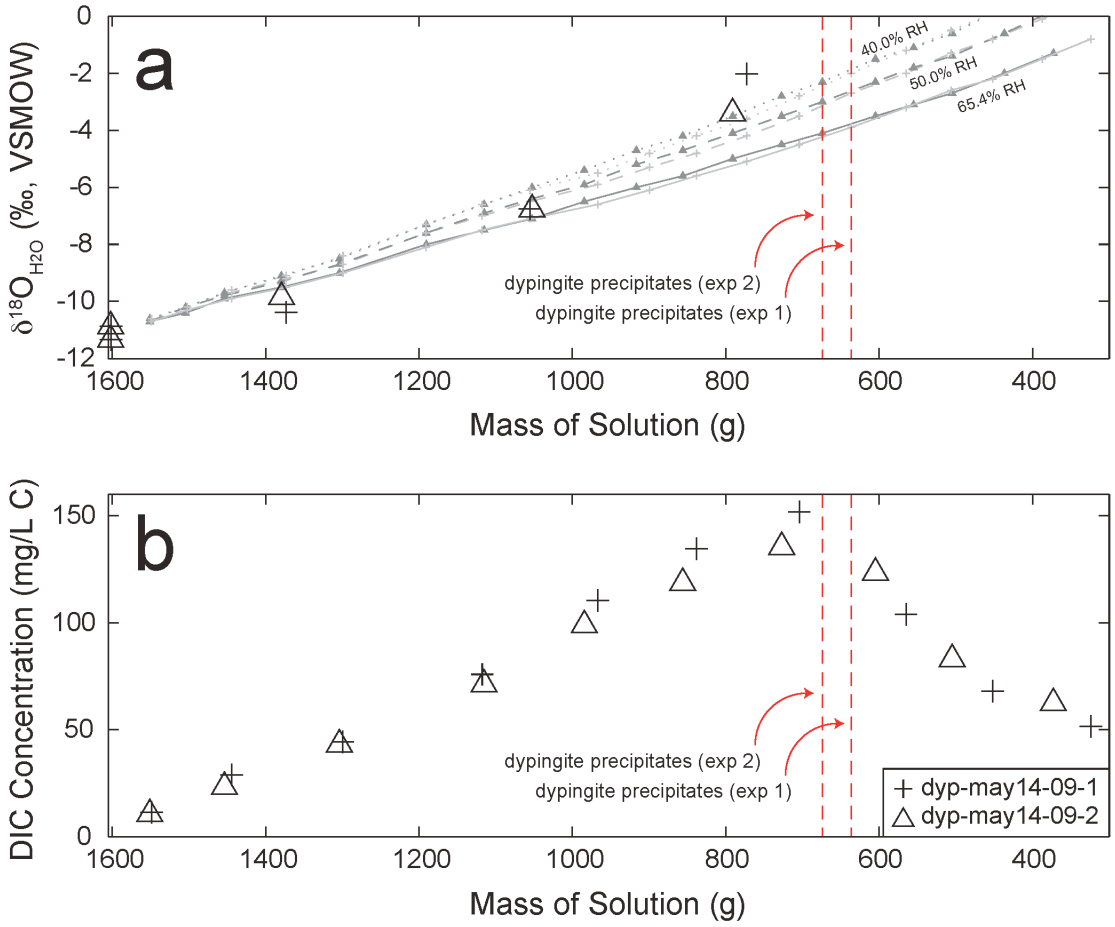

Figure 3.10: Stable oxygen isotopic data and concentrations of dissolved inorganic carbon (DIC) versus mass loss of solution. $\delta^{18}O$ values of water are given in (a) and concentrations of DIC in solution are given in (b). Evaporative water loss is modelled as a Rayleigh distillation effect in (a) at three different values of relative humidity (models for experiments 1 and 2 are denoted by crosses and triangles, respectively). Uncertainties on measured values are smaller than the symbols employed. The masses of solution corresponding to the points at which dypingite was first identified are marked by dashed lines.

3.5 Discussion

3.5.1 Mineralogy of final precipitates

Ultimately, both precipitation experiments, dyp-may14-09-1 and dyp-may14-09-2, produced a synthetic mineral phase that gives XRPD patterns that are in excellent agreement with that for the mineral phase originally characterized as "yoshikawaite" by Suzuki and Ito (1973) and documented as dypingite by Inaba et al. (1985), Gore et al. (1996), and Power et al. (2007). XRPD patterns of the final precipitates from both experiments are plotted in Figure 3.5. Three additional patterns are provided for comparison. One of these was collected from a natural specimen of dypingite from Yoshikawa, Shinshiro Cho, Aichi Prefecture, Japan (purchased from Roger's Minerals, http://www.rogersminerals.com). The remaining two patterns are replotted from Power et al. (2007) and were collected using micro-XRD techniques. These patterns were collected from dypingite that precipitated in association with filamentous cyanobacteria from (1) groundwater and (2) wetland water that were sampled from the area surrounding a hydromagnesite playa deposit near Atlin, British Columbia, Canada.

"Yoshikawaite" is generally considered to be dypingite, and the pattern collected by Suzuki and Ito (1973) is labelled as dypingite in the ICDD PDF 4+ database. Although it suffers from preferred orientation, the XRPD pattern for the sample of naturally occurring dypingite, from the same locality as that studied by Suzuki and Ito (1973), gives an excellent match to their ICDD reference pattern (Fig. 3.5). The XRPD patterns for dypingite precipitated from experiments dyp-may14-09-1 and dyp-may14-09-2 are in similarly good agreement with the pattern from Suzuki and Ito (1973) (Fig. 3.5). Both experimental precipitates contain halite, but only the precipitate from dyp-may14-09-2 contains residual brucite.

Microbial precipitation experiments done by Power et al. (2007) produced a phase that is more similar to the type dypingite, originally described by Raade (1970) and documented by Canterford et al. (1984) (Fig. 3.5). The most notable differences between XRPD patterns of the dypingite described by Raade (1970) and that of Suzuki and Ito (1973) are the extreme loss of intensity from two superstructure peaks at *d*-spacings of 33.2 Å and 16.4 Å, and a shift in these two peaks and one higher-angle harmonic

reflection [found at approximately 10.8 Å in the dypingite of Suzuki and Ito (1973)] toward smaller values of *d*. XRPD data alone, suggest that partial decomposition of "Raade's dypingite" toward hydromagnesite [$Mg_5(CO_3)_4(OH)_2{\cdot}4H_2O$] may be the cause of this inconsistency. Dypingite is known to decompose to hydromagnesite and to be an intermediate phase in the decomposition of nesquehonite [$MgCO_3{\cdot}3H_2O$] to hydromagnesite (e.g., Davies and Bubela 1973; Suzuki and Ito 1973; Canterford et al. 1984; Han and Lee 1985; Botha and Strydom 2001). Furthermore, Suzuki and Ito (1973) observed the disappearance of higher order peaks and the shift of the peak at 10.8 Å to 9.2 Å on heating at 150˚C, which produces a material with an XRPD pattern consistent with that of hydromagnesite. Therefore, in keeping with previous interpretations, we consider "yoshikawaite" to be dypingite and treat our precipitates as synthetic dypingite.

Brucite is known to produce hydromagnesite on weathering under conditions of temperature and pressure that prevail at the Earth's surface (e.g., Hostetler et al. 1966). In addition, Botha and Strydom (2001) and Xiong and Lord (2008) have synthesized hydromagnesite by slow replacement of brucite in aqueous solution. The gradual decline in the relative abundance of brucite in experiments dyp-may14-09-1 and dyp-may14-09-2 suggests that dypingite, like hydromagnesite, can form by the carbonation of brucite according to the following reactions:

$$4CO_{2(g)} \rightarrow 4CO_{2(aq)} \quad \text{(Eq. 3.1)}$$

$$4CO_{2(aq)} + 4OH^- \rightarrow 4HCO_3^- \quad \text{(Eq. 3.2)}$$

$$4HCO_3^- \rightarrow 4H^+ + 4CO_3^{2-} \quad \text{(Eq. 3.3)}$$

$$4H^+ + 4OH^- \rightarrow 4H_2O \quad \text{(Eq. 3.4)}$$

$$5Mg^{2+} + 4CO_3^{2-} + 2OH^- + 5H_2O \rightarrow Mg_5(CO_3)_4(OH)_2{\cdot}5H_2O \quad \text{(Eq. 3.5)}$$

which give the net reaction

$$4CO_{2(g)} + 5Mg^{2+} + 10OH^- + H_2O \rightarrow Mg_5(CO_3)_4(OH)_2{\cdot}5H_2O \quad \text{(Eq. 3.6)}$$

or

$$4CO_{2(g)} + 5Mg(OH)_2 + H_2O \rightarrow Mg_5(CO_3)_4(OH)_2{\cdot}5H_2O \quad \text{(Eq. 3.7)}$$

Although dypingite is usually referred to by the formula $Mg_5(CO_3)_4(OH)_2{\cdot}5H_2O$ (as expressed in Eqs. 3.6 and 3.7) the amount of structural water in its formula is quite variable. CHN data were recalculated on the basis of four atoms of carbon per formula unit (apfu), using the idealized stoichiometry of Raade (1970) for dypingite (Table 3.4). In addition, it was assumed that two H-atoms per formula unit (pfu) formed hydroxyl groups within the structure of dypingite. The number of structurally-bound water molecules in specimens of synthetic dypingite (produced according to the same method used to precipitate dypingite in dyp-may14-09-1 and dyp-may14-09-2) varies from 6.40 to 6.90 pfu. A considerably lower value of 5.80 water molecules per formula unit was determined for natural dypingite from Yoshikawa. This range of values is considerably more narrow than that obtained from a compilation of previous studies (i.e., Raade 1970; Davies and Bubela 1973; Suzuki and Ito 1973; Canterford et al. 1984). Previous determinations of elemental abundances in dypingite, give estimates of 4.35 to 9.05 water molecules per formula unit for different specimens of the same mineral (Table 3.4). In contrast, precipitation experiments of the design described in this study give a relatively narrow range in water content (i.e., 6.40-6.90 H_2O pfu).

3.5.2 Fractionation of stable isotopes during precipitation of dypingite

3.5.2.1 Stable isotopic fractionation in DIC and water

The evolution of $\delta^{13}C_{DIC}$ and $\delta^{18}O_{H_2O}$ with time is illustrated in Figure 3.8. Initial $\delta^{13}C_{DIC}$ values for experiments dyp-may14-09-1 and dyp-may14-09-2 are -19.2‰ and -19.3‰, respectively. In the range of pH under which these experiments were conducted (i.e., 8.48-9.36) bicarbonate is known to be the dominant aqueous carbonate species by several orders of magnitude (e.g., Faure 1986). Using the equilibrium carbon isotopic fractionation factor of Mook et al. (1974), $10^3 \ln\alpha_{HCO_3^- - CO_{2(g)}} = 7.9‰$ at 25˚C, and assuming that CO_2 in the laboratory atmosphere has a similar value of $\delta^{13}C$ to the bulk atmosphere [i.e. ~ -8‰, e.g., Clark and Fritz (1997) and Keeling et al. (2005)], DIC in equilibrium with the atmosphere should be characterized by $\delta^{13}C_{DIC} \approx 0‰$. The large deviation from

this expected equilibrium value could be explained by (1) diffusive fractionation of carbon isotopes caused by preferential uptake of $^{12}CO_2$(g) into solution or (2) extremely ^{13}C-deplected CO_2 in the laboratory atmosphere.

A potential cause of the depleted $\delta^{13}C$ signature of DIC in the precipitation experiments is a kinetic fractionation effect that can sometimes accompany diffusion of CO_2 into a solution. O'Neil and Barnes (1971) describe near-instantaneous precipitation of travertines and scums made of calcite and aragonite from high-pH (i.e., pH>11), Ca^{2+}-OH^--waters. They observed extreme depletion of ^{13}C in the resulting calcite and aragonite and were able to explain this depletion with the use of Graham's Law, $\alpha_{m^*\text{-}m}=(m/m^*)^{1/2}$, in which α is the observed diffusive fractionation between a molecule of mass m^* that bears a heavier isotope and a molecule of mass m that bears a lighter isotope. Considering the diffusion of $^{13}CO_2$ relative to $^{12}CO_2$, and assuming that these molecules can be modelled as point masses exhibiting simple harmonic motion, O'Neil and Barnes (1971) predicted that a kinetic isotope effect of ~11.2‰ would accompany diffusion of gaseous CO_2 into high-pH, Ca^{2+}-OH^--water. Assuming that laboratory CO_2 has a $\delta^{13}C$ value of -8‰, this kinetic diffusion effect would produce water with $\delta^{13}C_{DIC}\approx$-19.2‰, which is consistent with the initial carbon isotopic composition of DIC in both experiments.

Another possibility is that the depleted $\delta^{13}C$ signature of the DIC is the result of anomalously light CO_2 in our laboratory atmosphere. Operating under the assumption of equilibrium isotopic exchange between DIC and atmospheric CO_2, the gaseous CO_2 in our laboratory should have a $\delta^{13}C$ in the range of -27.2‰ to -27.1‰. In a study of kinetic isotopic fractionation during low-temperature dissolution of calcite, Skidmore et al. (2004) found that the average $\delta^{13}C$ of the atmosphere within their laboratory refrigerator was -13.8‰. A study of $\delta^{13}C$ compositions of atmospheric CO_2 in Paris, France found that laboratory air varied from -9.2‰ to -9.5‰ and that CO_2 in a recently used classroom had a high concentration (4630 ppm) of depleted ($\delta^{13}C$=-24.4‰) CO_2 that reflected human respiration (Widory and Javoy 2003). These values for $\delta^{13}C$ of interior air do not reflect the same extreme ^{13}C-depletion required to produce an equilibrium value of $\delta^{13}C_{DIC}\approx$-27‰, but the possible influence of human respiration, or the influence of other

laboratory sources of ^{13}C-depleted CO_2, on the experiments cannot be ruled out until the $\delta^{13}C$ of the laboratory air has been measured.

It can be seen from Figure 3.8 that values of $\delta^{13}C_{DIC}$ become increasingly positive with time, reaching maximum values of -16.0‰ in experiment dyp-may14-09-1 and -16.9‰ in dyp-may14-09-2. This trend toward enrichment in ^{13}C may result from a shift in the carbon isotopic composition of CO_2 (in the case of a ^{13}C-depleted laboratory atmosphere), very slow equilibration with atmospheric CO_2 (of a composition similar to that of the bulk atmosphere), or degassing of light CO_2 from solution. Comparison of the trends in $\delta^{13}C_{DIC}$ with the concentration of DIC over time (Fig. 3.9) demonstrates a contemporaneous increase in DIC concentration with ^{13}C-enrichment. As a result the degassing scenario is not likely. Furthermore, the largest enrichments in $\delta^{13}C_{DIC}$ correspond to the greatest uptake of atmospheric CO_2 into solution as DIC.

After approximately 359 hours (i.e., by day 16 of the experiments), DIC concentrations began to decrease and became increasingly depleted in ^{13}C. This behaviour is contemporaneous with the formation of dypingite in both experiments. It would appear that concentration of sufficient DIC into solution was driven by two processes: (1) slow uptake of atmospheric CO_2 into solution and (2) evapoconcentration of the solution. The latter effect can be inferred from Figure 3.10, a plot of $\delta^{18}O_{H_2O}$ and DIC concentration against the mass of solution remaining in experiments dyp-may14-09-1 and dyp-may14-09-2. By the onset of dypingite precipitation, both experiments had lost 37 wt.% of their initial water to evaporation, which would have contributed to the increased concentration of DIC in solution.

The fractionation of oxygen isotopes in these experiments can be described by evaporative loss of ^{16}O at moderate humidity. This effect is modelled in Fig. 3.10a as a Rayleigh process using measured values of H_2O loss by evaporation, Δm (from Tables 3.2 and 3.3), and Gonfiantini's (1986) relation for the humidity-dependence of kinetic isotopic fractionation of oxygen during evaporation:

$$\delta^{18}O_{H_2O} = (\varepsilon_{H_2O(g)\text{-}H_2O(l)} + \Delta\varepsilon_{H_2O(g)\text{-}H_2O(l)})\cdot \ln f + \delta^{18}O_{H_2O(0)} \qquad \text{(Eq. 3.8)}$$

where $\varepsilon_{H_2O(g)\text{-}H_2O(l)}$ is the equilibrium isotopic separation factor between water vapour and liquid water, f is the fraction of liquid water remaining, and $\delta^{18}O_{H_2O(0)}$ is the initial oxygen isotopic composition of the solution. $\Delta\varepsilon_{H_2O(g)\text{-}H_2O(l)}$ describes the humidity-dependent effect of kinetic isotopic fractionation: $\Delta\varepsilon_{H_2O(g)\text{-}H_2O(l)} = -14.2(1-h)‰$ for $h \equiv$ relative humidity (RH) (Gonfiantini 1986). The equilibrium isotopic separation factor was calculated to be -9.4‰ at 25˚C from the results of Kakiuchi and Matsuo (1979). $\Delta\varepsilon_{H_2O(g)\text{-}H_2O(l)}$ was determined for three different values of relative humidity: (1) $\Delta\varepsilon_{H_2O(g)\text{-}H_2O(l)}$=-4.9‰ at 65.4% RH, which is the average for the month of May in Vancouver, BC, Canada (Environment Canada 2009), (2) $\Delta\varepsilon_{H_2O(g)\text{-}H_2O(l)}$=-7.1‰ for RH=50%, and (3) $\Delta\varepsilon_{H_2O(g)\text{-}H_2O(l)}$=-8.5‰ for RH=40%. The data for $\delta^{18}O_{H_2O}$ are broadly consistent with kinetic fractionation as a result of evaporation at values of relative humidity between 40% and 65.4%. Mismatches are most likely due to variations in the ambient temperature and relative humidity of the laboratory in which precipitation experiments were conducted. This analysis establishes a kinetic control on the oxygen isotopic composition of the experimental solutions. We are currently unable to determine the extent of kinetic control on the fractionation of carbon isotopes between DIC and the atmosphere without direct measurement of $\delta^{13}C$ for laboratory CO_2.

3.5.2.2 Stable isotopic fractionation of C and O in dypingite

Measurements of $\delta^{13}C$ and $\delta^{18}O$ from eight specimens of dypingite (four from each experiment) are plotted in Figure 3.8 with $\delta^{13}C_{DIC}$ and $\delta^{18}O_{H_2O}$ data. $\delta^{13}C_{dyp}$ was measured to be -14.0‰ and -12.0‰ (in experiments dyp-may14-09-1 and dyp-may14-09-2, respectively) in precipitates from the first day that dypingite was detected in XRPD patterns. In the first experiment, $\delta^{13}C_{dyp}$ appears to reach a relatively constant level by the third day of dypingite precipitation (day 18) and remains between -15.2‰ and -15.4‰ for all subsequent measurements. In spite of this, $\delta^{13}C_{DIC}$ in the first experiment continues to decline and reaches a value of -20.7‰ when the experiment concludes. As a result, the carbon isotopic separation between dypingite and DIC increases from an initial value of 2.3‰ to a final value of 5.5‰. The average isotopic fractionation between dypingite and DIC in experiment dyp-may14-09-1 is (3.8 ± 1.4)‰. In the second

experiment, $\delta^{13}C_{dyp}$ declines to a comparable value to that in experiment dyp-may14-09-1, but continues past this point to end with a lower value of -16.9‰. As the DIC pool becomes increasingly depleted by dypingite precipitation, the value of $\delta^{13}C_{DIC}$ decreases from -16.9‰ to -20.3‰. The carbon isotopic separation between dypingite and DIC in experiment dyp-may14-09-2 varies from 2.5‰ to 4.9‰. The average isotopic fractionation between dypingite and DIC in experiment dyp-may14-09-2 is (3.8 ± 1.1)‰, which is indistinguishable from the result obtained from the first experiment. Using the equilibrium isotopic fractionation factor of Mook et al. (1974) for exchange of carbon between aqueous bicarbonate and gaseous CO_2, gives an estimated fractionation of 11.7‰ between dypingite and gaseous CO_2 (Figs. 3.1 and 3.3), which is consistent with equilibrium fractionation factors for other carbonate minerals. Comparison with factors for magnesite-CO_2 shows that it is also consistent with the observed difference between mineral-CO_2 fractionation factors for hydrous and anhydrous pairs of chemically related minerals (Fig. 3.3).

In the upper portion of Figure 3.8, a relatively constant depletion of $\delta^{13}C_{DIC}$ is accompanied by a contemporaneous depletion of $\delta^{13}C_{dyp}$ on a similar scale. Also, as the carbonation reaction progresses, the $\delta^{13}C$ of dypingite approaches the initial $\delta^{13}C$ of the DIC pool and actually reaches the same value in dyp-may14-09-2. This is inconsistent with the increasing $\delta^{13}C_{dyp}$ and $\delta^{13}C_{DIC}$ values that would result from CO_2 degassing. Furthermore, these trends in DIC concentration and $\delta^{13}C$ suggest that the amount of DIC in solution was not buffered by influx of atmospheric CO_2 during precipitation of dypingite. This implies that, within these relatively high-pH, saline solutions, the exchange of CO_2 between DIC and the atmosphere is surprisingly slow. Exchange of CO_2 is sufficiently slow that – at least on the timescale of dypingite precipitation – the DIC-dypingite system appears to behave as though it were largely closed to the atmosphere for isotopic exchange of carbon. The large standard deviations on the average values for carbon isotopic separation between dypingite and DIC indicate incomplete mixing of product and reactant. Because carbon isotopic equilibrium between DIC and dypingite was only approached from one direction in these non-reversible experiments, it cannot be stated definitively that isotopic equilibrium was reached. However, the value of the fractionation factor obtained for exchange of ^{13}C between

dypingite and DIC is consistent with equilibrium fractionation factors for other carbonate minerals. This result provides significant support for the conclusion that equilibrium isotope exchange of carbon was reached between dypingite and DIC.

The solubility of gaseous CO_2 is notably reduced as the salinity of a solution increases (e.g., Markham and Kobe 1941; Harned and Davis 1943; Onda et al. 1970; Yasunishi and Yoshida 1979). Experiments dyp-may14-09-1 and dyp-may14-09-2 both had an initial concentration of 1.0 M NaCl. As a result of evaporation, the final concentrations of dissolved NaCl could have been as high as 2.1 M in the first experiment and 2.2 M in the second experiment. The high salinity of these experiments may have had an impact on the rate of diffusion of CO_2 into solution, but this remains to be tested.

Kim and O'Neil (1997) have suggested that equilibrium/disequilibrium fractionation of oxygen isotopes in precipitation experiments like these may be controlled in part by the concentration of aqueous bicarbonate and cations. They observed larger fractionations of oxygen isotopes between carbonate minerals and water with increasing concentrations of aqueous metal-chlorides and sodium bicarbonate, which suggests that higher ionic strengths lead to larger fractionations (at least for oxygen isotopes). Because only two measurements of equilibrium fractionation of oxygen isotopes between hydromagnesite and water have ever been reported (for 0˚ and 25˚C, O'Neil and Barnes 1971), and because of our sparse $\delta^{18}O_{H_2O}$ data, it is difficult to assess whether the concentration of NaCl had an impact on oxygen isotopic fractionation. However, within the resolution of our experiments none was detectable.

Due to the limited number of $\delta^{18}O_{H_2O}$ data available, it is not possible to give a factor for the fractionation of oxygen isotopes between dypingite and water under the conditions of the two precipitation experiments. However, the available data and simple Rayleigh distillation models suggest that it is on the order of 30‰. Assuming that the Rayleigh model for $\delta^{18}O_{H_2O}$ using values of $\Delta\varepsilon_{H_2O(g)\text{-}H_2O(l)}$=-4.9‰ at 65.4% RH is a good approximation to the behaviour of the experimental solutions, oxygen isotopic fractionations between 30.4‰ and 31.1‰ and between 30.0‰ and 31.5‰ might be expected for experiments dyp-may14-09-1 and dyp-may14-09-2, during the course of dypingite precipitation. It should be noted that the oxygen isotopic separation between

hydromagnesite and water would decrease with declining humidity (Fig. 3.10). Perhaps surprisingly, these predictions are consistent with the equilibrium isotopic fractionation factor of $10^3 \ln\alpha_{\text{hydromagnesite-H}_2\text{O}}$=31.2‰ that was measured by O'Neil and Barnes (1971) at 25˚C.

Although it cannot be stated decisively whether or not equilibrium exchange of carbon isotopes was reached between dypingite and DIC, the isotopic fractionation measured between these two carbon pools should be applicable to similar natural and built systems from which dypingite, and the closely related mineral hydromagnesite, precipitate. These experiments also suggest that the equilibrium fractionation factor reported by O'Neil and Barnes (1971) for exchange of oxygen between hydromagnesite and water provides a good approximation to oxygen isotopic exchange in evaporative, saline systems. Perhaps the most significant results of these experiments are (1) that the DIC pool in saline, Mg-rich water can have limited exchange with the atmosphere during precipitation of a carbonate mineral and (2) that a fractionation of $10^3 \ln\alpha_{\text{dypingite-DIC}}$=(3.8 ± 1.2)‰ may be expected for exchange of carbon between dypingite and DIC in saline water at 20˚C ≤ T ≤ 25˚C and 8.5 ≤ pH ≤ 9.4.

3.6 Implications for CO_2 sequestration in mine tailings

The conditions used in these experiments simulate those at the Mount Keith Nickel Mine, Western Australia, Australia (discussed in detail in Chapter 4), where ultramafic mine tailings are stored in an arid environment and are periodically exposed to highly saline, neutral to basic process water. In ultramafic mine tailings environments like that at Mount Keith, sub-potable water with high ionic strength may be used for mineral processing. Once ore has been processed, mineral waste is pumped suspended in process water into tailings impoundments for permanent storage. In this environment, wastewater can become enriched in Mg by dissolution of Mg-rich gangue minerals.

Wilson et al. (2009) have used stable carbon and oxygen isotopic data and radiocarbon data to demonstrate trapping of atmospheric CO_2 within hydrous Mg-carbonate minerals (i.e., nesquehonite and lansfordite) and hydrous, basic Mg-carbonate

minerals (i.e., dypingite and hydromagnesite) at two historical chrysotile mines at Clinton Creek, Yukon Territory, Canada and Cassiar, British Columbia, Canada. They found that many of their stable isotopic data for secondary Mg-carbonate minerals fell outside the ranges predicted by available equilibrium fractionation factors for magnesite. In fact, stable carbon and oxygen data for dypingite and hydromagnesite from the Clinton Creek mine were found to be dependent upon the depth at which they had precipitated within the mine tailings pile. Stable isotope signatures of Mg-carbonate minerals that had precipitated at the surface of the tailings were significantly more enriched in both $\delta^{13}C$ and $\delta^{18}O$ and were commonly consistent with predicted values for precipitation of magnesite in equilibrium with atmospheric CO_2 (Wilson et al. 2009). Contrastingly, samples found in the subsurface environment were significantly depleted in ^{13}C and ^{18}O relative to predicted values made using equilibrium isotopic fractionation factors, which suggested input of an isotopically depleted source of carbon or the action of a kinetic isotope effect during mineral precipitation. The stable carbon and oxygen isotopic results of Wilson et al. (2009) are more indicative of the processes by which carbon is cycled in mine tailings environments than the sources from which it is drawn into carbonate minerals. Using ^{14}C as a tracer, they found that atmospheric CO_2 was being sequestered into minerals with stable isotopic signatures that were both in and out of accord with predictions made using equilibrium fractionation factors. Ultimately, they relied upon the use of ^{14}C data to confirm trapping of atmospheric carbon within Mg-carbonate minerals.

Mine tailings storage facilities, particularly those at active mining operations, are subject to phases of wetting during deposition of new tailings and phases of drying as process water evaporates or is reclaimed. Skidmore et al. (2004) have demonstrated that significant kinetic isotopic fractionation can occur during the first few hours of carbonate mineral dissolution as a result of the influx of atmospheric CO_2. In open system calcite dissolution experiments, they report deviations between calculated values for $\delta^{13}C_{DIC}$ (from equilibrium fractionation factors) and measured values that are as large as -17.4‰. Based on the results of their experiments, Skidmore et al. (2004) suggest that, in geological systems characterized by short exposures to water and low water-rock ratios, kinetic fractionation processes will determine the carbon isotopic signature of the DIC pool. Although we have considered precipitation of carbonate minerals rather than their

dissolution, this observation implies that kinetic fractionation processes may also exert significant control over the isotopic signature of carbonate minerals precipitated during wet phases in typically unsaturated mine tailings.

Laboratory experiments designed to precipitate dypingite under conditions similar to those in tailings storage facilities demonstrate that stable isotopic data may provide ambiguous or misleading information about the sources from which environmental isotopes like oxygen and carbon are drawn. Perhaps the single most telling example from this study is that equilibrium fractionation factors may not provide an explanation for the $\delta^{13}C$ signature of DIC, even though the only available source of carbon was the atmosphere. Had similarly ^{13}C-depleted dypingite been collected from the tailings storage facility of an operational mine, this depletion could have been explained equally well by (1) diffusion fractionation of atmospheric CO_2 into solution (e.g., O'Neil and Barnes 1971; Van Strydonck et al. 1989; Kosednar-Legenstein et al. 2008), (2) mixing of process waters with oxidized dissolved organic carbon from mine sewage, (3) mixing of process waters with groundwater containing DIC derived from soil CO_2 (e.g., Cerling 1984), (4) use of ^{13}C-depleted chemicals during mineral processing, or (5) ^{13}C-depletion of local atmosphere as a result of high biological activity or fossil fuel emissions from mine site generators. The results of this study and the field-based evidence of Wilson et al. (2009) suggest that, in the mine tailings environment, stable isotope data describe the processes by which elements are cycled more than their provenance. In light of this, isotopic analogue experiments, rather than equilibrium precipitation experiments, may be more useful guides to the study of complex, low-temperature geological systems like tailings storage facilities. Consequently, a different tracer like radiogenic ^{14}C should be used for the purpose of verifying sequestration of atmospheric carbon within mine tailings.

3.7 References

Aharon, P. (1988) A stable-isotope study of magnesites from the Rum Jungle uranium field, Australia: Implications for the origin of strata-bound massive magnesites. Chemical Geology, 69, 127-145.

Akao, M. and Iwai, S. (1977a) The hydrogen bonding of artinite. Acta Crystallographica, Section B: Structural Crystallography and Crystal Chemistry, B33, 3951-3953.

Akao, M. and Iwai, S. (1977b) The hydrogen bonding of hydromagnesite. Acta Crystallographica, Section B: Structural Crystallography and Crystal Chemistry, B33, 1273-1275.

Akao, M., Marumo, F., and Iwai, S. (1974) Crystal structure of hydromagnesite. Acta Crystallographica, Section B: Structural Crystallography and Crystal Chemistry, B30, 2670-2672.

Barnes, I. and O'Neil, J.R. (1971) Calcium-magnesium carbonate solid solutions from Holocene conglomerate cements and travertines in the Coast Range of California. Geochimica et Cosmochimica Acta, 35, 699-718.

Botha, A. and Strydom, C.A. (2001) Preparation of a magnesium hydroxy carbonate form magnesium hydroxide. Hydrometallurgy, 62, 175-183.

Bottinga Y. (1968) Calculations of fractionation factors for carbon and oxygen isotopic exchange in the system calcite-carbon dioxide-water. Journal of Physical Chemistry, 2, 800-808.

Böttcher, M.E. (1994) $^{13}C/^{12}C$ partitioning during synthesis of $Na_2Ca(CO_3)_2{\cdot}2H_2O$. Journal of the Chemical Society, Chemical Communications, 1485.

Braithwaite, C.J.R. and Zedef, V. (1996) Hydromagnesite stromatolites and sediments in an alkaline lake, Salda Gölü, Turkey. Journal of Sedimentary Research, 66, 991-1002.

Bruker AXS (2008) DIFFRAC^{plus} EVA 14 Release 2008. Bruker AXS, Germany.

Canterford, J.H., Tsambourakis, G, and Lambert, B. (1984) Some observations of the properties of dypingite, $Mg_5(CO_3)_4(OH)_2{\cdot}5H_2O$, and related minerals. Mineralogical Magazine, 48, 437-442.

Cerling, T.E. (1984) The stable isotopic composition of modern soil carbonate and its relationship to climate. Earth and Planetary Science Letters, 71, 229-240.

Chacko, T. and Deines, P. (2008) Theoretical calculation of oxygen isotope fractionation factors in carbonate systems. Geochimica et Cosmochimica Acta, 72, 3642-3660.

Chacko, T., Mayeda, T.K., Clayton, R.N., and Goldsmith, J.R. (1991) Oxygen and carbon isotope fractionations between CO_2 and calcite. Geochimica et Cosmochimica Acta, 55, 2867-2882.

Chacko, T., Cole, D.R., and Horita, J. (2001) Equilibrium oxygen, hydrogen and carbon isotope fractionation factors applicable to geologic systems. In Stable Isotope Geochemistry. Valley, J.W. and Cole, D.R., Eds. Reviews in Mineralogy and Geochemistry, 43, 1-81.

Clark, I. and Fritz, P. (1997) Environmental Isotopes in Hydrogeology. CRC Press, U.S.A., 328 p.

Clayton, R.N., Jones, B.F., Berner, R.A. (1968) Isotopic studies of dolomite formation under sedimentary conditions. Geochimica et Cosmochimica Acta, 32, 415-432.

Coleyshaw, E.E., Crump, G., and Griffith, W.P. (2003) Vibrational spectra of the hydrated carbonate minerals ikaite, monohydrocalcite, lansfordite and nesquehonite. Spectrochimica Acta Part A, 59, 2231-2239.

Davies, P.J. and Bubela, B. (1973) The transformation of nesquehonite into hydromagnesite. Chemical Geology, 12, 289-300.

Deines, P. (2004) Carbon isotope effects in carbonate systems. Geochimica et Cosmochimica Acta, 68, 2659-2679.

Deines, P., Langmuir, D., and Harmon, R.S. (1974) Stable carbon isotope ratios and the existence of a gas phase in the evolution of carbonate ground waters. Geochimica et Cosmochimica Acta, 38, 1147-1164.

Deuser, W.G. and Degens, E.T. (1967) Carbon isotope fractionation in the system CO_2(gas)-CO_2(aqueous)-HCO_3^-(aqueous). Nature, 215, 1033-1035.

Emrich, K., Ehalt, D.H., and Vogel, J.C. (1970) Carbon isotope fractionation during the precipitation of calcium carbonate. Earth and Planetary Science Letters, 8, 363-371.

Environment Canada (2009) National Climate Data and Information Archieve. Vancouver International Airport. Retrieved 01 October 2009. [http://www.climate.weatheroffice.ec.gc.ca/climate_normals/stnselect_e.html].

Epstein, S. Buchsbaum, R., Lowenstam, H.A., Urey, H.C. (1953) Revised carbonate-water isotopic temperature scale. Geological Society of America Bulletin, 64, 1315-1326.

Fantidis, J. and Ehhalt, D.H. (1970) Variations of the carbon and oxygen isotopic composition in stalagmites and stalactites; evidence of non-equilibrium isotopic fractionation. Earth and Planetary Science Letters, 10, 136-144.

Faure, G. (1986) Principles of Isotope Geology. Wiley, U.S.A., 589 p.

Friedman, I. and O'Neil, J.R. (1977) Compilation of stable isotope fractionation factors of geochemical interest. In Data of Geochemistry. Fleischer, M., Ed. United States Geological Survey Professional Paper 440-KK.

Giester, G., Lengauer, C.L., and Rieck, B. (2000) The crystal structure of nesquehonite, $MgCO_3 \cdot 3H_2O$, from Lavrion, Greece. Mineralogy and Petrology, 70, 153-163.

Golyshev, S.I., Padalko, N.L., and Pechenkin, S.A. (1981) Fractionation of stable oxygen and carbon isotopes in carbonate systems. Geochemistry International, 18, 85-99.

Gonfiantini, R. (1986) Environmental isotopes in lake studies. In Handbook of Environmental Isotope Geochemistry, Vol. 2, The Terrestrial Environment. Fritz, P. and Fontes, J.-C., Eds. Elsevier, Amsterdam, The Netherlands, p.113-168.

Gore, D.B., Creagh, D.C., Burgess, J.S., Colhoun, E.A., Spate, A.P., and Baird, A.S. (1996) Composition, distribution and origin of surficial salts in the Vestfold Hills, East Antarctica, Antarctic Science, 8, 73-84.

Grossman, E.L. and Ku, T.-L. (1986) Oxygen and carbon isotope fractionation in biogenic aragonite: Temperature effects. Chemical Geology, 59, 59-74.

Han, S.-K. and Lee, M.-D. (1985) The formation mechanism of basic magnesium carbonate. Hwahak Konghak, 23, 69-78.

Harned, H.S. and Davis, R., Jr. (1943) The ionization constant of carbonic acid in water and the solubility of carbon dioxide in water and aqueous salt solutions from 0 to 50˚. Journal of the American Chemical Society, 65, 2030-2037.

Hendy, C.H. (1971) The isotopic geochemistry of speleothems – I. The calculation of the effects of different modes of formation on the isotopic composition of speleothems and their applicability as palaeoclimatic indicators. Geochimica et Cosmochimica Acta, 35, 801-824.

Hostetler, P.B., Coleman, R.G., Mumpton, F.A., Evans, B.W. (1966) Brucite in alpine serpentinites. American Mineralogist, 51, 75-98.

Inaba, S., Minakawa, T., and Noto, S. (1985) Nesquehonite and dypingite from Shiraki, Mie Prefecture, Japan. Chigaku Kenkyu, 34, 281-287.

Jiménez-López, C., Romanek, C.S., and Caballero, E. (2006) Carbon isotope fractionation in synthetic magnesian calcite. Geochimica et Cosmochimica Acta, 70, 1163-1171.

Jiménez-López, C., Caballero, E., Huertas, F.J., and Romanek, C.S. (2001) Chemical, mineralogical and isotope behavior, and phase transformation during the precipitation of calcium carbonate minerals from intermediate ionic solution at 25˚C. Geochimica et Cosmochimica Acta, 65, 3219-3231.

Jiménez-López, C., Romanek, C.S., Huertas, F.J., Ohmoto, H., and Caballero, E. (2004) Oxygen isotope fractionation in synthetic magnesian calcite. Geochimica et Cosmochimica Acta, 68, 3367-3377.

Kakiuchi, M. and Matsuo, S. (1979) Direct measurements of D/H and $^{18}O/^{16}O$ fractionation factors between vapor and liquid water in the temperature range from 10˚ to 40˚. Geochemical Journal, 13, 307-311.

Keeling, C.D., Bollenbacher, A.F., and Whorf, T.P. (2005) Monthly atmospheric $^{13}C/^{12}C$ isotopic ratios for 10 SIO stations. In Trends: A Compendium of Data on Global Change. Carbon Dioxide Information Analysis Center, Oak Ridge National Laboratory, U.S. Department of Energy, Oak Ridge, Tennessee, U.S.A.

Kieffer, S.W. (1982) Thermodynamics and lattice vibration of minerals: 5. Application to phase equilibria, isotopic fractionation, and high pressure thermodynamic properties. Reviews in Geophysics and Space Physics, 20, 827-849.

Kim, S.-T. and O'Neil, J.R. (1997) Equilibrium and nonequilibrium oxygen isotope effects in synthetic carbonates. Geochimica et Cosmochimica Acta, 61, 3461-3475.

Kosednar-Legenstein, B., Dietzel, M., Leis, A., and Stingl, K. (2008) Stable carbon and oxygen isotope investigation in historical lime mortar and plaster – Results from field and experimental study. Applied Geochemistry, 23, 2425-2437.

Kralik, M., Aharon, P., Schroll, E., and Zachmann, D. (1989) Carbon and oxygen isotope systematics of magnesites: a review. In Magnesite: Geology, Mineralogy, Geochemsitry, Formation of Mg-Carbonates. Möller, P., Ed. Monograph Series on Mineral Deposits 28, 197-223.

Land, L.S. (1998) Failure to precipitate dolomite at 25˚C from dilute solution despite 1000-fold oversaturation after 32 years. Aquatic Geochemistry, 4, 361-368.

Lesniak, P.M. and Sakai, H. (1989) Carbon isotope fractionation between dissolved carbonate (CO_3^{2-}) and CO_2(g) at 25˚ and 40˚C. Earth and Planetary Science Letters, 95, 297-301.

Léveillé, R.J., Longstaffe, F.J., and Fyfe, W.S. (2007) An isotopic and geochemical study of carbonate-clay mineralization in basaltic caves: abiotic versus microbial processes. Geobiology, 5, 235-249.

Li, Q., Ding, Y., Yu, G., Li, C., Li, F., and Qian, Y. (2003) Fabrication of light-emitting porous hydromagnesite with rosette-like architecture. Solid State Communication, 125, 117-120.

Liu, B.-N., Zhou, X.-T., Cui, X.-S., and Tang, J.-G. (1990) Synthesis of lansfordite $MgCO_3 \cdot 5H_2O$ and its crystal structure investigation. Science in China, Series B, 33, 1350-1356.

Markham, A.E. and Kobe, K.A. (1941) The solubility of carbon dioxide and nitrous oxide in aqueous salt solutions. Journal of the American Chemical Society, 63, 449-454.

Matsuo, S., Friedman, I., Smith, G.I. (1972) Studies of Quaternary saline lakes. I. Hydrogen isotope fractionation in saline minerals. Geochimica et Cosmochimica Acta, 36, 427-435.

McCrea, J.M. (1950) On the isotopic chemistry of carbonates and a paleotemperature scale. Journal of Chemical Physics, 18, 849-857.

Melchiorre, E.B., Criss, R.E., and Rose, T.P. (2000) Oxygen and carbon isotope study of natural and synthetic azurite. Economic Geology, 95, 621-628.

Melchiorre, E.B., Criss, R.E., and Rose, T.P. (1999) Oxygen and carbon isotope study of natural and synthetic malachite. Economic Geology, 94, 245-260.

Mickler, P.J., Stern, L.A., Banner, J.L. (2006) Large kinetic isotope effects in modern speleothems. Geological Society of America Bulletin, 118, 65-81.

Mickler, P.J., Banner, J.L., Stern, L., Asmerom, Y., Edwards, R.L., and Ito, E. (2004) Stable isotope variations in modern tropical speleothems: Evaluating applications to paleoenvironmental reconstructions. Geochimica et Cosmochimica Acta, 68, 4381-4393.

Mook, W.G., Bommerson, J.C., Staverman, W.H. (1974) Carbon isotope fractionation between dissolved bicarbonate and gaseous carbon dioxide. Earth and Planetary Science Letters, 22, 169-176.

Murdock, J. (1954) Unit cell of hydromagnesite. American Mineralogist, 39, 24-29.

Ohmoto, H. and Rye, R.O. (1979) Isotopes of sulfur and carbon. In Geochemistry of Hydrothermal Ore Deposits, Second Edition. Barnes, H.L., Ed. John Wiley & Sons, 509-567.

O'Neil, J.R. and Barnes, I. (1971) C^{13} and O^{18} compositions in some fresh-water carbonates associated with ultramafic rocks and serpentinites: western United States. Geochimica et Cosmochimica Acta, 35, 687-697.

O'Neil, J.R., Clayton, R.N., and Mayeda, T.K. (1969) Oxygen isotope fractionation in divalent metal carbonates. Journal of Chemical Physics, 51, 5547-5558.

Onda, K., Sada, E., Kobayashi, T., Kito, S., and Ito, K. (1970) Salting-out parameters of gas solubility in aqueous salt solutions. Journal of Chemical Engineering of Japan, 3, 18-24.

Patterson, W.P., Smith, G.R., and Lohmann, K.C. (1993) Continental paleothermometry and seasonality using the isotopic composition of aragonitic otoliths of freshwater fishes. In Climate Change in Continental Isotopic Records. Swart, P.K., Lohmann, K.C., McKenzie, J., and Savin, S., Eds. Geophysical Monograph Series, 78, 181-202.

Power, I.M., Wilson, S.A., Thom, J., Dipple, G.M., and Southam, G. (2007) Biologically induced mineralization of dypingite by cyanobacteria from an alkaline wetland near Atlin, British Columbia, Canada. Geochemical Transactions, 8, article 13.

Power, I.M., Wilson, S.A., Thom, J.M., Dipple, G.M., Gabites, J.E., and Southam, G. (2009) The hydromagnesite playas of Atlin, British Columbia, Canada: A biogeochemical model for CO_2 sequestration. Chemical Geology, 260, 286-300.

Raade, G. (1970) Dypingite, a new hydrous basic carbonate of magnesium, from Norway. American Mineralogist, 55, 1457-1465.

Révész, K.M. and Landwehr, J.M. (2002) $\delta^{13}C$ and $\delta^{18}O$ isotopic composition of $CaCO_3$ measured by continuous flow isotope ratio mass spectrometry: statistical evaluation and verification by application to Devils Hole core DH-11 calcite. Rapid Communications in Mass Spectrometry, 16, 2102-2114.

Robie, R.A. and Hemingway, B.S. (1972) The heat capacities at low-temperatures and entropies at 298.15 K of nesquehonite, $MgCO_3 \cdot 3H_2O$, and hydromagnesite. American Mineralogist, 57, 1768-1781.

Romanek, C.S., Grossman, E.L., and Morse, J.W. (1992) Carbon isotopic fractionation in synthetic aragonite and calcite: effects of temperature and precipitation rate. Geochimica et Cosmochimica Acta, 56, 419-430.

Romanek, C.S., Jiménez-López, C., Navarro, A.R., Sánchez-Román, M., Sahai, N., and Coleman, M. (2009) Inorganic synthesis of Fe-Ca-Mg carbonates at low temperature. Geochimica et Cosmochimica Acta, 73, 5361-5376.

Rubinson, M. and Clayton, R.N. (1969) Carbon-13 fractionation between aragonite and calcite. Geochimica et Cosmochimica Acta, 33, 997-1002.

Rustad, J.R., Nelmes, S.L., Jackson, V.E., and Dixon, D.A. (2008) Quantum-chemical calculations of carbon-isotope fractionation in CO_2(g), aqueous carbonate species, and carbonate minerals. Journal of Physical Chemistry A, 112, 542-555.

Salata, G.G., Roelke, L.A., and Cifuentes, L.A. (2000) A rapid and precise method for measuring stable carbon isotope ratios of dissolved inorganic carbon. Marine Chemistry, 69, 153-161.

Schauble, E.A., Ghosh, P., and Eiler, J.M. (2006) Preferential formation of 13C-18O bonds in carbonate minerals, estimated using first-principles lattice dynamics. Geochimica et Cosmochimica Acta, 70, 2510-2529.

Sheppard, S.M.F. and Schwarcz, H.P. (1970) Fractionation of carbon and oxygen isotopes and magnesium between coexisting metamorphic calcite and dolomite. Contributions to Mineralogy and Petrology, 26, 161-198.

Shiro, Y. and Sakai, H. (1972) Calculation of the reduced partition function ratios of α-, β-quartzs and calcite. Bulletin of the Chemical Society of Japan, 45, 2355-2359.

Skidmore, M., Sharp, M., and Tranter, M. (2004) Kinetic isotopic fractionation during carbonate dissolution in laboratory experiments: Implications for detection of microbial CO_2 signatures using δ^{13}C-DIC. Geochimica et Cosmochimica Acta, 68, 4309-4317.

Spötl, C. and Burns, S.J. (1994) Magnesite diagenesis in redbeds: a case study from the Permian of the Northern Calcareous Alps (Tyrol, Austria). Sedimentology, 41, 543-565.

Stephan, G.W. (1974) De Kristalstructuur van Enige Magnesiumcarbonaten. Unpublished Ph.D. thesis, The University of Amsterdam, Amsterdam, The Netherlands.

Stephan, G.W. and MacGillavry, C.H. (1972) The crystal structure of nesquehonite, $MgCO_3 \cdot 3H_2O$. Acta Crystallographica, Section B: Structural Crystallography and Crystal Chemistry, B28, 1031.

Stiller, M., Rounick, J.S., and Shasha, S. (1985) Extreme carbon-isotope enrichments in evaporating brines. Nature, 316, 434-435.

Suzuki, J. and Ito, M. (1973) A new magnesium carbonate hydrate mineral, $Mg_5(CO_3)_4(OH)_2 \cdot 8H_2O$, from Yoshikawa, Aichi Prefecture, Japan. Journal of the Japanese Association of Mineralogists, Petrologists and Economic Geologists, 68, 353-361.

Tarutani, T., Clayton, R.N., and Mayeda, T.K. (1969) The effect of polymorphism and magnesium substitution on oxygen isotope fractionation between calcium carbonate and water. Geochimica et Cosmochimica Acta, 33, 987-996.

Thompson, J.B. and Ferris, F.G. (1990) Cyanobacterial precipitation of gypsum, calcite, and magnesite from natural alkaline lake water. Geology, 18, 995-998.

Turner, J.V. (1982) Kinetic fractionation of carbon-13 during calcium carbonate precipitation. Geochimica et Cosmochimica Acta, 46, 1183-1191.

Van Strydonck, M.J.Y., Dupas, M., and Keppens, E. (1989) Isotopic fractionation of oxygen and carbon in lime mortar under natural environmental conditions. Radiocarbon, 31, 610-618.

Vasconcelos, C., McKenzie, J.A., Warthmann, R., and Bernasconi, S.M. (2005) Calibration of the $\delta^{18}O$ paleothermometer for dolomite precipitated in microbial cultures and natural environments. Geology, 33, 317-320.

Vogel, J.C., Grootes, P.M., and Mook, W.G. (1970) Isotopic fractionation between gaseous and dissolved carbon dioxide. Zeitschrift für Physik, 230, 225-238.

Wendt, L. (1968) Fractionation of carbon isotopes and its temperature dependence in the system CO_2-gas-CO_2 in solution and HCO_3-CO_3 in solution. Earth and Planetary Science Letters, 4, 64-68.

White, W.B. (1971) Infrared characterization of water and hydroxyl ion in the basic magnesium carbonate minerals. American Mineralogist, 56, 46-53.

Widory, D. and Javoy, M. (2003) The carbon isotope composition of atmospheric CO_2 in Paris. Earth and Planetary Science Letters, 215, 289-298.

Wilson, S.A., Raudsepp, M., and Dipple, G.M. (2006) Verifying and quantifying carbon fixation in minerals from serpentine-rich mine tailings using the Rietveld method with X-ray powder diffraction data. American Mineralogist, 91, 1331-1341.

Wilson, S.A., Dipple, G.M., Power, I.M., Thom, J.M., Anderson, R.G., Raudsepp, M., Gabites, J.E., and Southam, G. (2009) Carbon dioxide fixation within mine wastes of ultramafic-hosted ore deposits: Examples from the Clinton Creek and Cassiar chrysotile deposits, Canada. Economic Geology, 104, 95-112.

Xiong, Y. and Lord, A.S. (2008) Experimental investigations of the reaction path in the MgO-CO_2-H_2O system in solutions with various ionic strengths, and their applications to nuclear waste isolation. Applied Geochemistry, 23, 1634-1659.

Yasunishi, A. and Yoshida, F. (1979) Solubility of carbon dioxide in aqueous electrolyte solutions. Journal of Chemical & Engineering Data, 24, 11-14.

Zachmann, D.W. and Johannes, W. (1989) Cryptocrystalline magnesite. In Magnesite: Geology, Mineralogy, Geochemsitry, Formation of Mg-Carbonates. Möller, P., Ed. Monograph Series on Mineral Deposits 28, 15-28.

Zedef, V., Russell, M.J., Fallick, A.E., and Hall, A.J. (2000) Genesis of vein stockwork and sedimentary magnesite and hydromagnesite deposits in the ultramafic terranes of southwestern Turkey: a stable isotope study. Economic Geology, 95, 429-446.

Zhang, J., Quay, P.D., Wilbur, D.O. (1995) Carbon isotope fractionation during gas-water exchange and dissolution of CO_2. Geochimica et Cosmochimica Acta, 59, 107-114.

Zheng, Y.-F. (1999) Oxygen isotope fractionation in carbonate and sulfate minerals. Geochemical Journal, 33, 109-126.

Chapter 4

Carbon fixation in mineral waste from the Mount Keith Nickel Mine, Western Australia, Australia[1]

4.1. Introduction

Mineralization of carbon dioxide (CO_2) in ultramafic mine tailings has been proposed as a method by which the mining industry might reduce its greenhouse gas emissions (Wilson et al. 2006). Storage of CO_2 within the crystal structures of carbonate minerals is recognized as a safe and durable method for the sequestration of anthropogenic carbon (Seifritz 1990; Lackner et al. 1995; Lackner 2003). Natural weathering of bedrock silicate minerals by dissolution can lead to precipitation of carbonate minerals under atmospheric temperature and pressure conditions. This weathering process is one of the most significant mechanisms for geochemical exchange of CO_2 between the atmosphere and the terrestrial environment (Schwartzman and Volk 1989; Berner 1990). The considerable increase in mineral surface area afforded by mining and milling of ore can result in accelerated trapping of atmospheric CO_2 within secondary carbonate minerals in the tailings from some ultramafic-hosted mining operations (Wilson et al. 2009a).

Hydrated magnesium carbonate minerals are common low-temperature alteration products of serpentine-rich mine wastes (e.g., Raade 1970; Suzuki and Ito 1973, 1974; Wilson et al. 2006, 2009a, 2009b; Levitan et al. 2009). Previous studies of carbon mineralization in mine tailings have focussed on fixation of greenhouse gases within secondary carbonate minerals in the tailings of historical chrysotile mines (Wilson et al. 2006, 2009a) and active diamond mining operations in northern Canada (Rollo and Jamieson 2006; Wilson et al. 2009b). At the Mount Keith Nickel Mine, Western

[1] A version of this chapter will be submitted for publication.
Wilson, S.A., Dipple, G.M., Barker, S.L.L., Power, I.M., Fallon, S.J., Raudsepp, M., and Southam, G. Carbon fixation in mineral waste from the Mount Keith Nickel Mine, Western Australia, Australia.

Australia, Australia, the hydrated magnesium carbonate mineral hydromagnesite [$Mg_5(CO_3)_4(OH)_2 \cdot 4H_2O$] develops within mine tailings as a result of mineral processing. This hydromagnesite is being mineralized as a direct result of the mining operation at Mount Keith. Consequently, accounting of the amount of atmospheric CO_2 that is being trapped and stored within this mineral could be used to reduce the mine's greenhouse gas emissions in a carbon limited economy. Furthermore, accelerating the uptake of CO_2 into mine tailings at Mount Keith could have the potential to completely offset the net greenhouse gas emissions of this mine.

The mineral content of mine tailings is generally heterogeneous due to frequent changes in ore mineralogy, processing procedures, and tailings management practices. Mineralogy also tends to vary with time as tailings weather to produce secondary phases. As a result, geostatistical methods that rely on the presence of regular and predictable geological structures cannot be used to predict the mineralogy of a mine tailings pile. In order to estimate the total amount of CO_2 captured within secondary carbonate mineral phases at a mine, it is necessary that the mineralogy of its tailings storage facilities be well constrained. This requires extensive sampling and the construction of a database of quantitative mineralogical data.

Standard bulk geochemical methods (e.g., Leco analysis) for measuring abundance of CO_2 cannot be used to quantify carbon trapping in mine tailings because they cannot distinguish between carbonate mineral species, nor can they discern the source of the carbon in minerals (i.e., atmospheric, bedrock, industrial, or organic). Recent advances in image analysis have improved the accuracy and efficiency of quantitative phase analysis with electron microbeam instruments (e.g., Fandrich et al. 2007). However, these techniques cannot be used to quantify the modal abundance of fine-grained minerals or hydrous minerals that are easily vaporized by an electron beam (e.g., hydrated carbonate minerals, hydrated sulphate minerals, and hydrotalcite-group minerals – all of which are common at Mount Keith). Quantitative crystallographic methods that use X-ray powder diffraction (XRPD) data are not limited by fine grain size and do not damage samples to the same extent as techniques that employ electron microbeams. Quantitative phase analysis using XRPD data provides a measure of the weight-percent contribution of each carbonate mineral in a sample. From a measure of

modal abundance, the amount of CO_2 stored in specific carbonate minerals, which are known to be trapping atmospheric carbon, can be determined.

Several methods of quantitative phase analysis with XRPD data have been tested and calibrated for the purpose of verifying and quantifying CO_2 sequestration within mine tailings (Wilson et al. 2006, 2009b). We have used the Rietveld method and X-ray powder diffraction data (Rietveld 1969; Hill and Howard 1987; Bish and Howard 1988) to obtain quantitative mineralogical data for over 200 samples of Mount Keith tailings. Because the ages are known for many of the tailings flows at Mount Keith, we have been able to use our quantitative mineralogical results to obtain an empirical rate for hydromagnesite precipitation and to estimate the amount of CO_2 that is being trapped and stored within these tailings. The three-isotope system (i.e., $\delta^{13}C$, $\delta^{18}O$, and $F^{14}C$) employed by Wilson et al. (2009a) has been used to verify trapping of atmospheric CO_2 within hydromagnesite and to provide more precise constraints on the amount of CO_2 fixed within the tailings at Mount Keith.

4.2 Locality and sampling strategy

4.2.1 The Mount Keith Nickel Mine

The MKD5 orebody at Mount Keith in the North Eastern Goldfields district of Western Australia (Fig. 4.1) is the largest nickel producer in Australia (Grguric 2003). The deposit at Mount Keith occurs in the NNW/SSE-trending Agnew-Wiluna greenstone belt in the Archaean Yilgarn Craton (Hill et al. 1990). The Agnew-Wiluna greenstone belt is at its narrowest in the vicinity of Mount Keith, with a breadth of six kilometres (Grguric et al. 2006), and is surrounded by Archaean granitoids to the east and west (Barrett et al. 1977). The MKD5 orebody is hosted by komatiitic peridotite (primarly dunite), which attained mid-upper greenschist facies as a result of regional metamorphism (Barrett et al. 1977). Retrograde serpentinization and carbonation of the host peridotites resulted from infiltration by H_2O-CO_2-rich fluids (Barrett et al. 1977; Grguric et al. 2006). Resulting metamorphic assemblages (from proximal to distal) are

(1) talc-magnesite, (2) antigorite-magnesite, and (3) lizardite-brucite-hydrotalcite group (Grguric et al. 2006).

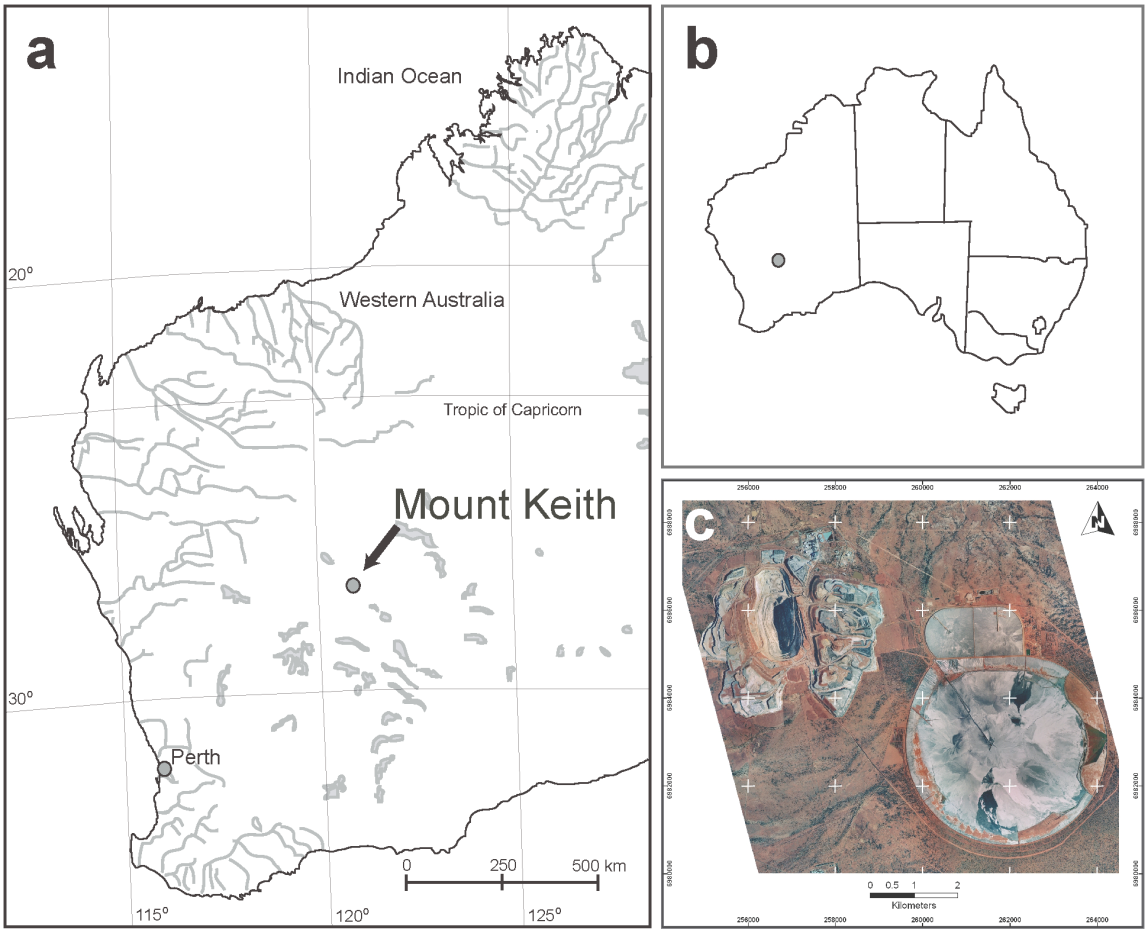

Figure 4.1: (a) and (b) Location of Mount Keith Nickel Mine, Western Australia, Australia. (c) Satellite photograph of the open pit at the MKD5 deposit and tailings storage facility, Mount Keith.

Conventional, staged-cutback, open pit mining methods are practiced at MKD5, yielding approximately 11 Mt of ore annually (Grguric 2003). The mining operation at MKD5 produces approximately 370,000 t of greenhouse gases (cited as CO_2 equivalent) and approximately 11 Mt of ultramafic tailings each year (BHP Billiton 2005). Ore from the MKD5 deposit is processed using froth flotation methods to concentrate sulphide minerals (Grguric et al. 2006). Additives used in processing include citric and sulphuric acids, guar gum, Na-dithionite, Na-ethyl xanthate, and (historically) soda ash. In 2004, ore reserves contained 0.52 wt.% nickel (Grguric et al. 2006), primarily in high-Ni pentlandite [$(Fe,Ni)_9S_8$], godlevskite [$(Ni,Fe)_9S_8$], heazlewoodite [Ni_3S_2], and millerite

[NiS]. Recovery of these minerals from the flotation circuit is typically about 70% (Grguric et al. 2006). The material rejected from the processing plant is piped to the second of two tailings storage facilities (TSF2, which is the only facility currently in operation), suspended in the hypersaline process water used in the flotation circuit. Tailings are deposited from spigots located on risers at nine points in TSF2 (Fig. 4.2).

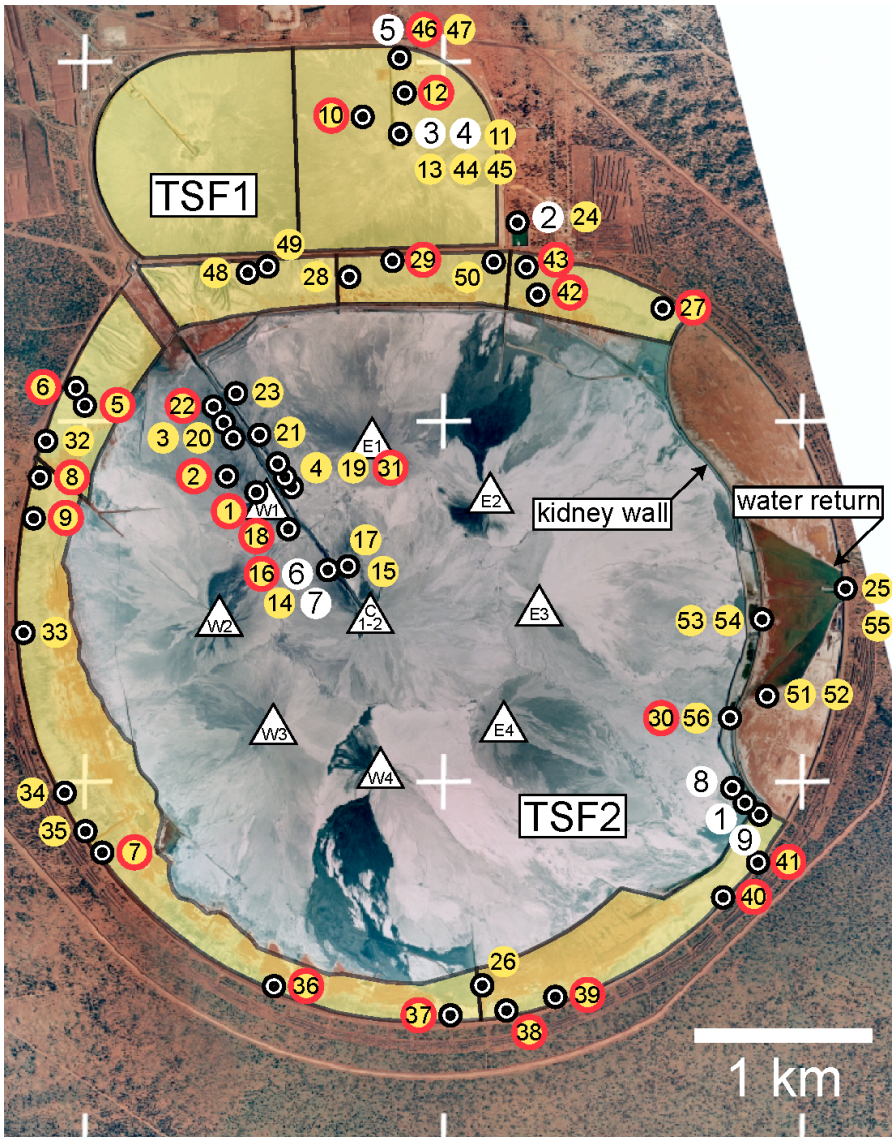

Figure 4.2: The Tailings Storage Facilities (TSFs) at Mount Keith. The roughly circular facility is TSF2 and the smaller, adjoining facility is TSF1. Samples were collected at 59 locations in TSF1 and TSF2. Sampling in TSF2 was done along the perimeter of the facility and on both sides of a radial access road. Sampling in TSF1 was done proximal to the access road in Cell 2 (the right-most cell of TSF1). White circles indicate sites sampled in 2005; yellow circles indicate sites sampled in 2006; red borders on circles indicate sites for which Rietveld refinements have been done; white triangles indicate locations of risers. Yellow shading denotes regions of the TSFs in which deposition of tailings had ceased as of 2006.

4.2.2 Strategy for sampling at Mount Keith

Limited sampling of the tailings storage facilities at Mount Keith was begun in April 2005. More extensive sampling was done in September and October of 2006. At this time, in excess of 800 samples were collected from TSF2 and the older, now-decommissioned TSF1.

Ideally, a tailings storage facility would be sampled randomly using a grid system; however, modern tailings management practices make this problematic if not impossible. Tailings saturated with water are more easily transported from a processing plant to a storage facility through a network of pipes. All tailings at Mount Keith have been and continue to be transported and deposited as slurry to the tailings storage facilities. Also, subaqueous storage of mine tailings is an effective strategy for preventing acid mine drainage and metal leaching from potentially acid-generating mine tailings (e.g., Robertson et al. 1997; Jambor and Blowes 1998; Price and Errington 1998). Consequently, it is common practise for many mining operations to retain some amount of process water in their stored tailings, either as a result of transportation by water or to mitigate acid generation. At the time of sampling, large regions of TSF2 were saturated with process water. These regions of the tailings facility were not accessible for sampling, making it impossible to collect a random set of samples on a grid.

In order to compensate for incomplete access to the tailings at Mount Keith, sampling of the main tailings storage facility (TSF2) was done along a radial maintenance road and around the perimeter of the roughly circular facility (Fig. 4.2). Sampling was done at random intervals along these two paths in TSF2 and within tailings situated along the access road of Cell 2 of the older, non-operational TSF1. Tailings were primarily sampled by coring on 5 m x 5 m and 10 m x 10 m grids (after Roselle et al. 1999) and from vertical profiles on exposed surfaces. A total of 501 samples were collected from 11 grids, three profiles, and one trench excavated using a backhoe. Grid sampling was undertaken to assess local homogeneity of tailings by sampling in a standard pattern, with cores taken at regular intervals of distance (0.25 m and 2.50 m) and depth (10-cm long samples centred at 5, 25, 50, 75, 100, and 125 cm depth). Profiles extended sampling to depths beyond the range accessible using a sediment-coring device to a maximum depth of approximately 4 m. One backhoe

excavation allowed otherwise inaccessible tailings from sampling site 30 (Fig. 4.2), which is near the Kidney Wall in TSF2, to be sampled to a depth of ~1.8 m. Twenty-six cores were sampled at random locations, providing an additional 144 samples. Seventy-nine samples of efflorescent crusts were collected in association with the grids, profiles, and individual cores. Approximately 820 samples of tailings, biofilms, water, and process chemicals were collected from Mount Keith in 2005 and 2006. Of these, 724 samples of mine tailings are suitable for quantitative phase analysis. Quantitative phase analysis with the Rietveld method was done on 204 of these. Sampling locations were selected for Rietveld refinement in a way that optimized coverage of the accessible regions of both tailings storage facilities. A random number generator was used to select subsets of samples collected from 5 m x 5 m and 10 m x 10 m grids for quantitative phase analysis.

Sampling did not extend to the base of the tailings deposits in most regions of TSF1 and TSF2 because depths greater than one to four metres were inaccessible using the collection techniques available (i.e., sampling with a sediment coring device, profiling, and limited access to a backhoe). In many of the thinner flows of tailings around the exterior of TSF2, the base of the deposits was accessible. However, basal deposits in the deeper, central regions of TSF1 and TSF2 could not be sampled.

4.3 Analytical methods

4.3.1 Qualitative X-ray powder diffraction methods

Qualitative mineralogy was done on selected specimens of efflorescent mineral crusts and microsamples from Mount Keith that were picked with fine tweezers under a binocular microscope. This was done in order to identify sulphate and halide minerals that were present at low abundances within the tailings. Qualitative XRPD was also done on acid-treated specimens of mine tailings prior to stable isotopic analysis. Finely ground aliquots of sample were smear-mounted onto petrographic slides with anhydrous ethanol and allowed to dry at room temperature. XRPD data for mineral identification were collected with a scanning step of 0.04° 2θ and counting time of 0.5 s/step on a Siemens

(Bruker) D5000 θ-2θ diffractometer equipped with a VÅNTEC-1 detector. The long, fine-focus Co X-ray tube was operated at 35 kV and 40 mA and an Fe monochromator foil was employed. Mineral phases were identified with reference to the ICDD PDF-4+ database using DIFFRAC^{plus} EVA Version 10.0 (Bruker AXS 2004).

4.3.2 Quantitative X-ray powder diffraction and Rietveld refinement

Quantitative phase analysis with the Rietveld method (Rietveld 1969; Hill and Howard 1987; Bish and Howard 1988) was done on 204 samples of mine tailings from the Mount Keith Nickel Mine. On return to the laboratory, samples were left in a drying hood under ambient conditions for a minimum of one week and were then homogenized mechanically with a spatula. From each dried and homogenized sample, a 50 g to 100 g subsample was taken and pulverized using a tungsten carbide ringmill. Three-gram aliquots of pulverized sample were weighed to a precision of ± 0.001 g. Ten weight-percent of annealed synthetic fluorite (an in-house standard) was added to each three-gram aliquot as an internal standard. Subsequently, the aliquots were ground for 10 minutes in a McCrone micronizing mill to reduce the mean grain size and ensure homogenization. Grinding was done under anhydrous ethanol using agate grinding elements. Ground samples were dried at room temperature under a fume hood and were disaggregated using an agate mortar and pestle once dry.

A specimen was prepared from each sample by mounting the powder into a back-loading aluminum cavity holder of the design described by Raudsepp and Pani (2003). Powdered samples were loaded against the roughened surface of a sheet of glass that covered the top of the cavity. This was done to reduce preferred orientation of crystallites, particularly those of phyllosilicate minerals, hydrotalcite-group minerals, and hydromagnesite. X-ray powder diffraction data were collected on the Siemens (Bruker) D5000 θ-2θ diffractometer under the same operating conditions used to collect data for qualitative mineralogy. Data for Rietveld refinement were collected with a step size of 0.04° 2θ and counting time of 1s/step over a range of 3-80° 2θ.

Rietveld refinements were done with Rietveld refinement software Topas Version 3 (Bruker AXS 2004) using the fundamental parameters approach (Cheary and Coelho

1992). Sources of crystal structure data for detectable mineral phases in the tailings samples are listed in Table 4.1.

Table 4.1: Sources of crystal structure data for Rietveld refinement.

Mineral	**Source**
Antigorite	Uehara (1998)
Blödite	Vizcayno and Garcia-Gonzalez (1999)
Brucite	Catti et al. (1995)
Calcite	Maslen et al. (1995)
Dolomite	Ross and Reeder (1992)
Epsomite	Calleri et al. (1984)
Fluorite	Batchelder and Simmons (1964)
Gypsum	Cole and Lancucki (1974)
Halite	Nickels et al. (1949)
Hexahydrite	Zalkin et al. (1964)
Hydromagnesite	Akao and Iwai (1977)
Iowaite	Braithwaite et al. (1994)
Kaolinite	Bish (1993)
Konyaite	Leduc et al. (2009)
Lepidocrocite	Zhukhlistov (2001)
Lizardite-1T	Mellini and Viti (1994)
Löweite	Fang and Robinson (1970)
Magnesite	Markgraf and Reeder (1985)
Magnetite	Tsukimura et al. (1997)
Muscovite-$2M_1$	Liang and Hawthorne (1996)
Plagioclase (An_{91})	Wenk and Kroll (1984)
Quartz	Glinnemann et al. (1992)
Rutile	Meagher and Lager (1979)
Talc	Perdikatsis and Burzlaff (1981)
Trona	Pertlik (1986)
Vermiculite	Shirozu and Bailey (1966)
Woodallite	Grguric et al. (2001) and Braithwaite et al. (1994)

The method of Wilson et al. (2006), initially developed for use with chrysotile-rich mine tailings, was used to compensate for structural disorder in lizardite and antigorite during refinement. This method was readily applied, with very little change of procedure, because of the mineralogical similarity between chrysotile mine tailings and the tailings from Mount Keith. Mineralogy and relative abundances of the major and minor phases in the tailings at Mount Keith are comparable to those for chrysotile mine tailings. Tailings from chrysotile mines and tailings from Mount Keith both contain one or more serpentine minerals, hydrotalcite-group minerals, minor spinel minerals (i.e., magnetite and/or chromite), occasional hydrated magnesium sulphate minerals, and low but detectable amounts of primary (i.e., bedrock) carbonate minerals and secondary precipitates of hydrated magnesium carbonate minerals. As a result, we were able to apply this established procedure for quantitative mineralogical analysis to samples from Mount Keith. Peak intensities for each serpentine mineral were extracted using the Pawley method (Pawley 1981), independent of atomic scattering, from X-ray powder diffraction patterns of high-purity standards. Fourth-order symmetrized harmonics were used to model anisotropic peak shape in lizardite and antigorite (Järvinen 1993). Without reference to atomic positions, the relative peak intensities of lizardite and antigorite are unconstrained. To compensate, the relative intensities of the serpentine peaks phases were initially held constant to prevent their peaks from interfering with those from other phases. The relative intensities of the peaks for lizardite and antigorite were refined only after the peaks of the other phases had been fitted. The weight-percent abundances of antigorite and lizardite are given together, because the method of Wilson et al. (2006) cannot quantify more than one disordered phase per sample.

Several poorly defined minerals are common constituents of Mount Keith tailings: mountkeithite $\{(Mg,Ni)_{11}(Fe^{3+},Cr^{3+},Al)_3[(OH)_{24}|(SO_4,CO_3)_{3.5}]\cdot 11H_2O\}$ and woodallite $[Mg_6Cr^{3+}_2(Cl_2)(OH)_{16}\cdot 4H_2O]$. Mountkeithite, occasionally detected in XRPD patterns, is generally present at abundances too low to refine reliably because only its most intense reflection is detectable at ~3σ above background. Woodallite is a minor phase in most samples and, to date, the details of its crystal structure have not been published. However, because of the known structural similarity and the solid solution series between woodallite and iowaite, the structure of woodallite can be approximated

using a modified structure based on that of iowaite (using the structure reported by Braithwaite et al. 1994). With this in mind, we replaced the lattice parameters of iowaite [$Mg_6Fe^{3+}_2(Cl_2)(OH)_{16}\cdot 4H_2O$] with those given for woodallite by Grguric et al. (2001) and substituted the scattering factor for the Fe^{3+} in the structure of iowaite with that for Cr^{3+}. Woodallite and iowaite in the ore from Mount Keith contain variable amounts of sulphate, carbonate, and chloride in their interlayer sites (Grguric 1999, 2003; Grguric et al. 2001, 2006; Woodhouse 2006). The grain-by-grain variability of chemical species in these interlayer sites commonly gives rise to broad, severely overlapped peaks for woodallite and iowaite. This makes it difficult to distinguish these mineral phases from XRPD patterns without resorting to the use of small angular steps and long counting times to acquire high-resolution XRPD data. Because of this, refined abundances for woodallite and iowaite are given here as a single value. Similarly, due to the structural similarity between magnetite and chromite and the difficulty in distinguishing between them using XRPD data, these phases have been refined using only the structure of magnetite and their abundances are reported together.

Second or third-order Chebychev polynomials were used to model the background and a $1/x$ term was included to assist in fitting the background curve at low angles of diffraction. Cell parameters and Lorentzian crystallite size were refined for all phases and zero error was refined for each XRPD pattern. The method of Brindley (1945) was used to correct for microabsorption contrast between phases, assuming a mean particle radius of 2.5 μm. Preferred orientation of hydrotalcite-group minerals was modeled using the March-Dollase correction (March 1932; Dollase 1986).

Quantification of hydromagnesite is of primary importance for estimates of carbon mineralization at Mount Keith. Unfortunately, trace amounts of this mineral are not always measurable using the methodology we employed to collect XRPD data for Rietveld refinement. The detection limit for hydromagnesite was determined to be approximately 0.5 wt.%. Hydromagnesite was successfully refined and quantified at an abundance of ~0.5 wt.% for only one sample, although it was present at close to this value in 22 of 204 samples for which Rietveld refinements were done. In this sample (06MKG10-4-3), the refined cell parameters of hydromagnesite gave reasonable values but the Lorentzian crystallite size refined for hydromagnesite gave an unrealistic value in

excess of 1000 nm. Although the most intense peaks of hydromagnesite (the overlapping 011 and 0-1-1 reflections) were detected at > 3σ of the background intensity for 22 samples, our attempts at including (and thereby quantifying) hydromagnesite in 21 of these refinements failed. Hard constraints on cell parameters and crystallite size were required to produce a reasonable fit to the observed data. Because constraints of this sort can bias Rietveld refinements, the crystal structure of hydromagnesite was removed from final refinements and a value of 0.5 wt.% (i.e., the detection limit) was imputed for the abundance of hydromagnesite in these samples. The numbers of samples for which hydromagnesite was quantifiable, imputed, and below detection are summarized in Table 4.2. Although there is error attached to imputed values for hydromagnesite, we consider this to be of an acceptable magnitude because it is almost certainly less than the error attached to refined values for mineral abundances less than 1 wt.% (which can exceed 50% relative, Wilson et al. 2006; 2009b).

Table 4.2: Numbers of samples for which hydromagnesite is quantifiable, imputed (at detection), or below detection.

Sample Subset	Quantified	At detection (0.5 wt.%)	Below detection (<0.5 wt.%)	Total
All samples	116	21	67	**204**
Samples included in statistical analyses	111	20	65	**196**

4.3.3 Scanning electron microscopy

Mineral habits and the textural relationships among minerals were characterized using a Philips XL-30 scanning electron microscope (SEM), equipped with a Princeton Gamma-Tech energy dispersive X-ray spectrometer (EDS) system. Selected samples of tailings were impregnated with epoxy and thin-sectioned for petrographic analysis. Backscattered electron (BSE) imaging was used to observe textural relationships in thin section and EDS was used for the identification of minerals.

4.3.4 Stable isotopic methods

A total of 100 specimens, taken from 45 geological samples and five samples of water, were analyzed for their stable carbon and oxygen isotopic compositions. Eighteen replicate analyses were done to assess reproducibility of the data. Thirty-two of these specimens of tailings were analyzed in bulk before and after treatment with one normal hydrochloric acid (1 N HCl) at room temperature (i.e., approximately 25ºC). Acid treatment was used to preferentially dissolve hydromagnesite, hydrotalcite-group minerals, and bedrock calcite and dolomite. The untreated specimens reflect the bulk isotopic compositions of all carbonate minerals in the tailings (i.e., bedrock and secondary carbonate minerals), while the acid-treated specimens reflect the isotopic composition of the more resistant bedrock magnesite. Stable isotopic data for the resulting 64 specimens, 16 other specimens of mine tailings, and the dissolved inorganic carbon (DIC) in five specimens of water, were collected using standard procedures for stable carbon and oxygen isotopic analyses (described in Subsections 4.3.4.1 and 4.3.4.2) employed at the Pacific Centre for Isotopic and Geochemical Research (PCIGR), The University of British Columbia. The stable isotopic compositions of hydromagnesite in 15 specimens of mine tailings were analyzed using the method for selective acid extraction of Barker et al. (2009), which is described in Subsection 4.3.4.3.

4.3.4.1 Standard methodology for carbonate minerals

Stable carbon and oxygen isotopic compositions of bulk samples of tailings and acid-treated tailings were determined using the standard procedure for routine analysis at PCIGR. Stable isotopic compositions were also measured in this way for highly pure subsamples of carbonate minerals that were picked with fine tweezers under a binocular microscope. A total of 80 aliquots of bulk tailings and mineral separates were analyzed using this standard methodology.

Specimens were analyzed using a gas bench attached to a Thermo Finnigan DeltaPlus XL isotope ratio mass spectrometer (IRMS). Aliquots weighing approximately 200 μg were loaded into septum vials, flushed with helium, and dissolved in 99% phosphoric acid at 72ºC for a minimum of one hour. Isotopic compositions of the evolved headspace gas were measured in a helium flow. The $\delta^{13}C$ compositions are given

relative to Vienna Pee Dee Belemnite (VPDB) and the $\delta^{18}O$ compositions are relative to Vienna Standard Mean Ocean Water (VSMOW). The external precision (1σ deviation) for isotopic analyses was < 0.1‰ $\delta^{13}C$ and < 0.2‰ $\delta^{18}O$, as estimated from repeated analysis of NBS-18, NBS-19, and in-house calcite standards (which are calibrated against the NBS standards). At least three standards were analyzed for every eight specimens.

As a result of their relative scarcity, fewer studies of stable isotopes in anhydrous magnesium carbonate minerals (e.g., magnesite, huntite, and dolomite) have been undertaken than for calcium carbonate minerals (Kralik et al. 1989). Even fewer detailed stable isotopic studies have been attempted for the hydrated magnesium carbonate minerals (i.e., O'Neil and Barnes 1971; Grady et al. 1989; Braithwaite and Zedef 1996; Zedef et al. 2000; Léveillé et al. 2007; Power et al. 2007, 2009; Wilson et al. 2009a). Because these minerals have not been studied thoroughly, the factors required to correct for fractionation of ^{18}O between hydromagnesite and phosphoric acid or other hydrated magnesium carbonate minerals and phosphoric acid are not known. As such, the acid fractionation factor for magnesite was used as a proxy for hydromagnesite. The $\delta^{18}O$ values of calcite, dolomite, and magnesite were corrected for reaction with phosphoric acid using the fractionation factors from Das Sharma et al. (2002), taking into account the approximate proportions of calcium and magnesium carbonate minerals in mixed specimens.

4.3.4.2 Standard procedure for dissolved inorganic carbon

Stable carbon isotopic compositions of total dissolved inorganic carbon (DIC) in five specimens of water from Mount Keith were determined using the Thermo Finnigan DeltaPlus XL IRMS. For each specimen, four to five drops of 99% phosphoric acid were loaded into an exetainer, which was then sealed with a rubber septum and flushed with helium for five minutes. A syringe was used to inject 600 μL of each water specimen into a sealed exetainer. The exetainer was shaken and the specimen left to react for a minimum of one hour at 25ºC. As with specimens of carbonate minerals, the isotopic composition of the evolved headspace gas was measured in a helium flow. The $\delta^{13}C$ compositions are given relative to VPDB. The external precision (1σ deviation) for

isotopic analyses was < 0.1‰ $\delta^{13}C$, as estimated from repeated analysis of NBS-18, NBS-19, and in-house calcite standards.

4.3.4.3 Procedures for selective analysis of carbonate minerals

The disseminated nature of hydromagnesite within Mount Keith tailings hinders isotopic analysis using standard analytical procedures. Efforts to manually separate pure hydromagnesite from these tailings have been unsuccessful. Alternatively, bulk dissolution of tailings extracts CO_2 from all carbonate minerals in a sample, including secondary carbonate minerals that may be storing atmospheric CO_2, bedrock carbonate minerals, and carbonate-bearing hydrotalcite-group minerals. Interpretation of stable carbon and oxygen isotopic data requires accounting of all carbonate-bearing mineral species due to the variability in isotopic fractionation with mineralogy. Stable isotopic results are more easily interpreted for single-phase specimens. Selective analysis of minerals allows the importance of different mineral species to CO_2 sequestration to be assessed.

Hydrated magnesium carbonate minerals like hydromagnesite are susceptible to dissolution in weak acids (e.g., Power et al. 2007; Wilson et al. 2009a), which can be used to leach them preferentially from samples of tailings. We have used the method of Barker et al. (2009) to determine the carbon and oxygen isotopic compositions of both the secondary hydromagnesite and bedrock magnesite in mine tailings from Mount Keith. This method exploits the difference in reactivity of hydrous and anhydrous magnesium carbonate minerals with phosphoric acid at room temperature (after Epstein et al. 1964; Al-Aasm et al. 1990). The hydrated magnesium carbonate minerals react quickly after addition of phosphoric acid to a bulk sample of pulverized tailings. Within the first 15 to 30 minutes of room-temperature reaction, most of the CO_2 evolved from a bulk sample is derived from decomposition of hydrated magnesium carbonate minerals. The evolved CO_2 can then be collected using a vacuum line and analyzed to determine the isotopic composition of the hydrated magnesium carbonate minerals in a sample. Once the hydrated magnesium carbonate minerals have reacted completely with the acid, the remainder of the evolved gas can be evacuated, and the acidified sample heated, in order to collect CO_2 from the bedrock carbonate minerals in the tailings. Using this

method, the CO_2 from hydromagnesite and magnesite (± calcite and dolomite) can be analyzed separately for stable carbon and oxygen and radiocarbon isotopic compositions. The resulting isotopic analyses give a more complete description of sources and cycles for CO_2 in carbonate minerals than can be gained from bulk analysis of mine tailings.

For each of 15 samples of pulverized tailings from Mount Keith, an aliquot was weighed out. The size of the aliquot was dependent upon (1) whether the sample was for stable isotopic or radiocarbon analysis (substantially more sample is required for radiocarbon analysis) and (2) the total percent by weight (wt.%) of carbonate minerals in each sample. Aliquots for stable isotopic analysis were weighed out such that each would provide at least 5 mg (of calcite-equivalent CO_2 content) of both hydromagnesite and magnesite. The amount of material required was calculated from the results of quantitative phase analysis with the Rietveld method. Each aliquot was deposited into a sterile, unlined 10 mL BD Vacutainer® with a resealable, 8-mm thick rubber septum. A small amount of glass wool was inserted into the top of each vial. This was done to contain the pulverized tailings within the bottom portion of the vial during reaction with phosphoric acid. It was also used to prevent any potential contamination of the vacuum line by finely powdered material.

Following the method of Barker et al. (2009), evacuated specimens were acidified with 99% phosphoric acid and allowed to react at 25ºC for 15-30 minutes. The evolved headspace gas from each vial was collected in the vacuum line described by Barker et al. (2009) for approximately 5 minutes and allowed to remain in contact with a water trap. Evolved gas was passed through a piece of glass tubing, that was cooled by a slush of anhydrous ethanol and dry ice, in order to trap evolved water (as ice) but let pass CO_2. Carbon dioxide was collected at the base of a 6-mm diameter glass ampoule, which was chilled in a bath of liquid nitrogen (T = 77 K) so that CO_2 could be collected in the solid state. A handheld propane torch was used to weld and seal the top of each ampoule so that the CO_2 could be contained and stored prior to analysis.

Following collection of CO_2 evolved from hydromagnesite, the room-temperature reaction was allowed to continue for two hours until dolomite, calcite, hydrotalcite-group minerals, and any residual hydromagnesite had reacted completely. Although hydrotalcite-group minerals are less susceptible to dissolution in weak acids than

hydromagnesite, they are prone to exchange of interlayer anions in some weakly acidic solutions (e.g., Bish 1980). There is also evidence that anionic clays (like the hydrotalcite-group minerals) are able to take up phosphate ions into their interlayers (e.g., Badreddine et al. 1999). The rate at which iowaite and woodallite dissolve in phosphoric acid, and the extent to which they may exchange interlayer CO_3^{2-} and Cl^- for phosphate ions, is not known.

The evolved gas from the reaction of hydromagnesite with phosphoric acid was removed from each vial using the vacuum line and vacuum was restored within the sample tubes. The evacuated vials were heated, in a 1 L bath of water on a laboratory heating plate, to 75ºC for 1 hour. Evolved headspace gas produced by reaction of phosphoric acid with magnesite was collected for approximately 5 minutes using the vacuum line. Carbon dioxide evolved from magnesite was trapped and stored within 6-mm diameter glass ampoules using the same procedure as for hydromagnesite.

Specimens were analyzed by loading into one bellows in the dual inlet of the Thermo Finnigan DeltaPlus XL IRMS. A reference gas was loaded into the other bellows. Isotopic ratios were measured using a standard dual-inlet technique, with 10 measurement cycles for each specimen. In-house standards were measured once for every five unknown specimens to monitor reference gas drift. Standards NBS-18 and NBS-19 were measured as "unknown" specimens to determine the accuracy of analyses. Values for $\delta^{13}C$ and $\delta^{18}O$ were measured to within ± 0.5‰ of accepted values for both international standards.

Samples containing hydromagnesite were not heated prior to acidification to remove crystallographic water from this mineral, as is standard practise for stable isotope studies of hydrated carbonates (e.g., O'Neil and Barnes 1971; Taylor 1975; Grady et al. 1989; Zedef et al. 2000). During analysis, exchange fractionation of oxygen may have occurred between H_2O and CO_2 evolved from acidified hydromagnesite. The phosphoric acid used to dissolve hydromagnesite is expected to have absorbed a component of the evolved crystallographic water, however, the extent to which this occurs has not been documented. As a result, the $\delta^{18}O$ values reported for selective extraction of CO_2 from hydromagnesite may reflect the oxygen isotopic composition of both carbonate and structurally bound water within this mineral.

4.3.5 Radiocarbon procedures

Radioactive ^{14}C can be used as an indicator of modern precipitation of carbonate minerals. As a result of the artificial enrichment of atmospheric ^{14}C caused by nuclear testing in the mid-twentieth century, minerals precipitated from modern atmospheric CO_2 will contain a greater proportion of ^{14}C than the reference standard (95% of the activity of oxalic acid derived from sugar beets grown in 1950) (Stuiver and Polach 1977). Since the discovery that nuclear testing had impacted the concentration of ^{14}C in the atmosphere (Rafter and Fergusson 1957), an effort has been made to document the history of the atmospheric "bomb curve" (e.g., Stuiver and Quay 1981; Nydal and Lövseth 1983; Levin et al. 1985; Olsson and Possnert 1992; Hua and Barbetti 2004; Levin and Kromer 2004; Quarta et al. 2005).

Because the "bomb curve" has a well-defined shape, it has been used to date tissues in forensic applications (e.g., Wild et al. 2000; Spalding et al. 2005), to measure the growth rate of speleothems (e.g., Genty and Massault 1997; Genty et al. 1998; Mattey et al. 2008), and to trace the exchange of carbon between the atmosphere, carbonate minerals, and soil (i.e., Genty et al. 1998; Milton and Kramer 1998; Hardie et al. 2007; Horvatincic et al. 2008). Two studies have used radiocarbon data to demonstrate recent precipitation of hydrated magnesium carbonate minerals from an atmospheric carbon source: Jull et al. (1988) with nesquehonite [$MgCO_3 \cdot 3H_2O$], and Wilson et al. (2009a) with nesquehonite and dypingite [$Mg_5(CO_3)_4(OH)_2 \cdot 5H_2O$].

Twenty-three specimens taken from 19 geological samples were analyzed for radiocarbon concentrations at The Australian National University. These comprised one specimen of industrial soda ash, three specimens of highly pure bedrock carbonate minerals, four specimens of CO_2 extracted from magnesite in bulk samples of tailings, and 15 specimens of CO_2 extracted from hydromagnesite in bulk tailings. Eight replicate analyses were done to assess reproducibility of radiocarbon data.

For radiocarbon analysis, specimen size was determined such that CO_2 would be evolved in a quantity equivalent to at least 1 mg of elemental carbon from each of (1) hydromagnesite and (2) bedrock magnesite. The required weight was determined from the results of Rietveld refinement on each sample of tailings, assuming ideal stoichiometric compositions for magnesium carbonate minerals and 100% recovery of

CO_2 during gas separation on the vacuum line. The remainder of the method is identical to that for stable isotopic analysis (as described in Subsection 4.3.4.3) save for one detail: 85% phosphoric acid was used in place of 99% phosphoric acid.

Specimens of CO_2 were sealed within glass ampoules at The University of British Columbia and were analyzed for ^{14}C content at the Research School of Earth Sciences at The Australian National University. There, the CO_2 contained within the ampoules was converted to graphite by hydrogen reduction in the presence of iron powder at 550ºC. Graphite targets were placed in a small mould and compressed into pellets. The pellets were run on the Single Stage Accelerator Mass Spectrometer (SSAMS) at The Australian National University. Background contamination, from preparation of graphite targets, was determined from analyses of ^{14}C-free coal and wood and was subtracted from sample data. The Cambridge half-life (5730 ± 40 years) was used to calculate the fraction of modern carbon ($F^{14}C$) as recommended by Donahue et al. (1990) and Reimer et al. (2004). Reservoir corrections were made to $F^{14}C$ values using $\delta^{13}C$ data collected with the SSAMS.

4.4 Field results and qualitative mineralogy

4.4.1 Qualitative mineralogy of Mount Keith mine tailings

Tailings at Mount Keith are composed primarily of antigorite and lizardite with hydrotalcite-group minerals (i.e., mostly iowaite and woodallite with occasional pyroaurite, stichtite, and mountkeithite). Minor amounts of brucite, chrysotile, talc, magnetite, chromite, quartz, magnesite, dolomite, and calcite are common. Trace vermiculite is also observed in the tailings. Sulphide minerals have not been detected with XRPD to a limit of approximately 0.5 wt.%.

Efflorescences of secondary minerals are abundant near surfaces within the tailings storage facilities and include carbonate minerals (listed in Table 4.3), halide minerals and sulphate minerals (listed in Table 4.4). Efflorescent halide and sulphate minerals are common within the upper 25 cm of the tailings storage facilities (although less so in TSF1 than in TSF2). Efflorescences of sulphate minerals commonly form at the

surface of mine tailings during dry conditions or in arid climates, and are leached from tailings during rainfall events (Jambor et al. 2000). At Mount Keith, halite, hexahydrite, and blödite dominate these efflorescences, and are commonly associated with lesser amounts of epsomite, konyaite, löweite, and gypsum. Sanderite, starkeyite, pentahydrite, and carnallite are less common and have only been observed at low abundance. Kainite and anhydrite may or may not be present near detection in a very few of the samples analyzed. Given that the hydration states of sulphate minerals are sensitive to changes in temperature and relative humidity (e.g., Chou and Seal 2003, 2007; Peterson and Grant 2005; Chipera and Vaniman 2007), the relative abundances of hydrated sulphate minerals measured in the laboratory may not reflect abundance in the field.

Table 4.3: Carbonate and hydrotalcite-group minerals detected at Mount Keith.

Mineral Name	Cation(s)	Formula	Detected at Surface	Detected at Depth
Hydromagnesite	Mg	$Mg_5(CO_3)_4(OH)_2{\cdot}4H_2O$	X	X
Magnesite	Mg	$MgCO_3$	X	X
Dolomite	Mg, Ca	$CaMg(CO_3)_2$	X	X
Calcite	Ca	$CaCO_3$	X	X
Siderite	Fe	$Fe^{2+}CO_3$	X	?
Trona	Na	$Na_3(CO_3)(HCO_3){\cdot}2H_2O$	X	
Iowaite	Mg, Fe	$Mg_6Fe^{3+}_2(OH)_{16}Cl_2{\cdot}4H_2O$	X	X
Pyroaurite	Mg, Fe	$Mg_6Fe^{3+}_2(OH)_{16}CO_3{\cdot}4H_2O$	X	X
Woodallite	Mg, Cr	$Mg_6Cr_2(OH)_{16}Cl_2{\cdot}4H_2O$	X	X
Stichtite	Mg, Cr	$Mg_6Cr_2(OH)_{16}CO_3{\cdot}4H_2O$	X	X
Hydrotalcite	Mg, Al	$Mg_6Al_2(OH)_{16}CO_3{\cdot}4H_2O$		
Mountkeithite	Mg, Ni, Fe, Cr	$(Mg,Ni)_{11}(Fe,Cr)_3(OH)_{24}(SO_4,CO_3)_{3.5}{\cdot}11H_2O$	X	X

Table 4.4: Sulphate and halide minerals detected at Mount Keith.

Mineral Name	Cation(s)	Formula	Detected at Surface	Detected at Depth
Sanderite	Mg	$MgSO_4 \cdot 2H_2O$	X	
Starkeyite	Mg	$MgSO_4 \cdot 4H_2O$	X	
Pentahydrite	Mg	$MgSO_4 \cdot 5H_2O$	X	
Hexahydite	Mg	$MgSO_4 \cdot 6H_2O$	X	
Epsomite	Mg	$MgSO_4 \cdot 7H_2O$	X	
Löweite	Na, Mg	$Na_{12}Mg_7(SO_4)_{13} \cdot 15H_2O$	X	
Blödite	Na, Mg	$Na_2Mg(SO_4)_2 \cdot 4H_2O$	X	
Konyaite	Na, Mg	$Na_2Mg(SO_4)_2 \cdot 5H_2O$	X	
Anhydrite	Ca	$CaSO_4$	?	?
Gypsum	Ca	$CaSO_4 \cdot 2H_2O$	X	X
Halite	Na	NaCl	X	X
Kainite	K, Mg	$Mg(SO_4)KCl \cdot 3H_2O$	?	
Carnallite	K, Mg	$KMgCl_3 \cdot 6H_2O$	X	

Scanning electron microscope (SEM) images of Mount Keith mine tailings commonly show fine crystals of hydromagnesite precipitating at the surface of grains of serpentine (Fig. 4.3). In some instances, hydromagnesite can be seen infilling fine cracks in grains of serpentine. Also, broad, irregular fissures in grains of serpentine are commonly filled with hydromagnesite (Fig. 4.3a). The latter texture suggests that hydromagnesite may be forming by replacement of serpentine. Micrometre-scale crystals of hydromagnesite radiate out into the spaces between tailings grains and commonly cement them together (Fig. 4.3b). These textures are reminiscent of those described by Wilson et al. (2009a) for dense cements of hydromagnesite and dypingite [$Mg_5(CO_3)_4(OH)_2 \cdot 5H_2O$] that form at depth within tailings at the Clinton Creek chrysotile mine, Yukon Territory, Canada. The textural relationship between hydromagnesite and serpentine minerals confirms the secondary origin of hydromagnesite as a weathering product of serpentine at Mount Keith. In all samples

examined using scanning electron microscopy, there was no indication from energy dispersive X-ray spectra that other divalent metal cations were substituting for Mg^{2+} in hydromagnesite. This is consistent with the Mg-rich, generally Fe-poor composition of Mount Keith mine tailings.

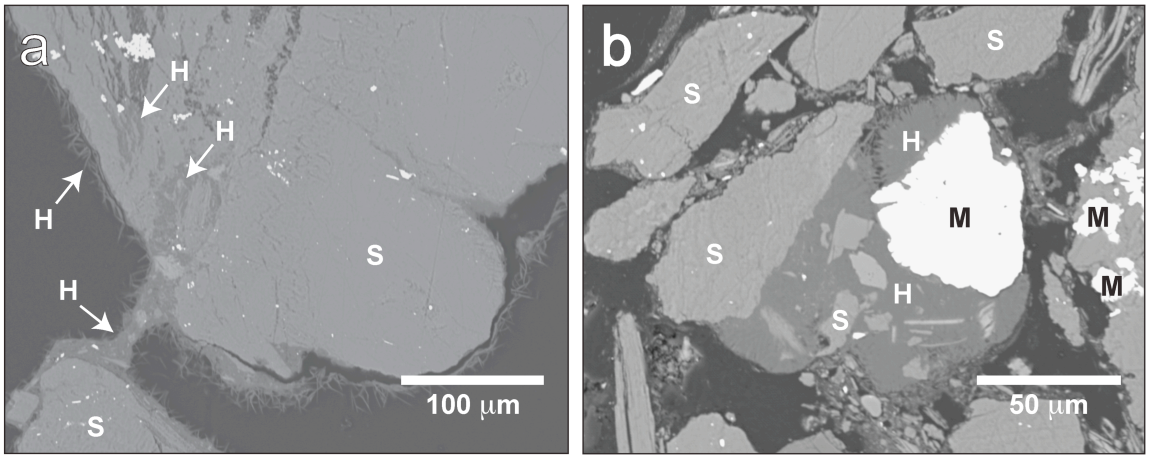

Figure 4.3: Backscattered electron images of hydromagnesite in Mount Keith mine tailings. Both (a) and (b) are from a particularly hydromagnesite-rich sample, 06MK9-9. (a) Hydromagnesite crystals precipitating at the surface of larger grains of serpentine and infilling cracks and fissures within them. (b) Hydromagnesite cementing both fine and larger grains of serpentine together. H – hydromagnesite; M – magnetite; S – serpentine.

Secondary hydromagnesite is typically concentrated within and just below efflorescent crusts of sulphate minerals, but hydromagnesite persists at depth within the tailings at Mount Keith whereas sulphate minerals generally do not. Although tailings that are heavily cemented with hydromagnesite commonly occur near the surface of TSF1 and TSF2, hydromagnesite-rich samples are encountered frequently at depth within the tailings storage facilities.

Excavating trenches within TSF2 to collect profile samples reveals distinct horizons of tailings material. Within these profiles, layers of clay and silt sized tailings commonly overly layers of sand sized tailings. These well-sorted layers are clearly indicative of mass settling within tailings flows during distinct depositional events. This layering trend occurs at least four times within the upper 2 m of the profile at sampling site 1 (i.e., 06MKP1) and is illustrated in Figures 4.4a and b. The most recently deposited tailings in 06MKP1 are covered by an efflorescent crust of blödite and halite and are enriched in hydromagnesite (samples labelled 1-3 in Fig. 4.4a). Hydromagnesite and

sulphate minerals are not detectable in the layers of fine sand (4) and coarse sand (5) beneath the surficial samples. However, hydromagnesite is present in deeper samples (6-8) that are associated with filled desiccation cracks (located between samples 7 and 8). Again, hydromagnesite is absent from sample 9, which grades into medium to coarse sand, but it reappears in sample 10. Although sample 10 is of coarse sand, it is in contact with a deeper, silty layer (11) that also contains hydromagnesite. The same trend of coarsening grain size with increasing depth occurs between samples 11 and 14, all of which contain hydromagnesite. Filled desiccation cracks appear once again between sample 14 and the fine-grained, hydromagnesite-rich tailings from sample 15. Beneath this level, at a depth of approximately 160 cm, the tailings become darker in colour and smell faintly of organic chemicals.

Desiccation cracks are a common feature within mine tailings at the surfaces of TSF1 and TSF2. Within weeks to months of tailings deposition, desiccation cracks begin to appear within the upper few centimetres of new tailings flows. Shallow, distantly spaced desiccation cracks can be seen in the newly deposited tailings at sampling site 30 (Fig. 4.4c). After approximately 6 months to year, many more cracks will have propagated within the hardened efflorescences on tailings surfaces (Fig. 4.4d). If the tailings are left exposed for a significant amount of time, the desiccation cracks can become deeper features as efflorescent sulphate minerals are leached from the surficial tailings, leaving behind hardened layers of hydromagnesite-cemented tailings (Fig. 4.4e).

The prevalence of desiccation cracks at tailings surfaces, the proximity to desiccation features, and the higher abundance of hydromagnesite within samples 06MKP1-8 and 06MKP1-15 indicate that the horizons from which they were taken were once exposed at the surface. It is particularly notable that these former surfaces and the horizons adjacent to them are enriched in hydromagnesite compared to the hydromagnesite-poor horizons of tailings that separate them. While hydromagnesite is most abundant near tailings surfaces, this suggests that (1) it may continue to precipitate at depth as a cement between tailings grains or that (2) it may becomes reworked at depth as former surfaces settle under the weight of the overlying deposits.

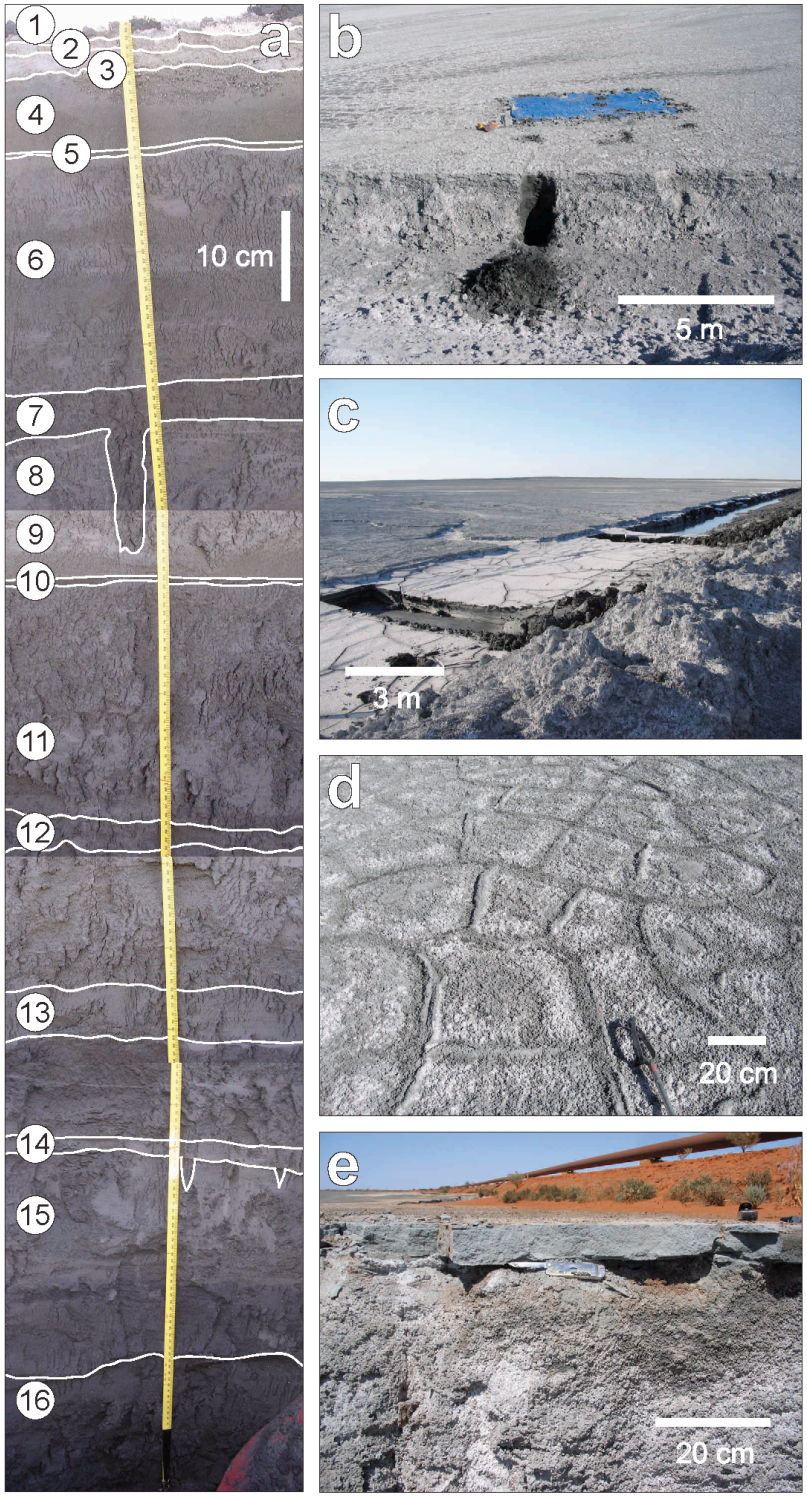

Figure 4.4: Mount Keith mine tailings at the surface and at depth within TSF2. (a) The upper half of the profile at sampling site 1 (06MKP1). Numbers label specific samples (e.g., "1" denotes sample "06MKP1-1") and white lines separate distinct horizons. (b) The profile excavation from (a) and a 5m x 5m grid sample (delineated by the blue tarpaulin) at sampling site 1. (c) Backhoe excavation at sampling site 30, showing near surface water and metre-scale desiccation cracks. (d) An older surface in TSF2 (~1-year old) showing well-developed efflorescences and more pervasive desiccation features. (e) The 7-8-year old surface of TSF2 at sampling site 9 (showing sample 06MK9-6) is heavily cemented with hydromagnesite.

4.4.2 Timing and depth of tailings deposition

The tailings storage facility at Mount Keith was constructed in two phases. The two cells of TSF1 were the sole receptacles for tailings from July 1994 (Environmental Protection Authority 1996; Ventnor Consulting Group 2003; Stolberg 2005) until the facility was decommissioned in January 1997 (Stolberg 2005). A centralized discharge tailings storage facility (TSF2) was commissioned to replace TSF1 in December 1996 (ICME and UNEP 1998) or January 1997 (Stolberg 2005) and remains in operation today. Along the circumference of TSF2, the outer 100 to 400 m of the compound are dedicated to catching and storing tailings in the event that mineral waste from the interior of the facility should overflow. This design feature has been effective and provides snapshots of tailings compositions from several overflow events. Tailings in the various overflow cells were permitted to weather, without addition of new tailings or process water, for periods of one, three, and between seven and eight years prior to sampling in 2006. Samples collected from the interior of TSF2 (along the radial access road) were last deposited approximately zero or one half years prior to collection. Tailings from Cell 2 of the decommissioned TSF1 were last deposited 10 years prior to collection.

To the best of our knowledge, all of the tailings (shallow and deep) sampled from the overflow cells around the exterior of TSF2 are of a specific age (either one, three, or between seven and eight years). Contrastingly, only the ages of tailings sampled from near the surfaces in the central regions of TSF1 and TSF2 are well constrained (as zero, one half, and 10 years).

Most of the sampling in the central regions of TSF1 and TSF2 was done to depths between zero and 130 cm using a sediment-coring device. The risers from which tailings are deposited to TSF2 are between 35 and 45 m high (ICME and UNEP 1998). At the time of sampling, the W1 riser (which is nearest to sampling sites 1 and 2, Fig. 4.2) extended approximately 16 m above the surface of the tailings (Fig. 4.5). Assuming that the W1 riser is 35-metres high and was buried in tailings to a depth of approximately 19 m, this would represent an average deposition of approximately 2 m of tailings each year from the time TSF2 was commissioned up until the time of sampling. However, mine tailings deposits are commonly less than 1 m deep within the exterior overflow cells and at the edges of the central, main cell of TSF2. Mining at Mount Keith produces

approximately 11 Mt of tailings each year. If this mass of tailings were deposited uniformly throughout TSF2 it would be approximately 31 cm in depth. After 10 years (i.e., from January 1997 to October 2006) of uniformly thick deposition, tailings deposits would be 3.1 m deep. Clearly, the deep deposits that surround risers are not typical of all regions within TSF2, which suggests that depths on the order of metres are more common than those on the order of decametres.

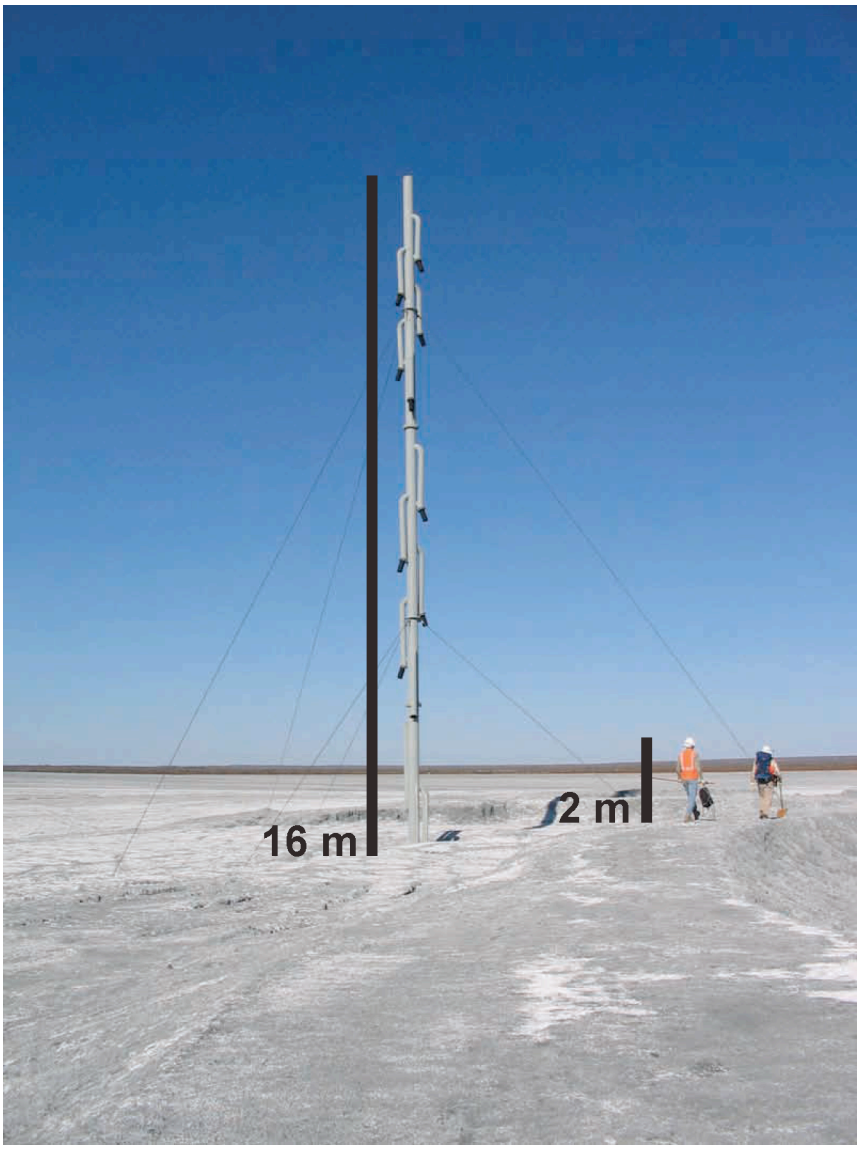

Figure 4.5: The W1 riser in TSF2. This riser extended approximately 16 m above the surface of the tailings flows in September and October 2006. Risers are between 35 and 45 m high (ICME and UNEP 1998). With boots and hardhat, Prof. G. Southam (used for scale here) is 2.00 ± 0.05 m tall.

Stolberg (2005) gives values of 3.0 to 3.8 m for the depth of the tailings deposited near the centre of Cell 2 in TSF1 and values as high as 10 m for the depth of tailings near discharge points along the perimeter of Cell 2. As such, deep grid samples in TSF1 and near the risers in TSF2 would most likely be accessing tailings deposited within one year of last deposition at the surface. Following this line of reasoning, we have attributed the same ages known for the surface deposits to the deeper tailings in our analyses. Notably, some of the deepest samples collected from the profile at sampling site 1 (i.e., 06MKP1) in TSF2 may be accessing tailings deposited one to two years before last deposition at the surface. Also, some of the cores collected from near the edge of the central cell of TSF2 (i.e., from sampling sites 3 and 20-23) may be sampling thinner flows of tailings deposited over the course of several years. However, Rietveld refinements were not done for the latter set of samples.

Mount Keith experiences an average pan evaporation of 2,400 mm/year and limited rainfall (220 mm/year on average), most of which is lost to evapotranspiration (Stolberg 2005). Our field investigations have confirmed Stolberg's (2005) observation that no watertable is present (to a depth of at least 1.3 m) within Cell 2 of TSF1 under dry conditions. However, the location of the watertable within TSF2 was difficult to assess by coring. Recently deposited tailings from some areas of TSF2 were wetted beneath efflorescent crusts and coring holes through these damp tailings had a tendency to swell shut within minutes of sampling. At sampling site 30, samples collected with a backhoe excavator were saturated with water, indicating that they had been collected from beneath the vadose (unsaturated) zone. This suggests that in parts of TSF2, the vadose zone is only representative of the upper few metres of tailings.

Darkly coloured, fragrant samples were collected from the base of the profile at sampling site 1 (Figs. 4.4a and b) and from the base of the backhoe trench at sampling site 30 (Fig. 4.4c). In addition, two samples of darkly coloured, anoxic sediments mixed with mine tailings were collected from shallow depth (i.e., < 20 cm) near the water return inside the Kidney Wall. These samples may reflect a prevalent compositional change within the deeper, anoxic tailings that are located within the saturated zone of TSF2. Hydromagnesite was present – at abundances comparable to those in the unsaturated zone – within samples collected from the base of the backhoe trench and the base of the

profile at sampling site 1. This confirms that hydromagnesite persists at depth within the saturated zone of TSF2. Hydromagnesite was not detected in the two samples of darkly coloured sediments collected from within the Kidney Wall. However, the latter samples of anoxic sediments are not representative of bulk tailings from TSF2. These samples are compositionally different and were deposited under very different conditions to those collected from other regions of TSF2. They were collected near the water return within the Kidney Wall in a region that often contains standing water and were mixed with desert sediment.

4.5 Analytical results

4.5.1 Rietveld refinement results

Rietveld refinement results for 204 samples of tailings from Mount Keith are given in Appendix A1. Graphical representations of these data are given in Figures 4.6-4.12. Data from eight samples were excluded from statistical analyses and figures (as summarized in Table 4.2). These samples include: (1) the two samples of anoxic sediments mixed with mine tailings from near the water return inside the Kidney Wall (06MKblackseds and 06MKdarkseds) and (2) six samples from a continuous core collected from within a mound of soil at the surface of TSF1 (06MK12-1-1 through 06MK12-1-6). Plots of soil were part of a remediation study initiated by D.J. Stolberg and D.J. Williams of the Division of Civil Engineering at The University of Queensland in 2001. This study is described in detail by Stolberg (2005). These samples and the anoxic sediments were excluded because they were not representative of the bulk of the tailings observed at and collected from Mount Keith (as discussed in Subsection 4.4.2).

Refined abundances and median abundances for hydromagnesite in 196 samples are plotted in Figure 4.6. Shaded envelopes denote the median plus or minus the median absolute deviation (e.g., Upton and Cook 2009) for depth intervals (in cm) of [0, 25), [25, 50), [50, 75), [75, 100), [100, 125), [125, 150), and [150, max depth]. Data are plotted similarly in Figures 4.7-4.12, but over more limited ranges of depth. These data are plotted for six different ages of tailings (measured since last deposition of tailings): 0

years, 0.5 years, 1 year, 3 years, 7 to 8 years, and 10 years. We chose to use the median and median absolute deviation (MAD) as measures of central tendency because Rietveld refinement results (Appendix A1) produce a sparse set of log-normally distributed data. The heterogeneity of Mount Keith tailings results in a significant number of "below-detection" measurements of weight-percent mineral abundance, which are reported here as zero-values. Imputed values may be used to obtain means and standard deviations from log-normally distributed datasets containing rounded zeroes (i.e., values below detection limits that have been rounded to zero). Here, imputation has been used sparingly for a limited number of detectable abundances of hydromagnesite (Table 4.2). However, extensive use of imputation can distort the properties of geochemical datasets and, consequently, it is not recommended for datasets with more than 10% rounded zeroes (e.g., Sandford 1993; Martín-Fernández et al. 2003; Palarea-Albaladejo et al. 2007). One of the benefits of using the median and MAD is that these measures are less biased toward outlier values than the mean and standard deviation of a distribution. This is an important consideration to this study, because sampling within vertical profiles and the backhoe trench was restricted to intervals of visually homogeneous material. As a result, a range of sampling lengths from 1 cm to 60 cm was used. By using median and MAD as measures of central tendency the bias toward shallow, hydromagnesite-rich samples is mitigated.

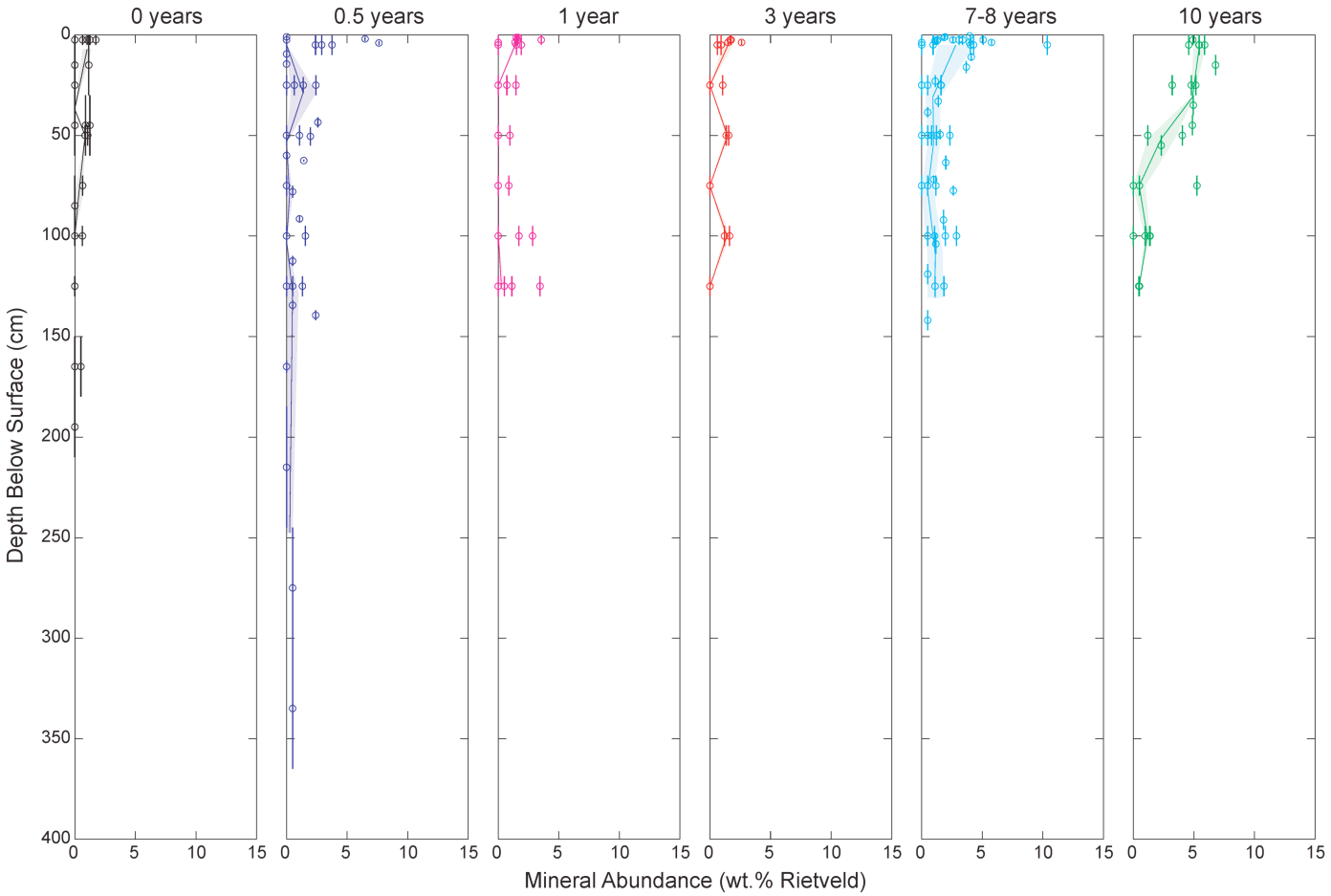

Figure 4.6: Variation of hydromagnesite abundance with depth beneath the surface of TSF1 and TSF2 over time. Tailings aged zero to eight years are from TSF2 and tailings aged 10 years are from TSF1. Age is measured relative to 2006, the date of sampling. Open circles indicate the median depth from which a sample was taken. The associated vertical lines represent intervals of depth over which individual samples were collected. Lines drawn through the data for tailings of each age connect six points (corresponding to six depth intervals). These points denote the mean depth of sampling (based on median depths) and the median abundance of hydromagnesite for samples from similar depths. Shaded regions are the median value ± the median absolute deviation.

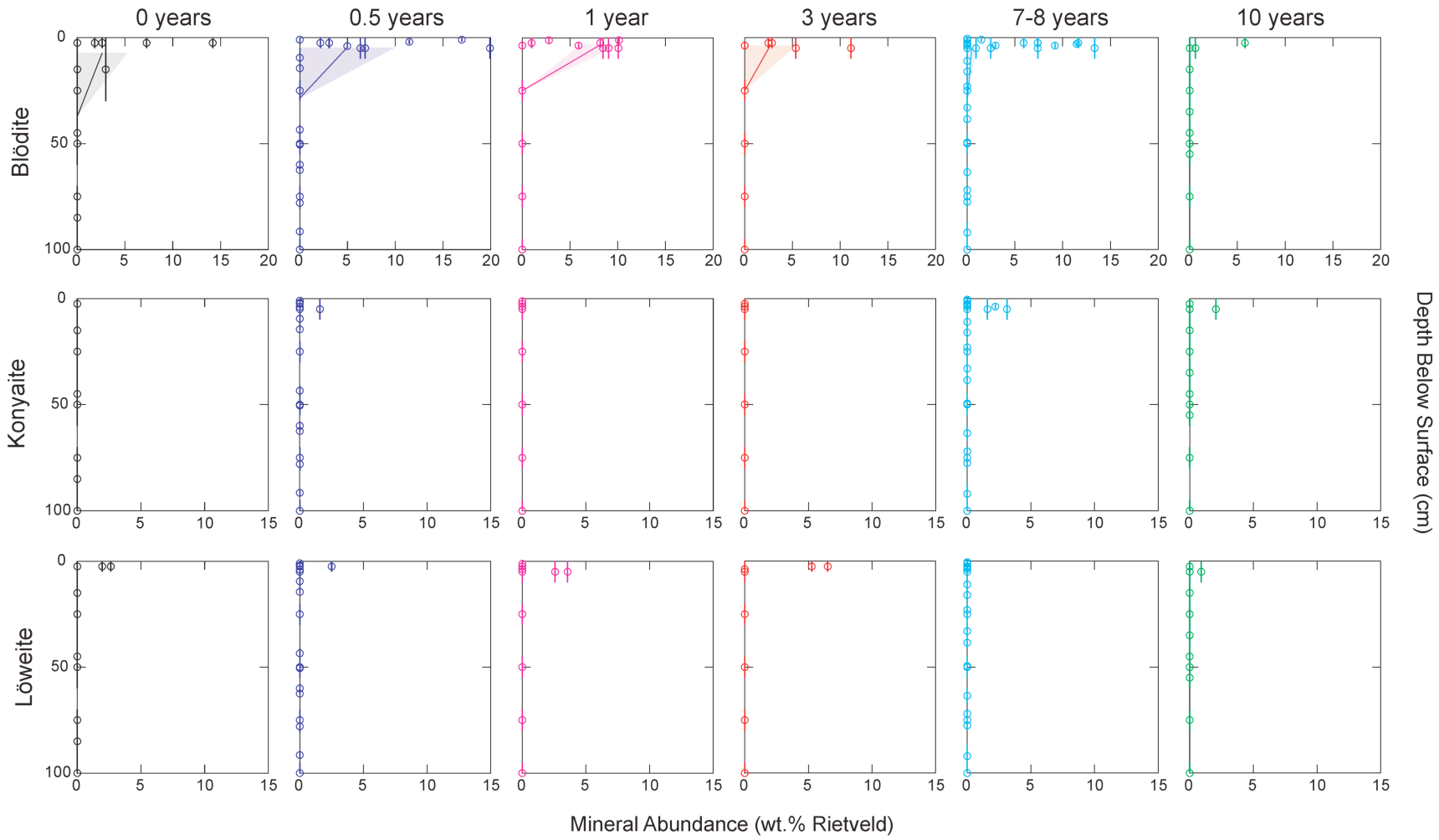

Figure 4.7: Variation of Na-Mg-sulphate mineral abundances with depth beneath the surface of TSF1 and TSF2 over time. Tailings aged zero to eight years are from TSF2 and tailings aged 10 years are from TSF1. Age is measured relative to 2006, the date of sampling.

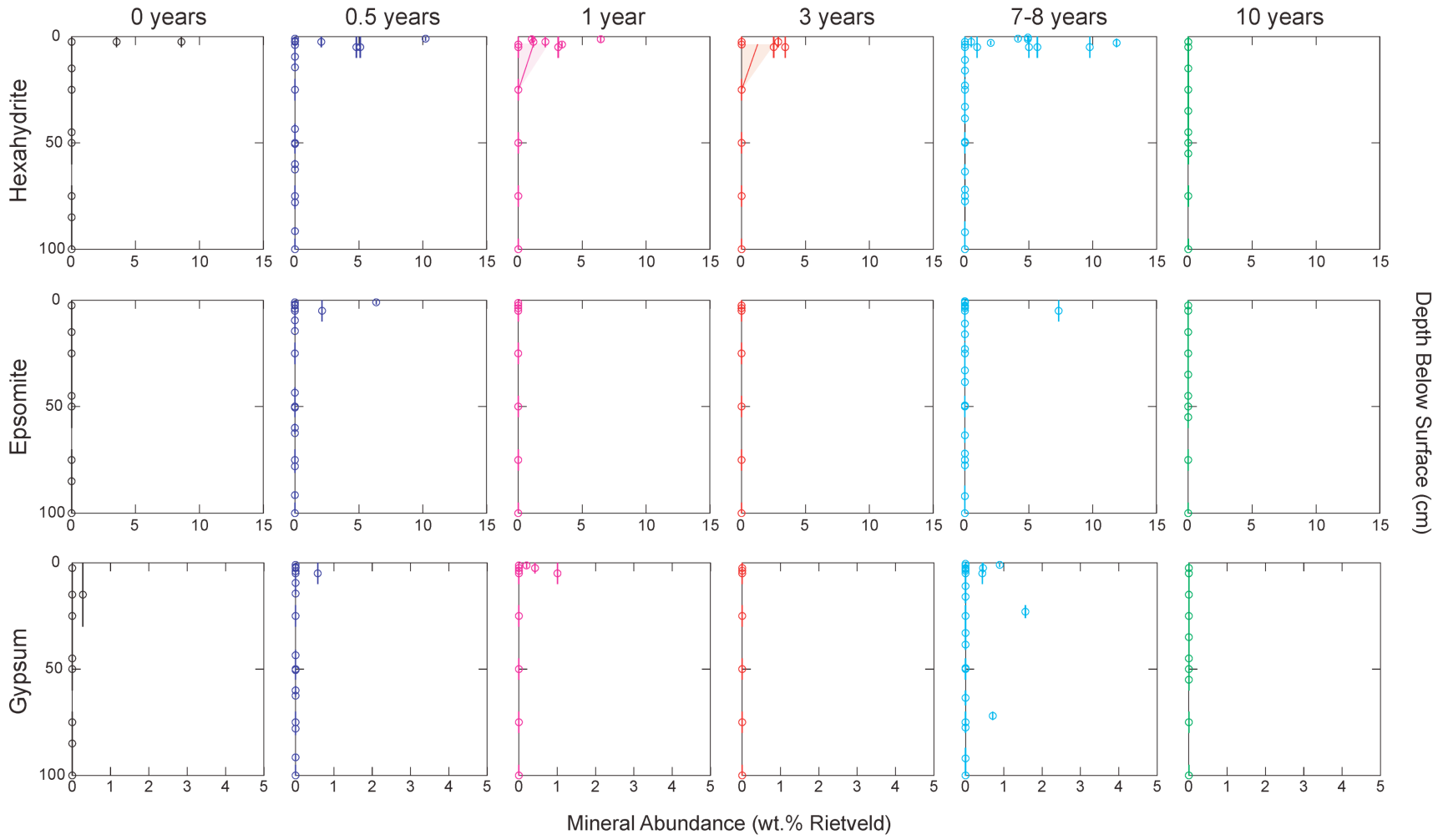

Figure 4.8: Variation of Mg-sulphate and Ca-sulphate mineral abundances with depth beneath the surface of TSF1 and TSF2 over time. Tailings aged zero to eight years are from TSF2 and tailings aged 10 years are from TSF1. Age is measured relative to 2006, the date of sampling.

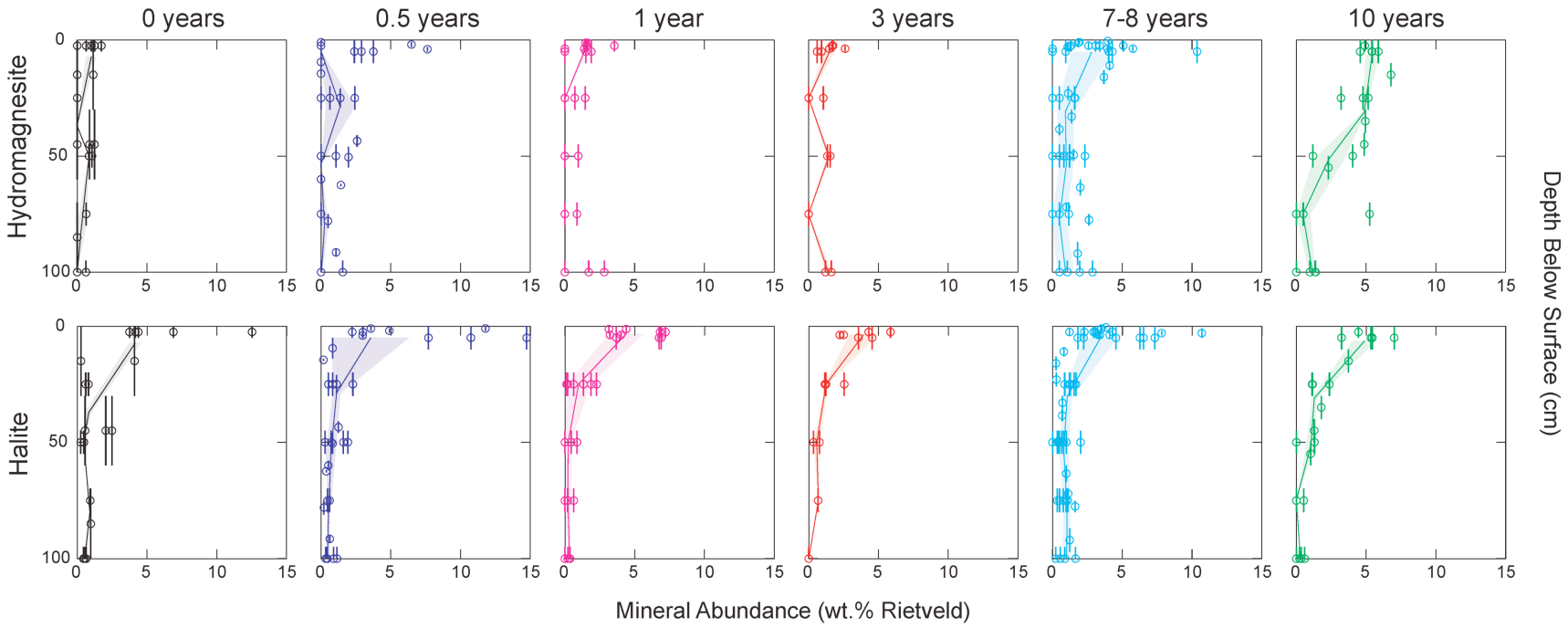

Figure 4.9: Variation of hydromagnesite and halite abundances with depth beneath the surface of TSF1 and TSF2 over time. Tailings aged zero to eight years are from TSF2 and tailings aged 10 years are from TSF1. Age is measured relative to 2006, the date of sampling.

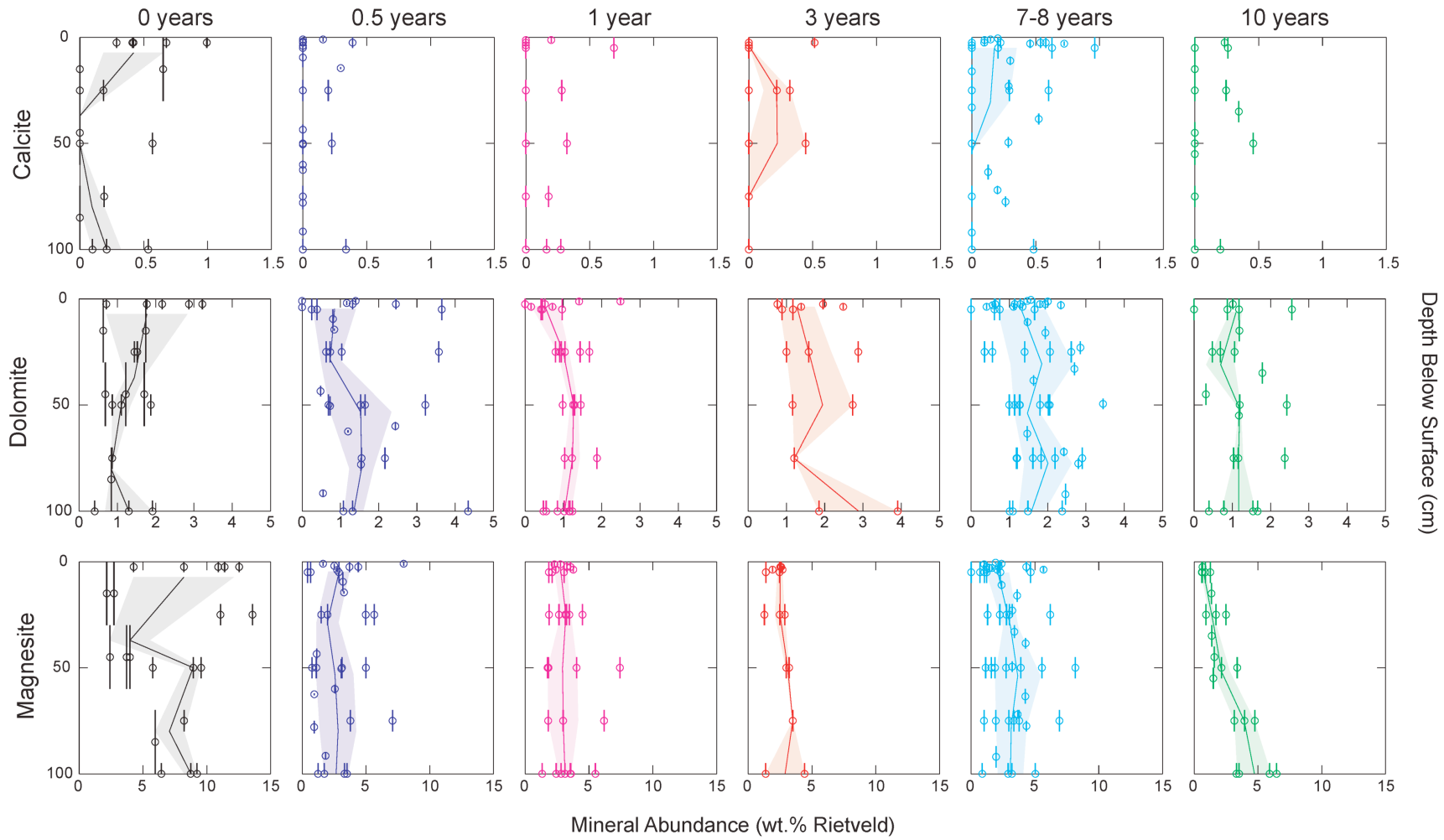

Figure 4.10: Variation of abundance for primary (bedrock) carbonate minerals with depth beneath the surface of TSF1 and TSF2 over time. Tailings aged zero to eight years are from TSF2 and tailings aged 10 years are from TSF1. Age is measured relative to 2006, the date of sampling.

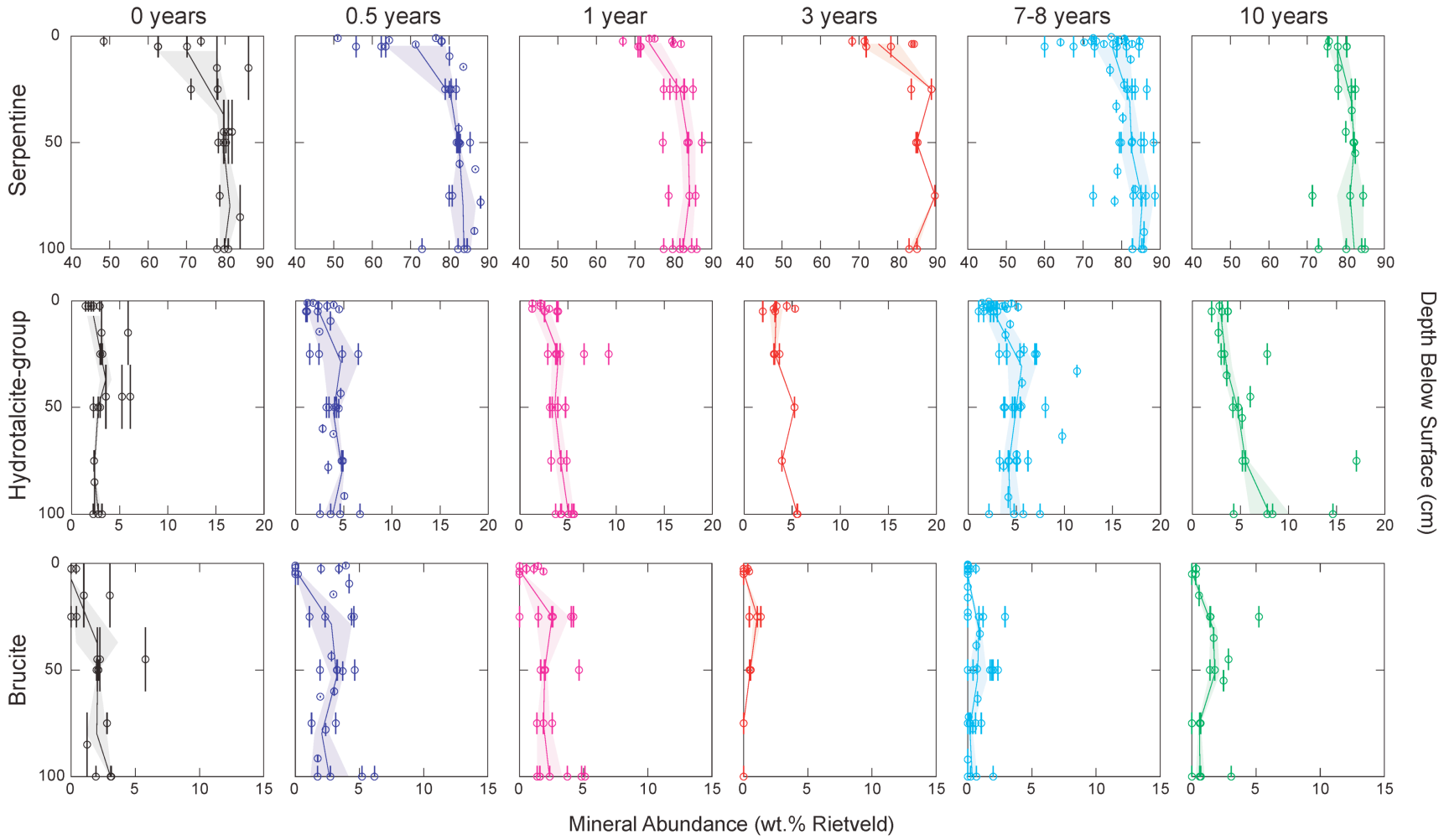

Figure 4.11: Variation of the abundance of select gangue minerals (serpentine-group, hydrotalcite-group, and brucite) with depth beneath the surface of TSF1 and TSF2 over time. Tailings aged zero to eight years are from TSF2 and tailings aged 10 years are from TSF1. Age is measured relative to 2006, the date of sampling.

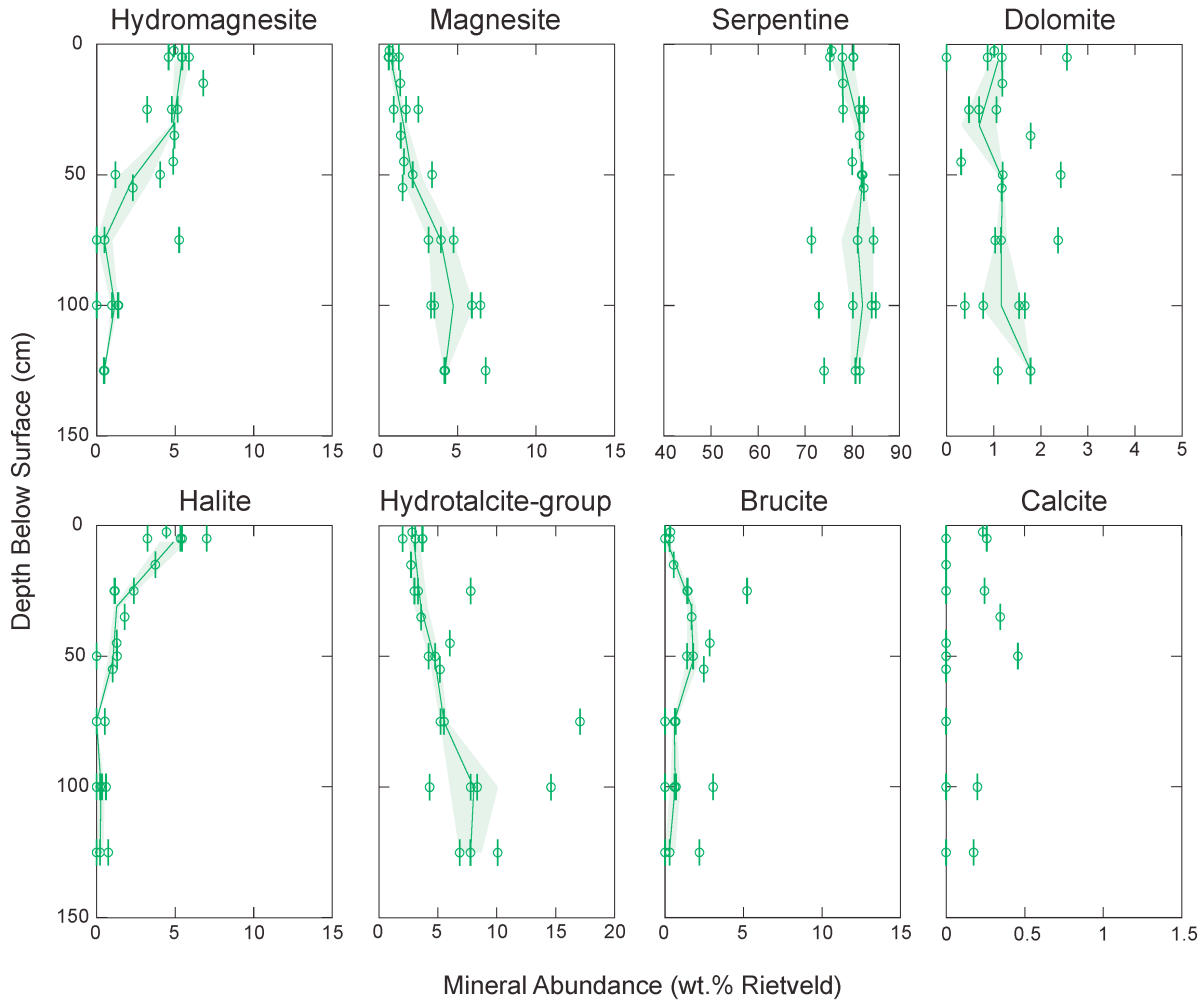

Figure 4.12: Variation of select mineral abundances with depth for 10-year old tailings from TSF1. Trends in gangue mineralogy and secondary mineralogy suggest decreased abundance of magnesite at the surface of TSF1 reflects a primary compositional change in the ore being processed (as opposed to dissolution of magnesite and reprecipitation as hydromagnesite).

4.5.2 Stable isotopic results

The $\delta^{13}C$ data for carbonate minerals from Mount Keith mine tailings (Appendix A1, Fig. 4.13) vary from -8.56‰ to 1.04‰ (VPDB), with $\delta^{18}O$ ranging from 7.81‰ to 39.89‰ (VSMOW). There is no significant relationship between $\delta^{13}C$, mineralogy, and mode of occurrence in the carbonate minerals at Mount Keith. There is, however, a trend in $\delta^{18}O$ with mineralogy and occurrence.

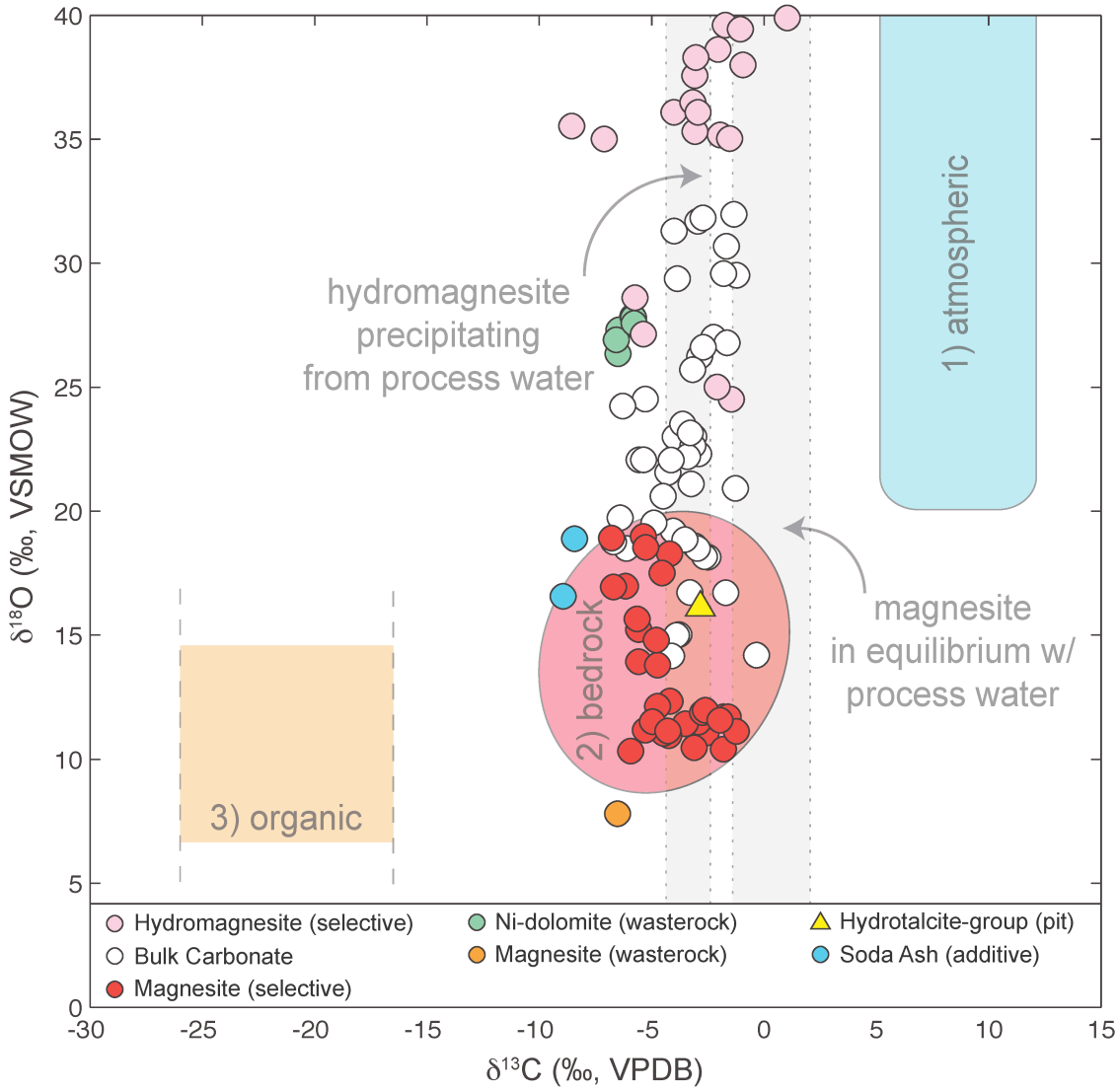

Figure 4.13: Stable oxygen and carbon isotope data for different modes of occurrence and mineralogy of carbonate minerals at Mount Keith. Numbers label fields for Mg-carbonate minerals in equilibrium with specific reservoirs for carbon. Measurement errors (as 2σ) are smaller than the symbols employed.

One specimen of bedrock magnesite from a sample of wasterock is characterized by $\delta^{13}C$ = -6.52‰ and $\delta^{18}O$ = 7.91‰. A specimen of iowaite (a hydrotalcite-group mineral) from the mine pit gives values of $\delta^{13}C$ = -2.83‰ and $\delta^{18}O$ = 16.11‰. Specimens of late-stage Ni-dolomite alteration give -6.58‰ ≤ $\delta^{13}C$ ≤ -5.78‰ and 26.35‰ ≤ $\delta^{18}O$ ≤ 27.86‰ ($\delta^{13}C_{av}$ = -6.16‰ and $\delta^{18}O_{av}$ = 27.30‰). Bedrock magnesite, isolated from tailings by selective acid dissolution, gives values of -6.79‰ ≤ $\delta^{13}C$ ≤ -1.23‰ and 10.33‰ ≤ $\delta^{18}O$ ≤ 18.98‰ ($\delta^{13}C_{av}$ = -4.11‰ and $\delta^{18}O_{av}$ = 13.27‰). Notably, stable isotopic data for magnesite extracted from bulk tailings are slightly more enriched in ^{13}C and significantly enriched in ^{18}O over the specimen of pure magnesite that was sampled from wasterock. Duplicate analyses of one sample of soda ash (used historically as an industrial process chemical) give average values of $\delta^{13}C$ = -8.69‰ and $\delta^{18}O$ = 17.73‰. Dissolved inorganic carbon in tailings water gives values of –8.16‰ ≤ $\delta^{13}C$ ≤ -6.20‰ ($\delta^{13}C_{av}$ = -7.36‰). Water from the processing plant gives values of -6.91‰ and -4.60‰ ($\delta^{13}C_{av}$ = -5.76‰).

Analyses done on bulk carbonate minerals give -6.70‰ ≤ $\delta^{13}C$ ≤ -0.33‰ and 14.16‰ ≤ $\delta^{18}O$ ≤ 31.97‰ ($\delta^{13}C_{av}$ = -3.46‰ and $\delta^{18}O_{av}$ = 22.60‰). On average, secondary hydromagnesite is enriched over magnesite by approximately 1‰ in $\delta^{13}C$ and approximately 22‰ in $\delta^{18}O$. Hydromagnesite (isolated using the method of Barker et al. 2009) is characterized by –8.56‰ ≤ $\delta^{13}C$ ≤ -1.04‰ and 24.51‰ ≤ $\delta^{18}O$ ≤ 39.89‰ ($\delta^{13}C_{av}$ = -3.04‰ and $\delta^{18}O_{av}$ = 34.81‰).

4.5.3 Radiocarbon results

The $F^{14}C$ data for carbonate minerals at Mount Keith range from 0.004 to 1.052 and are given in Appendix A1 and Figure 4.14. One specimen of bedrock Ni-dolomite gives an $F^{14}C$ of 0.004 and two specimens of highly pure bedrock magnesite are characterized by 0.005 and 0.009 (the latter value is an average of two analyses). These results for highly pure bedrock carbonate minerals are consistent with ^{14}C-free carbon and the level of atmospheric contamination expected from our vacuum line. Carbon dioxide extracted from magnesite in four bulk samples of tailings is defined by 0.024 ≤ $F^{14}C$ ≤ 0.365 ($F^{14}C_{av}$ = 0.147), the upper end of this range of values being significantly

higher than expected from measurements on highly pure specimens. One specimen of soda ash (used historically as a process chemical in the flotation circuit at Mount Keith) has an $F^{14}C$ of 0.052.

Analysis of CO_2 selectively extracted from hydromagnesite is characterized by $0.572 \leq F^{14}C \leq 1.052$ ($F^{14}C_{av} = 0.921$).

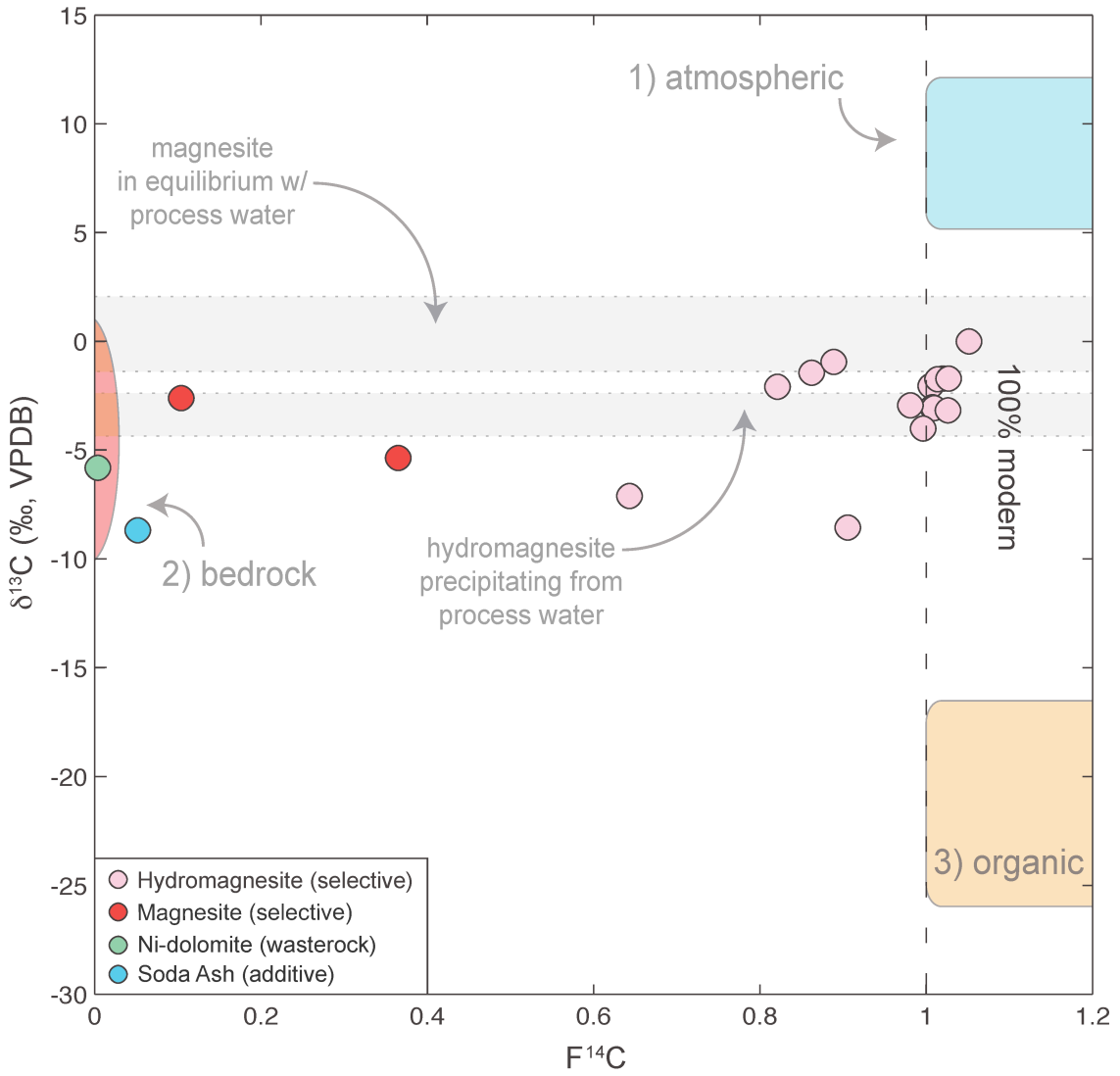

Figure 4.14: Stable carbon ($\delta^{13}C$) and fraction modern carbon ($F^{14}C$) data for secondary precipitates of hydromagnesite, bedrock carbonate minerals, and soda ash (a process additive) from Mount Keith. Numbers label fields for Mg-carbonate minerals in equilibrium with specific reservoirs for carbon. Values for $\delta^{13}C$ were determined in the Pacific Centre for Isotopic and Geochemical Research at the University of British Columbia. Values for $F^{14}C$ are corrected for machine fractionation using AMS results for $\delta^{13}C$. Measurement errors are smaller than the symbols employed.

4.6 Discussion

4.6.1 Abundance and distribution of minerals in Mount Keith mine tailings

Because ages are known for many of the tailings deposits at Mount Keith, we have been able to use Rietveld refinement results to track the mineralogical evolution of these mine tailings and to estimate the rate at which hydromagnesite precipitates.

4.6.1.1 Sulphate minerals

Acero et al. (2007, 2009) have used unsaturated column experiments and geochemical modelling to study mineral transformations in the vadose zone of pyritic tailings in arid to semiarid climates. Their results demonstrate that gypsum precipitates rapidly throughout the vadose zone of these tailings. Precipitation of gypsum is followed by precipitation of other hydrated sulphate minerals near the tailings surface. Hydrated sulphate minerals continue to precipitate within pore spaces at increasing depth within the tailings (Acero et al. 2007, 2009). Eventually, formation of a thick efflorescent crust reduces diffusivity and intrinsic permeability of the tailings, leading to a corresponding decrease in the evaporation rate (Acero et al. 2007, 2009) and limiting the depth to which efflorescent crusts may extend.

Our quantitative mineralogical data for Na-Mg, Mg, and Ca-sulphate minerals are consistent with the results of these previous studies. Figures 4.7 and 4.8 indicate that sulphate minerals are uncommon below 10 cm and are almost entirely absent below a depth of 25 cm in the tailings at Mount Keith. As deeper tailings become increasingly cut off from the oxygen in the atmosphere, oxidative weathering of residual sulphide minerals ceases to occur, which would restrict sulphate minerals to the upper centimetres of the tailings. Gypsum appears to be the only sulphate mineral that persists at depth (Fig. 4.8), but this occurrence is highly uncommon (i.e., occurring in only two samples aged 7-9 years). Notably, the Na-Mg sulphate minerals blödite, konyaite, and löweite persist at reduced abundance in a very few samples at the surface of 10-year old tailings from TSF1 (Fig. 4.7), whereas the absence of Mg and Ca-sulphate minerals (Fig. 4.8) suggests that the have been leached from the oldest tailings by rainfall (after Jambor et al. 2000).

4.6.1.2 Halite and hydromagnesite

The formation of halide crusts within tailings in arid climates is known to result from strong capillary transport of aqueous species toward tailings surfaces (Dold 2006). As with the sulphate minerals, the highest concentrations of halite occur at shallow depths, typically above 25 cm (Fig. 4.9). However, the similarity in these trends ends at the surface. Halite is much more persistent at depth within the tailings, even 10 years after last deposition, and is found at low abundances in the vast majority of samples that have been analyzed. This suggests that halite, unlike the ephemeral sulphate minerals, remains supersaturated within tailings and likely reprecipitates during occasional rainfall events.

Hydromagnesite abundance follows a similar trend to that for halite (Fig. 4.9). Most recent research into secondary minerals in mine tailings has focussed on precipitation of sulphate minerals by oxidative weathering of primary sulphide minerals, a process that has important implications for acid mine drainage (e.g., Jambor and Blowes 1998; Jambor et al. 2000). In spite of their differing behaviour, some of the processes by which secondary sulphate minerals form in mine tailings may also influence precipitation of secondary carbonate minerals that are associated with them.

Previous studies have shown that efflorescent crusts in mine tailings are able to reduce upward diffusion of gases, trapping them within pore spaces near tailings surfaces (Blowes et al. 1991; Tasse et al. 1997; Agnew and Taylor 2000). Agnew and Taylor (2000) measured concentrations of up to 10 times that of atmospheric CO_2 in pore spaces beneath a crust of hydrated Fe-sulphate minerals at the Elura Ag-Pb-Zn Mine near Booroondarra, New South Wales, Australia. The high concentrations of hydromagnesite within and just below tailings crusts at Mount Keith may result in part from high partial pressure of CO_2 within pore spaces below this physical barrier. Agnew and Taylor (2000) also describe “pop-up” and “tee-pee” structures forming in the hardpan at the surface of tailings from the Elura Mine. They attribute the formation of these structures to rapid mineral-water reactions and the large increases in solid volume that can accompany such reactions. These features are reminiscent of the desiccation cracks we have observed in the efflorescent crusts covering tailings at Mount Keith - features that temporarily expose

underlying tailings and which may allow for limited gas exchange between the deeper tailings and the atmosphere after efflorescences have formed at the surface.

The abundance of hydromagnesite (and that of halite) becomes relatively constant at depths below approximately 25 cm in zero to eight-year old tailings and below approximately 50 cm in 10-year old tailings. High abundances of hydromagnesite are sometimes measured at greater depths (Appendix A1 and Figs. 4.6 and 4.9), which may reflect partial preservation of crusts from former tailings surfaces (as discussed in Subsection 4.4.1). It is possible that hydromagnesite from buried crusts is being reworked at depth as the tailings settle under their own weight. Both hydromagnesite and halite may also be remobilized to some extent by water percolating through the tailings (primarily process water in active tailings and only meteoric water in inactive tailings from TSF1 and the exterior cells of TSF2). In TSF1 and TSF2, mineralization of higher abundances of hydromagnesite appears to be taking place within 0.25 to 0.50-m deep horizons (respectively) at the surface of tailings deposits that were between 3 and 20 m deep at the time of sampling.

4.6.1.3 Primary, bedrock carbonate minerals

Variations in the abundances of mined bedrock calcite, dolomite, and magnesite with depth and time are plotted in Figure 4.10. Although median values for the abundances of calcite, dolomite, and magnesite vary, they generally show no consistent trends in their behaviour with either depth or time. In almost all cases, the abundances of bedrock carbonate minerals stay relatively constant in comparison to results for hydromagnesite, halite, and sulphate minerals which show distinct and predictable behaviours with time and depth.

Bedrock carbonate minerals represent a reservoir from which secondary carbonate minerals like hydromagnesite could precipitate. Under the near-neutral pH conditions (i.e., pH of 5 to 8) that dominate within the tailings waters at Mount Keith, dissolution of bedrock carbonate minerals will proceed most readily for calcite, then dolomite, and least readily for magnesite (Palandri and Kharaka 2004). However, hydromagnesite is known to dissolve rapidly in 5% acetic acid (Wilson et al. 2009a) – an acid that has little effect on calcite, the least resistant of the bedrock carbonate minerals.

The near-constant abundance of less resistant bedrock carbonate minerals and the increasing abundance of hydromagnesite (the carbonate mineral least resistant to dissolution in weak acids within these tailings) toward the surface of TSF1 is very strong evidence that bedrock carbonate minerals are not being dissolved and remineralized in the shallow tailings. Moreover, the solubility of the bedrock carbonate minerals that occur at Mount Keith increases with the molar abundance of $CaCO_3$, with calcite being the most soluble of these minerals. Secondary Ca-bearing minerals (i.e., gypsum and anhydrite) are relatively uncommon in the tailings at Mount Keith, particularly when compared to the high abundances of secondary Mg-minerals. This evidence for only extremely limited dissolution of calcite essentially rules out bedrock carbonate minerals as the source of carbon in secondary hydromagnesite.

4.6.1.4 Serpentine, hydrotalcite-group minerals, and brucite

The compositional data for serpentine, hydrotalcite-group minerals, and brucite display a consistent trend toward decreasing abundance with proximity to tailings surfaces (Fig. 4.11). Abundances of these minerals are relatively constant to a depth of approximately 25 cm in tailings aged 0 to 7-8 years, but decline rapidly within shallow tailings. This effect is particularly marked for brucite, of which the median abundance and MAD decline to zero for all tailings that were sampled. For serpentine, median values decline on the order of 10 wt.% over the span of 25 cm.

In the 10-year old tailings from TSF1, part of this trend is the result of a first-order change in the composition of tailings during the first few years of mine operation (Fig. 4.11 and 4.12). Over time, the abundances of magnesite and hydrotalcite-group minerals decrease to a similar extent, reaching their lowest recorded abundances at the surface of TSF1. Serpentine minerals and brucite were deposited at relatively constant abundances for some time, but eventually they exhibit a shift toward lower abundances – the result of which is seen in lower abundances of these minerals near the surface of TSF1.

At first, a decrease in abundance of serpentine-group minerals may not seem consistent with a decrease in hydrotalcite-group minerals and magnesite, which are both indicators of increasing metamorphic grade and are typically found in ore that is less rich

in serpentine minerals. However, secondary minerals in surface efflorescences have precipitated to a large extent from dissolved atmospheric gasses, dissolved aqueous species within process water, and from process water itself (discussed further in Section 4.7). This significant input of crystalline mass that was not contained initially within the processed ore results in a dilution effect in mineral abundances. This occurs because Rietveld refinement results provide a relative measure of crystalline mass, normalized to 100 wt.%.

The dilution effect is negligible in serpentine at the surface of 10-year old tailings when compared to serpentine abundance in all younger tailings (Fig. 4.11). However, many of the younger surface samples contain abundant sulphate minerals, which the older tailings lack, and a significant trend toward decreasing abundance of serpentine is still apparent for 10-year tailings. Observations that (1) hydromagnesite nucleates on grains of serpentine and forms within what may be dissolution fissures within these grains (Fig. 4.3) and that (2) brucite virtually disappears from surficial tailings suggest that dissolution of Mg-rich bedrock minerals is a source for Mg in secondary carbonate and sulphate minerals.

Previous studies of mineral carbonation in ultramafic mine tailings were undertaken at deposits where brucite is uncommon. At the Clinton Creek and Cassiar chrysotile mines in northern Canada, serpentine minerals (primarily chrysotile) act as the source of Mg from which hydrated magnesium carbonate minerals precipitate (Wilson et al. 2006, 2009a). At the Diavik Diamond Mine, the primary sources for Mg are serpentine (primarily lizardite) and high-Mg forsterite (Wilson et al. 2009b, Chapter 2). Brucite is known to produce hydromagnesite on weathering under conditions of temperature and pressure that prevail at the Earth's surface (e.g., Hostetler et al. 1966; Xiong and Lord 2008). Although the results of Chapter 3 suggest that some of the brucite in the tailings at Mount Keith could have a secondary origin, our field observations and quantitative mineralogical work suggest this is unlikely. For instance, the partial pressure of CO_2 within Mount Keith tailings would have been considerably higher than in the initially carbon-poor precipitation experiments, making precipitation of brucite much less favourable. Additionally, brucite concentrations are at their lowest in those portions of

the tailings that contain the richest deposits of secondary precipitates, suggesting that brucite did not form as part of the suite of secondary minerals.

Therefore, in addition to serpentine minerals, the dissolution of brucite may also be contributing Mg for carbon mineralization at Mount Keith. This result implies that the decrease in the abundances of serpentine and brucite are very likely the result of both dissolution to produce secondary Mg-rich minerals, and a dilution effect caused by incorporation of water and atmospheric gasses into these newly formed minerals.

4.6.2 Summary of spatial and temporal changes in mineralogy

Similar trends can be seen in the data for (1) sulphate minerals, (2) hydromagnesite and halite, (3) bedrock carbonate minerals, and (4) serpentine, hydrotalcite-group minerals, and brucite. Sulphate minerals are ephemeral phases at the surface of the tailings at Mount Keith and are leached almost entirely from inactive tailings on a timescale of less than 10 years. Hydromagnesite and halite are most abundant near the surface of tailings deposits and persist at depth – hydromagnesite being associated with former tailings surfaces, and both minerals possibly having been reworked by mass settling and infiltration of water. Bedrock calcite, dolomite, and magnesite are present throughout the tailings and do not display a consistent change in abundance with depth. The only exception being the trend toward increasing abundance of magnesite at depth within 10-year old tailings from TSF1, which is the result of a compositional change in ore mineralogy. Serpentine, brucite, and hydrotalcite-group minerals display a trend toward lower abundance at shallow depth within tailings of all ages. In all three phases, the lower abundances result from a dilution effect as secondary sulphate, carbonate, and halide minerals precipitate at the surface of the tailings. Dissolution of serpentine and brucite almost certainly contributes to the decreased abundance of these minerals in near surface tailings environments.

4.6.3 Rate and scale of hydromagnesite precipitation

A conservative estimate of hydromagnesite abundance must consider the material that best reflects the bulk properties of tailings throughout the TSF1 and TSF2. The shallow zone at the surface of the tailings may provide insight into the mineralogical

processes that are active within tailings in contact with the atmosphere, but it reflects a comparatively small volume of the tailings, and for most of the rapidly resurfaced deposits in TSF2, only a brief snapshot of their mineralogical evolution. To estimate hydromagnesite abundance, an approximate depth limit to active mineralization of hydromagnesite needs to be selected. Abundances of both hydromagnesite and halite decrease asymptotically with increasing distance from the surface (Fig. 4.9) until reaching relatively constant values at depths of approximately 25 cm (for tailings aged zero to eight years) and 50 cm (for tailings aged 10 years). Based on this observation, we have taken these depths to represent the approximate limits to active precipitation of hydromagnesite and have determined a conservative rate for hydromagnesite precipitation in tailings below these depths. The different behaviour of hydromagnesite and halite between tailings from TSF1 and TSF2 may result from differences in the way the two storage facilities have been managed. More specifically, the tailings in TSF1 had been allowed to weather freely for 10 years (at the time of sampling) without addition of process water, whereas tailings from many parts of TSF2 had experienced more recent exposure to water.

The median abundance of hydromagnesite (± MAD) is plotted in Figure 4.15 against the approximate age of the tailings at the time of sampling. Only Rietveld refinement results for tailings collected from beneath the actively mineralizing surfaces of TSF1 and TSF2 are plotted in Figure. 4.15. A best linear least-squares fit (through the origin) to the data for median abundance of hydromagnesite gives the following result:

$$X_t = 0.126t \qquad \text{(Eq. 4.1)}$$

where X_t is abundance of hydromagnesite in wt.% and t is time since last deposition of tailings in years. This result suggests that on the order of 0.1 wt.% hydromagnesite accumulates at depth within the tailings for every year after deposition. The fit to the data plotted in Figure 4.15 suggests that old tailings may continue to mineralize CO_2 after deposition. The mining operation at Mount Keith produces approximately 11 Mt of tailings and emits approximately 370,000 t of CO_2 equivalent greenhouse gases each

year. The total amount of CO_2 sequestered within hydromagnesite to date can be calculated as follows:

$$M_{CO_2} = c\sum_{t=1}^{n} X_t M_t \qquad \text{(Eq. 4.2)}$$

for $\{n \geq 1: n \in \mathbb{N}\}$ and where M_{CO_2} is the mass of CO_2 mineralized as hydromagnesite, c is a constant equal to the fractional amount of CO_2 (by mass) in hydromagnesite (i.e., 0.3764) divided by 100, and M_t is the mass of tailings deposited to the TSFs for a given year, and n is the number of years tailings have been deposited. Eq. 4.3 gives the amount of CO_2 mineralized as hydromagnesite in a given year:

$$\frac{dM_{CO_2}}{dt} = c\sum_{t=1}^{n}(0.126)M_t \qquad \text{(Eq. 4.3)}$$

These equations are presented here with initial values of t=1, in which case it is assumed that hydromagnesite begins to accumulate at depth within the first year of tailings deposition. However, surface-based mineralization of hydromagnesite is more likely to have dominated for at least the first year of tailings deposition in TSF1 and again in TSF2. Because of this, our calculation for TSF1 begins with t=0 for the first year of tailings deposition (i.e., 1994-1995). Likewise, our calculation for TSF2 begins with t=0 for the first year of deposition in that facility (i.e, 1996-1997).

We have used available data for the mass of tailings produced at Mount Keith, which are available for each year between 2000 and 2004 (Table 4.5, BHP Billiton 2005). For the remaining years, we have assumed that 8.5 Mt of tailings were deposited to TSF1 in the first two years of operation (Environmental Protection Authority 1996) and that 11 Mt of tailings were deposited to TSF2 every year (beginning in the third year of mining operations) for 13 years (BHP Billiton 2005). Using Eq. 4.3, to calculate the amount of CO_2 mineralized as hydromagnesite at depth within TSF1 and TSF2 in 2009, we obtain a value of approximately 64,900 t. Based on CO_2 equivalent emissions of 370,000 t/year, this could represent an offsetting of nearly 18% of emissions for 2009 if

all CO_2 within hydromagnesite was sourced from the atmosphere. Assuming that Eq. 4.1 holds throughout TSF1 and TSF2, we can use Eq. 4.2 to estimate the total amount of CO_2 mineralized and stored within the deep tailings at Mount Keith since mining operations began. The result is that an estimated 449,000 t of CO_2 may have been mineralized as hydromagnesite between 1994 and 2009.

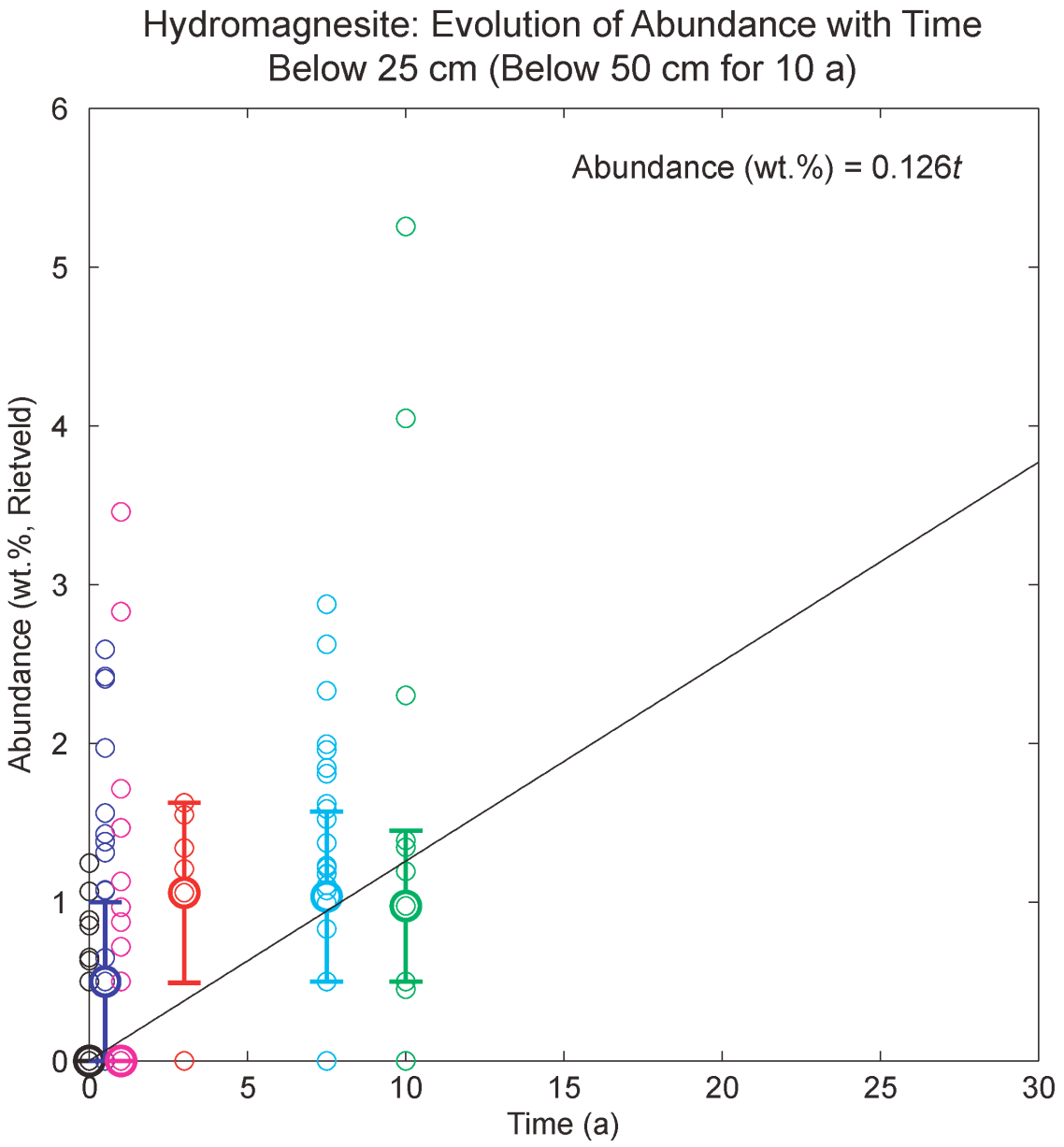

Figure 4.15: Development of hydromagnesite (as wt.% abundance) at depth within Mount Keith tailings, from zero to 10 years prior to sampling. A linear least squares fit to median abundances is shown and the equation for the curve is given.

A comparison can be made between Figures 4.15 and 4.16, in the latter of which is given the abundance of hydromagnesite within the enriched upper 50 cm of TSF1 and upper 25 cm of TSF2 versus time since last deposition of tailings. A best linear least-squares fit (through the origin) to the data for median abundance of hydromagnesite in surficial tailings gives the following relation:

$$X_t = 0.463t \qquad \text{(Eq. 4.4)}$$

This best fit to the data plotted in Figure 4.16 suggests that the annual rate of hydromagnesite precipitation at shallow depth is nearly four times as much as the rate for deep tailings. This high rate could result from (1) higher partial pressure of CO_2 beneath the efflorescent halide/sulphate minerals crust, or (2) ease of infiltration of atmospheric CO_2 through "tee-pee" and "pop-up" desiccation features. The rate of uptake of CO_2 into surface tailings may be calculated as:

$$\frac{dM_{CO_2}}{dt} = (0.463)cM_t \qquad \text{(Eq. 4.5)}$$

for $M_t = AD\rho$ where A is the combined surface area of TSF1 and TSF2, D is the depth to which surficial mineralization of hydromagnesite occurs (i.e., 50 cm for TSF1 and 25 cm for TSF2), and ρ is the density of tailings. Using an approximate combined volume (AD) of 4.1 x 10^{12} cm^3 for TSF1 and TSF2 and assuming perfect packing of tailings with a density of 2.6 g/cm^3 (i.e., the density of serpentine), gives an approximate rate of 18,000 t/year of CO_2 (in an estimated 10.7 Mt of surficial tailings). This estimate implies that in 2009, approximately 24% of the CO_2 mineralized within hydromagnesite at Mount Keith may have been trapped and stored in the upper 25-50 cm of the tailings storage facilities.

The above results can be used to estimate the annual rate of CO_2 mineralization within hydromagnesite and the cumulative uptake of CO_2 into Mount Keith tailings over the lifetime the mine. Nickel mining at Mount Keith began in 1994 and it is anticipated that operations may last until 2024 (based on a projected mine life of up to 30 years, Grguric et al. 2006). Projections are done assuming: (1) that the rate of tailings hold

steady, (2) that tailings mineralize hydromagnesite at the surface rate in their first year since deposition (Eq. 4.4), and (3) that tailings older than one year abide by the rate determined for deep samples (Eq. 4.1). Projections for the annual rate of CO_2 trapping within deep and surficial tailings and for cumulative CO_2 trapping within deep samples are reported in Table 4.5 and plotted in Figure 4.17. No such projection is reported here for the actively mineralizing zone at the surfaces of TSF1 and TSF2 because it has been assumed that this zone is buried and becomes subject to the mineralization regime that is active at depth within a year of deposition (i.e., described by Eq. 4.1). Cumulative trapping of CO_2 is projected to increase annually, eventually reaching a value of 2.05 Mt CO_2 in 2024 (Fig. 4.17a). According to this model, mineralization of hydromagnesite in near surface tailings dominates during CO_2 sequestration during the first few years of production at Mount Keith (Fig. 4.17b). However, after five years the annual rate of CO_2 trapping within deep tailings increases dramatically as tailings age and fresh material is deposited. If annual greenhouse gas emissions were to remain relatively constant to 2024 and all CO_2 trapped within hydromagnesite were sourced from the atmosphere, this model suggests that passive CO_2 sequestration at Mount Keith could offset approximately 19% of total emissions produced over the lifetime of this mine.

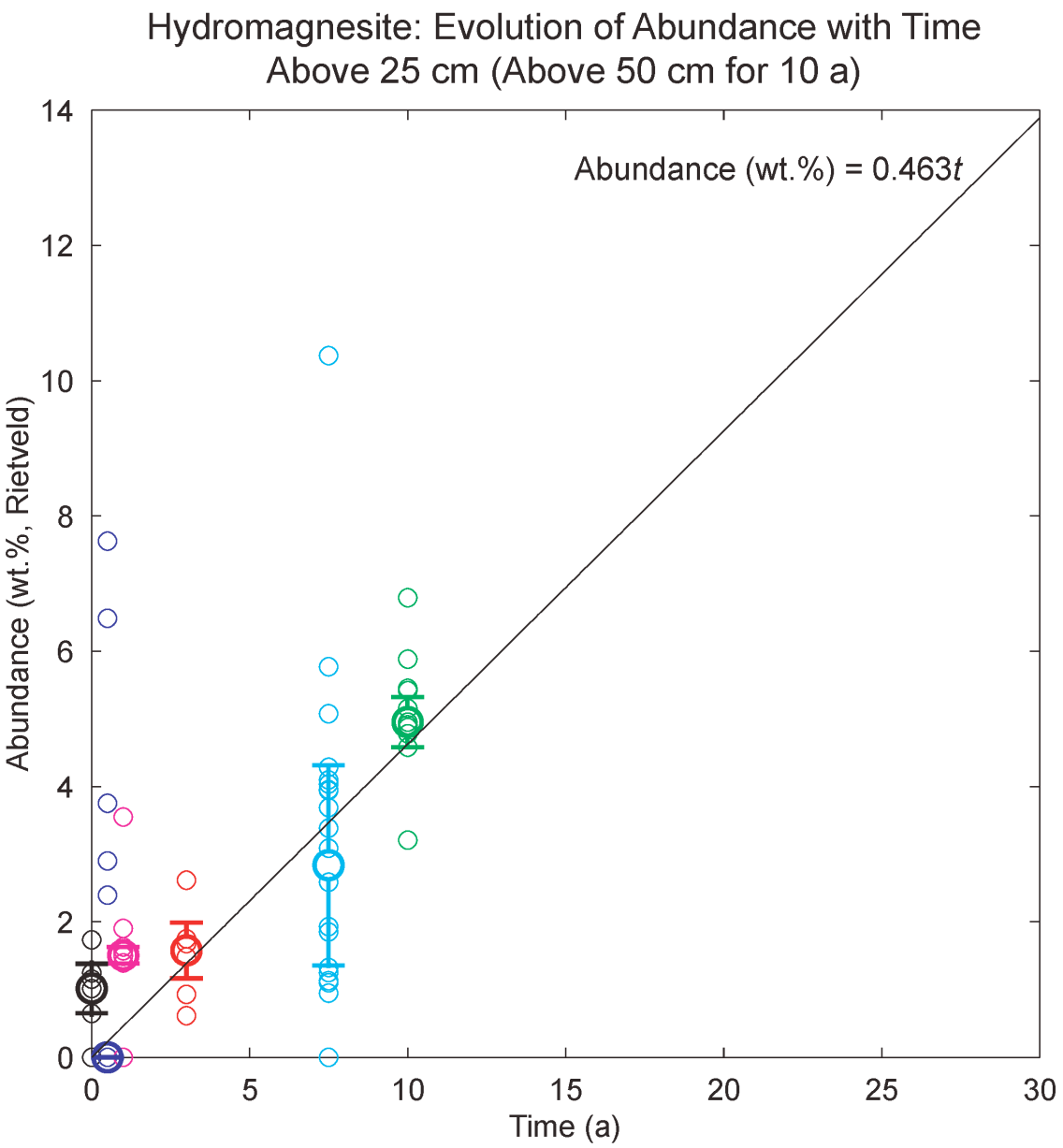

Figure 4.16: Development of hydromagnesite (as wt.% abundance) near the surface of Mount Keith tailings, from zero to 10 years prior to sampling. A linear least squares fit to mean abundances is shown and the equation for the curve is given.

Table 4.5: Annual rate of CO_2 mineralization and cumulative trapping at Mount Keith.

No. Years	Year[a]	Tailings Production (Mt/year)	Rate, Depth (Mt CO_2/year)	Rate, Surface (Mt CO_2/year)	Cumulative, Depth (Mt CO_2)
1	1995	8.50	0.00	2.77×10^{-3}	0.00
2	1996	8.50	4.03×10^{-3}	2.77×10^{-3}	4.03×10^{-3}
3	1997	11.00	8.06×10^{-3}	2.19×10^{-2}	1.21×10^{-2}
4	1998	11.00	8.06×10^{-3}	2.19×10^{-2}	2.02×10^{-2}
5	1999	11.00	1.33×10^{-2}	2.19×10^{-2}	3.34×10^{-2}
6	2000	10.44	1.85×10^{-2}	2.10×10^{-2}	5.19×10^{-2}
7	2001	10.67	2.37×10^{-2}	2.14×10^{-2}	7.56×10^{-2}
8	2002	10.84	2.87×10^{-2}	2.17×10^{-2}	1.04×10^{-1}
9	2003	10.96	3.37×10^{-2}	2.19×10^{-2}	1.38×10^{-1}
10	2004	10.94	3.89×10^{-2}	2.18×10^{-2}	1.77×10^{-1}
11	2005	11.00	4.41×10^{-2}	2.19×10^{-2}	2.21×10^{-1}
12	2006	11.00	4.93×10^{-2}	2.19×10^{-2}	2.70×10^{-1}
13	2007	11.00	5.45×10^{-2}	2.19×10^{-2}	3.25×10^{-1}
14	2008	11.00	5.97×10^{-2}	2.19×10^{-2}	3.84×10^{-1}
15	2009	11.00	6.49×10^{-2}	2.19×10^{-2}	4.49×10^{-1}
16	2010	11.00	7.01×10^{-2}	2.19×10^{-2}	5.19×10^{-1}
17	2011	11.00	7.53×10^{-2}	2.19×10^{-2}	5.95×10^{-1}
18	2012	11.00	8.06×10^{-2}	2.19×10^{-2}	6.75×10^{-1}
19	2013	11.00	8.58×10^{-2}	2.19×10^{-2}	7.61×10^{-1}
20	2014	11.00	9.10×10^{-2}	2.19×10^{-2}	8.52×10^{-1}
21	2015	11.00	9.62×10^{-2}	2.19×10^{-2}	9.48×10^{-1}
22	2016	11.00	1.01×10^{-1}	2.19×10^{-2}	1.05
23	2017	11.00	1.07×10^{-1}	2.19×10^{-2}	1.16
24	2018	11.00	1.12×10^{-1}	2.19×10^{-2}	1.27
25	2019	11.00	1.17×10^{-1}	2.19×10^{-2}	1.39
26	2020	11.00	1.22×10^{-1}	2.19×10^{-2}	1.51
27	2021	11.00	1.28×10^{-1}	2.19×10^{-2}	1.64
28	2022	11.00	1.33×10^{-1}	2.19×10^{-2}	1.77
29	2023	11.00	1.38×10^{-1}	2.19×10^{-2}	1.91
30	2024	11.00	1.43×10^{-1}	2.19×10^{-2}	2.05

[a] For the production year ending in the calendar year listed (e.g., 1995 denotes the end of the production year beginning in Summer 1994 and ending in Summer 1995).

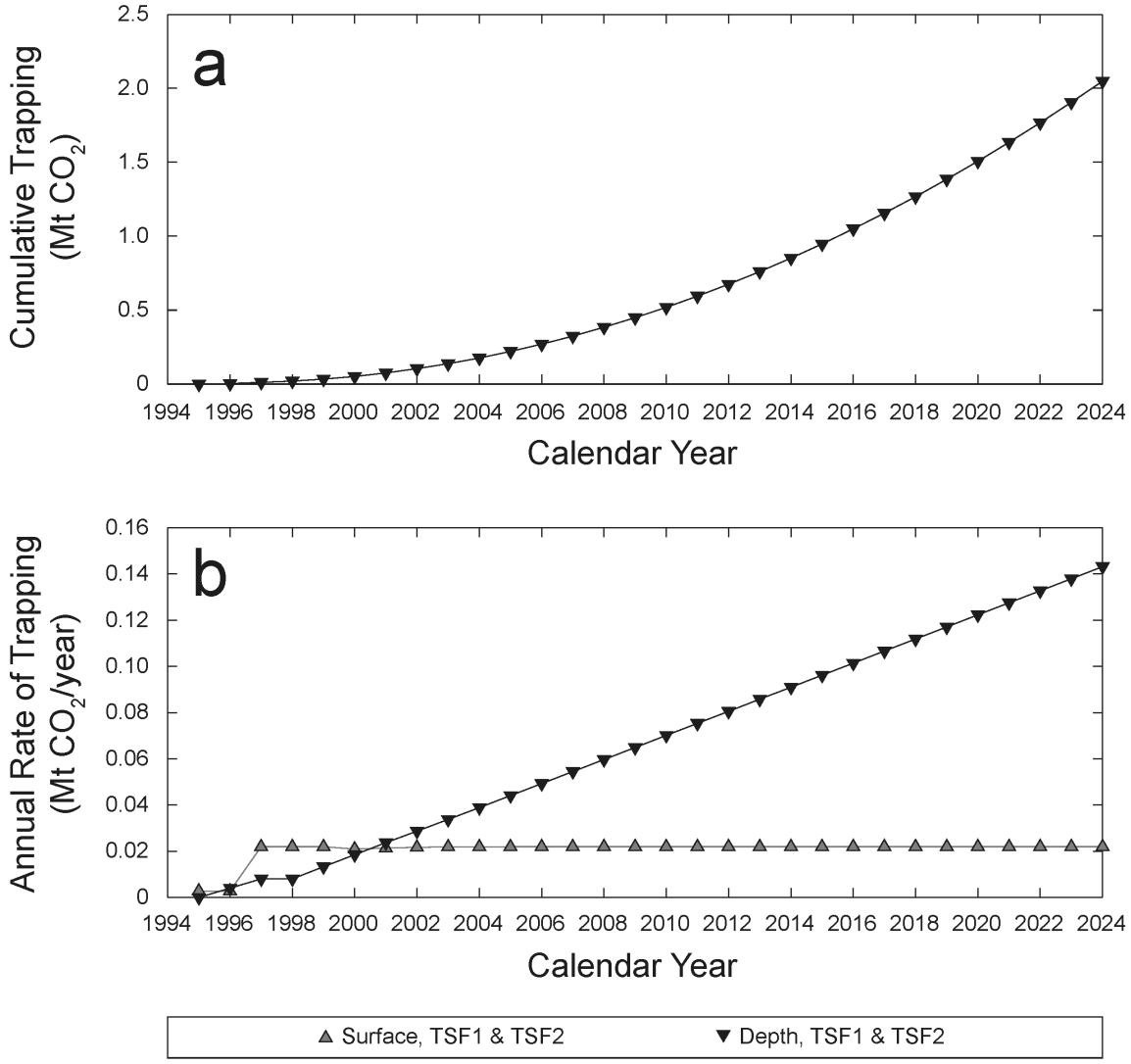

Figure 4.17: Estimated cumulative and annual mineralization of CO_2 within Mount Keith mine tailings. Estimates for cumulative (a) and annual (b) trapping of CO_2 within hydromagnesite are given in Mt. Predictions are made for the anticipated 30-year lifetime of the mine beginning in 1994 and ending in 2024.

4.7 Carbon reservoir fingerprinting

There are four potential sources of carbon in tailings from operating mines like Mount Keith; one or more of which may be accessed during recent precipitation of carbonate minerals. These sources are: (1) atmospheric carbon, (2) bedrock carbon from mined carbonate minerals, (3) carbon from industrial additives, and (4) organic carbon (i.e., mine camp sewage, mined organic sediments, decay of local biota, or microbial pathways). Net sequestration of CO_2 requires that there be a non-carbonate mineral source for cations and a non-mineral source for carbon. Therefore, net sequestration of CO_2 can only occur in mine tailings when atmospheric carbon (either directly from the atmosphere or indirectly from modern organic matter) is trapped and stored within the crystal structures of carbonate minerals. X-ray powder diffraction techniques are well suited to identifying and quantifying carbonate minerals. However, these techniques cannot discern which minerals are trapping and storing atmospheric CO_2 nor to what extent CO_2 is being sequestered.

Stable and radiogenic carbon and stable oxygen isotope data can be used to: (1) identify the sources for CO_2 stored in carbonate minerals, (2) elucidate the mechanisms by which minerals form, and (3) trace the processes by which carbon is cycled. We have used these stable and radiogenic isotopes to verify that hydromagnesite is trapping and storing atmospheric carbon at Mount Keith. Subsequently, we have used our isotopic results to estimate the proportion of atmospheric CO_2 bound within hydromagnesite.

4.7.1 Fingerprinting with stable isotopes

Values for $\delta^{13}C$ between -10‰ and +1‰ with $\delta^{18}O$ in the range of approximately 10‰ to 20‰ commonly reflect the isotopic compositions of metamorphic magnesite (e.g., Kralik et al. 1989; Hansen 2005). The majority of the stable isotopic data for magnesite fall within this range of values (Fig. 4.15) and are consistent with a metamorphic origin for this mineral at Mount Keith. One specimen of a hydrotalcite-group mineral (iowaite) has a similar stable isotopic signature to the specimens of magnesite. Specimens of Ni-dolomite are also similarly depleted in ^{13}C, but are significantly enriched in ^{18}O relative to the other bedrock carbonate minerals. This is

consistent with their origin as fracture coatings and vugh linings in oxidized ore (Grguric 2003). Soda ash, which was used historically as a process chemical, is slightly depleted in ^{13}C relative to bedrock carbonate minerals and gives $\delta^{18}O$ values that are comparable to the upper range for specimens of magnesite.

Samples of bulk carbonate are consistently, and often significantly, enriched in ^{18}O relative to bedrock magnesite. Furthermore, many of the isotopic analyses for bulk carbonate minerals are enriched in ^{18}O over the specimens of Ni-dolomite. Analyses of hydromagnesite, done using selective acid extraction, indicate further enrichment in ^{18}O (up to 40‰) accompanied by a small enrichment in ^{13}C of ~1‰ on average. The significant enrichment in ^{18}O in hydromagnesite relative to magnesite suggests precipitation in an evaporative environment. This is consistent with our interpretation that hydromagnesite forms as a secondary alteration mineral via weathering of serpentine and brucite.

The stable carbon isotopic signature of hydromagnesite is somewhat more difficult to interpret than that of oxygen. Carbonate minerals that have formed at low temperatures from atmospheric CO_2 typically show considerable enrichment in ^{13}C over bedrock carbonate minerals (e.g., Kralik et al. 1989; Zedef et al. 2000; Léveillé et al. 2007; Power et al. 2007; Wilson et al. 2009). In Figure 4.15, the blue field indicates the $\delta^{13}C$ composition of hydromagnesite in equilibrium with atmospheric CO_2. Magnesite-CO_2 isotopic fractionation factors are used here as a proxy for equilibrium fractionation of carbon isotopes between hydromagnesite and CO_2. Values for $10^3 ln\alpha_{magnesite\text{-}CO_2}$ are derived from the equilibrium fractionation factors of Deines (2004) and Romanek et al. (1992) for $10^3 ln\alpha_{magnesite\text{-}calcite}$ and $10^3 ln\alpha_{calcite\text{-}CO_2}$, respectively. The theoretical values shown in Figure 4.15 assume that atmospheric CO_2 has a $\delta^{13}C$ value between -8‰ and -7‰ and are calculated for a range of temperatures between 0˚ and 40˚C. Should data for hydromagnesite fall within this field they would be consistent with precipitation from dissolved inorganic carbon that was in exchange equilibrium: (1) with the atmosphere (e.g., Dugan and Borthwick 1986) and (2) with hydromagnesite during mineral precipitation (e.g., Chacko et al. 2001).

Because some of the sewage generated by the mine camp is disposed of within TSF2, another possibility is that hydromagnesite may be drawing carbon from oxidized

sewage (a subject that is discussed in detail in Chapter 5). The orange field in Figure 4.15 indicates the $\delta^{13}C$ composition of carbonate minerals precipitated from sewage (defined by values derived from Burnett and Schaeffer 1980; Spies et al. 1989; Gearing et al. 1991; Van Dover et al. 1992; Bachtiar et al. 1996; deBruyn and Rasmussen 2002; Fernandes et al. 2005; Ramírez-Álvarez et al. 2007).

None of the data for hydromagnesite at Mount Keith fall within the field defined for mineral precipitation in equilibrium with the atmosphere or mine camp sewage. Using $\delta^{13}C$ values for the DIC of TSF water, we have calculated that magnesite (as a proxy for hydromagnesite) precipitating in equilibrium with TSF water will have $\delta^{13}C$ values between -1.40‰ and +2.06‰ over the range of temperatures from 0˚ and 40˚C. This result (for carbon isotopic fractionation between magnesite and aqueous bicarbonate) was calculated using equilibrium isotopic fractionation factors derived from Deines (2004) for $10^3 ln\alpha_{magnesite\text{-}calcite}$, Romanek et al. (1992) for $10^3 ln\alpha_{calcite\text{-}CO_2}$, and Mook et al. (1974) for $10^3 ln\alpha_{HCO_3^-\text{-}CO_2}$. Alternatively, the average value of carbon isotopic fractionation between dypingite and DIC obtained in Chapter 3 can be used as a proxy for hydromagnesite-DIC fractionation in this similar system. Using the result from Chapter 3, it is expected that hydromagnesite in equilibrium with process water would have $\delta^{13}C$ values between -4.36‰ and -2.40‰ at 25˚C. The extents of these fields are plotted in Figures 4.15. Very few data for any of the mined carbonate minerals, bulk carbonate minerals, or hydromagnesite fall within the field for magnesite in equilibrium with process water. However, several data for bedrock magnesite do fall within the field for magnesite in equilibrium with process water. Additionally, the range of $\delta^{13}C$ values predicted for magnesite in equilibrium with process water falls between the reservoir fields for bedrock magnesite and magnesite in equilibrium with the atmosphere. Although this suggests mixing between these reservoirs via dissolution of bedrock carbonate minerals, it is inconsistent with our quantitative mineralogical results. Approximately one third of the data for hydromagnesite are consistent with values obtained using the dypingite-DIC fractionation factor for precipitation from process water at 25˚C. Based on comparison with carbon isotopic fractionation between other carbonate minerals and DIC, it is likely that inclusion of temperature dependence for

dypingite-DIC fractionation (using results from Chapter 3) would increase the breadth of this field by several per mil to include the remaining data for hydromagnesite.

A number of scenarios may be invoked to explain the ^{13}C-depletion observed in hydromagnesite: (1) diffusion fractionation of atmospheric CO_2 into solution (as discussed in Chapter 3), (2) mixing between process waters and mine sewage, (3) infiltration into the TSFs of groundwater with DIC derived from soil CO_2, (4) the use of ^{13}C-depleted chemicals during processing, or (5) ^{13}C-depletion of the local atmosphere by fossil fuel emissions from the mine site power generators or high biological activity. Because of this, it is difficult to confirm an atmospheric origin for carbon within hydromagnesite using stable isotopes alone.

4.7.2 Improved discrimination with radiocarbon

The ambiguity in the stable isotopic data can be resolved using radiocarbon, which is a more sensitive tracer for atmospheric CO_2. Radiocarbon data are provided for 15 specimens of hydromagnesite, six specimens of bedrock magnesite, one specimen of bedrock Ni-dolomite, and one specimen of soda ash (a process additive). These data are given as $F^{14}C$ values, the fraction modern carbon (after Donahue et al. 1990 and Reimer et al. 2004). Radiocarbon data can be used to distinctly fingerprint incorporation of modern, atmospheric carbon into minerals. Results with $F^{14}C > 1$ can be used to confirm precipitation of carbonate minerals from a modern (i.e., post-1950s) and ultimately atmospheric carbon source. A value of $F^{14}C=1.06$ reflects the ^{14}C concentration of the atmosphere in 2006, the year of sampling at Mount Keith (Levin et al. 2008).

Radiocarbon data are given in Appendix A1 and are plotted against $\delta^{13}C$ in Figure. 4.16. Average values of $F^{14}C$ and $\delta^{13}C$ are plotted for samples on which replicate analyses have been done. Because $\delta^{13}C$ data for four specimens of magnesite are not available, radiocarbon results are plotted for two of these specimens only (i.e., magnesite selectively extracted from samples 06MKG-2-7-3 and 06MKG10-5-1).

Fraction modern carbon values for CO_2 selectively extracted from hydromagnesite range from 0.572 to 1.052 and all but one specimen has $F^{14}C > 0.8$ (Fig. 4.16). The highest values in this range are consistent with 100% of the CO_2 in hydromagnesite having been drawn from the mid-2000s atmosphere. The remaining

results suggest that most of the carbon mineralized within hydromagnesite at Mount Keith is modern. The only known large reservoir for modern carbon at Mount Keith is the atmosphere and, based on our radiocarbon results, it can be inferred that almost all CO_2 mineralized as hydromagnesite originated from this source. However, the excursion of some of these data below $F^{14}C$ of unity suggests the possibility of: (1) partial dissolution and reprecipitation of bedrock carbonate minerals as hydromagnesite, (2) mixing with carbon bearing process additives during mineral precipitation, or (3) contamination of CO_2 from modern hydromagnesite with ^{14}C-dead magnesite during selective acid extraction.

The very small amount of ^{14}C measured in Ni-dolomite sample 06MKNi-dol ($F^{14}C = 0.004$) is consistent with the amount of atmospheric contamination typically observed in our vacuum line for samples of ^{14}C-free bedrock carbonate minerals. The sample of soda ash has $F^{14}C = 0.052$. This may reflect sourcing of this process additive from a Quaternary evaporite deposit (Warren 2006). Six specimens of magnesite give values of $0.005 \leq F^{14}C \leq 0.365$. Two of these analyses are of highly pure samples of magnesite found in wasterock at sampling sites 53 and 54 (i.e., 06MK53 and 06MK54), which give $F^{14}C$ values between 0.005 and 0.009. These values are consistent with vacuum line contamination of samples with $F^{14}C=0$, as expected of bedrock magnesite that formed by carbonate alteration of serpentinized komatiite (Barrett et al. 1977; Grguric et al. 2006). The remaining analyses were done on CO_2 selectively extracted from magnesite in four samples of tailings (06MKG2-6-3-mags, 06MKG2-7-3-mags, 06MKG10-5-1-mags, and 06MKP9-4-mags). Magnesite in these samples gives $F^{14}C$ values ranging from 0.024 to 0.365. These values are higher than expected for bedrock magnesite at Mount Keith, which should not contain detectable ^{14}C. Similarly to the anomalously low $F^{14}C$ values for hydromagnesite, this deviation toward enrichment in ^{14}C within magnesite could reflect (1) partial dissolution and reprecipitation of bedrock magnesite to hydromagnesite and subsequent decomposition back to magnesite, (2) contamination of CO_2 from ^{14}C-dead magnesite with modern CO_2 from residual, unreacted hydromagnesite during acid extraction, or (3) partial conversion of secondary hydromagnesite to magnesite.

The decomposition of hydromagnesite to magnesite has been observed in hydromagnesite playas on the Cariboo Plateau, interior British Columbia, Canada (e.g., Renaut and Long 1989; Renaut 1990; Renaut and Stead 1991). Hydromagnesite represents the dominant mineral phase in these modern lacustrine environments, but magnesite is observed at the surface of the playas during the summer months as a product of the decomposition of hydromagnesite. It may be possible that some amount of recently precipitated hydromagnesite may undergo a similar transformation to magnesite in the mine tailings at Mount Keith. In fact, the specimen of magnesite with the highest $F^{14}C$ value (i.e., 06MKG10-5-1-mags with $F^{14}C$=0.365) comes from the 10-year old surface of TSF1. In this case, the mixing trend for magnesite in Figure. 4.16 could result from precipitation of hydromagnesite and its decomposition to magnesite.

Alternatively, the finely intergrown nature of secondary hydromagnesite (i.e., as a cement between grains of primary tailings minerals) may be preventing complete reaction with phosphoric acid during sample processing. Subsequent processing of these samples at higher temperature and for a longer period of time would then dissolve not only the desired magnesite but also the residual, unreacted hydromagnesite. This would result in higher values of $F^{14}C$ than anticipated for magnesite. Additionally, the finest fractions of less acid resistant phases like calcite, dolomite, and hydrotalcite-group minerals may be reacting to some extent during extraction of CO_2 from hydromagnesite. This would produce a dilution in ^{14}C, resulting in artificially low values of $F^{14}C$ for hydromagnesite. Under this interpretation, the mixing trend observed in Figure 4.16 may be an artefact of the technique used for sample preparation. Nonetheless, a conservative estimate for trapping of atmospheric CO_2 within hydromagnesite will take the ^{14}C data at face value. Using the average $F^{14}C$ value of hydromagnesite ($F^{14}C_{av} = 0.921 \pm 0.145$) and assuming that modern atmospheric CO_2 at Mount Keith has an $F^{14}C$ of approximately 1.06, an estimated 56,400 t of atmospheric CO_2 were mineralized into hydromagnesite in 2009. This conservative estimate for mineralization of atmospheric CO_2 represents an offset of more than 15% of annual greenhouse gas emissions from the operations at Mount Keith. According to this estimate, approximately 390,000 t of atmospheric CO_2 should have been trapped and stored in the mine tailings at Mount Keith between 1994 and 2009. Our projections suggest that by 2024, 1.78 Mt of atmospheric CO_2 may have

become trapped and stored within Mount Keith tailings over the 30-year life of the mine (Fig. 4.18).

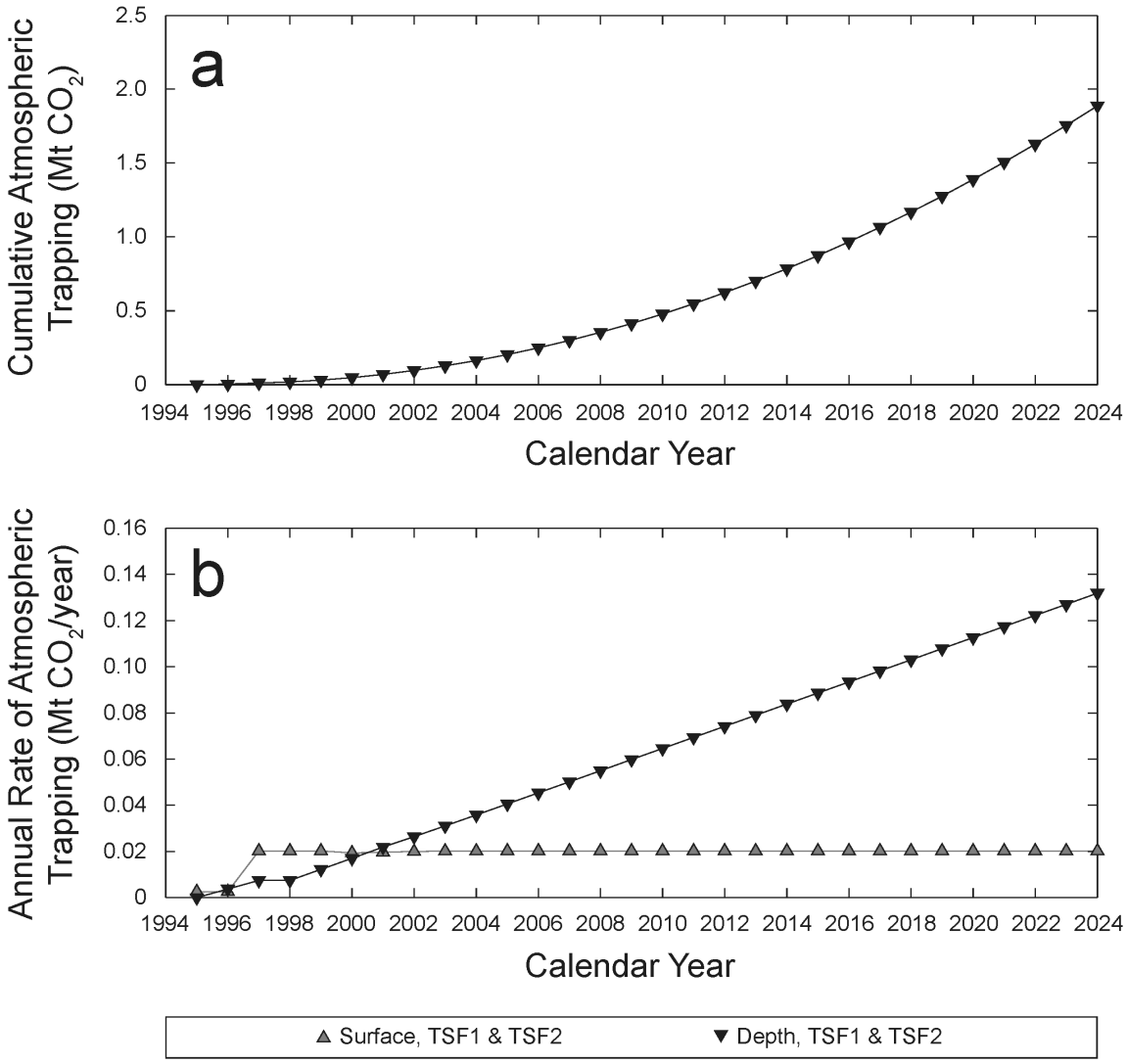

Figure 4.18: Estimated cumulative and annual mineralization of atmospheric CO_2 within Mount Keith mine tailings. Estimates for cumulative (a) and annual (b) trapping of atmospheric CO_2 within hydromagnesite are given in Mt. Predictions are made for the anticipated 30-year lifetime of the mine beginning in 1994 and ending in 2024.

4.8 Conclusions

At the Mount Keith Nickel Mine, the hydrated magnesium carbonate mineral, hydromagnesite [$Mg_5(CO_3)_4(OH)_2 \cdot 4H_2O$], forms as a secondary weathering product of serpentine-rich mine tailings and acts as a mineral trap for atmospheric CO_2. The near ubiquity of hydromagnesite at depth beneath efflorescent crusts of hydrated sulphate minerals may indicate in situ mineralization of hydromagnesite throughout the tailings or the reworking of hydromagnesite-rich horizons upon burial. At Mount Keith, hydromagnesite is commonly detectable at abundances greater than 0.5 wt.% within the tailings to depths of at least 1 to 4 m. As a result, the Rietveld method and X-ray powder diffraction data can be used to quantify the abundance of hydromagnesite and the amount of CO_2 trapped within it. The design of the tailings storage facilities (TSFs) at Mount Keith has led to preservation of historical mine tailings of various ages (from 0 to 10 years at the time of sampling in 2006). We have made use of Rietveld refinement results and this mineralogical and geochemical record to produce an empirical curve that measures the increase in concentrations of hydromagnesite within the TSFs over the life of the mine. From this curve, we have been able to extract an empirical rate law for carbon mineralization within hydromagnesite at Mount Keith. Using this rate law, it is possible to estimate the amount of carbon (including carbon from atmospheric, bedrock, industrial, and organic sources) that has been crystallographically stored in the tailings and to predict the scale of CO_2 trapping that may be expected over the life of the mine.

Hydromagnesite may be precipitating out of equilibrium with the atmosphere in the tailings at Mount Keith. This gives rise to a set of stable isotopic data that cannot be used unambiguously to fingerprint the source of CO_2 bound within secondary hydromagnesite. Radiocarbon data provide an unambiguous tool for fingerprinting modern carbon within hydromagnesite at Mount Keith. On average, 87% of the carbon in samples of hydromagnesite analyzed has been sequestered from a modern (and ultimately atmospheric) source. A conservative estimate indicates that at least 56,400 t of atmospheric CO_2 were mineralized into hydromagnesite at the Mount Keith Nickel Mine in 2009. This suggests that approximately 15% of the 2009 greenhouse gas emissions of

the Mount Keith operation were offset by uptake of CO_2 into mine tailings by a passive, and previously unrecognized, weathering process.

The rate at which atmospheric CO_2 is taken up by tailings in the upper 25 to 50 cm of the storage facilities is nearly four times higher than at depth. It may be possible to increase the rate of hydromagnesite precipitation within a greater mass of tailings by exposing a higher fraction of tailings to surface conditions. This could potentially be done by periodic aeration of tailings or by changing rotation patterns for tailings deposition from the nine risers in TSF2 and the pipelines around the circumference of the facility. Depositing tailings in thinner flows (approximately 25 cm deep) and allowing them to weather for longer periods of time could help to achieve this effect.

Lackner (2002) proposed that carbon mineralization could be stimulated within ponds of highly alkaline water built specifically for the purpose of sequestering CO_2. He suggested that biological mediation of silicate weathering and carbonate mineral precipitation could be incorporated into industrial processes for carbon mineralization. Since then, Power et al. (2009; in review) have described a natural analogue to this process in the hydromagnesite playas near Atlin, British Columbia, Canada (Power et al. 2009), and have developed a procedure for accelerated bioleaching of Mg from ultramafic mine tailings (Power et al. in review). Introduction of biologically mediated processes for carbon mineralization at Mount Keith and other ultramafic-hosted mines could help to accelerate trapping of atmospheric CO_2 in minerals. The amount of tailings produced at Mount Keith in one year has the capacity to bind approximately 4 Mt of CO_2 (after Lackner et al. 1995 and estimates from Wilson et al. 2009). This exceeds the annual emissions of the mine by more than a factor of ten. It also signifies a doubling of projected values for total CO_2 trapping up to 2024 and represents more than a 60-fold increase of sequestration capacity over the current, passive rate of carbon mineralization in these tailings. Accelerating the rate of mineral carbonation within Mount Keith tailings to make use of 11% of its total capacity to capture and store atmospheric CO_2 would completely offset the greenhouse gas emissions produced by this mine.

4.9 References

Acero, P., Ayora, C., Carrera, J., Saaltink, M.W., Olivella, S. (2009) Multiphase flow and reactive transport model in vadose tailings. Applied Geochemistry, 7, 1238-1250.

Acero, P., Ayora, C., Carrera, J. (2007) Coupled thermal, hydraulic and geochemical evolution of pyretic tailings in unsaturated column experiments. Geochimica et Cosmochimica Acta, 71, 5325-5338.

Agnew, M. and Taylor, G. (2000) Laterally extensive surface hardpans in tailings storage facilities as possible inhibitors of acid rock drainage. Proceedings of the 5th International Conference on Acid Rock Drainage, Society for Mining, Metallurgy, and Exploration, Inc., 1337-1346.

Akao, M. and Iwai, S. (1977) The hydrogen bonding of hydromagnesite. Acta Crystallographica, Section B: Structural Crystallography and Crystal Chemistry, B33, 1273-1275.

Al-Aasm, I.S., Taylor, B.E., and South, B. (1990) Stable isotope analysis of multiple carbonate samples using selective acid extraction. Chemical Geology, 80, 119-125.

Bachtiar, T., Coakley, J.P., and Risk, M.J. (1996) Tracing sewage-contaminated sediments in Hamilton Harbour using selected geochemical indicators. The Science of the Total Environment, 179, 3-16.

Badreddine, M., Legrouri, A., Barroug, A., De Roy, A., and Besse, J.P. (1999) Ion exchange of different phosphate ions into the zinc-aluminium-chloride layered double hydroxide. Materials Letters, 38, 391-395.

Barker, S.L.L., Wilson, S.A., Dipple, G.M., and Fallon, S.J. (2009) A method for separation and isotopic analysis of primary and secondary carbonate minerals found in ultramafic mine tailings. The Geological Society of America 2009 Annual Meeting, Abstracts with Programs, 41(7), 325.

Barrett, F.M., Binns, R.A., Groves, D.I., Marston, F.J., and McQueen, K.G. (1977) Structural history and metamorphic modification of Archean volcanic-type nickel deposits, Yilgarn Block, Western Australia. Economic Geology, 77, 1195-1223.

Barshad, I. (1965) Thermal analysis techniques for mineral identification and mineralogical composition. Agronomy, 9, 699-742.

Batchelder, D.N. and Simmons, R.O. (1964) Lattice constants and thermal expansivities of silicon and of calcium fluoride between 6 and 322 °K. Journal of Chemical Physics, 41, 2324-2329.

BHP Billiton (2005) Mt Keith Nickel Operations: Environmental Data. BHP Billiton Sustainable Development Reports. http://hsecreport.bhpbilliton.com/wmc/2004/performance/mko/data/index.htm.

Bish, D.L. (1980) Anion-exchange in takovite: Applications to other hydroxide minerals. Bulletin de Minéralogie, 103, 170-175.

Bish, D.L. (1993) Rietveld refinement of the kaolinite structure at 1.5 K. Clays and Clay Minerals, 41, 738-744.

Bish, D.L. and Howard, S.A. (1988) Quantitative phase analysis using the Rietveld method. Journal of Applied Crystallography, 21, 86-91.

Blowes, D.W., Reardon, E.J., Jambor, J.L., and Cherry, J.A. (1991) The formation and potential importance of cemented layers in inactive sulfide mine tailings. Geochimica et Cosmochimica Acta, 55, 965-978.

Braithwaite, C.J.R. and Zedef, V. (1996) Hydromagnesite stromatolites and sediments in an alkaline lake, Salda Gölü, Turkey. Journal of Sedimentary Research, 66, 991-1002.

Braithwaite, R.S.W., Dunn, P.J., Pritchard, R.G., and Paar, W.H. (1994) Iowaite, a re-investigation. Mineralogical Magazine, 58, 79-85.

Brindley, G.W. (1945) The effect of grain or particle size on X-ray reflections from mixed powders and alloys, considered in relation to the quantitative determination of crystalline substances by X-ray methods. Philosophy Magazine, 36, 347-369.

Bruker AXS (2004) EVA V. 10.0: Release 2004 – User's Manual: Karlsruhe, Germany, Bruker AXS.

Bruker AXS (2004) Topas V. 3.0: General Profile and Structure Analysis Software for Powder Diffraction Data. Bruker AXS, Germany.

Burnett, W.C. and Schaeffer, O.A. (1980) Effect of ocean $^{13}C/^{12}C$ ratios in marine sediments from the New York Bight. Estuarine and Coastal Marine Sciences, 11, 605-611.

Calleri, M., Gavetti, A., Ivaldi, G., and Rubbo, M. (1984) Synthetic epsomite, $MgSO_4 \cdot 7H_2O$: Absolute configuration and surface features of the complementary {111} forms. Acta Crystallographica Section B: Structural Science, B40, 218-222.

Catti, M., Ferraris, G., Hull, S., and Pavese, A. (1995) Static compression and H disorder in brucite, $Mg(OH)_2$, to 11 GPa: A powder diffraction study. Physics and Chemistry of Minerals, 22, 200-206.

Chacko, T., Cole, D.R., and Horita, J. (2001) Equilibrium oxygen, hydrogen and carbon isotope fractionation factors applicable to geologic systems. In Stable Isotope Geochemistry. Valley, J.W. and Cole, D.R., Eds. Reviews in Mineralogy and Geochemistry, 43, 1-81.

Cheary, R.W. and Coelho, A.A. (1992) A fundamental parameters approach to X-ray line-profile fitting. Journal of Applied Crystallography, 25, 109-121.

Chipera, S. and Vaniman, D.T. (2007) Experimental stability of magnesium sulfate hydrates that may be present on Mars. Geochimica et Cosmochimica Acta, 71, 241-250.

Chou, I.M. and Seal, R.R., II (2007) Magnesium and calcium sulfate stabilites and the water budget of Mars. Journal of Geophysical Research, 112, E11004, doi: 10.1029/2007JE002898.

Chou, I.M. and Seal, R.R., II (2003) Determination of epsomite-hexahydrite equilibria by the humidity-buffer technique at 0.1 MPa with implications for phase equilibria in the system $MgSO_4$-H_2O. Astrobiology, 3, 619-630.

Cole, W.F. and Lancucki, C.J. (1974) Refinement of the crystal structure of gypsum $CaSO_4 \cdot 2H_2O$. Acta Crystallographica, Section B: Structural Crystallography and Crystal Chemistry, 30, 921-929.

Das Sharma, S., Patil, D.J., and Gopalan, K., 2002, Temperature dependence of oxygen isotope fractionation of CO_2 from magnesite-phosphoric acid reaction: Geochimica et Cosmochimica Acta, v. 66, p. 589-593.

deBruyn, A.M.H. and Rasmussen, J.B. (2002) Quantifying assimilation of sewage-derived organic matter by riverine benthos. Ecological Applications, 12, 511-520.

Deines, P. (2004) Carbon isotope effects in carbonate systems. Geochimica et Cosmochimica Acta, 68, 2659-2679.

Deines, P., Langmuir, D., and Harmon, R.S. (1974) Stable carbon isotope ratios and the existence of a gas phase in the evolution of carbonate ground waters. Geochimica et Cosmochimica Acta, 38, 1147-1164.

Dold, B. (2006) Element flows associated with marine shore mine tailings deposits. Environmental Science & Technology, 40, 752-758.

Dollase, W.A. (1986) Correction of intensities for preferred orientation in powder diffractometry: application of the March model. Journal of Applied Crystallography, 19, 267-72.

Donahue, D.J., Linick, T.W., and Jull, A.J.T. (1990) Isotope-ratio and background corrections for accelerator mass spectrometry radiocarbon measurements. Radiocarbon, 32, 135-142.

Dugan, J.P., Jr. and Borthwick, J. (1986) Carbon dioxide-water oxygen isotope fractionation factor using chlorine trifluoride and guanidine hydrochloride techniques. Analytical Chemistry, 58, 3052-3054.

Engler, P. and Iyengar, S.S. (1987) Analysis of mineral samples using combined instrument (XRD, TGA, ICP) procedures for phase quantification. American Mineralogist, 72, 832-838.

Environmental Protection Authority (1996) Mt Keith Nickel Project: Tailings storage upgrade, Western Mining Corporation Limited: Report and recommendations of the Environmental Protection Authority. Environmental Protection Authority Bulletin 812, Perth, Australia.

Epstein, S., Graf, D.L., and Degens, E.T. (1964) Oxygen isotope studies on the origin of dolomites. In Isotopic and Cosmic Chemistry. Craig, H., Miller, S.L., and Wasserburg, G.T., Eds. North-Holland, Amsterdam, pp. 169-180.

Fandrich, R., Gu, Y., Burrows, D., Moeller, K. (2007) Modern SEM-based mineral liberation analysis. International Journal of Mineral Processing, 84, 310-320.

Fang, J.H. and Robinson, P.D. (1970) Crystal structures and mineral chemistry of double-salt hydrates: II. The crystal structure of loeweite. American Mineralogist, 55, 378-386.

Fernandes, S.A.P., Bettiol, W., Cerri, C.C., and Camargo, P. (2005) Sewage sludge effects on gas fluxes at the soil-atmosphere interface, on soil $\delta^{13}C$ and on total soil carbon and nitrogen. Geoderma, 125, 49-57.

Gearing, P.J., Gearing, J.N., Maughan, J.T., and Ovlatt, C.A. (1991) Isotopic distribution of carbon from sewage sludge and eutrophication in the sediments and food web of estuarine ecosystems. Environmental Science & Technology, 25, 295-301.

Genty, D. and Masssault, M. (1997) Bomb ^{14}C recorded in laminated speleothems: calculation of dead carbon proportion. Radiocarbon, 39, 33-48.

Genty, D., Vokal, B., Obelic, B., and Massault, M. (1998) Bomb ^{14}C time history recorded in two modern stalagmites – importance for soil organic matter dynamics and bomb 14C distribution over continents. Earth and Planetary Science Letters, 160, 795-809.

Glinnemann, J., King, H.E., Jr., Schulz, H., Hahn, T., La Placa, S.J., and Dacol, F. (1992) Crystal structures of the low-temperature quartz-type phases of silica and germanium dioxide at elevated pressure. Zeitschrift für Kristallographie, 198, 177-212.

Grady, M.M., Gibson, E.K., Wright, I.P., and Pillinger, C.T. (1989) The formation of weathering products on the LEW 85320 ordinary chondrite: Evidence from carbon and oxygen stable isotope compositions and implications for carbonates in SNC meteorites. Meteoritics, 24, 1-7.

Grguric, B.A., Rosengren, N.M., Fletcher, C.M., and Hronsky, J.M.A. (2006) Type 2 deposits: geology, mineralogy and processing of the Mount Keith and Yakabindi orebodies, Western Australia. Society of Economic Geologists Special Publications, 13, 119-138.

Grguric, B.A. (2003) Minerals of the MKD5 nickel deposit, Mount Keith, Western Australia. Australian Journal of Mineralogy, 9, 55-71.

Grguric, B.A., Madsen, I.C., and Pring, A. (2001) Woodallite, a new chromium analogue of iowaite from the Mount Keith nickel deposit, Western Australia. Mineralogical Magazine, 65, 427-435.

Grguric, B.A. (1999) The distribution and mineralogy of chlorine in concentrates and the MKD5 Ultramafic Unit: relationship to retrograde alteration and implications for mineral processing. WMC Resources Ltd., Internal Report. Unpublished, 86 pp.

Hansen, L.D. (2005) Geologic setting of listwanite, Atlin, B.C.: Implications for carbon dioxide sequestration and lode-gold mineralization. Unpublished M.Sc. thesis. The University of British Columbia, Vancouver, Canada, 174 pp.

Hardie, S.M.L., Garnett, M.H., Fallick, A.E., Rowland, A.P., and Ostle, N.J. (2007) Spatial variability of bomb ^{14}C in an upland peat bog. Radiocarbon, 49, 1055-1063.

Hill, R.E.T., Barnes, S.J., Gole, M.J., and Dowling, S.E. (1990) The physical volcanology of komatiites in the Norseman-Wiluna belt. In Third International Archean Symposium, Perth 1990, Excursion Guidebook. Ho, S.E., Glover, J.E., Myers, J.S., and Muhling, J.R., Eds., University of Western Australia, pp. 362-397.

Hill, R.J. and Howard, C.J. (1987) Quantitative phase analysis from neutron powder diffraction data using the Rietveld method. Journal of Applied Crystallography, 20, 467-474.

Horvatincic, N., Baresic, J., Babinka, S., Obelic, B., Bronic, I.K., Vreca, P., and Suckow, A. (2008) Towards a deeper understanding of how carbonate isotopes (^{14}C, ^{13}C, ^{18}O) reflect environmental changes: a study with recent 210Pb-dated sediments of the Plitvice lakes, Croatia. Radiocarbon, 50, 233-253.

Hostetler, P.B., Coleman, R.G., Mumpton, F.A., Evans, B.W. (1966) Brucite in alpine serpentinites. American Mineralogist, 51, 75-98.

Hua, Q. and Barbetti, M. (2004) Review of tropospheric bomb 14C data for carbon cycle modeling and age calibration purposes. Radiocarbon, 46, 1273-1298.

ICME and UNEP (1998) Case Studies on Tailings Management. The International Council on Metals and the Environment and the United Nations Environment Programme, Ottawa, Canada, 58 pp.

Jambor, J.L., Nordstrom, D.K., and Alpers, C.N. (2000) Metal-sulfate salts from sulfide mineral oxidation. In Sulfate Minerals: Crystallography, Geochemistry, and Environmental Significance. Alpers, C.N., Jambor, J.L., and Nordstrom, D.K., Eds. Reviews in Mineralogy & Geochemistry 40. Washington, DC, Mineralogical Society of America and Geochemical Society, 303-350.

Jambor, J.L. and Blowes, D.W. (1998) Theory and applications of mineralogy in environmental studies of sulfide-bearing mine wastes. In Modern Approaches to Ore and Environmental Mineralogy. Cabri, L.J. and Vaughn, D.J., Eds. Mineralogical Association of Canada Short Course 27, 367-401.

Järvinen, M. (1993) Application of symmetrized harmonics expansion to correction of the preferred orientation effect. Journal of Applied Crystallography, 26, 525-531.

Jull, A.J.T., Cheng, S., Gooding, J.L., and Velbel, M.A. (1988) Rapid growth of magnesium-carbonate weathering products in a stony meteorite from Antarctica. Science, 242, 417-419.

Kralik, M., Aharon, P., Schroll, E., and Zachmann, D. (1989) Carbon and oxygen isotope systematics of magnesites: a review. In Magnesite: Geology, Mineralogy, Geochemsitry, Formation of Mg-Carbonates. Möller, P., Ed. Monograph Series on Mineral Deposits 28, 197-223.

Lackner, K.S. (2002) Carbonate chemistry for sequestering fossil carbon. Annual Reivew of Energy and the Environment, 27, 193-232.

Leduc, E.M.S., Peterson, R.C., and Wang, R. (2009) The crystal structure and hydrogen bonding of synthetic konyaite, $Na_2Mg(SO_4)_2 \cdot 5H_2O$. American Mineralogist, 94, 1005-1011.

Léveillé, R.J., Longstaffe, F.J., and Fyfe, W.S. (2007) An isotopic and geochemical study of carbonate-clay mineralization in basaltic caves: abiotic versus microbial processes. Geobiology, 5, 235-249.

Levin, I. and Kromer, B. (2004) The tropospheric $^{14}CO_2$ level in mid-latitudes of the northern hemisphere (1959-2003). Radiocarbon, 46, 1261-1272.

Levin, I., Hammer, S., Kromer, B., Meinhardt, F. (2008) Radiocarbon observations in atmospheric CO_2: Determining fossil fuel CO_2 over Europe using Jungfraujoch observations as background. Science of the Total Environment, 391, 211-216.

Levin, I., Kromer, B., Schoch-Fischer, H., Bruns, M., Munnich, M., Berdau, D., Vogel, J.C., and Munnich, K.O. (1985) 25 years of tropospheric ^{14}C observations in Central Europe. Radiocarbon, 27, 1-19.

Levitan, D.M., Hammarstrom, J.M., Gunter, M.E., Seal, R.R., II, Chou, I.-M., and Piatak, N.M. (2009) Mineralogy of mine waste at the Vermont Asbestos Group mine, Belvidere Mountain, Vermont. American Mineralogist, 94, 1063-1066.

Liang, J.-J. and Hawthorne, F.C. (1996) Rietveld refinement of micaceous materials; muscovite-$2M_1$, a comparison with single-crystal structure refinement. Canadian Mineralogist, 34, 115-122.

Maharaj, S., Barton, C.D., Karathanasis, T.A.D., Rowe, H.D., and Rimmer, S.M. (2007) Distinguishing "new" from "old" organic carbon on reclaimed coal mine sites using thermogravimetry: I. method development. Soil Science, 172, 292-301.

March, A. (1932) Mathematische theorie der regelung nach der korngestalt bei affiner deformation. Zeitschrift für Kristallographie, 81, 285-297.

Markgraf, S.A. and Reeder, R.J. (1985) High-temperature structure refinements of calcite and magnesite. American Mineralogist, 70, 590-600.

Martín-Fernández, J.A., Barceló-Vidal, C., and Pawlowsky-Glahn, V. (2003) Dealing with zeros and missing values in compositional data sets using nonparametric imputation. Mathematical Geology, 35, 253-278.

Maslen, E.N., Streltsov, V.A., Streltsova, N.R., and Ishizawa, N. (1995) Electron density and optical anisotropy in rhombohedral carbonates. III. Synchrotron x-ray studies of $CaCO_3$, $MgCO_3$ and $MnCO_3$. Acta Crystallographica, Section B: Structural Science, B51, 929-939.

Mattey, D., Lowry, D., Duffet, J., Fisher, R., Hodge, E., and Frisia, S. (2008) A 53 year seasonally resolved oxygen and carbon isotope record from a modern Gibraltar speleothem: reconstructed drip water and relationship to local precipitation. Earth and Planetary Science Letters, 269, 80-95.

Meagher, E.P. and Lager, G.A. (1979) Polyhedral thermal expansion in the TiO_2 polymorphs: Refinement of the crystal structures of rutile and brookite at high temperature. Canadian Mineralogist, 17, 77-85.

Mellini, M. and Viti, C. (1994) Crystal structure of lizardite-1T from Elba, Italy. American Mineralogist, 79, 1194-1198.

Milton, G.M. and Kramer, S.J. (1998) Using 14C as a tracer of carbon accumulation and turnover in soils. Radiocarbon, 40, 999-1011.

Mook, W.G., Bommerson, J.C., Staverman, W.H. (1974) Carbon isotope fractionation between dissolved bicarbonate and gaseous carbon dioxide. Earth and Planetary Science Letters, 22, 169-176.

Nickels, J.E., Fineman, M.A., and Wallace, W.E. (1949) X-ray diffraction studies of sodium chloride-sodium bromide solid solutions. Journal of Physical Chemistry, 53, 625-628.

Nieto, F., Abad, I., and Azañón, J.M. (2008) Smectite quantification in sediments and soils by thermogravimetric analyses. Applied Clay Science, 38, 288-296.

Nydal, R. and Lövseth, K. (1983) Tracing bomb ^{14}C in the atmosphere 1962-1980. Journal of Geophysical Research, 88, 3621-3642.

Olsson, I.U. and Possnert, G. (1992) ^{14}C activity in different sections and chemical fractions of oak tree rings, AC 1938-1981. Radiocarbon, 34, 757-767.

O'Neil, J.R. and Barnes, I. (1971) C^{13} and O^{18} compositions in some fresh-water carbonates associated with ultramafic rocks and serpentinites: western United States. Geochimica et Cosmochimica Acta, 35, 687-697.

Palandri, J.L. and Kharaka, Y.K. (2004) A compilation of rate parameters of water-mineral interaction kinetics for application to geochemical modelling. U.S. Geological Survey Open File Report 2004-1068.

Palarea-Albaladejo, J., Martín-Fernández, J.A., and Gómez-García, J. (2007) A parametric approach for dealing with compositional rounded zeros. Mathematical Geology, 39, 625-645.

Pawley, G.S. (1981) Unit-cell refinement from powder diffraction scans. Journal of Applied Crystallography, 14, 357-361.

Perdikatsis, B. and Burzlaff, H. (1981) Strukturverfeinerung am Talk $Mg_3[(OH)_2Si_4O_{10}]$. Zeitschrift für Kristallographie, 156, 177-186.

Pertlik, F. (1986) Comparison of the results of routine structure determination by X-ray and neutron single-crystal data for trona, $Na_3H(CO_3)_2 \cdot 2H_2O$. Mitteilungen der Österreichischen Mineralogischen Gesellschaft, 131, 7-14.

Peterson, R.C. and Grant, A.H. (2005) Dehydration and crystallization reactions of secondary sulfate minerals found in mine waste: In situ powder-diffraction experiments. Canadian Mineralogist, 43, 1171-1181.

Power, I.M., Dipple, G.M., and Southam, G. Bioleaching of ultramafic tailings by *Acidithiobacillus* spp. for CO_2 sequestration. Environmental Science & Technology, in review.

Power, I.M., Wilson, S.A., Thom, J.M., Dipple, G.M., Gabites, J.E., and Southam, G. (2009) The hydromagnesite playas of Atlin, British Columbia, Canada: A biogeochemical model for CO_2 sequestration. Chemical Geology, 260, 286-300.

Power, I.M., Wilson, S.A., Thom, J., Dipple, G.M., and Southam, G. (2007) Biologically induced mineralization of dypingite by cyanobacteria from an alkaline wetland near Atlin, British Columbia, Canada. Geochemical Transactions, 8, article 13.

Price, W.A. and Errington, J.C. (1998) Guidelines for metal leaching and acid rock drainage at minesites in British Columbia. Retieved June 6, 2008 from the website of the British Columbia Ministry of Energy, Mines and Petroleum Resources. http://www.em.gov.bc.ca/Subwebs/mining/Project_Approvals/guidelines.htm#Metal%20Leaching%20and%20Acid%20Rock%20Drainage.

Quarta, G., D'Elia, M., Valzano, D., and Calcagnile, L. (2005) New bomb pulse radiocarbon records from annual tree rings in the Northern Hemisphere temperate region. Radiocarbon, 47, 27-30.

Raade, G. (1970) Dypingite, a new hydrous basic carbonate of magnesium, from Norway. American Mineralogist, 55(9-10), 1457-1465.

Rafter, T.A. and Fergusson, G.J. (1957) Atom bomb effect – recent increase of carbon-14 content of the atmosphere and biosphere. Science, 126, 557-558.

Ramírez-Álvarez, N., Macías-Zamora, J.V., Burke, R.A., and Rodríguez-Villanueva, L.V. (2007) Use of $\delta^{13}C$, $\delta^{15}N$, and carbon to nitrogen ratios to evaluate the impact of sewage-derived particulate organic matter on the benthic communities

of the Southern California Bight. Environmental Toxicology and Chemistry, 26, 2332-2338.

Raudsepp, M., and Pani, E. (2003) Application of Rietveld analysis to environmental mineralogy. In Environmental Mineralogy of Mine Wastes. Jambor, J.L., Blowes, D.W., and Ritchie, A.I.M., Eds. Mineralogical Association of Canada Short Course, 31, 165-180.

Reimer, P.J., Brown, T.A., and Reimer, R.W. (2004) Discussion: Reporting and calibration of post-bomb ^{14}C data. Radiocarbon, 46, 1299-1304.

Renaut, R.W. and Stead, D. (1991) Recent magnesite-hydromagnesite sedimentation in the playa basins of the Cariboo Plateau, British Columbia. Geological Fieldwork (BCGSB), Paper 1991-1, 279-288.

Renaut, R.W. (1990) Recent carbonate sedimentation and brine evolution in the saline lake basins of the Cariboo Plateau, British Columbia, Canada. Hydrobiologia, 197, 67-81.

Renaut, R.W. and Long, P.R. (1989) Sedimentology of the saline lakes of the Cariboo Plateau, Interior British Columbia, Canada. Sedimentary Geology, 64, 239-264.

Rietveld, H.M. (1969) A profile refinement method for nuclear and magnetic structures. Journal of Applied Crystallography, 2, 65-71.

Robertson, J.D., Tremblay, G.A., and Fraser, W.W. (1997) Subaqueous tailing disposal: a sound solution for reactive tailings. Proceedings of the 4th International Conference on Acid Rock Drainage, MEND, Natural Resources Canada, 1027-1044.

Romanek, C.S., Grossman, E.L., and Morse, J.W. (1992) Carbon isotopic fractionation in synthetic aragonite and calcite: effects of temperature and precipitation rate. Geochimica et Cosmochimica Acta, 56, 419-430.

Roselle, G.T., Baumgartner, L.P., and Valley, J.W. (1999) Stable isotope evidence of heterogeneous fluid infilration at the Ubehebe Peak contact aureole, Death Valley National Park, California. American Journal of Science, 299, 93-138.

Ross, N.L. and Reeder, R.J. (1992) High-pressure structural study of dolomite and ankerite. American Mineralogist, 77, 412-421.

Sandford, R.F., Pierson, C.T., and Crovelli, R.A. (1993) An objective replacement method for censored geochemical data. Mathematical Geology, 25, 59-80.

Shirozu, H. and Bailey, S.W. (1966) Crystal structure of a two-layer Mg-vermiculite. American Mineralogist, 51, 1124-1143.

Spalding, K.L., Buchholz, B.A., Bergman, L.-E., Druid, H., and Frisén (2005) Age written in teeth by nuclear tests. Nature, 437, 333-334.

Spies, R.B., Kruger, H., Ireland, R., and Rice, D.W., Jr. (1989) Stable isotope ratios and contaminant concentrations in a sewage-distorted food web. Marine Ecology Progress Series, 54, 157-170.

Stolberg, D.J. (2005) Rehabilitation studies on tailings storage facilities in an arid hypersaline region. Unpublished Ph.D. thesis. The University of Queensland, Brisbane, Australia, 304 pp.

Stuiver, M. and Polach, H.A. (1977) Discussion: reporting of ^{14}C data. Radiocarbon, 19, 355-363.

Stuiver, M. and Quay, P.D. (1981) Atmospheric ^{14}C changes resulting from fossil fuel CO_2 release and cosmic ray flux variability, Earth and Planetary Science Letters, 53, 349-362.

Suzuki, J. and Ito, M. (1974) Nesquehonite from Yoshikawa, Aichi Prefecture, Japan: occurrence and thermal behaviour. Journal of the Japanese Association of Mineralogists, Petrologists and Economic Geologists, 69, 275-284.

Suzuki, J. and Ito, M. (1973) A new magnesium carbonate hydrate mineral, $Mg_5(CO_3)_4(OH)_2 \cdot 8H_2O$, from Yoshikawa, Aichi Prefecture, Japan. Journal of the Japanese Association of Mineralogists, Petrologists and Economic Geologists, 68, 353-361.

Tasse, N., Germain, D, Dufour, C., and Tremblay, R. (1997) Hardpan formation in the Canadian Malartic Mine tailings: Implications for the reclamation of the abandoned impoundments. Proceedings of the 4th International Conference on Acid Rock Drainage, MEND, Natural Resources Canada, 1797-1812.

Taylor, G.F., 1975, The occurrence of monohydrocalcite in two small lakes in the South-East of South Australia: American Mineralogist, v. 60, p. 690-697.

Tsukimura, K., Sasaki, S., Kimizuka, N. (1997) Cation distributions in nickel ferrites. Japanese Journal of Applied Physics, Part 1: Regular Papers, Short Notes & Review Papers, 36, 3609-3612.

Uehara, S. (1998) TEM and XRD study of antigorite superstructures. Canadian Mineralogist, 36, 1595-1605.

Upton, G. and Cook, I. (2008) A Dictionary of Statistics. Oxford University Press, U.S.A., 512 p.

Van Dover, C.L., Grassle, J.F., Fry, B., Garritt, R.H., and Starczak, V.R. (1992) Stable isotope evidence for entry of sewage-derived organic material into a deep-sea food web. Nature, 360, 153-156.

Ventnor Consulting Group (2003) Report for Goldfields Gas Transmission Pty Ltd: Goldfields Gas Pipeline: Relevant Downstream Markets. Ventnor Consulting Group, North Fremantle, Australia, 58 pp.

Vizcayno, C. and Garcia-Gonzalez, M.T. (1999) $Na_2Mg(SO_4)_2{\cdot}4H_2O$, the Mg end-member of the bloedite-type of mineral. Acta Crystallographica, Section C: Crystal Structure Communications, C55, 8-11.

Warren, J.K. (2006) Evaporites: Sediments, Resources, and Hydrocarbons. Springer-Verlag, Germany, 1035 p.

Wenk, H.R. and Kroll, H. (1984) Analysis of P1, I1, and C1-plagioclase structures. Bulletin de Minéralogie, 107, 467-487.

Wild, E.M., Arlamovsky, K.A., Golser, R., Kutschera, W., Priller, A., Puchegger, S., Rom, W., Steier, P., and Vycudilik, W. (2000) 14C dating with the bomb peak: an application to forensic medicine. Nuclear Instruments and Methods in Physics Research B, 172, 944-950.

Wilson, S.A., Dipple, G.M., Power, I.M., Thom, J.M., Anderson, R.G., Raudsepp, M., Gabites, J.E., and Southam, G. (2009a) Carbon dioxide fixation within mine wastes of ultramafic-hosted ore deposits: Examples from the Clinton Creek and Cassiar chrysotile deposits, Canada. Economic Geology, 104, 95-112.

Wilson, S.A., Raudsepp, M., and Dipple, G.M. (2009b) Quantifying carbon fixation in trace minerals from processed kimberlite: A comparative study of quantitative methods using X-ray powder diffraction data with applications to the Diavik

Diamond Mine, Northwest Territories, Canada. Applied Geochemistry, 24, 2312-2331. doi:10.1016/j.apgeochem.2009.09.018.

Wilson, S.A., Raudsepp, M., and Dipple, G.M. (2006) Verifying and quantifying carbon fixation in minerals from serpentine-rich mine tailings using the Rietveld method with X-ray powder diffraction data. American Mineralogist, 91, 1331-1341.

Woodhouse, J.N. (2006) The characterization of hydrotalcite-group minerals and their anion exchange capabilities at Mount Keith Nickel Mine, Western Australia. B.Sc. Thesis, University of British Columbia, Vancouver, BC, Canada.

Xiong, Y. and Lord, A.S. (2008) Experimental investigations of the reaction path in the MgO-CO_2-H_2O system in solutions with various ionic strengths, and their applications to nuclear waste isolation. Applied Geochemistry, 23, 1634-1659.

Zalkin, A., Ruben, H., and Templeton, D.H. (1964) Crystal structure and hydrogen bonding of magnesium sulfate hexahydrate. Acta Crystallographica, 17, 235-240.

Zedef, V., Russell, M.J., Fallick, A.E., and Hall, A.J. (2000) Genesis of vein stockwork and sedimentary magnesite and hydromagnesite deposits in the ultramafic terranes of southwestern Turkey: a stable isotope study. Economic Geology, 95, 429-446.

Zhukhlistov, A.P. (2001) Crystal structure of lepidocrocite FeO(OH) from electron diffraction data. Kristallografiya, 46, 805-808.

Chapter 5

Isotopic fingerprinting of mineralized carbon in ultramafic mine tailings[1]

5.1 Introduction

Most of the carbon on Earth is stored within minerals with a mean residence time on the order of 10^6 years or more (Sundquist 1985; Sundquist 1993). Because of this, storage of carbon within the crystal structures of minerals is considered a safe and essentially permanent method for sequestering anthropogenic carbon dioxide (CO_2) (Seifritz 1990; Lackner et al. 1995). In situ dissolution of silicate minerals and precipitation of carbonate minerals in mine tailings represents an implementation of this process.

Secondary sulphate, carbonate, and halide minerals are common products of mineral weathering in mine tailings (e.g., Jambor and Blowes 1998; Al et al. 2000; Dold 2006). The development of these secondary minerals, carbonates in particular, has important implications for fixation of CO_2 in mine tailings. Wilson et al. (2006, 2009a) have documented trapping and storage of atmospheric CO_2 within hydrated Mg-carbonate minerals at two inactive chrysotile mines at Clinton Creek, Yukon Territory, Canada, and Cassiar, British Columbia, Canada. They demonstrated that a combination of (1) quantitative mineralogical and (2) isotope geochemical techniques can be used to verify and quantify mineralization of atmospheric CO_2 within secondary carbonate minerals in mine tailings.

In mine tailings, the rate of mineral-fluid reaction is greatly accelerated because milling and mineral processing lead to significant increases in reactive surface area (e.g., White et al. 1996; Molson et al. 2005). The atmosphere, industrial process chemicals, milled bedrock carbonate minerals, local biota, and organic waste products from mine

[1] A version of this chapter will be submitted for publication.
Wilson, S.A., Dipple, G.M., Power, I.M., Barker, S.L.L., Fallon, S.J., and Southam, G. Isotopic fingerprinting of mineralized carbon in ultramafic mine tailings.

camps are all potential sources of carbon from which secondary carbonate minerals may precipitate. The potential for inputs of carbon from multiple reservoirs, can give rise to stable carbon and oxygen isotopic data that are ambiguous or misleading. In geological systems for which uncommon minerals are locally abundant, this ambiguity can be compounded by a lack of constraint on isotopic fractionation factors. Kinetic isotope fractionation may also play a role in the mineralization of carbon in the tailings from some mines (Chapters 3 and 4). Under these conditions, it can be challenging to implicate specific reservoirs in the precipitation of minerals.

Commonly occurring carbonate minerals that are relatively straightforward to precipitate in the laboratory typically have well-constrained equilibrium isotopic fractionation factors. For instance, low-temperature isotopic fractionation of carbon and oxygen in calcite has been very well studied (e.g., Epstein 1953; Rubinson and Clayton 1969; O'Neil et al. 1969; Deines et al. 1974; Friedman and O'Neil 1977; Romanek et al. 1992; Kim and O'Neil 1997; Jiménez-López et al. 2001). Contrastingly, only two fractionation factors have ever been published for any of the hydrated Mg-carbonate minerals (s.l., meaning both hydrous and basic Mg-carbonate minerals), which are the primary hosts to atmospheric CO_2 in ultramafic mine tailings (Wilson et al. 2009a). These values are for the fractionation of stable oxygen isotopes between hydromagnesite [$Mg_5(CO_3)_4(OH)_2{\cdot}4H_2O$] and water at 0˚ and 25˚C (reported by O'Neil and Barnes 1971). The availability of oxygen isotopic fractionation factors for hydromagnesite (O'Neil and Barnes 1971) and the carbon isotopic fractionation factor for dypingite [$Mg_5(CO_3)_4(OH)_2{\cdot}5H_2O$] (Chapter 3), which is chemically similar (and likely to be structurally similar) to hydromagnesite, now enable predictions to be made about isotopic fractionation effects during precipitation of hydrated Mg-carbonate minerals in mine tailings.

This work is part of a broader study of natural analogues to CO_2 sequestration via carbon mineralization (Hansen et al. 2005; Power et al. 2007, 2009, in review) and passive methods for mineralizing atmospheric CO_2 within mine tailings (Wilson et al. 2006, 2009a, 2009b). Here, we present new radiocarbon and stable carbon and oxygen isotopic data for primary and secondary carbonate minerals from processed kimberlite mine tailings at the Diavik Diamond Mine, Northwest Territories, Canada. Of significant

concern to CO_2 sequestration is that the presence of secondary carbonate minerals at sites like Diavik may not represent net trapping of atmospheric CO_2. Although stable carbon and oxygen isotopic compositions for carbonate minerals (that have precipitated in equilibrium with atmospheric CO_2) can be predicted using isotopic fractionation factors, there are other ways of producing carbonate minerals with a similar stable isotopic signature.

During dissolution of carbonate minerals in a system open to the atmosphere, CO_2 is drawn into solution (Holland et al. 1964; Drever 1982). Conversely, CO_2 is degassed during precipitation of carbonate minerals. In this way, dissolution and reprecipitation of carbonate minerals can lead to efficient mixing of carbon from atmospheric and bedrock reservoirs. Recycling of bedrock carbonate minerals can therefore produce atmospheric C and O isotopic signatures, but with no net mineralization of carbon.

We have modelled three scenarios by which carbon may be mixed and cycled between different reservoirs in mine tailings. One model reflects mechanical mixing of minerals precipitated from two isotopically distinct reservoirs. The other two models reflect recycling of carbon from mined, bedrock carbonate minerals into newly precipitated carbonate minerals. The first of the recycling scenarios describes batch mixing of two isotopic end-members (bedrock carbonate minerals and secondary Mg-carbonate minerals precipitated in equilibrium with the atmosphere) in a closed system and is dependent upon the water-rock ratio of the system. The second scenario considers cyclic dissolution and reprecipitation of mined, bedrock carbonate minerals in an open system. The resulting models are used to interpret stable carbon and oxygen and radiogenic carbon isotopic data for the Diavik Diamond Mine. Models are then applied to isotopic data sets from three other mines: the Mount Keith Nickel Mine, Western Australia, Australia (using data from Chapter 4) and the historical chrysotile mines at Clinton Creek, Yukon Territory, Canada, and Cassiar, British Columbia, Canada (using data from Wilson et al. 2009a). Based on comparison with modelled results, we assess the impact of mechanical mixing and bedrock carbonate recycling on CO_2 sequestration at these four mines, and the validity of using stable isotopes of carbon and oxygen as the primary tools for verifying sequestration of atmospheric CO_2 within mine tailings.

5.2 Secondary carbonate minerals at the Diavik Diamond Mine

The Diavik Diamond Mine (DDMI) is located on East Island in Lac de Gras, approximately 300 km northeast of Yellowknife, Northwest Territories, Canada (Fig. 5.1). There are four mineable kimberlite pipes on the Diavik property that are part of the current mine plan. Two kimberlite pipes, A154 North and A154 South, are mined from a single open pit and a third pipe, A418, is located to the south of the A154 pipes. The fourth pipe, A21, is not currently being developed.

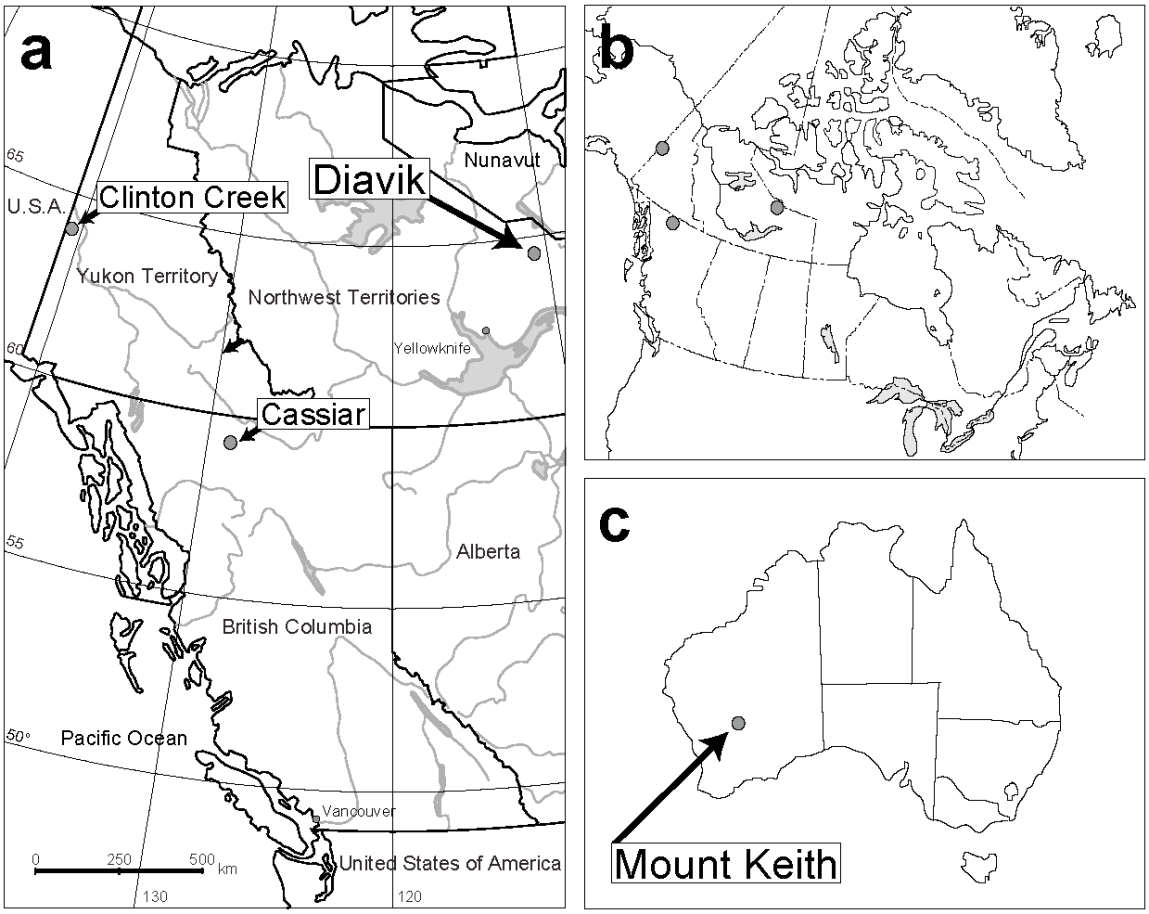

Figure 5.1: Locations of four mines. (a) and (b) Locations of the Diavik Diamond Mine, Northwest Territories, Canada, and the chrysotile mines at Clinton Creek, Yukon Territory, Canada, and Cassiar, British Columbia, Canada. (c) Location of the Mount Keith Nickel Mine, Western Australia, Australia.

The kimberlites at Lac de Gras, including those at Diavik, intrude Late Archean granitoids and supracrustal rocks of the Yellowknife Supergroup in the Slave Structural Province (Graham et al. 1998). Approximately 2 Mt/year of kimberlite ore are currently

being mined from the A154 open pit with increasing input from the A418 pit, which began production in 2008. After undergoing processing to remove diamonds, the residual kimberlite is transported to one of two locations for permanent storage. Most of this material is piped, suspended in water, into a natural basin (called the Fine Processed Kimberlite Containment Facility or fine PKC) where it is stored subaqueously in a pond of process water. A much smaller amount of coarse-grained waste material is stored subaerially in a pile (called the Coarse Processed Kimberlite Containment Facility or coarse PKC).

Processed kimberlite from the fine PKC is characterized by serpentine minerals (predominantly lizardite) and high-Mg forsterite with minor amounts of calcite, Cr-diopside, Mg-rich garnet, plagioclase, phlogopite, quartz, and clay minerals (e.g., vermiculite and possibly interstratified clays). Traces of chromite, dolomite, muscovite, perovskite, and an amphibole group mineral have been observed. The mineralogy of the coarse PKC is similar to that of the fine PKC, but differs notably in the presence of trace amounts of pyrite and jarosite. Pyrite has not been detected (to a limit of approximately 0.5 wt.%) in X-ray powder diffraction patterns of tailings samples.

Efflorescent crusts of secondary minerals are commonly observed in the fine PKC and occasionally in the coarse PKC at Diavik. Wilson et al. (2009b, Chapter 2) have defined four distinct modes in which these efflorescences occur: (1) white, powdery films of nesquehonite or sulphate minerals (commonly gypsum) that form on vertical and horizontal surfaces in the fine PKC, (2) white, loosely-aggregated crusts of Mg and Ca-sulphate minerals (typically a combination of anhydrite, gypsum, epsomite, hexahydrite, syngenite, and possibly butlerite), or occasionally of nesquehonite, that are found just below the surface of the coarse PKC, (3) preserved efflorescences of nesquehonite located at depth within the fine PKC, and (4) thick (> 1 mm) crusts of portlandite, Ca and Na-carbonate minerals (primarily calcite, gaylussite, natrite, thermonatrite, trona, and vaterite), with occasional nesquehonite, gypsum, and ettringite, that occur in parts of the fine PKC where processed sewage and waste water have been deposited.

Ten species of carbonate minerals have been detected in crust samples from Diavik (Table 5.1). Calcite and dolomite, the latter of which occurs less commonly, are gangue minerals in kimberlite and are observed in the fine and coarse PKC. Calcite is

found in most samples of bulk tailings and efflorescent crusts, although some of the calcite and vaterite found in Group 4 crusts appears to have precipitated from the sewage deposits.

Table 5.1: Carbonate mineral phases detected at Diavik.

Mineral Name	Cation(s)	Formula	Occurrence at Diavik
Nesquehonite	Mg	$MgCO_3 \cdot 3H_2O$	Efflorescent Precipitate
Dolomite	Ca, Mg	$CaMg(CO_3)_2$	Bedrock
Calcite	Ca	$CaCO_3$	Efflorescent Precipitate, Bedrock
Vaterite	Ca	$CaCO_3$	Efflorescent Precipitate
Gaylussite	Na, Ca	$CaNa_2(CO_3)_2 \cdot 5H_2O$	Efflorescent Precipitate
Natrite	Na	Na_2CO_3	Efflorescent Precipitate
Natron	Na	$Na_2CO_3 \cdot 10H_2O$	Efflorescent Precipitate
Thermonatrite	Na	$Na_2CO_3 \cdot H_2O$	Efflorescent Precipitate
Trona	Na	$Na_3(CO_3)(HCO_3) \cdot 2H_2O$	Efflorescent Precipitate
Northupite	Na, Mg	$Na_3Mg(CO_3)_2Cl$	Efflorescent Precipitate

Nesquehonite has been observed forming directly on the surfaces of grains of forsterite (Fig. 5.2a), suggesting precipitation from dissolved forsterite and/or serpentine mined from kimberlite. Nesquehonite typically forms continuous films (i.e., Group 1 crusts) at the surface of the tailings at Diavik (Fig. 5.2b), but it has also been detected in trace (or greater) amounts in all other types of crust. Sodium carbonate minerals like natrite, thermonatrite, trona, and gaylussite (Fig. 5.2c) are common in Group 4 crusts and occur at low abundance in Group 1 crusts. Natron and northupite are less common and have only been detected at low abundances. In the Group 1 crusts that lack nesquehonite, the most common sulphate minerals are epsomite, gypsum, hexahydrite, and syngenite

(Table 5.2). It is likely that these minerals form from sulphur released by dissolution of pyrite (Chapter 2). Gypsum is commonly found as a thin film on horizontal and vertical surfaces of the fine PKC and at shallow depth within the coarse PKC. Sulphate-rich efflorescences can develop very quickly in the fine PKC at Diavik. For instance, the gypsum in Figure 5.2d precipitated by the morning after a rainfall event, along the edges of a footprint made the previous evening. Contrastingly, the rainfall event did not have a noticeable effect on carbonate-rich crusts.

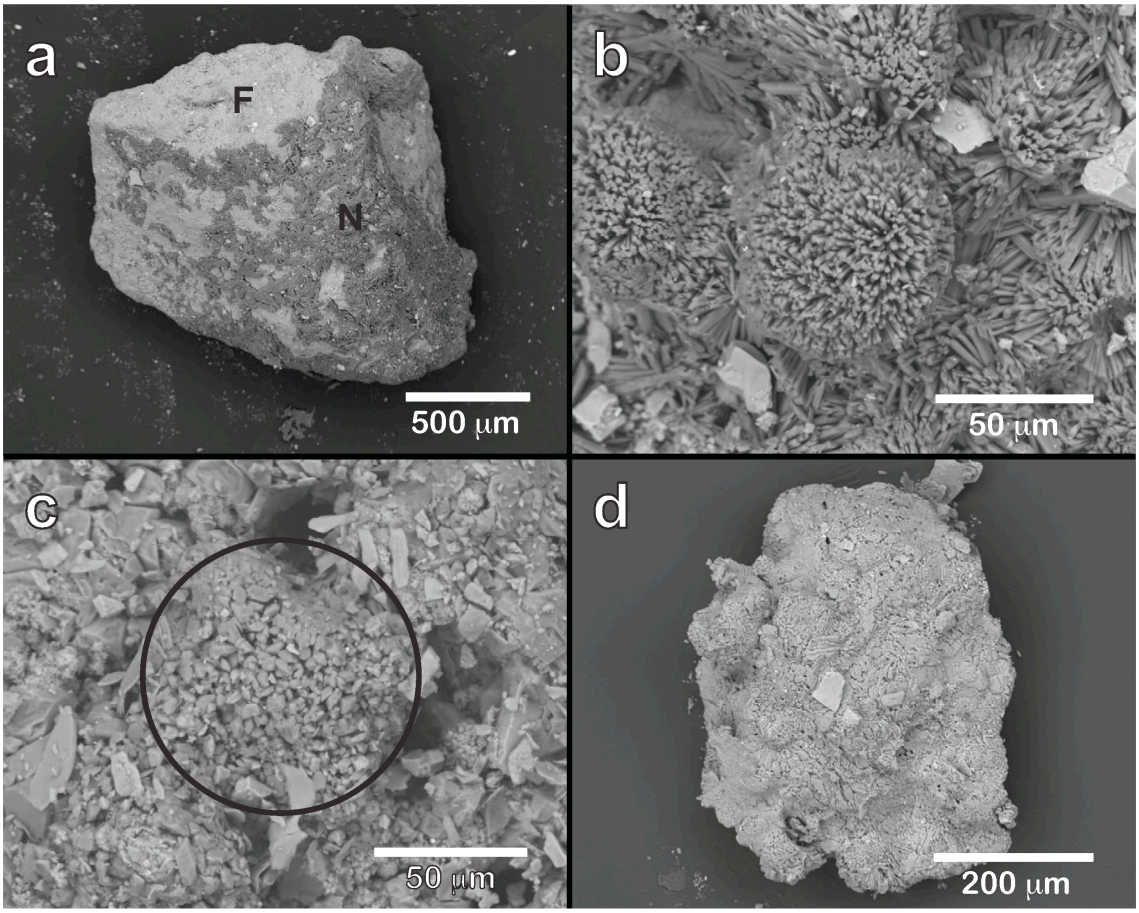

Figure 5.2: Backscattered electron SEM images of efflorescences from the surface of the tailings at Diavik. (a) Nesquehonite (N) encrusting a grain of forsterite (F) in sample 06DVK28; (b) rosettes made up of acicular crystals of nesquehonite from the surface of the fine PKC (06DVK37); (c) a cluster of gaylussite crystals (circled) in sample 06DVK13 from the coarse PKC; (d) a crust of gypsum from the surface of the fine PKC (06DVK49). The gypsum in (d) precipitated the morning after a rainfall event, along the edges of a footprint made the previous evening.

Table 5.2: Sulphate mineral phases detected at Diavik.

Mineral Name	Cation(s)	Formula	Occurrence at Diavik
Pentahydrite	Mg	$MgSO_4 \cdot 5H_2O$	Efflorescent Precipitate
Hexahydrite	Mg	$MgSO_4 \cdot 6H_2O$	Efflorescent Precipitate
Epsomite	Mg	$MgSO_4 \cdot 7H_2O$	Efflorescent Precipitate
Anhydrite	Ca	$CaSO_4$	Efflorescent Precipitate
Bassanite	Ca	$CaSO_4 \cdot 0.5H_2O$	Efflorescent Precipitate
Gypsum	Ca	$CaSO_4 \cdot 2H_2O$	Efflorescent Precipitate
Ettringite	Ca, Al	$Ca_6Al_2(SO_4)_3(OH)_{12} \cdot 26H_2O$	Efflorescent Precipitate
Langbeinite	K, Mg	$K_2Mg_2(SO_4)_3$	Efflorescent Precipitate
Syngenite	K, Ca	$K_2Ca(SO_4)_2 \cdot H_2O$	Efflorescent Precipitate
Jarosite	Fe, K	$KFe^{3+}_3(SO_4)_2(OH)_6$	Efflorescent Precipitate
Butlerite [a]	Fe	$Fe^{3+}(SO_4)(OH) \cdot 2H_2O$	Efflorescent Precipitate

[a] Butlerite may have been detected in XRPD patterns, by its most intense peak, at > 3σ above background intensity.

Nesquehonite is a common low-temperature alteration product of serpentinite and serpentine-rich mine wastes (e.g., Suzuki and Ito 1973; Suzuki and Ito 1974; Inaba et al. 1985; Giester et al. 2000; Wilson et al. 2006, 2009a, 2009b). Nesquehonite also forms by evaporation in creeks and playa environments that are fed by groundwater derived in part from drainage through ultramafic rock units (e.g., O'Neil and Barnes 1971; Power et al. 2007, 2009). In instances for which radiocarbon and stable carbon isotopic concentrations have been measured, naturally occurring nesquehonite tends to have a distinctly atmospheric source for carbon (e.g., O'Neil and Barnes 1971; Jull et al. 1988; Power et al. 2007; Wilson et al. 2009a). Despite the surface expression of Group 1 and Group 4 efflorescences, preserved efflorescent (Group 3) crusts of nesquehonite found at

depth within the fine PKC likely represent the bulk of carbon mineralization in the tailings at Diavik (Wilson et al. 2009b, Chapter 2).

In August 2006, samples of efflorescences were collected from the fine and coarse PKC using a knife edge and fine tweezers. Bulk samples of processed kimberlite mine tailings were collected using a sediment coring device. Detailed descriptions of sampling techniques and sampling locations are given by Wilson et al. (2009b, Chapter 2).

5.3 Analytical methods

5.3.1 Qualitative X-ray powder diffraction methods

Mineral phases in all specimens analyzed for isotopic concentrations were identified from X-ray powder diffraction (XRPD) patterns. Finely ground aliquots of sample were mounted as slurry onto a zero-background quartz plate with anhydrous ethanol and allowed to dry at room temperature. XRPD data were collected on a Siemens (Bruker) D5000 θ-2θ diffractometer equipped with a VÅNTEC-1 detector. A long, fine-focus Co X-ray tube was operated at 35 kV and 40 mA and an Fe monochromator foil was employed. Data for mineral identification were collected with a step size of 0.04° 2θ and counting time of 0.8 s/step over a range of 3-80° 2θ. Constituent mineral phases were identified from XRPD patterns with reference to the ICDD PDF-4+ 2008 database using the program DIFFRAC^{plus} EVA 10 (Bruker AXS 2004).

5.3.2 Stable isotopic methods

Specimens were analyzed using a gas bench attached to a Thermo Finnigan DeltaPlus XL IRMS at the Pacific Centre for Isotopic and Geochemical Research (PCIGR), The University of British Columbia. Aliquots weighing approximately 200 μg were loaded into septum vials, flushed with helium, and dissolved in 99% phosphoric acid at 72ºC for a minimum of one hour. Isotopic compositions of the evolved headspace gas were measured in a helium flow. The $\delta^{13}C$ compositions are given relative to Vienna Pee Dee Belemnite (VPDB) and the $\delta^{18}O$ compositions are given relative to Vienna

Standard Mean Ocean Water (VSMOW). The external precision (1σ deviation) for isotopic analyses was < 0.1‰ $\delta^{13}C$ and < 0.2‰ $\delta^{18}O$, as estimated from repeated analysis of NBS-18, NBS-19, and in-house calcite standards (which are calibrated against the NBS standards). At least three standards were analyzed for every eight specimens.

Stable carbon isotopic compositions of dissolved inorganic carbon (DIC) in five specimens of water from Diavik were determined using the Thermo Finnigan DeltaPlus XL IRMS at PCIGR. For each specimen, four to five drops of 99% phosphoric acid were loaded into an exetainer, which was then sealed with a rubber septum and flushed with helium for five minutes. A syringe was used to inject 600 μL of each water specimen into a sealed exetainer. The exetainer was shaken and the specimen left to react for a minimum of one hour at 25ºC. As with specimens of carbonate minerals, the isotopic composition of the evolved headspace gas was measured in a helium flow. The $\delta^{13}C$ compositions are given relative to VPDB. The external precision (1σ deviation) for isotopic analyses was < 0.1‰ $\delta^{13}C$, as estimated from repeated analysis of NBS-18, NBS-19, and in-house calcite standards. At least three standards were analyzed for every eight specimens.

Because isotope fractionation effects in hydrated Mg-carbonate minerals have not been studied thoroughly, the factors required to correct for fractionation of ^{18}O between these minerals and phosphoric acid are not known. The oxygen isotopic fractionation factor for magnesite and phosphoric acid was used as a proxy for those of the hydrated Mg-carbonate minerals. The $\delta^{18}O$ values of carbonate minerals were corrected for reaction with phosphoric acid using the fractionation factors from Das Sharma et al. (2002), taking into account the approximate proportions of calcium and magnesium carbonate minerals in mixed specimens. Specimens of hydrated carbonate minerals were analyzed in bulk, without removing crystallographic water by heating, as is standard practice for stable isotopic studies of these minerals (e.g., O'Neil and Barnes 1971; Taylor 1975; Grady et al. 1989; Zedef et al. 2000). As a consequence, exchange fractionation of oxygen may have occurred between H_2O and CO_2 evolved from acidification of specimens of hydrous minerals. The extent to which this exchange occurs has not been documented and, as a result, the $\delta^{18}O$ values reported for specimens of

hydrous minerals may reflect the isotopic composition of both carbonate and structurally bound water from these minerals.

5.3.3 Radiocarbon procedures

Six specimens of secondary carbonate minerals were picked under a binocular microscope with fine tweezers to maintain high purity. Powdered specimens were acidified to extract CO_2 using the vacuum line described by Barker et al. (2009) in the Department of Earth and Ocean Sciences, The University of British Columbia. The CO_2 contained within the ampoules was converted to graphite by hydrogen reduction in the presence of iron powder at 550ºC at the Research School of Earth Sciences, The Australian National University. Graphite targets were placed in a small mould and compressed into pellets. The pellets were run on the Single Stage Accelerator Mass Spectrometer (SSAMS) at The Australian National University. Background contamination, from preparation of graphite targets, was determined from analyses of ^{14}C-free coal and wood and was subtracted from sample data. The Cambridge half-life (5730 ± 40 years) was used to calculate the fraction of modern carbon ($F^{14}C$) as recommended by Donahue et al. (1990) and Reimer et al. (2004). Reservoir corrections were made to $F^{14}C$ values using $\delta^{13}C$ data collected with the SSAMS.

5.4 Results of isotopic analyses for the Diavik Diamond Mine

5.4.1 Stable carbon and oxygen isotopic results

The $\delta^{13}C$ data for specimens of carbonate minerals from Diavik (Table 5.3, Fig. 5.3) vary from -26.34‰ to 8.40‰ (VPDB), with $\delta^{18}O$ values ranging from 5.39‰ to 22.60‰ (VSMOW). A relationship between mineralogy, mode of occurrence, and $\delta^{13}C$ is observed in the stable isotopic data. Samples rich in efflorescent Ca and Na-carbonate minerals (e.g., calcite, gaylussite, natron, northupite, thermonatrite, trona, vaterite), and containing occasional nesquehonite, are characterized by $-26.34‰ \leq \delta^{13}C \leq -12.98‰$ and $7.59‰ \leq \delta^{18}O \leq 13.97‰$. Bedrock carbonate minerals (i.e., calcite ± dolomite) from the A154 mine pit have $-13.78‰ \leq \delta^{13}C \leq -1.78‰$ and $10.92‰ \leq \delta^{18}O \leq 14.92‰$, and

calcite ± dolomite from bulk tailings are defined by -9.69‰ ≤ $\delta^{13}C$ ≤ -3.92‰ and 5.39‰ ≤ $\delta^{18}O$ ≤ 10.96‰. Calcite ± dolomite from bulk tailings is on average more depleted in ^{13}C and ^{18}O than samples of the same minerals collected from the A154 mine pit. Highly pure aliquots of efflorescent nesquehonite give values of -4.39‰ ≤ $\delta^{13}C$ ≤ 8.40‰ and 9.40‰ ≤ $\delta^{18}O$ ≤ 22.60‰. Aliquots of nesquehonite contaminated with calcite give relatively depleted values of -5.65‰ ≤ $\delta^{13}C$ ≤ -0.90‰ and 7.07‰ ≤ $\delta^{18}O$ ≤ 16.08‰.

Dissolved inorganic carbon (DIC) in five specimens of filtered water gives a range of values from -17.85‰ ≤ $\delta^{13}C$ ≤ -4.62‰. The lowest value, -17.85‰ comes from water in the North Inlet (06DVK24), which is susceptible to algal blooms in the warm summer months (personal communication, C. English, DDMI). DIC in stored process water, collected from near the centre of the pond in the fine PKC (06DVK9), has a $\delta^{13}C$ of -10.39‰. Three splits from a large sample of processed water from the sewage treatment plant at Diavik (07DVK-sewage) contain DIC with values from -5.55‰ ≤ $\delta^{13}C$ ≤ -4.62‰.

5.4.2 Radiocarbon results

Radiocarbon analysis of nesquehonite and samples of Na and Ca-carbonate minerals from Diavik provides values of $F^{14}C$, the fraction modern carbon (after Donahue et al. 1990 and Reimer et al. 2004). These values are given in Table 5.3 and are plotted with $\delta^{13}C$ data in Figure 5.4. Three highly pure specimens of nesquehonite from Group 1 crusts sampled from the fine PKC give $F^{14}C$ values of 0.954 ± 0.006 (06DVK36-purest), 0.972 ± 0.009 (06DVK37-purest), and 0.972 ± 0.006 (06DVK39-purest). No other mineral phases were detected to a limit of approximately 0.5 wt.% in the XRPD patterns collected on these specimens of nesquehonite. Three specimens of secondary minerals collected from Group 4 crusts have $F^{14}C$ values of 0.946 ± 0.007 (06DVK7-crust, which contains calcite, nesquehonite, northupite, and trona), 1.057 ± 0.005 (06DVK10-purest, which contains calcite and gaylussite), and 1.009 ± 0.006 (06DVK4-isolate, which contains gaylussite, calcite, and thermonatrite).

Table 5.3: Stable carbon and oxygen isotopic data and radiocarbon data for carbonate minerals and DIC from Diavik.

Sample	Mode	Major Carbonate Phases[a]	Minor Carbonate Phases[a]	$\delta^{13}C$ (‰, VPDB)	$2\sigma_{\delta}{}^{13}C$ (‰, VPDB)	$\delta^{18}O$ (‰, VSMOW)	$2\sigma_{\delta}{}^{18}O$ (‰, VSMOW)	$F^{14}C$	$\sigma_{F}{}^{14}C$	NAD 27 Easting[b]	NAD 27 Northing[b]	Sample Depth (m)
06DG1-1	bulk tailings, fine PKC	Cal	–	-6.26	0.30	8.93	0.40	–	–	0533287	7152052	<0.1
06DG1-3	bulk tailings, fine PKC	Cal	–	-7.26	0.28	10.96	0.28	–	–	0533287	7152052	1
06DG1-3	bulk tailings, fine PKC	Cal	–	-7.11	0.12	9.23	0.16	–	–	0533287	7152052	1
06DG3-1	bulk tailings, fine PKC	Cal	–	-6.66	0.22	9.19	0.12	–	–	0533287	7152052	<0.1
06DG3-3	bulk tailings, fine PKC	Cal	–	-6.55	0.18	9.98	0.20	–	–	0533287	7152052	1
06DG3-3	bulk tailings, fine PKC	Cal	–	-6.62	0.08	9.45	0.18	–	–	0533287	7152052	1
06DG7-1	bulk tailings, fine PKC	Cal	–	-6.23	0.30	9.05	0.26	–	–	0533287	7152052	<0.1
06DG7-3	bulk tailings, fine PKC	Cal	–	-7.34	0.22	10.43	0.18	–	–	0533287	7152052	1
06DG8-1	bulk tailings, fine PKC	Cal	–	-5.95	0.40	8.31	0.40	–	–	0533287	7152052	<0.1
06DG9-1	bulk tailings, fine PKC	Cal	–	-6.17	0.16	8.56	0.18	–	–	0533287	7152052	<0.1
06DG9-2	bulk tailings, fine PKC	Cal	–	-6.00	0.14	9.49	0.14	–	–	0533287	7152052	0.5
06DG9-3	bulk tailings, fine PKC	Cal	–	-6.63	0.32	10.11	0.32	–	–	0533287	7152052	1
06DG11-3	bulk tailings, fine PKC	Cal	–	-6.77	0.28	10.16	0.20	–	–	0533287	7152052	1
06DG14-2	bulk tailings, fine PKC	Cal	Dol	-6.34	0.22	9.27	0.20	–	–	0533287	7152052	0.5
06DVK22	bulk tailings, coarse PKC	Cal	–	-6.67	0.14	9.92	0.14	–	–	0534030	7151721	surface
06DVK31	bulk tailings, fine PKC	Cal	–	-6.77	0.18	8.34	0.22	–	–	0533198	7152105	<0.1
06DVK33-1	bulk tailings, fine PKC	Cal	–	-7.10	0.22	7.62	0.22	–	–	0533015	7152116	<0.1
06DVK33-1	bulk tailings, fine PKC	Cal	–	-6.79	0.16	7.54	0.12	–	–	0533015	7152116	<0.1
06DVK33-3	bulk tailings, fine PKC	Cal	–	-6.24	0.36	9.10	0.18	–	–	0533015	7152116	1
06DVK34-3	bulk tailings, fine PKC	Cal	–	-6.50	0.14	9.00	0.14	–	–	0532802	7151825	1
06DVK42-1	bulk tailings, fine PKC	Cal	–	-3.92	0.20	5.38	0.12	–	–	0532470	7151627	<0.1
06DVK42-3	bulk tailings, fine PKC	Cal	–	-3.93	0.22	5.56	0.30	–	–	0532470	7151627	1
06DVK46-1	bulk tailings, fine PKC	Cal	–	-6.44	0.30	6.65	0.16	–	–	0533690	7151915	<0.1
06DVK46-1	bulk tailings, fine PKC	Cal	–	-6.64	0.12	5.96	0.20	–	–	0533690	7151915	<0.1
06DVK46-3	bulk tailings, fine PKC	Cal	–	-6.74	0.22	9.01	0.12	–	–	0533690	7151915	1

[a] Cal – Calcite, Dol – Dolomite, Gyl – Gaylussite, Nsq – Nesquehonite, Nor - Northupite, Tht - Thermonatrite, Tna - Trona.

[b] The Diavik Diamond Mine is in NAD 27 Zone 12.

[c] Denotes that grains were picked under a binocular microscope to maintain high sample purity.

Table 5.3 (continued): Stable carbon and oxygen isotopic data and radiocarbon data for carbonate minerals and DIC from Diavik.

Sample	Mode	Major Carbonate Phases[a]	Minor Carbonate Phases[a]	$\delta^{13}C$ (‰, VPDB)	$2\sigma_{\delta}{}^{13}C$ (‰, VPDB)	$\delta^{18}O$ (‰, VSMOW)	$2\sigma_{\delta}{}^{18}O$ (‰, VSMOW)	$F^{14}C$	$\sigma_{F}{}^{14}C$	NAD 27 Easting[b]	NAD 27 Northing[b]	Sample Depth (m)
06DVK48[c]	group 1 crust (gypsum), fine PKC	Dol, Cal	–	-7.74	0.18	10.35	0.22	–	–	0533554	7152029	surface
06DVK48-isolate[c]	group 1 crust (gypsum), fine PKC	Dol, Cal	–	-7.34	0.32	10.81	0.42	–	–	0533554	7152029	surface
06DVK49-crust[c]	group 1 crust (gypsum), fine PKC	Cal	–	-9.68	0.78	10.84	0.56	–	–	0533768	7151847	surface
06DVK53-1	bulk tailings, fine PKC	Cal	–	-5.35	0.48	7.74	0.22	–	–	0533544	7151450	<0.1
06DVK53-3	bulk tailings, fine PKC	Cal	–	-5.74	0.16	9.96	0.14	–	–	0533544	7151450	1
280s-06	carbonate in kimberlite	Cal	–	-4.90	0.14	10.91	0.12	–	–	0536644	7152699	280 m ASL
A154S-280-13	carbonate in kimberlite	Cal	–	-2.82	0.14	14.92	0.16	–	–	0536635	7152692	280 m ASL
A418-30-04-1	carbonate in kimberlite	Cal	–	-2.35	0.10	13.04	0.16	–	–	0536235	7151741	2 m ASL
A418-30-04-2	carbonate in kimberlite	Cal	–	-2.31	0.10	11.80	0.12	–	–	0536235	7151741	2 m ASL
GK ball	carbonate in kimberlite	Cal	–	-13.60	0.24	11.89	0.22	–	–	0536901	7152950	335 m ASL
GK ball	carbonate in kimberlite	Cal	–	-13.78	0.10	12.64	0.16	–	–	0536901	7152950	335 m ASL
GTH-79-02-1	carbonate in kimberlite	Cal	–	-1.80	0.06	13.39	0.08	–	–	0536655	7153154	8 m ASL
GTH-79-02-2	carbonate in kimberlite	Cal	–	-2.25	0.14	12.79	0.08	–	–	0536655	7153154	8 m ASL
RVK-CC-balls	carbonate in kimberlite	Cal	–	-4.77	0.10	11.87	0.10	–	–	0536840	7152970	295 m ASL
06DVK12-isolote[c]	group 4 crust, fine PKC	Cal	–	-12.98	0.08	13.97	0.12	–	–	0533375	7152062	surface
06DVK13-isolate[c]	group 2 crust, coarse PKC	Cal	–	-19.35	0.08	12.40	0.10	–	–	0534033	7151715	surface
06DVK1	group 4 crust	Cal	Tna	-18.97	0.12	9.26	0.14	–	–	0533359	7152087	surface
06DVK2	group 4 crust	Cal	Tna	-17.45	0.08	9.78	0.12	–	–	0533359	7152087	surface
06DVK5-subset[c]	group 4 crust	Cal	Tht	-23.72	0.08	9.38	0.10	–	–	0533359	7152087	surface
06DVK7-crust[c]	group 4 crust	Cal	Nsq, Nor, Tna	-26.34	0.24	7.59	0.18	0.946	0.007	0533359	7152087	surface
06DVK10	group 4 crust	Cal	Gyl	-16.46	0.18	13.14	0.26	–	–	0533375	7152062	surface
06DVK10-isolate[c]	group 4 crust	Cal	Gyl	-18.46	0.08	12.93	0.12	–	–	0533375	7152062	surface
06DVK10-crust[c]	group 4 crust	Cal	Gyl	-21.49	0.12	11.83	0.12	–	–	0533375	7152062	surface
06DVK10-purest[c]	group 4 crust	Cal	Gyl	-21.58	0.20	11.72	0.16	1.057	0.005	0533375	7152062	surface
06DVK4	group 4 crust	Gyl	Cal	-17.37	0.08	12.90	0.16	–	–	0533359	7152087	surface

[a] Cal – Calcite, Dol – Dolomite, Gyl – Gaylussite, Nsq – Nesquehonite, Nor - Northupite, Tht - Thermonatrite, Tna - Trona.
[b] The Diavik Diamond Mine is in NAD 27 Zone 12.
[c] Denotes that grains were picked under a binocular microscope to maintain high sample purity.

Table 5.3 (continued): Stable carbon and oxygen isotopic data and radiocarbon data for carbonate minerals and DIC from Diavik.

Sample	Mode	Major Carbonate Phases[a]	Minor Carbonate Phases[a]	$\delta^{13}C$ (‰, VPDB)	$2\sigma_{\delta}{}^{13}{}_{C}$ (‰, VPDB)	$\delta^{18}O$ (‰, VSMOW)	$2\sigma_{\delta}{}^{18}{}_{O}$ (‰, VSMOW)	$F^{14}C$	$\sigma_{F}{}^{14}{}_{C}$	NAD 27 Easting[b]	NAD 27 Northing[b]	Sample Depth (m)
06DVK4-isolate[c]	group 4 crust	Gyl	Cal, Tht	-18.51	0.08	13.15	0.10	1.009	0.006	0533359	7152087	surface
06DVK4-isolate-2[c]	group 4 crust	Gyl	Cal, Tht	-17.58	0.44	13.73	0.48	–	–	0533359	7152087	surface
06DVK11-isolate[c]	group 4 crust	Tna, Tht	Cal, Nsq	-1.03	0.22	20.00	0.20	–	–	0533375	7152062	surface
06DVK36-bulk	group 1 crust	Cal	Nsq	-5.65	0.18	7.07	0.12	–	–	0532504	7151711	surface
06DVK36-isolate[c]	group 1 crust	Nsq	–	-4.39	0.26	9.40	0.32	–	–	0532504	7151711	surface
06DVK36-purest[c]	group 1 crust	Nsq	–	2.36	0.36	20.88	0.42	0.954	0.006	0532504	7151711	surface
06DVK-37-bulk-crust[c]	group 1 crust	Nsq	Cal	-2.35	0.08	16.08	0.12	–	–	0532504	7151711	surface
06DVK37-isolate[c]	group 1 crust	Nsq	–	-3.45	0.12	21.73	0.34	–	–	0532504	7151711	surface
06DVK37-isolate-2[c]	group 1 crust	Nsq	–	-1.06	0.18	21.85	0.18	–	–	0532504	7151711	surface
06DVK37-purest[c]	group 1 crust	Nsq	–	-0.31	0.28	21.77	0.34	0.972	0.009	0532504	7151711	surface
06DVK39	group 1 crust	Nsq, Cal	–	-0.90	0.24	12.01	0.22	–	–	0532462	7151689	surface
06DVK39-opaque[c]	group 1 crust	Nsq	–	8.02	0.22	22.42	0.18	–	–	0532462	7151689	surface
06DVK39-trans-opaque[c]	group 1 crust	Nsq	–	8.40	0.12	22.34	0.12	–	–	0532462	7151689	surface
06DVK39-translucent[c]	group 1 crust	Nsq	–	8.40	0.16	22.07	0.16	–	–	0532462	7151689	surface
06DVK39-purest[c]	group 1 crust	Nsq	–	7.43	0.70	22.60	0.32	0.972	0.006	0532462	7151689	surface
06DVK24	DIC, North Inlet water	–	–	-17.85	0.12	–	–	–	–	0535290	7153065	–
06DVK9	DIC, fine PKC barge water	–	–	-10.39	0.08	–	–	–	–	0533266	7151772	–
07DVK-sewage-1	DIC, process plant water	–	–	-4.62	0.52	–	–	–	–	–	–	–
07DVK-sewage-2	DIC, process plant water	–	–	-5.55	0.38	–	–	–	–	–	–	–
07DVK-sewage-3	DIC, process plant water	–	–	-4.71	0.40	–	–	–	–	–	–	–
07CC17	DIC, toe of northern lobe of pile	–	–	-15.78	0.03	–	–	–	–	0514035	7147995	–

[a] Cal – Calcite, Dol – Dolomite, Gyl – Gaylussite, Nsq – Nesquehonite, Nor - Northupite, Tht - Thermonatrite, Tna - Trona.
[b] The Diavik Diamond Mine is in NAD 27 Zone 12 and the Clinton Creek Chrysotile Mine is in NAD 27 Zone 07.
[c] Denotes that grains were picked under a binocular microscope to maintain high sample purity.

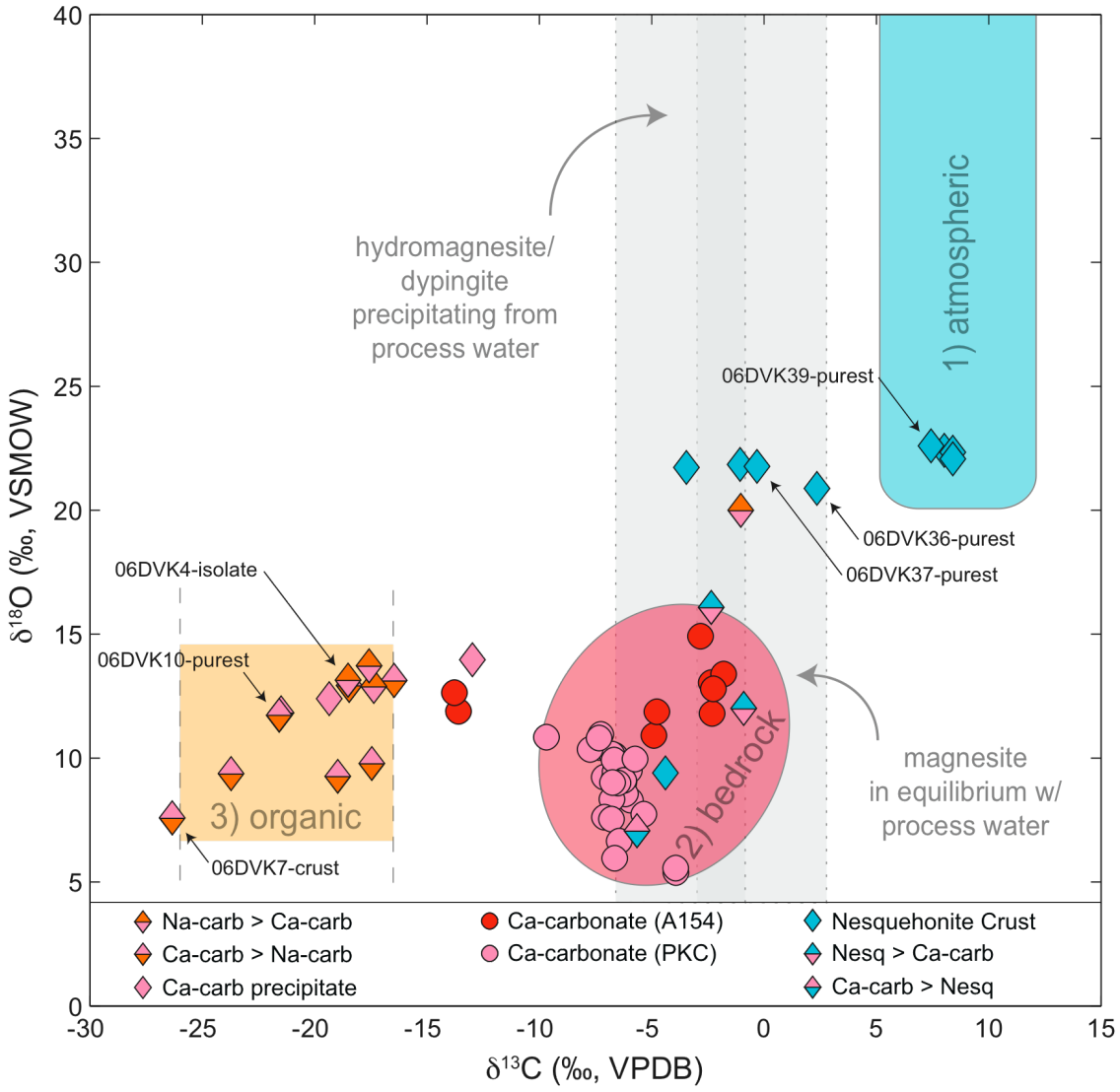

Figure 5.3: Stable oxygen and carbon isotope data by mode of occurrence and mineralogy for Diavik. Numbers indicate fields for carbonate minerals in equilibrium with specific reservoirs for carbon and oxygen. In most cases, 2σ measurement errors are smaller than the symbols employed.

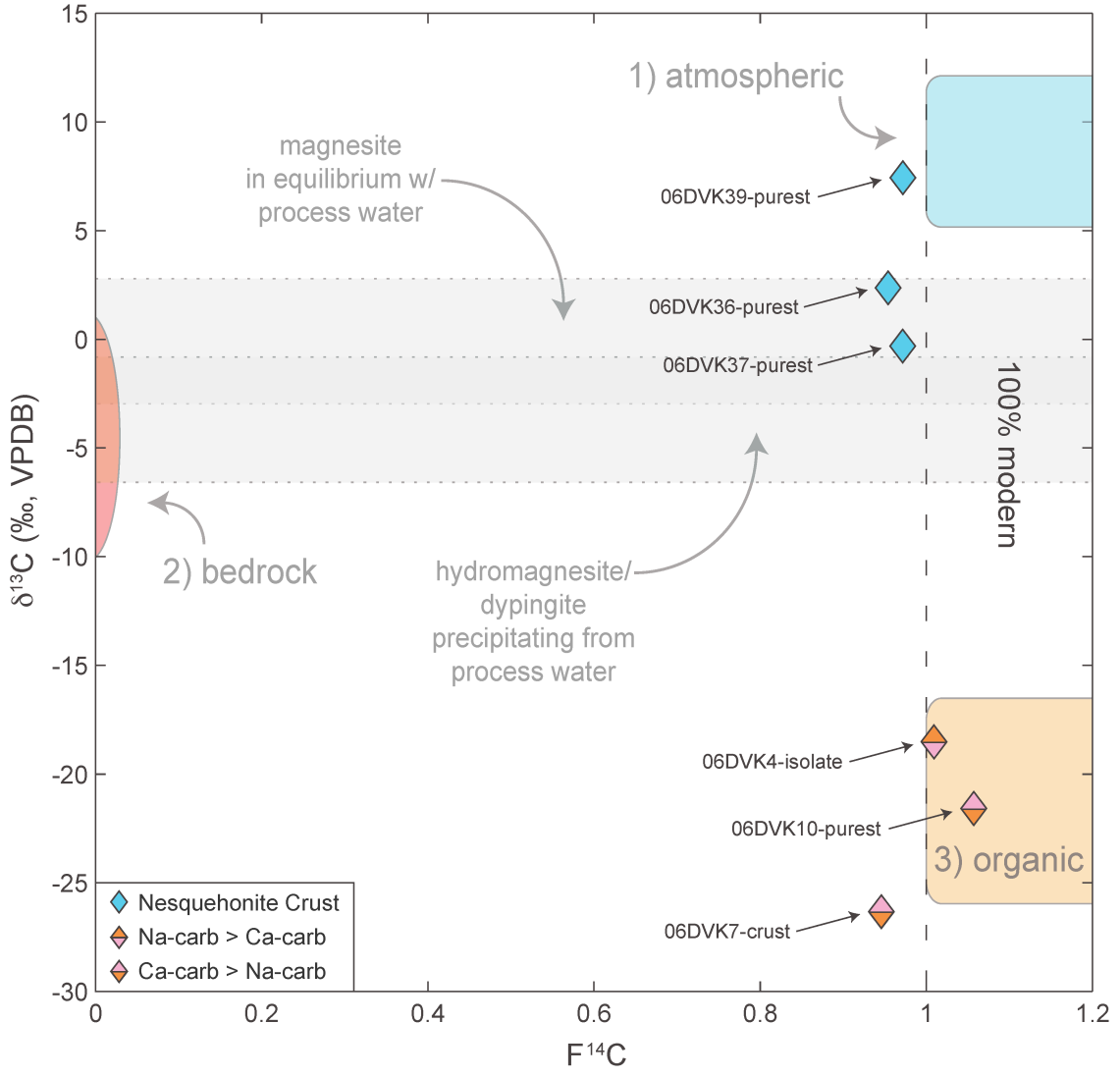

Figure 5.4: Variation of $\delta^{13}C$ with $F^{14}C$ for samples from Diavik. Numbers indicate fields for carbonate minerals in equilibrium with specific reservoirs for carbon and oxygen. In most cases, measurement errors are smaller than the symbols employed.

5.5 Isotopic fingerprinting at Diavik

5.5.1 Stable isotopic results

5.5.1.1 Secondary Na and Ca-carbonate minerals

The depleted $\delta^{13}C$ signature and relatively high $\delta^{18}O$-values of the Na and Ca-carbonate minerals in the fine PKC at Diavik suggest precipitation from an organic source of carbon in an evaporative environment. At Diavik, treated sewage from the mine camp has been disposed of at the surface of the tailings in the fine PKC. Sewage is deposited near the road that follows the perimeter of the fine PKC where crusts of Na and Ca-carbonate minerals were observed. The lowest values of $\delta^{13}C$ for these minerals are consistent with precipitation from sewage, which typically has $\delta^{13}C$ values for dissolved organic carbon (DOC) and particulate organic matter (POM) between approximately -26‰ and -21‰ (e.g., Burnett and Schaeffer 1980; Gearing et al. 1991; Van Dover et al. 1992; Bachtiar et al. 1996; deBruyn and Rasmussen 2002; Fernandes et al. 2005; Ramírez-Álvarez et al. 2007) but which can be as enriched as -16‰ (e.g., Spies et al. 1989).

Because aerobic oxidation of organic matter produces CO_2 with a carbon isotopic ratio close that of the parent material (Ogrinc et al. 2008), carbonate minerals precipitated from an organic source will have a similarly depleted isotopic signature. For instance, calcite precipitated from sewage-derived aqueous HCO_3^-, at temperatures from 0˚ to 40˚C, and under equilibrium conditions, is expected to be more enriched by 0.8‰ to 1.1‰ in $\delta^{13}C$ than the aqueous species from which it formed [using fractionation factors from Mook et al. (1974) and Romanek et al. (1992) for $10^3 \ln\alpha_{HCO_3^-(aq)\text{-}CO_2(g)}$ and $10^3 \ln\alpha_{calcite\text{-}CO_2(g)}$, respectively]. Although most data for secondary Na and Ca-carbonate minerals are consistent with precipitation from oxidized sewage organic matter, it is notable that data for one aliquot of Na and Ca-carbonate minerals (06DVK11-isolate) lie well outside the expected range of values (Fig. 5.3). Sample 06DVK11-isolate is considerably more enriched in ^{13}C and ^{18}O than other mineralogically similar aliquots.

We did not investigate the potential role of microbes in carbonate mineralization in this setting, however it is entirely possible that microbial communities within the

sewage deposits contributed to the breakdown and mineralization of sewage organic matter. In future investigations, culturing and in situ sampling of CO_2 could be used to evaluate the role of microbes in precipitating these Na and Ca-carbonate minerals.

We collected $\delta^{13}C$ data for dissolved inorganic carbon (DIC) in water obtained from the sewage treatment plant at Diavik (Table 5.3), but our results ($-5.55‰ \leq \delta^{13}C \leq -4.62‰$) suggest that the DIC may have equilibrated with atmospheric CO_2 after sampling and prior to analysis. No measurements were done on POM or DOC in this water and samples of sewage were not available for direct analysis. In the absence of isotopic data for sewage from Diavik, we have defined the field for organic carbon in Figures 5.3 and 5.4 to reflect literature values for sewage from cities in North, Central, and South America (cited above).

5.5.1.2 Primary bedrock carbonate minerals

Primary calcite in kimberlite typically exhibits values between approximately -10‰ and -1‰ in $\delta^{13}C$ and approximately 7‰ to 27‰ in $\delta^{18}O$ (reviewed by Mitchell 1986). Secondary calcite, associated with bituminous matter is usually more depleted in ^{13}C, with $\delta^{13}C$ values in the range of approximately -32‰ to -10‰ (Mamchur et al. 1980). Some samples of calcite from the A154 mine pit at Diavik have $\delta^{13}C$ values lower than expected for primary calcite (Fig. 5.3). These samples were found in association with lenses of mud and fragments of preserved wood (personal communication, S. Moss, UBC-EOS), suggesting possible input of organic carbon during precipitation.

Lighter values for $\delta^{13}C$ and $\delta^{18}O$ in calcite ± dolomite sampled from the fine PKC may reflect different sources within the A154 mine pit for fresh samples versus mine tailings or partial dissolution and reprecipitation of primary bedrock calcite ± dolomite with an input of organic carbon, which would manifest as carbonate minerals with an intermediate isotopic signature. With regard to the latter interpretation, Al et al. (2000) describe precipitation of secondary siderite on grains of ankerite at the Kidd Creek copper-zinc mine near Timmins, Ontario, Canada, and Paktunc and Davé (2002) document secondary Ca-siderite overgrowing grains of calcite in mine tailings at the Lower Williams Lake uranium mine near Elliot Lake, Ontario, Canada. We have not undertaken the sort of detailed scanning electron microscope work required to identify

zoning in calcite ± dolomite, but it is possible that primary carbonate minerals may have dissolved and reprecipitated to some extent within the fine PKC. However, the relatively small footprint of sewage deposits at the surface of the fine PKC suggests that the input of organic carbon via sewage is probably too localized and volumetrically insufficient to influence the isotopic composition of calcite ± dolomite throughout the fine PKC. Also, the studies done by Al et al. (2000) and Paktunc and Davé (2002) were done in mine tailings with neutral to acidic pore waters. It is unlikely that calcite would be prone to significant dissolution and reprecipitation under the neutral to basic conditions of pH in the fine PKC at Diavik (Palandri and Kharaka 2004).

5.5.1.3 Secondary nesquehonite, $MgCO_3 \cdot 3H_2O$

The wide range of stable carbon and oxygen isotopic values for nesquehonite may imply precipitation from several distinct and mixed sources of carbon.

Highly pure aliquots of nesquehonite, picked from sample 06DVK39 under a binocular microscope, are interpreted as having developed in an evaporative environment with an atmospheric source of CO_2 based on significant enrichment in ^{13}C and ^{18}O. $\delta^{13}C$ values for nesquehonite from this sample are consistent with mineral precipitation in isotopic equilibrium with atmospheric CO_2 (Fig. 5.3).

Data for highly pure aliquots of nesquehonite, picked from samples 06DVK36 and 06DVK37, show similar enrichment in ^{18}O, but give $\delta^{13}C$ values that are inconsistent with precipitation from atmospheric CO_2. These data fall in a region of $\delta^{18}O$-$\delta^{13}C$ space that lies between the three reservoir fields identified as sources of carbon at Diavik (i.e., the atmosphere, mined carbonate minerals, and sewage organic matter). Using $\delta^{13}C$ values for the DIC in the fine PKC pond, and the DIC in water from the sewage treatment plant, we have calculated that nesquehonite precipitating in equilibrium with tailings water will have $\delta^{13}C$ values between -6.59‰ and -0.82‰ at 25˚C (using the fractionation factor for dypingite obtained in Chapter 3). Because typical temperatures at Diavik are considerably less than 25˚C, inclusion of temperature dependence for dypingite-DIC fractionation would increase the breadth of this field toward higher $\delta^{13}C$. The field for magnesite in equilibrium with process water extends from -2.98‰ to 2.79‰ at 25˚C. Data for all remaining aliquots of highly pure nesquehonite are

consistent with equilibrium precipitation from DIC. Kinetic diffusion fractionation of atmospheric CO_2 into solution (as discussed in Chapters 3 and 4) may be invoked to explain the ^{13}C-depletion observed in these specimens of nesquehonite. However, there is a large spread in the $\delta^{13}C$ data for nesquehonite at Diavik, and some samples are consistent with precipitation under isotopic equilibrium, which suggests that mixing processes could have produced some of the observed trends under isotopic equilibrium.

Data for four nesquehonite-rich aliquots (representing the three samples analyzed: 06DVK36, 06DVK37, and 06DVK39) plot within the field defined by bedrock carbonate minerals. This may result from contamination by bedrock minerals or incorporation into nesquehonite of carbon recycled from dissolved bedrock carbonate minerals. Contamination by calcite from kimberlite has been confirmed by XRPD for three of the four aliquots. No calcite was observed in the XRPD pattern of the remaining aliquot, 06DVK36-isolate, which suggests that certain occurrences of nesquehonite at Diavik may be mineralizing bedrock carbon to some extent. However, data for other aliquots of nesquehonite from the same sample (i.e., 06DVK36) are inconsistent with recycling of bedrock calcite, suggesting the possibility that calcite contamination may have been missed in the XRPD pattern, which did not use the entire aliquot that was analyzed for its isotopic composition.

5.5.2 Radiocarbon results

Values of $F^{14}C$ for six aliquots of secondary carbonate minerals range from 0.946 to 1.057 (Fig. 5.4). This result suggests that most (at least 90%) of the carbon bound within these efflorescences was derived from atmospheric carbon, either directly from the atmosphere, indirectly through the biosphere (i.e., sewage carbon), or via recycling of bedrock carbonate minerals. Data for two specimens of Na and Ca-carbonate minerals fall within the field defined for precipitation from sewage organic carbon. One of these two specimens, 06DVK10-purest (which contains calcite and gaylussite), has an $F^{14}C$ value of 1.057, which is consistent with the composition of the atmosphere in 2006, the year of sampling. The remaining four specimens give $F^{14}C$ values slightly less than one, suggesting input from a source of ^{14}C-free carbon.

5.6 Modelling mixing and recycling of carbonate minerals in mine tailings

Mechanical mixtures of minerals precipitated from different sources of carbon can give isotopic data that are intermediate between the isotopic signatures of distinct reservoirs for carbon and oxygen. Also, dissolution and reprecipitation of primary, bedrock carbonate minerals may play a role in production of new carbonate minerals in some mine tailings storage facilities. The latter process can also give mixed isotopic signals in secondary carbonate minerals.

We have modelled three mixing scenarios in order to improve our ability to recognize (1) mechanical mixing of minerals precipitated from two distinct reservoirs and (2) dissolution and reprecipitation of mined bedrock carbonate minerals. The first model describes simple, linear mixing between two populations of minerals with distinct isotopic signatures. The second scenario describes batch mixing of two isotopic end-members (bedrock carbonate minerals and secondary carbonate minerals precipitated in equilibrium with the atmosphere) in a closed system and is dependent upon the water-rock ratio during reaction. The third scenario describes sequential dissolution and reprecipitation of bedrock carbonate minerals in an open system. The second scenario describes a single dissolution-reprecipitation event, whereas the third scenario depicts repeated cycles of carbonate mineral dissolution and reprecipitation.

5.6.1 Reservoir values and isotopic fractionation factors used in models

Four different sets of starting conditions are used in all three scenarios (outlined in Table 5.4) to model (1) precipitation of a hydrated Mg-carbonate mineral [using fractionation factors for dypingite from Chapter 3 and for hydromagnesite from O'Neil and Barnes (1971)] from water of a typical isotopic composition, (2) precipitation of magnesite from water of a typical isotopic composition, (3) precipitation of a hydrated Mg-carbonate mineral from highly evaporated water, and (4) precipitation of magnesite from a highly evaporated water. Models 1 and 2 are based on isotopic data from the Diavik Diamond Mine and models 3 and 4 are based on data from the Mount Keith Nickel Mine.

Table 5.4: Values input to models for scenarios 1 through 3.

Reservoir[a]	**$\delta^{13}C$ (‰, VPDB)**	**$\delta^{18}O$ (‰, VSMOW)**	**$F^{14}C$**
Atmosphere (year 2006)	-8	40	1.06
Diavik water	-10.39	-10	–
Diavik bedrock (calcite)	-6.39	8.69	0
Diavik secondary ppt. (hymag/dyp)	3.67	20.85	1.06
Diavik secondary ppt. (magnesite)	7.35	21.85	1.06
Diavik sewage (Group 4) crust	-26.34	7.59	1.06
Mt. Keith water	-7.71	7	–
Mt. Keith bedrock (magnesite)	-4.11	13.27	0
Mt. Keith secondary ppt. (hymag/dyp)	3.67	38	1.06
Mt. Keith secondary ppt. (magnesite)	7.35	39	1.06
Fractionation factors between reservoirs[a]	**$\Delta^{13}C$ (‰)**	**$\Delta^{18}O$ (‰)**	
DIC (HCO_3^-) – $CO_2(g)$[b]	7.94		
$H_2O(l)$ – $CO_2(g)$		-9.96	
DIC (HCO_3^-) – magnesite	-7.41		
$H_2O(l)$ – magnesite		-32.23	
DIC (HCO_3^-) – hymag/dyp	-3.8		
$H_2O(l)$ – hymag/dyp		-31.19	

[a] Sources of initial values and selection criteria are discussed in detail in the text.
[b] DIC (dissolved inorganic carbon) in assumed to be bicarbonate (HCO_3^-).

The isotopic composition of the atmosphere is assumed to be $\delta^{18}O_{CO_2(g)}$=40‰, $\delta^{13}C_{CO_2(g)}$=-8‰, and $F^{14}C$=1.06 using values from Clark and Fritz (1997), Keeling et al. (2005), and Levin et al. (2008), respectively. All minerals of bedrock origin are assumed to contain zero ^{14}C and all minerals precipitated in equilibrium with the atmosphere are assumed to have an $F^{14}C$ value of 1.06 (reflecting the modern atmosphere, Levin et al. 2008). Starting conditions for models with unevaporated water (i.e., models 1 and 2) use average values for bedrock calcite at Diavik for the initial values of $\delta^{18}O_{carb}$ (8.69‰) and $\delta^{13}C_{carb}$ (-6.39‰). A measured value for DIC of pond water in the fine PKC at Diavik is

used for $\delta^{13}C_{H_2O}$ (-10.39‰), and a typical value of $\delta^{18}O_{H_2O}$=-10‰ for near surface ground water (Clark and Fritz 1997), are used in models 1 and 2.

Average values for bedrock magnesite at Mount Keith ($\delta^{18}O_{carb}$=13.27‰ and $\delta^{13}C_{carb}$=-4.11‰) are used in models with evaporated water (i.e., models 3 and 4). A measured value for DIC in Tailings Storage Facility 2 (TSF2) at Mount Keith (from Chapter 4) is used for $\delta^{13}C_{H_2O}$ (-7.71‰), and a value of $\delta^{18}O_{H_2O}$=7‰ is assumed for highly evaporated water. This value of $\delta^{18}O_{H_2O}$ is consistent with Raleigh fractionation resulting from evaporation of 70% of a pool of surface water with an initial $\delta^{18}O_{H_2O}$ of 0‰ at 25˚C and 30% relative humidity (Gonfiantini 1986; Clark and Fritz 1997). This value was selected based on (1) data for average humidity from the nearby town of Kalgoorlie, Western Australia (Government of Australia, Bureau of Meteorology 2009), (2) the observation that only 30% of process water deposited to TSF2 is returned for reuse (personal communication, J. Levitt, BHPB), and (3) that desert ground water can be relatively enriched in ^{18}O (e.g., Ma and Yang 2008).

The carbon isotopic composition of magnesite in equilibrium with the atmosphere was calculated (at 25˚C) as

$$\delta^{13}C_{magnesite} \approx 10^3 ln\alpha_{magnesite\text{-}calcite} + 10^3 ln\alpha_{calcite\text{-}CO_2(g)} + \delta^{13}C_{CO_2(g)} \qquad \text{(Eq. 5.1)}$$

using the theoretical fractionation factor of Deines (2004) for $10^3 ln\alpha_{magnesite\text{-}calcite}$, the experimental results of Romanek et al. (1992) for $10^3 ln\alpha_{calcite\text{-}CO_2(g)}$, and using a value of $\delta^{13}C_{CO_2(g)}$ = -8‰ for atmospheric CO_2. Considering direct fractionation between magnesite and atmospheric CO_2 assumes that dissolved inorganic carbon is in exchange equilibrium with the atmosphere (e.g., Dugan and Borthwick 1986) and with secondary Mg-carbonate minerals during precipitation (e.g., Chacko et al. 2001). The fractionation factor for carbon between dypingite and DIC (Chapter 3) was used similarly to calculate an isotopic composition for dypingite/hydromagnesite in equilibrium with the atmosphere. Calculated values are $\delta^{13}C$=3.67‰ for dypingite and $\delta^{13}C$=7.35‰ for magnesite.

In scenarios 1 and 2, model values of $\delta^{18}O$ for secondary minerals were chosen to represent efflorescent Mg-carbonate minerals at Diavik and Mount Keith. An average

value of 20.85‰ from the narrowly distributed $\delta^{18}O$ values for highly pure nesquehonite was taken as representative of secondary Mg-carbonate minerals at Diavik. At Mount Keith, where $\delta^{18}O$ values for secondary hydromagnesite are more variable (Chapter 4), a typical value of 38‰ was used. In addition, an oxygen isotopic fractionation of $10^3\ln\alpha_{magnesite\text{-}hydromagnesite} \approx 1‰$ was used to model precipitation of magnesite using the same approach as for hydrated Mg-carbonate minerals in scenarios 1 and 2. This isotopic separation between magnesite and hydromagnesite is derived from oxygen isotopic fractionation factors from O'Neil and Barnes (1971) for hydromatnesite-H_2O and from Spötl and Burns (1994) for magnesite-H_2O.

In addition to the four models described above, which are used in all three scenarios, two additional models are used in scenario 1. Scenario 1 also describes mechanical mixing between dypingite/hydromagnesite precipitated in equilibrium with the atmosphere and (1) bedrock magnesite and (2) carbonate minerals precipitated in equilibrium with isotopically light C derived from sewage. The isotopically lightest specimen of Group 4 crust from Diavik was chosen to represent the sewage carbonate reservoir. This specimen (06DVK7-crust) is characterized by: $\delta^{18}O$=7.59‰ and $\delta^{13}C$=-26.34‰.

Fractionation factors (used to model scenario 3) are calculated at 25˚C and are as follows: (1) $\Delta^{18}O_{H_2O\text{-}carb}$ = -31.19‰ for hydromagnesite (O'Neil and Barnes 1971) and $\Delta^{18}O_{H_2O\text{-}carb}$ = -32.23‰ for magnesite (Spötl and Burns 1994), (2) $\Delta^{18}O_{H_2O\text{-}CO_2(g)}$ = -9.96‰ calculated as $10^3\ln\alpha_{HCO_3^-(aq)\text{-}H_2O(l)} - 10^3\ln\alpha_{CO_2(g)\text{-}H_2O(l)}$ from Halas and Wolacewicz (1982) and Bottinga (1968), respectively, (3) $\Delta^{13}C_{H_2O\text{-}carb}$ = -3.8‰ for dypingite (using the average value from Chapter 3) and $\Delta^{13}C_{H_2O\text{-}carb}$ = -7.41‰ for magnesite (using fractionation factors from Mook et al. 1974; Romanek et al. 1992; Deines 2004), and (4) $\Delta^{13}C_{H_2O\text{-}CO_2(g)}$ = 7.94‰ using $10^3\ln\alpha_{HCO_3^-(aq)\text{-}CO_2(g)}$ from Mook et al. (1974).

5.6.2 Scenario 1: Mechanical mixing between two reservoirs

Mechanical mixing between two populations of carbonate minerals, precipitated from distinct reservoirs for carbon and oxygen, is modelled using the following equations:

$$\delta^{18}O_{bulk} = \delta^{18}O_{carb1}p + (1-p)\delta^{18}O_{carb2} \quad \text{(Eq. 5.2)}$$

$$\delta^{13}C_{bulk} = \delta^{13}C_{carb1}p + (1-p)\delta^{13}C_{carb2} \quad \text{(Eq. 5.3)}$$

$$F^{14}C_{bulk} = F^{14}C_{carb1}p + (1-p)F^{14}C_{carb2} \quad \text{(Eq. 5.4)}$$

where $\delta^{18}O_{bulk}$, $\delta^{13}C_{bulk}$, and $F^{14}C_{bulk}$ (Eqs. 5.2-5.4) characterize the bulk oxygen and carbon isotopic signature of a geological sample. $\delta^{18}O_{carb1}$, $\delta^{13}C_{carb1}$, $F^{14}C_{carb1}$ characterize the isotopic signature of reservoir 1, and $\delta^{18}O_{carb2}$, $\delta^{13}C_{carb2}$, $F^{14}C_{carb2}$ describe a second reservoir with which the first mixes. The variable *p* is the fraction of carbon in the system input from reservoir 1 and (1-*p*) is the fraction of carbon from reservoir 2. Mixing is modelled between (1) Diavik bedrock calcite and each of secondary magnesite and hydromagnesite/dypingite, (2) Mount Keith bedrock magnesite and each of secondary magnesite and hydromagnesite/dypingite, and (3) carbonate minerals precipitated from Diavik sewage organic matter and each of secondary hydromagnesite/dypingite and magnesite.

5.6.3 Scenario 2: Single-event dissolution and reprecipitation of carbonate minerals

Scenario 2 uses a model for binary mixing in a closed system via water-rock interaction. Both the model and the formalism used here are adapted from Albarède (1995). Because we did not know the initial isotopic ratios of the water from which secondary carbonate minerals formed at Diavik and the other mines, we adapted the model of Albarède (1995) such that we could choose our "water" end member to reflect the isotopic composition of a Mg-carbonate mineral (assumed to have precipitated in equilibrium with the atmosphere). The MATLAB script is available for reference in Appendix A2.

Here, the isotopic signature of the post-reaction mineral is a function of (1) the amount of water introduced to the system, $Q = f_w/f_r$, where f_w and f_r are the fractions of water and rock respectively, (2) the concentrations of the relevant elements in each end-member in the mixing scenario, ${C_1}^O$, ${C_1}^C$, ${C_2}^O$, and ${C_2}^C$, where the superscript indicates the element and the subscript indicates the end-member (1 for bedrock carbonate minerals and 2 for secondary Mg-carbonate minerals), (3) the initial isotopic composition of the reacting mineral, $\delta^{18}O_{1(0)}$, $\delta^{13}C_{1(0)}$, $F^{14}C_{1(0)}$ (using average compositions of calcite

at Diavik and magnesite at Mount Keith, Table 5.4) and the final composition of the reprecipitated mineral, $\delta^{18}O_{2(f)}$, $\delta^{13}C_{2(f)}$, and $F^{14}C_{2(f)}$ (using ideal values for magnesite and dypingite/hydromagnesite in equilibrium with atmospheric CO_2, Table 5.4).

By assuming end-member isotopic compositions for the reprecipitated Mg-carbonate minerals, and by embedding information about fractionation effects in this system into these values, Albarède's (1995) equations for the final (post-reaction) values of $\delta^{18}O_1$, $\delta^{13}C_1$ and $F^{14}C_1$ reduce to

$$\delta^{18}O_1 = \varphi_2{}^{O}\delta^{18}O_{2(f)} + (1-\varphi_2{}^{O})\delta^{18}O_{1(0)} \quad \text{(Eq. 5.5)}$$

$$\delta^{13}C_1 = \varphi_2{}^{C}\delta^{13}C_{2(f)} + (1-\varphi_2{}^{C})\delta^{13}C_{1(0)} \quad \text{(Eq. 5.6)}$$

$$F^{14}C_1 = \varphi_2{}^{C}F^{14}C_{2(f)} + (1-\varphi_2{}^{C})F^{14}C_{1(0)} \quad \text{(Eq. 5.7)}$$

where $\varphi_2{}^{O}$ and $\varphi_2{}^{C}$ are the fractions of total oxygen and carbon (respectively) held by the water from which secondary Mg-carbonate minerals are precipitating. These values are given by the expressions

$$\varphi_2{}^{O} = \frac{Q(C_2{}^{O}/C_1{}^{O})}{Q(C_2{}^{O}/C_1{}^{O})+1} \quad \text{(Eq. 5.8)}$$

$$\varphi_2{}^{C} = \frac{Q(C_2{}^{C}/C_1{}^{C})}{Q(C_2{}^{C}/C_1{}^{C})+1} \quad \text{(Eq. 5.9)}$$

Values of $C_2{}^{O}/C_1{}^{O}$ and $C_2{}^{C}/C_1{}^{C}$ are calculated assuming that the second end-member in the model (i.e., a secondary Mg-carbonate mineral) is precipitated at equilibrium from dissolved species carried by water. The value of $C_2{}^{O}/C_1{}^{O}$ was estimated to be 37.1 for the Diavik model. This value was estimated using the weight percent abundance of oxygen in pure water for $C_2{}^{O}$ and the weight percent abundance of oxygen in a rock containing 5 wt.% calcite for $C_1{}^{O}$. This abundance represents the upper limit to the range of refined abundances for calcite at Diavik (Chapter 2). This approach assumes that only the oxygen from calcite is available for reaction. An estimate for $C_2{}^{C}/C_1{}^{C}$ of 0.0167 was obtained for Diavik using the weight percent abundance of dissolved

inorganic carbon, using a typical concentration of 100 ppm (personal communication, C. English, DDMI), in otherwise pure water for C_2^C and the weight percent abundance of carbon in a rock containing 5 wt.% calcite for C_1^C. The former definition implies (1) that DIC is in exchange equilibrium with the atmosphere and (2) that secondary Mg-carbonate minerals will precipitate from this DIC and dissolved bedrock carbonate minerals under equilibrium conditions. The model for Diavik assumes that Mg is sourced from silicate minerals, but does not account for oxygen isotopic effects of silicate dissolution. Values of C_2^O/C_1^O = 31.2 and C_2^C/C_1^C = 0.0138 were assumed for Mount Keith using the same arguments, except that C_1^O and C_1^C were determined assuming a rock containing 5 wt.% magnesite (in keeping with the estimate for Diavik and the upper end of median values for Mount Keith, Chapter 4). Equations 5.5 to 5.7, for $\delta^{18}O_1$ and $\delta^{13}C_1$, were solved using values for the water-rock ratio, Q, from 0 to 10^4 in increments of 0.05.

5.6.4 Scenario 3: Cyclical dissolution and reprecipitation of carbonate minerals

The third scenario uses a mixing model for cyclical dissolution and reprecipitation of bedrock carbonate minerals from dissolved inorganic carbon (DIC) in a system with access to atmospheric CO_2 (MATLAB script is available in Appendix A2). Here, the isotopic signature of the post-reaction mineral is obtained by solving a system of six linear equations that describe the initial isotopic composition of the geological system and the fractionation of stable carbon and oxygen isotopes within it:

$$\delta^{18}\mathrm{O}_{\mathrm{bulk}} = \sum_i^m X_{O_i}\delta^{18}\mathrm{O}_i = \left(\frac{n_{O_{H_2O}}}{n_{O_{bulk}}}\right)\delta^{18}\mathrm{O}_{\mathrm{H_2O}} + \left(\frac{n_{O_{carb}}}{n_{O_{bulk}}}\right)\delta^{18}\mathrm{O}_{\mathrm{carb}} + \left(\frac{n_{O_{CO_2(g)}}}{n_{O_{bulk}}}\right)\delta^{18}\mathrm{O}_{\mathrm{CO_2(g)}} \quad \text{(Eq. 5.10)}$$

$$\delta^{13}\mathrm{C}_{\mathrm{bulk}} = \sum_i^m X_{C_i}\delta^{13}\mathrm{C}_i = \left(\frac{n_{C_{H_2O}}}{n_{C_{bulk}}}\right)\delta^{13}\mathrm{C}_{\mathrm{H_2O}} + \left(\frac{n_{C_{carb}}}{n_{C_{bulk}}}\right)\delta^{13}\mathrm{C}_{\mathrm{carb}} + \left(\frac{n_{C_{CO_2(g)}}}{n_{C_{bulk}}}\right)\delta^{13}\mathrm{C}_{\mathrm{CO_2(g)}} \quad \text{(Eq. 5.11)}$$

$$\Delta^{18}\mathrm{O}_{\mathrm{H_2O-carb}} = \delta^{18}\mathrm{O}_{\mathrm{H_2O}} - \delta^{18}\mathrm{O}_{\mathrm{carb}} \quad \text{(Eq. 5.12)}$$

$$\Delta^{18}\mathrm{O}_{\mathrm{H_2O-CO_2(g)}} = \delta^{18}\mathrm{O}_{\mathrm{H_2O}} - \delta^{18}\mathrm{O}_{\mathrm{CO_2(g)}} \quad \text{(Eq. 5.13)}$$

$$\Delta^{13}\mathrm{C}_{\mathrm{H_2O-carb}} = \delta^{13}\mathrm{C}_{\mathrm{H_2O}} - \delta^{13}\mathrm{C}_{\mathrm{carb}} \quad \text{(Eq. 5.14)}$$

$$\Delta^{13}\mathrm{C}_{\mathrm{H_2O-CO_2(g)}} = \delta^{13}\mathrm{C}_{\mathrm{H_2O}} - \delta^{13}\mathrm{C}_{\mathrm{CO_2(g)}} \quad \text{(Eq. 5.15)}$$

$\delta^{18}O_{bulk}$ and $\delta^{13}C_{bulk}$ (Eqs. 5.10 and 5.11) characterize the bulk oxygen and carbon isotopic signature of the reacting geological system. $\delta^{18}O_{H_2O}$, $\delta^{18}O_{carb}$, and $\delta^{18}O_{CO_2(g)}$, are the oxygen isotopic compositions for liquid water, the carbonate mineral precipitating from the system (either magnesite or a hydrated Mg-carbonate mineral), and gaseous CO_2, respectively. $\delta^{13}C_{H_2O}$ is the carbon isotopic composition of liquid water or, more precisely, the carbon isotopic composition of HCO_3^-(aq), which is the dominant DIC species at near-neutral to basic pH (e.g., Faure 1986). $\delta^{13}C_{carb}$ and $\delta^{13}C_{CO_2(g)}$ are the carbon isotopic concentrations for the carbonate mineral precipitating from the system (either magnesite or a hydrated Mg-carbonate mineral) and gaseous CO_2, respectively. Values of n_O and n_C are molar concentrations of oxygen and carbon in the various components of the system and $n_{O_{bulk}}$ and $n_{C_{bulk}}$ are values for total molar concentrations of oxygen and carbon. Equations 5.12 through 5.15 are isotopic fractionation factors for oxygen and carbon isotopes between the components input to the system and are listed in Table 5.4.

Starting inputs are assumed to be 0.100 g of DIC in isotopic equilibrium with the atmosphere (a quantity consistent with measurements from Mount Keith and Diavik, personal communication, C. English, DDMI, and J. Levitt, BHBP), 4.000 g of dissolved Mg (consistent with the highest concentrations measured in tailings water at Mount Keith), and 1000 g of water. The size of the system is constrained by the mass of water (i.e., 1000 g or 1.000 L). Conditions built into this model assume (1) that magnesite or a hydrated Mg-carbonate mineral will precipitate out of solution when a concentration of 4.000 g/L of Mg is reached and (2) that corresponding molar amounts of carbon and oxygen are present in solution strictly as a result of the dissolution of bedrock carbonate minerals. In the case of Mount Keith, this implies that mined bedrock magnesite is the sole source of Mg and provides the bulk of dissolved inorganic carbon. At Diavik, where magnesite is absent, this implies dissolution of Mg-silicate minerals and bedrock calcite (although the oxygen isotopic effect of silicate dissolution is not considered by this model). During carbonate dissolution and reprecipitation, one mole of atmospheric CO_2 is drawn into solution for every mole of mineral carbonate dissolved (Holland et al. 1964; Drever 1982) and one mole of CO_2 is released back to the atmosphere when new carbonate minerals are precipitated. Thus, a corresponding molar quantity of atmospheric

carbon (and twice this amount for oxygen) is drawn into solution to match the concentration of carbon that results from dissolution of carbonate minerals.

Models were run for eight cycles, using the same starting concentrations at each step. After each cycle, the values solved for $\delta^{18}O_{H_2O}$, $\delta^{18}O_{carb}$, and $\delta^{18}O_{CO_2(g)}$, $\delta^{13}C_{H_2O}$, $\delta^{13}C_{carb}$, and $\delta^{13}C_{CO_2(g)}$ were used to determine $\delta^{18}O_{bulk}$ and $\delta^{13}C_{bulk}$ for the next cycle of dissolution and reprecipitation. Initial values are given in Table 5.4.

Radiocarbon values for the system were estimated at each cycle using a method adapted from Polach and Golson (1966). The fraction of modern carbon after *n* cyles of dissolution and reprecipitation is calculated as

$$F^{14}C = F^{14}C_0\left(1 - \frac{1}{2^n}\right) \qquad \text{(Eq. 5.16)}$$

where $F^{14}C_0$ is the fraction modern carbon value for the year of sample collection (i.e., 1.06 in 2006, Levin et al. 2008).

5.6.5 Model results

5.6.5.1 Results for scenario 1: Mechanical mixing

Scenario 1 results are plotted for (1) mechanical mixing between bedrock carbonate minerals and Mg-carbonate minerals precipitated in equilibrium with the atmosphere and (2) mechanical mixing between carbonate minerals precipitated in equilibrium with each of sewage organic matter and atmospheric CO_2 (Fig. 5.5). Model trends plot as lines between endmember isotopic compositions that represent specific reservoirs for carbon and oxygen. Models for mixing between bedrock carbonate minerals and secondary hydromagnesite/dypingite give similar values of $\delta^{18}O$ as those for mixing between bedrock carbonate minerals and secondary magnesite. This similarity results from the small oxygen isotopic separation between hydromagnesite and magnesite. Because there is a larger stable isotopic separation in carbon between dypingite and magnesite, the models for hydromagnesite/dypingite and magnesite diverge from each other as they approach 100% abundance of atmospheric C (Fig. 5.5a).

The same divergence in $\delta^{13}C$ is seen in the mixing trends between the organic and atmospheric reservoirs. The four models for mixing between bedrock carbonate minerals and Mg-carbonate minerals have end members with either $F^{14}C=0$ or $F^{14}C=1.06$ (Fig. 5.5b). As a result, $F^{14}C$ values vary identically with the percent of Mg-carbonate that is in equilibrium with atmospheric CO_2, in the mixtures. The models for mixing of sewage derived carbonate minerals with Mg-carbonate minerals in equilibrium with atmospheric CO_2 remain constant in $F^{14}C$, but vary across a broad range of $\delta^{13}C$ values (Fig. 5.5b).

5.6.5.2 Results for scenario 2: Single-event dissolution and reprecipitation

Both dissolution/reprecipitation models (i.e., scenarios 2 and 3) give hyperbolic trends in $\delta^{18}O$-$\delta^{13}C$-space and linear trends between endmember compositions in $\delta^{13}C$-$F^{14}C$-space (Figs. 5.6 and 5.7). As a consequence, dissolution and reprecipitation of secondary Mg-carbonate minerals can be expected to produce similar trends in isotopic data for either mechanism of dissolution and reprecipitation.

In scenario 2, for single-step batch reaction in a closed system, large values of *Q*, the water-rock ratio, are required on approach to the horizontal asymptote of the mixing curves in $\delta^{18}O$-$\delta^{13}C$-space (Fig. 5.6a). In all models, values of *Q* in excess of 1 still plot on the upward trend in $\delta^{18}O$, and show no change in $\delta^{13}C$ relative to the bedrock carbonate endmember. Values of *Q* in excess of 1000 are required to approach the isotopic composition of the secondary Mg-carbonate endmembers. Evidently, closed-system batch precipitation of Mg-carbonate minerals under the conditions input to the first model require very large water-rock ratios for isotopic mixing trends to become evident from plots of $\delta^{18}O$ versus $\delta^{13}C$. Increasing the initial DIC content to values in excess of 1000 ppm diminishes the curvature of the hyperbolic mixing trends and enables heavier isotopic signatures in the vicinity of the secondary Mg-carbonate end-member to be attained using much smaller water-rock ratios (i.e., $\delta^{13}C > 7‰$ is obtained with a water-rock ratio of less than 50:1 for a concentrations in excess of 1000 ppm). However, DIC concentrations significantly in excess of 100 ppm are seldom observed at Diavik and Mount Keith. Although very high concentrations may exist locally and for short durations, they have not been measured and would be unlikely to persist within large volumes of a tailings storage facility in order to feed such a batch reaction. The linear

model trends in $\delta^{13}C$-$F^{14}C$-space suggest that secondary Mg-carbonate minerals precipitated with Q=1 will have an $F^{14}C$ value much less than 1 (Fig. 5.6b). In this scenario, DIC is in exchange equilibrium with the atmosphere and, other than bedrock carbonate minerals, is the only other source of carbon available during precipitation of new minerals. Because DIC is the only source of modern atmospheric CO_2, values of Q on the order of 100 are required to produce secondary Mg-carbonate minerals with $F^{14}C>0.5$ and values of Q in excess of 1000 are needed to precipitate Mg-carbonate minerals with $F^{14}C>1$.

5.6.5.3 Results for scenario 3: Cyclical dissolution and reprecipitation

Scenario 3 (for cyclic dissolution/reprecipitation in a system open to the atmosphere) produces similar model trends in $\delta^{18}O$-$\delta^{13}C$-space and $\delta^{13}C$-$F^{14}C$-space to those obtained from scenario 2. Isotopic compositions for eight cycles of dissolution and reprecipitation are plotted in Figures 5.7. Because isotopic compositions were modelled for discrete cycles, the curvature of the model trends in $\delta^{18}O$-$\delta^{13}C$-space is not known (Fig. 5.7a). Nonetheless, for ease of use, hyperbolae with the same curvature as the model results from scenario 2 are displayed in Figure 5.7a and are overlain by results for scenario 3.

In all models for scenario 3, the water-dominated $\delta^{18}O$ values have plateaued within one cycle of dissolution and reprecipitation (Fig. 5.7a). Although the upper limit to equilibrium oxygen isotopic fractionation is achieved rapidly, it takes approximately eight cycles of dissolution and reprecipitation to approach the limit to $\delta^{13}C$ under the conditions built into this model. It is notable that after three cycles of dissolution and reprecipitation, magnesite formed in equilibrium with the atmosphere at 25˚C will have a stable carbon and oxygen isotopic signature that is indistinguishable from that of magnesite formed at 40˚C from a silicate source for cations and a strictly atmospheric source for carbon. This is, however, not the case in $\delta^{13}C$-$F^{14}C$-space. When the same model lines are plotted in $\delta^{13}C$-$F^{14}C$-space (Fig. 5.7b), thrice-recycled bedrock carbonate minerals will plot outside of the field defined by magnesite precipitated in equilibrium with the atmosphere. Model results suggest that cyclical dissolution and reprecipitation of bedrock carbonate minerals in an open system is able to produce secondary Mg-

carbonate minerals with a modern radiocarbon signature (i.e., $F^{14}C>1$) after five cycles of dissolution and reprecipitation. Within eight cycles, recycled bedrock carbonate minerals may be indistinguishable from secondary minerals precipitated in equilibrium with atmospheric CO_2.

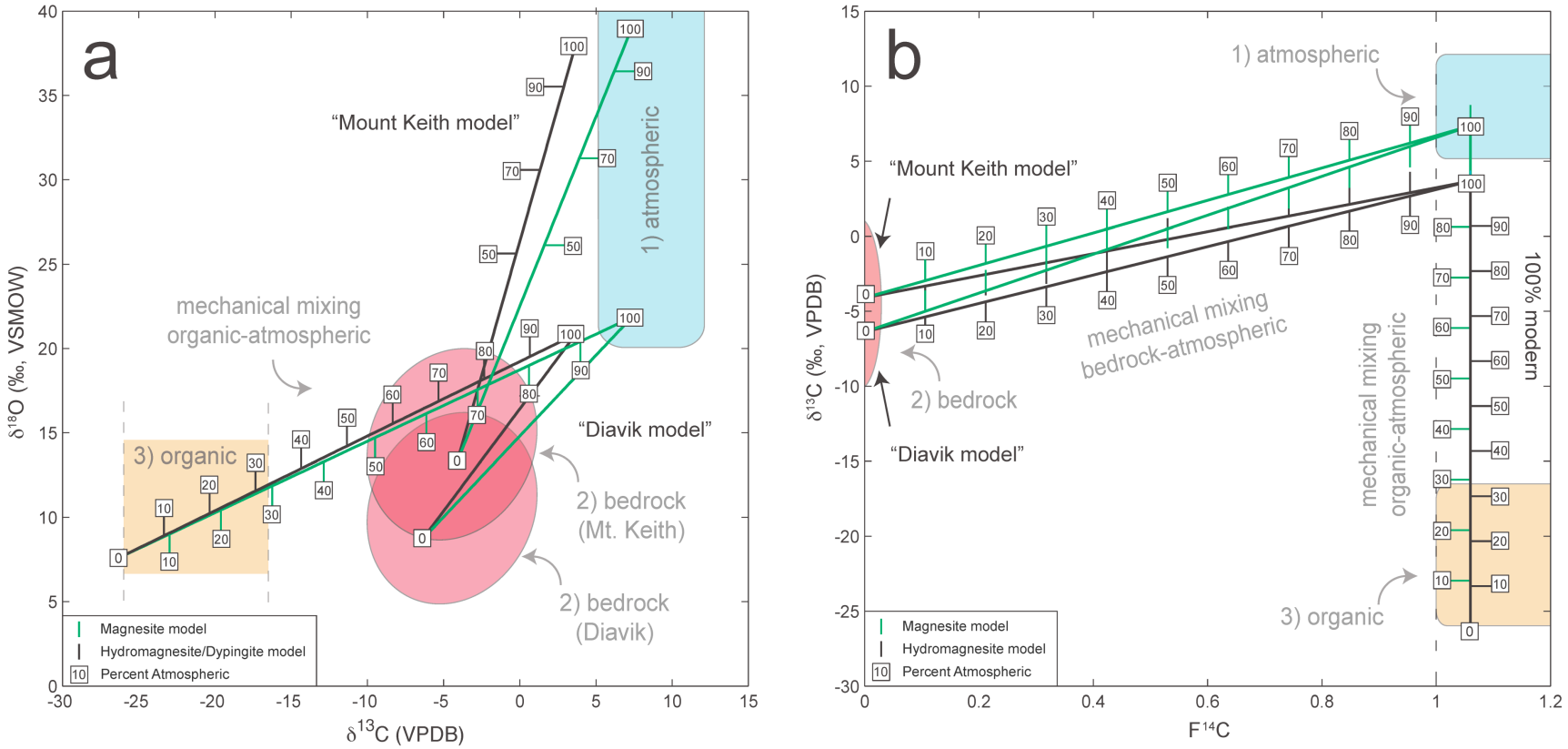

Figure 5.5: Models for scenario 1, mechanical mixing of carbonate minerals from two distinct reservoirs. (a) Models in stable oxygen and carbon isotope space and (b) in stable carbon isotope and radiocarbon space. Shaded, numbered fields indicate the ranges of values for carbonate minerals in equilibrium with specific reservoirs for carbon and oxygen. A number within a box indicates the percent of atmospheric carbon within a sample plotting at a specific point.

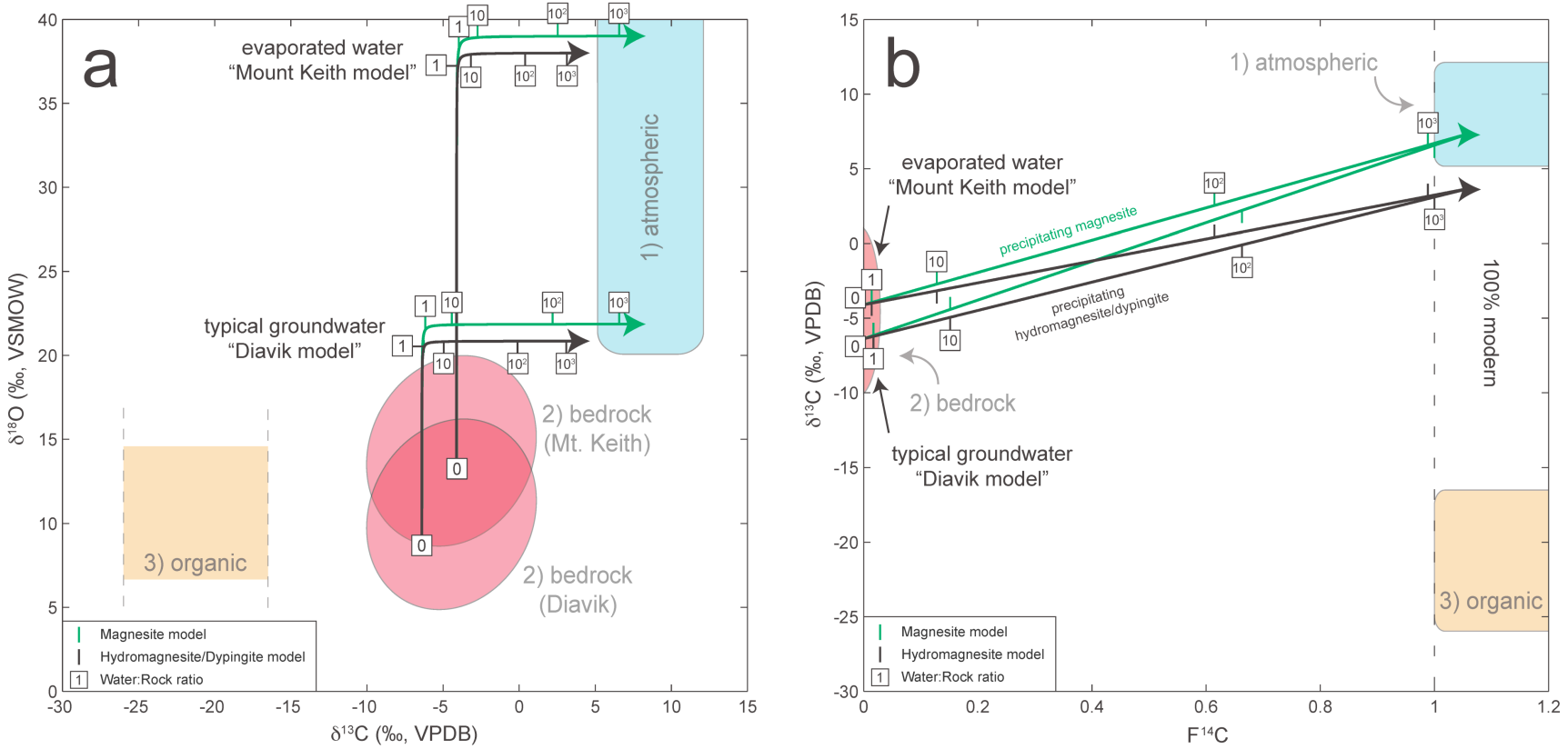

Figure 5.6: Models for scenario 2, batch dissolution and reprecipitation of carbonate minerals with dependence upon the water-rock ratio. (a) Models in stable oxygen and carbon isotope space and (b) in stable carbon isotope and radiocarbon space. Shaded, numbered fields indicate the ranges of values for carbonate minerals in equilibrium with specific reservoirs for carbon and oxygen. A number within a box indicates the water-rock ratio required to produce a sample plotting at that point.

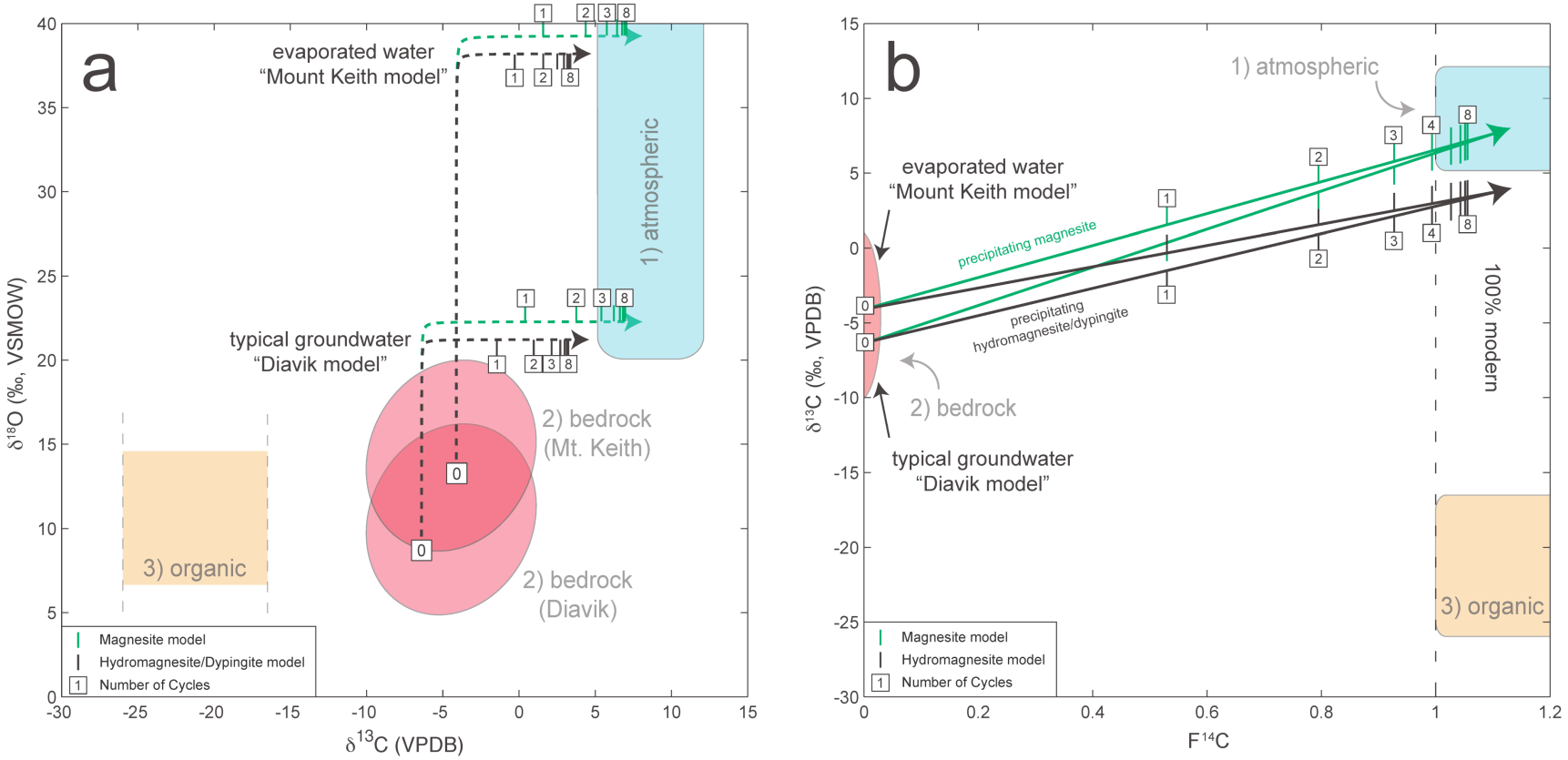

Figure 5.7: Models for scenario 3, cyclic dissolution and reprecipitation of carbonate minerals. (a) Models in stable oxygen and carbon isotope space and (b) in stable carbon isotope and radiocarbon space. Shaded, numbered fields indicate the ranges of values for carbonate minerals in equilibrium with specific reservoirs for carbon and oxygen. A number within a box indicates the number of dissolution/reprecipitation cycles required to produce a sample plotting at that point.

5.7 Application of mixing scenarios to Diavik

Modelled trends for mixing scenarios 1-3 are overlaid on plots of isotopic data for Diavik in Figures 5.8-5.10.

5.7.1 Application of scenario 1 to Diavik

In Figure 5.8, mechanical mixing is modelled between bedrock calcite and secondary Mg-carbonate minerals, and secondary carbonate minerals precipitated from sewage organic matter and secondary Mg-carbonate minerals. In $\delta^{18}O$-$\delta^{13}C$-space, data for the majority of calcite-contaminated specimens of nesquehonite fall very near to the trends for mechanical mixing between the bedrock and atmospheric reservoirs (Fig. 5.8a). According to the model trend, these samples contain between 70% and 100% carbon derived from a bedrock carbonate source. The specimen most heavily contaminated by calcite, 06DVK36-bulk, plots closest to the bedrock endmember of the model. The next most heavily contaminated specimen, 06DVK39, plots further from the bedrock endmember, and the least contaminated of these specimens, 06DVK37-bulk-crust, plots the furthest from the bedrock endmember.

Almost all of the samples of secondary Na and Ca-carbonate minerals and the highly pure samples of nesquehonite fall near the mechanical mixing trend between the organic and atmospheric reservoirs (Fig. 5.8a). This model suggests that secondary carbonate minerals formed near sewage deposits (i.e., the majority of the secondary mineral specimens) may represent mechanical mixtures, of separate mineral populations, that have precipitated from either atmospheric CO_2 or sewage organic matter. Six specimens of secondary minerals that were analyzed for radiocarbon content plot along the same trend for sewage-atmospheric mixing when viewed in $\delta^{13}C$-$F^{14}C$-space (Fig. 5.8b). Also, approximately 10% of the nesquehonite, in the three specimens analyzed for $F^{14}C$, could be interpreted as having precipitated from ^{14}C-free bedrock calcite (Fig. 5.8b).

Mechanical mixing provides a good explanation for some of the obviously calcite-contaminated specimens of nesquehonite. However, there is little to no mineralogical support for mechanical mixing for most of the remaining specimens of

secondary minerals. For instance, many data for specimens of highly pure nesquehonite are consistent with mechanical mixing between sewage-derived Na and Ca-carbonate minerals and nesquehonite precipitated from atmospheric CO_2, even though they contain no Na or Ca-carbonate minerals. The same problem exists for the Na- and Ca-carbonate minerals. Only two of the specimens that fall on this mixing trend, 06DVK7-crust and 06DVK11-isolate, contain any nesquehonite. In spite of this, these two samples fall on opposite ends of the mixing trend: 06DVK11-isolate is enriched in ^{13}C above all other specimens of Na and Ca-carbonate minerals and 06DVK7-crust is the most depleted in ^{13}C of these specimens.

Mechanical mixing between two isotopically distinct populations of minerals does not give a satisfactory description of the $\delta^{18}O$ and $\delta^{13}C$ data for most samples of nesquehonite and Na and Ca-carbonate minerals.

5.7.2 Application of scenario 2 to Diavik

The model curves for scenario 2, batch dissolution and reprecipitation of bedrock calcite, are plotted with data from Diavik in Figure 5.9. The models for single-event dissolution of bedrock calcite and reprecipitation of secondary Mg-carbonate minerals indicate that very large water-rock ratios are required to produce the data from Diavik. Values of Q between 10 and 1000 must be invoked to explain precipitation of most specimens of nesquehonite via single-event dissolution/reprecipitation (Figs. 5.9a and 5.9b). Furthermore, values of Q in excess of 1000 are required to explain the stable isotopic data for the specimens of nesquehonite that are most enriched in ^{13}C (Fig. 5.9a).

The water-rock ratio of the storage facility for fine processed kimberlite (fine PKC) at Diavik is not known. However, the water-rock ratio of Tailings Storage Facility 2 (TSF2) at Mount Keith can be estimated. Both mines, at Diavik and Mount Keith, employ similar technology for deposition of tailings as slurry and reclamation of process water from tailings storage facilities. It is not unreasonable to expect that the water-rock ratio in the fine PKC at Diavik will be of a similar order to that in TSF2 at Mount Keith. Values for total water consumption and tailings production at Mount Keith are available for the years 2000 to 2004 (BHP Billiton 2005). Assuming that all water used at Mount Keith is ultimately deposited to TSF2, water-tailings ratios between 0.92 and 1.07 result

for the years between 2000 and 2004. Because the ratio of water to magnesite (at an abundance of 5 wt.%) was used to model scenario 2 for Mount Keith, the water rock ratio is estimated to be between 18.4 and 21.4. This assumption undoubtedly gives an overestimate for the water-rock ratio at Mount Keith, but it implies that water-rock ratios on the order of 20 can be expected within the fine PKC at Diavik. This water-rock ratio is consistent with isotopic data for one specimen of nesquehonite (Fig. 5.9a). The remaining data require significantly higher water-rock ratios. Therefore, scenario 2 is largely inconsistent with isotopic results from Diavik and the expected water-rock ratio of the fine PKC.

5.7.3 Application of scenario 3 to Diavik

Model curves for scenario 3, cyclic dissolution/reprecipitation of bedrock calcite, are plotted with data from Diavik in Figure 5.10. Most of the data points for nesquehonite (barring data for those samples contaminated by primary calcite) are bracketed by the reprecipitation trends for magnesite and hydromagnesite/dypingite (Fig. 5.10a). Stable isotopic data for specimens of nesquehonite that plot within the bedrock reservoir field do not fall near the model trends for scenario 3. Stable isotopic data for most specimens of nesquehonite are consistent with less than one to greater than eight cycles of dissolution and reprecipitation. However, the radiocarbon data for nesquehonite from Diavik (Fig. 5.10b) do not follow the model trends as faithfully as the stable isotopic data. Instead, radiocarbon data conflict with results in $\delta^{18}O$-$\delta^{13}C$-space, and are consistent with between 3 and 4 cycles of dissolution and reprecipitation.

Additionally, the secondary carbonate minerals collected from the fine PKC were located near active tailings discharge points and locations along the service road from which sewage from the mine camp is deposited. It is unlikely that these active surfaces had been left to weather for very long at the time of sampling. It should be considered that the process of dissolving and reprecipitating nesquehonite in situ, and in some cases in excess of eight times, may not have had sufficient time to occur between deposition of fresh tailings and sampling of nesquehonite from the surface of those tailings.

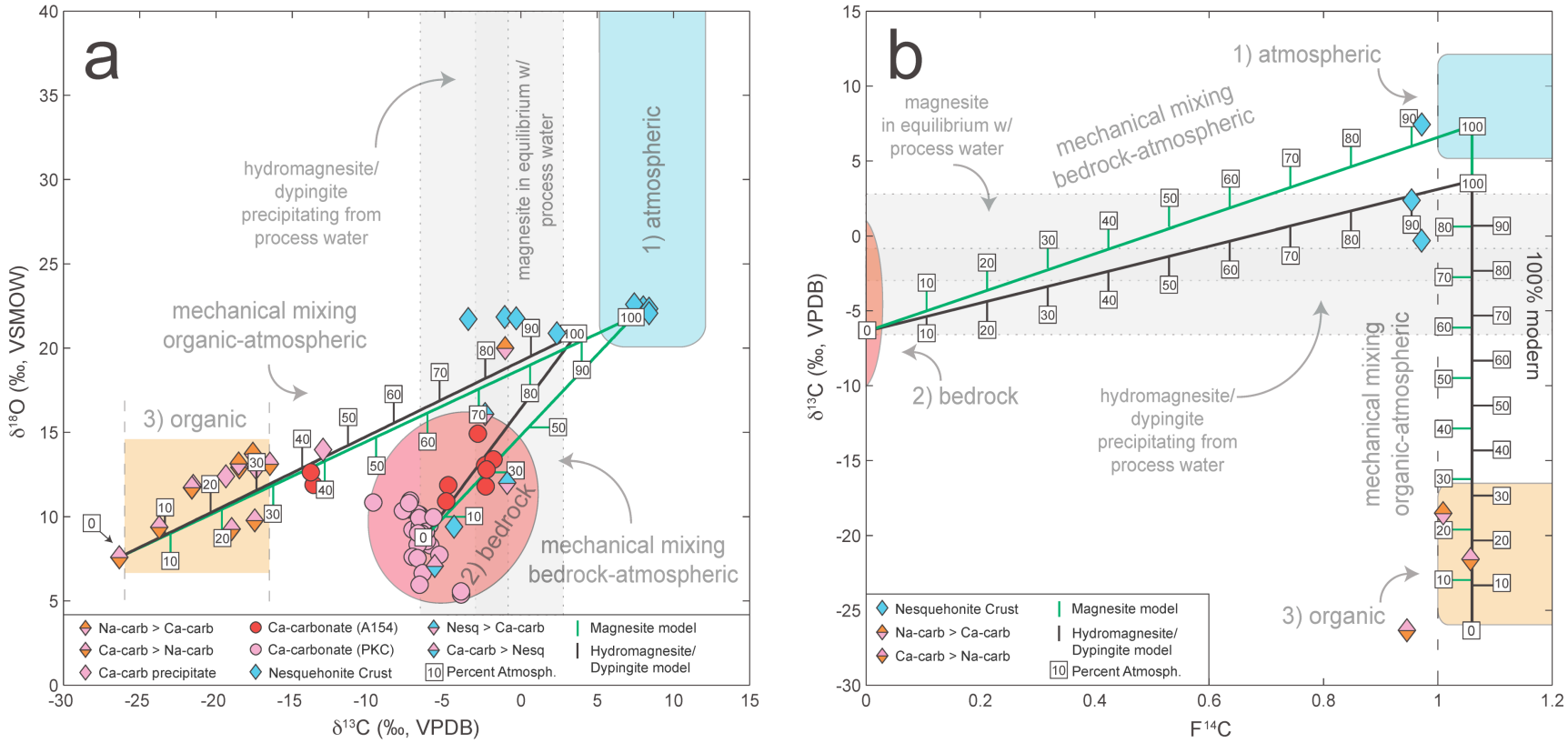

Figure 5.8: Stable isotope and radiocarbon data from Diavik overlain by modelled predictions for scenario 1 (mechanical mixing). Stable carbon and oxygen isotope data are given in (a) and stable carbon and radiocarbon ($F^{14}C$) isotope data are given in (b). Shaded, numbered fields indicate the ranges of values for carbonate minerals in equilibrium with specific reservoirs for carbon and oxygen. A number within a box indicates the percent of atmospheric carbon within a sample plotting at a specific point.

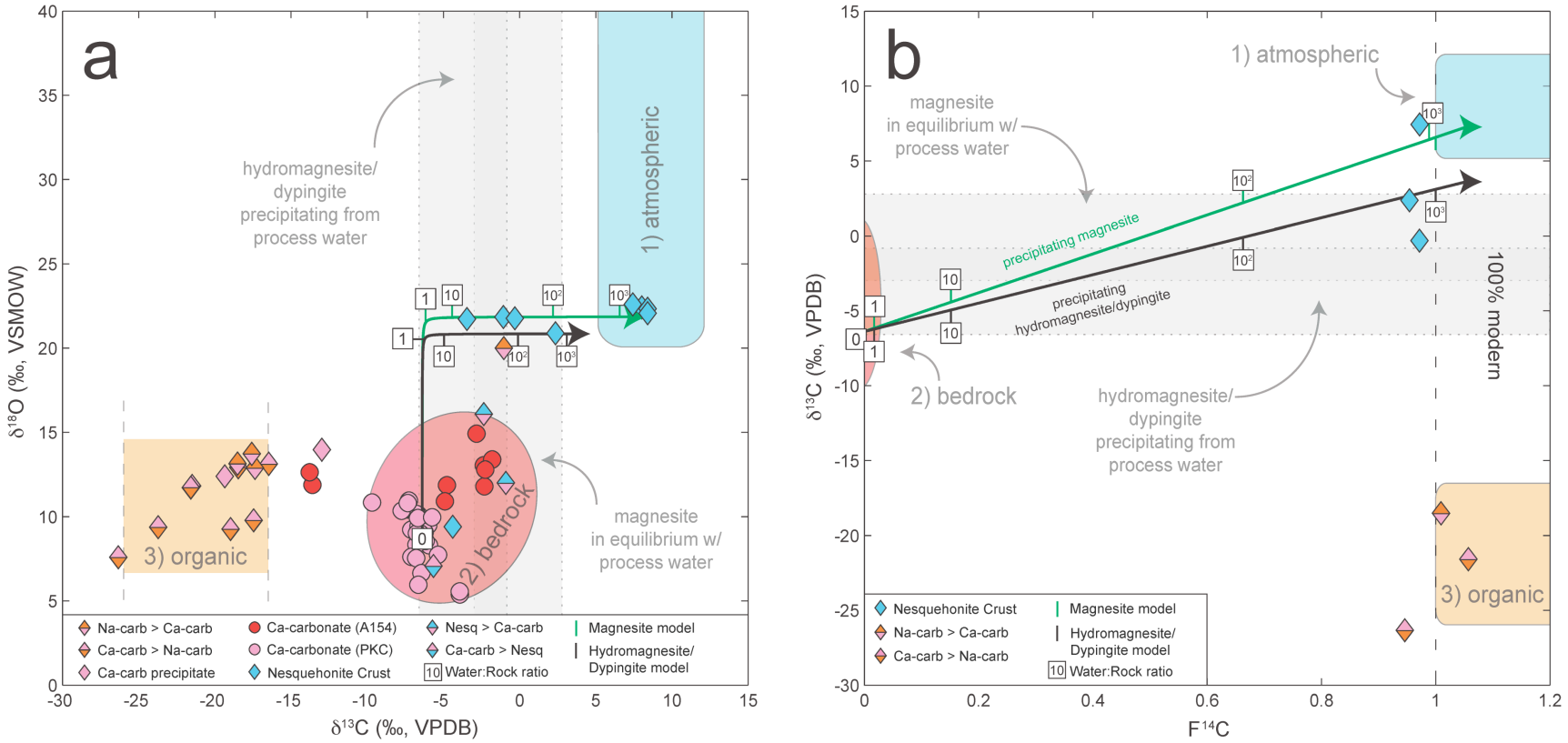

Figure 5.9: Stable isotope and radiocarbon data from Diavik overlain by modelled predictions for scenario 2 (batch dissolution/reprecipitation). Stable carbon and oxygen isotope data are given in (a) and stable carbon and radiocarbon ($F^{14}C$) isotope data are given in (b). In most cases, measurement errors are smaller than the symbols employed. Shaded, numbered fields indicate the ranges of values for carbonate minerals in equilibrium with specific reservoirs for carbon and oxygen. A number within a box indicates the water-rock ratio required to produce a sample plotting at that point.

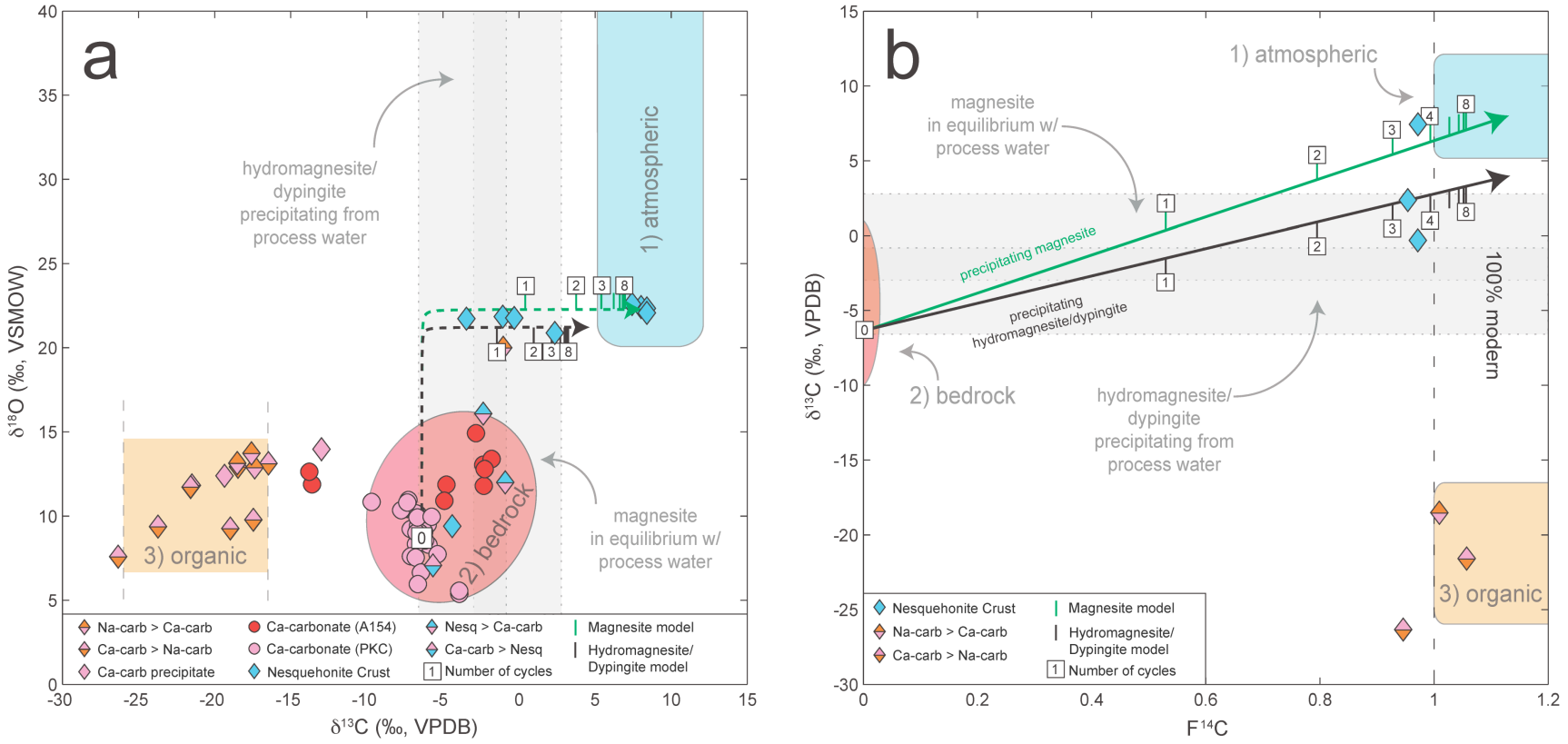

Figure 5.10: Stable isotope and radiocarbon data from Diavik overlain by modelled predictions for scenario 3 (cyclic dissolution/reprecipitation). Stable carbon and oxygen isotope data are given in (a) and stable carbon and radiocarbon ($F^{14}C$) isotope data are given in (b). In most cases, measurement errors are smaller than the symbols employed. Shaded, numbered fields indicate the ranges of values for carbonate minerals in equilibrium with specific reservoirs for carbon and oxygen. A number within a box indicates the number of dissolution/reprecipitation cycles required to produce a sample plotting at that point.

5.7.4 Implications of modelled results for CO_2 sequestration at Diavik

One model from scenario 1, for mechanical mixing between isotopically distinct populations of minerals, is consistent with a known instance of mechanical mixing (i.e., contamination of nesquehonite by calcite). However, the mass-balance predicted by the remaining models is not supported by mineralogical observations. The dissolution/reprecipitation models produced for scenarios 2 and 3 imply that dissolved C from a Ca-carbonate mineral, calcite, is being recycled into a secondary Mg-carbonate mineral, nesquehonite. Secondary Ca-bearing minerals are relatively uncommon at the surface of the fine PKC and have not been observed at depth within the tailings. Nesquehonite is also uncommon in the fine PKC, but it does persist within deep tailings at trace amounts (Chapter 2). Primary Mg-carbonate minerals (e.g., dolomite) are rare at Diavik. The common presence of trace amounts of nesquehonite and Mg-sulphate minerals in the fine PKC suggests that they precipitated from a more common mineral or minerals. Furthermore, textural relationships between nesquehonite and primary Mg-silicate minerals (Fig. 5.2) suggest that silicate minerals are the source of Mg in secondary minerals.

Forsterite and serpentine (predominantly lizardite) comprise 76 to 93 wt.% of the fine processed kimberlite tailings at Diavik (Chapter 2). Contrastingly, calcite has only been found at abundances less than 5 wt.%. There is no trend in the Rietveld refinement data from Chapter 2 to suggest that a significant amount of calcite is being dissolved within the fine PKC at Diavik. Under similar pH conditions, and temperature conditions more beneficial to mineral weathering, bedrock carbonate minerals from the Mount Keith Nickel Mine show no evidence of dissolution (Chapter 4). Multiple lines of evidence suggest that dissolution of bedrock calcite is unlikely to be the main source of C mineralized as nesquehonite at Diavik: (1) contradictory radiocarbon and stable isotopic data, (2) collection of secondary minerals from active surfaces in the fine PKC, (3) the lack of quantitative mineralogical evidence for calcite dissolution, and (4) high abundance non-carbonate sources of Mg.

None of the three scenarios, which assume isotopic equilibrium, is sufficient to describe the stable isotopic and radiocarbon data for secondary nesquehonite at Diavik. The only remaining explanation for these data is the simplest one proposed: That most

occurrences of nesquehonite are precipitating in equilibrium with process water DIC (as suggested in subsection 5.5.1.3), which is out of isotopic exchange equilibrium with the atmosphere. Stable and radiogenic isotope data from Diavik are consistent with observations (Chapter 3), which indicate that kinetic diffusion fractionation can produce isotopically depleted DIC and carbonate minerals from an atmospheric source of CO_2. Only the radiocarbon data for Diavik are able to distinctly and easily fingerprint atmospheric CO_2 in nesquehonite (and Na and Ca-carbonate minerals). Notably, in the case of sample 06DVK39, equilibrium precipitation from atmospheric CO_2 did occur. Sample 06DVK39, which produced the only aliquots of nesquehonite with $\delta^{13}C$ values consistent with equilibrium precipitation from atmospheric CO_2, was collected further from the fine PKC pond than any other sample of nesquehonite. This sample was likely isolated from the DIC pool and may have received a greater proportion of DIC from rainwater than any of the other samples.

5.8 Carbon fingerprinting in ultramafic mine tailings

5.8.1 The Mount Keith Nickel Mine

Stable and radiogenic isotope data for samples of tailings from Mount Keith (Chapter 4) are replotted with model results from mixing scenarios 1 to 3 in Figures 5.11 through 5.13.

Model lines from scenario 1, for mechanical mixing between bedrock magnesite and each of atmospheric hydromagnesite and magnesite, are plotted in Figure 5.11. The stable oxygen isotopic data, for CO_2 selectively extracted from magnesite and hydromagnesite, fall at opposite ends of the mixing trends between the bedrock and atmospheric reservoirs (Fig. 5.11a). Analyses for bulk carbonate minerals (i.e., tailings containing bedrock magnesite, dolomite, calcite, and hydrotalcite-group minerals plus secondary hydromagnesite) span the range between these endmember populations. Rietveld refinement results (Chapter 4), for the relative amount of CO_2 contributed by hydromagnesite and bedrock carbonate minerals, are broadly consistent with predictions made by the model for mechanical mixing. The stable carbon isotope data are more in

keeping with the model for hydromagnesite/dypingite than that for magnesite. However, the data for Mount Keith span a much smaller range of $\delta^{13}C$ values than predicted by either model (Fig. 5.11a). None of the data for recently precipitated hydromagnesite at Mount Keith plot within the field defined for Mg-carbonate minerals precipitated in equilibrium with the atmosphere. However, $\delta^{13}C$ data for hydromagnesite are broadly consistent with precipitation from DIC in the process water from the tailings storage facility at Mount Keith (as described in Chapter 4). The same data, plotted in $\delta^{13}C$-$F^{14}C$-space (Fig. 5.11b), give similar results in that hydromagnesite appears to be precipitating in equilibrium with process water DIC and out of equilibrium with the atmosphere. Also, the same mechanical mixing trend between bedrock magnesite and hydromagnesite appears in $\delta^{13}C$-$F^{14}C$-space, and it remains offset from the model lines.

In Figure 5.12, modelled results for scenario 2, single-event dissolution/ reprecipitation, are plotted with isotope data from Mount Keith. In $\delta^{18}O$-$\delta^{13}C$-space, the models imply that nearly half of the stable isotopic data for hydromagnesite were produced by reactions with water-rock ratios between 10-1000 (Fig. 5.12a). Water-rock ratios of at least 100 must be invoked to produce the large values of $F^{14}C$ observed for hydromagnesite in Figure 5.12b. As mentioned in subsection 5.7.2, the water-rock ratio in TSF2 at Mount Keith is at most 21.4. Therefore, most isotopic data from Mount Keith are inconsistent with single-event dissolution of magnesite and reprecipitation of hydromagnesite.

Model results for scenario 3, cyclic dissolution/reprecipitation of carbonate minerals, are plotted with data from Mount Keith in Figure 5.13. According to the model lines for scenario 3, stable carbon and oxygen isotope data reflect less than one cycle of dissolution and reprecipitation of secondary minerals from bedrock magnesite (Fig. 5.13a). In $\delta^{13}C$-$F^{14}C$-space, the $F^{14}C$ data for hydromagnesite from Mount Keith are consistent with no less than 1 cycle of dissolution and reprecipitation and most of the data are consistent with model predictions for four to eight cycles of dissolution and reprecipitation (Fig. 5.13b). Once again, the radiocarbon data and the stable isotopic data give mutually conflicting results when viewed in light of the dissolution/reprecipitation models. Post-deposition, the hydromagnesite within these Mount Keith mine tailings had little exposure to process water and meteoric precipitation, significantly reducing

opportunities for carbonate mineral recycling. Also, precipitation of hydrous, basic Mg-carbonates, like hydromagnesite and dypingite, is a slow process (Chapter 3). On the basis of these field and laboratory observations, is it very unlikely that hydromagnesite could have dissolved and reprecipitated fully from these samples on the order of eight times – in some cases within a matter of weeks to months between deposition and sampling.

Furthermore, Rietveld refinement results for Mount Keith tailings show no evidence of bedrock carbonate mineral dissolution (Chapter 4). The same Rietveld refinement results show a decrease in the abundance of Mg-rich serpentine minerals and brucite with a concurrent increase in the abundance of secondary hydromagnesite (Chapter 4). It is clear from the results of Chapter 4 that bedrock carbonate minerals are not the primary source of carbon in secondary hydromagnesite at Mount Keith. As a consequence, the two dissolution/reprecipitation scenarios may be ruled out as mechanisms by which hydromagnesite forms at this site. And, as discussed in Chapter 4, it is probable that this mechanical mixing trend is an artefact of the method used for selective extraction of CO_2.

The equilibrium isotopic mixing models are insufficient to explain the isotopic data for Mount Keith. Therefore, the conclusion reached in Chapter 4 still provides the best explanation: Secondary hydromagnesite precipitates in isotopic exchange equilibrium with a DIC pool that is out of equilibrium with atmospheric CO_2.

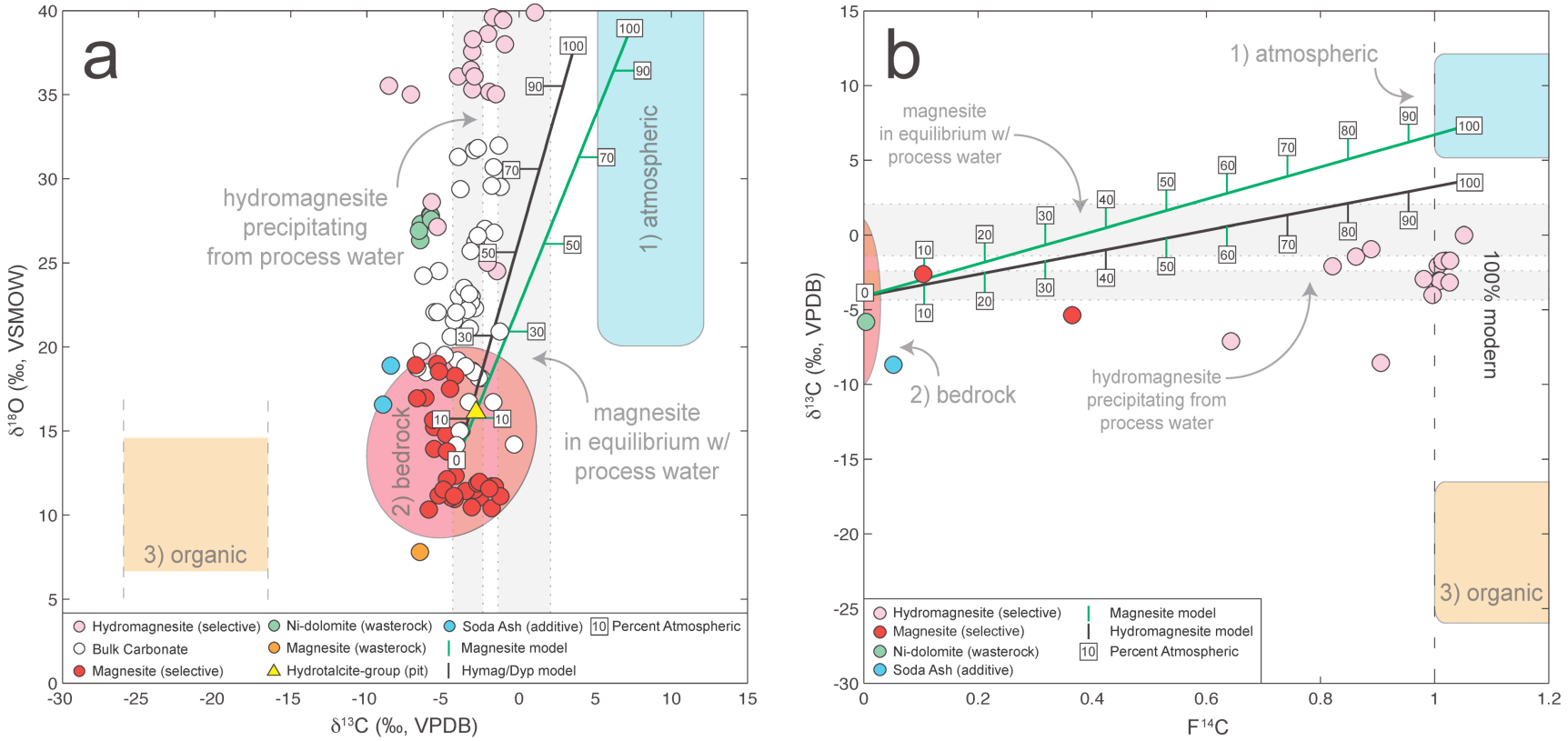

Figure 5.11: Stable isotope and radiocarbon data from Mount Keith overlain by modelled predictions for scenario 1 (mechanical mixing). Stable carbon and oxygen isotope data are given in (a) and stable carbon and radiocarbon ($F^{14}C$) isotope data are given in (b). In most cases, measurement errors are smaller than the symbols employed. Shaded, numbered fields indicate the ranges of values for carbonate minerals in equilibrium with specific reservoirs for carbon and oxygen. A number within a box indicates the percent of atmospheric carbon within a sample plotting at a specific point.

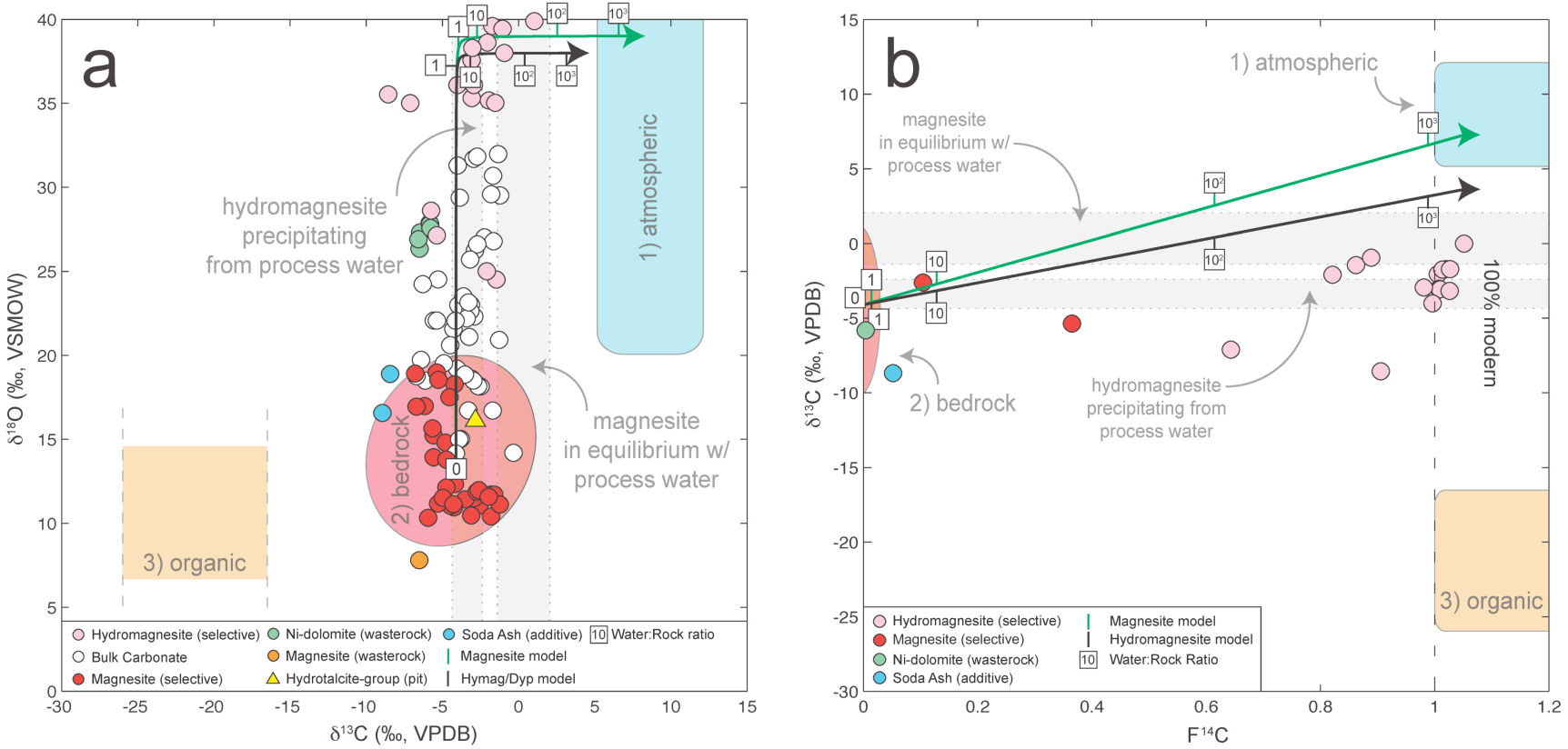

Figure 5.12: Stable isotope and radiocarbon data from Mount Keith overlain by modelled predictions for scenario 2 (batch dissolution/reprecipitation). Stable carbon and oxygen isotope data are given in (a) and stable carbon and radiocarbon ($F^{14}C$) isotope data are given in (b). In most cases, measurement errors are smaller than the symbols employed. Shaded, numbered fields indicate the ranges of values for carbonate minerals in equilibrium with specific reservoirs for carbon and oxygen. A number within a box indicates the water-rock ratio required to produce a sample plotting at that point.

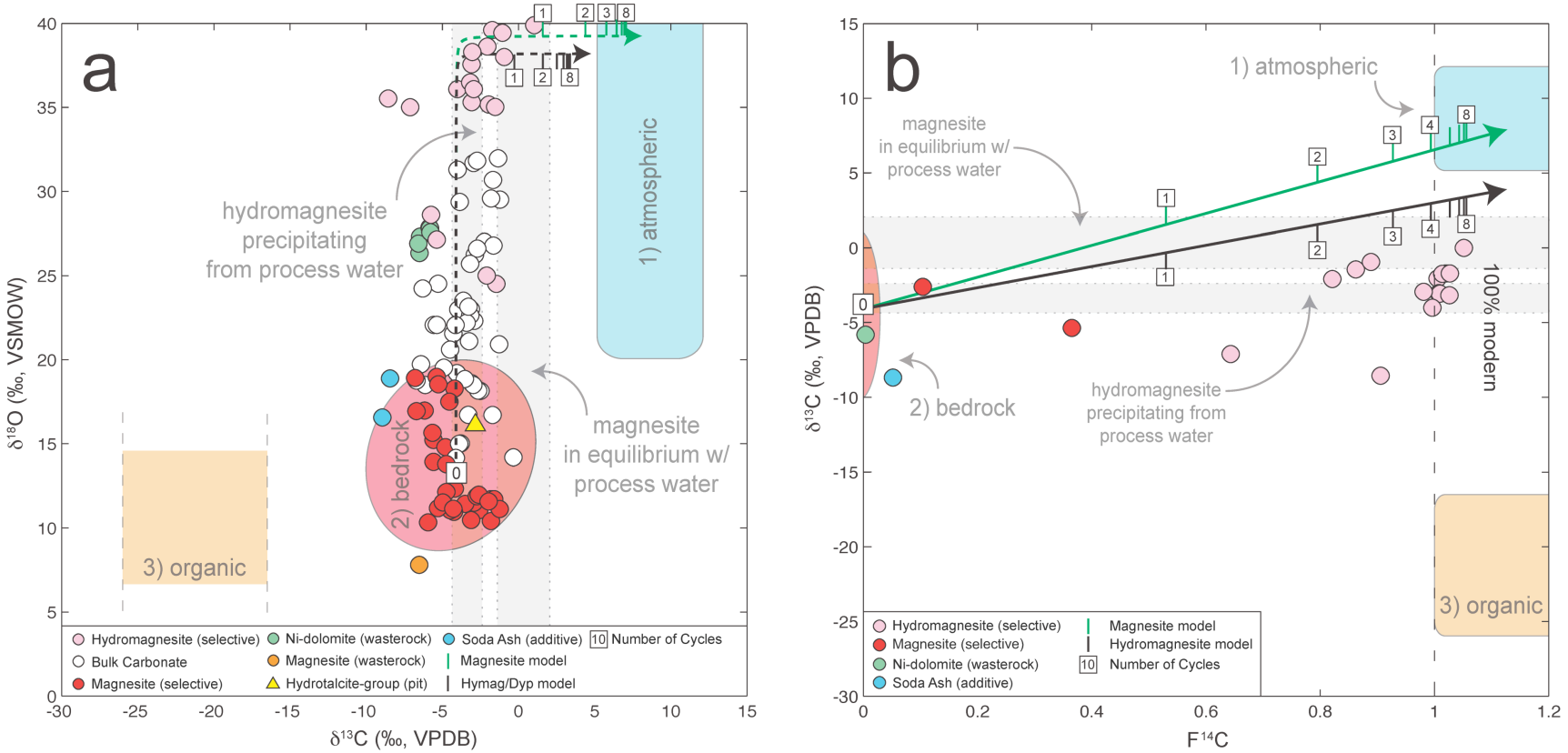

Figure 5.13: Stable isotope and radiocarbon data from Mount Keith overlain by modelled predictions for scenario 3 (cyclic dissolution/reprecipitation) Stable carbon and oxygen isotope data are given in (a) and stable carbon and radiocarbon ($F^{14}C$) isotope data are given in (b). Shaded, numbered fields indicate the ranges of values for carbonate minerals in equilibrium with specific reservoirs for carbon and oxygen. A number within a box indicates the number of dissolution/reprecipitation cycles required to produce a sample plotting at that point.

5.8.2 Active and historical mines

Data from four ultramafic mines are plotted in Figures 5.14 and 5.15 for samples with complete sets of $F^{14}C$-$\delta^{13}C$-$\delta^{18}O$ data. Stable oxygen and carbon isotope data and radiocarbon data are plotted for the active operations at the Diavik Diamond Mine and the Mount Keith Nickel Mine (Chapter 4). Data from the historical chrysotile mining operations at Clinton Creek, Yukon Territory, Canada, and Cassiar, British Columbia, Canada are replotted from Wilson et al. (2009a). Data points from these mines are numbered so that pairs of $\delta^{18}O$-$\delta^{13}C$ data points (Fig. 5.14) and $\delta^{13}C$-$F^{14}C$ data points (Fig. 5.15) may be compared more readily between figures. An interesting result, that is made more evident in Figures 5.14 and 5.15, is that some data points that plot adjacent to one another in $\delta^{18}O$-$\delta^{13}C$-space do not necessarily share a close relationship in $\delta^{13}C$-$F^{14}C$-space, and vice versa. One example from Mount Keith involves data for samples 06MK41-3-hydro (No. 9) and 06MKP9-12-hydro (No. 20). These data plot adjacent to one another in $\delta^{18}O$-$\delta^{13}C$-space (indicated with arrows in Figs. 5.14 and 5.15), but plot in drastically different regions of $\delta^{13}C$-$F^{14}C$-space (Fig. 5.15). Many data give consistent results between $\delta^{18}O$-$\delta^{13}C$ and $\delta^{13}C$-$F^{14}C$-space, but significant inconsistencies, as in the previous example, remain.

Stable isotope data from the Clinton Creek chrysotile mine fall between fields for bedrock carbonate minerals and Mg-carbonate minerals in equilibrium with atmospheric CO_2 (Figs. 5.14). Although data from Clinton Creek could be interpreted as being indicative of dissolution/reprecipitation of bedrock magnesite in $\delta^{18}O$-$\delta^{13}C$-space (Fig. 5.14), what may be a mixing trend (between atmospheric CO_2 and a modern organic source for carbon) is seen when viewed in $\delta^{13}C$-$F^{14}C$-space (Fig. 5.15, replotted from Wilson et al. 2009a). Wilson et al. (2009a) observed that samples of hydrated Mg-carbonate minerals taken from increasing depth within the tailings pile at Clinton Creek are increasingly depleted in ^{13}C and ^{18}O relative to surface samples. Data for one sample of tailings water (07CC17, Table 5.3), collected from the toe of the northern lobe of the mine tailings pile at Clinton Creek has a $\delta^{13}C_{DIC}$ value of -15.78‰. This value is consistent with aqueous bicarbonate in equilibrium with soil CO_2 derived from C_3 vegetation (e.g., Clark and Fritz 1997). It may be that tailings deeper within the thinly deposited tailings flows at this site have better access to relatively modern groundwater

from the surrounding forest, producing a mixing trend between two modern (and ultimately atmospheric) sources of carbon.

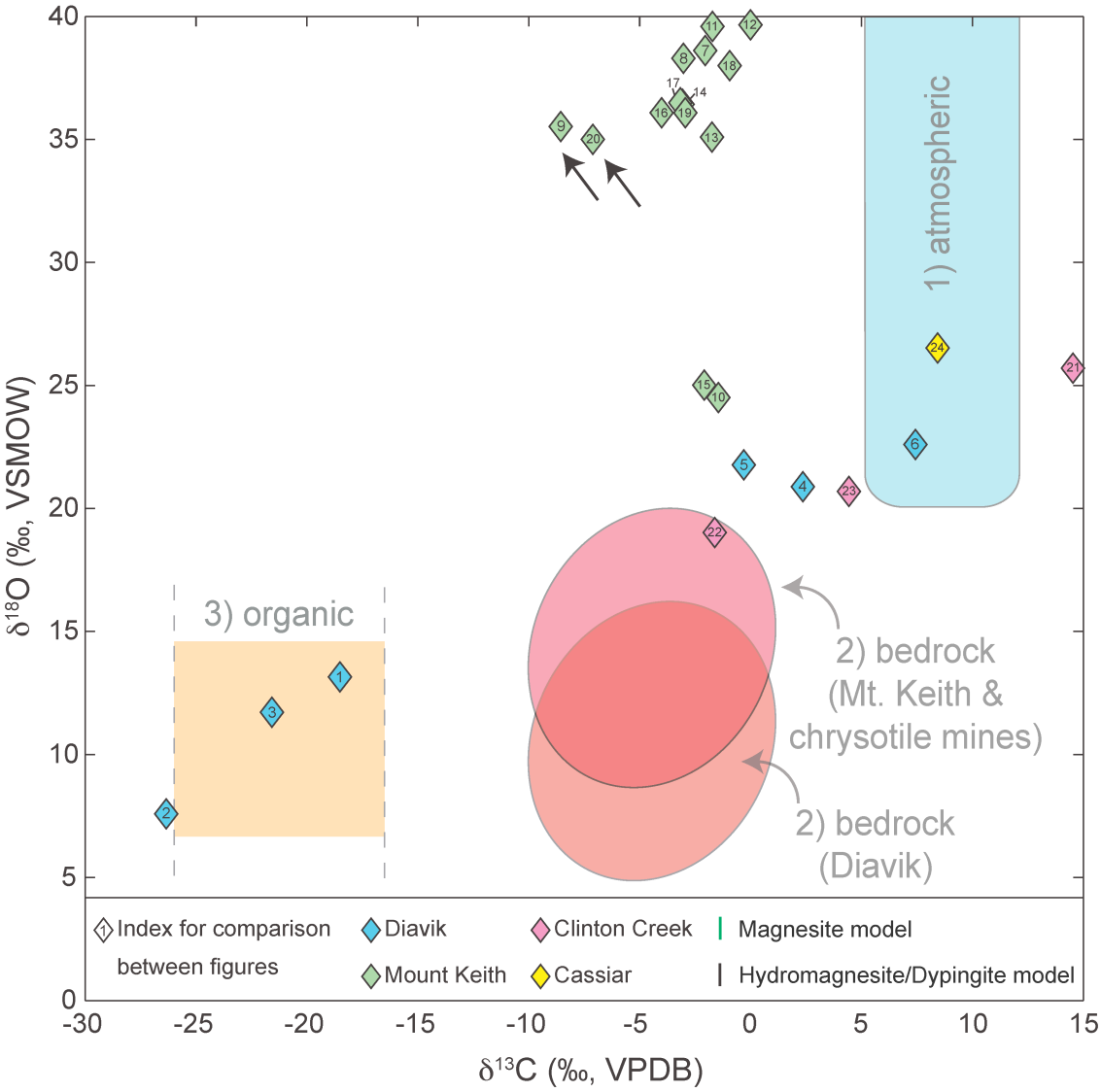

Figure 5.14: Stable oxygen and carbon isotope data from samples for which radiocarbon data are available. These data come from four ultramafic-hosted mines: The Diavik Diamond Mine, the Mount Keith Nickel Mine, and the historical mines at Clinton Creek and Cassiar. Shaded, numbered fields indicate carbonate minerals in equilibrium with specific reservoirs for carbon and oxygen. In most cases, measurement errors are smaller than the symbols employed.

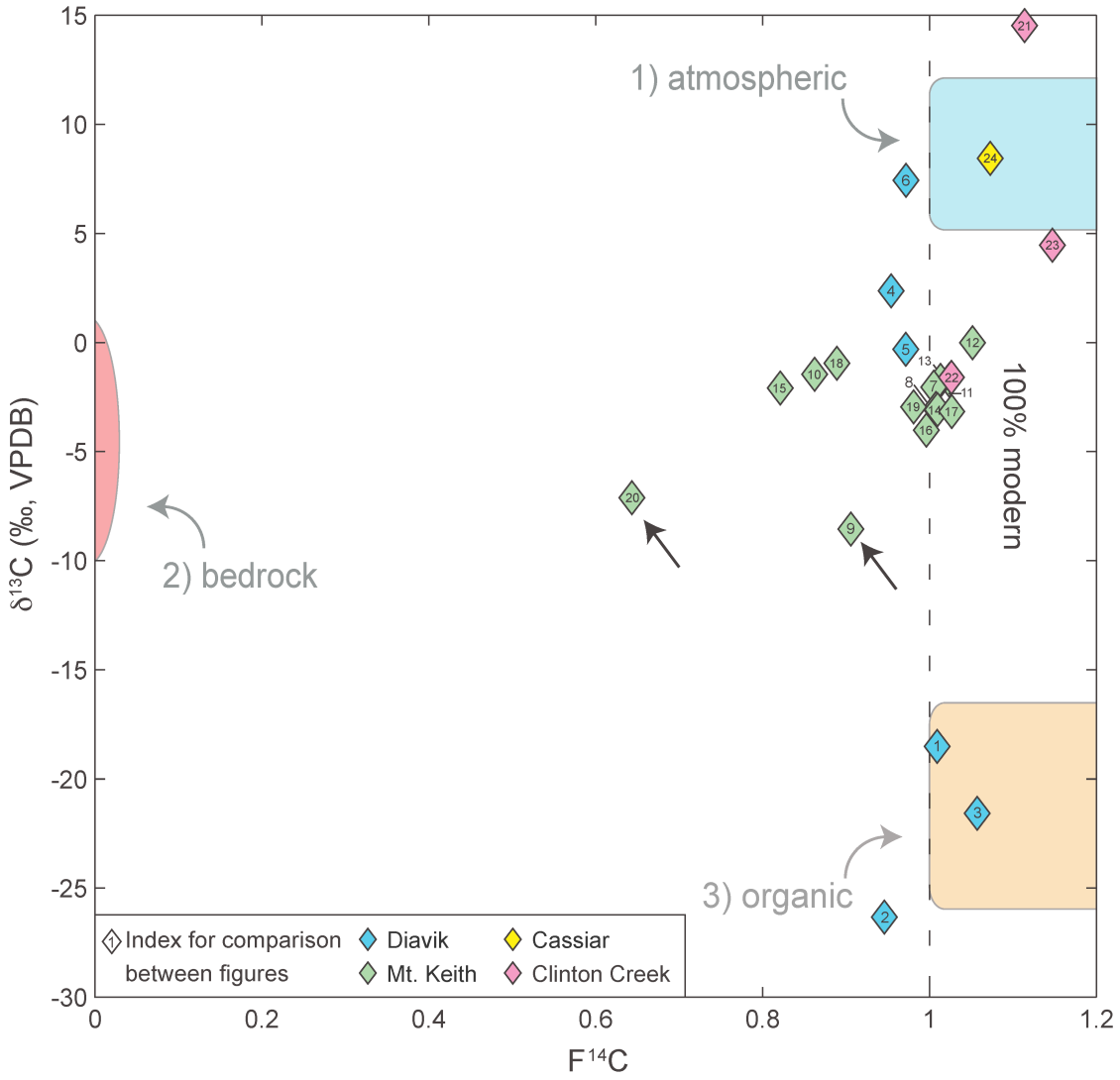

Figure 5.15: Stable carbon isotope data and radiocarbon data from four ultramafic-hosted mines. These data come from the Diavik Diamond Mine, the Mount Keith Nickel Mine, and the historical mines at Clinton Creek and Cassiar. Shaded, numbered fields indicate carbonate minerals in equilibrium with specific reservoirs for carbon. In most cases, measurement errors are smaller than the symbols employed.

However, many of the data for nesquehonite precipitated at the surface of mine tailings from Clinton Creek and Cassiar are consistent with equilibrium precipitation from atmospheric CO_2 (Figs. 5.14 and 5.15, Wilson et al. 2009a). In light of this, an alternative explanation to the mixing scenario proposed by Wilson et al. (2009a), is that equilibrium isotopic fractionation occurs at the surface of these chrysotile mine tailings and that kinetic isotope fractionation becomes increasingly prevalent at depth.

In long abandoned mine tailings facilities, like Clinton Creek and Cassiar, the most significant source of water is meteoric precipitation. This may also be the case for the isolated crust of nesquehonite at Diavik (i.e., 06DVK39), which appears to have precipitated in isotopic equilibrium with the atmosphere. Atmospheric CO_2 will become dissolved in meteoric or surface water as bicarbonate, which may react to precipitate Mg-carbonate minerals from Mg sourced from dissolved silicate minerals (after Berner 1990). Stable isotopic data suggest that, in the unsaturated surficial tailings at Clinton Creek and Cassiar, and the isolated and unsaturated tailings at Diavik, carbonate minerals precipitate in isotopic exchange equilibrium with atmospheric CO_2 (e.g., Dugan and Borthwick 1986). This suggests that these minerals are precipitating from a DIC pool that is in equilibrium with atmospheric CO_2 (Chacko et al. 2001). Contrastingly, kinetic diffusion isotope exchange is observed between atmospheric CO_2 and DIC in the process water at Mount Keith, and in most instances at Diavik. At the active mines, atmospheric CO_2 is likely drawn into solution via the following reactions for dissolution of forsterite (Eq. 5.17) and serpentine (Eq. 5.18):

$$Mg_2SiO_4 + 4CO_2 + 4H_2O \rightarrow 2Mg^{2+} + 4HCO_3^- + Si(OH)_4 \quad \text{(Eq. 5.17)}$$

$$Mg_3Si_2O_5(OH)_4 + 6CO_2 + 5H_2O \rightarrow 3Mg^{2+} + 6HCO_3^- + 2Si(OH)_4 \quad \text{(Eq. 5.18)}$$

Therefore, for every mole of forsterite dissolved in a storage facility for ultramafic mine tailings, four moles of CO_2 are drawn into solution. Six moles of CO_2 are drawn into solution for every mole of serpentine dissolved. Atmospheric CO_2, in pore spaces within the unsaturated zones of active mine tailings, may be drawn into solution during silicate weathering. Also, these dissolution reactions have the potential to draw a large amount of atmospheric CO_2 into solution very rapidly, producing a kinetic isotope fractionation between atmospheric CO_2 and DIC, of the sort described by O'Neil and Barnes (1971) in natural travertines. In abandoned mine tailings, this same mechanism of CO_2 drawn down may produce the increasingly depleted isotopic signature that is observed as deeper mine tailings receive less circulation of atmospheric gasses and are increasingly cut off from fresh meteoric water.

5.9 Summary and Conclusions

Tailings storage facilities can access some surprising isotopic reservoirs, as evidenced by precipitation of Na and Ca-carbonate minerals from sewage at Diavik. During fieldwork, this exotic carbon source and the carbonate minerals that precipitated from it could easily have been overlooked. In addition, poor constraint on stable isotopic fractionation factors for Mg-carbonate minerals, and many other hydrated carbonate minerals, can compound the challenge of interpreting stable isotopic data from these minerals. Additionally, kinetic isotope effects may play a significant role in precipitation of carbonate minerals from process water in tailings storage facilities, particularly at active mines. All of these factors have the potential to confound interpretation of stable isotope data in the ultramafic mine tailings environment.

Isotopic data sets for the Diavik Diamond Mine and Mount Keith Nickel Mine have been compared with equilibrium models for mechanical mixing of carbonate minerals from multiple reservoirs and for carbonate mineral dissolution and reprecipitation. Models for dissolution and reprecipitation may provide convincing fits to stable isotopic data while giving predictions that conflict with $F^{14}C$ data, field-based observations, and laboratory-based analyses. Radiocarbon data and field observations from all four mine sites discussed in this study strongly suggest that most of the carbon within secondary Mg-carbonate minerals is sourced from the modern atmosphere.

Radiocarbon data clearly and reliably identify the signature of the atmosphere in carbonate minerals even when stable isotopic data are ambiguous. Nuclear weapons testing in the 1950s and 1960s nearly doubled the amount of ^{14}C in Earth's atmosphere. Although atmospheric ^{14}C concentrations were initially at their highest in the Northern Hemisphere, the distribution of bomb ^{14}C reached a global equilibrium in the late 1960s (Telgadas 1971). During the 1960s and 1970s exchange with the biosphere and oceans contributed significantly to a decrease in atmospheric ^{14}C (Levin and Hesshaimer 2000). As of the late 2000s, nearly all of the observed decrease in atmospheric $F^{14}C$ levels is the result of dilution by fossil fuel CO_2 and is balanced somewhat by release of nuclear-era ^{14}C from the biosphere (Naegler and Levin 2006). In 2006 and 2007, the $F^{14}C$ of the atmosphere was approximately 1.06 [based on $\Delta^{14}C \approx 50‰$ as reported by Levin et al.

(2008) and converted to $F^{14}C$ using the Internet-based program CALIBomb (Reimer et al. 2004)]. The relatively homogeneous distribution of ^{14}C in the atmosphere and the residual enrichment in atmospheric $^{14}CO_2$ can be used very effectively to trace uptake of modern atmospheric carbon into minerals.

Although local atmospheric ^{14}C concentrations may be more or less enriched in radiocarbon, these depletions are typically not large enough to detract from the usefulness of radiocarbon as a tracer for the modern atmosphere. For instance, Levin et al. (2008) have measured depletions of as much as $\Delta^{14}C \approx -32‰$ ($F^{14}C=0.974$) in tropospheric CO_2 sampled from Heidelberg, Germany. Even this extreme depletion may be used reliably to fingerprint the atmosphere in recently precipitated carbonate minerals. Furthermore, secondary carbonate minerals precipitated from mine tailings in the past 20 years will have seen a decline in atmospheric $F^{14}C$ of approximately 0.10 and those from mining operations initiated within the past 10 years will have seen a decline of less than 0.05 (Levin et al. 2008; Reimer et al. 2004). Thus, secondary carbonate minerals from recently initiated mining operations will always have a limited range of $F^{14}C$ values if ~100% of the carbon within their structures is derived from the atmosphere.

Stable carbon and oxygen isotopic signatures of secondary carbonate minerals in mine tailings are not so well constrained as the ^{14}C composition of the atmosphere. For instance, ^{13}C-depleted carbonate minerals like those found in association with sewage deposits at Diavik could be the result of precipitation from oxidized sewage organic matter or diffusion fractionation of atmospheric CO_2 into a high-pH, high-ionic strength solution (e.g., O'Neil and Barnes 1971; Van Strydonck et al. 1989; Kosednar-Legenstein et al. 2008). Our field evidence suggests that Na and Ca- carbonate minerals at Diavik precipitated from an oxidized organic source of carbon. Nonetheless, a case can be made for diffusion fractionation of the sort described in Chapter 3, for dypingite synthesis experiments, and in previous studies of (1) natural travertines associated with high-pH, Ca^{2+}-OH^--water (O'Neil and Barnes 1971) and (2) calcite precipitated during setting of mortar (e.g., Van Strydonck et al. 1989; Kosednar-Legenstein et al. 2008). In both scenarios, modern carbon would be trapped and stored within carbonate minerals in mine tailings. The only difference is the process by which trapping occurs, either directly from the atmosphere or indirectly through the biosphere. Although both processes trap and

store atmospheric CO_2 within carbonate minerals, the stable isotope signature they produce is drastically different from that predicted for carbonate minerals precipitated in equilibrium with atmospheric CO_2.

Mixing of process waters with groundwater may also impact the stable isotopic signature of secondary carbonate minerals. This is more likely to be an issue in older mine tailings storage facilities that are not sealed off from the local environment by walls and liners. For example, the tailings at the Clinton Creek chrysotile mine were initially deposited in a pile on a topographic high that overlooks a creek. Between 1974 and 1985, the tailings slumped into the creek, burying a forest and forming a thin layer over the slope of a mountainside (Wilson et al. 2009a). The secondary carbonate minerals that form near the surface of this mine tailings pile are highly enriched in ^{13}C and ^{18}O and are generally consistent with equilibrium precipitation of Mg-carbonate minerals from atmospheric CO_2. However, the same minerals, precipitated at depth within the tailings, become increasingly depleted in ^{13}C and ^{18}O with increasing depth below the surface of the tailings pile. The trend toward increasing ^{13}C and ^{18}O depletion at depth within the tailings at Clinton creek may be interpreted in a number of different ways (as discussed previously). Nonetheless, radiocarbon data indicate that all of this mineralization is trapping modern (and ultimately atmospheric) carbon (Fig. 5.15, Wilson et al. 2009a).

The use of carbon-bearing chemicals during mineral processing may change the initial isotopic composition process water DIC. Addition of carbon-bearing process chemicals may even change the isotopic composition of some minerals, like hydrotalcite-group minerals, that are prone to anionic exchange in solution (Grguric 1999; Grguric et al. 2006).

Depletion of ^{13}C in local atmosphere may occur as a result of high primary productivity or fossil fuel emissions from mine site generators. Although this effect is typically minimal in $F^{14}C$ data, it may have a more significant impact on the stable isotopic composition of local atmosphere (Widory and Javoy 2003). Such a depletion could result in carbonate minerals, precipitated in equilibrium with atmospheric CO_2, with slightly depleted $\delta^{13}C$ signatures.

Contrastingly, colonization of mine tailings by micro-organisms has the potential to enrich secondary carbonate minerals in ^{13}C, as bicarbonate ions containing ^{12}C are

preferentially metabolized by micro-organisms (e.g., Pentecost and Spiro 1990; Power et al. 2009). However, similar enrichments may also be caused by infiltration of atmospheric CO_2 into mine tailings or by degassing of CO_2 during precipitation of carbonate minerals. These processes by which carbon may be cycled in mine tailings could provide misleading stable isotopic signatures, by precipitating some isotopically enriched or mixed fraction of the bedrock carbon pool.

In this study, significant disagreement of radiocarbon data, field observations, and laboratory testing with equilibrium models based on stable isotopic data are observed in tailings storage facilities from both active and historical mining operations. The results of this study are in accord with the experimental results of Chapter 3 and the field-based observations and analytical results of Chapter 4: In the mine tailings environment, stable isotope data describe the processes by which elements are cycled more than their provenance. The results of our models also provide further evidence that kinetic isotope fractionation may control the isotopic signature of DIC in tailings waters from active mines. Therefore, a best approach to verifying CO_2 sequestration in mine tailings relies upon use of bomb ^{14}C as an atmospheric tracer rather than light stable isotopic data. In spite of the often ambiguous stable carbon and oxygen isotopic data, $F^{14}C$ data confirm that CO_2 is being sequestered from the atmosphere at the Diavik Diamond Mine, the Mount Keith Nickel Mine, and the historical chrysotile mines at Clinton Creek and Cassiar.

5.10 References

Al, T.A., Martin, C.J., Blowes, D.W. (2000) Carbonate-mineral/water interactions in sulfide-rich mine tailings. Geochimica et Cosmochimica Acta, 64, 3933-3948.

Albarède, F. (1995) Introduction to Geochemical Modeling. Cambridge University Press, Cambridge, U.K, 543 p.

Australian Government, Bureau of Meteorology (2009) Climate statistics for Australian locations: Summary statistics Kalgoorie-Boulder Airport. (http://www.bom.gov.au/climate/averages/tables/cw_012038.shtml).

Bachtiar, T., Coakley, J.P., and Risk, M.J. (1996) Tracing sewage-contaminated sediments in Hamilton Harbour using selected geochemical indicators. The Science of the Total Environment, 179, 3-16.

Barker, S.L.L., Wilson, S.A., Dipple, G.M., and Fallon, S.J. (2009) A method for separation and isotopic analysis of primary and secondary carbonate minerals found in ultramafic mine tailings. The Geological Society of America 2009 Annual Meeting, Abstracts with Programs, 41(7), 325.

BHP Billiton (2005) Mt Keith Nickel Operations: Environmental Data. BHP Billiton Sustainable Development Reports. http://hsecreport.bhpbilliton.com/wmc/2004/performance/mko/data/index.htm.

Bottinga, Y. (1968) Calculations of fractionation factors for carbon and oxygen isotopic exchange in the system calcite-carbon dioxide-water. Journal of Physical Chemistry, 72, 800-808.

Bruker AXS (2004) DIFFRAC^{plus} EVA 10.0 Release 2004. Bruker AXS, Germany.

Burnett, W.C. and Schaeffer, O.A. (1980) Effect of ocean $^{13}C/^{12}C$ ratios in marine sediments from the New York Bight. Estuarine and Coastal Marine Sciences, 11, 605-611.

Cerling, T.E. (1984) The stable isotopic composition of modern soil carbonate and its relationship to climate. Earth and Planetary Science Letters, 71, 229-240.

Chacko, T., Cole, D.R., and Horita, J. (2001) Equilibrium oxygen, hydrogen and carbon isotope fractionation factors applicable to geologic systems. In Stable Isotope

Geochemistry. Valley, J.W. and Cole, D.R., Eds. Reviews in Mineralogy and Geochemistry, 43, 1-81.

Clark, I. and Fritz, P. (1997) Environmental Isotopes in Hydrogeology. CRC Press, U.S.A., 328 p.

Das Sharma, S., Patil, D.J., and Gopalan, K., 2002, Temperature dependence of oxygen isotope fractionation of CO_2 from magnesite-phosphoric acid reaction: Geochimica et Cosmochimica Acta, v. 66, p. 589-593.

deBruyn, A.M.H. and Rasmussen, J.B. (2002) Quantifying assimilation of sewage-derived organic matter by riverine benthos. Ecological Applications, 12, 511-520.

Deines, P. (2004) Carbon isotope effects in carbonate systems. Geochimica et Cosmochimica Acta, 68, 2659-2679.

Deines, P., Langmuir, D., and Harmon, R.S. (1974) Stable carbon isotope ratios and the existence of a gas phase in the evolution of carbonate ground waters. Geochimica et Cosmochimica Acta, 38, 1147-1164.

Dold, B. (2006) Element flows associated with marine shore mine tailings deposits. Environmental Science & Technology, 40, 752-758.

Donahue, D.J., Linick, T.W., and Jull, A.J.T. (1990) Isotope-ratio and background corrections for accelerator mass spectrometry radiocarbon measurements. Radiocarbon, 32, 135-142.

Drever, J.I. (1982) The geochemistry of natural waters. Prentice-Hall, U.S.A., 388 p.

Dugan, J.P., Jr. and Borthwick, J. (1986) Carbon dioxide-water oxygen isotope fractionation factor using chlorine trifluoride and guanidine hydrochloride techniques. Analytical Chemistry, 58, 3052-3054.

Epstein, S. Buchsbaum, R., Lowenstam, H.A., Urey, H.C. (1953) Revised carbonate-water isotopic temperature scale. Geological Society of America Bulletin, 64, 1315-1326.

Faure, G. (1986) Principles of Isotope Geology. Wiley, U.S.A., 589 p.

Fernandes, S.A.P., Bettiol, W., Cerri, C.C., and Camargo, P. (2005) Sewage sludge effects on gas fluxes at the soil-atmosphere interface, on soil $\delta^{13}C$ and on total soil carbon and nitrogen. Geoderma, 125, 49-57.

Friedman, I. and O'Neil, J.R. (1977) Compilation of stable isotope fractionation factors of geochemical interest. In Data of Geochemistry. Fleischer, M., Ed. United States Geological Survey Professional Paper 440-KK.

Gearing, P.J., Gearing, J.N., Maughan, J.T., and Ovlatt, C.A. (1991) Isotopic distribution of carbon from sewage sludge and eutrophication in the sediments and food web of estuarine ecosystems. Environmental Science & Technology, 25, 295-301.

Giester, G., Lengauer, C.L., and Rieck, B. (2000) The crystal structure of nesquehonite, $MgCO_3 \cdot 3H_2O$, from Lavrion, Greece. Mineralogy and Petrology, 70, 153-163.

Gonfiantini, R. (1986) Environmental isotopes in lake studies. In Handbook of Environmental Isotope Geochemistry, Vol. 2, The Terrestrial Environment. Fritz, P. and Fontes, J.-C., Eds. Elsevier, Amsterdam, The Netherlands, p.113-168.

Grady, M.M., Gibson, E.K., Wright, I.P., and Pillinger, C.T. (1989) The formation of weathering products on the LEW 85320 ordinary chondrite: Evidence from carbon and oxygen stable isotope compositions and implications for carbonates in SNC meteorites. Meteoritics, 24, 1-7.

Graham, I., Burgess, J.L., Bryan, D., Ravenscroft, P.J., Thomas, E., Doyle, B.J., Hopkins, R., and Armsrong, K.A. (1998) Exploration history and geology of the Diavik kimberlites, Lac de Gras, Northwest Territories, Canada. In: Gurney, J.J., Gurney, J.L., Pascoe, M.D., and Richardson, S.H. (Eds.), Proceedings of the VIIth International Kimberlite Conference, vol. 1. Red Roof Design, Cape Town, South Africa, pp. 262-279.

Grguric, B.A., Rosengren, N.M., Fletcher, C.M., and Hronsky, J.M.A. (2006) Type 2 deposits: geology, mineralogy and processing of the Mount Keith and Yakabindi orebodies, Western Australia. Society of Economic Geologists Special Publications, 13, 119-138.

Grguric, B.A. (1999) The distribution and mineralogy of chlorine in concentrates and the MKD5 Ultramafic Unit: relationship to retrograde alteration and implications for mineral processing. WMC Resources Ltd., Internal Report. Unpublished, 86 pp.

Halas, S. and Wolacewicz, W. (1982) The experimental study of oxygen isotope exchange reaction between dissolved bicarbonate and water. Journal of Chemical Physics, 76, 5470-5472.

Hansen, L.D. (2005) Geologic setting of listwanite, Atlin, B.C.: Implications for carbon dioxide sequestration and lode-gold mineralization. Unpublished M.Sc. thesis. The University of British Columbia, Vancouver, Canada, 174 pp.

Holland, H.D., Kirsipu, R.V., Huebner, J.S., and Oxburgh, U.M. (1964) On some aspects of the chemical evolution of cave waters. Journal of Geology, 72, 36-67.

Inaba, S., Minakawa, T., and Noto, S. (1985) Nesquehonite and dypingite from Shiraki, Mie Prefecture, Japan. Chigaku Kenkyu, 34, 281-287.

Jambor, J.L. and Blowes, D.W. (1998) Theory and applications of mineralogy in environmental studies of sulfide-bearing mine wastes. In Modern Approaches to Ore and Environmental Mineralogy. Cabri, L.J. and Vaughn, D.J., Eds. Mineralogical Association of Canada Short Course 27, 367-401.

Jiménez-López, C., Caballero, E., Huertas, F.J., and Romanek, C.S. (2001) Chemical, mineralogical and isotope behavior, and phase transformation during the precipitation of calcium carbonate minerals from intermediate ionic solution at 25˚C. Geochimica et Cosmochimica Acta, 65, 3219-3231.

Jull, A.J.T., Cheng, S., Gooding, J.L., and Velbel, M.A. (1988) Rapid growth of magnesium-carbonate weathering products in a stony meteorite from Antarctica. Science, 242, 417-419.

Keeling, C.D., Bollenbacher, A.F., and Whorf, T.P. (2005) Monthly atmospheric $^{13}C/^{12}C$ isotopic ratios for 10 SIO stations. In Trends: A Compendium of Data on Global Change. Carbon Dioxide Information Analysis Center, Oak Ridge National Laboratory, U.S. Department of Energy, Oak Ridge, Tennessee, U.S.A.

Kim, S.-T. and O'Neil, J.R. (1997) Equilibrium and nonequilibrium oxygen isotope effects in synthetic carbonates. Geochimica et Cosmochimica Acta, 61, 3461-3475.

Kosednar-Legenstein, B., Dietzel, M., Leis, A., and Stingl, K. (2008) Stable carbon and oxygen isotope investigation in historical lime mortar and plaster – Results from field and experimental study. Applied Geochemistry, 23, 2425-2437.

Lackner, K.S., Wendt, C.H., Butt, D.P., Joyce, G.L., and Sharp, D.H. (1995) Carbon dioxide disposal in carbonate minerals. Energy, 20, 1153-1170.

Levin, I. and Hesshaimer, V. (2000) Radiocarbon – a unique tracer of global carbon cycle dynamics. Radiocarbon, 42, 69-80.

Levin, I., Hammer, S., Kromer, B., Meinhardt, F. (2008) Radiocarbon observations in atmospheric CO_2: Determining fossil fuel CO_2 over Europe using Jungfraujoch observations as background. Science of the Total Environment, 391, 211-216.

Ma, N. and Yang, X. (2008) Environmental isotopes and water chemistry in the Badain Jaran desert and in its southeastern adjacent areas, Inner Mongolia and their hydrological implications. Disiji Yanjiu, 28, 702-711.

Mamchur, G.P., Melnik, Y.M., Kharkiv, A.D., and Yarynych, O.A. (1980) Origin of carbonates and bitumens in kimberlites according to carbon isotope data. Geochemistry International, 17, 118-124.

Mitchell, R.H. (1986) Kimberlites: Mineralogy, Geochemistry and Petrology. Plenum Press, New York.

Molson, J.W., Fala, O., Aubertin, M., and Bussière, B. (2005) Numerical simulations of pyrite oxidation and acid mine drainage in unsaturated waste rock piles. Journal of Contaminant Hydrology, 78, 343-371.

Mook, W.G., Bommerson, J.C., Staverman, W.H. (1974) Carbon isotope fractionation between dissolved bicarbonate and gaseous carbon dioxide. Earth and Planetary Science Letters, 22, 169-176.

Naegler, T. and Levin, I. (2006) Closing the global radiocarbon budget 1945-2005. Journal of Geophysical Research, 111, D12311.

Ogrinc, N., Markovics, R., Kanduc, T., Walter, L.M., and Hamilton, S.K. (2008) Sources and transport of carbon and nitrogen in the River Sava watershed, a major tributary of the River Danube. Applied Geochemistry, 23, 3685-3698.

O'Neil, J.R. and Barnes, I. (1971) C^{13} and O^{18} compositions in some fresh-water carbonates associated with ultramafic rocks and serpentinites: western United States. Geochimica et Cosmochimica Acta, 35, 687-697.

O'Neil, J.R., Clayton, R.N., and Mayeda, T.K. (1969) Oxygen isotope fractionation in divalent metal carbonates. Journal of Chemical Physics, 51, 5547-5558.

Paktunc, A.D. and Davé, N.K. (2002) Formation of secondary pyrite and carbonate minerals in the Lower Williams Lake tailings basin, Elliot Lake, Ontario, Canada. American Mineralogist, 87, 593-602.

Palandri, J.L. and Kharaka, Y.K. (2004) A compilation of rate parameters of water-mineral interaction kinetics for application to geochemical modelling. U.S. Geological Survey Open File Report 2004-1068.

Pentecost, A. and Spiro, B. (1990) Stable carbon and oxygen isotope composition of calcites associated with modern freshwater cyanobacteria and algae. Geomicrobiology Journal, 8, 17-26.

Polach, H.A. and Golson, J. (1966) Collection of Specimens for Radiocarbon Dating and Interpretation of Results, Manual 2. Australian Institute of Aboriginal Studies, Canberra, ACT, Australia.

Power, I.M., Dipple, G.M., and Southam, G. Bioleaching of ultramafic tailings by *Acidithiobacillus* spp. for carbon capture and storage. Environmental Science & Technology, in review.

Power, I.M., Wilson, S.A., Thom, J.M., Dipple, G.M., Gabites, J.E., and Southam, G. (2009) The hydromagnesite playas of Atlin, British Columbia, Canada: A biogeochemical model for CO_2 sequestration. Chemical Geology, 260, 286-300.

Power, I.M., Wilson, S.A., Thom, J., Dipple, G.M., and Southam, G. (2007) Biologically induced mineralization of dypingite by cyanobacteria from an alkaline wetland near Atlin, British Columbia, Canada. Geochemical Transactions, 8, article 13.

Ramírez-Álvarez, N., Macías-Zamora, J.V., Burke, R.A., and Rodríguez-Villanueva, L.V. (2007) Use of $\delta^{13}C$, $\delta^{15}N$, and carbon to nitrogen ratios to evaluate the impact of sewage-derived particulate organic matter on the benthic communities of the Southern California Bight. Environmental Toxicology and Chemistry, 26, 2332-2338.

Reimer, P.J., Brown, T.A., and Reimer, R.W. (2004) Discussion: Reporting and calibration of post-bomb ^{14}C data. Radiocarbon, 46, 1299-1304.

Romanek, C.S., Grossman, E.L., and Morse, J.W. (1992) Carbon isotopic fractionation in synthetic aragonite and calcite: effects of temperature and precipitation rate. Geochimica et Cosmochimica Acta, 56, 419-430.

Rubinson, M. and Clayton, R.N. (1969) Carbon-13 fractionation between aragonite and calcite. Geochimica et Cosmochimica Acta, 33, 997-1002.

Seifritz, W. (1990) CO_2 disposal by means of silicates. Nature, 345, 486.

Spies, R.B., Kruger, H., Ireland, R., and Rice, D.W., Jr. (1989) Stable isotope ratios and contaminant concentrations in a sewage-distorted food web. Marine Ecology Progress Series, 54, 157-170.

Spötl, C. and Burns, S.J. (1994) Magnesite diagenesis in redbeds: a case study from the Permian of the Northern Calcareous Alps (Tyrol, Austria). Sedimentology, 41, 543-565.

Sundquist, E.T. (1993) The global carbon dioxide budget. Science, 259, 934-941.

Sundquist, E.T. (1985) Geological perspectives on carbon dioxide and the carbon cycle. In E.T. Sundquist and W.S. Broecker, Eds., The Carbon Cycle and Atmospheric CO_2: Natural Variations Archaen to Present, Geophysical Monographs, 32, 5-60. American Geophysical Union, Washington, DC, USA.

Suzuki, J. and Ito, M. (1973) A new magnesium carbonate hydrate mineral, $Mg_5(CO_3)_4(OH)_2{\cdot}8H_2O$, from Yoshikawa, Aichi Prefecture, Japan. Journal of the Japanese Association of Mineralogists, Petrologists and Economic Geologists, 68, 353-361.

Suzuki, J. and Ito, M. (1974) Nesquehonite from Yoshikawa, Aichi Prefecture, Japan: occurrence and thermal behaviour. Journal of the Japanese Association of Mineralogists, Petrologists and Economic Geologists, 69, 275-284.

Taylor, G.F. (1975) The occurrence of monohydrocalcite in two small lakes in the South-East of South Australia. American Mineralogist, 60, 690-697.

Telegadas, K. (1971) The seasonal atmospheric distribution and inventories of excess carbon-14 from March 1955 to July 1969. U.S. Atomic Energy Commission Report, HASL-243.

Van Dover, C.L., Grassle, J.F., Fry, B., Garritt, R.H., and Starczak, V.R. (1992) Stable isotope evidence for entry of sewage-derived organic material into a deep-sea food web. Nature, 360, 153-156.

Van Strydonck, M.J.Y., Dupas, M., and Keppens, E. (1989) Isotopic fractionation of oxygen and carbon in lime mortar under natural environmental conditions. Radiocarbon, 31, 610-618.

White, A.F., Blum, A.E., Schulz, M.S., Bullen T.D., Harden, J.W., and Peterson, M.L. (1996) Chemical weathering rates of a soil chronosequence on granitic alluvium: I. Quantification of mineralogical and surface area changes and calculation of primary silicate reaction rates. Geochimica et Cosmochimica Acta, 60, 2533-2550.

Widory, D. and Javoy, M. (2003) The carbon isotope composition of atmospheric CO_2 in Paris. Earth and Planetary Science Letters, 215, 289-298.

Wilson, S.A., Dipple, G.M., Power, I.M., Thom, J.M., Anderson, R.G., Raudsepp, M., Gabites, J.E., and Southam, G. (2009a) Carbon dioxide fixation within mine wastes of ultramafic-hosted ore deposits: Examples from the Clinton Creek and Cassiar chrysotile deposits, Canada. Economic Geology, 104, 95-112.

Wilson, S.A., Raudsepp, M., and Dipple, G.M. (2009b) Quantifying carbon fixation in trace minerals from processed kimberlite: A comparative study of quantitative methods using X-ray powder diffraction data with applications to the Diavik Diamond Mine, Northwest Territories, Canada. Applied Geochemistry, 24, 2312-2331. doi:10.1016/j.apgeochem.2009.09.018.

Wilson, S.A., Raudsepp, M., and Dipple, G.M. (2006) Verifying and quantifying carbon fixation in minerals from serpentine-rich mine tailings using the Rietveld method with X-ray powder diffraction data. American Mineralogist, 91, 1331-1341.

Zedef, V., Russell, M.J., Fallick, A.E., and Hall, A.J. (2000) Genesis of vein stockwork and sedimentary magnesite and hydromagnesite deposits in the ultramafic terranes of southwestern Turkey: a stable isotope study. Economic Geology, 95, 429-446.

Chapter 6

Conclusions

6.1 Summary of research outcomes

The primary goals of this research have been to develop mineralogical and geochemical strategies for assessing carbon mineralization in mine tailings, and to apply these methods to the Mount Keith Nickel Mine and the Diavik Diamond Mine. The primary result of this thesis is that secondary Mg-carbonate minerals can precipitate within ultramafic mine tailings from active mines, via a previously unrecognized passive weathering process. Furthermore, these Mg-carbonate minerals can act as traps for atmospheric CO_2 at active mines.

At the Diavik Diamond Mine, trace amounts of nesquehonite [$MgCO_3 \cdot 3H_2O$] precipitate at the surface of the fine PKC and persist at depth within the tailings upon burial (Chapter 2). In the fine PKC, nesquehonite forms as a secondary weathering product of Mg-silicate minerals, the most abundant of which are serpentine-group minerals and forsterite. The Rietveld method (Rietveld 1969; Hill and Howard 1987; Bish and Howard 1988) and the method of normalized reference intensity ratios (Chung 1974) were found to be effective for quantifying nesquehonite at abundances ≥ 0.5 wt.% in kimberlite mine tailings. However, the internal standard method (Alexander and Klug 1948) provides significantly more accurate results for abundances < 0.5 wt.%. Based on the results of quantitative X-ray powder diffraction in Chapter 2, on the order of 1,800 tonnes of CO_2 may be trapped within nesquehonite in the fine PKC at Diavik. Radiocarbon data for nesquehonite from Chapter 5, suggest that most (in excess of 90%) of this CO_2 has an atmospheric origin. Although this represents only a small offsetting of greenhouse gas emissions at Diavik, it is significant that this passive weathering process is operating at Diavik and trapping atmospheric CO_2 under extremely cold conditions in tailings that are largely saturated with water.

In Chapter 3, isotopic analogue experiments were used study the fractionation of stable carbon isotopes during precipitation of dypingite [$Mg_5(CO_3)_4(OH)_2 \cdot 5H_2O$] from an evaporating, saline system that was open to the atmosphere. The conditions of these experiments were chosen to simulate those under which the structurally and chemically related mineral, hydromagnesite, precipitates at Mount Keith. A carbon isotopic fractionation factor for exchange between dypingite and DIC (i.e., aqueous bicarbonate) was obtained under conditions similar to those in effect within ultramafic mine tailings at active mines. This fractionation factor is consistent with previously determined fractionation factors for carbonate minerals. It was also confirmed that the equilibrium oxygen isotopic fractionation factor for hydromagnesite reported by O'Neil and Barnes (1971) provides a good description of oxygen isotopic fractionation between dypingite and water under evaporative and saline conditions. The precipitation experiments undertaken in Chapter 3 demonstrate that equilibrium fractionation factors do not always provide an explanation for the $\delta^{13}C$ signature of DIC. Furthermore, it strongly suggests that stable isotope data may fail to unambiguously fingerprint trapping of atmospheric CO_2 within Mg-carbonate minerals.

At the Mount Keith Nickel Mine (Chapter 4), hydromagnesite [$Mg_5(CO_3)_4(OH)_2 \cdot 4H_2O$], forms as a secondary weathering product of serpentine-rich mine tailings and acts as a mineral trap for atmospheric CO_2. Hydromagnesite is commonly detectable at abundances greater than 0.5 wt.%, which facilitates quantitative mineralogy with the Rietveld method and X-ray powder diffraction data, and permits estimates of CO_2 trapping to be made. In Chapter 4, trends in quantitative mineralogical data have been used effectively to identify brucite and serpentine minerals as the primary sources of Mg in secondary minerals and to establish that primary bedrock minerals are not being dissolved and reprecipitated as hydromagnesite. Refined abundances for hydromagnesite from tailings of various ages have been used to produce an empirical rate law for carbon mineralization within hydromagnesite at Mount Keith. In Chapter 4, this rate law is used to estimate the amount of CO_2 stored within hydromagnesite at Mount Keith and to predict the scale of future CO_2 trapping over the projected life of the mine. The fractionation factor for dypingite, obtained in Chapter 3, was used to demonstrate that secondary hydromagnesite at Mount Keith precipitated in equilibrium

with tailings water DIC, which was almost certainly out of isotopic exchange equilibrium with the atmosphere. Because the stable isotopic data for hydromagnesite at Mount Keith were ambiguous, and could not be used to identify the source of carbon trapped within this mineral, radiocarbon data were employed as an alternative tracer. Radiocarbon data unambiguously identify the atmosphere as the primary source of carbon stored within hydromagnesite. Based on Rietveld refinement results and radiocarbon data, it was concluded that approximately 15% of 2009 greenhouse gas emissions from Mount Keith were offset by mineralization of atmospheric CO_2 within hydromagnesite.

In Chapter 5, a computational model for mechanical mixing of isotopically distinct populations of carbonate minerals, and two equilibrium isotopic models for dissolution and reprecipitation of primary carbonate minerals, were developed. The models for dissolution and reprecipitation of primary carbonate minerals, to precipitate secondary Mg-carbonate minerals, gave good fits to stable isotopic data. However, these models consistently conflicted with field observations, quantitative mineralogical results, and radiocarbon data. Equilibrium isotopic models failed to give a satisfactory description of the isotopic data for secondary nesquehonite at Diavik and secondary hydromagnesite at Mount Keith. The only internally consistent explanation for these data is that kinetic fractionation processes control the stable isotopic composition of the DIC pools at Diavik and Mount Keith. A more significant implication is that secondary Mg-carbonate minerals that precipitate within the tailings at active mines may reflect the isotopic composition of DIC, rather than that predicted by models for equilibrium precipitation from atmospheric CO_2. Radiocarbon data clearly fingerprint trapping of atmospheric CO_2 within secondary Mg-carbonate minerals, but stable isotopic data are difficult to interpret because they are inconsistent with commonly used models for equilibrium isotopic fractionation. As seen before, in Chapters 3 and 4, stable isotopic data for secondary carbonate minerals in mine tailings describe the processes by which elements are cycled more than their provenance. Therefore, a more reliable tracer like radiocarbon should be used in place of stable carbon and oxygen isotopes to fingerprint sequestration of atmospheric carbon within minerals.

6.2 Suggestions for future research

This thesis describes a first attempt at constructing a large database of quantitative mineralogical data for the purpose of estimating CO_2 sequestration within a mine tailings storage facility. Ideally, a tailings storage facility would be sampled randomly using a grid system; however, modern tailings management practices make this problematic if not impossible. Tailings saturated with water are more easily transported from a processing plant to a storage facility through a network of pipes. Subaqueous storage of mine tailings is an effective strategy for preventing acid mine drainage and metal leaching from potentially acid-generating mine waste (e.g., Robertson et al. 1997, Jambor and Blowes 1998, Price and Errington 1998). As a consequence, it is common practise for many mining operations to retain some amount of process water in their stored tailings, either as a result of transportation by water or to mitigate acid generation. I was able to compensate somewhat for incomplete access to the tailings at Mount Keith and Diavik, by using available symmetry of the tailings storage facilities, undertaking extensive sampling at random intervals on pre-determined paths, and selecting samples for analysis using a random number generator. It would be appropriate to improve upon this strategy using geostatistical techniques so that sampling bias could be further reduced and estimates for CO_2 trapping improved.

It would also be worthwhile to continue open system and closed system precipitation experiments for dypingite and other hydrated Mg-carbonate minerals. Because bonding environment, and thus crystal structure, controls isotopic fractionation effects between minerals and their environments, it is reasonable to assume that equilibrium and kinetic fractionation factors for dypingite, magnesite, hydromagnesite, nesquehonite, and other Mg-carbonate minerals will differ. Availability of (1) equilibrium oxygen and carbon isotopic fractionation factors for these minerals and (2) kinetic fractionation factors obtained from isotopic analogue experiments are likely to improve understanding of stable isotopic data sets for secondary carbonate minerals in mine tailings.

An other line of research that may be worth pursuing is the development of portable, cost-effective analytical equipment for measuring the ^{14}C composition of

gasses, water, and minerals in the field. Accelerator mass spectrometric analyses of radiocarbon are expensive and samples require precise and time-consuming preparation prior to analysis. Development of a portable laser spectroscopic isotope analyzer for ^{14}C would greatly facilitate future isotopic studies of carbon mineralization within mine tailings. Furthermore, it could be used for on-site monitoring of CO_2 capture and storage by mine personnel.

6.3 References

Alexander, L. and Klug, H.P. (1948) Basic aspects of X-ray absorption in quantitative diffraction analysis of powder mixtures. Analytical Chemistry, 20, 886-889.

Bish, D.L. and Howard, S.A. (1988) Quantitative phase analysis using the Rietveld method. Journal of Applied Crystallography, 21, 86-91.

Chung, F.H. (1974) Quantitative interpretation of X-ray diffraction patterns of mixtures. II. Adiabatic principle of X-ray diffraction analysis of mixtures. Journal of Applied Crystallography, 7, 526-531.

Hill, R.J. and Howard, C.J. (1987) Quantitative phase analysis from neutron powder diffraction data using the Rietveld method. Journal of Applied Crystallography, 20, 467-474.

Jambor, J.L. and Blowes, D.W. (1998) Theory and applications of mineralogy in environmental studies of sulfide-bearing mine wastes. In L.J. Cabri and D.J. Vaughn, Eds., Modern Approaches to Ore and Environmental Mineralogy, 27, 367-401. Mineralogical Association of Canada, Ottawa, ON, Canada.

O'Neil, J.R. and Barnes, I. (1971) C^{13} and O^{18} compositions in some fresh-water carbonates associated with ultramafic rocks and serpentinites: western United States. Geochimica et Cosmochimica Acta, 35, 687-697.

Price, W.A. and Errington, J.C. (1998) Guidelines for metal leaching and acid rock drainage at minesites in British Columbia. Retrived June 6, 2008 from the website of the British Columbia Ministry of Energy, Mines and Petroleum Resources: http://www.em.gov.bc.ca/Subwebs/mining/Project_Approvals/guidelines.htm#Metal%20Leaching%20and%20Acid%20Rock%20Drainage.

Rietveld, H.M. (1969) A profile refinement method for nuclear and magnetic structures. Journal of Applied Crystallography, 2, 65-71.

Robertson, J.D., Tremblay, G.A., and Fraser, W.W. (1997) Subaqueous tailing disposal: a sound solution for reactive tailings. In Proceedings of the Fourth International Conference on Acid Rock Drainage, 3, 1027-1044. MEND, Natural Resources Canada, Ottawa, ON, Canada.

Appendix A1

Appendix to Chapter 4

This appendix consists of two large tables of data discussed in Chapter 4. Appendix Table A1.1 gives Rietveld refinement results for 204 samples of mine tailings from the Mount Keith Nickel Mine. Appendix Table A1.2 gives stable carbon and oxygen isotope data and radiocarbon data for specimens of carbonate minerals, dissolved inorganic carbon (DIC), and bulk tailings.

Appendix Table A1.1: Rietveld refinement results for samples from Mount Keith.

Sample	**06MK30-1**	**06MK30-2**	**06MK30-3**	**06MK30-4**	**06MK30-5**	**06MK30-6**	**06MK30-7**	**06MK30-8**
Age (years)	0	0	0	0	0	0	0	0
Depth (cm)	0-30	0-30	30-60	30-60	30-60	70-100	150-180	150-180
Sample Type	Trench Sample	Trench Sample	Trench Sample	Trench Sample	Trench Sample	Trench Sample	Trench Sample	Trench Sample
Easting (UTM 51J WGS 84)	263550	263550	263550	263550	263550	263550	263550	263550
Northing (UTM 51J WGS 84)	6982329	6982329	6982329	6982329	6982329	6982329	6982329	6982329
Error on GPS Location (m)	5.8	5.8	5.8	5.8	5.8	5.8	5.8	5.8
Elevation at Surface (m OSL)	525.8	525.8	525.8	525.8	525.8	525.8	525.8	525.8
serpentine	77.9	86.1	81.8	80.9	79.7	83.9	81.6	80.6
kaolinite	–	–	–	–	–	–	–	–
brucite	1.0	3.0	2.0	2.2	5.8	1.2	3.4	3.4
talc	–	–	–	–	–	–	–	–
vermiculite	–	–	–	–	–	–	–	–
muscovite	–	–	–	–	–	–	–	–
hydrotalcite-group	5.9	3.1	6.1	5.2	3.6	2.4	4.7	5.9
gypsum	0.3	–	–	–	–	–	–	–
hexahydrite	–	–	–	–	–	–	–	–
epsomite	–	–	–	–	–	–	–	–
blödite	3.0	–	–	–	–	–	–	–
konyaite	–	–	–	–	–	–	–	–
löweite	tr	–	–	–	–	–	–	–
lepidocrocite	–	–	–	–	–	–	–	–
magnetite & chromite	2.8	3.5	2.2	3.2	6.4	4.7	3.8	4.5
quartz	–	tr	tr	–	tr	tr	–	–
rutile	–	–	–	–	–	–	–	–
plagioclase	–	–	–	–	–	–	–	–
halite	4.1	0.3	2.5	2.0	0.6	1.0	2.4	1.9
magnesite	2.2	2.7	3.7	4.0	2.4	6.0	2.9	3.2
dolomite	1.7	0.6	1.7	1.2	0.7	0.8	1.0	tr
calcite	–	0.7	tr	tr	–	tr?	0.3	–
trona	–	–	–	–	–	–	–	–
hydromagnesite	**1.2**	**–**	**–**	**1.2**	**0.9**	**–**	**–**	**0.5**
Total	100.0	100.0	100.0	100.0	100.0	100.0	100.0	100.0
R_{wp} [a]	5.9	4.3	4.3	4.1	4.0	3.9	4.2	4.3
χ^2 [b]	3.8	3.1	3.2	3.0	3.0	3.0	3.0	3.1
d [c]	1.4	2.2	2.1	2.3	2.3	2.3	2.3	2.1

[a] R_{wp} is the weighted pattern index, a function of the least-squares residual.

[b] χ^2 is the reduced chi-squared statistic for the least-squares fit.

[c] d is the Durbin-Watson statistic, a measure of serial correlation for the least-squares fit.

Appendix Table A1.1 (continued): Rietveld refinement results for samples from Mount Keith.

Sample	**06MK31-1**	**06MK31-2**	**06MKG31-1-3**	**06MKG31-2-2**	**06MKG31-7-1**	**06MKG31-7-2**	**06MKG31-7-3**	**06MKG31-9-2**
Age (years)	0	0	0	0	0	0	0	0
Depth (cm)	0-5	2.5-5	100	75	0	50	100	50
Sample Type	Crust Sample	Fines Sample	Tarpaulin Grid	Tarpaulin Grid	Tarpaulin Grid	Tarpaulin Grid	Tarpaulin Grid	Tarpaulin Grid
Easting (UTM 51J WGS 84)	261079	261079	261079	261079	261079	261079	261079	261079
Northing (UTM 51J WGS 84)	6983710	6983710	6983710	6983710	6983710	6983710	6983710	6983710
Error on GPS Location (m)	6.1	6.1	6.1	6.1	6.1	6.1	6.1	6.1
Elevation at Surface (m OSL)	542.5	542.5	542.5	542.5	542.5	542.5	542.5	542.5
serpentine	48.5	73.7	79.8	78.6	70.1	78.2	80.8	79.6
kaolinite	–	–	–	–	–	–	–	–
brucite	–	–	3.1	2.8	–	2.0	3.1	2.1
talc	5.0	2.5	–	–	2.5	–	–	–
vermiculite	–	–	–	–	–	–	–	–
muscovite	–	–	–	–	–	–	–	–
hydrotalcite-group	1.5	2.0	3.2	2.3	2.9	2.3	2.3	3.0
gypsum	–	–	–	–	–	–	–	–
hexahydrite	8.6	–	–	–	–	–	–	–
epsomite	–	–	–	–	–	–	–	–
blödite	14.2	–	–	–	2.6	–	–	–
konyaite	–	–	–	–	–	–	–	–
löweite	tr	–	–	–	2.0	–	–	–
lepidocrocite	–	–	–	–	–	–	–	–
magnetite & chromite	2.7	1.7	4.7	5.2	1.6	5.3	3.4	4.4
quartz	–	0.4	tr	0.2	–	–	tr	tr
rutile	–	–	–	–	–	–	–	–
plagioclase	–	–	–	–	–	–	–	–
halite	12.5	4.2	0.6	0.9	4.4	0.5	0.5	0.3
magnesite	4.3	10.9	6.4	8.2	12.5	9.6	8.7	8.9
dolomite	1.8	2.9	1.9	0.9	0.7	1.1	0.4	0.9
calcite	0.4	0.4	0.2	0.2	0.7	tr	0.1	tr
trona	–	–	–	–	–	–	–	–
hydromagnesite	**0.6**	**1.2**	**–**	**0.6**	**–**	**1.1**	**0.6**	**0.9**
Total	100.0	100.0	100.0	100.0	100.0	100.0	100.0	100.0
R_{wp} [a]	5.2	4.4	4.3	3.6	3.6	3.6	3.5	3.6
χ^2 [b]	3.0	2.9	3.0	3.0	3.0	3.1	3.1	3.1
d [c]	2.2	2.2	2.3	2.2	2.1	2.2	2.0	2.1

[a] R_{wp} is the weighted pattern index, a function of the least-squares residual.

[b] χ^2 is the reduced chi-squared statistic for the least-squares fit.

[c] d is the Durbin-Watson statistic, a measure of serial correlation for the least-squares fit.

Appendix Table A1.1 (continued): Rietveld refinement results for samples from Mount Keith.

Sample	06MKG31-10-1	06MKG31-11-1	06MKG31-12-1	06MKG31-12-2	06MKG31-12-3	06MKG31-14-3	06MKG31-16-1	06MKP1-2
Age (years)	0	0	0	0	0	0	0	0.5
Depth (cm)	0	25	0	50	100	125	25	1-3
Sample Type	Tarpaulin Grid	Tarpaulin Grid	Tarpaulin Grid	Tarpaulin Grid	Tarpaulin Grid	Tarpaulin Grid	Tarpaulin Grid	Vertical Profile
Easting (UTM 51J WGS 84)	261079	261079	261079	261079	261079	261079	261079	260984
Northing (UTM 51J WGS 84)	6983710	6983710	6983710	6983710	6983710	6983710	6983710	6983591
Error on GPS Location (m)	6.1	6.1	6.1	6.1	6.1	6.1	6.1	5.7
Elevation at Surface (m OSL)	542.5	542.5	542.5	542.5	542.5	542.5	542.5	540.3
serpentine	62.6	78.1	62.5	80.2	77.9	80.4	71.1	64.4
kaolinite	–	–	–	–	–	–	–	–
brucite	0.4	–	–	2.1	1.9	2.7	0.4	–
talc	4.5	1.4	3.3	–	–	–	2.7	–
vermiculite	–	–	–	–	–	tr	–	–
muscovite	–	–	–	–	–	–	–	–
hydrotalcite-group	2.3	3.0	1.7	2.8	2.8	3.3	3.2	3.9
gypsum	–	–	–	–	–	–	–	–
hexahydrite	–	–	3.5	–	–	–	–	–
epsomite	–	–	–	–	–	–	–	–
blödite	1.8	–	7.3	–	–	–	–	11.5
konyaite	–	–	–	–	–	–	–	–
löweite	2.6	–	–	–	–	–	–	–
lepidocrocite	–	–	–	–	–	–	–	–
magnetite & chromite	4.6	4.4	1.4	5.3	5.9	4.2	6.3	5.1
quartz	tr	tr	tr?	tr	tr	tr	0.2	–
rutile	–	–	–	–	–	–	–	–
plagioclase	–	–	–	–	–	–	–	–
halite	3.7	0.6	6.9	0.5	0.4	0.4	0.8	4.9
magnesite	11.4	11.1	8.2	5.8	9.2	6.8	13.6	2.5
dolomite	2.2	1.4	3.2	1.9	1.3	1.9	1.5	1.2
calcite	1.0	tr	0.3	0.6	0.5	0.4	0.2	–
trona	1.1	–	0.6	–	–	tr?	–	–
hydromagnesite	**1.7**	–	**1.0**	**0.9**	–	**–**	–	**6.5**
Total	100.0	100.0	100.0	100.0	100.0	100.0	100.0	100.0
R_{wp} [a]	5.6	3.8	4.3	3.8	3.4	3.6	3.5	4.3
χ^2 [b]	4.3	3.3	3.1	3.2	2.9	3.1	3.0	2.9
d [c]	1.2	1.9	2.1	2.0	2.2	2.1	2.1	2.3

[a] R_{wp} is the weighted pattern index, a function of the least-squares residual.
[b] χ^2 is the reduced chi-squared statistic for the least-squares fit.
[c] d is the Durbin-Watson statistic, a measure of serial correlation for the least-squares fit.

Appendix Table A1.1 (continued): Rietveld refinement results for samples from Mount Keith.

Sample	**06MKP1-3**	**06MKP1-4**	**06MKP1-5**	**06MKP1-6**	**06MKP1-7**	**06MKP1-8**	**06MKP1-9**	**06MKP1-10**
Age (years)	0.5	0.5	0.5	0.5	0.5	0.5	0.5	0.5
Depth (cm)	3-5	5-14	14-15	21-29	41-46	46-55	58-62	62-63
Sample Type	Vertical Profile	Vertical Profile	Vertical Profile	Vertical Profile	Vertical Profile	Vertical Profile	Vertical Profile	Vertical Profile
Easting (UTM 51J WGS 84)	260984	260984	260984	260984	260984	260984	260984	260984
Northing (UTM 51J WGS 84)	6983591	6983591	6983591	6983591	6983591	6983591	6983591	6983591
Error on GPS Location (m)	5.7	5.7	5.7	5.7	5.7	5.7	5.7	5.7
Elevation at Surface (m OSL)	540.3	540.3	540.3	540.3	540.3	540.3	540.3	540.3
serpentine	71.3	80.0	83.6	80.0	82.5	82.9	82.7	86.8
kaolinite	–	–	–	–	–	–	–	–
brucite	–	4.2	3.0	4.4	2.8	3.7	3.0	1.9
talc	–	–	–	–	–	–	–	–
vermiculite	–	–	–	–	–	–	–	–
muscovite	–	–	–	–	–	–	–	–
hydrotalcite-group	4.5	3.6	2.5	4.8	4.7	4.5	2.8	3.9
gypsum	–	–	–	–	–	–	–	–
hexahydrite	–	–	–	–	–	–	–	–
epsomite	–	–	–	–	–	–	–	–
blödite	5.0	–	–	–	–	–	–	–
konyaite	–	–	–	–	–	–	–	–
löweite	–	–	–	–	–	–	–	–
lepidocrocite	–	–	–	–	–	–	–	–
magnetite & chromite	5.9	7.3	6.3	5.7	4.6	2.4	6.0	3.4
quartz	–	–	–	tr	tr	tr	tr?	–
rutile	–	–	–	–	–	–	–	–
plagioclase	–	–	–	–	–	–	–	–
halite	3.0	0.8	0.2	1.1	1.3	0.8	0.5	0.4
magnesite	2.7	3.2	3.3	1.5	1.1	3.1	2.6	0.9
dolomite	–	0.8	0.8	1.0	0.5	0.7	2.4	1.2
calcite	–	–	0.3	tr	tr	tr	tr	tr
trona	–	–	–	–	–	–	–	–
hydromagnesite	**7.6**	–	–	**1.4**	**2.6**	**2.0**	**–**	**1.4**
Total	100.0	100.0	100.0	100.0	100.0	100.0	100.0	100.0
R_{wp} [a]	4.3	3.7	4.0	4.0	4.0	5.1	3.9	4.0
χ^2 [b]	3.2	2.9	3.2	3.0	3.0	3.9	3.1	3.0
d [c]	2.1	2.1	2.1	2.2	2.2	1.6	2.3	2.2

[a] R_{wp} is the weighted pattern index, a function of the least-squares residual.

[b] χ^2 is the reduced chi-squared statistic for the least-squares fit.

[c] d is the Durbin-Watson statistic, a measure of serial correlation for the least-squares fit.

Appendix Table A1.1 (continued): Rietveld refinement results for samples from Mount Keith.

Sample	**06MKP1-11**	**06MKP1-12**	**06MKP1-13**	**06MKP1-14**	**06MKP1-15**	**06MKP1-16**	**06MKP1-17**	**06MKP1-18**
Age (years)	0.5	0.5	0.5	0.5	0.5	0.5	0.5	0.5
Depth (cm)	75-81	90-93	110-115	132-137	137-142	162-168	185-245	245-305
Sample Type	Vertical Profile	Vertical Profile	Vertical Profile	Vertical Profile	Vertical Profile	Vertical Profile	Vertical Profile	Vertical Profile
Easting (UTM 51J WGS 84)	260984	260984	260984	260984	260984	260984	260984	260984
Northing (UTM 51J WGS 84)	6983591	6983591	6983591	6983591	6983591	6983591	6983591	6983591
Error on GPS Location (m)	5.7	5.7	5.7	5.7	5.7	5.7	5.7	5.7
Elevation at Surface (m OSL)	540.3	540.3	540.3	540.3	540.3	540.3	540.3	540.3
serpentine	88.1	86.5	88.0	88.4	83.9	83.3	87.3	84.7
kaolinite	–	–	–	–	–	–	–	–
brucite	2.4	1.7	1.1	1.3	2.6	2.6	2.1	1.9
talc	–	–	–	–	–	–	–	–
vermiculite	–	–	–	tr	–	–	–	–
muscovite	–	–	–	–	–	–	–	–
hydrotalcite-group	3.4	5.0	3.7	3.0	3.8	2.9	2.8	2.7
gypsum	–	–	–	–	–	–	–	–
hexahydrite	–	–	–	–	–	–	–	–
epsomite	–	–	–	–	–	–	–	–
blödite	–	–	–	–	–	–	–	–
konyaite	–	–	–	–	–	–	–	–
löweite	–	–	–	–	–	–	–	–
lepidocrocite	–	–	–	–	–	–	–	–
magnetite & chromite	2.9	2.6	2.8	3.0	3.0	4.4	2.8	3.4
quartz	–	–	–	tr?	tr	tr	tr	tr
rutile	–	–	–	–	–	–	–	–
plagioclase	–	–	–	–	–	–	–	–
halite	0.2	0.6	0.3	–	0.7	0.2	0.6	0.5
magnesite	0.9	1.8	2.6	3.1	3.1	3.9	3.3	3.7
dolomite	1.5	0.5	1.0	0.7	0.6	2.3	1.2	2.5
calcite	tr	tr	tr	tr	tr	0.4	–	tr
trona	–	–	–	–	–	–	–	–
hydromagnesite	**0.5**	**1.1**	**0.5**	**0.5**	**2.4**	–	–	**0.5**
Total	100.0	100.0	100.0	100.0	100.0	100.0	100.0	100.0
R_{wp} [a]	4.1	3.8	4.1	3.8	4.4	3.8	4.9	3.9
χ^2 [b]	3.1	2.8	3.0	3.0	3.2	2.9	3.6	3.0
d [c]	2.3	2.3	2.2	2.3	2.0	2.4	1.8	2.3

[a] R_{wp} is the weighted pattern index, a function of the least-squares residual.

[b] χ^2 is the reduced chi-squared statistic for the least-squares fit.

[c] d is the Durbin-Watson statistic, a measure of serial correlation for the least-squares fit.

Appendix Table A1.1 (continued): Rietveld refinement results for samples from Mount Keith.

Sample	**06MKP1-19**	**06MKG2-5-2**	**06MKG2-6-1**	**06MKG2-6-3**	**06MKG2-7-2**	**06MKG2-7-3**	**06MKG2-9-1**	**06MKG2-12-3**
Age (years)	0.5	0.5	0.5	0.5	0.5	0.5	0.5	0.5
Depth (cm)	305-365	50	25	125	50	100	0	100
Sample Type	Vertical Profile	Tarpaulin Grid	Tarpaulin Grid	Tarpaulin Grid	Tarpaulin Grid	Tarpaulin Grid	Tarpaulin Grid	Tarpaulin Grid
Easting (UTM 51J WGS 84)	260984	260833	260833	260833	260833	260833	260833	260833
Northing (UTM 51J WGS 84)	6983591	6983692	6983692	6983692	6983692	6983692	6983692	6983692
Error on GPS Location (m)	5.7	5.3	5.3	5.3	5.3	5.3	5.3	5.3
Elevation at Surface (m OSL)	540.3	537.4	537.4	537.4	537.4	537.4	537.4	537.4
serpentine	85.0	85.4	80.5	82.0	81.9	73.0	63.5	83.9
kaolinite	–	–	–	–	–	–	–	–
brucite	1.9	3.3	2.3	4.5	4.6	6.2	–	5.2
talc	–	–	–	–	–	–	–	–
vermiculite	–	–	–	–	–	–	–	–
muscovite	–	–	–	–	–	–	–	–
hydrotalcite-group	2.5	3.2	6.5	3.6	4.2	6.7	2.3	3.6
gypsum	–	–	–	–	–	–	–	–
hexahydrite	–	–	–	–	–	–	5.1	–
epsomite	–	–	–	–	–	–	–	–
blödite	–	–	–	–	–	–	6.4	–
konyaite	–	–	–	–	–	–	1.6	–
löweite	–	–	–	–	–	–	–	–
lepidocrocite	–	–	–	–	–	–	–	0.6
magnetite & chromite	5.2	2.7	3.4	4.6	4.7	7.0	3.3	3.0
quartz	–	tr	–	–	–	–	0.4	0.5
rutile	–	–	–	–	–	–	–	–
plagioclase	–	–	–	–	–	–	–	–
halite	0.4	1.9	2.3	0.5	1.6	1.1	10.7	0.9
magnesite	2.1	0.8	2.0	2.2	1.1	1.7	0.7	1.2
dolomite	2.4	1.6	0.6	1.3	1.5	4.3	3.7	1.1
calcite	tr	tr	0.0	0.2	0.2	–	–	tr
trona	–	–	–	–	–	–	–	–
hydromagnesite	**0.5**	**1.1**	**2.4**	**1.3**	–	–	**2.4**	**–**
Total	100.0	100.0	100.0	100.0	100.0	100.0	100.0	100.0
R_{wp} [a]	4.0	3.8	4.3	3.8	3.8	3.8	4.9	6.2
χ^2 [b]	3.0	3.0	3.4	3.0	3.0	3.1	3.1	4.9
d [c]	2.2	2.2	1.9	2.1	2.2	2.3	2.1	1.1

[a] R_{wp} is the weighted pattern index, a function of the least-squares residual.

[b] χ^2 is the reduced chi-squared statistic for the least-squares fit.

[c] d is the Durbin-Watson statistic, a measure of serial correlation for the least-squares fit.

Appendix Table A1.1 (continued): Rietveld refinement results for samples from Mount Keith.

Sample	**06MKG2-13-3**	**06MKG2-15-1**	**06MKG2-16-3**	**06MK16-1**	**06MK16-2**	**06MK16-3**	**06MK16-4**	**06MK16-5**
Age (years)	0.5	0.5	0.5	0.5	0.5	0.5	0.5	0.5
Depth (cm)	125	0	125	0-5	25	50	75	100
Sample Type	Tarpaulin Grid	Tarpaulin Grid	Tarpaulin Grid	Core Sample	Core Sample	Core Sample	Core Sample	Core Sample
Easting (UTM 51J WGS 84)	260833	260833	260833	261330	261330	261330	261330	261330
Northing (UTM 51J WGS 84)	6983692	6983692	6983692	6983263	6983263	6983263	6983263	6983263
Error on GPS Location (m)	5.3	5.3	5.3	7.1	7.1	7.1	7.1	7.1
Elevation at Surface (m OSL)	537.4	537.4	537.4	544.3	544.3	544.3	544.3	544.3
serpentine	81.1	62.4	76.9	77.9	81.8	82.3	80.0	84.7
kaolinite	–	–	–	–	–	–	–	–
brucite	4.5	–	5.2	3.4	4.6	3.2	1.3	1.7
talc	tr	–	–	–	–	–	1.0	–
vermiculite	–	0.1	–	–	–	–	–	–
muscovite	–	–	–	–	–	–	–	–
hydrotalcite-group	3.8	1.1	4.9	2.4	1.5	3.5	4.9	4.6
gypsum	–	–	–	–	–	–	–	–
hexahydrite	–	5.1	–	2.1	–	–	–	–
epsomite	–	–	–	–	–	–	–	–
blödite	–	6.9	–	3.1	–	–	–	–
konyaite	–	–	–	–	–	–	–	–
löweite	–	–	–	–	–	–	–	–
lepidocrocite	–	–	–	–	–	–	–	–
magnetite & chromite	5.0	5.2	6.1	3.5	4.9	4.4	3.3	3.4
quartz	0.4	–	0.4	tr	0.2	0.2	0.3	–
rutile	–	–	–	–	–	–	–	–
plagioclase	–	–	–	–	–	–	–	–
halite	1.2	14.7	1.1	2.2	0.5	0.7	0.6	0.4
magnesite	1.4	0.4	3.0	3.7	5.0	5.0	7.1	3.5
dolomite	2.5	0.4	2.3	1.3	0.7	0.7	1.6	1.3
calcite	tr?	–	–	0.4	0.2	tr	tr	0.3
trona	–	–	–	–	–	–	–	–
hydromagnesite	**–**	**3.8**	–	–	**0.6**	–	–	–
Total	100.0	100.0	100.0	100.0	100.0	100.0	100.0	100.0
R_{wp} [a]	3.8	4.4	3.9	4.8	3.7	3.8	4.1	4.1
χ^2 [b]	3.1	2.9	3.6	3.7	3.0	3.1	3.3	3.0
d [c]	2.2	2.1	2.2	1.5	2.2	2.2	1.9	2.2

[a] R_{wp} is the weighted pattern index, a function of the least-squares residual.

[b] χ^2 is the reduced chi-squared statistic for the least-squares fit.

[c] d is the Durbin-Watson statistic, a measure of serial correlation for the least-squares fit.

Appendix Table A1.1 (continued): Rietveld refinement results for samples from Mount Keith.

Sample	**06MK16-6**	**06MK16-10**	**06MK18-7**	**06MK22-1**	**06MK22-2**	**06MK22-3**	**06MK22-4**	**06MK22-5**
Age (years)	0.5	0.5	0.5	0.5	0.5	0.5	0.5	0.5
Depth (cm)	125	0	0-2	0-5	25	50	75	100
Sample Type	Core Sample	Crust Sample	Crust Sample	Core Sample	Core Sample	Core Sample	Core Sample	Core Sample
Easting (UTM 51J WGS 84)	261330	261330	261158	260718	260718	260718	260718	260718
Northing (UTM 51J WGS 84)	6983263	6983263	6983481	6984191	6984191	6984191	6984191	6984191
Error on GPS Location (m)	7.1	7.1	4.4	5.2	5.2	5.2	5.2	5.2
Elevation at Surface (m OSL)	544.3	544.3	542.0	534.1	534.1	534.1	534.1	534.1
serpentine	80.1	55.8	76.6	78.1	78.9	82.6	80.8	82.3
kaolinite	–	–	–	–	–	–	–	–
brucite	2.0	0.2	3.9	2.0	1.1	1.9	3.2	2.7
talc	–	–	–	–	3.0	0.9	–	–
vermiculite	–	–	–	–	0.2	0.1	0.2	–
muscovite	–	–	–	–	–	–	–	–
hydrotalcite-group	5.5	1.2	1.8	3.3	2.4	4.0	4.8	2.5
gypsum	–	0.6	–	–	–	–	–	–
hexahydrite	–	4.8	–	–	–	–	–	–
epsomite	–	2.1	–	–	–	–	–	–
blödite	–	19.9	–	2.2	–	–	–	–
konyaite	–	–	–	–	–	–	–	–
löweite	–	–	–	2.5	–	–	–	–
lepidocrocite	–	–	–	–	–	–	–	–
magnetite & chromite	5.8	1.7	4.6	2.1	4.0	3.8	4.6	5.8
quartz	tr	–	tr	tr	0.3	tr	0.1	0.2
rutile	–	–	–	–	–	–	–	–
plagioclase	–	–	–	–	–	–	–	–
halite	2.2	7.7	3.6	3.0	0.8	0.3	0.5	0.3
magnesite	2.4	2.9	8.0	4.4	5.6	3.1	3.8	3.3
dolomite	1.6	0.3	1.4	2.5	3.6	3.2	2.2	1.3
calcite	tr	–	0.2	tr	–	tr	tr?	–
trona	–	–	–	–	–	–	–	–
hydromagnesite	**0.5**	**2.9**	–	–	–	–	–	**1.6**
Total	100.0	100.0	100.0	100.0	100.0	100.0	100.0	100.0
R_{wp} [a]	4.1	4.6	5.2	4.2	5.2	3.8	4.2	4.0
χ^2 [b]	3.0	3.1	4.2	2.9	4.0	3.0	3.3	3.1
d [c]	2.2	2.0	1.4	2.3	1.4	2.1	2.0	2.0

[a] R_{wp} is the weighted pattern index, a function of the least-squares residual.

[b] χ^2 is the reduced chi-squared statistic for the least-squares fit.

[c] d is the Durbin-Watson statistic, a measure of serial correlation for the least-squares fit.

Appendix Table A1.1 (continued): Rietveld refinement results for samples from Mount Keith.

Sample	**06MK22-6**	**06MK22-7**	**06MKG29-1-1**	**06MKG29-1-2**	**06MKG29-1-3**	**06MKG29-3-3**	**06MKG29-4-3**	**06MKG29-6-1**
Age (years)	0.5	0.5	0.83	0.83	0.83	0.83	0.83	0.83
Depth (cm)	125	0-2	0	50	100	100	125	25
Sample Type	Core Sample	Crust Sample	10m Pipe Grid	10m Pipe Grid	10m Pipe Grid	10m Pipe Grid	10m Pipe Grid	10m Pipe Grid
Easting (UTM 51J WGS 84)	260718	260718	261675	261675	261675	261675	261675	261675
Northing (UTM 51J WGS 84)	6984191	6984191	6984906	6984906	6984906	6984906	6984906	6984906
Error on GPS Location (m)	5.2	5.2	6.9	6.9	6.9	6.9	6.9	6.9
Elevation at Surface (m OSL)	534.1	534.1	527.2	527.2	527.2	527.2	527.2	527.2
serpentine	83.9	51.0	71.5	87.4	86.1	84.7	80.0	79.1
kaolinite	–	–	–	–	–	–	–	–
brucite	2.0	tr	–	1.7	1.6	1.4	0.8	–
talc	–	–	–	–	–	–	–	–
vermiculite	–	–	0.1	0.2	0.2	0.2	0.2	0.1
muscovite	–	–	–	–	–	–	–	–
hydrotalcite-group	3.1	1.2	4.0	3.9	5.6	5.6	7.0	9.2
gypsum	–	–	–	–	–	–	–	–
hexahydrite	–	10.2	–	–	–	–	–	–
epsomite	–	6.4	–	–	–	–	–	–
blödite	–	17.0	8.5	–	–	–	–	–
konyaite	–	–	–	–	–	–	–	–
löweite	–	–	2.6	–	–	–	–	–
lepidocrocite	–	–	–	–	–	–	–	–
magnetite & chromite	5.0	0.7	2.2	3.2	2.7	3.9	3.1	2.7
quartz	0.2	–	tr?	–	tr?	–	0.3	–
rutile	–	–	–	–	–	–	–	–
plagioclase	–	–	–	–	–	–	–	–
halite	0.7	11.8	6.9	0.5	0.3	0.4	0.5	2.3
magnesite	3.1	1.6	1.9	1.8	1.3	2.4	3.6	3.5
dolomite	2.0	tr?	0.4	1.3	0.5	1.2	0.7	1.7
calcite	tr	–	–	tr?	tr	0.2	0.4	tr
trona	–	–	–	–	–	–	–	–
hydromagnesite	–	–	**1.9**	**–**	**1.7**	**–**	**3.5**	**1.5**
Total	100.0	100.0	100.0	100.0	100.0	100.0	100.0	100.0
R_{wp} [a]	3.7	6.8	5.4	4.2	4.1	4.3	4.7	7.4
χ^2 [b]	2.9	4.4	3.3	2.9	2.8	3.1	3.2	5.1
d [c]	2.3	1.2	1.8	2.3	2.3	2.2	1.8	1.0

[a] R_{wp} is the weighted pattern index, a function of the least-squares residual.

[b] χ^2 is the reduced chi-squared statistic for the least-squares fit.

[c] d is the Durbin-Watson statistic, a measure of serial correlation for the least-squares fit.

Appendix Table A1.1 (continued): Rietveld refinement results for samples from Mount Keith.

Sample	**06MKG29-6-2**	**06MKG29-6-3**	**06MKG29-7-1**	**06MKG7-2-1**	**06MKG7-2-3**	**06MKG7-4-1**	**06MKG7-5-2**	**06MKG7-5-3**
Age (years)	0.83	0.83	0.83	1	1	1	1	1
Depth (cm)	75	125	0	25	125	25	50	100
Sample Type	10m Pipe Grid	10m Pipe Grid	10m Pipe Grid	Tarpaulin Grid	Tarpaulin Grid	Tarpaulin Grid	Tarpaulin Grid	Tarpaulin Grid
Easting (UTM 51J WGS 84)	261675	261675	261675	260146	260146	260146	260146	260146
Northing (UTM 51J WGS 84)	6984906	6984906	6984906	6981564	6981564	6981564	6981564	6981564
Error on GPS Location (m)	6.9	6.9	6.9	4.4	4.4	4.4	4.4	4.4
Elevation at Surface (m OSL)	527.2	527.2	527.2	532.4	532.4	532.4	532.4	532.4
serpentine	85.8	86.6	70.8	77.5	80.4	82.7	83.6	82.5
kaolinite	–	–	–	–	–	–	–	–
brucite	1.4	0.5	–	2.6	4.6	2.5	4.6	4.8
talc	–	–	–	–	–	–	–	–
vermiculite	0.3	0.2	–	tr	–	–	–	–
muscovite	–	–	–	–	–	–	–	–
hydrotalcite-group	4.9	4.9	3.8	4.2	4.9	3.9	4.7	3.7
gypsum	–	–	–	–	–	–	–	–
hexahydrite	–	–	–	–	–	–	–	–
epsomite	–	–	–	–	–	–	–	–
blödite	–	–	9.0	–	–	–	–	–
konyaite	–	–	–	–	–	–	–	–
löweite	–	–	3.6	–	–	–	–	–
lepidocrocite	–	–	–	–	–	–	–	–
magnetite & chromite	3.3	3.5	2.0	10.1	5.0	6.3	4.2	4.9
quartz	–	–	0.2	0.3	0.4	–	–	–
rutile	–	–	–	–	–	–	–	–
plagioclase	–	–	–	–	–	–	–	–
halite	0.6	0.4	6.8	0.1	tr	1.9	tr	–
magnesite	1.8	2.4	2.1	3.1	3.4	1.9	1.8	2.8
dolomite	1.0	1.0	1.0	1.4	1.3	1.0	1.0	1.2
calcite	–	tr	0.7	tr	tr	tr	tr	tr?
trona	–	–	–	–	–	–	–	–
hydromagnesite	**0.9**	**0.5**	**–**	**0.7**	–	–	–	–
Total	100.0	100.0	100.0	100.0	100.0	100.0	100.0	100.0
R_{wp} [a]	4.1	4.3	5.3	3.6	3.7	3.6	3.6	3.7
χ^2 [b]	2.9	3.1	3.1	3.0	3.0	3.0	3.1	3.1
d [c]	2.3	2.2	2.0	2.2	2.1	2.3	2.1	2.1

[a] R_{wp} is the weighted pattern index, a function of the least-squares residual.

[b] χ^2 is the reduced chi-squared statistic for the least-squares fit.

[c] d is the Durbin-Watson statistic, a measure of serial correlation for the least-squares fit.

Appendix Table A1.1 (continued): Rietveld refinement results for samples from Mount Keith.

Sample	**06MKG7-6-1**	**06MKG7-7-1**	**06MKG7-7-3**	**06MKG7-13-3**	**06MKG7-17-3**	**06MK36-1**	**06MK36-2**	**06MK36-3**
Age (years)	1	1	1	1	1	1	1	1
Depth (cm)	25	0	100	125	100	0-5	0-2.5	2.5-5.0
Sample Type	Tarpaulin Grid	Tarpaulin Grid	Tarpaulin Grid	Tarpaulin Grid	Tarpaulin Grid	Core Sample	Crust Sample	Fines Sample
Easting (UTM 51J WGS 84)	260146	260146	260146	260146	260146	260982	260982	260982
Northing (UTM 51J WGS 84)	6981564	6981564	6981564	6981564	6981564	6980885	6980885	6980885
Error on GPS Location (m)	4.4	4.4	4.4	4.4	4.4	6.0	6.0	6.0
Elevation at Surface (m OSL)	532.4	532.4	532.4	532.4	532.4	531.5	531.5	531.5
serpentine	80.8	71.3	77.5	81.4	79.8	66.9	75.1	80.1
kaolinite	–	–	–	–	–	–	–	–
brucite	4.0	tr	5.1	5.0	3.7	0.5	–	tr
talc	–	–	–	–	–	–	–	–
vermiculite	–	0.2	–	–	–	–	–	–
muscovite	–	–	–	–	–	–	–	–
hydrotalcite-group	6.7	2.6	5.4	3.5	4.3	2.1	1.3	1.3
gypsum	–	1.0	–	–	–	0.4	0.2	–
hexahydrite	–	3.1	–	–	–	2.1	1.1	3.4
epsomite	–	–	–	–	–	–	–	–
blödite	–	10.1	–	–	–	8.2	10.1	5.9
konyaite	–	–	–	–	–	–	–	–
löweite	–	–	–	–	–	–	–	–
lepidocrocite	–	–	–	–	–	–	–	–
magnetite & chromite	4.2	3.0	6.6	5.2	5.0	5.7	3.0	3.5
quartz	–	–	tr	tr	0.1	–	–	–
rutile	–	–	–	–	–	–	–	–
plagioclase	–	–	–	–	–	–	–	–
halite	0.6	3.7	0.4	0.9	0.2	7.2	3.2	3.2
magnesite	2.7	3.0	3.6	2.9	3.1	3.3	2.8	2.4
dolomite	0.8	0.5	1.1	1.1	0.8	tr	1.4	0.2
calcite	0.3	tr	0.3	tr	tr	–	0.2	tr
trona	–	–	–	–	–	–	–	–
hydromagnesite	**–**	**1.5**	–	–	**2.8**	**3.5**	**1.6**	**–**
Total	100.0	100.0	100.0	100.0	100.0	100.0	100.0	100.0
R_{wp} [a]	4.6	4.2	3.6	3.8	3.7	3.9	4.2	4.0
χ^2 [b]	3.8	3.1	2.9	3.2	3.0	2.8	3.0	2.9
d [c]	1.7	2.0	2.3	2.0	2.3	2.2	2.1	2.2

[a] R_{wp} is the weighted pattern index, a function of the least-squares residual.

[b] χ^2 is the reduced chi-squared statistic for the least-squares fit.

[c] d is the Durbin-Watson statistic, a measure of serial correlation for the least-squares fit.

Appendix Table A1.1 (continued): Rietveld refinement results for samples from Mount Keith.

Sample	**06MK36-4**	**06MK36-5**	**06MK36-6**	**06MK36-7**	**06MK36-8**	**06MK37-1**	**06MK37-2**	**06MK37-3**
Age (years)	1	1	1	1	1	1	1	1
Depth (cm)	25	50	75	100	125	0-5	0-2.5	2.5-5.0
Sample Type	Core Sample	Core Sample	Core Sample	Core Sample	Core Sample	Core Sample	Crust Sample	Fines Sample
Easting (UTM 51J WGS 84)	260982	260982	260982	260982	260982	262100	262100	262100
Northing (UTM 51J WGS 84)	6980885	6980885	6980885	6980885	6980885	6980682	6980682	6980682
Error on GPS Location (m)	6.0	6.0	6.0	6.0	6.0	4.2	4.2	4.2
Elevation at Surface (m OSL)	531.5	531.5	531.5	531.5	531.5	529.8	529.8	529.8
serpentine	85.1	84.0	84.2	82.7	81.9	79.7	73.8	82.0
kaolinite	–	–	–	–	–	–	–	–
brucite	1.5	1.9	1.9	1.6	1.9	1.1	1.5	1.9
talc	–	–	–	–	–	–	–	–
vermiculite	–	–	–	–	–	–	–	–
muscovite	–	–	–	–	–	–	–	–
hydrotalcite-group	2.9	3.4	3.2	4.2	3.5	2.1	2.2	3.0
gypsum	–	–	–	–	–	–	–	–
hexahydrite	–	–	–	–	–	1.2	6.5	–
epsomite	–	–	–	–	–	–	–	–
blödite	–	–	–	–	–	1.0	2.8	–
konyaite	–	–	–	–	–	–	–	–
löweite	–	–	–	–	–	–	–	–
lepidocrocite	–	–	–	–	–	–	–	–
magnetite & chromite	4.9	5.4	5.9	6.9	4.9	2.4	2.7	3.2
quartz	–	–	–	–	–	–	–	–
rutile	–	–	–	–	–	–	–	–
plagioclase	–	–	–	–	–	–	–	–
halite	0.2		tr?	tr?	tr	6.8	4.4	4.0
magnesite	4.5	4.0	3.0	3.5	5.6	3.6	2.3	3.8
dolomite	0.9	1.3	1.9	1.0	1.1	0.5	2.5	0.7
calcite	tr	tr	–	–	–	–	–	tr?
trona	–	–	–	–	–	–	–	–
hydromagnesite	–	–	–	–	**1.1**	**1.6**	**1.5**	**1.4**
Total	100.0	100.0	100.0	100.0	100.0	100.0	100.0	100.0
R_{wp} [a]	3.6	3.8	3.7	3.7	3.6	4.5	4.7	5.7
χ^2 [b]	3.0	3.2	3.1	3.1	2.9	2.9	2.9	3.2
d [c]	2.2	2.2	2.1	2.1	2.2	2.3	2.2	2.0

[a] R_{wp} is the weighted pattern index, a function of the least-squares residual.

[b] χ^2 is the reduced chi-squared statistic for the least-squares fit.

[c] d is the Durbin-Watson statistic, a measure of serial correlation for the least-squares fit.

Appendix Table A1.1 (continued): Rietveld refinement results for samples from Mount Keith.

Sample	**06MK37-4**	**06MK37-5**	**06MK37-6**	**06MK37-7**	**06MK37-8**	**06MKG27-1-1**	**06MKG27-1-2**	**06MKG27-1-3**
Age (years)	1	1	1	1	1	3	3	3
Depth (cm)	25	50	75	100	125	0	50	100
Sample Type	Core Sample	Core Sample	Core Sample	Core Sample	Core Sample	10m Pipe Grid	10m Pipe Grid	10m Pipe Grid
Easting (UTM 51J WGS 84)	262100	262100	262100	262100	262100	263178	263178	263178
Northing (UTM 51J WGS 84)	6980682	6980682	6980682	6980682	6980682	6984701	6984701	6984701
Error on GPS Location (m)	4.2	4.2	4.2	4.2	4.2	6.3	6.3	6.3
Elevation at Surface (m OSL)	529.8	529.8	529.8	529.8	529.8	523.7	523.7	523.7
serpentine	82.9	77.3	78.8	81.7	79.8	71.9	85.2	83.0
kaolinite	–	–	–	–	–	–	–	–
brucite	4.2	2.0	2.6	2.4	2.3	–	0.5	–
talc	–	–	–	–	–	–	–	–
vermiculite	–	–	–	–	–	–	–	–
muscovite	–	–	–	–	–	–	–	–
hydrotalcite-group	3.7	3.1	4.3	5.1	4.8	2.0	5.2	5.6
gypsum	–	–	–	–	–	–	–	–
hexahydrite	–	–	–	–	–	3.4	–	–
epsomite	–	–	–	–	–	–	–	–
blödite	–	–	–	–	–	11.1	–	–
konyaite	–	–	–	–	–	–	–	–
löweite	–	–	–	–	–	–	–	–
lepidocrocite	–	–	–	–	–	–	–	–
magnetite & chromite	3.6	6.6	6.6	4.5	4.6	3.9	1.0	4.4
quartz	–	–	–	–	tr	–	0.2	0.5
rutile	–	–	–	–	–	–	–	–
plagioclase	–	–	–	–	–	–	–	–
halite	1.3	0.9	0.2	0.4	0.6	4.6	0.4	–
magnesite	3.2	7.4	6.2	5.5	6.2	1.4	3.0	1.4
dolomite	1.0	1.5	1.2	0.6	1.7	1.2	2.7	3.9
calcite	tr?	0.3	0.2	tr	tr	–	0.4	tr
trona	–	–	–	–	–	–	–	–
hydromagnesite	**–**	**1.0**	–	–	–	**0.6**	**1.3**	**1.2**
Total	100.0	100.0	100.0	100.0	100.0	100.0	100.0	100.0
R_{wp} [a]	5.7	5.1	5.3	4.9	5.6	4.1	3.6	3.5
χ^2 [b]	3.4	3.0	3.1	2.9	3.4	2.9	3.0	2.9
d [c]	1.9	2.3	2.1	2.3	1.9	2.3	2.2	2.3

[a] R_{wp} is the weighted pattern index, a function of the least-squares residual.

[b] χ^2 is the reduced chi-squared statistic for the least-squares fit.

[c] d is the Durbin-Watson statistic, a measure of serial correlation for the least-squares fit.

Appendix Table A1.1 (continued): Rietveld refinement results for samples from Mount Keith.

Sample	**06MKG27-2-1**	**06MKG27-5-1**	**06MK42-1**	**06MK42-3**	**06MK42-4**	**06MK43-1**	**06MK43-3**	**06MK43-6**
Age (years)	3	3	3	3	3	3	3	3
Depth (cm)	25	0	0-5	2.5-5.0	25	0-5	2.5-5.0	25
Sample Type	10m Pipe Grid	10m Pipe Grid	Core Sample	Fines Sample	Core Sample	Core Sample	Fines Sample	Core Sample
Easting (UTM 51J WGS 84)	263178	263178	262475	262475	262475	262427	262427	262427
Northing (UTM 51J WGS 84)	6984701	6984701	6984742	6984742	6984742	6984907	6984907	6984907
Error on GPS Location (m)	6.3	6.3	6.8	6.8	6.8	6.6	6.6	6.6
Elevation at Surface (m OSL)	523.7	523.7	525.6	525.6	525.6	530.8	530.8	530.8
serpentine	88.8	78.3	68.2	84.3	88.8	71.5	83.8	83.6
kaolinite	–	–	–	–	–	–	–	–
brucite	0.4	–	0.3	0.4	1.1	–	–	1.3
talc	–	–	3.2	–	–	1.7	–	–
vermiculite	–	–	0.5	0.3	0.1	–	0.1	0.2
muscovite	–	–	–	–	–	–	–	–
hydrotalcite-group	3.1	3.2	3.4	3.1	3.2	4.4	5.3	3.7
gypsum	–	–	–	–	–	–	–	–
hexahydrite	–	2.5	2.9	–	–	–	–	–
epsomite	–	–	–	–	–	–	–	–
blödite	–	5.3	2.5	–	–	2.9	–	–
konyaite	–	–	–	–	–	–	–	–
löweite	–	–	5.3	–	–	6.5	–	–
lepidocrocite	–	–	–	–	–	–	–	–
magnetite & chromite	1.5	2.8	2.6	2.4	3.3	2.2	3.0	1.9
quartz	0.3	–	–	–	tr	–	–	–
rutile	–	–	–	–	–	–	–	–
plagioclase	–	–	–	–	–	–	–	–
halite	1.2	3.6	4.3	2.5	1.2	5.9	2.2	2.6
magnesite	2.9	2.5	2.6	1.9	1.3	2.5	2.7	2.5
dolomite	1.6	0.9	2.0	2.5	1.0	0.8	1.4	2.9
calcite	0.2	tr?	0.5	tr	tr	–	tr?	0.3
trona	–	–	–	–	–	–	–	–
hydromagnesite	**–**	**0.9**	**1.8**	**2.6**	**–**	**1.7**	**1.5**	**1.1**
Total	100.0	100.0	100.0	100.0	100.0	100.0	100.0	100.0
R_{wp} [a]	3.7	5.1	5.8	5.3	4.5	7.8	6.4	4.5
χ^2 [b]	3.0	3.9	2.8	2.9	3.1	4.6	4.3	3.0
d [c]	2.2	1.5	2.3	2.2	2.3	1.1	1.3	2.3

[a] R_{wp} is the weighted pattern index, a function of the least-squares residual.

[b] χ^2 is the reduced chi-squared statistic for the least-squares fit.

[c] d is the Durbin-Watson statistic, a measure of serial correlation for the least-squares fit.

Appendix Table A1.1 (continued): Rietveld refinement results for samples from Mount Keith.

Sample	06MK43-7	06MK43-8	06MK43-9	06MK43-10	06MKG5-1-2	06MKG5-1-3	06MKG5-4-2	06MKG5-5-1
Age (years)	3	3	3	3	7-8	7-8	7-8	7-8
Depth (cm)	50	75	100	125	50	100	75	0
Sample Type	Core Sample	Core Sample	Core Sample	Core Sample	Tarpaulin Grid	Tarpaulin Grid	Tarpaulin Grid	Tarpaulin Grid
Easting (UTM 51J WGS 84)	262427	262427	262427	262427	259940	259940	259940	259940
Northing (UTM 51J WGS 84)	6984907	6984907	6984907	6984907	6984050	6984050	6984050	6984050
Error on GPS Location (m)	6.6	6.6	6.6	6.6	4.0	4.0	4.0	4.0
Elevation at Surface (m OSL)	530.8	530.8	530.8	530.8	531.1	531.1	531.1	531.1
serpentine	84.8	89.7	85.1	83.2	82.6	85.7	86.3	60.0
kaolinite	–	–	–	–	–	–	–	–
brucite	0.6	–	–	–	1.9	tr	tr	–
talc	–	–	–	–	–	–	–	–
vermiculite	tr	–	–	–	–	tr	0.2	–
muscovite	–	–	–	–	–	–	–	–
hydrotalcite-group	5.3	3.9	5.5	5.8	5.4	2.2	5.0	1.6
gypsum	–	–	–	–	–	–	–	–
hexahydrite	–	–	–	–	–	–	–	9.8
epsomite	–	–	–	–	–	–	–	–
blödite	–	–	–	–	–	–	–	13.3
konyaite	–	–	–	–	–	–	–	–
löweite	–	–	–	–	–	–	–	–
lepidocrocite	–	–	–	–	–	–	–	–
magnetite & chromite	2.6	1.0	1.5	2.3	3.9	3.5	1.4	3.2
quartz	tr?	tr	tr	tr	0.2	0.7	0.6	–
rutile	–	–	–	–	–	–	–	–
plagioclase	–	–	–	–	–	–	–	–
halite	0.8	0.7	tr	0.2	2.0	1.6	1.1	7.3
magnesite	3.2	3.5	4.4	5.9	1.6	2.9	3.8	0.7
dolomite	1.2	1.2	1.9	2.5	1.3	1.5	1.6	–
calcite	–	–	tr	tr	–	–	–	–
trona	–	–	–	–	–	–	–	–
hydromagnesite	**1.5**	**–**	**1.6**	**–**	**1.2**	**2.0**	**–**	**4.0**
Total	100.0	100.0	100.0	100.0	100.0	100.0	100.0	100.0
R_{wp} [a]	5.1	4.5	4.3	4.5	3.9	3.8	4.6	4.7
χ^2 [b]	3.5	3.1	3.0	3.2	3.1	3.0	3.8	3.2
d [c]	1.8	2.2	2.3	2.2	2.1	2.1	1.5	2.1

[a] R_{wp} is the weighted pattern index, a function of the least-squares residual.

[b] χ^2 is the reduced chi-squared statistic for the least-squares fit.

[c] d is the Durbin-Watson statistic, a measure of serial correlation for the least-squares fit.

Appendix Table A1.1 (continued): Rietveld refinement results for samples from Mount Keith.

Sample	**06MKG5-9-1**	**06MKG5-9-2**	**06MKG5-16-1**	**06MKG5-16-2**	**06MKP6-1**	**06MKG8-1-2**	**06MKG8-3-1**	**06MKG8-7-1**
Age (years)	7-8	7-8	7-8	7-8	7-8	7-8	7-8	7-8
Depth (cm)	0	50	25	75	0-5	50	0	0
Sample Type	Tarpaulin Grid	Tarpaulin Grid	Tarpaulin Grid	Tarpaulin Grid	Vertical Profile	10m Pipe Grid	10m Pipe Grid	10m Pipe Grid
Easting (UTM 51J WGS 84)	259940	259940	259940	259940	259940	259725	259725	259725
Northing (UTM 51J WGS 84)	6984050	6984050	6984050	6984050	6984050	6983721	6983721	6983721
Error on GPS Location (m)	4.0	4.0	4.0	4.0	4.0	4.3	4.3	4.3
Elevation at Surface (m OSL)	531.1	531.1	531.1	531.1	531.1	529.4	529.4	529.4
serpentine	67.5	88.3	86.5	83.0	81.0	79.4	73.0	78.7
kaolinite	–	–	–	–	–	–	–	–
brucite	–	1.7	1.2	tr	0.6	–	–	–
talc	–	–	–	–	–	–	–	–
vermiculite	–	tr	0.3	0.3	–	tr	–	–
muscovite	–	–	–	–	–	–	–	–
hydrotalcite-group	2.7	3.7	4.0	3.3	2.1	8.0	1.1	2.6
gypsum	–	–	–	–	–	–	0.4	–
hexahydrite	5.7	–	–	–	–	–	5.0	1.0
epsomite	7.3	–	–	–	–	–	–	–
blödite	7.4	–	–	–	–	–	2.5	0.9
konyaite	–	–	–	–	–	–	1.6	3.1
löweite	–	–	–	–	–	–	–	–
lepidocrocite	–	–	–	–	–	–	–	–
magnetite & chromite	2.2	2.7	1.6	5.6	5.8	3.8	2.3	2.9
quartz	–	tr	tr	tr	–	0.2	3.6	0.5
rutile	–	–	–	–	–	–	–	–
plagioclase	–	–	–	–	–	–	–	–
halite	6.3	0.8	1.6	1.1	3.1	0.5	6.5	4.5
magnesite	–	1.1	2.8	3.3	1.2	5.5	2.3	4.7
dolomite	–	1.1	2.1	2.9	0.6	2.0	1.7	0.7
calcite	–	–	–	–	0.6	–	–	0.2
trona	–	–	–	–	–	–	–	–
hydromagnesite	**0.9**	**0.5**	**–**	**0.5**	**5.1**	**0.5**	–	–
Total	100.0	100.0	100.0	100.0	100.0	100.0	100.0	100.0
R_{wp} [a]	5.1	4.0	3.9	4.0	4.2	5.7	4.5	4.1
χ^2 [b]	3.6	3.3	3.1	3.3	2.9	4.8	3.1	3.0
d [c]	1.8	2.0	2.1	2.0	2.3	1.2	2.1	2.1

[a] R_{wp} is the weighted pattern index, a function of the least-squares residual.

[b] χ^2 is the reduced chi-squared statistic for the least-squares fit.

[c] d is the Durbin-Watson statistic, a measure of serial correlation for the least-squares fit.

Appendix Table A1.1 (continued): Rietveld refinement results for samples from Mount Keith.

Sample	**06MKG8-8-2**	**06MKG8-8-3**	**06MK9-1**	**06MK9-2**	**06MK9-6**	**06MK9-7**	**06MKG9-1-2**	**06MKG9-2-3**
Age (years)	7-8	7-8	7-8	7-8	7-8	7-8	7-8	7-8
Depth (cm)	75	100	0-2	2-4	0-10	0	50	125
Sample Type	10m Pipe Grid	10m Pipe Grid	Surface Crust	Surface Fines	Surface Cement	Surface Cement	8m Pipe Grid	8m Pipe Grid
Easting (UTM 51J WGS 84)	259725	259725	259674	259674	259674	259674	259674	259674
Northing (UTM 51J WGS 84)	6983721	6983721	6983486	6983486	6983486	6983486	6983486	6983486
Error on GPS Location (m)	4.3	4.3	5.4	5.4	5.4	5.4	5.4	5.4
Elevation at Surface (m OSL)	529.4	529.4	540.3	540.3	540.3	540.3	540.3	540.3
serpentine	85.0	82.8	72.6	70.3	81.3	84.5	85.0	84.5
kaolinite	–	–	–	–	–	–	–	–
brucite	1.1	2.0	–	–	–	–	0.4	0.3
talc	–	–	–	–	–	–	–	–
vermiculite	tr	tr	–	–	–	–	–	0.1
muscovite	–	–	–	–	–	–	–	–
hydrotalcite-group	6.2	5.7	1.4	1.6	2.3	3.0	4.6	7.1
gypsum	–	–	0.9	–	–	–	–	–
hexahydrite	–	–	4.2	2.0	–	–	–	–
epsomite	–	–	–	–	–	–	–	–
blödite	–	–	1.5	11.5	–	–	–	–
konyaite	–	–	–	–	–	–	–	–
löweite	–	–	–	–	–	–	–	–
lepidocrocite	–	–	–	–	–	–	–	–
magnetite & chromite	1.9	3.8	4.9	1.4	2.5	2.8	2.8	2.9
quartz	0.4	0.1	5.1	1.2	–	0.4	tr	0.2
rutile	–	–	–	–	–	–	–	–
plagioclase	–	–	–	–	–	–	–	–
halite	0.5	0.2	3.5	7.8	1.8	2.2	0.3	0.1
magnesite	1.9	3.2	2.4	1.6	1.0	1.2	2.7	1.6
dolomite	1.8	1.0	1.5	0.6	–	0.6	1.8	1.1
calcite	–	–	0.1	0.7	0.6	1.0	tr	0.4
trona	–	–	–	–	–	–	–	–
hydromagnesite	**1.2**	**1.1**	**1.9**	**1.2**	**10.4**	**4.3**	**2.3**	**1.8**
Total	100.0	100.0	100.0	100.0	100.0	100.0	100.0	100.0
R_{wp} [a]	3.8	4.1	4.2	7.2	4.3	5.3	4.0	4.1
χ^2 [b]	3.0	3.2	2.7	4.2	3.0	3.7	3.0	2.8
d [c]	2.2	1.9	2.2	1.4	2.4	1.5	2.3	2.3

[a] R_{wp} is the weighted pattern index, a function of the least-squares residual.

[b] χ^2 is the reduced chi-squared statistic for the least-squares fit.

[c] d is the Durbin-Watson statistic, a measure of serial correlation for the least-squares fit.

Appendix Table A1.1 (continued): Rietveld refinement results for samples from Mount Keith.

Sample	**06MKG9-4-1**	**06MKG9-6-2**	**06MKG9-9-3**	**06MKP9-1**	**06MKP9-2**	**06MKP9-3**	**06MKP9-4**	**06MKP9-5**
Age (years)	7-8	7-8	7-8	7-8	7-8	7-8	7-8	7-8
Depth (cm)	25	75	100	137-147	114-124	99-109	87-97	75-80
Sample Type	8m Pipe Grid	8m Pipe Grid	8m Pipe Grid	Vertical Profile	Vertical Profile	Vertical Profile	Vertical Profile	Vertical Profile
Easting (UTM 51J WGS 84)	259674	259674	259674	259674	259674	259674	259674	259674
Northing (UTM 51J WGS 84)	6983486	6983486	6983486	6983486	6983486	6983486	6983486	6983486
Error on GPS Location (m)	5.4	5.4	5.4	5.4	5.4	5.4	5.4	5.4
Elevation at Surface (m OSL)	540.3	540.3	540.3	540.3	540.3	540.3	540.3	540.3
serpentine	81.4	88.7	82.8	84.9	85.1	83.3	85.8	78.2
kaolinite	–	–	–	–	–	–	–	–
brucite	0.9	0.2	0.2	0.8	1.5	–	–	0.4
talc	–	–	–	–	–	–	–	–
vermiculite	–	0.2	–	–	tr	–	–	–
muscovite	–	–	–	–	–	–	–	–
hydrotalcite-group	7.1	4.2	4.8	3.5	3.2	4.2	4.2	3.7
gypsum	–	–	–	–	–	–	–	–
hexahydrite	–	–	–	–	–	–	–	–
epsomite	–	–	–	–	–	–	–	–
blödite	–	–	–	–	–	–	–	–
konyaite	–	–	–	–	–	–	–	–
löweite	–	–	–	–	–	–	–	–
lepidocrocite	–	–	–	–	–	–	–	–
magnetite & chromite	2.4	2.2	1.4	2.8	4.9	4.4	2.5	5.8
quartz	0.3	0.2	tr	–	–	0.1	–	0.2
rutile	–	–	–	–	–	–	–	–
plagioclase	–	–	–	–	–	–	–	–
halite	1.3	0.3	0.6	1.0	1.2	1.1	1.2	1.6
magnesite	3.0	3.0	5.0	5.1	2.1	4.0	2.0	4.3
dolomite	1.4	1.2	2.4	1.4	1.3	1.5	2.5	2.8
calcite	0.6	tr	tr	–	–	0.3	–	0.3
trona	–	–	–	–	–	–	–	–
hydromagnesite	**1.6**	**–**	**2.9**	**0.5**	**0.5**	**1.2**	**1.8**	**2.6**
Total	100.0	100.0	100.0	100.0	100.0	100.0	100.0	100.0
R_{wp} [a]	4.5	3.9	3.8	3.8	4.0	4.3	3.7	3.6
χ^2 [b]	3.3	2.9	2.8	3.1	3.3	3.8	3.1	3.0
d [c]	1.9	2.2	2.4	2.2	2.1	1.6	2.1	2.2

[a] R_{wp} is the weighted pattern index, a function of the least-squares residual.

[b] χ^2 is the reduced chi-squared statistic for the least-squares fit.

[c] d is the Durbin-Watson statistic, a measure of serial correlation for the least-squares fit.

Appendix Table A1.1 (continued): Rietveld refinement results for samples from Mount Keith.

Sample	**06MKP9-6**	**06MKP9-7**	**06MKP9-8**	**06MKP9-9**	**06MKP9-10**	**06MKP9-11**	**06MKP9-12**	**06MKP9-13**
Age (years)	7-8	7-8	7-8	7-8	7-8	7-8	7-8	7-8
Depth (cm)	70-74	60-67	47-52	36-41	30-36	20-26	13-19	9-13
Sample Type	Vertical Profile	Vertical Profile	Vertical Profile	Vertical Profile	Vertical Profile	Vertical Profile	Vertical Profile	Vertical Profile
Easting (UTM 51J WGS 84)	259674	259674	259674	259674	259674	259674	259674	259674
Northing (UTM 51J WGS 84)	6983486	6983486	6983486	6983486	6983486	6983486	6983486	6983486
Error on GPS Location (m)	5.4	5.4	5.4	5.4	5.4	5.4	5.4	5.4
Elevation at Surface (m OSL)	540.3	540.3	540.3	540.3	540.3	540.3	540.3	540.3
serpentine	83.5	78.9	82.8	80.3	78.6	80.6	77.0	82.3
kaolinite	–	–	–	–	–	–	–	–
brucite	0.1	0.8	0.7	0.7	0.9	–	–	–
talc	0.5	–	–	–	–	–	–	–
vermiculite	tr	–	–	–	–	–	–	–
muscovite	–	–	–	–	–	–	–	–
hydrotalcite-group	5.0	9.8	5.5	5.6	11.3	5.8	3.9	4.4
gypsum	0.7	–	–	–	–	1.6	–	–
hexahydrite	–	–	–	–	–	–	–	–
epsomite	–	–	–	–	–	–	–	–
blödite	–	–	–	–	–	–	–	–
konyaite	–	–	–	–	–	–	–	–
löweite	–	–	–	–	–	–	–	–
lepidocrocite	–	–	–	–	–	–	0.2	–
magnetite & chromite	1.8	1.7	1.9	5.8	0.9	4.2	9.5	4.2
quartz	–	–	0.2	–	–	–	–	–
rutile	–	–	–	–	–	–	–	–
plagioclase	–	–	–	–	–	–	–	–
halite	1.1	1.0	0.4	0.7	0.7	0.3	0.3	0.8
magnesite	3.7	4.2	3.2	4.3	3.4	3.2	3.6	2.4
dolomite	2.4	1.5	3.4	1.6	2.7	2.9	1.9	1.5
calcite	0.2	0.1	0.3	0.5	–	0.3	–	0.3
trona	–	–	–	–	–	–	–	–
hydromagnesite	**1.0**	**2.0**	**1.5**	**0.5**	**1.4**	**1.1**	**3.7**	**4.1**
Total	100.0	100.0	100.0	100.0	100.0	100.0	100.0	100.0
R_{wp} [a]	3.5	5.0	3.4	3.6	6.3	3.2	3.5	3.6
χ^2 [b]	2.8	4.2	2.9	3.0	5.3	2.9	3.1	2.9
d [c]	2.3	1.3	2.3	2.2	1.0	2.3	2.2	2.2

[a] R_{wp} is the weighted pattern index, a function of the least-squares residual.

[b] χ^2 is the reduced chi-squared statistic for the least-squares fit.

[c] d is the Durbin-Watson statistic, a measure of serial correlation for the least-squares fit.

Appendix Table A1.1 (continued): Rietveld refinement results for samples from Mount Keith.

Sample	06MKP9-14	06MKP9-15	06MKP9-16	06MK38-2	06MK39-1	06MK39-3	06MK39-4	06MK39-5
Age (years)	7-8	7-8	7-8	7-8	7-8	7-8	7-8	7-8
Depth (cm)	1-4	1-5	0-1	0-2.5	0-5	2.5-5.0	25	50
Sample Type	Vertical Profile	Vertical Profile	Vertical Profile	Crust Sample	Core Sample	Fines Sample	Core Sample	Core Sample
Easting (UTM 51J WGS 84)	259674	259674	259674	262378	262641	262641	262641	262641
Northing (UTM 51J WGS 84)	6983486	6983486	6983486	6980726	6980807	6980807	6980807	6980807
Error on GPS Location (m)	5.4	5.4	5.4	4.2	4.9	4.9	4.9	4.9
Elevation at Surface (m OSL)	540.3	540.3	540.3	529.5	530.2	530.2	530.2	530.2
serpentine	84.7	64.1	77.3	80.7	72.2	82.7	83.5	85.8
kaolinite	–	–	–	–	–	–	–	–
brucite	–	–	–	–	tr	–	2.9	2.4
talc	–	–	–	–	–	–	–	–
vermiculite	–	0.1	–	–	–	–	–	–
muscovite	–	–	–	–	–	–	–	–
hydrotalcite-group	3.6	5.2	2.1	4.5	3.8	4.0	6.9	4.9
gypsum	–	–	–	–	–	–	–	–
hexahydrite	–	11.9	4.9	4.9	0.5	–	–	–
epsomite	–	–	–	–	–	–	–	–
blödite	–	–	–	–	11.6	–	–	–
konyaite	–	–	–	–	–	–	–	–
löweite	–	–	–	–	–	–	–	–
lepidocrocite	–	–	–	–	–	–	–	–
magnetite & chromite	3.8	2.7	3.0	1.1	1.7	1.6	3.6	3.2
quartz	–		1.2	0.3	–	–	–	tr
rutile	–	–	–	–	–	–	–	–
plagioclase	–	–	–	–	–	–	–	–
halite	1.2	10.7	3.8	3.5	2.9	3.4	0.9	tr?
magnesite	2.2	1.4	1.9	1.0	2.2	2.0	1.3	1.9
dolomite	1.8	2.3	1.6	2.0	1.1	0.4	0.4	1.0
calcite	0.1	0.5	0.2	0.1	0.5	tr	tr	tr
trona	–	–	–	–	–	–	–	–
hydromagnesite	**2.6**	**1.1**	**4.0**	**1.9**	**3.4**	**5.8**	**0.5**	**0.8**
Total	100.0	100.0	100.0	100.0	100.0	100.0	100.0	100.0
R_{wp} [a]	3.5	4.8	3.7	5.4	4.2	3.9	3.8	3.9
χ^2 [b]	3.0	3.4	3.0	2.8	3.0	3.1	3.0	3.2
d [c]	2.3	1.9	2.2	2.2	2.2	2.3	2.2	2.0

[a] R_{wp} is the weighted pattern index, a function of the least-squares residual.

[b] χ^2 is the reduced chi-squared statistic for the least-squares fit.

[c] d is the Durbin-Watson statistic, a measure of serial correlation for the least-squares fit.

Appendix Table A1.1 (continued): Rietveld refinement results for samples from Mount Keith.

Sample	**06MK40-1**	**06MK40-4**	**06MK40-5**	**06MK40-6**	**06MK40-7**	**06MK41-1**	**06MK41-3**	**06MK41-4**
Age (years)	7-8	7-8	7-8	7-8	7-8	7-8	7-8	7-8
Depth (cm)	0-5	2.5-5.0	25	50	75	0-5	2.5-5.0	25
Sample Type	Core Sample	Fines Sample	Core Sample	Core Sample	Core Sample	Core Sample	Fines Sample	Core Sample
Easting (UTM 51J WGS 84)	263602	263602	263602	263602	263602	263817	263817	263817
Northing (UTM 51J WGS 84)	6981428	6981428	6981428	6981428	6981428	6981688	6981688	6981688
Error on GPS Location (m)	5.4	5.4	5.4	5.4	5.4	4.9	4.9	4.9
Elevation at Surface (m OSL)	522.9	522.9	522.9	522.9	522.9	525.9	525.9	525.9
serpentine	73.4	77.7	81.5	79.9	72.6	79.1	75.4	82.7
kaolinite	–	–	–	–	–	–	–	–
brucite	0.2	–	–	–	0.2	–	–	0.9
talc		tr?	–	2.7	3.0	–	–	–
vermiculite	0.3	0.2	0.3	0.1	0.1	–	tr	–
muscovite	–	–	–	–	–	–	–	–
hydrotalcite-group	2.9	2.2	3.2	4.8	4.3	2.4	2.2	5.4
gypsum	0.5	–	–	–	–	–	–	–
hexahydrite	–	–	–	–	–	–	–	–
epsomite	–	–	–	–	–	–	–	–
blödite	5.9	3.0	–	–	–	7.4	9.2	–
konyaite	–	2.2	–	–	–	–	–	–
löweite	–	–	–	–	–	–	–	–
lepidocrocite	–	–	–	–	–	–	–	–
magnetite & chromite	4.0	4.3	5.0	2.1	4.6	1.7	2.6	4.5
quartz	1.0	0.3	tr	tr	5.2	0.3	–	0.1
rutile	–	–	–	–	–	–	–	–
plagioclase	–	–	–	–	–	–	–	–
halite	4.3	3.3	1.2	1.0	1.0	2.3	4.1	1.7
magnesite	4.3	5.7	6.2	8.2	6.9	2.2	1.2	2.3
dolomite	1.9	1.1	2.6	1.3	2.2	1.3	1.3	0.6
calcite	–	–	tr	tr	–	0.2	tr?	0.3
trona	–	–	–	–	–	–	–	–
hydromagnesite	**1.3**	–	–	–	–	**3.1**	**3.9**	**1.6**
Total	100.0	100.0	100.0	100.0	100.0	100.0	100.0	100.0
R_{wp} [a]	4.0	3.9	4.0	3.8	3.8	4.0	4.1	3.8
χ^2 [b]	3.0	3.0	3.3	3.0	2.9	2.9	3.0	3.0
d [c]	2.1	2.2	2.1	2.2	2.1	2.3	2.1	2.3

[a] R_{wp} is the weighted pattern index, a function of the least-squares residual.

[b] χ^2 is the reduced chi-squared statistic for the least-squares fit.

[c] d is the Durbin-Watson statistic, a measure of serial correlation for the least-squares fit.

Appendix Table A1.1 (continued): Rietveld refinement results for samples from Mount Keith.

Sample	06MK41-5	06MK41-6	06MK41-7	06MK41-8	06MKG10-3-3	06MKG10-4-1	06MKG10-4-2	06MKG10-4-3
Age (years)	7-8	7-8	7-8	7-8	13	13	13	13
Depth (cm)	50	75	100	125	100	25	75	125
Sample Type	Core Sample	Core Sample	Core Sample	Core Sample	Tarpaulin Grid	Tarpaulin Grid	Tarpaulin Grid	Tarpaulin Grid
Easting (UTM 51J WGS 84)	263817	263817	263817	263817	261554	261554	261554	261554
Northing (UTM 51J WGS 84)	6981688	6981688	6981688	6981688	6985677	6985677	6985677	6985677
Error on GPS Location (m)	4.9	4.9	4.9	4.9	4.8	4.8	4.8	4.8
Elevation at Surface (m OSL)	525.9	525.9	525.9	525.9	539.1	539.1	539.1	539.1
serpentine	82.6	88.7	85.2	83.2	80.1	78.0	81.1	80.7
kaolinite	–	–	–	–	–	–	–	–
brucite	2.0	0.6	0.7	1.9	3.1	5.2	0.7	2.2
talc	–	–	–	–	–	–	–	–
vermiculite	–	0.2	0.3	–	–	–	–	–
muscovite	–	–	–	–	–	–	–	–
hydrotalcite-group	3.8	5.1	7.5	6.1	8.3	7.8	5.5	7.8
gypsum	–	–	–	–	–	–	–	–
hexahydrite	–	–	–	–	–	–	–	–
epsomite	–	–	–	–	–	–	–	–
blödite	–	–	–	–	–	–	–	–
konyaite	–	–	–	–	–	–	–	–
löweite	–	–	–	–	–	–	–	–
lepidocrocite	–	–	–	–	–	–	–	–
magnetite & chromite	3.8	1.9	2.4	3.0	2.7	2.1	5.8	2.5
quartz	–	–	0.1	–	–	–	–	–
rutile	–	–	–	–	–	–	–	–
plagioclase	–	–	–	–	–	–	–	–
halite	0.7	0.8	0.9	0.6	0.2	1.2	0.5	0.2
magnesite	3.9	1.0	0.9	2.7	3.3	1.7	3.9	4.2
dolomite	2.1	1.2	1.1	1.4	0.8	0.5	2.4	1.8
calcite	–	tr	0.5	–	tr	0.2	tr	0.2
trona	–	–	–	–	–	–	–	–
hydromagnesite	**1.2**	**0.5**	**0.5**	**1.1**	**1.4**	**3.2**	**–**	**0.5**
Total	100.0	100.0	100.0	100.0	100.0	100.0	100.0	100.0
R_{wp} [a]	3.5	3.8	3.8	3.7	4.1	4.5	3.6	3.8
χ^2 [b]	2.9	3.1	3.1	2.9	3.3	3.6	3.0	3.0
d [c]	2.3	2.2	2.1	2.2	2.0	1.7	2.2	2.2

[a] R_{wp} is the weighted pattern index, a function of the least-squares residual.

[b] χ^2 is the reduced chi-squared statistic for the least-squares fit.

[c] d is the Durbin-Watson statistic, a measure of serial correlation for the least-squares fit.

Appendix Table A1.1 (continued): Rietveld refinement results for samples from Mount Keith.

Sample	**06MKG10-5-1**	**06MKG10-6-2**	**06MKG10-9-1**	**06MKG10-9-2**	**06MKG10-9-3**	**06MKG10-10-1**	**06MKG10-16-3**	**06MKG10-17-3**
Age (years)	13	13	13	13	13	13	13	13
Depth (cm)	0	75	0	50	100	0	125	100
Sample Type	Tarpaulin Grid	Tarpaulin Grid	Tarpaulin Grid	Tarpaulin Grid	Tarpaulin Grid	Tarpaulin Grid	Tarpaulin Grid	Tarpaulin Grid
Easting (UTM 51J WGS 84)	261554	261554	261554	261554	261554	261554	261554	261554
Northing (UTM 51J WGS 84)	6985677	6985677	6985677	6985677	6985677	6985677	6985677	6985677
Error on GPS Location (m)	4.8	4.8	4.8	4.8	4.8	4.8	4.8	4.8
Elevation at Surface (m OSL)	539.1	539.1	539.1	539.1	539.1	539.1	539.1	539.1
serpentine	80.2	71.3	77.9	82.0	72.9	80.3	74.0	84.1
kaolinite	–	–	–	–	–	–	–	–
brucite	–	–	–	1.4	0.7	–	0.3	0.6
talc	–	–	–	–	–	–	–	–
vermiculite	tr	–	0.1	0.6	–	tr	–	tr
muscovite	–	–	–	–	–	–	–	–
hydrotalcite-group	3.1	17.1	3.7	4.8	14.6	3.7	10.1	7.8
gypsum	–	–	–	–	–	–	–	–
hexahydrite	–	–	–	–	–	–	–	–
epsomite	–	–	–	–	–	–	–	–
blödite	–	–	0.6	–	–	–	–	–
konyaite	–	–	2.1	–	–	–	–	–
löweite	–	–	–	–	–	0.9	–	–
lepidocrocite	–	–	–	–	–	–	–	–
magnetite & chromite	1.7	2.2	2.1	3.7	1.6	2.3	8.4	2.2
quartz	tr	–	–	–	–	–	tr	–
rutile	–	–	–	–	–	–	–	–
plagioclase	–	–	–	–	–	–	–	–
halite	5.5	tr	7.0	1.3	0.6	5.3	0.7	0.4
magnesite	1.3	3.1	0.6	2.1	6.5	0.9	4.2	3.5
dolomite	2.6	1.0	–	2.4	1.5	1.2	1.8	0.4
calcite	0.3	–	–	0.5	0.2	tr	tr	tr
trona	–	–	–	–	–	–	–	–
hydromagnesite	**5.5**	**5.3**	**5.9**	**1.2**	**1.3**	**5.4**	**0.5**	**1.0**
Total	100.0	100.0	100.0	100.0	100.0	100.0	100.0	100.0
R_{wp} [a]	4.1	5.5	4.2	4.0	4.8	4.1	3.8	3.5
χ^2 [b]	3.1	4.7	3.0	3.2	3.9	3.1	3.2	2.9
d [c]	2.1	1.1	2.2	2.0	1.5	2.1	2.1	2.2

[a] R_{wp} is the weighted pattern index, a function of the least-squares residual.

[b] χ^2 is the reduced chi-squared statistic for the least-squares fit.

[c] d is the Durbin-Watson statistic, a measure of serial correlation for the least-squares fit.

Appendix Table A1.1 (continued): Rietveld refinement results for samples from Mount Keith.

Sample	**06MK12-1-1**	**06MK12-1-2**	**06MK12-1-3**	**06MK12-1-4**	**06MK12-1-5**	**06MK12-1-6**	**06MK12-2-1**	**06MK12-2-2**
Age (years)	13	13	13	13	13	13	13	13
Depth (cm)	0-10	10-20	20-30	30-40	40-50	50-60	0-10	10-20
Sample Type	Core Sample	Core Sample	Core Sample	Core Sample	Core Sample	Core Sample	Core Sample	Core Sample
Easting (UTM 51J WGS 84)	261766	261766	261766	261766	261766	261766	261766	261766
Northing (UTM 51J WGS 84)	6985850	6985850	6985850	6985850	6985850	6985850	6985850	6985850
Error on GPS Location (m)	5.1	5.1	5.1	5.1	5.1	5.1	5.1	5.1
Elevation at Surface (m OSL)	534.9	534.9	534.9	534.9	534.9	534.9	534.9	534.9
serpentine	80.7	66.9	67.1	81.7	72.7	75.5	75.3	78.0
kaolinite	–	–	–	–	–	–	–	–
brucite	1.8	2.2	2.4	4.1	3.0	3.3	0.3	0.6
talc	–	–	–	–	–	–	–	–
vermiculite	0.3	0.3	tr	–	–	–	0.1	0.2
muscovite	–	3.8	5.3	–	–	–	–	–
hydrotalcite-group	5.0	4.0	2.9	4.3	3.1	4.0	2.0	2.7
gypsum	–	–	–	–	–	–	–	–
hexahydrite	–	–	–	–	–	–	–	–
epsomite	–	–	–	–	–	–	–	–
blödite	–	–	–	–	–	–	–	–
konyaite	–	–	–	–	–	–	–	–
löweite	–	–	–	–	–	–	–	–
lepidocrocite	–	–	–	–	–	–	–	–
magnetite & chromite	4.7	2.4	4.1	3.0	3.4	3.5	4.8	2.8
quartz	0.2	6.8	6.3	0.6	4.2	3.4	1.8	1.0
rutile	–	–	–	–	–	–	–	–
plagioclase	–	10.0	8.0	2.4	9.8	6.0	6.4	1.7
halite	0.3	0.3	0.4	tr	0.2	0.6	3.2	3.7
magnesite	2.5	1.0	0.9	0.9	1.3	1.2	0.6	1.4
dolomite	1.5	1.0	1.2	2.6	0.7	1.5	0.9	1.2
calcite	tr	–	–	tr	–	tr?	–	tr?
trona	–	–	–	–	–	–	–	–
hydromagnesite	**3.0**	**1.4**	**1.3**	**0.5**	**1.6**	**1.0**	**4.6**	**6.8**
Total	100.0	100.0	100.0	100.0	100.0	100.0	100.0	100.0
R_{wp} [a]	4.1	5.6	4.1	4.0	4.1	4.2	4.2	4.0
χ^2 [b]	3.0	3.7	2.8	2.9	2.9	3.0	2.9	2.8
d [c]	2.2	1.4	2.2	2.2	2.3	2.3	2.2	2.4

[a] R_{wp} is the weighted pattern index, a function of the least-squares residual.

[b] χ^2 is the reduced chi-squared statistic for the least-squares fit.

[c] d is the Durbin-Watson statistic, a measure of serial correlation for the least-squares fit.

Appendix Table A1.1 (continued): Rietveld refinement results for samples from Mount Keith.

Sample	**06MK12-2-3**	**06MK12-2-4**	**06MK12-2-5**	**06MK12-2-6**	**06MK46-1**	**06MK46-4**	**06MK46-5**	**06MK46-6**
Age (years)	13	13	13	13	13	13	13	13
Depth (cm)	20-30	30-40	40-50	50-60	0-5	25	50	75
Sample Type	Core Sample	Core Sample	Core Sample	Core Sample	Core Sample	Core Sample	Core Sample	Core Sample
Easting (UTM 51J WGS 84)	261766	261766	261766	261766	261704	261704	261704	261704
Northing (UTM 51J WGS 84)	6985850	6985850	6985850	6985850	6986062	6986062	6986062	6986062
Error on GPS Location (m)	5.1	5.1	5.1	5.1	6.0	6.0	6.0	6.0
Elevation at Surface (m OSL)	534.9	534.9	534.9	534.9				
serpentine	81.4	81.6	80.0	82.4	75.6	82.5	82.2	84.5
kaolinite	–	–	–	–	–	–	–	–
brucite	1.4	1.7	2.9	2.5	0.3	1.5	1.8	0.6
talc	–	–	–	–	–	–	–	–
vermiculite	0.2	tr?	–	–	0.2	–	–	0.2
muscovite	–	–	–	–	–	–	–	–
hydrotalcite-group	3.0	3.6	6.0	5.2	2.8	3.3	4.2	5.2
gypsum	–	–	–	–	–	–	–	–
hexahydrite	–	–	–	–	–	–	–	–
epsomite	–	–	–	–	–	–	–	–
blödite	–	–	–	–	5.8	–	–	–
konyaite	–	–	–	–	–	–	–	–
löweite	–	–	–	–	–	–	–	–
lepidocrocite	–	–	–	–	–	–	–	–
magnetite & chromite	4.7	2.9	3.1	3.7	3.0	3.2	3.2	3.0
quartz	tr	–	–	0.2	0.9	tr	–	tr
rutile	–	–	–	–	–	–	–	–
plagioclase	–	–	–	–	–	–	–	–
halite	2.4	1.8	1.3	1.0	4.4	1.1	–	–
magnesite	0.9	1.4	1.6	1.5	0.7	2.5	3.4	4.8
dolomite	1.1	1.8	0.3	1.2	1.0	0.7	1.2	1.2
calcite	tr?	0.3	–	–	0.2	–	–	tr
trona	–	–	–	–	–	–	–	–
hydromagnesite	**4.8**	**5.0**	**4.9**	**2.3**	**4.9**	**5.2**	**4.0**	**0.5**
Total	100.0	100.0	100.0	100.0	100.0	100.0	100.0	100.0
R_{wp} [a]	4.1	4.2	4.6	4.7	4.1	3.8	3.7	3.7
χ^2 [b]	3.0	3.0	3.4	3.5	2.9	3.0	3.0	3.2
d [c]	2.2	2.2	1.9	1.7	2.2	2.1	2.2	2.0

[a] R_{wp} is the weighted pattern index, a function of the least-squares residual.

[b] χ^2 is the reduced chi-squared statistic for the least-squares fit.

[c] d is the Durbin-Watson statistic, a measure of serial correlation for the least-squares fit.

Appendix Table A1.1 (continued): Rietveld refinement results for samples from Mount Keith.

Sample	**06MK46-7**	**06MK46-8**	**06MKdarkseds**	**06MKblackseds**
Age (years)	13	13	?	?
Depth (cm)	100	125	?	?
Sample Type	Core Sample	Core Sample	Sediment Sample	Sediment Sample
Easting (UTM 51J WGS 84)	261704	261704	–	–
Northing (UTM 51J WGS 84)	6986062	6986062	–	–
Error on GPS Location (m)	6.0	6.0	–	–
Elevation at Surface (m OSL)	–	–	–	–
serpentine	85.0	81.6	60.8	47.6
kaolinite	–	–	9.8	14.5
brucite	–	–	–	–
talc	–	–	–	–
vermiculite	0.1	tr	–	–
muscovite	–	–	–	–
hydrotalcite-group	4.3	6.9	0.7	0.3
gypsum	–	–	0.8	1.4
hexahydrite	–	–	6.2	5.5
epsomite	–	–	–	–
blödite	–	–	–	–
konyaite	–	–	–	–
löweite	–	–	–	–
lepidocrocite	–	–	–	–
magnetite & chromite	3.0	3.2	0.4	–
quartz	tr?	–	15.8	26.6
rutile	–	–	tr	0.6
plagioclase	–	–	–	–
halite	–	–	5.0	3.5
magnesite	5.9	6.8	0.4	–
dolomite	1.7	1.1	tr	–
calcite	tr	tr	tr	–
trona	–	–	–	–
hydromagnesite	**–**	**0.5**	–	–
Total	100.0	100.0	100.0	100.0
R_{wp} [a]	4.0	4.0	4.6	4.9
χ^2 [b]	3.3	3.4	3.1	3.1
d [c]	2.1	2.0	2.0	2.0

[a] R_{wp} is the weighted pattern index, a function of the least-squares residual.

[b] χ^2 is the reduced chi-squared statistic for the least-squares fit.

[c] d is the Durbin-Watson statistic, a measure of serial correlation for the least-squares fit.

Appendix Table A1.2: Stable and radiogenic isotope data for carbonate minerals and DIC from Mount Keith.

Sample[a]	Mode	Major Carbonate-Bearing Phases[b]	Minor Carbonate-Bearing Phases[b]	$\delta^{13}C$ (‰, VPDB)	$2\sigma_{\delta}{}^{13}{}_{C}$ (‰, VPDB)	$\delta^{18}O$ (‰, VSMOW)	$2\sigma_{\delta}{}^{18}{}_{O}$ (‰, VSMOW)	$F^{14}C$	$\sigma_{F}{}^{14}{}_{C}$	WGS 84 Easting	WGS 84 Northing	Sample Depth (m)
04MK-iowaite	mineral specimen, mine pit	Ht-group		-2.83	0.33	16.11	0.26					
05MK3	mineral specimen, TSF1	Ni-Dol		-6.46 -6.50	0.23 0.14	27.31 26.35	0.39 0.15			0261747	6985588	surface
05MK5	crust	Hmg, Mgs	Ht-group, Dol, Cal	-1.34 -1.67	0.20 0.09	31.97 30.68	0.35 0.20			0261704	6986062	surface
05MK7	crust	Mgs, Hmg	Ht-group	-2.50 -2.65	0.19 0.28	18.14 18.16	0.25 0.28			0261388	6983185	surface
05MK9	crust	Hmg, Mgs	Ht-group, Dol, Cal	-3.07	0.20	18.60	0.19			0263779	6981819	surface
05MK10	ore, float	Mgs		-6.52	0.10	7.81	0.15					
05MK11	process chemical	Nat, Tna, Tht		-8.94 -8.43	0.09 0.15	16.56 18.89	0.21 0.30	0.052	0.001			
06MKNi-dol	mineral specimen, TSF1	Ni-Dol						0.004	0.000	0261727	6985559	surface
06MK1-crust-bulk	crust	Hmg	Mgs, Dol	-2.86	0.14	26.24	0.34			0260984	6983591	<0.10
06MK1-crust-mags[c]	crust	Mgs		-2.58	0.14	11.06	0.11					
06MK16-10-bulk	crust	Hmg, Mgs	Dol, Ht-group	-3.95	0.23	22.99	1.16					
06MK16-10-mags[c]	crust	Mgs		-1.81	0.14	10.41	0.21			0261330	6983263	<0.10
06MK16-10-hydro	crust	Hmg		-1.95 -1.53		35.17 35.03		1.014	0.005			
06MK39-1-bulk	crust	Hmg, Ht-group, Mgs	Dol, Cal	-1.21	0.31	29.51	0.75			0262641	6980807	<0.10
06MK39-1-mags[c]	crust	Mgs		-1.80	0.15	11.64	0.16					
06MK39-2-bulk	crust	Hmg, Ht-group, Mgs	Dol, Cal	-2.24	0.19	27.01	0.13			0262641	6980807	<0.10
06MK39-2-mags[c]	crust	Mgs		-3.11	0.06	10.47	0.14					
06MK39-3-hydro	crust	Hmg		-1.72		39.60		1.027 1.020	0.006 0.005	0262641	6980807	<0.10
06MK41-3-hydro	crust	Hmg		-1.05 1.04		39.44 39.89		1.052	0.004	0263817	6981688	<0.10

[a] The following denote: bulk - bulk analysis of carbonate minerals, mags - magnesite only, hydro - hydromagnesite only.

[b] Cal – Calcite, Dol – Dolomite, Hmg - Hydromagnesite, Ht-group - Hydrotalcite group, Mgs - Magnesite, Nat - Natrite, Ni-Dol - Nickel Dolomite, Tht - Thermonatrite, Tna - Trona.

[c] Samples for stable isotopic analysis were immersed in 1N HCl for 1 hour.

[d] Samples for stable isotopic analysis were immersed in 0.1N HCl for 1 hour.

Appendix Table A1.2 (continued): Stable and radiogenic isotope data for carbonate minerals and DIC from Mount Keith.

Sample[a]	Mode	Major Carbonate-Bearing Phases[b]	Minor Carbonate-Bearing Phases[b]	$\delta^{13}C$ (‰, VPDB)	$2\sigma_{\delta}{}^{13}{}_{C}$ (‰, VPDB)	$\delta^{18}O$ (‰, VSMOW)	$2\sigma_{\delta}{}^{18}{}_{O}$ (‰, VSMOW)	$F^{14}C$	$\sigma_{F}{}^{14}{}_{C}$	WGS 84 Easting	WGS 84 Northing	Sample Depth (m)
06MK42-2-bulk	crust	Hmg, Ht-group, Mgs, Dol	Cal	-2.91	0.13	22.31	0.24			0262475	6984742	<0.10
06MK42-2-mags[c]	crust	Mgs		-2.92	0.12	11.50	0.10					
06MK44-1	mineral specimen, TSF1	Ni-Dol		-6.58	0.14	26.91	0.07			0261727	6985559	surface
06MK44-2-1	mineral specimen, TSF1	Ni-Dol		-5.84	0.12	27.86	0.15					
06MK44-2-2	mineral specimen, TSF1	Ni-Dol		-5.81	0.05	27.81	0.11			0261727	6985559	surface
06MK44-2-3	mineral specimen, TSF1	Ni-Dol		-5.78	0.06	27.58	0.08					
06MK46-2-bulk	crust	Hmg, Ht-group	Dol, Mgs, Cal	-1.80	0.80	29.58	0.86			0261704	6986062	<0.10
06MK46-2-mags[c]	crust	Mgs		-6.16	0.07	16.97	0.06					
06MK47	crust, within tailings pipeline	Mgs	Hmg	-3.24	0.07	21.10	0.04			0261704	6986062	<0.10
06MK47-mags[c]	crust, within tailings pipeline	Mgs		-4.18	0.18	12.34	0.16					
06MK48-2-bulk	crust	Ht-group	Mgs, Dol	-3.13 -3.17	0.53 0.20	23.01 22.63	0.37 0.31			0260913	6984794	<0.10
06MK48-2-mags[c]	crust	Mgs		-3.50	0.20	11.43	0.12					
06MK49-9-bulk	crust	Ht-group, Hmg	Mgs	-5.28	0.38	24.52	0.29			0261335	6984898	<0.10
06MK49-9-mags[c]	crust	Mgs		-5.58	0.08	13.93	0.10					
06MK53	mineral specimen, TSF2	Mgs						0.009 0.008	0.000 0.000	0263732	6982836	surface
06MK54	mineral specimen, TSF2	Mgs						0.005	0.000	0263732	6982836	surface
06MKG2-6-1-bulk	subsurface	Hmg, Ht-group, Mgs	Dol	-2.97	0.08	18.49	0.07			0260833	6983692	0.25
06MKG2-6-1-mags[c]	subsurface	Mgs		-2.74	0.08	11.89	0.14					
06MKG2-6-3-mags	subsurface	Mgs						0.095	0.001	0260833	6983692	1.25
06MKG2-6-3-hydro	subsurface	Hmg		-1.45		24.51		0.862	0.004			
06MKG2-7-3-bulk	subsurface	Dol, Ht-group	Mgs, Hmg	-1.70	0.11	16.71	0.06					
06MKG2-7-3-mags[c]	subsurface	Mgs		-2.61	0.14	11.98	0.08	0.104	0.002	0260833	6983692	1.00
06MKG2-7-3-hydro	subsurface	Hmg		-2.09		25.01		0.821	0.004			

[a] The following denote: bulk - bulk analysis of carbonate minerals, mags - magnesite only, hydro - hydromagnesite only.

[b] Cal – Calcite, Dol – Dolomite, Hmg - Hydromagnesite, Ht-group - Hydrotalcite group, Mgs - Magnesite, Nat - Natrite, Ni-Dol - Nickel Dolomite, Tht - Thermonatrite, Tna - Trona.

[c] Samples for stable isotopic analysis were immersed in 1N HCl for 1 hour.

[d] Samples for stable isotopic analysis were immersed in 0.1N HCl for 1 hour.

Appendix Table A1.2 (continued): Stable and radiogenic isotope data for carbonate minerals and DIC from Mount Keith.

Sample[a]	Mode	Major Carbonate-Bearing Phases[b]	Minor Carbonate-Bearing Phases[b]	$\delta^{13}C$ (‰, VPDB)	$2\sigma_{\delta}{}^{13}C$ (‰, VPDB)	$\delta^{18}O$ (‰, VSMOW)	$2\sigma_{\delta}{}^{18}O$ (‰, VSMOW)	$F^{14}C$	$\sigma_F{}^{14}C$	WGS 84 Easting	WGS 84 Northing	Sample Depth (m)
06MKG2-15-1-hydro	crust	Hmg		-3.07 -3.08		35.31 37.56		1.006 1.013	0.005 0.006	0260833	6983692	<0.10
06MKG5-5-1-bulk	crust	Hmg	Ht-group, Mgs	-3.41	0.28	22.20	0.27					
06MKG5-5-1-mags[c]	crust	Mgs		-1.81	0.18	11.72	0.13			0259940	6984050	<0.10
06MKG5-5-1-hydro	crust	Hmg		-4.01		36.09		0.993 1.000	0.004 0.005			
06MKG5-9-1-bulk	crust	Ht-group	Hmg	-3.86 -3.62	0.45 0.33	29.38 23.51	0.68 0.44					
06MKG5-9-1-mags[c]	crust	Mgs		-1.60	0.10	11.72	0.09			0259940	6984050	<0.10
06MKG5-9-1-hydro	crust	Hmg		-3.17		36.49		1.033 1.019	0.004 0.003			
06MKG7-6-1-bulk	subsurface	Ht-group, Mgs	Hmg, Dol, Cal	-0.33	0.11	14.19	0.10			0260146	6981564	0.25
06MKG7-6-1-mags[c]	subsurface	Mgs		-1.23	0.11	11.13	0.05					
06MKG7-7-1-bulk	crust	Mgs, Ht-group	Hmg, Dol, Cal	-1.27	0.28	20.92	0.33					
06MKG7-7-1-mags[c]	crust	Mgs		-1.96	0.10	11.58	0.09			0260146	6981564	<0.10
06MKG7-7-1-hydro	crust	Hmg		-0.94		38.00		0.889 0.888	0.005 0.004			
06MKG8-3-1-bulk	crust	Mgs	Dol, Ht-group	-3.79 -3.90	0.28 0.51	15.02 14.99	0.36 0.49			0259725	6983721	<0.10
06MKG8-7-1-bulk	crust	Mgs	Ht-group, Dol, Cal	-3.30	0.31	16.72	1.33			0259725	6983721	<0.10
06MKG8-7-1-mags[c]	crust	Mgs		-4.20	0.65	18.28	0.44					
06MKG10-3-3-bulk	subsurface	Ht-group, Mgs	Hmg, Dol, Cal	-4.12	0.09	14.16	0.11			0261554	6985677	1.00
06MKG10-3-3-mags[c]	subsurface	Mgs		-4.74	0.09	13.79	0.09					
06MKG10-4-1-bulk	subsurface	Ht-group, Hmg	Mgs, Dol, Cal	-6.29	0.13	24.24	0.22			0261554	6985677	0.25
06MKG10-4-1-mags[c]	subsurface	Mgs		-4.49	0.13	11.12	0.16					

[a] The following denote: bulk - bulk analysis of carbonate minerals, mags - magnesite only, hydro - hydromagnesite only.

[b] Cal – Calcite, Dol – Dolomite, Hmg - Hydromagnesite, Ht-group - Hydrotalcite group, Mgs - Magnesite, Nat - Natrite, Ni-Dol - Nickel Dolomite, Tht - Thermonatrite, Tna - Trona.

[c] Samples for stable isotopic analysis were immersed in 1N HCl for 1 hour.

[d] Samples for stable isotopic analysis were immersed in 0.1N HCl for 1 hour.

Appendix Table A1.2 (continued): Stable and radiogenic isotope data for carbonate minerals and DIC from Mount Keith.

Sample[a]	Mode	Major Carbonate-Bearing Phases[b]	Minor Carbonate-Bearing Phases[b]	$\delta^{13}C$ (‰, VPDB)	$2\sigma_{\delta}{}^{13}{}_{C}$ (‰, VPDB)	$\delta^{18}O$ (‰, VSMOW)	$2\sigma_{\delta}{}^{18}{}_{O}$ (‰, VSMOW)	$F^{14}C$	$\sigma_{F}{}^{14}{}_{C}$	WGS 84 Easting	WGS 84 Northing	Sample Depth (m)
06MKG10-5-1	crust	Hmg, Ht-group	Mgs, Dol, Cal	-1.65	0.20	26.79	0.43					
06MKG10-5-1-bulk	crust	Hmg, Ht-group	Mgs, Dol, Cal	-2.95	0.17	31.69	0.19					
06MKG10-5-1-mags[c]	crust	Mgs		-5.37	0.12	18.98	0.17	0.365	0.002	0261554	6985677	<0.10
06MKG10-5-1-hydro	crust	Hmg		-2.05		38.62		1.006	0.008			
06MKG10-5-1-0.1N[d]	crust	Hmg, Ht-group	Mgs, Dol, Cal	-2.86	0.09	21.70	0.06					
06MKG10-5-1-1N[c]	crust	Mgs		-5.58	0.21	15.22	0.34					
06MKG10-6-2-bulk	subsurface	Ht-group, Hmg	Mgs, Dol	-4.28	0.07	21.56	0.10			0261554	6985677	0.75
06MKG10-6-2-mags[c]	subsurface	Mgs		-4.80	0.18	14.80	0.16					
06MKG10-9-1-bulk	crust	Hmg, Ht-group	Mgs	-4.00	0.20	31.30	0.22					
06MKG10-9-1-mags[c]	crust	Mgs		-5.26	0.09	18.54	0.12			0261554	6985677	<0.10
06MKG10-9-1-hydro	crust	Hmg		-8.56		35.53		0.906	0.003			
06MKG10-10-1	crust	Hmg, Ht-group	Mgs, Dol, Cal	-2.71 -3.18	0.42 0.85	26.61 25.71	0.28 1.79					
06MKG10-10-1-bulk	crust	Hmg, Ht-group	Mgs, Dol, Cal	-2.72	0.09	31.83	0.20					
06MKG10-10-1-mags[c]	crust	Mgs		-4.54	1.19	17.50	0.93			0261554	6985677	<0.10
06MKG10-10-1-hydro	crust	Hmg		-3.03		38.30		1.008	0.007			
06MKG10-10-1-0.1N[d]	crust	Hmg, Ht-group	Mgs, Dol, Cal	-4.22	0.09	17.40	0.11					
06MKG10-10-1-1N[c]	crust	Mgs		-6.79 -6.70	0.16 0.14	18.91 16.94	0.15 0.18					
06MKG10-11-2-bulk	subsurface	Ht-group, Hmg, Mgs	Dol	-4.49	0.14	20.60	0.18			0261554	6985677	0.75
06MKG10-11-2-mags[c]	subsurface	Mgs		-5.65	0.08	15.65	0.10					
06MKG27-1-1-bulk	crust	Ht-group, Mgs	Dol, Hmg	-4.04	0.36	19.20	0.33			0263178	6984701	<0.10
06MKG27-1-1-mags[c]	crust	Mgs		-4.74	0.11	12.14	0.06					
06MKG27-5-1-bulk	crust	Ht-group, Mgs	Hmg, Dol, Cal?	-3.52	0.43	18.85	0.41					
06MKG27-5-1-mags[c]	crust	Mgs		-4.24	0.09	10.96	0.11			0263178	6984701	<0.10
06MKG27-5-1-hydro	crust	Hmg		-2.94		36.09		0.990 0.972	0.004 0.004			

[a] The following denote: bulk - bulk analysis of carbonate minerals, mags - magnesite only, hydro - hydromagnesite only.

[b] Cal – Calcite, Dol – Dolomite, Hmg - Hydromagnesite, Ht-group - Hydrotalcite group, Mgs - Magnesite, Nat - Natrite, Ni-Dol - Nickel Dolomite, Tht - Thermonatrite, Tna - Trona.

[c] Samples for stable isotopic analysis were immersed in 1N HCl for 1 hour.

[d] Samples for stable isotopic analysis were immersed in 0.1N HCl for 1 hour.

Appendix Table A1.2 (continued): Stable and radiogenic isotope data for carbonate minerals and DIC from Mount Keith.

Sample[a]	Mode	Major Carbonate-Bearing Phases[b]	Minor Carbonate-Bearing Phases[b]	$\delta^{13}C$ (‰, VPDB)	$2\sigma_{\delta}{}^{13}{}_{C}$ (‰, VPDB)	$\delta^{18}O$ (‰, VSMOW)	$2\sigma_{\delta}{}^{18}{}_{O}$ (‰, VSMOW)	$F^{14}C$	$\sigma_{F}{}^{14}{}_{C}$	WGS 84 Easting	WGS 84 Northing	Sample Depth (m)
06MKP9-3-hydro	subsurface	Hmg		-5.37 -5.74		27.14 28.61				0259674	6983486	0.99-1.09
06MKP9-4-mag	subsurface	Mgs						0.024	0.001	0259674	6983486	0.87-0.97
06MKP9-4-hydro	subsurface	Hmg						0.572	0.007			
06MKP9-11-bulk	subsurface	Ht-group, Mgs	Dol, Hmg, Cal	-6.13	0.11	18.49	0.10			0259674	6983486	0.20-0.26
06MKP9-11-mags[c]	subsurface	Mgs		-4.47	0.22	11.05	0.19					
06MKP9-12-bulk	subsurface	Ht-group, Hmg, Mgs	Dol	-6.40	0.09	19.73	0.22			0259674	6983486	0.13-0.19
06MKP9-12-mags[c]	subsurface	Mgs		-5.93	0.14	10.33	0.15					
06MKP9-12-hydro	subsurface	Hmg		-7.11		35.01		0.652 0.635	0.004 0.005			
06MKP9-13	subsurface	Ht-group, Hmg	Mgs, Dol, Cal	-5.56 -6.70	0.48 0.89	22.07 18.76	1.11 0.73					
06MKP9-13-bulk	subsurface	Ht-group, Hmg	Mgs, Dol, Cal	-5.36 -4.90	0.11 0.05	22.07 19.53	0.21 0.10			0259674	6983486	0.09-0.13
06MKP9-13-mags[c]	subsurface	Mgs		-4.42 -5.28	0.16 0.13	11.24 11.18	0.17 0.30					
06MKP9-14-bulk	crust	Ht-group, Hmg	Mgs, Dol, Cal	-4.13	0.10	22.06	0.17			0259674	6983486	0.01-0.04
06MKP9-14-mags[c]	crust	Mgs		-4.97	0.13	11.52	0.15					
06MKP9-16-bulk	crust	Hmg	Ht-group, Mgs, Dol, Cal	-3.28	0.17	23.15	0.08			0259674	6983486	<0.01
06MKP9-16-mags[c]	crust	Mgs		-4.28	0.09	11.14	0.08					
06MK56	DIC, water			-8.16	0.14							
Kidney water pump station	DIC, water			-7.71	0.13							
MKO side pond	DIC, water			-6.20	0.11							
MKO thickener tailings	DIC, water			-6.91	0.22							
Tailings thickener overflow	DIC, water			-4.60	0.10							

[a] The following denote: bulk - bulk analysis of carbonate minerals, mags - magnesite only, hydro - hydromagnesite only.
[b] Cal – Calcite, Dol – Dolomite, Hmg - Hydromagnesite, Ht-group - Hydrotalcite group, Mgs - Magnesite, Nat - Natrite, Ni-Dol - Nickel Dolomite, Tht - Thermonatrite, Tna - Trona.
[c] Samples for stable isotopic analysis were immersed in 1N HCl for 1 hour.
[d] Samples for stable isotopic analysis were immersed in 0.1N HCl for 1 hour.

Appendix A2

Appendix to Chapter 5

This appendix consists of seven MATLAB scripts that are used in Chapter 5. The scripts mixing11.m and mixing12.m model single-event dissolution of bedrock carbonate minerals and reprecipitation of secondary Mg-carbonate minerals (scenario 2, Chapter 5). The function, F14C_xValues.m, produces values of $F^{14}C$ for cyclic dissolution and reprecipitation (scenario 3, Chapter 5) and is called by the scripts react2f.m, react3f.m, react4f.m, and react5f.m. The react*n*f.m series of scripts model cyclic dissolution and reprecipitation of bedrock carbonate minerals from a mixed source of carbon, according to scenario 3 (Chapter 5).

A2.1 mixing11.m

```
% mixing11.m
% Programmer: S. Wilson
% Date Created: 24 April 2006
% Date Modified: 22 October 2009
%Purpose: Plots mixing hyperbolae for scenario 3 in Chapter 5 (for hydromagnesite/dypingite). Mixing
%hyperbolae predict fractionation based on water-rock (mass) ratio and represent closed system batch
%mixing between bedrock carbonate minerals and water equilibrated with the atmosphere at T = 25C and
%pH = 8.0. The amount of dissolved atmospheric carbon is very small under these conditions, and demands
%a high water-to-rock mass ratio for significant mixing to occur. The values used in this initial instance of the
%script are for water having an ideal composition reflecting the precipitation of hydromagnesite/dypingite.
%The bedrock end-member values come from primary magnesite at Mount Keith and primary calcite at
%Diavik. Secondary hydromagnesite/dypingite is taken as the "water" end-member.
%
figure (1)
% for Mount Keith
Ro1=31.227; %estimate of Ro=Cwo/Cro
Rc1=0.0138; %estimate of (Rc=Cwc/Crc) - dissolved C in the water is low. 0.0138 is for 100 ppm C and 0.72
% %C in 5 wt.% magnesite in tailings
% control1=1/Rc1; %gives an idea of how much water is needed
d18Ow01=38; %for hypothetical hydromagnesite
d13Cw01=3.67; %hydromagnesite from Chapter 3 - Mook et al. (1974) for hco3- - co2
d18Or01=13.27; %from MK magnesite
d13Cr01=-4.11; %from MK magnesite
D18Orw1=0; %working in MINERAL SPACE - so set to zero.
D13Crw1=0; %working in MINERAL SPACE - so set to zero.
Q=[0:0.05:10000]; %range for Q, the water-rock ratio (can scale by "control" function by %multiplying upper
% limit by "control")
psiwO1=(Q.*Ro1)./((Q.*Ro1)+ones(size(Q))); % psi for O
psiwC1=(Q.*Rc1)./((Q.*Rc1)+ones(size(Q))); % psi for C
d18Orock1=psiwO1*(d18Ow01+D18Orw1) + (ones(size(psiwO1))-psiwO1)*d18Or01; %d18O for the mineral
d13Crock1=psiwC1*(d13Cw01+D13Crw1) + (ones(size(psiwC1))-psiwC1)*d13Cr01; %d13C for the mineral
F14Crock1=psiwC1*(1.06)+(ones(size(psiwC1))-psiwC1)*0; %F14C for the mineral
hold on
plot(d13Crock1,d18Orock1,'b')
hold on
box
axis([-30 15 0 40]);
xlabel('\delta^{13}C (VPDB)')
ylabel('\delta^{18}O (VSMOW)')
title('Mixing Trends for Mount Keith and Diavik (hydromagnesite/dypingite): \delta^{18}O versus
\delta^{13}C')
%
hold on
Qa=[0:100:10000]; %range for Q, the water-rock ratio (can scale by "control" function by multiplying upper
% limit by "control")
psiwOa=(Qa.*Ro1)./((Qa.*Ro1)+ones(size(Qa))); % psi for O
psiwCa=(Qa.*Rc1)./((Qa.*Rc1)+ones(size(Qa))); % psi for C
d18Orocka=psiwOa*(d18Ow01+D18Orw1) + (ones(size(psiwOa))-psiwOa)*d18Or01; %d18O for the mineral
d13Crocka=psiwCa*(d13Cw01+D13Crw1) + (ones(size(psiwCa))-psiwCa)*d13Cr01; %d13C for the mineral
F14Crocka=psiwCa*(1.06)+(ones(size(psiwCa))-psiwCa)*0; %F14C for the mineral
plot(d13Crocka,d18Orocka,'+','MarkerEdgeColor','r','MarkerSize',6)
%
Qaa=[0:10:100]; %range for Q, the water-rock ratio (can scale by "control" function by multiplying upper limit
% by "control")
psiwOaa=(Qaa.*Ro1)./((Qaa.*Ro1)+ones(size(Qaa))); % psi for O
psiwCaa=(Qaa.*Rc1)./((Qaa.*Rc1)+ones(size(Qaa))); % psi for C
d18Orockaa=psiwOaa*(d18Ow01+D18Orw1) + (ones(size(psiwOaa))-psiwOaa)*d18Or01; %d18O for the
% mineral
```

```
d13Crockaa=psiwCaa*(d13Cw01+D13Crw1) + (ones(size(psiwCaa))-psiwCaa)*d13Cr01; %d13C for the
% mineral
plot(d13Crockaa,d18Orockaa,'+','MarkerEdgeColor','c','MarkerSize',6)
%
Qaaa=[0:0.2:1];
psiwOaaa=(Qaaa.*Ro1)./((Qaaa.*Ro1)+ones(size(Qaaa))); % psi for O
psiwCaaa=(Qaaa.*Rc1)./((Qaaa.*Rc1)+ones(size(Qaaa))); % psi for C
d18Orockaaa=psiwOaaa*(d18Ow01+D18Orw1) + (ones(size(psiwOaaa))-psiwOaaa)*d18Or01; %d18O for
% the mineral
d13Crockaaa=psiwCaaa*(d13Cw01+D13Crw1) + (ones(size(psiwCaaa))-psiwCaaa)*d13Cr01; %d13C for
% the mineral
plot(d13Crockaaa,d18Orockaaa,'+','MarkerEdgeColor','g','MarkerSize',6)
%
hold on
% for Diavik
Ro2=37.068; %estimate of Ro=Cwo/Cro
Rc2=0.0167; %estimate of (Rc=Cwc/Crc) - dissolved C in the water is low. 0.0167 is for 5wt% calcite in
% tailings at Diavik
% control2=1/Rc2; %gives an idea of how much water is needed
d18Ow02=20.85; %for hypothetical nesquehonite
d13Cw02=3.67; %hydromagnesite from Chapter 3 - Mook et al. (1974) for hco3- - co2
d18Or02=8.69; %from DVK calcite
d13Cr02=-6.39; %from DVK calcite
D18Orw2=0; %working in MINERAL SPACE - so set to zero.
D13Crw2=0; %working in MINERAL SPACE - so set to zero.
Q=[0:0.05:10000]; %range for Q, the water-rock ratio (can scale by "control" function by %multiplying upper
% limit by "control")
psiwO2=(Q.*Ro2)./((Q.*Ro2)+ones(size(Q))); % psi for O
psiwC2=(Q.*Rc2)./((Q.*Rc2)+ones(size(Q))); % psi for C
d18Orock2=psiwO2*(d18Ow02+D18Orw2) + (ones(size(psiwO2))-psiwO2)*d18Or02; %d18O for the mineral
d13Crock2=psiwC2*(d13Cw02+D13Crw2) + (ones(size(psiwC2))-psiwC2)*d13Cr02; %d13C for the mineral
hold on
plot(d13Crock2,d18Orock2,'b')
%
Qb=[0:100:10000]; %range for Q, the water-rock ratio (can scale by "control" function by multiplying upper
% limit by "control")
psiwOb=(Qb.*Ro2)./((Qb.*Ro2)+ones(size(Qb))); % psi for O
psiwCb=(Qb.*Rc2)./((Qb.*Rc2)+ones(size(Qb))); % psi for C
d18Orockb=psiwOb*(d18Ow02+D18Orw2) + (ones(size(psiwOb))-psiwOb)*d18Or02; %d18O for the mineral
d13Crockb=psiwCb*(d13Cw02+D13Crw2) + (ones(size(psiwCb))-psiwCb)*d13Cr02; %d13C for the mineral
plot(d13Crockb,d18Orockb,'+','MarkerEdgeColor','r','MarkerSize',6)
%
Qbb=[0:10:100]; %range for Q, the water-rock ratio (can scale by "control" function by multiplying upper limit
% by "control")
psiwObb=(Qbb.*Ro2)./((Qbb.*Ro2)+ones(size(Qbb))); % psi for O
psiwCbb=(Qbb.*Rc2)./((Qbb.*Rc2)+ones(size(Qbb))); % psi for C
d18Orockbb=psiwObb*(d18Ow02+D18Orw2) + (ones(size(psiwObb))-psiwObb)*d18Or02; %d18O for the
% mineral
d13Crockbb=psiwCbb*(d13Cw02+D13Crw2) + (ones(size(psiwCbb))-psiwCbb)*d13Cr02; %d13C for the
% mineral
plot(d13Crockbb,d18Orockbb,'+','MarkerEdgeColor','c','MarkerSize',6)
%
Qbbb=[0:0.2:1]; %range for Q, the water-rock ratio (can scale by "control" function by multiplying upper limit
% by "control")
psiwObbb=(Qbbb.*Ro2)./((Qbbb.*Ro2)+ones(size(Qbbb))); % psi for O
psiwCbbb=(Qbbb.*Rc2)./((Qbbb.*Rc2)+ones(size(Qbbb))); % psi for C
d18Orockbbb=psiwObbb*(d18Ow02+D18Orw2) + (ones(size(psiwObbb))-psiwObbb)*d18Or02; %d18O for
% the mineral
d13Crockbbb=psiwCbbb*(d13Cw02+D13Crw2) + (ones(size(psiwCbbb))-psiwCbbb)*d13Cr02; %d13C for
% the mineral
plot(d13Crockbbb,d18Orockbbb,'+','MarkerEdgeColor','g','MarkerSize',6)
%
```

```
%
figure (2)
hold on
box
axis([0,1.2,-30,15])
xlabel('F^{14}C')
ylabel('\delta^{13}C (VPDB)')
title('Mixing Trends for Mount Keith and Diavik (hydromagnesite/dypingite): \delta^{13}C versus F^{14}C')
%
F14Crock1=psiwC1*(1.06)+(ones(size(psiwC1))-psiwC1)*0; %F14C for the mineral
plot(F14Crock1,d13Crock1,'b')
F14Crocka=psiwCa*(1.06)+(ones(size(psiwCa))-psiwCa)*0; %F14C for the mineral
plot(F14Crocka,d13Crocka,'+','MarkerEdgeColor','r','MarkerSize',6)
F14Crockaa=psiwCaa*(1.06)+(ones(size(psiwCaa))-psiwCaa)*0; %F14C for the mineral
plot(F14Crockaa,d13Crockaa,'+','MarkerEdgeColor','c','MarkerSize',6)
F14Crockaaa=psiwCaaa*(1.06)+(ones(size(psiwCaaa))-psiwCaaa)*0; %F14C for the mineral
plot(F14Crockaaa,d13Crockaaa,'+','MarkerEdgeColor','g','MarkerSize',6)
F14Crock2=psiwC2*(1.06)+(ones(size(psiwC2))-psiwC2)*0; %F14C for the mineral
plot(F14Crock2,d13Crock2,'b')
F14Crockb=psiwCb*(1.06)+(ones(size(psiwCb))-psiwCb)*0; %F14C for the mineral
plot(F14Crockb,d13Crockb,'+','MarkerEdgeColor','r','MarkerSize',6)
F14Crockbb=psiwCbb*(1.06)+(ones(size(psiwCbb))-psiwCbb)*0; %F14C for the mineral
plot(F14Crockbb,d13Crockbb,'+','MarkerEdgeColor','c','MarkerSize',6)
F14Crockbbb=psiwCbbb*(1.06)+(ones(size(psiwCbbb))-psiwCbbb)*0; %F14C for the mineral
plot(F14Crockbbb,d13Crockbbb,'+','MarkerEdgeColor','g','MarkerSize',6)
%
%fin
```

A2.2 mixing12.m

```
% mixing12.m
% Programmer: S. Wilson
% Date Created: 24 April 2006
% Date Modified: 22 October 2009
%Purpose: Plots mixing hyperbolae for scenario 3 in Chapter 5 (for secondary magnesite). Mixing
%hyperbolae predict fractionation based on water-rock (mass) ratio and represent closed system batch
%mixing between bedrock carbonate minerals and water equilibrated with the atmosphere at T = 25C and
%pH = 8.0. The amount of dissolved atmospheric carbon is very small under these conditions, and demands
%a high water-to-rock mass ratio for significant mixing to occur. The values used in this initial instance of the
%script are for water having an ideal composition reflecting the precipitation of magnesite. The bedrock end-
%member values come from primary magnesite at Mount Keith and primary calcite at Diavik. Secondary
%magnesite is taken as the "water" end-member.
%
figure (3)
% for Mount Keith
Ro1=31.227; %estimate of Ro=Cwo/Cro
Rc1=0.0138; %estimate of (Rc=Cwc/Crc) - dissolved C in the water is low. 0.0138 is for 100 ppm C and
% 0.72% C in 5 wt.% magnesite in tailings
% control1=1/Rc1; %gives an idea of how much water is needed
d18Ow01=39; %from hypothetical secondary magnesite
d13Cw01=7.35; %from hypothetical magnesite from Deines et al. (2004) for mags-cal + Romanek et al.
% (1992) for cal-co2 - Mook et al. (1974) for hco3- - co2
d18Or01=13.27; %from MK magnesite
d13Cr01=-4.11; %from MK magnesite
D18Orw1=0; %working in MINERAL SPACE - so set to zero.
D13Crw1=0; %working in MINERAL SPACE - so set to zero.
Q=[0:0.05:10000]; %range for Q, the water-rock ratio (can scale by "control" function by multiplying upper
% limit by "control")
psiwO1=(Q.*Ro1)./((Q.*Ro1)+ones(size(Q))); % psi for O
psiwC1=(Q.*Rc1)./((Q.*Rc1)+ones(size(Q))); % psi for C
d18Orock1=psiwO1*(d18Ow01+D18Orw1) + (ones(size(psiwO1))-psiwO1)*d18Or01; %d18O for the mineral
d13Crock1=psiwC1*(d13Cw01+D13Crw1) + (ones(size(psiwC1))-psiwC1)*d13Cr01; %d13C for the mineral
hold on
plot(d13Crock1,d18Orock1,'b')
hold on
axis([-30 15 0 40]);
xlabel('\delta^{13}C (VPDB)')
ylabel('\delta^{18}O (VSMOW)')
title('Mixing Trends for Mount Keith and Diavik (magnesite): \delta^{18}O versus \delta^{13}C')
%
hold on
Qa=[0:100:10000]; %range for Q, the water-rock ratio (can scale by "control" function by multiplying upper
% limit by "control")
psiwOa=(Qa.*Ro1)./((Qa.*Ro1)+ones(size(Qa))); % psi for O
psiwCa=(Qa.*Rc1)./((Qa.*Rc1)+ones(size(Qa))); % psi for C
d18Orocka=psiwOa*(d18Ow01+D18Orw1) + (ones(size(psiwOa))-psiwOa)*d18Or01; %d18O for the mineral
d13Crocka=psiwCa*(d13Cw01+D13Crw1) + (ones(size(psiwCa))-psiwCa)*d13Cr01; %d13C for the mineral
plot(d13Crocka,d18Orocka,'+','MarkerEdgeColor','r','MarkerSize',6)
%
Qaa=[0:10:100]; %range for Q, the water-rock ratio (can scale by "control" function by multiplying upper limit
% by "control")
psiwOaa=(Qaa.*Ro1)./((Qaa.*Ro1)+ones(size(Qaa))); % psi for O
psiwCaa=(Qaa.*Rc1)./((Qaa.*Rc1)+ones(size(Qaa))); % psi for C
d18Orockaa=psiwOaa*(d18Ow01+D18Orw1) + (ones(size(psiwOaa))-psiwOaa)*d18Or01; %d18O for the
% mineral
d13Crockaa=psiwCaa*(d13Cw01+D13Crw1) + (ones(size(psiwCaa))-psiwCaa)*d13Cr01; %d13C for the
% mineral
plot(d13Crockaa,d18Orockaa,'+','MarkerEdgeColor','c','MarkerSize',6)
```

```
%
%
hold on
% for Diavik
Ro2=37.068; %estimate of Ro=Cwo/Cro
Rc2=0.0167; %estimate of (Rc=Cwc/Crc) - dissolved C in the water is low. 0.0167 is for 5wt% calcite in
% tailings at Diavik
% control2=1/Rc2; %gives an idea of how much water is needed
d18Ow02=21.85; %from hypothetical secondary magnesite
d13Cw02=7.35; %from hypothetical magnesite from Deines et al. (2004) for mags-cal + Romanek et al.
% (1992) for cal-co2 - Mook et al. (1974) for hco3- - co2
d18Or02=8.69; %from DVK calcite
d13Cr02=-6.39; %from DVK calcite
D18Orw2=0; %working in MINERAL SPACE - so set to zero.
D13Crw2=0; %working in MINERAL SPACE - so set to zero.
Q=[0:0.05:10000]; %range for Q, the water-rock ratio (can scale by "control" function by multiplying upper
% limit by "control")
psiwO2=(Q.*Ro2)./((Q.*Ro2)+ones(size(Q))); % psi for O
psiwC2=(Q.*Rc2)./((Q.*Rc2)+ones(size(Q))); % psi for C
d18Orock2=psiwO2*(d18Ow02+D18Orw2) + (ones(size(psiwO2))-psiwO2)*d18Or02; %d18O for the mineral
d13Crock2=psiwC2*(d13Cw02+D13Crw2) + (ones(size(psiwC2))-psiwC2)*d13Cr02; %d13C for the mineral
hold on
plot(d13Crock2,d18Orock2,'b')
%
Qb=[0:100:10000]; %range for Q, the water-rock ratio (can scale by "control" function by multiplying upper
% limit by "control")
psiwOb=(Qb.*Ro2)./((Qb.*Ro2)+ones(size(Qb))); % psi for O
psiwCb=(Qb.*Rc2)./((Qb.*Rc2)+ones(size(Qb))); % psi for C
d18Orockb=psiwOb*(d18Ow02+D18Orw2) + (ones(size(psiwOb))-psiwOb)*d18Or02; %d18O for the mineral
d13Crockb=psiwCb*(d13Cw02+D13Crw2) + (ones(size(psiwCb))-psiwCb)*d13Cr02; %d13C for the mineral
plot(d13Crockb,d18Orockb,'+','MarkerEdgeColor','r','MarkerSize',6)
%
Qbb=[0:10:100]; %range for Q, the water-rock ratio (can scale by "control" function by multiplying upper limit
% by "control")
psiwObb=(Qbb.*Ro2)./((Qbb.*Ro2)+ones(size(Qbb))); % psi for O
psiwCbb=(Qbb.*Rc2)./((Qbb.*Rc2)+ones(size(Qbb))); % psi for C
d18Orockbb=psiwObb*(d18Ow02+D18Orw2) + (ones(size(psiwObb))-psiwObb)*d18Or02; %d18O for the
% mineral
d13Crockbb=psiwCbb*(d13Cw02+D13Crw2) + (ones(size(psiwCbb))-psiwCbb)*d13Cr02; %d13C for the
% mineral
plot(d13Crockbb,d18Orockbb,'+','MarkerEdgeColor','c','MarkerSize',6)
%
Qbbb=[0:0.2:1]; %range for Q, the water-rock ratio (can scale by "control" function by multiplying upper limit
% by "control")
psiwObbb=(Qbbb.*Ro2)./((Qbbb.*Ro2)+ones(size(Qbbb))); % psi for O
psiwCbbb=(Qbbb.*Rc2)./((Qbbb.*Rc2)+ones(size(Qbbb))); % psi for C
d18Orockbbb=psiwObbb*(d18Ow02+D18Orw2) + (ones(size(psiwObbb))-psiwObbb)*d18Or02; %d18O for
% the mineral
d13Crockbbb=psiwCbbb*(d13Cw02+D13Crw2) + (ones(size(psiwCbbb))-psiwCbbb)*d13Cr02; %d13C for
% the mineral
plot(d13Crockbbb,d18Orockbbb,'+','MarkerEdgeColor','g','MarkerSize',6)
%
%
figure (4)
hold on
box
axis([0,1.2,-30,15])
xlabel('F^{14}C')
ylabel('\delta^{13}C (VPDB)')
title('Mixing Trends for Mount Keith and Diavik (magnesite): \delta^{13}C versus F^{14}C')
%
F14Crock1=psiwC1*(1.06)+(ones(size(psiwC1))-psiwC1)*0; %F14C for the mineral
```

```
plot(F14Crock1,d13Crock1,'b')
F14Crocka=psiwCa*(1.06)+(ones(size(psiwCa))-psiwCa)*0; %F14C for the mineral
plot(F14Crocka,d13Crocka,'+','MarkerEdgeColor','r','MarkerSize',6)
F14Crockaa=psiwCaa*(1.06)+(ones(size(psiwCaa))-psiwCaa)*0; %F14C for the mineral
plot(F14Crockaa,d13Crockaa,'+','MarkerEdgeColor','c','MarkerSize',6)
F14Crockaaa=psiwCaaa*(1.06)+(ones(size(psiwCaaa))-psiwCaaa)*0; %F14C for the mineral
plot(F14Crockaaa,d13Crockaaa,'+','MarkerEdgeColor','g','MarkerSize',6)
F14Crock2=psiwC2*(1.06)+(ones(size(psiwC2))-psiwC2)*0; %F14C for the mineral
plot(F14Crock2,d13Crock2,'b')
F14Crockb=psiwCb*(1.06)+(ones(size(psiwCb))-psiwCb)*0; %F14C for the mineral
plot(F14Crockb,d13Crockb,'+','MarkerEdgeColor','r','MarkerSize',6)
F14Crockbb=psiwCbb*(1.06)+(ones(size(psiwCbb))-psiwCbb)*0; %F14C for the mineral
plot(F14Crockbb,d13Crockbb,'+','MarkerEdgeColor','c','MarkerSize',6)
F14Crockbbb=psiwCbbb*(1.06)+(ones(size(psiwCbbb))-psiwCbbb)*0; %F14C for the mineral
plot(F14Crockbbb,d13Crockbbb,'+','MarkerEdgeColor','g','MarkerSize',6)
%
%fin
```

A2.3 F14C_xValues.m

```
function y=F14C_xValues(length)
   values=ones(1,length);
   for i=1:length
      values(i)=values(i)-2^(-(i-1));
   end
   y=1.06*values;
end
```

A2.4 react2f.m

```
% react2f.m
% Programmer: S. Wilson with assistance from J.R. Gare
% Date Created: 10 September 2009
% Date Modified: 22 October 2009
% Purpose: Models cyclic dissolution and reprecipitation of bedrock calcite to precipitate secondary
%hydromagnesite from a mixed atmospheric and bedrock source for carbon. Initial values are for
%unevaporated water at the Diavik Diamond Mine.
%
% Fractionation factors (all calculated at 25C)
D18Odicco2=-9.96;   % 10^3lna(HCO3-(aq)-H2O(l)) Halas & Wolacewicz (1982) J Chem Phys 76, 5470-
5472 [30.19 per mil] - 10^3lna(co2(g)-h2o(l) Bottinga (1968) J Phys Chem 72, 800-808 [40.15 per mil]
D13Cdicco2=7.94;    % Mook et al. (1974) for 10^3lna(HCO3-(aq)-CO2(g))
D18Odicmags=-31.19; % O'Neil & Barnes (1971) for 10^3lna(hydromagnesite-H2O(l))
D13Cdicmags=-3.8;  %  -3.8 per mil from Chapter 3

% Starting compositions for reservoirs
d13Ch2o=-10.39;  % Measured from fine PKC pond
d18Oh2o=-10;    % Assumed for lack of data to be a typical value for shallow groundwater, river water - from
% Clark & Fritz (1997)
d13Cmags=-6.39; % Measured for pure calcite sample
d18Omags=8.69;  % Measured for pure calcite sample
d13Cco2=-8;     % Median value for atmosphere ? Keeling et al. (2005)
d18Oco2=40;    % Median value for atmosphere - from Clark & Fritz (1997), p.25

% Setting up the C & O composition of the system:
% The size of the system is based on the condition that there is a maximum
% of 1 L of pure water.
%
% Molecular mass of reservoir components:
Gmmh2o=(2*1.00794)+15.9994; %water in g/mol
Gmmdic=1.00794+12.011+(3*15.9994); %dic = HCO3- in g/mol
Gmmmags=24.3050+12.011+(3*15.9994); %magnesite in g/mol
Gmmhymags=(5*24.3050)+(4*12.011)+(18*15.9994)+(10*1.00794); %hydromagnesite in g/mol
%
% Starting concentrations of reservoir components:
ch2o=0.100;   % in g/L - 0.100 g/L (100 ppm) of dissolved inorganic C
oh2o=1000;    % in g/L
mgmags=4.000; % in g/L (default assumes 4000 ppm Mg for hydromagnesite to precipitate)
%
% Moles of reservoir components:
nch2o=ch2o/Gmmdic; % moles/L of dic in H2O
noh2o=oh2o/Gmmh2o; % moles/L of O in H2O
%
%ncmags=mgmags/Gmmmags; % moles/L of C (same as moles/L of Mg & MgCO3) in MgCO3
%nomags=3*ncmags;       % moles/L of O in MgCO3
nchymags=4*mgmags/Gmmhymags; % moles/L of C (4x moles/L of Mg) in Mg5(CO3)4(OH2)*4H2O
nohymags=(18/4)*nchymags; % moles/L of O in Mg5(CO3)4(OH)2*4H2O
%
ncco2=nchymags;   % match the input of carbon from the atmosphere to the input from dissolved hydromag
noco2=2*nchymags; % twice the molar amount of O is in CO2 as there is for C
%
% Summation of moles of C & O in the system:
ncbulk=nch2o+nchymags+ncco2;
nobulk=noh2o+nohymags+noco2;

% Setting up the system of equations that controls mixing and precipitation:
d18Obulk=((noh2o/nobulk)*d18Oh2o)+((nohymags/nobulk)*d18Omags)+((noco2/nobulk)*d18Oco2);
d13Cbulk=((nch2o/ncbulk)*d13Ch2o)+((nchymags/ncbulk)*d13Cmags)+((ncco2/ncbulk)*d13Cco2);
```

```
%
y=[d18Obulk; d13Cbulk; D18Odicmags; D18Odicco2; D13Cdicmags; D13Cdicco2];
A=[(noh2o/nobulk) (nohymags/nobulk) (noco2/nobulk) 0 0 0; 0 0 0 (nch2o/ncbulk) (nchymags/ncbulk)
(ncco2/ncbulk); 1 -1 0 0 0 0; 1 0 -1 0 0 0; 0 0 0 1 -1 0; 0 0 0 1 0 -1];

x=A\y % this vector is [d18Odic; d18Omags; d18Oco2; d13Cdic; d13Cmags; d13Cco2]
note1='this vector, x, is [d18Odic; d18Omags; d18Oco2; d13Cdic; d13Cmags; d13Cco2]'
%
% X will be matrix with each successive result x in the columns
X=x;
numCycles=8;  %Change this if you want more cycles.
for i=2:numCycles
   %
   % Cycle i
   d18Obulk2=((noh2o/nobulk)*d18Oh2o)+((nohymags/nobulk)*X(2,i-1))+((noco2/nobulk)*d18Oco2);
   d13Cbulk2=((nch2o/ncbulk)*d13Ch2o)+((nchymags/ncbulk)*X(5,i-1))+((ncco2/ncbulk)*d13Cco2);
   %
   y=[d18Obulk2; d13Cbulk2; D18Odicmags; D18Odicco2; D13Cdicmags; D13Cdicco2];
   x=A\y % this vector is [d18Odic; d18Omags; d18Oco2; d13Cdic; d13Cmags; d13Cco2]
   note1='this vector, x, is [d18Odic; d18Omags; d18Oco2; d13Cdic; d13Cmags; d13Cco2]'
   X=[X x];
end

% Plotting results:
carbons=vertcat(d13Cmags, X(5,:)');
oxygens=vertcat(d18Omags, X(2,:)');
figure (1)
hold on
plot(carbons,oxygens,'+','MarkerEdgeColor','m','MarkerSize',10)
axis([-30,15,0,40])
box
%
%
figure (2)
%
hold on

F14C=F14C_xValues(numCycles+1)
plot(F14C,carbons,'+','MarkerEdgeColor','m','MarkerSize',10)
axis([0,1.2,-30,15])
box
%
%fin.
```

A2.5 react3f.m

```
% react3f.m
% Programmer: S. Wilson with assistance from J.R. Gare
% Date Created: 10 September 2009
% Date Modified: 22 October 2009
% Purpose: Models cyclic dissolution and reprecipitation of bedrock magnesite to precipitate secondary
%hydromagnesite from a mixed atmospheric and bedrock source for carbon. Initial values are for highly
%evaporated water at the Mount Keith Nickel Mine.
%
% Fractionation factors (all calculated at 25C)
D18Odicco2=-9.96;   % 10^3lna(HCO3-(aq)-H2O(l)) Halas & Wolacewicz (1982) J Chem Phys 76, 5470-
% 5472 [30.19 per mil] - 10^3lna(co2(g)-h2o(l) Bottinga (1968) J Phys Chem 72, 800-808 [40.15 per mil]
D13Cdicco2=7.94;    % Mook et al. (1974) for 10^3lna(HCO3-(aq)-CO2(g))
D18Odicmags=-31.19; % O'Neil & Barnes (1971) for 10^3lna(hydromagnesite-H2O(l))
D13Cdicmags=-3.8;  %  -3.8 per mil from Chapter 3

% Starting compositions for reservoirs
d13Ch2o=-7.71;  % Measured at Kidney water station, Mount Keith TSF2
d18Oh2o=7;    % Assumed for lack of data to be a highly evaporated water. Assuming about 50-70% loss to
% evaporation under low humidity conditions and an initial water d18O of about 0 per mil
d13Cmags=-4.11; % Measured for pure magnesite wasterock sample
d18Omags=13.27;  % Measured for pure magnesite wasterock sample
d13Cco2=-8;     % Median value for atmosphere ? Keeling et al. (2005)
d18Oco2=40;    % Median value for atmosphere - from Clark & Fritz (1997), p.25

% Setting up the C & O composition of the system:
% The size of the system is based on the condition that there is a maximum
% of 1 L of pure water.
%
% Molecular mass of reservoir components:
Gmmh2o=(2*1.00794)+15.9994; %water in g/mol
Gmmdic=1.00794+12.011+(3*15.9994); %dic = HCO3- in g/mol
Gmmmags=24.3050+12.011+(3*15.9994); %magnesite in g/mol
Gmmhymags=(5*24.3050)+(4*12.011)+(18*15.9994)+(10*1.00794); %hydromagnesite in g/mol
%
% Starting concentrations of reservoir components:
ch2o=0.100;   % in g/L - 0.100 g/L (100 ppm) of dissolved inorganic C - consistent with measured values in
% TSF2
oh2o=1000;    % in g/L
mgmags=4.000; % in g/L (default assumes 4000 ppm Mg for hydromagnesite to precipitate)
%
% Moles of reservoir components:
nch2o=ch2o/Gmmdic; % moles/L of dic in H2O
noh2o=oh2o/Gmmh2o; % moles/L of O in H2O
%
%ncmags=mgmags/Gmmmags; % moles/L of C (same as moles/L of Mg & MgCO3) in MgCO3
%nomags=3*ncmags;       % moles/L of O in MgCO3
nchymags=4*mgmags/Gmmhymags; % moles/L of C (4x moles/L of Mg) in Mg5(CO3)4(OH2)*4H2O
nohymags=(18/4)*nchymags; % moles/L of O in Mg5(CO3)4(OH)2*4H2O
%
ncco2=nchymags;   % match the input of carbon from the atmosphere to the input from dissolved hydromag
noco2=2*nchymags; % twice the molar amount of O is in CO2 as there is for C
%
% Summation of moles of C & O in the system:
ncbulk=nch2o+nchymags+ncco2;
nobulk=noh2o+nohymags+noco2;

% Setting up the system of equations that controls mixing and precipitation:
d18Obulk=((noh2o/nobulk)*d18Oh2o)+((nohymags/nobulk)*d18Omags)+((noco2/nobulk)*d18Oco2);
```

```
d13Cbulk=((nch2o/ncbulk)*d13Ch2o)+((nchymags/ncbulk)*d13Cmags)+((ncco2/ncbulk)*d13Cco2);
%
y=[d18Obulk; d13Cbulk; D18Odicmags; D18Odicco2; D13Cdicmags; D13Cdicco2];
A=[(noh2o/nobulk) (nohymags/nobulk) (noco2/nobulk) 0 0 0; 0 0 0 (nch2o/ncbulk) (nchymags/ncbulk)
(ncco2/ncbulk); 1 -1 0 0 0 0; 1 0 -1 0 0 0; 0 0 0 1 -1 0; 0 0 0 1 0 -1];

x=A\y % this vector is [d18Odic; d18Omags; d18Oco2; d13Cdic; d13Cmags; d13Cco2]
note1='this vector, x, is [d18Odic; d18Omags; d18Oco2; d13Cdic; d13Cmags; d13Cco2]'
%
% X will be matrix with each successive result x in the columns
X=x;
numCycles=8;  %Change this if you want more cycles.
for i=2:numCycles
   %
   % Cycle i
   d18Obulk2=((noh2o/nobulk)*d18Oh2o)+((nohymags/nobulk)*X(2,i-1))+((noco2/nobulk)*d18Oco2);
   d13Cbulk2=((nch2o/ncbulk)*d13Ch2o)+((nchymags/ncbulk)*X(5,i-1))+((ncco2/ncbulk)*d13Cco2);
   %
   y=[d18Obulk2; d13Cbulk2; D18Odicmags; D18Odicco2; D13Cdicmags; D13Cdicco2];
   x=A\y % this vector is [d18Odic; d18Omags; d18Oco2; d13Cdic; d13Cmags; d13Cco2]
   note1='this vector, x, is [d18Odic; d18Omags; d18Oco2; d13Cdic; d13Cmags; d13Cco2]'
   X=[X x];
end

% Plotting results:
carbons=vertcat(d13Cmags, X(5,:)');
oxygens=vertcat(d18Omags, X(2,:)');
figure (1)
hold on
plot(carbons,oxygens,'+','MarkerEdgeColor','m','MarkerSize',10)
axis([-30,15,0,40])
box
%
%
figure (2)
%
hold on

F14C=F14C_xValues(numCycles+1)
plot(F14C,carbons,'+','MarkerEdgeColor','m','MarkerSize',10)
axis([0,1.2,-30,15])
box
%
%fin.
```

A2.6 react4f.m

```
% react4f.m
% Programmer: S. Wilson with assistance from J.R. Gare
% Date Created: 10 September 2009
% Date Modified: 22 October 2009
% Purpose: Models cyclic dissolution and reprecipitation of bedrock calcite to precipitate secondary
%magnesite from a mixed atmospheric and bedrock source for carbon. Initial values are for unevaporated
%water at the Diavik Diamond Mine.
%
% Fractionation factors (all calculated at 25C)
D18Odicco2=-9.96;   % 10^3lna(HCO3-(aq)-H2O(l)) Halas & Wolacewicz (1982) J Chem Phys 76, 5470-
% 5472 [30.19 per mil] - 10^3lna(co2(g)-h2o(l) Bottinga (1968) J Phys Chem 72, 800-808 [40.15 per mil]
D13Cdicco2=7.94;    % Mook et al. (1974) for 10^3lna(HCO3-(aq)-CO2(g))
D18Odicmags=-32.23; % from Spˆtl & Burns (1994) 10^3lna(H2o(l)-mags)
D13Cdicmags=-7.41;  % Deines (2004) 10^3lna(mags-cal) + Romanek et al. (1992) 10^3lna(cal-co2) is
% collectively [15.3539] - 10^3lna(Hco3- - co2(g)) from Mook et al. (1974) [7.94 per mil]

% Starting compositions for reservoirs
d13Ch2o=-10.39;  % Measured from fine PKC pond
d18Oh2o=-10;    % Assumed for lack of data to be a normal value for near surface groundwater or river
% water. From Clark & Fritz (1997).
d13Cmags=-6.39; % Measured for pure calcite sample
d18Omags=8.69;  % Measured for pure calcite sample
d13Cco2=-8;     % Median value for atmosphere – Keeling et al. (2005)
d18Oco2=40;    % Median value for atmosphere - from Clark & Fritz (1997), p.25

% Setting up the C & O composition of the system:
% The size of the system is based on the condition that there is a maximum
% of 1 L of pure water.
%
% Molecular mass of reservoir components:
Gmmh2o=(2*1.00794)+15.9994; %water in g/mol
Gmmdic=1.00794+12.011+(3*15.9994); %dic = HCO3- in g/mol
Gmmmags=24.3050+12.011+(3*15.9994); %magnesite in g/mol
%
% Starting concentrations of reservoir components:
ch2o=0.100;   % in g/L - 0.100 g/L (100 ppm) of dissolved inorganic C - consistent with measured values in
% TSF2
oh2o=1000;    % in g/L
mgmags=4.000; % in g/L (default assumes 4000 ppm Mg for hydromagnesite to precipitate)
%
% Moles of reservoir components:
nch2o=ch2o/Gmmdic; % moles/L of dic in H2O
noh2o=oh2o/Gmmh2o; % moles/L of O in H2O
%
ncmags=mgmags/Gmmmags; % moles/L of C (same as moles/L of Mg & MgCO3) in MgCO3
nomags=3*ncmags;       % moles/L of O in MgCO3
%
ncco2=ncmags;   % match the input of carbon from the atmosphere to the input from dissolved magnesite
noco2=2*ncmags; % twice the molar amount of O is in CO2 as there is for C
%
% Summation of moles of C & O in the system:
ncbulk=nch2o+ncmags+ncco2;
nobulk=noh2o+nomags+noco2;

% Setting up the system of equations that controls mixing and precipitation:
d18Obulk=((noh2o/nobulk)*d18Oh2o)+((nomags/nobulk)*d18Omags)+((noco2/nobulk)*d18Oco2);
d13Cbulk=((nch2o/ncbulk)*d13Ch2o)+((ncmags/ncbulk)*d13Cmags)+((ncco2/ncbulk)*d13Cco2);
%
```

```
y=[d18Obulk; d13Cbulk; D18Odicmags; D18Odicco2; D13Cdicmags; D13Cdicco2];
A=[(noh2o/nobulk) (nomags/nobulk) (noco2/nobulk) 0 0 0; 0 0 0 (nch2o/ncbulk) (ncmags/ncbulk)
(ncco2/ncbulk); 1 -1 0 0 0 0; 1 0 -1 0 0 0; 0 0 0 1 -1 0; 0 0 0 1 0 -1];

x=A\y % this vector is [d18Odic; d18Omags; d18Oco2; d13Cdic; d13Cmags; d13Cco2]
note1='this vector, x, is [d18Odic; d18Omags; d18Oco2; d13Cdic; d13Cmags; d13Cco2]'
%
% X will be matrix with each successive result x in the columns
X=x;
numCycles=8;  %Change this if you want more cycles.
for i=2:numCycles
   %
   % Cycle i
   d18Obulk2=((noh2o/nobulk)*d18Oh2o)+((nomags/nobulk)*X(2,i-1))+((noco2/nobulk)*d18Oco2);
   d13Cbulk2=((nch2o/ncbulk)*d13Ch2o)+((ncmags/ncbulk)*X(5,i-1))+((ncco2/ncbulk)*d13Cco2);
   %
   y=[d18Obulk2; d13Cbulk2; D18Odicmags; D18Odicco2; D13Cdicmags; D13Cdicco2];
   x=A\y % this vector is [d18Odic; d18Omags; d18Oco2; d13Cdic; d13Cmags; d13Cco2]
   note1='this vector, x, is [d18Odic; d18Omags; d18Oco2; d13Cdic; d13Cmags; d13Cco2]'
   X=[X x];
end

% Plotting results:
carbons=vertcat(d13Cmags, X(5,:)');
oxygens=vertcat(d18Omags, X(2,:)');
figure (1)
hold on
plot(carbons,oxygens,'+','MarkerEdgeColor','g','MarkerSize',10)
axis([-30,15,0,40])
box
%
%
figure (2)
%
hold on

F14C=F14C_xValues(numCycles+1)
plot(F14C,carbons,'+','MarkerEdgeColor','g','MarkerSize',10)
axis([0,1.2,-30,15])
box
%
%fin.
```

A2.7 react5f.m

```
% react5.m
% Programmer: S. Wilson with assistance from J.R. Gare
% Date Created: 10 September 2009
% Date Modified: 22 October 2009
% Purpose: Models cyclic dissolution and reprecipitation of bedrock magnesite to precipitate secondary
%magnesite from a mixed atmospheric and bedrock source for carbon. Initial values are for highly
%evaporated water at the Mount Keith Nickel Mine.
%
% Fractionation factors (all calculated at 25C)
D18Odicco2=-9.96;   % 10^3lna(HCO3-(aq)-H2O(l)) Halas & Wolacewicz (1982) J Chem Phys 76, 5470-
% 5472 [30.19 per mil] - 10^3lna(co2(g)-h2o(l) Bottinga (1968) J Phys Chem 72, 800-808 [40.15 per mil]
D13Cdicco2=7.94;    % Mook et al. (1974) for 10^3lna(HCO3-(aq)-CO2(g))
D18Odicmags=-32.23; % from Spˆtl & Burns (1994) 10^3lna(H2o(l)-mags)
D13Cdicmags=-7.41;  % Deines (2004) 10^3lna(mags-cal) + Romanek et al. (1992) 10^3lna(cal-co2) is
% collectively [15.3539] - 10^3lna(Hco3- - co2(g)) from Mook et al. (1974) [7.94 per mil]

% Starting compositions for reservoirs
d13Ch2o=-7.71;  % Measured at Kidney water station, Mount Keith TSF2
d18Oh2o=7;    % Assumed for lack of data to be a highly evaporated water. Assuming about 50-70% loss to
% evaporation under low humidity conditions and an initial water d18O of about 0 per mil
d13Cmags=-4.11; % Measured for pure magnesite wasterock sample
d18Omags=13.27;  % Measured for pure magnesite wasterock sample
d13Cco2=-8;     % Median value for atmosphere ? Keeling et al. (2005)
d18Oco2=40;    % Median value for atmosphere - from Clark & Fritz (1997), p.25

% Setting up the C & O composition of the system:
% The size of the system is based on the condition that there is a maximum
% of 1 L of pure water.
%
% Molecular mass of reservoir components:
Gmmh2o=(2*1.00794)+15.9994; %water in g/mol
Gmmdic=1.00794+12.011+(3*15.9994); %dic = HCO3- in g/mol
Gmmmags=24.3050+12.011+(3*15.9994); %magnesite in g/mol
%
% Starting concentrations of reservoir components:
ch2o=0.100;   % in g/L - 0.100 g/L (100 ppm) of dissolved inorganic C - consistent with measured values in
% TSF2
oh2o=1000;    % in g/L
mgmags=4.000; % in g/L (default assumes 4000 ppm Mg for hydromagnesite to precipitate)
%
% Moles of reservoir components:
nch2o=ch2o/Gmmdic; % moles/L of dic in H2O
noh2o=oh2o/Gmmh2o; % moles/L of O in H2O
%
ncmags=mgmags/Gmmmags; % moles/L of C (same as moles/L of Mg & MgCO3) in MgCO3
nomags=3*ncmags;       % moles/L of O in MgCO3
%
ncco2=ncmags;   % match the input of carbon from the atmosphere to the input from dissolved magnesite
noco2=2*ncmags; % twice the molar amount of O is in CO2 as there is for C
%
% Summation of moles of C & O in the system:
ncbulk=nch2o+ncmags+ncco2;
nobulk=noh2o+nomags+noco2;

% Setting up the system of equations that controls mixing and precipitation:
d18Obulk=((noh2o/nobulk)*d18Oh2o)+((nomags/nobulk)*d18Omags)+((noco2/nobulk)*d18Oco2);
d13Cbulk=((nch2o/ncbulk)*d13Ch2o)+((ncmags/ncbulk)*d13Cmags)+((ncco2/ncbulk)*d13Cco2);
%
```

```
y=[d18Obulk; d13Cbulk; D18Odicmags; D18Odicco2; D13Cdicmags; D13Cdicco2];
A=[(noh2o/nobulk) (nomags/nobulk) (noco2/nobulk) 0 0 0; 0 0 0 (nch2o/ncbulk) (ncmags/ncbulk)
(ncco2/ncbulk); 1 -1 0 0 0 0; 1 0 -1 0 0 0; 0 0 0 1 -1 0; 0 0 0 1 0 -1];

x=A\y % this vector is [d18Odic; d18Omags; d18Oco2; d13Cdic; d13Cmags; d13Cco2]
note1='this vector, x, is [d18Odic; d18Omags; d18Oco2; d13Cdic; d13Cmags; d13Cco2]'
%
% X will be matrix with each successive result x in the columns
X=x;
numCycles=8;  %Change this if you want more cycles.
for i=2:numCycles
   %
   % Cycle i
   d18Obulk2=((noh2o/nobulk)*d18Oh2o)+((nomags/nobulk)*X(2,i-1))+((noco2/nobulk)*d18Oco2);
   d13Cbulk2=((nch2o/ncbulk)*d13Ch2o)+((ncmags/ncbulk)*X(5,i-1))+((ncco2/ncbulk)*d13Cco2);
   %
   y=[d18Obulk2; d13Cbulk2; D18Odicmags; D18Odicco2; D13Cdicmags; D13Cdicco2];
   x=A\y % this vector is [d18Odic; d18Omags; d18Oco2; d13Cdic; d13Cmags; d13Cco2]
   note1='this vector, x, is [d18Odic; d18Omags; d18Oco2; d13Cdic; d13Cmags; d13Cco2]'
   X=[X x];
end

% Plotting results:
carbons=vertcat(d13Cmags, X(5,:)');
oxygens=vertcat(d18Omags, X(2,:)');
figure (1)
hold on
plot(carbons,oxygens,'+','MarkerEdgeColor','g','MarkerSize',10)
axis([-30,15,0,40])
box
%
%
figure (2)
%
hold on

F14C=F14C_xValues(numCycles+1)
plot(F14C,carbons,'+','MarkerEdgeColor','g','MarkerSize',10)
axis([0,1.2,-30,15])
box
%
%fin.
```